WOODHEAD PUBLISHING SERIES IN ELECTRONIC AND OPTICAL MATERIALS

MEMS for automotive and aerospace applications

Edited by Michael Kraft and Neil M. White

WP
WOODHEAD PUBLISHING

VISIT…

MEMS for automotive and aerospace applications

© Woodhead Publishing Limited, 2013

Related titles:

Handbook of MEMS for wireless and mobile applications
(ISBN 978-0-85709-271-7)

MEMS for biomedical applications (ISBN 978-0-85709-129-1)

Ultrasonic transducers (ISBN 978-1-84569-989-5)

Details of these and other Woodhead Publishing books can be obtained by:

- visiting our web site at www.woodheadpublishing.com
- contacting Customer Services (e-mail: sales@woodheadpublishing.com; fax: +44 (0) 1223 832819; tel.: +44 (0) 1223 499140 ext. 130; address: Woodhead Publishing Limited, 80 High Street, Sawston, Cambridge CB22 3HJ, UK)
- contacting our US office (e-mail: usmarketing@woodheadpublishing.com; tel. (215) 928 9112; address: Woodhead Publishing, 1518 Walnut Street, Suite 1100, Philadelphia, PA 19102-3406, USA)

If you would like e-versions of our content, please visit our online platform: www.woodheadpublishingonline.com. Please recommend it to your librarian so that everyone in your institution can benefit from the wealth of content on the site.

We are always happy to receive suggestions for new books from potential editors. To enquire about contributing to our Electronic and Optical Materials series, please send your name, contact address and details of the topic/s you are interested in to laura.pugh@woodheadpublishing.com. We look forward to hearing from you.

The Woodhead team responsible for publishing this book:
Commissioning Editor: Laura Pugh
Publications Coordinator: Anneka Hess
Project Editor: Sarah Lynch
Editorial and Production Manager: Mary Campbell
Production Editor: Adam Hooper
Project Manager: Annette Wiseman
Copyeditor: Jo Egré
Proofreader: Simon Webber
Cover Designer: Terry Callanan

© Woodhead Publishing Limited, 2013

Woodhead Publishing Series in Electronic and Optical Materials:
Number 32

MEMS for automotive and aerospace applications

Edited by
Michael Kraft and
Neil M. White

Oxford Cambridge Philadelphia New Delhi

© Woodhead Publishing Limited, 2013

Published by Woodhead Publishing Limited,
80 High Street, Sawston, Cambridge CB22 3HJ, UK
www.woodheadpublishing.com
www.woodheadpublishingonline.com

Woodhead Publishing, 1518 Walnut Street, Suite 1100, Philadelphia,
PA 19102-3406, USA

Woodhead Publishing India Private Limited, G-2, Vardaan House,
7/28 Ansari Road, Daryaganj, New Delhi – 110002, India
www.woodheadpublishingindia.com

First published 2013, Woodhead Publishing Limited
© Woodhead Publishing Limited, 2013. The publisher has made every effort to ensure that permission for copyright material has been obtained by authors wishing to use such material. The authors and the publisher will be glad to hear from any copyright holder it has not been possible to contact.
The authors have asserted their moral rights.

This book contains information obtained from authentic and highly regarded sources. Reprinted material is quoted with permission, and sources are indicated. Reasonable efforts have been made to publish reliable data and information, but the authors and the publishers cannot assume responsibility for the validity of all materials. Neither the authors nor the publishers, nor anyone else associated with this publication, shall be liable for any loss, damage or liability directly or indirectly caused or alleged to be caused by this book.

Neither this book nor any part may be reproduced or transmitted in any form or by any means, electronic or mechanical, including photocopying, microfilming and recording, or by any information storage or retrieval system, without permission in writing from Woodhead Publishing Limited.

The consent of Woodhead Publishing Limited does not extend to copying for general distribution, for promotion, for creating new works, or for resale. Specific permission must be obtained in writing from Woodhead Publishing Limited for such copying.

Trademark notice: Product or corporate names may be trademarks or registered trademarks, and are used only for identification and explanation, without intent to infringe.

British Library Cataloguing in Publication Data
A catalogue record for this book is available from the British Library.

Library of Congress Control Number: 2012950810

ISBN 978-0-85709-118-5 (print)
ISBN 978-0-85709-648-7 (online)
ISSN 2050-1501 Woodhead Publishing Series in Electronic and Optical Materials (print)
ISSN 2050-151X Woodhead Publishing Series in Electronic and Optical Materials (online)

The publisher's policy is to use permanent paper from mills that operate a sustainable forestry policy, and which has been manufactured from pulp which is processed using acid-free and elemental chlorine-free practices. Furthermore, the publisher ensures that the text paper and cover board used have met acceptable environmental accreditation standards.

Typeset by RefineCatch Limited, Bungay, Suffolk
Printed and bound in the UK by the MPG Books Group

Contents

Contributor contact details *ix*
Woodhead Publishing Series in Electronic and Optical Materials *xiii*

Part I MEMS for automotive applications 1

1 MEMS for passenger safety in automotive vehicles 3
J. Swingler, Heriot-Watt University, UK

1.1 Introduction 3
1.2 Passenger safety systems 4
1.3 Accelerometers for crash sensing systems 8
1.4 Angular rate sensors for rollover detection systems 13
1.5 Strain gauges for occupant sensing systems 19
1.6 Future trends in safety sensing systems 23
1.7 Conclusion 25
1.8 References 26

2 MEMS sensors for automotive vehicle stability control applications 29
M. Reze and M. Osajda, Freescale Halbleiter Deutschland GmbH, Germany

2.1 Introduction to vehicle stability control (VSC) 29
2.2 What is vehicle stability control? 30
2.3 MEMS accelerometers in electronic stability control (ESC) 35
2.4 MEMS angular rate sensors 39
2.5 Vehicle architecture challenges and sensor fusion 46
2.6 MEMS accelerometers used in active suspension 51
2.7 Conclusion 52
2.8 References 53

© Woodhead Publishing Limited, 2013

3 MEMS for automotive tire pressure monitoring systems 54
M. Löhndorf and T. Lange, Infineon Technologies AG, Germany

3.1 Introduction 54
3.2 Tire pressure monitoring systems (TPMS) applications and solutions 55
3.3 MEMS-based pressure sensors and technologies 59
3.4 TPMS requirements 65
3.5 Power management 67
3.6 Future TPMS applications 74
3.7 Conclusion 76
3.8 References 76

4 MEMS pressure and flow sensors for automotive engine management and aerospace applications 78
D. Sparks, Hanking Electronics Ltd, China

4.1 Sensors used in system and engine management 78
4.2 The MEMS design process 81
4.3 Pressure sensors 86
4.4 Flow sensors 89
4.5 Concentration, density and fuel quality sensors 95
4.6 Sensor signal conditioning 97
4.7 Packaging MEMS sensors for harsh environments 99
4.8 Conclusion and future trends 103
4.9 References 103

5 RF MEMS for automotive radar sensors 106
J. Oberhammer, N. Somjit, U. Shah and Z. Baghchehsaraei, KTH Royal Institute of Technology, Sweden

5.1 Introduction 106
5.2 Radio-frequency (RF) MEMS components for automotive radar 110
5.3 Examples of RF MEMS-based automotive radar front-end technology 121
5.4 Unconventional MEMS radar beam steering technologies 126
5.5 Conclusion 133
5.6 References 134

6 MEMS for passenger comfort in vehicles 137
S. J. Lee, San Jose State University, USA

6.1 Introduction 137
6.2 Seating 140
6.3 Climate control 142
6.4 Visual comfort 144

© Woodhead Publishing Limited, 2013

6.5 Auditory comfort 145
6.6 Conclusion and future trends 146
6.7 References 146

Part II MEMS for aerospace applications 151

7 MEMS devices for active drag reduction in aerospace applications 153
J. F. Morrison, Imperial College, London UK
7.1 Introduction 153
7.2 Surface sensors 160
7.3 Actuators 166
7.4 Conclusion and future trends 172
7.5 Acknowledgements 173
7.6 References 173

8 MEMS inertial navigation systems for aircraft 177
Y. Dong, Colibrys SA, Switzerland
8.1 Introduction 177
8.2 Microfabrication 189
8.3 Integrated inertial navigation systems (INS) with global positioning system (GPS) 207
8.4 Conclusion and future trends 216
8.5 References 217

9 MEMS for structural health monitoring in aircraft 220
M. Giglio, A. Manes and C. Sbarufatti, Politecnico di Milano, Italy
9.1 Introduction 220
9.2 State-of-the-art structural health monitoring (SHM) for aerospace structures 223
9.3 MEMS devices for embedded SHM 228
9.4 Conclusion and future trends 240
9.5 References 242

10 MEMS for harsh environment sensors in aerospace applications: selected case studies 245
N. Tiliakos, Alliant Techsystems Operations, LLC, USA
10.1 Micro-electromechanical systems (MEMS) 245
10.2 Examples of MEMS harsh environment sensors in aerospace applications 251
10.3 Conclusion and future trends 277
10.4 Sources of further information 279
10.5 References 280

© Woodhead Publishing Limited, 2013

11 MEMS thrusters for nano- and pico-satellites 283
P. Lozano, Massachusetts Institute of Technology, USA

11.1 Introduction 283
11.2 Propulsion requirements 285
11.3 Propulsion technologies 287
11.4 Miniaturizing propulsion systems 293
11.5 MEMS thrusters 298
11.6 Design considerations of MEMS thrusters 299
11.7 Future trends 308
11.8 References 309

12 MEMS enabling space exploration and exploitation 311
R. Osiander and A. Darrin, The Johns Hopkins University Applied Physics Laboratory, USA

12.1 Introduction 311
12.2 Future trends in spacecraft – small satellites 312
12.3 MEMS in spacecraft subsystems 313
12.4 MEMS in space science instrumentation 320
12.5 Reliability concerns in the space environment 325
12.6 Conclusion 328
12.7 References 329

Index *331*

© Woodhead Publishing Limited, 2013

Contributor contact details

(* = main contact)

Editors

Professor Michael Kraft* and Professor Neil M. White
School of Electronics and Computer Science
Southampton University
Southampton
SO17 1BJ
UK

E-mail: mk1@ecs.soton.ac.uk; nmw@ecs.soton.ac.uk

Chapter 1

Dr Jonathan Swingler
School of Engineering and Physical Sciences
Heriot-Watt University
Edinburgh
EH14 4AS
UK

E-mail: j.swingler@hw.ac.uk

Chapter 2

Matthieu Reze* and Marc Osajda
Freescale Halbleiter Deutschland GmbH
Schatzbogen 7
81829 Munich
Germany

E-mail: Matthieu.Reze@Micronas.com

Chapter 3

Dr Markus Löhndorf* and Thomas Lange
Business Line Sense and Control
Infineon Technologies AG
81726 Munich
Germany

E-mail: markus.loehndorf@infineon.com

Chapter 4

Dr Douglas Sparks
Executive Vice President
Hanking Electronics Ltd
227 Qingnian Ave.
Shenyang
Liaoning
110016
PR China

E-mail: sparksdr@hanking.com

© Woodhead Publishing Limited, 2013

Chapter 5

Joachim Oberhammer*, Nutapong Somjit, Umer Shah and Zargham Baghchehsaraei
KTH Royal Institute of Technology
School of Electrical Engineering
Microsystem Technology Lab
Osquldas väg 10
SE-100 44 Stockholm
Sweden

E-mail: joachim.oberhammer@ee.kth.se

Chapter 6

Professor John Lee
Mechanical and Aerospace Engineering
San Jose State University
One Washington Square
San Jose
California 95192 -0087
USA

E-mail: sang-joon.lee@sjsu.edu

Chapter 7

Professor Jonathan Morrison
Department of Aeronautics
Imperial College
London
SW7 2AZ
UK

E-mail: j.morrison@imperial.ac.uk

Chapter 8

Dr Yufeng Dong
Core Technology
Colibrys SA
2000 Neuchâtel
Switzerland

E-mail: yufeng.dong@ieee.org

Chapter 9

M. Giglio*, A. Manes and C. Sbarufatti
Politecnico di Milano
Department of Mechanical Engineering
Via la Masa 1
20156 Milano
Italy

E-mail: marco.giglio@polimi.it; andrea.manes@polimi.it; claudio.sbarufatti@mail.polimi.it

Chapter 10

Dr Nicholas Tiliakos
Senior Research and Development Engineer
Advanced Programs
Alliant Techsystems Operations, LLC (ATK)
Defense Components Business
GASL Operations
77 Raynor Avenue
Ronkonkoma
New York 11779
USA

E-mail: Nicholas.Tiliakos@ATK.com

© Woodhead Publishing Limited, 2013

Chapter 11

Paulo Lozano
Massachusetts Institute of Technology
77 Massachusetts Avenue, 37-401
Cambridge
Massachusetts 02139
USA

E-mail: plozano@MIT.EDU

Chapter 12

Dr Robert Osiander* and Ann Garrison Darrin
The Johns Hopkins University Applied Physics Laboratory
11100 Johns Hopkins Road
Laurel
Maryland 20723
USA

E-mail: robert.osiander@jhuapl.edu; ann.darrin@jhuapl.edu

© Woodhead Publishing Limited, 2013

Woodhead Publishing Series in Electronic and Optical Materials

1 **Circuit analysis**
J. E. Whitehouse

2 **Signal processing in electronic communications: For engineers and mathematicians**
M. J. Chapman, D. P. Goodall and N. C. Steele

3 **Pattern recognition and image processing**
D. Luo

4 **Digital filters and signal processing in electronic engineering: Theory, applications, architecture, code**
S. M. Bozic and R. J. Chance

5 **Cable engineering for local area networks**
B. J. Elliott

6 **Designing a structured cabling system to ISO 11801: Cross-referenced to European CENELEC and American Standards**
Second edition
B. J. Elliott

7 **Microscopy techniques for materials science**
A. Clarke and C. Eberhardt

8 **Materials for energy conversion devices**
Edited by C. C. Sorrell, J. Nowotny and S. Sugihara

9 **Digital image processing: Mathematical and computational methods**
Second edition
J. M. Blackledge

10 **Nanolithography and patterning techniques in microelectronics**
Edited by D. Bucknall

11 **Digital signal processing: Mathematical and computational methods, software development and applications**
Second edition
J. M. Blackledge

© Woodhead Publishing Limited, 2013

12 **Handbook of advanced dielectric, piezoelectric and ferroelectric materials: Synthesis, properties and applications**
Edited by Z.-G. Ye

13 **Materials for fuel cells**
Edited by M. Gasik

14 **Solid-state hydrogen storage: Materials and chemistry**
Edited by G. Walker

15 **Laser cooling of solids**
S. V. Petrushkin and V. V. Samartsev

16 **Polymer electrolytes: Fundamentals and applications**
Edited by C. A. C. Sequeira and D. A. F. Santos

17 **Advanced piezoelectric materials: Science and technology**
Edited by K. Uchino

18 **Optical switches: Materials and design**
Edited by S. J. Chua and B. Li

19 **Advanced adhesives in electronics: Materials, properties and applications**
Edited by M. O. Alam and C. Bailey

20 **Thin film growth: Physics, materials science and applications**
Edited by Z. Cao

21 **Electromigration in thin films and electronic devices: Materials and reliability**
Edited by C.-U. Kim

22 ***In situ* characterization of thin film growth**
Edited by G. Koster and G. Rijnders

23 **Silicon-germanium (SiGe) nanostructures: Production, properties and applications in electronics**
Edited by Y. Shiraki and N. Usami

24 **High-temperature superconductors**
Edited by X. G. Qiu

25 **Introduction to the physics of nanoelectronics**
S. G. Tan and M. B. A. Jalil

26 **Printed films: Materials science and applications in sensors, electronics and photonics**
Edited by M. Prudenziati and J. Hormadaly

27 **Laser growth and processing of photonic devices**
Edited by N. A. Vainos

28 **Quantum optics with semiconductor nanostructures**
Edited by F. Jahnke

29 **Ultrasonic transducers: Materials and design for sensors, actuators and medical applications**
Edited by K. Nakamura

30 **Waste electrical and electronic equipment (WEEE) handbook**
Edited by V. Goodship and A. Stevels

© Woodhead Publishing Limited, 2013

31 **Applications of ATILA FEM software to smart materials: Case studies in designing devices**
Edited by K. Uchino and J.-C. Debus

32 **MEMS for automotive and aerospace applications**
Edited by M. Kraft and N. M. White

33 **Semiconductor lasers: Fundamentals and applications**
Edited by A. Baranov and E. Tournie

34 **Handbook of terahertz technology for imaging, sensing, and communications**
Edited by D. Saeedkia

35 **Handbook of solid-state lasers: Materials, systems and applications**
Edited by B. Denker and E. Shklovsky

36 **Organic light-emitting diodes: Materials, devices and applications**
Edited by A. Buckley

37 **Lasers for medical applications: Diagnostics, therapy and surgery**
Edited by H. Jelínková

38 **Semiconductor gas sensors**
Edited by R. Jaaniso and O. K. Tan

39 **Handbook of organic materials for optical and optoelectronic devices: Properties and applications**
Edited by O. Ostroverkhova

40 **Metallic films for electronic, optical and magnetic applications: Structure, processing and properties**
Edited by K. Barmak and K. Coffey

41 **Handbook of laser welding technologies**
Edited by S. Katayama

42 **Nanolithography: The art of fabricating nanoelectronics, nanophotonics and nanobiology devices and systems**
Edited by M. Feldman

43 **Laser spectroscopy for sensing: Fundamentals, techniques and applications**
Edited by M. Baudelet

44 **Chalcogenide glasses: Preparation, properties and applications**
Edited by J.-L. Adam and X. Zhang

45 **Handbook of MEMS for wireless and mobile applications**
Edited by D. Uttamchandani

46 **Subsea optics and imaging**
Edited by J. Watson and O. Zielinski

47 **Carbon nanotubes and graphene for photonic applications**
Edited by S. Yamashita, Y. Saito and J. H. Choi

48 **Optical biomimetics: Materials and applications**
Edited by M. Large

© Woodhead Publishing Limited, 2013

1

MEMS for passenger safety in automotive vehicles

J. SWINGLER, Heriot-Watt University, UK

DOI: 10.1533/9780857096487.1.3

Abstract: Passenger safety is a high priority for vehicle manufacturers and over recent decades many advances have been made in a number of technologies to more effectively implement protection devices. This chapter starts with an overview of the rationale behind safety systems, introduces the protection systems employed against crash and rollover events, and then focuses on three sensing devices used in such systems, which have been implemented adopting MEMS technology. Much research and development effort continues to create novel safety systems. This chapter finishes by reviewing progress in the three distinct areas of passenger monitoring systems, vehicle monitoring systems and environment monitoring systems.

Key words: crash, rollover, occupant, accelerometer, angle rate, strain gauge.

1.1 Introduction

MEMS (Micro-electromechanical systems) implemented in automotive electronics began in the early 1980s with pressure sensors for engine management systems. In the early 1990s, this technology was introduced to safety systems with the implementation of accelerometers (Fleming, 2001, 2008). Over the decades, MEMS technology has found many applications within the motor car, enabling innovative electronic systems and the reduction of production and assembly costs of safety systems.

Passenger safety is a high priority for the vehicle manufacturer, often making it a selling feature for the vehicle. Many advances have been made in a number of technologies to more effectively implement protection devices to ensure the safety of occupants in a crash event.

The World Heath Organisation reported in 2007 that Western Europe, Canada, Australia and Japan have some of the lowest death rates per annum caused by vehicle crash events. These are between 4.8 per 100 000 persons for the Netherlands (UK 5.4) to 10 per 100 000 persons for Iceland. The USA has a death rate of 13.8 per 100 000 persons compared with Eastern Europe, for example with Bulgaria at 13.2 per 100 000 and Poland of 14.7 per 100 000 persons. Some of the worst death rates are in North Africa, with around 40 per 100 000 persons per annum. Causes of such crash events are made up of a mixture of road and vehicle conditions, and driver behavior.

Road fatalities in the UK started to decrease in the early 1970s, from 7500 deaths per annum, with the introduction of speed limits, annual vehicle testing

© Woodhead Publishing Limited, 2013

(the MOT) and other measures, to less than 6000 death per annum in the early 1980s. Further reductions have occurred during the introduction of the compulsory use of seat belts and the development of vehicle safety systems to less than 2500 deaths per annum in recent years. The UK Department of Transport reports that 1850 persons were killed on the roads in 2010. This reduction is mirrored in other countries with the US Department of Transportation reporting that 32 788 persons were killed in 2010, which is a death rate of 10.6 per 100 000 persons.

The reduction in deaths cannot simply be explained in terms of one or two improvements in road conditions or vehicle performance, but consists of a complex mixture of many factors. An important factor is the development of vehicle safety systems and along with this are the developments in MEMS sensors.

Frontal crash, side impact and rollover are the main events that a safety system has been developed to deploy protection devices. MEMS sensing devices are used in such systems to detect the condition of the vehicle in terms of undesirable accelerations and angular rate changes, as well as the detection of the position of occupants. Research and development effort continues worldwide on creating novel safety systems by monitoring passenger position and behavior, vehicle behavior and environmental conditions.

The main suppliers of MEMS for the automotive industry are identified in the chart in Fig. 1.1, showing their market share in terms of sale value worldwide. Bosch dominates but there are multiple companies involved in MEMS production as illustrated by the chart, which is not an exhaustive list of players.

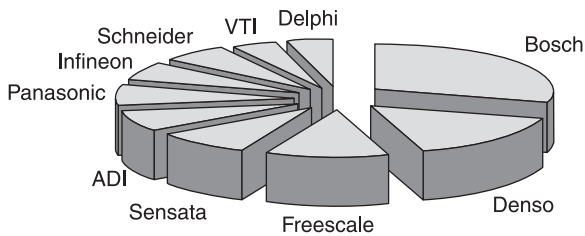

1.1 Market share of automotive MEMS in 2009 (source: Marek 2011).

1.2 Passenger safety systems

A vehicle manufacturer, such as Daimler AG (Mercedes-Benz), has classified their safety systems into several technological domains. 'Prevention' technologies help the driver to become more aware of road conditions, as well as minimizing driver distractions and stress. For example, radar and cameras improve visibility. 'Response' technologies assist the driver when things start to go wrong. For example, anti-lock breaking (ABS) improves breaking and steerability. 'Protection' technologies are designed to mitigate the consequences of accidents for the

© Woodhead Publishing Limited, 2013

passenger and other road users. For example, restraint systems minimize injury to the passenger. The final domain is 'rescue' technologies for helping the emergency services.

1.2.1 Passenger protection systems

Electronically controlled passenger protection systems are commonplace in most vehicles to some degree. These consist of various airbags, seat belt pretensioners and rollover protection devices, all controlled by an electronic control unit(s) (ECU). These systems are typically integrated into one centrally controlled system made up of the following component parts:

- Sensors:
  - for indicating an event, which may require action.
- The ECU:
  - for signal processing to identify the critical event that requires action;
  - for supplying the appropriate signals to deploy the protection device;
  - for system diagnostics to ensure robust behavior.
- The protection device:
  - for delivering the appropriate protection.

Figure 1.2 illustrates this system consisting of a sensing part, a control unit and an actuation part. Three types of protection devices are shown in this example, for airbag deployment, pretensioner firing and rollover protection. Also three types of sensing devices are shown, each of which is the focus of this chapter concerning crash sensing, vehicle rollover and occupant detection.

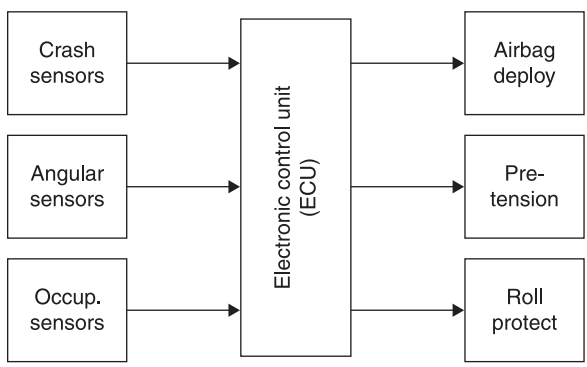

1.2 The protection system.

© Woodhead Publishing Limited, 2013

1.2.2 The crash event

A vehicle in a crash event is usually undergoing a rapid change in velocity in some direction caused by contact with an external obstacle. In a frontal collision of the moving vehicle, there is a rapid deceleration of the vehicle, whereas an unrestrained occupant continues to move forward until abruptly stopped by contact with a rigid part of the interior of the vehicle (such as a steering wheel or windscreen). Any protection system employed looks to ensure smooth deceleration of the occupant to minimize injury. Pretensioned seat belts and airbags are designed specifically to achieve this.

Pretentioners on seat belts are fired by igniting a pyrotechnic charge in the frontal crash event to maximize the restrain of the occupant with the use of the seat belt. This tightens the seat belt to prevent the occupant from jerking forward, which typically takes between 5 and 10 ms (Jurgen, 1999).

Depending on the specification of the vehicle, there are numerous arrangements of airbags and curtain systems. The frontal airbag is the most standard, which is placed in the steering wheel or dashboard to restrict frontal motion of the occupant. Pyroelectric igniters activate gas generators to inflate the airbag within around 30 ms (Jurgen, 1999).

Rollover protection such as roll-bars (Wanden and Kinnanen, 2001) and headrest-bars (Hehl and Remm, 1999) are usually spring-loaded and released on command. They maintain a volume of space in the occupant's head area during a vehicular roll to minimize injury. Convertible are the typical vehicles with these devices fitted. However, non-convertible vehicles are also considered to require rollover protection devices (Bozzini *et al.*, 2010).

Depending on the crash event (see next section on frontal, oblique, offset, pole, under-ride and side crash events), the firing of the different protection systems is crucial to allow the displacement of the occupant to be within certain limits to ensure time to activate the relevant devices.

1.2.3 Classification of crash events

A passenger vehicle has 6 degrees of freedom, 3 translational movements with usually only the longitudinal translation as desirable, and 3 rotational movements, which are usually all undesirable. Figure 1.3 shows these translational movements.

Forward longitudinal crashes have been classified into different types (Fig. 1.4) (Iyoda, 2001). The frontal crash is where the impact has equal force along the front of the vehicle, whereas the oblique crash exhibits a gradient of force level from one side to the other. The oblique crash may cause a yaw rotation. Pole and offset crashes concentrate an impact force at particular areas at the front of the vehicle. The under-ride crash is where forces are concentrated at the upper parts of the vehicle's front, whereas the interference crash affects the underside of the vehicle.

© Woodhead Publishing Limited, 2013

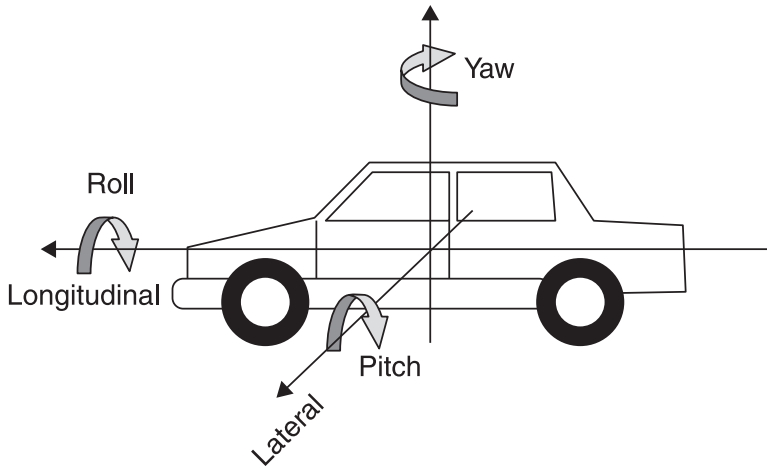

1.3 Vehicular translations.

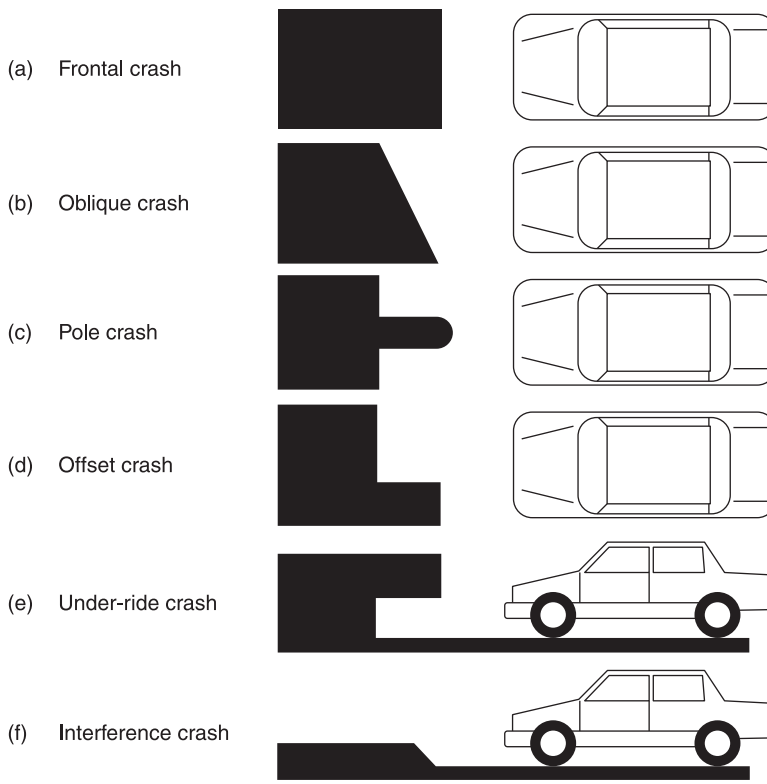

1.4 (a–f) Forward longitudinal crash types.

© Woodhead Publishing Limited, 2013

Side or latitude crashes and rear longitudinal crashes can similarly be described as depicted in Fig. 1.4. Understanding the types and likelihood of each type of crash is important to identify the requirements of the sensing device of a safety system.

1.3 Accelerometers for crash sensing systems

1.3.1 Background to crash sensing systems

One of the first crash sensing systems was the 'distributed front airbag sensing system' based on electromechanical discrimination sensors fitted in the front crash zone of the vehicle (Jurgen, 1999). Positioning these sensors at the front of the vehicle enabled early detection of deceleration during the first stages of a crash event. One major disadvantage of using these sensors today is the cost of manufacture and installation.

Two types of electromechanical sensing units are used in these early crash sensing systems, based on the 'ball-in-tube' and the rolamite principles. The ball-in-tube sensor relies on a ball being held by a permanent magnet or a spring mechanism until the ball experiences sufficient force acting on it due to deceleration of the vehicle. When the ball is released, it travels along a narrow tube (Fig. 1.5a), to close a mechanical switch at the end of the tube to close the electric circuit.

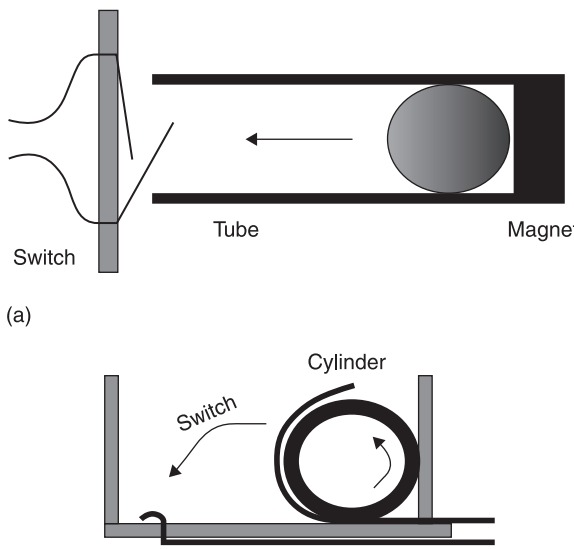

1.5 Schematic diagrams of early types of sensors: (a) the 'ball-in-tube' sensor; (b) the rolamite sensor.

© Woodhead Publishing Limited, 2013

The rolamite sensor consists of a metal cylinder with a sheet metal spring wrapped partially around it to stop it from rolling (Tyebkham, 1991; Jurgen, 1999). Given a sufficient force, the wrapped spring unwinds, allowing the metal cylinder to roll and make an electrical contact to indicate the crash event (Fig. 1.5b).

The macroscopically manufactured piezoelectric-based accelerometers came after these electromechanical type sensors for simplicity and reduced costs of manufacture and installation. An important advantage is that these sensors are robust against electromagnetic interference.

1.3.2 Principles of operation for the MEMS sensors

The principle of operation of the accelerometer in MEMS application is similar to macroscopic applications. A seismic mass is restrained by a spring, appropriately damped, and sensed using one of many different techniques (Turner, 1988). When a MEMS device undergoes acceleration or deceleration, the seismic mass moves relative to the device housing. Removing any acceleration applied to the device results in the mass returning to its original position. This is illustrated in Fig. 1.6, where the position of the housing is identified with y and the position of the mass is identified with x relative to some external reference.

The dynamics of this system can be described by a second-order differential equation, the mass-spring-damper system:

$$m\ddot{x} = -c(\dot{x} - \dot{y}) - k(x - y) \qquad [1.1]$$

where the seismic mass has mass m, the damper is damped with constant c and the spring has a spring constant k.

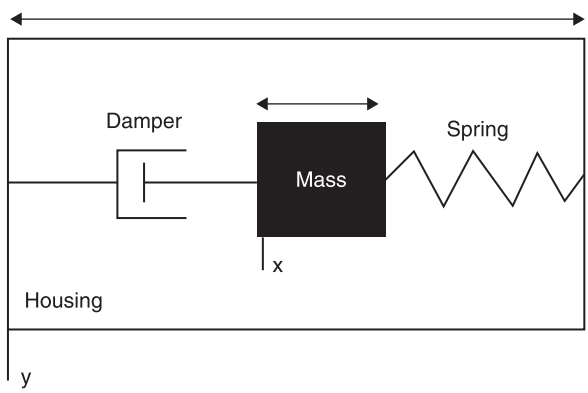

1.6 The mass-spring damper system.

© Woodhead Publishing Limited, 2013

The sensing element will detect the position x or force $m\ddot{x}$, using one of the following effects:

Piezoelectric effect

The piezoelectric effect causes an electrical potential difference to occur across an appropriate material, when it is put under strain or deflected with an applied stress. This type of material has symmetrically distributed positively and negatively charged forming unit cells, which contribute to domains of a particular alignment of polarity. Normally, these domains are arranged randomly with a net zero polarity of the material. Once the material is compressed, a proportion of domains start to align resulting in a polar material and the development of a potential difference. The polarization, P, is given by Eq. 1.2 for the applied stress, σ:

$$P = k_P \sigma \qquad [1.2]$$

where k_p is a piezoelectric constant of the material. The developed voltage, V, across a length of the materials, l, is related to the polarization, P:

$$dV = \frac{P}{\varepsilon} dl \qquad [1.3]$$

where ε is the dielectric constant (permittivity) of the material.

As an example, a block of piezoelectric material with an area of 1 × 1 mm, which has an applied stress across its thickness of length, l = 0.1 mm, can be used to produce a potential difference. The force can be calculated to require an open circuit voltage of 10 mV, given the typical values of:

- the piezoelectric constant of the material is 289 pC/N;
- the dielectric contact is 8.85 nF/m.

Rearranging Eq. 1.2 and Eq. 1.3:

$$\sigma = \frac{V\varepsilon}{k_p l} \qquad [1.4]$$

gives a force of 3 mN (where the applied stress is force per area).

Piezoresistive effect

The piezoresistive effect occurs in materials such as silicon, which gives a change in electrical resistance due to changes in its physical geometry (as with metals) plus changes in the material resistivity due to modifications in charge carrier mobility. The charge carrier mobility, μ, is determined by the charge per carrier, q, mean free time between carrier collisions, t, and the effective mass of the carrier in the lattice, m*, as in Eq. 1.5 (Geyling and Forst, 1960; Liu, 2005):

$$\mu = \frac{qt}{m^*} \qquad [1.5]$$

© Woodhead Publishing Limited, 2013

The mean free time of carrier collisions and the carrier effective mass are both influenced by the strain applied to the material. When the material is put under strain or deflected, the electrical resistance will change accordingly, remaining at the new value until restored back to its original geometry (Turner, 2009).

If a rectilinear piezoresistive member has length, l, the change in resistance, R, along its length is given by:

$$\frac{dR}{R} = k\frac{dl}{l} \qquad [1.6]$$

where k is the sensitivity of this example member (or gauge factor).

Capacitive effect

The capacitive effect involves the detection of changes in capacitance of sensing elements, which are brought into proximity. These changes are caused by a seismic mass moving due to external effects. This seismic mass is supported on a substrate and is able to move in one direction (Fig. 1.7). One part of the sensing element is anchored to the substrate, the other is fitted to the moveable seismic mass.

Equation 1.7 governs the output for the sensor, where the capacitance, C, is related to the distance, s, separating the plates of the sensing element of an area, A:

$$C = \varepsilon\frac{A}{s} \qquad [1.7]$$

where ε is the permittivity of the air gap between the plates.

1.3.3 Implementation of the MEMS sensor

The electronic airbag control unit (ECU) requires an accelerometer sensor, which will monitor decelerations for frontal collisions in the order of 35 to 100 g and accelerations for side impacts of up to 250 g.

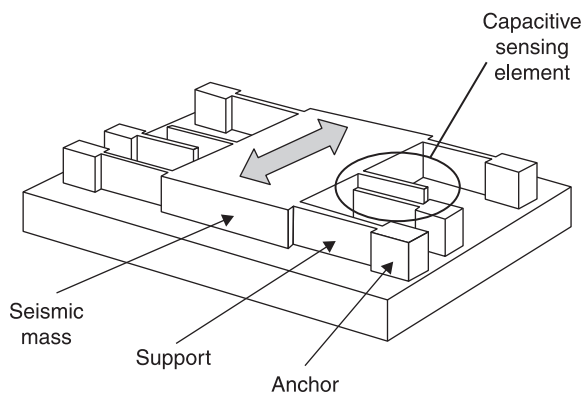

1.7 Schematic of MEMS capacitive sensor.

© Woodhead Publishing Limited, 2013

Technical details of typical devices

One of the first MEMS accelerometer devices on the market is the Analog Device ADXL50, which uses a capacitive sensing principle. The sensing element consists of many differential capacitor units with the center plate of each unit joined to a movable beam. The two outer plates of each unit are anchored to the device's substrate to form two series capacitors (C_1 and C_2) with the center plate. The moveable beam responds to positive or negative acceleration in the sensing direction. During no acceleration, the center plate of each unit is positioned equidistant between each outer plate. During positive acceleration, the moveable beam will position the center plate of each unit closer to one of the outer plates, and further away from the other, depending upon the magnitude of the acceleration. The result is that capacitor C_1 will increase in capacitance, whereas capacitor C_2 will decrease in capacitance. The outer plates of the two capacitors are driven deferentially with a 1 MHz square waveform, so that the outer plate of C_1 sees a positive signal when the outer plate of C_2 sees a negative signal, and visa versa. When there is no acceleration, the capacitors C_1 and C_2 are equal in value, resulting in zero voltage on the center plate. When a positive acceleration occurs, the voltage output from the center plate is in phase with the original waveform. When a negative acceleration occurs, the voltage output on the center plate is 180° out of phase with the original waveform. The magnitude of the voltage output is a function of the magnitude of the acceleration. The signal from the center plate is demodulated to give a differential output from the device of ±0.95 V for a ±50 g of acceleration (Analog Devices, 1996).

Later versions of this type of sensor from Analog Devices include the ADXL78, which has built-in filtering techniques for delivering robust output signals. During a crash event, the sensing element can generate signals with high amplitudes and high frequency components, which are of no use for detecting the crash event. In addition, these signals might interfere with the proper operation of the system. Therefore, a 2-pole Bessel filter is fitted into the ADXL78 at the output stage to remove these undesired signals (Analog Devices, 2010).

Comments on manufacturing processes

The Analog Devices DXL50 is a single-chip monolithic integrated device consisting of a polysilicon micromachined sensing element and a signal conditioning circuit on the same substrate. The conditioning circuit is fabricated first using bipolar junction transistor and complementary metal oxide semiconductor technologies (BiCMOS). Following this high temperature stage, the polysilicon MEMS structure is deposited. A low temperature metal and passivation process is finally employed (Martin, 2007).

The Bosch fabrication processes also combine BiCMOS with the MEMS structural deposition. Offenberg *et al.* (1995) gives a comprehensive description of the process, where the polysilicon MEMS structure is deposited earlier in the

© Woodhead Publishing Limited, 2013

fabrication. The MEMS structure is embedded in the epitaxial layer by depositing it simultaneously with the growth of the epitaxial layer of the BiCMOS fabrication process.

Integration as a system

Figure 1.8 shows the approximate position of these sensors in the vehicle, the airbags located on the dashboard and inflatable curtains for side impact crash protection. This type of sensing system is generally called a multi-point sensing system. The single-point system has no satellite sensors and the sensors are integrated into the ECU package.

In the typical crash detection systems used today, sensors communicate to the ECU by one of the standardized sensor buses, such as the Peripheral Sensor Interface 5 (PSI5), see http://www.psi5.org, or the Distributed System Interface (DSI), see http://www.dsiconsortium.org

Systems that are currently available are, for example, Bosch's 4th Generation CG101, CG102 and CG103 airbag chip set. Inputs include buckle switch sensors, seat position sensors, and for each module, two analog inputs and two external sensor interfaces (PSI5). Outputs include four firing channels for each module to activate protection devices.

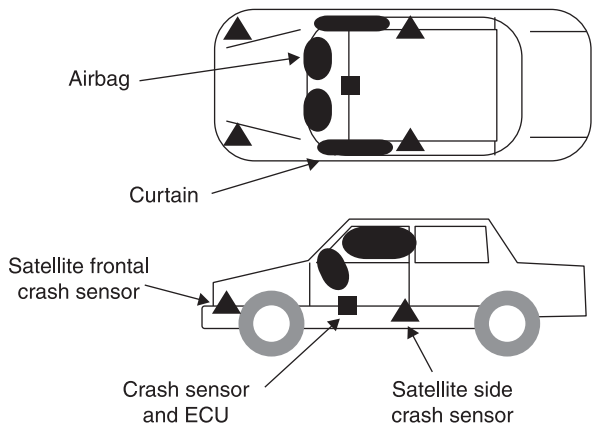

1.8 Schematic of vehicle showing sensors.

1.4 Angular rate sensors for rollover detection systems

1.4.1 Background to rollover detection systems

Passenger vehicles can undesirably roll and pitch and in the late 1980s the first protection system of its kind was developed for convertibles to protect the

© Woodhead Publishing Limited, 2013

occupants against such events. The activation time for these first systems was approximately 200 ms to detect the roll event and a further 300 ms to activate the protection devices.

Initially, several sensor types were used based on an on/off switching mechanism. The tilt switch was employed to identify a greater than ±22° angle around the roll axis. These switches consisted of a rocker cylinder fitted with a permanent magnet within the housing. A Hall effect sensing element was used to identify the position of the rocker to indicate tilt. The axle switch was employed to identify when an axle became unloaded due to the wheels leaving the ground. This was a switch that opened during this event. The spirit level switch used a bubble in a liquid to identify the level. This required a light source from typically an LED and a photo transistor to identify the position of the bubble. All these types of devices are complex to manufacture and assemble in the vehicle. MEMS bring great advantages in this regard for mass production vehicle systems.

1.4.2 Principles of operation for the MEMS sensor

The principle of operation of the angular rate MEMS sensors is based around the Coriolis phenomena of oscillating structures (seismic masses) moving in an inertial frame of reference.

Oscillating structures

An oscillating structure or seismic mass tends to continue to oscillate in the same plane or direction, even though the supporting structure is perturbated orthogonally to that plane or direction (Fig. 1.9). Figures 1.9a and 1.9b show a mass oscillating within a housing (started by some means not shown on the diagram). Once the housing is rotated with an angular acceleration, a_{roll}, the mass tends to continue to oscillate within the same plane of the inertial frame of reference external to the housing. Viewed relative to the housing, the mass has the tendency to move toward the bottom right of the housing and the top left of the housing as is oscillates (Fig. 1.9c). This is exhibiting the Coriolis effect. In addition, from the housing reference frame, the springs apply a force to the mass to give it an angular acceleration, a_{cen}, due to the roll of the housing in the inertia frame of reference.

The Coriolis effect

The Coriolis effect acting on a seismic mass can be detected between the mass and a datum frame of reference, which is rotating in an inertial frame of reference. The

© Woodhead Publishing Limited, 2013

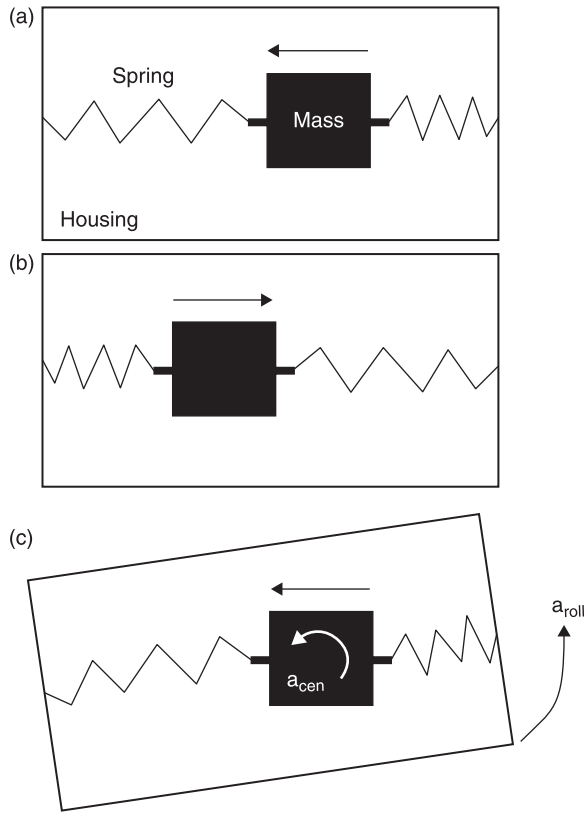

1.9 Oscillating mass: (a) and (b) mass oscillating within a housing; (c) movement of mass due to oscillation.

acceleration of the seismic mass, $a_{0,2}$, with respect to the inertial frame of reference is given by (Neul *et al.*, 2007):

$$\begin{aligned} a_{0,2} &= a_{0,1} + a_{1,2} \\ &\quad + \boldsymbol{\alpha}_{1,2} \times \mathbf{r}_{1,2} \\ &\quad + \boldsymbol{\omega}_{0,1} \times (\boldsymbol{\omega}_{0,1} \times \mathbf{r}_{1,2}) \\ &\quad + 2\boldsymbol{\omega}_{0,1} \times \mathbf{v}_{1,2} \end{aligned} \qquad [1.8]$$

where:

- $a_{0,2}$ is the acceleration of the seismic mass wrt, the inertial frame of reference;
- $a_{0,1}$ is the acceleration of the datum frame of reference wrt, the inertial frame of reference;
- $a_{1,2}$ is the acceleration of the seismic mass wrt, the datum frame of reference;

© Woodhead Publishing Limited, 2013

- $\alpha_{0,1}$ is the angular acceleration of the seismic mass wrt, the inertial frame of reference;
- $r_{1,2}$ is the distance vector from the datum frame of reference origin wrt, the seismic mass;
- $\omega_{0,1}$ is the angular velocity of the datum frame of reference wrt, the inertial frame of reference;
- $v_{1,2}$ is the velocity of the seismic mass wrt, the datum frame of reference.

Figure 1.10 illustrates a generalized embodiment of this principle with the Coriolis acceleration, a_{cor}, given by $2\boldsymbol{\omega}_{0,1} \times \mathbf{v}_{1,2}$ being the term of interest during a roll event of acceleration $a_{roll} = \boldsymbol{\alpha}_{1,2} \times \mathbf{r}_{1,2}$. Coriolis acceleration, a_{cor}, is then sensed in the device by some technique.

In Fig. 1.10, the inertial frame of reference is designated as the frame of reference 0 in which the car is traveling, the datum frame of reference is designated as the frame of reference 1 to which any measurement is compared, and the seismic mass frame of reference is frame of reference 2 from which measurements are taken. Figure 1.10 also shows the linear accelerations of $a_{0,1}$ and $a_{1,2}$, and the centripetal acceleration $a_{cen} = \boldsymbol{\omega}_{0,1} \times (\boldsymbol{\omega}_{0,1} \times \mathbf{r}_{1.2})$ restraining the seismic masses during the roll. Any undesirable perturbation from this system on the sensing technique can be removed by adopting two seismic mass structures (Fig. 1.10) oscillating in anti-parallel and then taking measurements from both to give a differential signal.

Driving and sensing techniques

The oscillation of the seismic masses in the MEMS sensor is driven using similar technologies to sensing techniques, but in reverse. Table 1.1 shows some characteristics of a few devices available for the automotive industry.

Systron Donner's devices use a piezoelectric driving mechanism and a separate piezoelectric detection mechanism. The design consists of a double-ended tuning

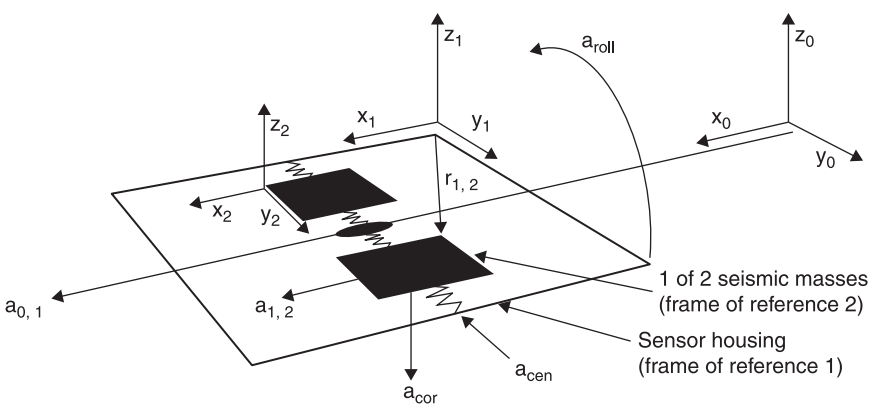

1.10 The roll sensor.

© Woodhead Publishing Limited, 2013

Table 1.1 Driving and sensing in MEMS sensors

Supplier	MEMS manufacturing technology	Driving mechanism	Sensing mechanism
Systron Donner	Quartz wet etch	Piezoelectric	Piezoelectric
Bosch	Si bulk DRIE	Capacitive	Capacitive
Silicon Sensing	Si bulk DRIE	Inductive	Inductive
Panasonic	Quartz wet etch	Piezoelectric	Piezoelectric
Analog Devices	Si surface	Capacitive	Capacitive

Source: data from Acar, 2009.

fork being driven to oscillate at 10 kHz (Voss *et al.*, 1997; Sassen *et al.*, 2000). Bosch's DRS-MMx devices use an electrostatic (capacitive) driving mechanism and a capacitive detection mechanism. The design consists of two 11 μm polysilicon seismic masses forming a tuning fork structure. This is driven at 15 kHz (Neul *et al.*, 2007). Bosch also adopt piezoresistive sensing techniques (Pan *et al.*, 2008).

1.4.3 Implementation of the MEMS sensor

The rollover protection system requires that the sensor detects a less aggressive event than compared to frontal or side crash events. This has been estimated at between 3 and 10 g in terms of acceleration (Jurgen, 1999). Strictly speaking, the angular rate sensor detects angular velocity of between 1.5°/sec (noise level) to 300°/sec.

Technical details of typical devices

The Analog Devices ADXRS612 is an angular rate sensor, which uses the principle of oscillating structures and the Coriolis effect. Two seismic masses form two 'dither frames', which are caused to oscillate asymmetrically at 14 kHz in a linear fashion. An electrostatic means is used to drive the oscillation, which requires between 18 and 20 V to achieve the required amplitude. A charge pump circuit is included if only lower voltages are available to supply the device. A finger structure is fitted to each of the outer parts of each dither frame to enable the sensing of movement orthogonal to the oscillations. This detects the Coriolis movement. The fingers are positioned between fixed fingers to take a capacitive measurement similar to that employed in the ADXL50 accelerator. The signal is demodulated to give an output voltage of 7 mV per angular rate °/sec (Analog Devices, 2007).

Figure 1.11 shows the Bosch SMG061 surface mount angular rate sensor. The cut-open package shows two chips, one being the MEMS sensor and the second being the conditioning electronics and interface. Again, the principle of oscillating structures and the Coriolis effect is utilized to sense the angular rate. A single

© Woodhead Publishing Limited, 2013

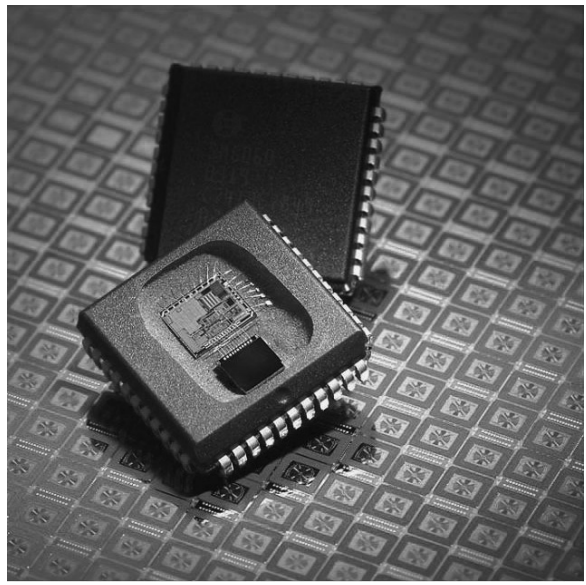

1.11 Example of sensor (source: Bosch).

seismic mass is caused to oscillate at 15 kHz by electrostatic means in a rotational fashion. Any movement orthogonal to the plane of the oscillation (due to angular rate movement) causes a rocking motion, which is out of plane of the oscillating seismic mass. This rocking motion is detected with an electrode under the seismic mass by capacitive means. The signal generated is demodulated to give an output voltage of 7 mV per angular rate °/sec.

Comments on manufacturing processes

Classen *et al.* (2007) give a comprehensive description of the developments in the fabrications processes used by Bosch for the angular rate MEMS sensor. These build on the bulk and surface micromachining techniques employed in the accelerometer devices. The silicon wafer is deposited with various combinations of oxide layers and polysilicon layers with an aluminium conductive layer. The oscillating masses are constructed from these layers by the anisotropic deep reactive ion etching method, which has come to be known as the Bosch Process. The formed MEMS structural components are freed by removing the oxide layers using hydrogen fluoride vapor phase etching.

Integration as a system

Rollover protection technology is often integrated with the airbag crash system. Rollover events are not the most frequent type of crash; however, they do incur

© Woodhead Publishing Limited, 2013

the most serious injuries. The most common rollover events are due to a soil trip, fall over and curb trip (Viano and Parenteau, 2004).

This system is employed on non-convertible vehicles as well as convertibles for the benefits it brings. Once a rollover event is detected, several protection devices can be deployed. Inflatable side curtains are the most common in non-convertible vehicles, for protecting against head and upper body injuries.

1.5 Strain gauges for occupant sensing systems

1.5.1 Background to occupant sensing systems

Occupant classification and position detection have been significant research areas in intelligent safety systems in the automotive field (Hannan *et al.*, 2006). The first occupant detection systems were concerned with identifying whether a seat was occupied.

Occupant sensing has become of critical importance where airbag and inflatable curtains are concerned, as many child and small adults have been injured and killed due to their deployment. An airbag can inflate at over 200 mph. In the USA since 1990, nearly 300 children and small adults have been killed as the result of airbag deployment (source: NHTSA, The National Highway Traffic Safety Administration).

Figure 1.12 gives a typical example of an occupant detection and classification system, which is fitted into a seat. This is Delphi's 'Passive Occupant Detection System – B', which was launched in the early 2000s. The great advantage of such a system is that it does not require action by the driver to suppress the airbag system. The occupancy of the seat is classified by the system and judges whether the airbag system should be suppressed due to the seat being empty, the occupant being an adult or infant/child. The seat is fitted with a fluid-filled bladder connected to a pressure sensor. The ECU processes data from the seat sensor, and if certain criteria are met, the airbag deployment will be allowed when necessary.

The advantages of MEMS pressure sensors in these types of systems are the relatively low costs and the small physical size of the units. MEMS give the options for multiple sensor use for enhanced occupant classification.

1.5.2 Principles of operation for the MEMS sensor

Force deflector types

Force deflector types of the electronic pressure sensors use a deflection, for example in a diaphragm, to measure the applied force on the deflector. This is illustrated in Fig. 1.13, where an external pressure supplies a force per the area of the diaphragm to cause the deflection.

© Woodhead Publishing Limited, 2013

1.12 Delphi's 'Passive Occupant Detection System – B' (Figure is property of Delphi and used with permission).

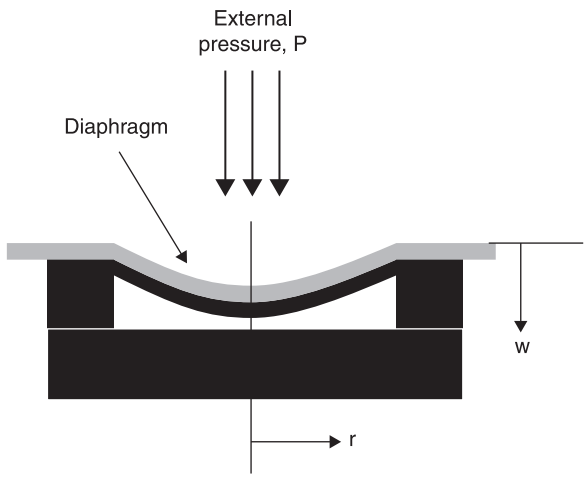

1.13 Force deflection types.

© Woodhead Publishing Limited, 2013

The deflection of a circular diaphragm, w(r), can be found from the relationship:

$$\nabla^2 w(r) \nabla^2 D(r) = P \qquad [1.9]$$

where D(r) is the bending rigidity of the diaphragm across the plane at radius, r. Assuming a constant rigidity, the deflection of any point in a diaphragm (total radius a) can be found to be as (Eaton and Smith, 1997; Hezarjaribi *et al.*, 2008):

$$w(r) = \frac{Pa^4}{64D}\left(1 - \left(\frac{r}{a}\right)^2\right)^2 \qquad [1.10]$$

Piezoresistive techniques are one of the most frequently used methods to sense a deflection in a diaphragm structure (Sing *et al.*, 2002; Zaiazmin, 2006). Piezoresistive components are fitted to the diaphragm and electrically connected in a bridge arrangement. Capacitive techniques are also often employed (Hezarijaribi *et al.*, 2008).

Resonant structure types

Resonant structure types use the changes in the resonant frequency of the structure caused by the applied force on the structure to determine that force. This is illustrated in Fig. 1.14, where an external pressure applies a force across the area of the structure.

The structure can be forced to resonate by various means. Welham *et al.* (1996) report an electrostatic driven comb arrangement with a seismic mass, M. A bias voltage, V_p, is placed on the comb and is oscillated at a resonant angular frequency, ω_0, with an alternating voltage of magnitude, V_d. If a sense voltage, V_s is applied

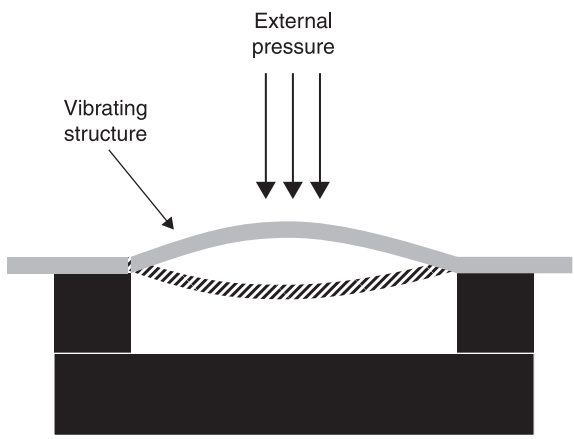

1.14 Resonance structure types.

© Woodhead Publishing Limited, 2013

to a sensing comb linked to the driving comb, a current can be detected to measure the movement in the comb. This current is given by:

$$|i_s| = \left(\frac{dC}{dx}\right)^2 \frac{V_s V_p V_d Q}{M\omega_0} \quad [1.11]$$

where the C/x term is a constant relating to the capacitor dimensions and Q is the Q-factor of the resonator. Welham *et al.* (1996) report empirical data relating pressure to the resonant angular frequency, ω_0, as in the second-order polynomial:

$$f = \frac{1}{2\pi}\left(C_0 + C_1 P + C_2 P^2\right) \quad [1.12]$$

where $C_0 = 58$; $C_1 = 3.8$ and $C_2 = -0.271$ are all constants depending on the device.

Some examples of other structures have been reported in Tang *et al.* (1989), giving a good overview of comb type structures. Burns *et al.* (1995) report on a microbeam type structure. Chuan and Can (2010) report on a MEMS device, with double resonant beams of TiN connected to a diaphragm. This structure is made to resonate by the passage of a current. Baldi *et al.* (2003) report on a MEMS device driven by inductive means, a ferrite core connected to a diaphragm, which is driven by a current carrying coil. Southworth *et al.* (2009) report on a piezoelectric resonator device.

1.5.3 Implementation of the MEMS sensor

The USA have developed airbag standards to ensure airbag systems do 'no harm' to passengers and thus occupant sensors have been developed specifically to enable compliance with such standards (Fleming, 2008).

Technical details of typical devices

The Melexis MLX80807/8 is a device that measures relative or absolute pressure. Piezoresistive material is deposited onto the edges of a diaphragm, which deflects due to pressure differences between the two sides. Four piezoresistive resistors are used at the edge of the diaphragm in a Wheatstone bridge arrangement to modify an electrical signal. Included is a facility to compensate for offset draft due to temperature variations (Melexis, 2011).

To ensure that the Wheatstone bridge delivers a change in resistance due to deflection of the diaphragm, typically two of the piezoresistors elements are deposited with positive piezoresistive characteristics and two are deposited with negative piezoresistive characteristics (Adam *et al.*, 2008).

Comments on manufacturing processes

The Melexis MLX80807/8 integrates both the MEMS sensing element and signal processing on a single silicon die. The sensing element consists of a square silicon diaphragm formed by backside etching.

© Woodhead Publishing Limited, 2013

Bosch's MEMS pressure sensor fabrication uses surface micromachining of the sensing diaphragm (Adam *et al.*, 2008). A monocrystalline starter layer is first formed and a porous silicon layer is created by using a wet chemical etching process. An epitaxial monocrystalline silicon layer is then applied to the whole wafer. This epitaxial process and subsequent high temperature steps cause silicon atoms from the porous silicon layer to migrate, leaving a void and creating the cavity for the diaphragm.

Integration as a system

Four types of occupant sensor, or occupant behavior sensor, have been the focus of attention by many (Fleming, 2008).

The occupant weight sensor measures the passenger's weight to identify whether they are a child or a small adult. If the system identifies that there is no passenger or child seated, then the airbag system is deactivated. If the system identifies a small adult, then the airbag system is programmed to deploy a 'softer' airbag with, for example, less explosive gas injection or other means. A fluid-filled bladder with a pressure sensor is one measuring device that has been patented by Waidner and Fortune (2007). Oestreicher *et al.* (2006) have patented an idea, which involves strain-gauge sensors placed strategically within the seat.

The seatbelt tension sensor is designed to identify a child seat fitted on the passenger seat. The issue is that the occupant weight sensor can return an adult weight when a child seat is fitted. Therefore, a means needs to be employed to make this differentiation. When a child seat is fitted, the seatbelt tension sensor detects a larger force (than compared to an adult), due to the child seat being tightly belted into place. A typical type of sensor employed uses a magnet and a Hall effect probe to identify displacement of a spring mechanism (Stanley and Takehara, 2007).

The seatbelt buckle sensor identifies whether a seat belt is buckled. If it is not buckled, and the seat is occupied, a higher rate of airbag inflation is used to try to restrain the occupant in a crash event. The type of sensor typically used is a magnet and Hall effect probe arrangement to identify the latched buckle (Almaraz and Martinez, 2006).

The seat position sensor can be used to identify the position of the occupant relative to the airbags. This is particularly relevant for the driver's seat, because if the seat is a long way forward, this may indicate a small adult. Also the driver would then be close to the steering wheel and close to the steering wheel airbag. All this needs to be considered when deploying the protection measures in a crash event. The typical sensor employed is a magnet and Hall effect probe arrangement to identify position (Ventura and Tokarz, 2008).

1.6 Future trends in safety sensing systems

MEMS technology brings several advantages to mass produced vehicles and their systems. The main advantage is cost reduction for a protection system that might

© Woodhead Publishing Limited, 2013

otherwise be employed with macro-sensing devices. In addition, more complex systems can be implemented with high reliability, which more accurately assess the crash event and more accurately make the appropriate response. There is still much room for improvement in occupant safety and new technologies give the opportunity to push this area of science and engineering forward.

Volvo Cars (2012) set themselves an ambitious safety challenge, when in 2008 they published their 'Vision 2020'. This stated that by 2020 nobody should be seriously injured or killed in a new Volvo. Watson (2010) reports that Volvo plans to achieve this by a combination of crash prediction and technologies that avoid crash events in the first place. The technologies under consideration include pedestrian avoidance and the ability to see around corners, which use camera, radar, GPS and GSM mobile phone devices. The idea includes the communication between vehicles so that any one vehicle's sensing range is extended beyond its own sensors to vehicles that are 'around corners'. MEMS sensors are expected to play an important role in this.

This section discusses future trends in three main areas of sensing (namely, passenger monitoring, vehicle monitoring and environmental monitoring) and speculates about opportunities.

1.6.1 Passenger monitoring systems

Vehicle interior surveillance systems for driver alertness monitoring are likely to be implemented. Eyelid monitoring is one means to determine alertness but there are other types of driver behavior that can be considered (Boverie, 2002). The increases in processing ability has made visual monitoring feasible (Chan, 2007). Such systems can be used to map the position of occupants and thus optimize any deployment of protection devices for driver and passenger. Stature of the occupant, position and posture are the main parameters that are considered. The challenge for the future is to implement these surveillance sensors, or novel versions, using MEMS technology to reduce the size and cost of the sensing units.

Taking driver alertness further would be driver's health monitoring for anticipating any likely problem during the journey. What MEMS could be employed to implement such systems?

1.6.2 Vehicle monitoring systems

The future prospects for monitoring vehicle behavior are likely to be the continual refinement of current types of sensors for more accurate and robust sensing. This is to *in situ* characterize the exact dynamic behavior of the vehicle, millisecond by millisecond. The type of safety systems likely to be developed with such sensors will focus on gaining information to predict vehicular behavior to take appropriate safety measures.

© Woodhead Publishing Limited, 2013

With the drive for lighter vehicles, there is an opportunity to replace mechanical structural 'crash zone' components with protection devices. These will require appropriate robust sensors for the intelligent systems to handle the crash event.

1.6.3 Environment monitoring systems

The motor vehicle is expected to become more automated to enable more fuel efficiency, to reduce traffic congestion, and deliver higher safety for occupants and pedestrians. This will require more sensors and novel types of sensing technology, as well as novel systems. Currently, long-range distance sensors are used on adaptive cruise control to not only maintain a constant speed but to maintain a safe distance from the car in front. The adaptive cruise control slows the vehicle as it gets too close to one in front. These sensor types are already used for warning of a forward collision. Sensor types current used are 'pulse doppler radar', 'frequency-modulated/continuous-wave radar', 'monopulse radar' and 'laser radar' (Fleming, 2008). The challenge for the future is to implement these, or novel versions, using MEMS technology to reduce the size of the sensing units.

Short-range distance sensors are used for parking assist and lane changing assist systems, to help the driver minimize collisions. Sensor types available are 'ultra-wideband radar', 'multibeam-forming radar', 'laser radar', 'camera vision' and 'ultrasonic sensors' (Fleming, 2008). Again the challenge for the future is to implement these, or novel versions, using MEMS technology, without the need for larger structures being attached to the micro-fabricated components. The ideal is to integrate as much as possible onto a single micro-fabricated substrate.

These long-range and short-range sensors are used to assist the driver to prevent any crash in the first instance. However, another area that is likely to expand is to adopt technology to anticipate a crash event in the moments before it actually occurs (pre-crash sensing). Then the on-board systems can prepare the vehicle and occupants with appropriate protection measures. The anticipation of a crash event gives more time for early triggering of multiple protection devices.

1.7 Conclusion

The past few decades have seen the development and implementation of a range of safety systems that rely on MEMS sensing technology. These safety systems have contributed to the reduction of the annual death rate on the world's roads, where generally we can expect less than 10 out of 100 000 persons killed annually. The airbag system is one system that has contributed significantly to safety. Such systems have adopted several sensing devices, which include MEMS sensors for acceleration, angular rate and strain gauge measurements.

The volume and diversity of different types of sensors are expected to grow with the increase in different safety systems, which need to monitor passengers,

© Woodhead Publishing Limited, 2013

vehicle behavior and the conditions in the external environment. There are many future opportunities for novel MEMS sensors to exploit concerning safety in the automotive vehicle. The sensor development scientists will need to work even closer with safety system design engineers to exploit new ideas and extend the technological limits in sensing. It is expected that sensor developers will work closely with vehicle stylists to ensure best location (Prosser, 2007).

1.8 References

Acar C, Schofield A R, Trusov A A, Costlow L E and Shkel A M (2009), 'Environmentally robust MEMS vibratory gyroscopes for automotive applications', *IEEE Sens J*, 9(12), 1895–1906.

Adam B, Brandt T, Henn R, Reiss S and Lang M, *et al.* (2008) 'A new micromechanical pressure sensor for automotive airbag applications, in advanced microsystems for automotive applications', *VDI-Buch*, 6, 259–284.

Almaraz J and Martinez D (2006), 'Seat belt latch sensor assembly', US Patent 7,116,220.

Analog Devices (1996), *Data Sheet ADXL50*.

Analog Devices (2007), *Data Sheet ADXRS612*.

Analog Devices (2010), *Data Sheet ADXL78*.

Baldi A, Choi W and Ziaie B (2003), 'A self-resonant frequency-modulated micromachined passive pressure transensor', *IEEE Sens J*, 3(6), 728–733.

Boverie S (2002), 'A new class of intelligent sensors for the inner space monitoring of the vehicle of the future', *J of Cont Eng*, 10, 1169–1178.

Bozzini S, Josh A, Jimenez R G and Friedman D (2010), 'Roll over protection – a meaningful and effective solution', *SPE International Conference on Health, Safety and Environment in Oil and Gas Exploration and Production*, 12–14 April 2010, Rio de Janeiro, Brazil.

Burns D W, Zook J D, Horning R D, Herb W R and Guckel H (1995), 'Sealed-cavity resonant microbeam pressure sensor', *Sens Actuat*, A48, 179–186.

Chan C Y (2007), 'Trends in crash detection and occupant restraint technology', *Proc of IEEE*, 95(2), 388–396.

Chuan Y and Can G (2010), 'Structure design on MEMS TiN resonant pressure sensors', *Proceedings of the 2010 5th IEEE International Conference on Nano/Micro Engineered and Molecular Systems*, 20–23 January 2010, Xiamen, China.

Classen J, Frey J, Kuhlmann B and Ernst P (2007), 'MEMS gyroscopes for automotive applications', in *Advanced Microsystems for Automotive Applications 2007, VDI-Buch*, Part 5, 291–306.

Eaton W P and Smith J H (1997), 'Micromachined pressure sensors: Review and recent developments', *Smart Mater Struct*, 6, 530–539.

Fleming W J (2001), 'Overview of automotive sensors', *IEEE Sens J*, 1(4), 296–308.

Fleming W J (2008), 'New automotive sensors – a review', *IEEE Sens J*, 8(11), 1900–1921.

Geyling F T and Forst J J (1960), 'Semiconductor strain transducers', *The Bell Syst Tech J*, 39, 705–731.

Hannan M A, Hussain A, Samad S A, *et al.* (2006), 'Development of occupant classification and position detection for intelligent safety system', *Int J Auto Tech*, 7(7), 827–832.

Hehl O and Remm G (1999), 'Rollover protection system for passenger car', US Patent 5,927,803.

© Woodhead Publishing Limited, 2013

Hezarjaribi Y, Hamidon M N, Keshmiri S H and Bahadorimehr A R (2008), 'Capacitive pressure sensor based on MEMS, operating in harsh environments', *Proc IEEE Conf on ICSE*, Johor Bahru, Malaysia, pp. 184–187.

Iyoda, M (2001), 'Activation controlling apparatus for passive safety device', US Patent 6,196,578.

Jurgen R K (1999), *Automotive Electronics Handbook, Second Edition*, New York: McGraw-Hill.

Liu C (2005), *Foundation in MEMS*, New Jersey: Prentice Hall.

Marek J (2011), 'Automotive MEMS sensors – trends and applications', *Proceedings of International Symposium on VLSI Technology, Systems, and Applications*, VLSI-TSA, p. 5–7.

Martin J (2007), Section 55, in Bhusban B (Ed.), *Springer Handbook of Nanotechnology*, 2. 1749–1772.

Melexis (2011) *MLX90807/90808 Data Sheet*.

Neul R, Gomez U-M, Kehr K, Bauer W, Classen J, *et al.* (2007), 'Micromachined angular rate sensors for automotive applications', *IEEE Sens J*, 7(2), 302–309.

NHTSA, Department of Transportation, National Highway Traffic Safety Administration, 49 CFR Part 595 (Docket No. 74-14; Notice 107), RIN 2127 – AG61, Air Bag Deactivation.

Offenberg M, Bosch R, Laermer F, Elsner B, Muenzel H, *et al.* (1995), 'Novel process for a monolithic integrated accelerometer', *Proceedings of International Conference on Solid-State Sensors and Actuators, and Eurosensors IX*, volume 1, pp. 589–592.

Pan Z, Lang C and Yama G (2008), 'Dual-axis yaw rate sensing unit having a tuning fork gyroscope arrangement', US Patent 7,401,517.

Oestreicher R, Homann M, Lichtinger H, Morell S and Reich D (2006), 'Method and system for determining weight and position of a vehicle seat occupant', US Patent 7,082,360.

Prosser S J (2007), 'Automotive sensors: past, present and future', *IoP J Phys: Conf Series*, 76, 012001.

Sassen S, Voss R, Schalk J, Stenzel E, Gleissner T, *et al.* (2000), 'Tuning fork silicon angular rate sensor with enhanced performance for automotive applications', *Sens and Act*, 83, 80–84.

Singh R, Ngo L L, Seng H S and Mok, F N C (2002), 'A silicon piezoresistive pressure sensor', *Proc IEEE Computer Society, The First IEEE International Workshop on Electronic Design, Test and Applications (DELTA '02)*, pp. 181–184.

Southworth D R, Craighead H G and Paria J M (2009), 'Pressure dependent resonant frequency of micromechanical drumhead resonatros', *App Phys Lett*, 94, 213506.

Stanley J and Takehara H (2007), 'Seat belt device', US Patent 7,273,231.

Turner J D (1988), *Instrumentation for Engineers*, London: MacMillan.

Turner J D (2009), *Automotive Sensors*, New Jersey: Momentum Press.

Tyebkham Y M (1991), 'Rolanite sensor', US Patent 4,985,604.

Ventura K and Tokarz S (2008), 'Seat track assembly for a motor vehicle having an integrated position sensor', US Patent 7,322,605.

Viano D C and Parenteau C S (2004), 'Rollover crash sensing and safety overview', *SAE Technical Paper Series*, 2004-01-0342.

Volvo Cars (2012), Available at www.volvocars.com (accessed March 2012).

Voss R, *et al.* (1997), 'Silicon angular rate sensor for automotive applications with piezoelectric drive and piezoresistive read-out', *Proceedings of Transducers 1997: International Conference on Solid-State Sensors and Actuators*, Chicago, 16–19 June 1997, pp. 879–882.

© Woodhead Publishing Limited, 2013

Waidner J and Fortune D (2007), 'Fluid-filled seat bladder having integral interface panel', US Patent 7,188,536.

Wanden A and Kinnanen M (2001), 'Folding top mechanism for a convertible, rollover protection system, and a concertible', US Patent 6,322,130.

Watson M (2010), Volvo's shock safety pledge in *Auto Express*. Available at www.autoexpress.co.uk (accessed March 2012).

Welham C J, Gardner J W and Greenwood J (1996), 'A laterally driven micromachined resonant pressure sensor', *Sens and Act A*, 52, 86–91.

Zaiazmin Y N (2006), 'Comparison between ANSYS and CATIA simulation capability in simulating round shape diaphragm of MEMS piezoresistive pressure sensor', School of Manufacturing Engineering, Kolej University, Kejuruteraan Utara, Malaysia.

© Woodhead Publishing Limited, 2013

2

MEMS sensors for automotive vehicle stability control applications

M. REZE and M. OSAJDA, Freescale Halbleiter Deutschland GmbH, Germany

DOI: 10.1533/9780857096487.1.29

Abstract: Electronic safety systems have been widely used in modern vehicles for the last 25 years. The first such systems were airbags and anti-lock braking system (ABS), while today they include new active systems that are able to intervene to compensate for driver error and to enhance vehicle handling. Active suspension and especially vehicle stability control (VSC) are part of these new dynamic systems. At a lower cost and a smaller size and weight than conventional systems, these MEMS deliver reliability to the overall vehicle system. After a brief history of VSC, this chapter will cover the different systems and their market impact, followed by a description of the various inertial MEMS sensors used, their evolution in the near future and the remaining challenges to be overcome. It finishes with a section on MEMS sensors used in active suspension.

Key words: electronic stability control (ESC), vehicle stability control (VSC), MEMS gyroscope, MEMS yaw rate sensors, MEMS accelerometer, active suspension.

2.1 Introduction to vehicle stability control (VSC)

Vehicle stability control (VSC) is a generic term referring to various electronic systems used in modern cars, with the aim of improving the road handling of the vehicle by means of an electronic aid. It can include a number of different systems, such as electronic stability control (ESC), active suspension or active cornering. Considered to be one of the greatest advances in road safety since the invention of the seatbelt, the ESC is an additional improvement to the anti-lock braking system (ABS) and traction control system (TCS), which were introduced in the 1980s. Its basic function is to stabilize the vehicle when it starts to skid, by applying differential braking force to individual wheels and in some cases also by reducing the torque transmitted to the wheel. It keeps the car on course even under extremely difficult conditions, such as icy or wet roads. Additional sensors must be added to the ABS system in order to implement ESC functionality, including a steering wheel angle sensor, a yaw rate sensor and a low g acceleration sensor to measure the dynamic response of the vehicle. Only the last two sensors use MEMS technology and will be part of the discussion in this chapter. This type of system is becoming popular, particularly now that many governments have introduced vehicle safety legislation programs whose focus has shifted from passive safety

© Woodhead Publishing Limited, 2013

systems such as airbags to active safety systems, helping to save thousands of lives annually. It is part of the standard equipment of many passenger cars and its penetration rate is greater than 70% in many developed countries.

Active damping is also a generic term used to describe semi- or full-active suspension systems that continuously adjust a vehicle's damping levels according to road and driving conditions. It controls the vertical movement of the wheels via an onboard system, with the aim of virtually eliminating variation in the vehicle's roll and pitch, which occurs in many driving situations such as cornering, accelerating and braking. Active damping enables car manufacturers to achieve a higher degree of ride quality and car handling, by keeping the tires in contact with the road, allowing much higher levels of grip and control. A vehicle's chassis movement and/or suspension displacement are detected by a range of sensors located throughout the vehicle. Contactless Hall effect sensors are often used for this purpose, but MEMS inertial sensors are also used, particularly for detecting the motion of the vehicle body. The data from these sensors are fed into a dedicated control unit, which will act on the suspension, adjusting damping characteristics as necessary. This chapter will present in detail a typical fully-active suspension architecture using MEMS low-g sensors, together with their requirements. Market trends and future developments will also be covered.

2.2 What is vehicle stability control?

2.2.1 A short history

The active stabilization of vehicles has long been the subject of engineering research, dating back to the 1960s. It was only a theory for nearly two decades until the advent of microelectronics made possible the use of sensors and control units that were able to measure inertial movement and to intervene with a stabilizing effect in just a few milliseconds.

The anti-lock braking system (ABS), which was first introduced in the Mercedes S-Class in 1978, was the foundation for the development of advanced braking systems. It served as the basis for other applications such as anti skid control (ASC), a system that was able to control the longitudinal forces between tires and road surface, not only during braking but also during acceleration, acting on both the brakes and the engine. A common feature of all these systems was the ability to record and limit wheel slip using advanced microelectronics and hydraulics techniques, with the aim of improving the so-called 'longitudinal dynamics' of the car.

After several earlier incarnations, the two earliest innovators of ESC, namely Mercedes-Benz and BMW, introduced their first real TCSs in 1987. These systems offered improved handling capabilities under various conditions such as evasive maneuvers, during cornering or in other transverse dynamic vehicle movements with a high risk of skidding. While they were able to maintain vehicle traction by automatically applying brakes on individual wheels and regulating engine output,

© Woodhead Publishing Limited, 2013

they were not designed to aid in steering and featured only a slip control function. However, in the early 1990s, several car manufacturers launched what are still called ESC systems. Mitsubishi introduced a new TCS called TCL, which also monitored the steering angle. Although it did not make use of a yaw rate sensor to measure the vehicle's angular speed, this active safety application was not that different from the systems used today. Furthermore, Mitsubishi improved the entire performance of their vehicles by using the TCL in conjunction with an electronic controlled suspension and four-wheel steering.

Some car original equipment manufacturers (OEMs) teamed up with automotive suppliers; for example, BMW with Continental Automotive Systems; and Mercedes-Benz with Robert Bosch GmbH, who co-developed a lateral slippage control system called 'Elektronisches Stabilitätsprogramm' trademarked as ESP or Electronic Stability Program. They were the first to implement an ESC with the W140 Mercedes S-Class model in 1995. Other car OEMs followed close behind, introducing similar ESC systems into their vehicles, such as Toyota's Crown Majesta in the same year. GM worked with the Delphi Corporation to develop its 'StabiliTrak' system, incorporated in some Cadillac models in 1997. Despite the fact that this system showed promising safety improvements, its penetration rate was very slow as it was mainly implemented in premium cars. It came to prominence in October 1997, when a Swedish journalist rolled a Mercedes A-Class without ESC at 78 km/h, during a moose test (also called 'the Elk test' in Germany), which is a sudden maneuver to avoid an obstacle in the road. This forced Mercedes-Benz to recall and retrofit 130 000 A-Class cars with ESC to save its reputation, which had been built on the safety of its cars. It was something of an 'eye opener' for the car industry and for the general public, and led to the increased penetration of ESC in subsequent years. It is fitted today as standard equipment on most medium and high end vehicle brands, or proposed as an option on nearly every model (Fig. 2.1).

Modern ESC systems are increasingly coupled with other active systems, such as steering modules (active cornering) and/or active suspension (variable dampers).

2.2.2 Description of an electronic stability control (ESC) system

The ESC system runs continuously in the background during normal driving conditions, and monitors the behavior of the driver and the vehicle by comparing the driver's intended direction to the vehicle's actual course (Bauer, 2004). Functioning on any road surfaces, it becomes operational only in the case of loss of steering control during critical driving situations, such as an emergency steering maneuver to avoid a crash, understeer or oversteer after misjudgment of a turn, or hydroplaning. By assessing the direction of the skid, preventing the vehicle's heading from changing too quickly (spinning out) or not quickly enough (plowing out), the ESC applies the brakes to individual wheels in an asymmetric fashion. It creates torque around the vehicle's vertical axis, thus counteracting the skid and

© Woodhead Publishing Limited, 2013

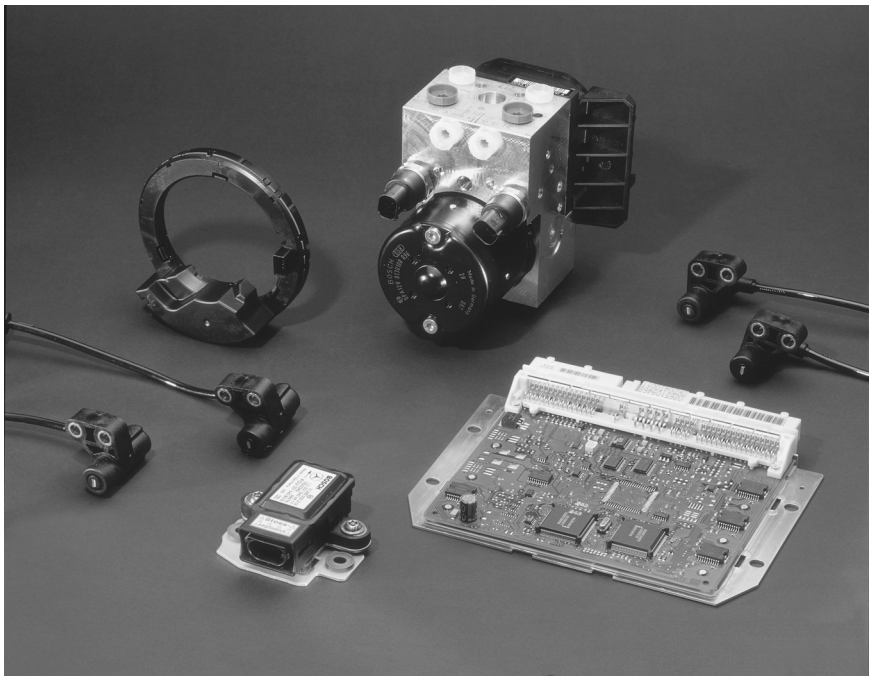

2.1 Sensotronic brake control system of Mercedes-Benz 211 series E-Class sedan (source: Mercedes-Benz).

bringing the vehicle back in line with the driver's intended direction. It may additionally reduce the engine power or operate the transmission to slow the vehicle down. The ESC reacts to and corrects skidding much faster and more effectively than a typical human driver, often before the driver is even aware of any imminent loss of control. Indeed, unlike professional racing drivers who are able to maintain control in many spinout or plowout conditions by using countersteering (momentarily turning away from the intended direction), an average driver would be unlikely to do so in a panic situation. However, an ESC system is not a performance enhancement nor a replacement for safe driving practices, but rather a safety technology to assist the driver in recovering from dangerous situations. It will not prevent cases of vehicles leaving the road due to lack of concentration or drowsiness on the part of the driver.

An ESC system uses a number of sensors to verify what the driver wants (input), while other sensors indicate the actual state of the vehicle (response). Speed and steering angle measurements are used to determine the driver's intended heading. The vehicle response is measured in terms of lateral acceleration and yaw rate by onboard silicon-based sensors, which are manufactured using micromachining technologies. Most automotive ESC systems now use these MEMS sensors, which over the last decade have been able to drastically improve

© Woodhead Publishing Limited, 2013

the ESC system in terms of size, cost and reliability, with the MEMS yaw rate replacing the conventional high-precision mechanical sensors.

Both the accelerometer and yaw rate sensors continuously send their data to the brain of the ESC system, a controller that stores the application algorithm, including the set of equations used to model the dynamics of the vehicle (Fig. 2.2). The control algorithm compares driver inputs to vehicle response and decides, when necessary, to apply the brakes driving the valves of the hydraulic modulator and/or to reduce throttle by a calculated amount. If the vehicle is responding correctly to the steering input, the yaw rate will be in balance with the speed and lateral acceleration. Since it is connected to the vehicle network (e.g. controller area network–CAN), the ESC controller is also able to receive data from and issue commands to other controllers such as an all-wheel drive system or an active suspension system, thereby allowing further improvements to vehicle stability and controllability. Most ESC systems have the option of disabling the function, which can be useful in various off-road driving conditions or when using a smaller-sized spare tire, which would interfere with the sensors. Some vehicle manufacturers offer an additional mode in which a driver can utilize the limits of car adhesion with less electronic intervention. However, the ESC system returns to normal operation when the ignition is re-started.

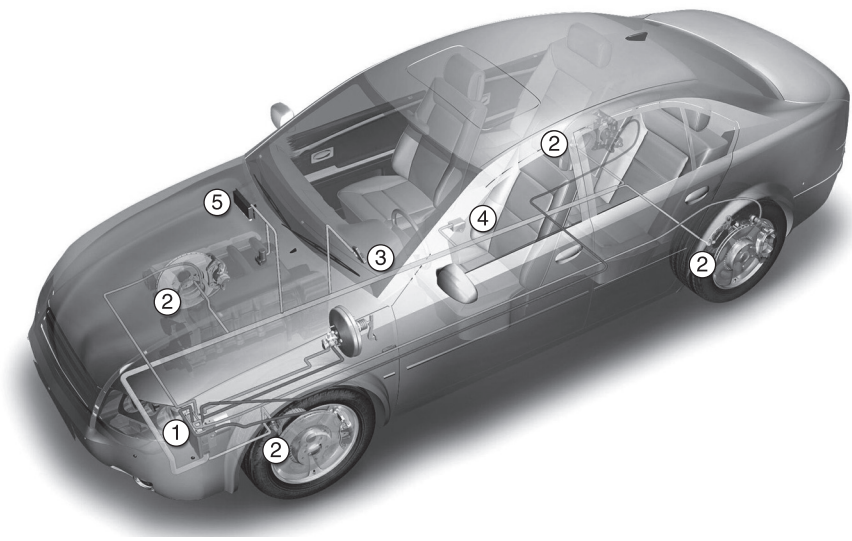

2.2 Main ESC components (source: Bosch): 1. Hydraulic bloc (valve actuation) with Electronic Control Unit (ECU); 2. Wheel speed sensor; 3. Steering wheel angle sensor; 4. Lateral and yaw rate sensors module; 5. Communication with engine management ECU.

© Woodhead Publishing Limited, 2013

The most important sensors of an ESC system are:

- *Steering wheel angle sensor*: determines where the driver wants to steer (intended heading). This kind of sensor is often based on Hall effect sensors.
- *Yaw rate sensor*: measures the rotation rate (or angular speed) of the car along the vertical axis. The data from the yaw sensor is compared with the data from the steering wheel angle sensor to determine regulating action. The concept of 'yaw rate' can be illustrated by imagining a car following a large circle painted on a parking lot, viewed from above. If the car begins pointing north and drives half way around the circle, its new heading is south. Its yaw angle has changed by 180° degrees. If it takes 10 seconds to travel half way around the circle, the yaw rate is 180°/10 sec or 18 °/sec. If the speed stays the same, the car is constantly rotating at a rate of 18 °/sec around a vertical axis that can be imagined to be piercing its roof. If the speed is doubled, the yaw rate increases to 36 °/sec.
- *Lateral acceleration sensor*: measures the lateral acceleration of the vehicle. Today this relies only on a MEMS-based single or dual-axis capacitive accelerometer, able to measure low-g signal up to 1.5 to 3 g (full scale). The use of a dual-axis low-g sensor also allows the integration of new functionalities, such as hill start assist and electric parking brake (EPB). through an accurate measurement of the tilt angle of the vehicle while on a slope.
- *Wheel speed sensor*: measures the wheel speed. This kind of sensor is mostly based on contactless magnetic sensors.

2.2.3 Market trends, legislation and mandates

In most developed nations, car accident fatalities and injuries are decreasing. For example, the estimated average reduction in the 27 member states of the EU was around 40% in the last decade (iSuppli, 2010a) and the US Department of Transportation's National Highway Traffic Safety Administration (NTHSA) disclosed that 2009 saw the lowest number of auto-related deaths since 1950. These achievements were made possible by focusing on several factors such as legislation, road infrastructure and driver behavior, but more importantly on improving overall vehicle safety. Passive restraint systems, such as seatbelts and airbags, have certainly played an important role in recent decades, helping to save thousands of lives. Many governments are now ready to go even further and mandate programs increasing the focus from passive to active safety. Between 2011 and 2020, a new range of active safety systems to prevent crashes will be widely deployed, including ESC (iSuppli, 2010a).

Large amounts of data compiled by a number of international studies have demonstrated that ESC systems significantly reduce the risk of a crash and help save thousands of lives annually (Bosch Automotive, 2009). Toyota and Daimler estimated that ESC could decrease the risk of single vehicle accident by 35 and 42%, respectively (Bosch Automotive, 2009). NTHSA estimated in 2006 that the risk could be slashed by more than 30%, thereby avoiding up to 9600 fatalities and

© Woodhead Publishing Limited, 2013

252 000 injuries every year. For example, it was demonstrated that Sport Utility Vehicles (SUVs), which are popular in the USA, are more subject to rollover or loss of steering control in difficult driving conditions due to their high center of gravity. When equipped with ESC, the potential for rollover can be drastically reduced by more than 80% (NTHSA. 2007). With such safety benefits, governments worldwide mandated ESC as a compulsory safety feature for passenger cars. All new vehicles up to 4.5 tons sold in the USA will have to be equipped with ESC by the end of 2012 (NTHSA. 2007). The European Commission has also adopted legislation requiring new cars to be fitted with ESC by November 2014, while major countries such as Brazil, Japan and South Korea have already announced their ESC mandates for 2012 and beyond (iSuppli, 2010b). The 2010 fit rate is around 40% on a worldwide basis (Europe as a whole at >65%; Sweden or Germany >85%); this provides an indication of the huge effort still required to reach full implementation, particularly in BRIC countries (Brazil, Russia, India, China).

All these mandates create a huge demand and market research firms such as Strategy Analytics (Strategy Analytics, 2009) have estimated that safety systems will be one of the highest growth areas in the period 2009 to 2014. This growth is mainly driven by the implementation of a number of active systems including ESC: the number of such systems will rise from 26 million today up to 44 million systems by 2014. Since some premium brand cars can include redundant sensors, iSuppli (2011) estimates that this would represent a market of more than 78 million MEMS accelerometer and yaw rate sensors by 2014, with 64 million of these being stand-alone dual-axis low-g accelerometers and angular rate sensors (32 million of each). Most of the remaining volume (14 million) would be combo devices, integrating a yaw rate sensor with a single or dual-axis low-g accelerometer. Indeed, the system requirements have evolved and been refined over the years to better take into account various vehicle types (i.e. four-wheel drive cars) and roads under a variety of weather conditions. These additional function requirements are a challenge for manufacturers of acceleration and yaw rate sensors, particularly as ESCs already demand an extremely high performance level for these products.

2.3 MEMS accelerometer in electronic stability control (ESC)

In an ESC system, the optimum mounting location of the corresponding sensors, particularly those for vehicle acceleration and yaw rate, is near the vehicle's center of gravity (if placed elsewhere, the acceleration signals must be transformed to take account of vehicle rotation). Together with a yaw rate sensor used to measure the vertical angular speed of the vehicle, a low-g acceleration sensor is used to detect the vehicle's lateral acceleration: the task of these two sensors is to continuously monitor any movements in the vehicle's chassis. Similar to airbag sensors, the devices used are mostly based on a surface micromachined capacitive sensing element and a control application-specific integrated circuit (ASIC) for

© Woodhead Publishing Limited, 2013

signal conditioning (conversion, amplification and filtering), assembled in a small ceramic or plastic package.

During a loss of control when the vehicle starts to skid, the maximum lateral acceleration due to friction is less than 1 g. Looking at the smaller measuring range, it is clear that the resolution of a so-called low-g acceleration sensor for vehicle dynamics is higher than that of a high-g crash sensor and a signal resolution of as low as 10 mg is required. The inertial sensor must therefore have high sensitivity to sense the low-g motion together with high accuracy. This translates into a requirement for the device output to have low noise and a small zero-g acceleration drift in temperature. Furthermore, the accelerometer must be immune to the parasitic high frequency content present in the car at the chassis level. Low energy signals with high frequency bandwidths can be found, from a few hundred Hz during normal driving conditions to a few kHz in the presence of poor surface conditions or gravel, for example, as a result of shocks coming from the road. Thus, frequencies above 1 kHz must be filtered out to avoid corrupting the sensor response. By definition, an acceleration sensor is highly sensitive to acceleration of any origin, since the micromachined sensing element is based on a seismic mass moving relative to a fixed plate. Parasitic high frequencies are usually removed from the sensor output signal via electronic low pass filtering. A sensor with an overdamped transducer, which can mechanically eliminate this unwanted higher frequency acceleration content, can also be of use.

2.3.1 MEMS transducer

Most state-of-the-art sensors use a thick transducer (>15 um), often using a silicon on insulator (SOI) wafer and deep reactive ion etching (DRIE) (Fig. 2.3). The thick

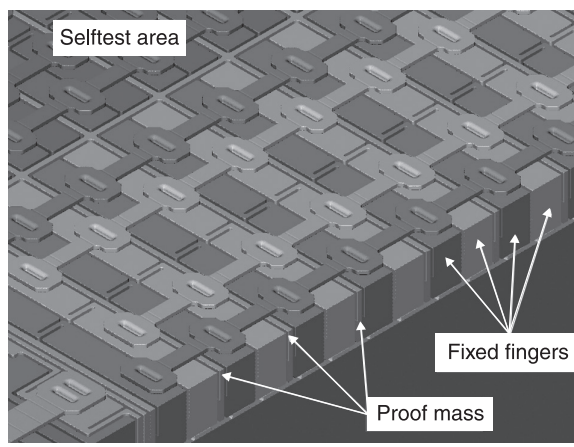

2.3 A closer look at an *x*-axis capacitive accelerometer, with thick SOI layers, narrow trenches and polysilicon bridges (source: Freescale Semiconductor Inc.).

© Woodhead Publishing Limited, 2013

SOI layer provides increased stiffness and greater mass for the moving mechanical element, along with increased electrical capacitance (Starr, 1990). The benefits of this are increased sensitivity with enhanced noise performance compared to standard surface micromachined processes (i.e. bulk micromachined processes), together with improved reliability, since it better mitigates possible stiction during use. Combined with the over-pressure hermetic sealing that is possible when glass frit wafer bonding is employed, the transducer experiences considerable air resistance as it moves, providing an overdamped mechanical response with a natural cut-off frequency below 1 kHz. Thicker capacitor plates mean less out-of-plane deformation of the sensor structure, due to package stress over temperature variation (when over-molded in the plastic package). Furthermore, the improved signal-to-noise ratios translate to lower gain of the transducer signal in the sensor system.

2.3.2 Application-specific integrated circuit (ASIC) improvements

A wide dynamic range is required for the MEMS accelerometer output for ESC application; full-scale/minimum signal, such as greater than 60 dB. The accelerometer must detect any small input or signal due to vehicle behavior change and the ASIC circuit must recognize and process these small signals over the full-scale operational range.

This wide dynamic range is achieved by limiting the noise generation sources, first by minimizing the first amplifier stage that receives the signal from the MEMS transducer (analog front end part), and second through careful design of the converter circuit. Since modern ASIC technologies available on the market contain very high density logic capabilities, the use of a sigma-delta ($\Sigma\Delta$) converter can reduce the noise component in low frequency regions through the noise-shaping effect of $\Sigma\Delta$ modulation. A high over-sampling frequency of the $\Sigma\Delta$ conversion further improves the detection resolution. As a result, the S/N ratio and dynamic range are improved. Therefore, the wide dynamic range is achieved through noise reduction of the analog input circuit and the improvement of the detection resolution of the converter circuit.

The ESC system also requires offset stability equivalent to within ±75 mg over the operational temperature range (for premium requirements this can be ±30 mg). Any intrinsic offset error creates an incorrect positional reading of a change in vehicle behavior. The offset shift caused by temperature change also leads to further errors. Sensor design is used to minimize the impact of the over-temperature offset shift. To further reduce these errors, the ASIC chip must initially include the trim capability of gain and offset; this adjustment centers the sensor within the specification. Furthermore, the ASIC chip can contain a directly integrated temperature sensor, providing temperature compensation capability. For some points within the operational temperature range, trim codes are stored in on-chip non-volatile memory during the calibration of the device. The correct trim code

© Woodhead Publishing Limited, 2013

can be reintroduced during real operation to compensate for the actual temperature. Thus, the gain/offset adjustment error reduction over temperature is achieved by the trim and the option of compensating with a temperature sensor and a non-volatile memory on the ASIC chip.

2.3.3 Digital communication capability

The accelerometer must include an analog/digital (A/D) converter and a digital communication interface circuit on the ASIC chip. A/D conversion is performed by a $\Sigma\Delta$ converter followed by an analog input circuit. The output is a pulsewidth modulated serial digital datastream, which is less affected by external noise. Compared to analog circuits, the digital datastream can be provided to a digital signal processor (DSP), which improves the accuracy of the signal information through the complicated filter functions. The digital data is sent to the ESC microcontroller via a communication interface. Serial peripheral interface (SPI) protocol is preferred for an automotive-dedicated communication bus, in which the ESC system and sensors are set up in a master and slave relationship.

The digital communication interface is therefore achieved through use of an $\Sigma\Delta$ converter, DSP and serial communication interface circuit on the ASIC chip.

2.3.4 Packaging

As with most MEMS sensors, package interactions are just as critical as the selection of device technology, and often contribute to significant performance variation between packages (Ristic *et al.*, 1992). The packaging is vital, as it directly influences the final characteristics of the product in terms of mechanical stress, shock transmission and so on, as well as its testability, reliability and cost. In addition to providing a mounting foundation for a printed circuit board (PCB), micromachined sensor packaging faces another unique challenge; the stresses induced by a mismatch in the thermal expansion coefficients of the materials used to fabricate the package and its external thermal loading must be controlled and kept at a level low enough to avoid impact to the sensor or to control circuitry performance. External package-induced stresses on an accelerometer die can produce up to 0.15 um curvature out of plane for the die from center to the edge, resulting in a device offset that would not be present for the die in wafer form. For capacitive devices capable of resolving displacement at the nanometer scale, excessive curvature due to stress on the die at a late point in the assembly can be catastrophic. In general, different MEMS devices have different stress tolerance levels. Therefore, each MEMS package must be uniquely designed and evaluated to meet specific requirements.

Package stresses are more significant for highly sensitive ESC devices than for airbag MEMS sensors. Many products were first introduced using a ceramic substrate, since this offers a lesser thermal mismatch and the ability to connect

© Woodhead Publishing Limited, 2013

passive components with good reliability. However, the higher cost of using these ceramic substrates compared to standard packages led to the development first of cavity packages and then of overmolded packages. This became possible due to improvements in the robustness of the sensor element (through a less stress-sensitive design), better signal conditioning circuitry, a profound understanding of material properties and substantial work on modeling and simulation techniques during the design phase to take into account the influence of mechanical, thermal, electrical and fluidic parameters.

These improvements formed the starting point for the move from bulky leaded devices to tiny plastic, industry standard quad-flat no-lead (QFN) packages, enabling smaller PCB designs and better resistance to parasitic frequency vibrations. As an example, the first package resonance frequency of this type of QFN package is greater than 100 kHz, far above the potential parasitic frequencies found in a vehicle that could disturb the MEMS sensing element (Fig. 2.4).

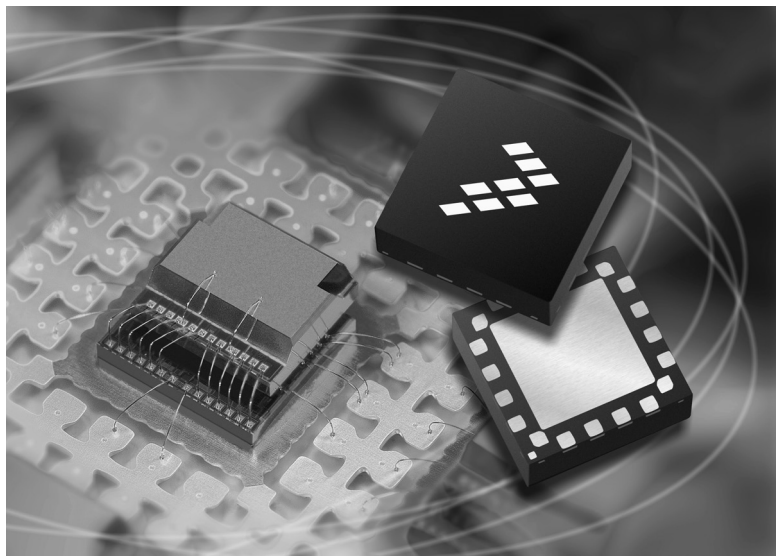

2.4 Stacked die configuration (ASIC + MEMS transducer) of a digital XY accelerometer in a QFN 6 × 6 mm package (source: Freescale Semiconductor Inc.).

2.4 MEMS angular rate sensors

2.4.1 Introduction to angular velocity sensors

Angular velocity sensors are used to measure the rotation rate of a body with respect to an inertial frame of reference. They measure the yaw rate, Ωz, at the vehicle's vertical axis.

© Woodhead Publishing Limited, 2013

Traditionally, angular velocity has been measured with a mechanical rotating wheel gyroscope, which is based on the conservation of angular momentum. This has been replaced by fiber optic and ring laser gyroscopes in high precision applications (e.g. in the military). Optical gyroscopes, based on the Sagnac effect, are the most accurate angular velocity sensors and are used, for instance, in avionics inertial navigation systems. However, these optical gyroscopes are too expensive and too bulky for automotive applications. VSC systems in particular have created a rapidly growing market for low- to medium-priced, medium-accuracy angular velocity sensors: MEMS technology allows the creation of sensors to meet this demand.

The earliest development leading to MEMS angular velocity sensors took place as early as 1835, as G. G. Coriolis (1792–1843) described the imaginary force that causes a moving particle to deviate within a rotating frame of reference. On the basis of this effect, Foucault used his pendulum to detect the Earth's rotation in 1851. In the 1950s, the Sperry Gyroscope Company invented the Gyrotron angular rate tachometer, a device similar to Foucault's pendulum. This device can be considered to be the first successful artificial vibratory gyroscope. The first actual MEMS gyroscopes were piezoelectric devices made out of quartz, first commercialized in the 1980s by Systron Donner Inertial. The first batch-fabricated silicon micromachined gyroscope is usually considered to be the device demonstrated by the Charles Stark Draper Laboratory in 1991. Several companies currently provide MEMS gyroscopes, consisting of both piezoelectric and silicon devices. However, all aspects of microgyroscope design – including the mechanics, electronics required, the system-level implementation and the packaging – have been and continue to be the subject of active research, both in industry and in academia.

Gyroscopes can generally be grouped into three different categories according to their performance, namely inertial-grade, tactical-grade and rate-grade. Table 2.1 summarizes the requirements for each of these categories. Over the past decade, much of the focus in the development of micromachined silicon gyroscopes has been on 'rate grade' devices, primarily because of their use in automotive applications (e.g. in VSC applications and to avoid rollover).

VSC applications generally require a full-scale range of at least ±70 to 100°/s, a resolution (bias) of about 0.5°/s in a bandwidth of more than 70 Hz with

Table 2.1 Performance requirements for different types of gyroscope

Parameter	Rate grade	Tactical grade	Inertial grade
Angle random walk, °/√h	>0.5	0.5–0.05	<0.001
Bias drift, °/h	10–1000	0.1–10	<0.01
Scale factor accuracy, %	0.1–1	0.01–0.1	<0.001
Full scale range (°/s)	50–1000	>500	>400
Max. shock in 1 msec, g	10e3	10e3–10e4	10e3
Bandwidth, Hz	>70	100	100

© Woodhead Publishing Limited, 2013

noise less than 0.01 °/s/sqrt(Hz). The operating temperature ranges from −40 to 105°C and can even be as high as 125°C for products designed to be placed beneath the hood.

2.4.2 Operating principles

Unlike an accelerometer, the transducer of a yaw-rate sensor needs to be driven into oscillation in order to function as a sensor (Bergstrom and Li, 2002). The transducer makes use of the Coriolis acceleration, which is generated when rotation, Ω, is coupled with an oscillatory component (velocity v) to a mass (m). In line with the familiar vector law, these accelerations are horizontal with respect to the x- and y-axis (Fig. 2.5), where Ω_z is the rate of rotation and v_x is the linear velocity of the structure due to the drive. An analogy may be drawn between the behavior of the yaw-rate sensor with that of the accelerometer, if the Coriolis term ($2\Omega_z dx/dt$) is considered as an acceleration. Assuming a typical automotive spec, where the full range of angular velocity is around 100°/s, then an equivalent acceleration, α, is given by:

$$a = 3.5\frac{dx}{dt} \qquad [2.1]$$

In general, the driving frequency is near resonance and the vibration amplitude of the transducer structure is about 1 μm. Assuming a natural frequency of 10 kHz, the resulting Coriolis acceleration of Eq. 2.1 is shown in Eq. 2.2, demonstrating that the acceleration induced by the Coriolis force is very small:

$$a = 0.022\,mg \qquad [2.2]$$

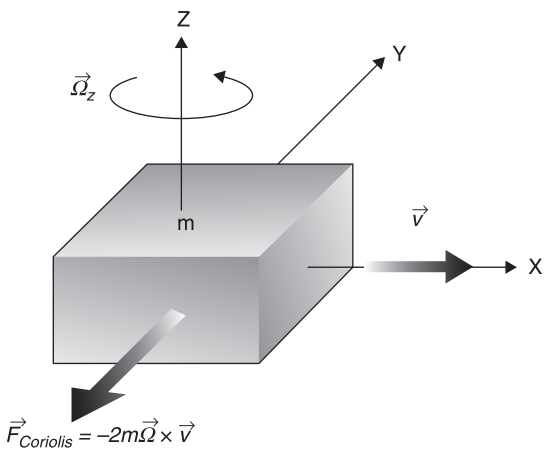

2.5 MEMS gyroscopes using the Coriolis effect to measure the angular rate.

© Woodhead Publishing Limited, 2013

For most applications, a single-axis angular rotation measurement is required. This type of single-axis rate sensor can be manufactured by sensing induced displacement, either from an oscillating rotor or from a linearly oscillating structure. Although these two types of rate sensor design appear to be different, the operation principles are the same. In both cases, when the reference frame, or device substrate, experiences a rotation along the input axis, the oscillating mass, which can be either translational or rotary, would induce a Coriolis force or torque in a direction perpendicular to both the input axis and the drive axis. When the amplitude of the drive oscillation is fixed and controlled, the amplitude of the sensing oscillation is proportional to the rate of rotation of the mounting foundation.

Because the coupling of the Coriolis effect is orthogonal to the vibratory motion in a micromachined gyroscopic device, two degrees of mechanical freedom are required. One degree of freedom is utilized for the excitation of the vibratory motion, and the second degree of freedom, orthogonal to the first, is required for sensing. This requirement is key in the choice of technology for the gyroscopic inertial sensor, as the axis of sensitivity defines which mechanical degrees of freedom are required to sense it.

2.4.3 Micromachined gyroscope technology

Almost all the micromachined angular velocity sensing elements reported in the literature have been vibratory gyroscopes, using vibrating mechanical elements (proof mass) to sense rotation (Putty and Najafi, 1994). The reason for this is that, unlike rotating wheel gyroscopes, they do not require bearings; this means their design is simpler, they can be easily manufactured using batch silicon techniques and they offer greater long-term reliability. However, as with accelerometers, a variety of technologies and sensing methodologies have been used, and new combinations are always under consideration. Some common designs from recent decades are discussed below.

Vibratory gyroscopes

Vibratory gyroscopes were demonstrated in the early 1980s. One example of this type of device is quartz tuning forks. Although vibratory gyroscopes can offer high quality at atmospheric pressure with an improved level of performance, their batch processing is not compatible with IC fabrication technology due to the use of quartz as the primary material. In the late 1980s, after a successful demonstration of batch-fabricated silicon accelerometers, attempts were made to replace quartz with silicon in micromachined vibratory gyroscopes. The Charles Stark Draper Laboratory demonstrated one of the first batch fabricated silicon micromachined rate gyroscopes in 1991 (Berstrom and Li, 2002).

© Woodhead Publishing Limited, 2013

Vibrating-wheel gyroscopes

Vibrating-wheel gyroscopes have a wheel that is driven to vibrate about its axis of symmetry. Rotation about either in-plane axis results in the tilting of the wheel, a change that can be detected with capacitive electrodes underneath the wheel (O'Brien *et al.*, 2002). Two axes of rotation can be sensed with a single vibrating wheel, as in the surface micromachined polysilicon vibrating wheel angular accelerometer depicted in Fig. 2.6

Tuning fork gyroscopes

Tuning fork gyroscopes contain a pair of masses that are driven to oscillate with equal amplitude, but in opposite directions. When rotated, the Coriolis force creates an orthogonal vibration that can be sensed by a variety of mechanisms (Fig. 2.7). Many sensors in production today use comb-type structures to drive the tuning fork into resonance, and rotation about either the in-plane or out-of-plane

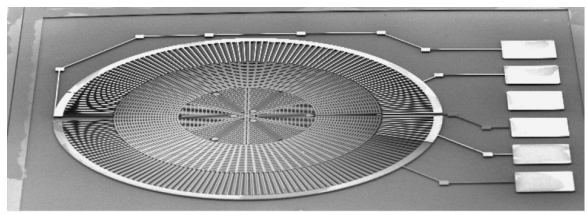

2.6 Vibrating wheel angular accelerometer with dual anchor support (source: Motorola, Inc.).

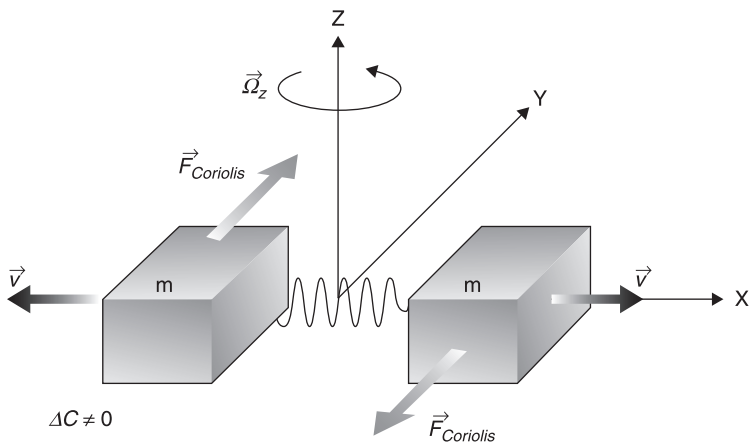

2.7 Tuning fork configuration when angular velocity along vertical axis is applied.

© Woodhead Publishing Limited, 2013

axis causes the moving masses to lift, a change that can be detected with capacitive electrodes beneath the mass.

This type of Coriolis vibratory gyroscope using an inverse tuning fork configuration is becoming increasingly popular in the industry (Kobayashi *et al.*, 1999; Classen *et al.*, 2007) (Figs 2.8 and 2.9). Each half consists

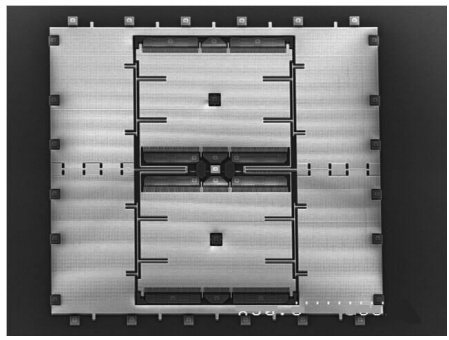

2.8 SEM picture of tuning fork gyroscope (source: Freescale Semiconductor Inc.).

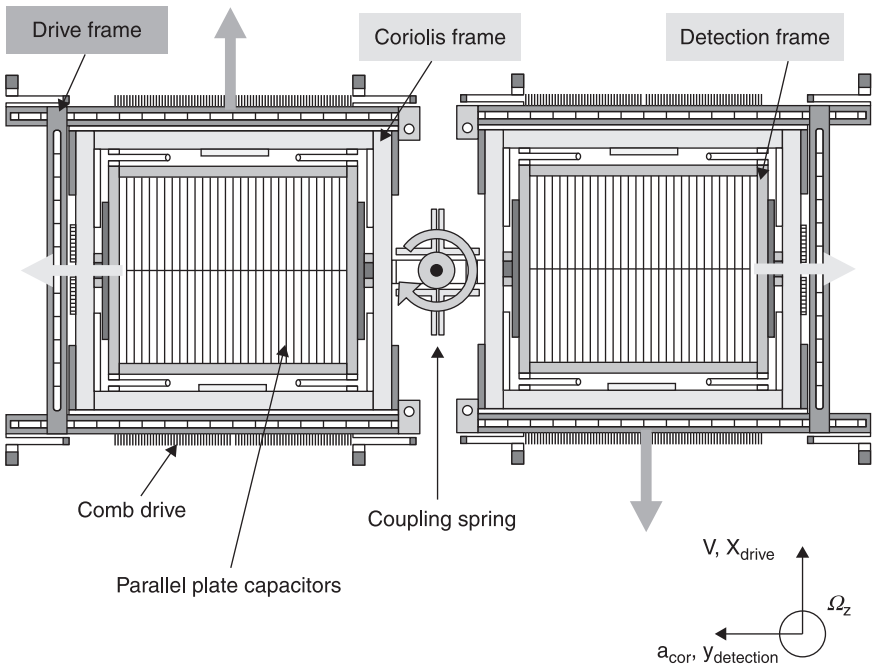

2.9 Principle operation of a tuning fork gyroscope (source: Bosch).

© Woodhead Publishing Limited, 2013

of three frames (drive, Coriolis and detection). Primary oscillation (drive) comprises movement of the drive and Coriolis frames in the *x*-direction (antiparallel mode) and excited via comb drive structures. The secondary mode (detection) is excited by Coriolis forces as a result of an angular rate around the z-axis; this is comprised of oscillation of the Coriolis and detection frames. Coriolis signals are detected by parallel plate capacitors within the detection frame. The U-shaped spring design guarantees low mechanical non-linearities, while decoupling of the detection frame from the primary oscillation significantly reduces electrical crosstalk. Mechanical crosstalk is reduced through close control of the critical MEMS processes, such as lithography and trench etching. High-quality factors for both drive and detection modes are provided by the enclosed small pressure of a few mbar.

2.4.4 Challenges in MEMS gyroscope design

Gyroscopes are much more challenging MEMS sensor products than acceleration or pressure sensors. Essentially, they must contain two high performing MEMS devices that are integrated into one single device and that have to work together to produce results, namely a self-tuned resonator in the drive axis and a micro-g sensor in the sensing axis. The absolute magnitude of the Coriolis force sensed is orders of magnitude lower than any high volume production MEMS accelerometer, as seen in Eq. 2.2. Gyroscope performance is sensitive to all potential manufacturing variations, including packaging, linear acceleration, temperature, and so on. To achieve high performance and low cost, the utmost care must be taken during the initial design, to obtain a product that is not affected by most of these potential variations. Gyroscope designers need to consider all three aspects, such as the mechanical element, electronics and packaging in one united system approach.

First, the mechanical element must be small and able to be mass produced; it should preferably not require any post-manufacturing trimming. Second, the electronics must be small, with only standard technology required to produce them. A key component for the performance of the sensor is the electromechanical $\Sigma\Delta$ modulator with a force rebalance control loop, including the micromechanical sensing element (Brosnihan *et al.*, 1995). By applying noise shaping design techniques, the SNR of the sensor can be drastically improved. Third, the encapsulation of the devices into a standard plastic package is preferred over special packaging. In particular, hermetic ceramic carriers dramatically increase the price of a single unit and must be avoided if possible. A careful system-level design is necessary to optimize the designs of individual parts and to minimize the manufacturing costs, while ensuring that the required performance targets are met. With regard to cost-saving, the testing can make a significant contribution to the overall costs in the production of microsystems and must therefore be carefully considered.

© Woodhead Publishing Limited, 2013

2.5 Vehicle architecture challenges and sensor fusion

A current challenge in the field of vehicle architectures is the incorporation of an increasing number of functions and features, causing a sharp rise in the number and complexity of electronic control units (ECUs) in the vehicle (Axten and Schier, 2007). The networking between these ECUs becomes ever more complex, leading to a higher bus load, increased effort and cost in wiring and potential impacts on controllability. Advanced self diagnostics and enhanced safety integrity (i.e. the forthcoming functional safety standard ISO26262) are an absolute necessity in these distributed logic systems, particularly given that car manufacturers' quality targets are taken into account. The increased number of ECUs and sensors, along with their added complexity, has also led to an increase in material and manufacturing costs. New concepts have been developed in recent years to optimize the various functions of the vehicle by merging some functions and re-using the information from the sensors.

2.5.1 Sensor fusion

As a consequence of this fusion at the system level, the inertial sensors will also have to merge (Fig. 2.10). Since the data from vehicle dynamics sensors, such as gyroscopes and accelerometers, will be used by numerous systems, it would clearly be beneficial to identify potential areas of synergy and to integrate various different types of sensing element, such as a gyroscope and accelerometer, in a multi-axis inertial measurement sensor or combo. The development of this type of integrated device has been possible due to advancements made over the last decade in the field of MEMS technology and processing power, along with advanced design (simulation, modeling) and packaging techniques (Mizuno *et al.*, 1999).

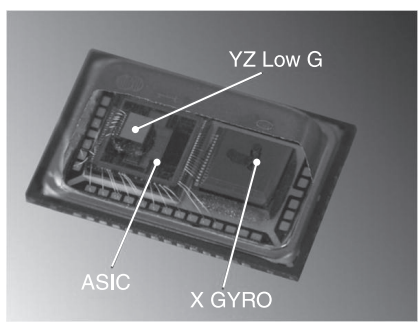

2.10 Combo sensors: integration of a gyroscope and low-g accelerometer (source: Freescale Semiconductor Inc.).

© Woodhead Publishing Limited, 2013

Simply meeting the sometimes contradictory demands of active and passive safety systems is a challenge in itself. Combo sensor elements must be as flexible as possible, to be suitable for use in a wide range of applications. This involves the use of flexible digital interfaces such as Serial Peripheral Interconnect (SPI), different supply voltages (3.3 and 5V), programmable circuits (filters, and so on) and robust packaging. However, it is also essential that the sensor elements also meet the specification requirements of the most demanding system to which they will supply the signal. Hence, the combo sensor not only has to overcome the challenges posed by integration, but also has to meet the demand for higher performance sensor elements compared to stand-alone products.

High end car manufacturers are increasingly making the decision to include more systems in their vehicles, and to add sophisticated features to safety systems in order to distinguish themselves from their competition. One obvious solution to keep costs under control is to reduce the number of ECUs in the car by finding synergies between the various functions. One of these approaches currently implemented in today's vehicles involves merging some of the sensors used in the airbag and ESC modules. However, several different approaches have been adopted by Tier 1 automotive suppliers and these are presented below.

2.5.2 ESC sensor cluster including various inertial devices

This is the option most frequently employed in modern vehicles. A sensor cluster consisting of different inertial sensor elements (accelerometer and gyroscope) communicates with the ESC ECU via a CAN bus (Fig. 2.11). Other ECUs in the vehicle can also use the sensor's signals, either through a direct connection to the CAN bus, or by receiving them from the ESC ECU via a different connection. Due to its small size, the sensor cluster can then be placed in a favorable position, in order to measure the dynamics of the vehicle (usually close to the center of gravity, in the middle of the car) without excessive vibration. The ESC system ECU can be placed wherever it is required, as there are no restrictions placed upon this by the

2.11 ESC sensor cluster including combo sensor (source: Continental).

© Woodhead Publishing Limited, 2013

inertial sensors. Furthermore, the ESC ECU benefits from sensor optimization due to the fusion of the low-g sensor with the gyroscope in one package.

2.5.3 ESC sensors integrated into the ESC electronic control unit (ECU)

ESC sensors can also be integrated directly into the ESC system ECU. This offers the advantage of eliminating the need for an extra connection or wiring harness connecting the sensors and the ECU. It also saves on module housing without the need to find a suitable sensor mounting position. Costs are further reduced as the additional microcontroller and CAN circuitry found in the sensor cluster are not required. However, the main challenge faced by this approach is the comparatively harsh environment (temperature, vibrations, electromagnetic compatibility (EMC) parasitic frequencies) that the inertial MEMS sensors have to withstand due to the location of ESC ECU in the engine compartment, mounted directly on the hydraulic block.

2.5.4 Integration of the ESC and airbag sensors into the airbag ECU

As the airbag ECU already contains accelerometers, its mounting position in the center of the vehicle and its relatively protected environment offers scope for sensor synergies. The addition of ESC inertial sensors saves on space in the vehicle as a whole, since the sensor cluster can be removed. This solution has been already adopted by some Tier 1 suppliers; it does not require a major change in the module architecture, and the functions of the sensors in airbag and ESC are kept discrete. This is the first step in merging passive and active safety systems before the integration (and data fusion) into a full domain controller.

2.5.5 Integration of all inertial sensors into a domain controller ECU

This approach involves the integration of all inertial sensors in the vehicle into one central ECU, meaning that the signals for a variety of system ECUs (ESC, automatic cruise control, roll stability control, airbag, and so on) can be housed together. In this way, the dynamic behavior of the vehicle can be measured as a whole and processed using model-based algorithms. The required signals can then be supplied to all active and passive safety chassis and restraint systems. One advantage of this approach is that the requirements of the inertial sensor elements can be taken into account when choosing a mounting position. There is no competition between two ECUs or between sensor clusters, which both require a mounting position suitable for vehicle dynamic management. Most synergy effects between the sensor elements and the signals required by active and passive

© Woodhead Publishing Limited, 2013

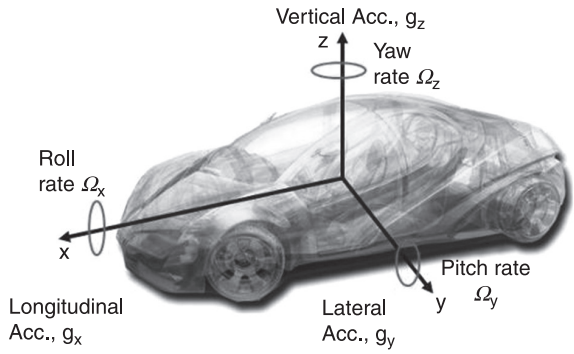

2.12 The six degrees of freedom (DoF) into a vehicle.

safety systems can then be employed. If the required systems use all the inertial sensing axes (up to 6 degrees of freedom, as shown in Fig. 2.12), the ECU could theoretically be mounted in an arbitrary position.

The misalignment with respect to the vehicle axes can then be calculated and automatically corrected for. The main challenge in using this integration method to house airbag sensors is that the energy reserve requirements for the restraint system must be met. This means that the buffer time for the airbag sensors in the domain ECU is increased, requiring intelligent energy management and interfacing logic.

With the introduction of a high speed bus system such as Flexray in new vehicles, higher data rates and more networking of different systems can be achieved. This increases the attractiveness of a centralized domain ECU to host all inertial sensors (Table 2.2).

Furthermore, the 'combo strategy' becomes an obvious choice when the information in Table 2.2 is taken into account, since a single device could then be used by several applications. The development of several combinations of combos

Table 2.2 Sensor cluster: a centralized vehicle inertial data center to share sensors information

Applications	g_x	g_y	Ω_x	Ω_y	Ω_z
ESC		X			X
Rollover		X	X		
Active cornering		X			X
Steer by wire					X
Active cruise control (ACC)					X
Chassis management				X	X
Navigation				X	X
Electrical parking brake (EPB)	X				

© Woodhead Publishing Limited, 2013

with a gyroscope in the *x*- and *z*-axis, including multi-axis low-g sensors, could cover most of the mentioned applications, thereby substantially reducing the number of packaged sensors. For example, a high runner device would be a gyro z with *xy* low-g to cover ESC and EPB applications when fitted as standard.

2.5.6 Functional safety challenges

Electronic safety systems have increasingly stringent requirements. The forthcoming functional Safety Standard ISO26262 is being applied in the automotive industry to ensure that electronic systems in cars are actually safe. The International Organization for Standardization (ISO) document defines four automotive safety integrated levels (ASILs), with ASIL D being the most stringent safety level. These new requirements affect the entire product development process in the same way as an Automotive Electronics Council (AEC) AEC-Q100 or ISO-9000 quality requirement. From the beginning of the design process, evidence must be collected to demonstrate that the product is being developed according to the Standard and to document that potential hazards have been identified and adequate mitigation is in place. New tools have been introduced to support this new approach to automotive quality. Failure modes and effects analysis (FMEA) has routinely been used in the past to address failure modes in automotive systems. Now ISO26262 requires an FMEDA (failure modes, effects and diagnostic analysis). In this approach, failures must be identified and quantified and a diagnostic performed to capture the failure. In addition, suppliers must provide customers with documentation in the form of a safety manual that explains how to implement the device in an ASIL D type of system.

As most of the sensors and new combinations of combos described earlier are used in safety critical applications, these will also have to comply with these new 'state-of-the-art' safety standards, which are to be introduced in 2014/2015. These additional requirements will therefore need to be taken into account at the beginning of the design. All sensor suppliers are developing devices, including the required documentation as well as innovative functions to guarantee failure detection and cover any deviations from the specification. This requires the implementation of dedicated 'failsafe' circuitry, which is able to monitor signals from the various sensing elements (driven in closed loop configuration) and all critical data from the control ASIC.

2.5.7 Future trends

In the future, the borders between the well-established vehicle domains will change. As described above, networking the active and passive safety systems with the driver assistance systems to create a modular safety system will become a reality due to the flexibility offered by MEMS integration. In the future it will be possible to provide an even greater level of protection to the passenger by

© Woodhead Publishing Limited, 2013

combining the airbag control unit with other systems and sensors in the vehicle. Advanced rollover sensing, for example, optimizes the protective benefits of the restraint systems when the vehicle rolls over, by including the ESC data about the state of the vehicle in the airbag control unit's calculations. This allows earlier and more reliable identification of the optimum point at which to trigger the belt tighteners, side and head airbags and the roll bar. Moreover, data from navigation systems will be included in the design of future safety features. Indeed, the ESC angular rate data can provide information on the local heading by integrating the sensor signals, since the information about the car's current position and the layout of the roads can be used to warn the driver in advance of potential dangers, such as dangerous crossings, tight curves or accident black spots.

2.6 MEMS accelerometers used in active suspension

The vision of cars with adaptive suspension has existed since 1980. An active suspension system guarantees the highest safety and comfort level for the driver in different driving and road conditions. It also allows the driver to alter the system performance and, for example, to choose between sporty or comfort suspension.

The basic principle of active suspension is to measure pitch, roll and vertical movement of the body of the vehicle. With this information, the system can adjust the dampers, depending on the type of technology used. A full-active system uses separate (hydraulic or electromagnetic) actuators, which can exert an independent force on the suspension to improve the riding characteristics. Semi-active systems can only change the viscous damping coefficient of the shock absorber, and do not add energy to the suspension system. In a simple system, the reaction speed is slow and control is based on the average movement of the car body. In advanced systems, the movement of the wheels is also measured and the dampers are controlled almost in real time.

The first systems had controllable dampers or an air suspension level control. However, the early systems provided poor feedback on the car's body and wheel movements. The situation improved with the introduction of the acceleration sensor in active and adaptive suspension systems. The best feedback for dynamic control can be achieved by measuring the information on the car's vertical acceleration in real time from every wheel damper, and then comparing this to car body accelerations.

Today there are many different active suspension systems on the market, most frequently found in high end vehicles. In the most common approach, three MEMS accelerometer modules are used to measure car chassis movement (Fig. 2.13). Other systems incorporate 2- or 4-wheel-MEMS acceleration modules, integrated with the dampers. Compared to vehicles relying only on information from ESC sensors, vehicles using this kind of system architecture benefit from accurate body dynamics data and from the use of a minimum number of sensor modules.

© Woodhead Publishing Limited, 2013

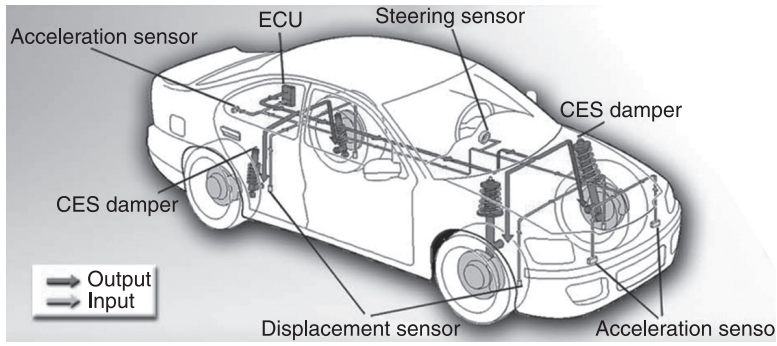

2.13 Active damping system using three single-axis low-g sensors located on the vehicle chassis (source: Tenneco).

The control unit processes this information and controls the damper actuators. Accelerometer modules with a wire harness, bracket and cabling, account for a significant proportion of the overall cost of an active suspension system. To reduce these costs, the acceleration sensor modules can be replaced with sensors that are located directly on the ECU board or integrated into the damper actuator units. In some systems, a displacement sensor (based on the Hall effect) is used to replace the wheel acceleration sensors, or to reduce the number of these required.

Future body MEMS acceleration modules will use a Peripheral Sensor Interface 5 (PSI5) digital communication interface (for the same as that used for airbag satellite crash sensors) with a bus connection to reduce cabling costs and to improve networking capabilities with other systems, such as ESC, hill start aids or burglar alarm systems. However, despite improved handling characteristics, the large-scale adoption of active suspension is still some distance away, since most drivers currently do not purchase the option for their new vehicle. iSuppli estimates that by 2014, 12 million MEMS sensors will be used in active suspension systems, representing around 4 million vehicles: this accounts for less than 5% of the total vehicle production.

2.7 Conclusion

Customer awareness and the various mandates of governments worldwide have caused an increase in the adoption of more safety systems in the vehicle. Automotive suppliers and car manufacturers are looking at new vehicle system partitions by integrating various functions together or by merging sensor information, such as with airbags and ESC. While this merge of passive and active safety systems certainly offers some advantages, it also has repercussions for MEMS sensors, which require a new level of integration. Multi-axis components will be needed, integrating different sensing elements such as yaw rate and low-g sensors, which are capable of addressing a variety of module configurations. In

© Woodhead Publishing Limited, 2013

order for this increased level of integration to function successfully, a certain degree of sensor synergy must be achieved: in this case, the application with the highest performance will always dictate the performance requirements of the sensor. Progress in MEMS technology, advanced design techniques and packaging will continue to be crucial in achieving further cost reductions and increasing the benefit to the customer.

2.8 References

Axten E and Schier J (2007), 'Inertial sensor performance for diverse integration strategies in automotive safety', in *Technical Digest Int Conf Advanced Microsystems for Automotive (AMAA '07)*, New York: Springer, pp. 251–263.

Bauer H (2004), *Automotive Electrics, Automotive Electronics, Systems and Components, New: Sensor/Microelectronics, Fourth Edition*, Robert Bosch GmbH, Plochingen, Professional Engineering Publishing Limited.

Bergstrom P and Li G (2002), 'Inertial Sensor', in Gad-el-Hak, *The MEMS Handbook*, Boca Raton: CRC Press.

Bosch Automotive (2009), Press Release on ESP, March 2009.

Brosnihan T J, Pisano A P and Howe R T (1995), 'Micromachined angular accelerometer with force feedback', *ASME Int Conf Expo*, pp. 941–947.

Classen J, Frey J, Kuhlmann B and Ernst P (2007), 'MEMS gyroscopes for automotive applications', in *Proceedings Int Conf Advanced Microsystems for Automotive (AMAA '07)*, New York: Springer, pp. 291–305.

iSuppli (2010a) *Market Watch*, 10(35), 27 September.

iSuppli (2010b) *Market Watch*, 10(39), 25 October.

iSuppli (2011) *Automotive MEMS Q1 2011 Market Tracker*, May.

Kobayashi S, Hara T, Ogichi T, Asaji Y, Yaji K, *et al.* (1999), 'Double-Frame silicon gyroscope packaged under low pressure by wafer bonding', in *Technical Digest IEEE Int Conf Solid State Sensors and Actuators (Transducers '99)*, New York: Institute of Electrical and Electronics Engineers, pp. 910–913.

Mizuno J, Nottmeyer K, Kanai Y, Berberig O, Kobayashi T, *et al.* (1999), 'A silicon bulk micromachined crash detection sensor with simultaneous angular and linear sensitivity', *IEEE Transducers*, 1302–1305.

NTSHA (2007), FMVSS. Available from: http://www.nhtsa.dot.gov/staticfiles/DOT/NHTSA/Rulemaking/Rules/Associated%20Files/ESC_FR_03_2007.pdf

O'Brien G J, Monk D J and Najafi K (2002), 'Dual anchor angular rate sensor (gyroscope)', *IEEE Solid State Sensors and Actuators*, 285–288.

Putty M and Najafi K (1994), 'A micromachined vibrating ring gyroscope', in *Technical Digest, Solid-State Sensor and Actuator Workshop*, Hilton Head, SC: Transducers Research Foundation, Cleveland, OH, pp. 213–220.

Ristic L J, Gutteridge R, Dunn B, Mietus D and Bennet P (1992), 'Surface micromachined polysilicon accelerometer', Hilton Head, SC: IEEE Solid State Sensors and Actuators Workshop', New York, pp. 118–121.

Starr J B (1990), 'Squeeze-film damping in sold-state accelerometers', in *Technical Digest IEEE Solid State Sensors and Actuators Workshop*, Hilton Head, SC: Institute of Electrical and Electronics Engineers, New York: pp. 44–47.

Strategy Analytics (2011) *Automotive Sensor Demand Forecast 2009 to 2018*, July 2011.

© Woodhead Publishing Limited, 2013

3

MEMS for automotive tire pressure monitoring systems

M. LÖHNDORF and T. LANGE, Infineon Technologies AG, Germany

DOI: 10.1533/9780857096487.1.54

Abstract: This chapter gives an overview of the requirements and status of tire pressure monitoring systems (TPMS) in view of MEMS sensors and the corresponding electronics. TPMS has become a nature market due to mandatory legal regulations for light vehicles in the USA. MEMS-based pressure sensors are used in the vast majority of so-called direct TPMS systems. After an introduction to the different processes of MEMS pressure sensors as well as the detection schemes, the power management of TPMS is discussed in detail. In addition, the use of energy harvesters as potential power sources for future TPMS systems, as well as the requirements and advantages of tire integrated TPMS systems, are discussed.

Key words: MEMS, pressure sensors, automotive, tire pressure monitoring.

3.1 Introduction

3.1.1 History of regulations

A series of fatal accidents in the USA in the late 1990s, due to tire tread separations, led the US administration to mandate tire pressure monitoring systems (TPMS). The TREAD Act (Transportation Recall Enhancement, Accountability and Documentation) mandated the use of TPMS to alert drivers in case of under-inflation of vehicle tires. The TREAD Act affected all light vehicles (<10 000 pounds, ~4500 kg) sold after 1 September 2007, with a phase-in starting in October 2005.

The Federal Motor Vehicle Safety Standard (FMVSS) 138 was released by the US National Highway Traffic and Safety Administration (NHTSA, 2005), to warn the driver when one or more tires were significantly under-inflated. In March 2006, an international standard was published (ISO 21750, 2006), but this ISO standard is not mandatory in contrast to the FVMSS 138. In the following years, several international workgroups and councils were established in order to find a harmonization of the TPMS regulations.

In 2010, the European Commission issued an amendment to Regulation 64 of the Inland Transport Committee for Tire Pressure Monitoring (UN/ECE, 2010). The key focus of this regulation is on the reduction of CO_2 emissions and on increased safety. It is most likely that in future other countries will also apply these regulations. Korea, Russia and Japan will follow the EU regulation and

© Woodhead Publishing Limited, 2013

Table 3.1 Short overview of TPMS regulations and standards by region

	USA	EU		Worldwide
Regulation	FMVSS138	ECE (GRRF-65-40)		ISO21750
Tires	1 or 4 tires	Puncture (1 tire)	Diffusion (4 tires)	TPAS (1 or 4 tires underinflated)
Speed range	50–100kph	40kph - v_max		25kph -v_max
		40–120kph (test)	50–100kph (test)	
Pressure Warning	25% (ref. cold pressure) under recommended inflation pressure	20% (ref. warm pressure) under recommended inflation pressure		(ref. cold pressure) 10kPa below threshold (3 min) 20kPa/min, 100kPa below threshold (5 min) 10kPa/min, 100kPa below threshold (10 min)
Detection time	20 min	10 min	60 min	3 min (10kPa below threshold) 5 min (20kPa/min, 100kPa below threshold) 10 min (10kPa/min, 100kPa below threshold)
Malfunction detection	20 min	10 min		10 min
Status	Phase in ended 9/2007 for all vehicles < 4.5 t	New vehicle types as from 11/2012 and all vehicles as from 11/2014 < 3.5 t		Voluntary since 2006

China is working on a separate proposal. Table 3.1 summarizes the key requirements from the known regulations and standards.

3.1.2 Market

Shortly after the mandatory regulation in the USA, several companies started to develop and commercialize dedicated TPMS systems. Most of these systems are based on a MEMS pressure sensor in conjunction with an electronic circuit (application-specific integrated circuit – ASIC), to compute the pressure signals and allow a wireless transmission of the information via RF (radio frequency). These systems are called direct TPMS, since the absolute tire pressure is measured and monitored. A different approach, the so-called indirect TPMS, makes use of wheel speed sensor information to detect under-inflation due to differences in the circumference of the tire.

In 2007, the US car sales for light vehicles was in the range of 15 million units, thus the total market for direct TPMS sensors was roughly 60 mio pcs/yr, taking into account an average of 4 TPMS sensors per vehicle. The worldwide economic crisis in 2009/2010 led to a significant downturn, but the US car market recovered and reached 12 million cars in 2011. With the new regulations in the EU starting from 2012 onwards and planned regulations in Japan, Russia and Korea, the total market for TPMS is expected to grow significantly. However, all regulations are open for different technical solutions (e.g. indirect, direct TPMS) as long as the defined requirements are met. With the legal enforcement of the implementation of tire pressure monitoring, the market became a high volume market. Thus, the major differentiation between the TPM systems is the feature set (e.g. localization, additional information) and the reduction of overall system costs.

3.2 Tire pressure monitoring systems (TPMS) applications and solutions

3.2.1 Direct and indirect TPMS systems

Direct and indirect TPMS systems compete to fulfill the regulations using different prerequisites. As direct systems measure the pressure via a MEMS pressure

© Woodhead Publishing Limited, 2013

sensor, the accuracy is high and the warning signal to the driver is sent immediately. The drawback of this solution is cost, as each tire requires its own tire pressure sensor module and a central receiver unit. Indirect systems instead use existing wheel speed sensors to measure the rotational speed of the tires. In cases of one or more tire leaks, the radius of the tires decrease and the wheel rotation speed increases. The difficulty is to achieve the required accuracy for every combination of road conditions and tire brands. To ensure a correct warning for the driver, the indirect system has to compare and compute the ABS signals for several minutes. Thus, indirect systems provide reduced system costs, but with the drawback of less accuracy and longer warning time for the driver compared to direct systems.

3.2.2 Direct systems

The schematic of a direct system is shown in Fig. 3.1. It is based on a TPMS pressure sensor module in each tire and central RF receiving unit placed in a location that provides a sufficient link margin to each of the four sensors. To differentiate TPMS sensors from the same car type, each sensor module has a unique sensor ID. Thus an integration step is required for the system to learn the sensor IDs belonging to the vehicle. After the learning phase, the sensor IDs are

3.1 Direct TPMS system.

© Woodhead Publishing Limited, 2013

stored in the central receiver unit. In case one of the monitored pressure signals drops below the warning threshold, a simple warning lamp is illuminated in the dashboard to inform the driver. Such a simple setup of a TPMS system provides no information about the position of the deflated tire. The feature to determine the position of the tire is called 'localization' and is often used to differentiate TPMS systems at the OEM and consumer levels.

3.2.3 Application – state-of-the-art TPMS module

Today's original equipment manufacturer (OEM) TPMS are safely installed on the rim. Due to high acceleration forces in the wheel, the wheel modules will be fixed directly, either on the rim or on the valve stem (Fig. 3.2). Inside the wheel module, a battery-based TPMS system is placed. A typical configuration is represented by a MEMS pressure sensor, a low power embedded micro controller for processing, an ultra high frequency (UHF) transmitter to transmit the data to a central receiving unit and a battery as power source.

The main electrical components of a state-of-the-art module are shown in Fig. 3.3. Optional components are represented by a dotted line. Basic systems will measure the pressure and temperature periodically, regardless of whether the car is driving or parked. To maximize the lifetime of the battery, as well as to minimize the current consumption, an additional acceleration sensing device is used for motion detection. Based on this information, the microcontroller will manage how often the pressure and temperature measurement is performed and transmitted via the UHF link. The supply voltage sensor monitors the battery voltage to control all internal operations and to predetermine the end of life for the wheel module. Setup and maintenance of the wheel modules are via the communication of the low frequency (LF) receiver. The UHF transmission from the wheel to the electronic central unit (ECU) takes place at 315 MHz (in USA/Japan) and

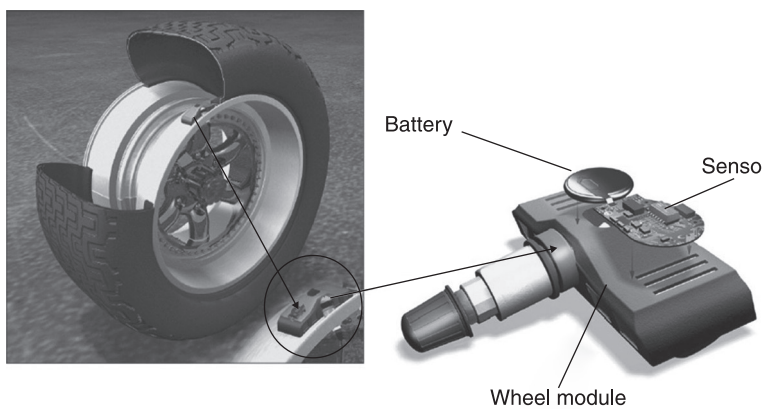

3.2 Rim-based mounting of an OEM-based TPMS module.

© Woodhead Publishing Limited, 2013

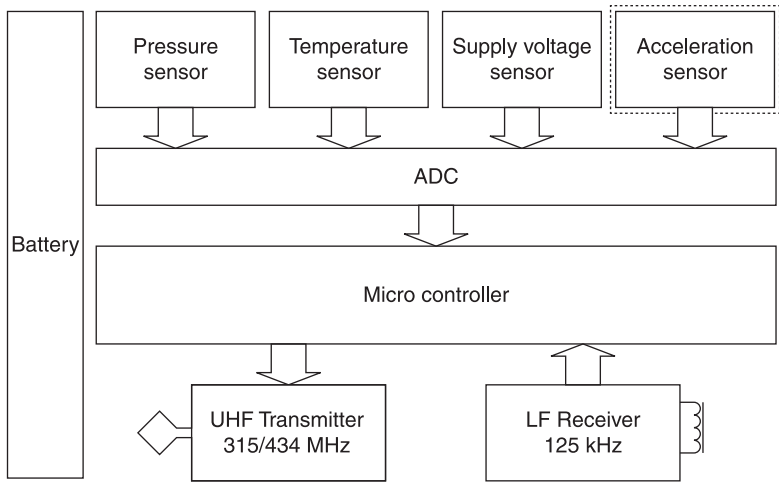

3.3 Electrical components of a battery-based TPMS module.

433.92 MHz (in Europe/Korea) with almost no exceptions (Löhndorf *et al.*, 2007b).

Systems without localization

Systems without localization provide no information about the position of the deflated tire. In the case of a pressure warning, the TPMS warning lamp is illuminated (Fig. 3.4) and the driver has to determine for himself which of the

3.4 Typical display of TPMS warning lamp for systems without localization.

© Woodhead Publishing Limited, 2013

tires is deflated. The majority of the direct systems have no localization feature, as this reduces the complexity and the costs.

Systems with localization

To determine the position of the tires, several localization methods have been developed. The most common solution uses LF transmitters. Up to four hard wired transmitters are positioned in proximity to the tires to trigger each sensor module via a special command. The sensor module responds immediately, thus the pressure information with the unique sensor ID can be mapped to the position of the LF transmitter. In such a system, a suitable display (Fig. 3.5) within the instrument cluster is required, that allows the driver to monitor the pressure for each tire and its position immediately after ignition. As multifunctional and complex driver information displays continue to grow in the marketplace and localization becomes increasingly important also for low end car platforms, cost optimized solutions have to be developed. Intelligent systems are able to reduce the number of LF transmitters or use the direction information of the sensor module in combination with the field strength information of the RF signal. The increased complexity of these systems is also driving the requirements of the sensors ICs.

3.5 Typical display of TPMS systems with localization.

3.3 MEMS-based pressure sensors and technologies

Pressure sensing was one of the first successful applications for MEMS in automotive and industrial applications. MEMS allows for cost reduction and miniaturization by integrating semiconductor electronics and tailoring or adjusting physical properties for the dedicated needs of the application environment.

In general, a MEMS pressure sensor consists of one or more pressure sensitive diaphragms or membranes and often an integrated transducer mechanism to translate the mechanical change into an electrical signal. By applying an external

© Woodhead Publishing Limited, 2013

pressure, the membrane will deflect and this deflection will be measured by various physical principles such as piezoresistive, capacitive, magneto resistive or optical means.

However, in order to provide a successful pressure sensor product, not only the MEMS process is of importance. Rather the optimal combination of a microelectronic sensor package with a reliable and robust MEMS technology for the dedicated application is necessary.

For silicon-based micromachined pressure sensors, two different manufacturing processes are used to form the pressure sensitive membrane or diaphragm, so-called bulk micromachining (BMM) and surface micromachining (SMM). Both processes have their benefits and their inherent weaknesses; depending upon which of the system approach, the sensor application, or the environment the sensor is used, one or the other technique might be preferred.

In recent years, MEMS-based pressure sensors have been widely used in the automotive industry for applications such as manifold air pressure (MAP), barometric air pressure (BAP), in-cylinder pressure measurement, oil pressure, braking pressure, fuel vapor pressure, differential pressure measurement of exhaust gas filters and safety relevant applications such as side airbag (SAB) pressure sensors and TPMS. The acceptance of MEMS-based pressure sensors from the automotive industry for all these different applications demonstrates the excellent reliability and overall quality level of these devices (Eaton and Smith, 1997; Bustillo *et al.*, 1998; Eaton *et al.*, 1998; Czarnocki and Schuster, 1999; Shaw *et al.*, 2008).

3.3.1 Bulk micromachining of sensor devices

Bulk micromachining (BMM) is the older process technology making use of single crystalline silicon. Here, chemical wet etching is still used to form structures and membranes. However, new plasma process technologies (e.g. the so-called Bosch Process) also allows for different geometries and membrane structures with almost vertical walls (Robert Bosch GmbH, 2007). The first MEMS-based pressure sensors have been developed using the KOH wet etch process to open the back side of the silicon wafer. Miniaturization of BMM structures are limited due to the size constraints given by the characteristic 54.7° angle of the anisotropic wet etching. Thus, depending on the design and membrane size, BMM pressure sensors are often larger in lateral dimensions compared to SMM sensors. However, BMM process equipment is less expensive and the process control and mechanical properties are very reliable, since the defect rate of a single crystalline silicon is small compared to polysilicon. In addition, the full wafer thickness can be used to obtain thick membranes or to use the higher mass for resonator or accelerometer structures. BMM in combination with anodic wafer bonding technologies also produces sealed cavities for absolute pressure measurements or high-Q resonators (Elwenspoek and Jansen, 1998).

© Woodhead Publishing Limited, 2013

The vast majority of BMM pressure sensors are so-called piezoresistive pressure sensors, since the diffusion or implantation of piezoresistors within the silicon membrane structure is feasible without huge effort and costs. A simple Wheatstone bridge design of the resistor elements enables a reliable measurement of the deflection of the membrane structure. However, temperature and lifetime drift effects have to be taken into account, therefore a dedicated calibration and characterization process must be performed prior to any use of the sensor in the application. Thus, a robust design and a reliable process control are of utmost importance in order to reduce calibration effort and failures during sensor operation.

Figure 3.6 shows a schematic cross-section of Infineon's bulk micromachined pressure sensor. The sensor consists of three different layers: first, an anodic bonded glass wafer to form the sealed cavity in order to allow an absolute pressure measurement, second, the silicon micro machined pressure membrane with integrated piezoresistors, and third, a second anodic bonded glass wafer to obtain an optimized pressure inlet as well as a robust design. The main benefit of such a design with a back-side opening is the improved media compatibility, because the electronic circuit is on the top side and not exposed to any media (Fischer, 2003).

Millions of these sensors have been sold into the automotive industry for TPMS within the last decade.

3.3.2 Surface micromachining of sensor devices

In contrast to BMM, SMM allows the formation of membrane structures and cavities from the front side of the silicon wafers. SMM is commonly based on thin-film deposition and sacrificial layer techniques. Thus, SMM MEMS processes

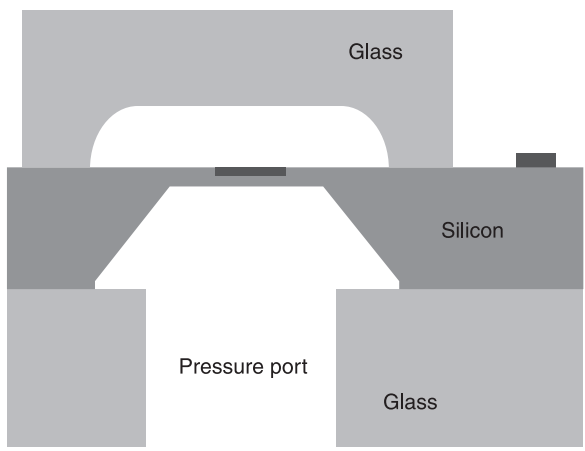

3.6 Bulk micromachined pressure sensor as triple stack.

© Woodhead Publishing Limited, 2013

can be more easily integrated into complementary metal oxide semiconductor (CMOS) technology process flow and SMM has a potential to obtain smaller sensor device dimensions. The main difficulty is the reliable etching process of the cavity structure using sacrificial layers and the (re-)formation of the membrane with excellent mechanical and electrical properties (e.g. low defect rate, high piezoresistive gauge factor and low stress).

From the beginning of SMM, polysilicon has been widely used as the material for membrane and sensor structures, as it can be well integrated into CMOS processes. Polysilicon's fair mechanical and electrical properties can be tailored over a wide range by changing the deposition technique as well as the process parameters. Usually silicon dioxide or silicon nitride, thin films are used as sacrificial layer material in combination with structural polysilicon formation. The cavity under the polysilicon membrane is mostly created by removing the sacrificial layer by a wet etch process through opening holes and finally sealed again using dedicated thin-film deposition steps. In general, piezoresistive or capacitive sensing principles are used to measure the deflection of the polysilicon membrane. Figure 3.7 shows a schematic cross-section of Infineon's BICMOS-based SMM pressure sensor (Infineon Technologies AG, 2004).

3.3.3 Detection schemes – capacitive/piezo-resistive

For MEMS-based pressure sensors, piezoresistive and capacitive detection schemes are mainly used to measure the deflection of the micromachined membrane. In piezoresistive detection, the piezoresistors are positioned onto the membrane in a full-bridge Wheatstone configuration (Fig. 3.8), in order to obtain a reliable signal without significant cross-talk.

When the bridge is fully balanced, the ratio of the resistors on the right side is identical to the ratio of the resistors on the left side; the voltage U(p) across the bridge is zero. If a small change in resistance on either side of the resistors occurs, the bridge becomes unbalanced and a voltage difference appears. Wheatstone bridges are widely used in all sorts of sensor devices, such as strain and pressure

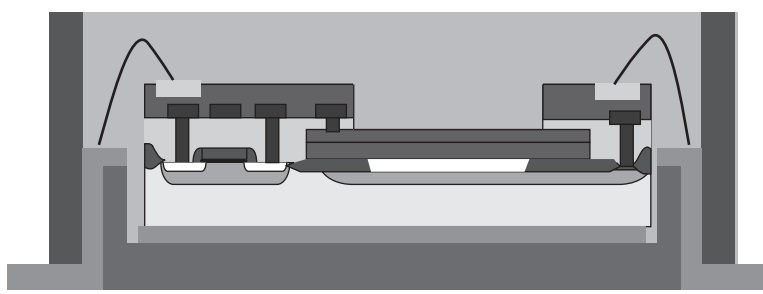

3.7 Schematic cross-section of BICMOS-based SMM pressure sensor including package.

© Woodhead Publishing Limited, 2013

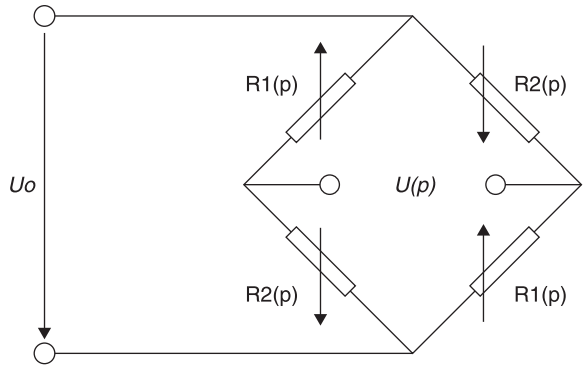

3.8 Possible piezoresistive Wheatstone bridge configuration for pressure sensors.

gauges. In this application, the resistor values are tuned in such a way that the voltage changes across the bridge are in the mV region, with a reasonable supply voltage in the range of 3 to 5 V. For the capacitive detection scheme, a similar configuration can be used. However, depending on the design and layout of the MEMS membrane, the changes in capacitance are small (e.g. pico- or femto-Farad). Thus, a fast conversion of the analog signal into a digital signal is mandatory, to reduce parasitic effects and enable a good signal-to-noise ratio (SNR). Figure 3.9 shows two variable capacitors and two similar fixed capacitors used in a Wheatstone bridge configuration. The analog voltage signal will be immediately converted into a digital signal using an analog-to-digital converter (ADC). Here, a sigma-delta ($\Sigma\Delta$) ADC has been used to convert the analog pressure signal into a digital signal.

Both piezoresistive and capacitive detection schemes have inherent advantages as well as some disadvantages. The linearization of the sensor signal might be less complex for piezoresistive sensors, since the single membrane is commonly larger

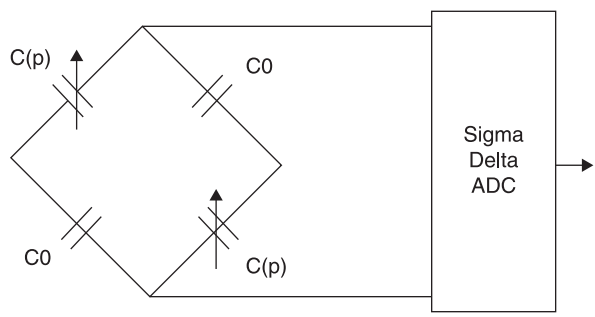

3.9 Capacitive detection scheme for pressure sensors with analog-to-digital conversion.

© Woodhead Publishing Limited, 2013

due to the required space of the piezoresistors and therefore non-linearity effects will be less pronounced. However, the resonance frequency of the larger membrane structure is lower (e.g. kHz region) and therefore the risk for production failures during the semiconductor process flow might be increased. Overall, both principles are used in commercially available products. Thus, potential risks are manageable; in the end the manufacturing costs and potential cost-down strategies are the main decision for the preferred technology.

3.3.4 Motion detection

Motion detection is a requirement for most TPMS system designs, in order to activate the system only when needed to conserve the limited energy of the battery.

In the following section, the power requirements are discussed in more detail. However, for the TPMS application, the tire pressure must be measured and transmitted to the ECU only while the vehicle is moving. Thus, a simple mechanical switch or a MEMS-based accelerometer could be used as a wake-up signal for the TPMS module. In the state-of-the-art TPMS modules, a MEMS accelerometer is used to measure the radial acceleration of the tire during the rotation. Depending upon the tire size and rim size, the threshold level must be adjusted in order to obtain the full TPMS functionality at a certain speed. Typically the acceleration threshold level is in the range of 6 to 8 g (1 g = 9.81 m/s^2). Figure 3.10 shows a monolithic MEMS integration of both the pressure membrane (front) as well as the single-axis accelerometer (back). Here, the accelerometer is designed to match the TPMS requirements and to be as robust as needed. Very high acceleration levels are known during manufacturing of the module, and mounting of the tires, as well as for severe driving conditions.

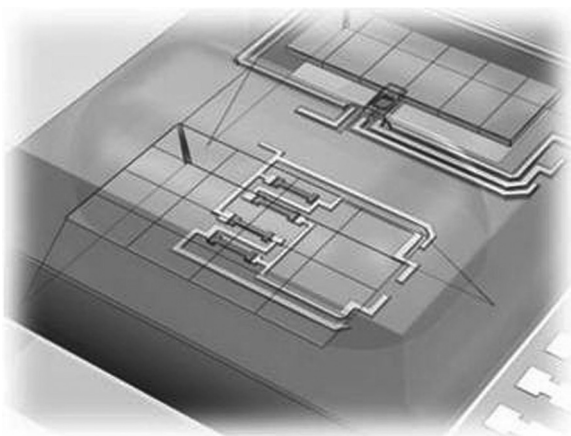

3.10 Monolithic MEMS integration of pressure membrane (front) and accelerometer (back).

© Woodhead Publishing Limited, 2013

In some TPMS applications, the accelerometer output data will also be used as part of the localization scheme, therefore different requirements are needed, such as dual-axis measurement, higher sensitivity and wider measurement range.

3.3.5 Summary

In summary, the different TPMS requirements are challenging for a MEMS sensor device in view of temperature range, accuracy, low power consumption, robustness and media compatibility. However, MEMS products are capable of handling all these requirements, even for a high volume market such as TPMS.

Bulk-MEMS pressure sensors have the advantage of the back-side opening of the pressure inlet, thus they exhibit excellent media compatibility. Surface micromachined pressure sensors often require an additional gel or glob top process to protect the wire bonds and pads from corrosion. Field failure rates are very low and well within the legal requirement and the internal Tier1/OEM targets.

3.4 TPMS requirements

The requirements for TPMS are given by the regulations and standards summarized in Fig. 1.1 in Chapter 1. For the RF link between the sensor modules and the receiver unit, the regional RF regulations (FCC, 2007; ETSI, 2010) have to be applied. Due to the fact that the LF and RF communication protocols are not regulated, the OEMs have developed their own protocols. Thus, the sensor modules from different OEMs are not compatible to each other.

3.4.1 Pressure sensor requirements

The TPMS system pressure performance is one of the most important requirements within the regulations. A breakdown from the application determines the specific MEMS pressure sensor requirements. For example, the types of vehicles applied for the regulation have a maximum weight of 4.5 t in the USA and 3.5 t in Europe. The overall weight and number of tires indirectly define the maximum pressure range. For light vehicles, this range is typically 100kPa up to 450 kPa absolute pressure. For some car platforms, even higher pressures of up to 900 kPa are required. In addition, the required accuracy of the absolute pressure is different between the regulations and standards. The new regulation in Europe has a tighter pressure accuracy requirement, since a pressure change of 20% referenced to the warm recommended inflation pressure must be obtained, in contrast to the FMVSS with 25% deflation referenced to recommended cold pressure.

Figure 3.11 shows a pressure error over temperature for a typical TPMS MEMS-based pressure sensor. In order to fulfill automotive quality requirements, the specification for the pressure sensor has to be valid for at least a 10-year

© Woodhead Publishing Limited, 2013

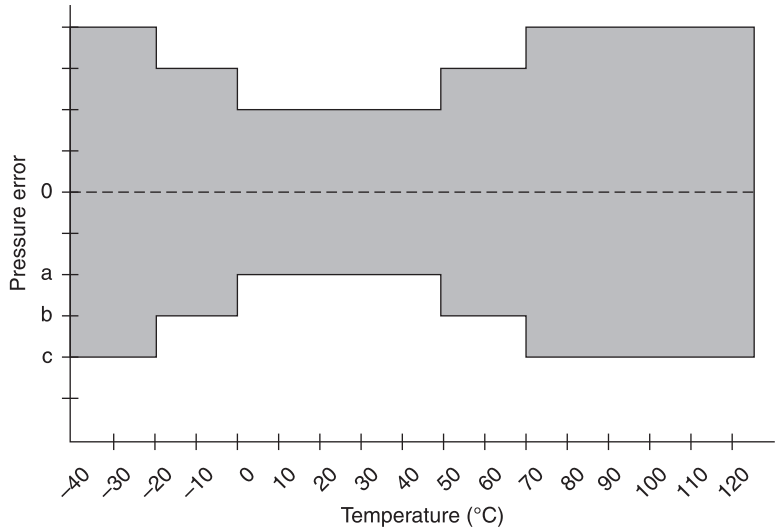

3.11 TPMS MEMs sensor pressure measurement over temperature.

lifetime of the product. Therefore, effects such as long-term drift have to be considered. The reliability of such a TPMS sensor system is tested during the qualification process, which determines the absolute maximum ratings for the sensor, such as overpressure, shock and chemical resistance.

3.4.2 Standards and protocols

Primarily two frequency bands for the RF communication of TPMS modules are used: either 315 MHz in USA/Japan or 434 MHz in Europe/Korea. These frequency bands are regulated by the following regional standards:

- USA: FCC (FCC, 2007);
- Europe: ETSI (ETSI, 2010);
- Japan: ARIB (ARIB, 2007);
- Korea: MIC (MIC, 2007).

These standards specify the requirements for the maximum allowed output power, harmonics and spurious emissions according to the band used. In addition, the standards for Korea and Japan specify an Occupied Bandwidth (OBW). The OBW defines the frequency band with 95% of the energy from the signal. At higher data rates (>10 kbit/s), and especially for Amplitude Shift Keying (ASK) modulation scheme, this requirement is difficult to achieve with a low-cost implementation.

Since the protocol is not part of the regional standards, the OEMs have defined their own protocols in the past. An easy exchange of different TPMS modules is

© Woodhead Publishing Limited, 2013

not possible, thus the effort for logistics for the supply chain is rather complicated. Therefore the German OEMs have initiated a working group to define a common TPMS protocol. This protocol includes a RF data rate of 19.2 kbit/s and is foreseen to be applied for the EU regulation starting from 2012.

3.4.3 Lifetime requirements versus current consumption

As mentioned earlier, the typically required lifetime of a TPMS module is 10 years. There is no reasonable size coin cell battery that could provide enough energy to power the TPMS system continuously for 10 years. Effective energy management allows maximization of the life of the battery as well as minimizing the current consumption (Löhndorf *et al.*, 2007a). The required battery capacity strongly depends on the application program, temperature profile, transmission power level and ASIC specifications. As an example, the average driving time of a privately owned light vehicle is less than 5% of the total 10-year lifetime.

During transmission mode, the highest current consumption occurs, therefore the data rate is very important for the lifetime of the battery. Within the TPMS application there is a trend toward higher data rates to allow the usage of smaller size batteries. Usually coin cells of the type 2450 (24 mm diameter and 5 mm height) with a battery capacity of about 450 to 600 mAh are utilized within commercial TPMS systems, to fulfill the requirements. In the future, coin cells of the type 2050 or even type 2032 with a battery capacity of about 250 to 350 mAh are targeted.

3.5 Power management

3.5.1 Battery lifetime model introduction

Effective power management is the key in the TPMS application, to reduce power consumption and allow the usage of smaller battery types. The energy consumption determines the size, weight and cost of the battery and therefore a significant part of the overall cost of the TPMS wheel module. As mentioned earlier, higher RF transmission data rates help to reduce the energy consumption, but in addition special low power circuits within the TPMS ASIC are required to achieve this target. Depending on the application program, an analysis of the current consumption will help to understand the consumption of each circuit block. Figure 3.12 shows the typical share of the energy consumption over the lifetime for a typical application with motion detection and no LF localization feature. Here, the peak RF transmission power level is assumed to be 5 dBm. The three main contributors to the overall current consumption are RF transmission, LF receiver and power down current. A more detailed analysis of these specific modes will be discussed in the following sections.

© Woodhead Publishing Limited, 2013

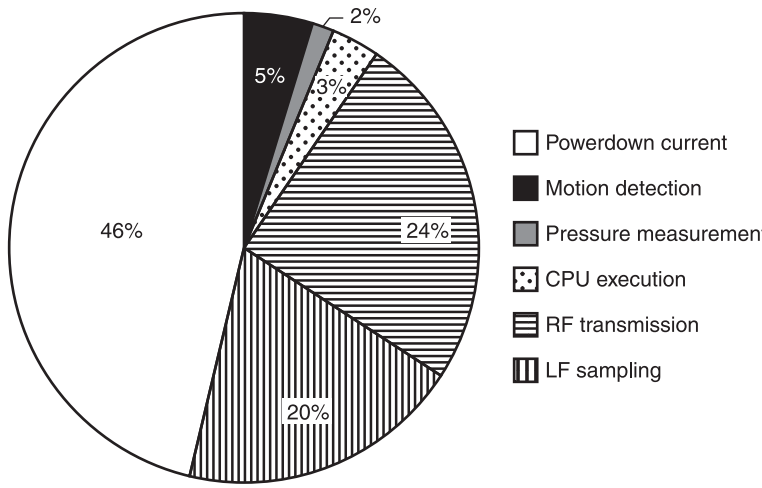

3.12 Typical share of the energy consumption over lifetime of a TPMS module.

3.5.2 Radio frequency (RF) transmission and protocol

The ECU controller is updated with the latest sensor information by periodic transmissions while the vehicle is in motion. The RF transmitter modulates the data provided by the sensor, amplifies the signal and sends it out via the RF antenna. Usually the RF transmitter is integrated into the TPMS ASIC, which allows smaller modules and better cost efficiency. The trend to reduce the size and weight of the TPMS modules drives the use of smaller battery types and therefore the need to reduce the overall current consumption of the RF transmitter. Here, the main challenge is to reduce the peak current, as smaller batteries have not only a smaller energy capacity, but also a higher internal resistance. To minimize the energy budget, higher data rates are utilized to shorten the transmission time significantly.

Table 3.2 shows a typical datagram of a current TPMS module. In order to allow the receiver in the body controller to learn which wheel modules belong to its system, a 32-bit unique identification number (ID) is provided. Pressure, temperature and diagnostic data are monitored. There are ideas to reduce the length of the datagram and in turn to save power. The basic idea of such a reduced smart datagram is to transmit only the ID as long as the overall pressure difference is zero. Thus, the pressure has to be measured on a regular basis and be compared with the stored previous values. Although the duration time of the application program, and as a consequence the CPU execution current, is increased, this approach improves transmission efficiency by a minimum of 3 bytes and thus approximately 25% of energy (Löhndorf *et al.*, 2007a).

© Woodhead Publishing Limited, 2013

Table 3.2 Typical RF datagram of current TPMS module

Byte	Description	Comments
1	Synchronization	Synchronization bytes for the receiver
2	Synchronization	
3	Identification ID3	Unique 32 bit ID number
4	Identification ID2	
5	Identification ID1	
6	Identification ID0	
7	Pressure	Pressure value
8	Temperature	Temperature value
9	Diagnostics	Status information
10	Check sum	CRC
11	End of message	1–2 bits

3.5.3 Low frequency (LF) receiver and protocol

In applications without LF localization, the LF receiver is used basically only during manufacturing and servicing. However, to allow a permanent communication, the LF receiver is turned on and off in a defined interval for the complete lifetime of the module to poll for the incoming datagram. The 125 kHz frequency allows the implementation of ultra low power receiver circuits. In order to minimize the current consumption even further, the right tradeoff between sensitivity, interferer stability and on/off polling must be found by the application. Figure 3.13 shows a typical datagram used for LF communication: during the on-time of the LF receiver, incoming datagram with correct sync pattern and wake-up ID are accepted. The payload counts typically two to five Manchester encoded data bytes. The datagram is transmitted with a data rate of about 3.9 kbit/s.

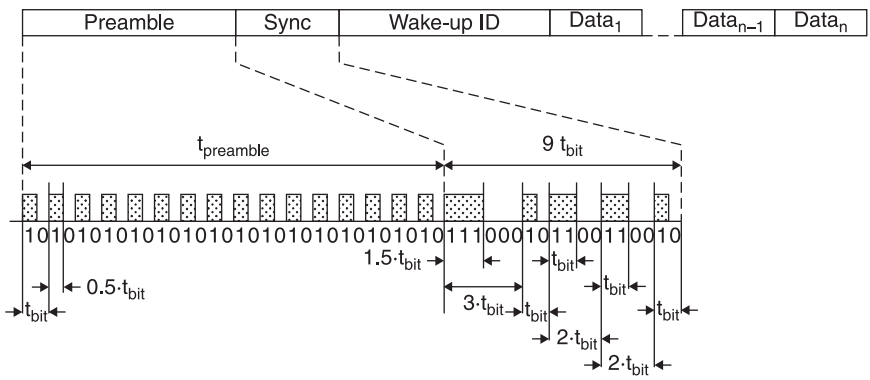

3.13 Typical LF datagram format of current TPMS module.

© Woodhead Publishing Limited, 2013

During datagram reception of the current, consumption is only slightly increased compared to an on-cycle; such higher data rates would not help to further reduce the energy budget of the LF Receiver.

3.5.4 Power down

By using the motion detection, which allows distinguishing between parking and driving, the TPMS system is in power-down mode more than 99% of the time. However, the power-down or standby current consumes approximately one-third of the overall battery capacity. During power-down, only a few parts of the TPMS system are active and the rest are switched off. Figure 3.14 shows a block diagram of the active (marked light gray) and inactive (marked dark gray) peripherals. The main current draw can be attributed to leakage currents within the ASIC itself. In general, the smaller the CMOS structures, the higher the contribution of the leakage current. Also, in the high temperature range, the leakage current increases dramatically. System integration and the need for low RF peak currents force the ASIC development to utilize smaller CMOS structures. However, utilizing smaller battery types requires reducing the power down current further, in order to keep the same lifetime of the wheel module. Therefore, several developments and technologies are explored to reduce the leakage currents.

To improve the situation with CMOS technology, several power domains have to be built into the ASIC architecture. In power-down mode, power switches are

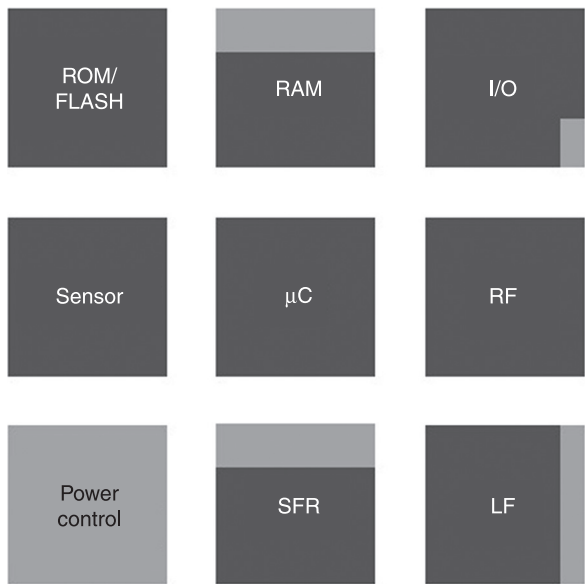

3.14 Active (light grey)and Inactive parts (dark grey) of a TPM sensor during power down mode.

© Woodhead Publishing Limited, 2013

used to cut off the power supply for all unused domains. Another solution could be to switch from bulk wafer to silicon on insulator wafer. The key advantage of this so-called SOI wafer technology is the improved isolation of the SOI area from the substrate.

3.5.5 Energy harvesting

To overcome the limitations of the battery capacity and the associated size and weight of a Li-Ion battery for the TPMS application, the use of Energy Harvesting Schemes have been discussed in recent years. A rotating tire is an inherent source of energy, thus vibration, thermal or rotational energy could be used for an energy harvesting concept (Roundy *et al.*, 2003). However, state-of-the-art TPMS systems allow an immediate read-out of the tire pressure, even at zero velocity. Therefore, a direct replacement of the battery with only an energy harvester is not sufficient. A successful replacement of the battery must consist of an energy harvester, an energy storage device and an efficient converter, in order to power the sensor IC under all conditions. In addition, the current consumption of the sensor ICs must be greatly reduced.

The reduction of current losses due to leakage and power-down is a focus topic of ongoing developments at TPMS IC suppliers. However, increasing transmission rates and optimization of the transmission boot routine and transmission power level will require a general change of the quasi-standard for RF transmission for TPMS, in view of transmission frequency and data protocols. Implementation of 100 kbit/sec transmission rates or higher, with further optimization, could reduce the average power consumption for each datagram to approximately 5–10 μWs (Löhndorf *et al.*, 2007a) Fig. 3.15 shows a TPMS demonstrator working at

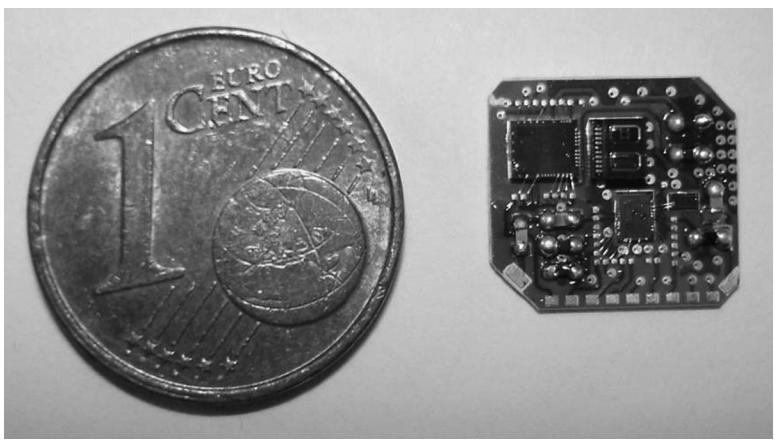

3.15 Top view of a 2.4 GHz TPMS demonstrator PCB (right side) with 1 Euro Cent coin for size comparison.

© Woodhead Publishing Limited, 2013

2.4 GHz. This small-sized demonstrator includes the MEMS pressure and acceleration sensor, the μC ASIC, the 2.4 GHz transceiver ASIC and the bulk-acoustic wave (BAW) based resonator. Not included is the energy harvesting circuit and the RF antenna (Flatscher *et al.*, 2010).

A more detailed block diagram is shown in Fig. 3.16. The gray shaded blocks are included in the PCB demonstrator. For the TPMS application, various energy harvesting concepts have been discussed, to make use of the inherent energy of a rotating tire (e.g. deformation of the tire, vibrations or acceleration variations). However, most concepts are based on so-called vibration energy harvesters. Here, the mechanical vibrations are coupled to a mechanical-to-electrical transducer, in order to generate the required power for the TPMS IC. In general, piezoelectric, capacitive or electromagnetic transducer mechanisms can be used for the mechanical energy conversion.

At the present time, most TPMS modules are mounted on the rim or at the valve stem of the tire. At this position, vibration harvesters could use the rotational energy or the changes of the gravitation (±1 g) at every revolution. For future TPMS systems, the integration of the modules into the rubber tire has been discussed, in order to combine the pressure surveillance with an increase of the functionality for vehicle stability systems (e.g. load distribution, friction estimation, etc.). But at the tire maximum, acceleration peaks of 4000 to 5000 g must be taken into account for the MEMS design, in order to fulfill the lifetime and automotive quality requirements. In general, the amount of harvested power is dependent upon the proof mass and the efficiency of conversion.

A vibration energy harvester mounted on the inside of a car tire at the so-called inner liner position is subject to acceleration in all three directions. The major accelerations are in the radial and the tangential directions, which are both

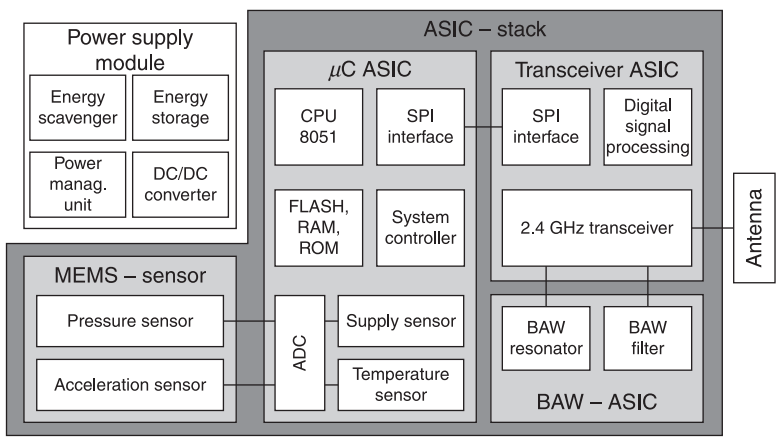

3.16 Block diagram of the 2.4 GHz demonstrator (only gray shaded areas are included on PCB).

© Woodhead Publishing Limited, 2013

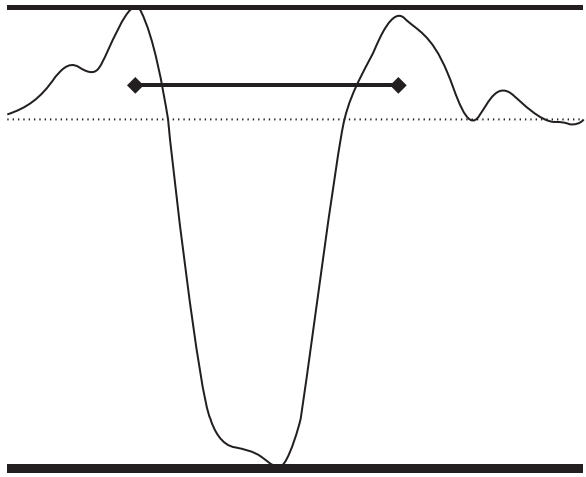

3.17 Filtered measurement data of the *z*-axis acceleration signal at the inner liner for the contact area. Dashed line indicates the level of the average rotational acceleration. Black bar shows the distance between leading and trailing edge and defines the contact area between ground and tire.

dominated by the revolution of the tire. The acceleration shows a characteristic signature (Fig. 3.17) when the part of the tire where the device is mounted hits or leaves the ground. These positions are known as the leading and trailing edges, defining the contact area of the tire with the road. However, other factors, such as surface roughness of the road, fluctuations in driving speed and the dynamics of the tire, contribute to the acceleration signal (Apollo Project, 2001). Measurements of the power density spectrum (PDS) at the inner liner position have shown that a successful vibration harvester concept must be sensitive to a wide range of frequencies between 5 and 1 kHz. Thus, increasing the average power level by making use of a resonant energy harvesting concept is not feasible for TPMS application.

The overall harvested energy is directly correlated to the proof mass and to the power loss due to conversion. To make use of the radial accelerations, the harvester device will need a proof mass with a motion out-of-plane, whereas for tangential accelerations, an in-plane proof mass motion is required. Figure 3.18 shows a schematic cross-section of an electrostatic vibration harvester with in-plane motion (Halvorsen, 2008; Halvorsen *et al.*, 2009). The first silicon device utilizes high aspect ratio micromachined springs, mechanical stoppers and a proof mass size of 5.4 × 6 mm (Fig. 3.19). Simulations with a total proof mass of 1.5 × 10 to 5 kg with the dimensions of 4× 4 × 400 μm and the silicon density of 2.33 g/cm^3, have shown that for a velocity of 25 km/h the average output power of this device was in the order of 3 μW, whereas for a velocity of 50 km/h the power was 8.5 μW.

© Woodhead Publishing Limited, 2013

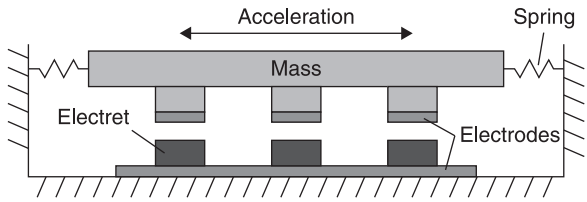

3.18 Schematic cross-section of an electrostatic vibration harvester with in-plane motion.

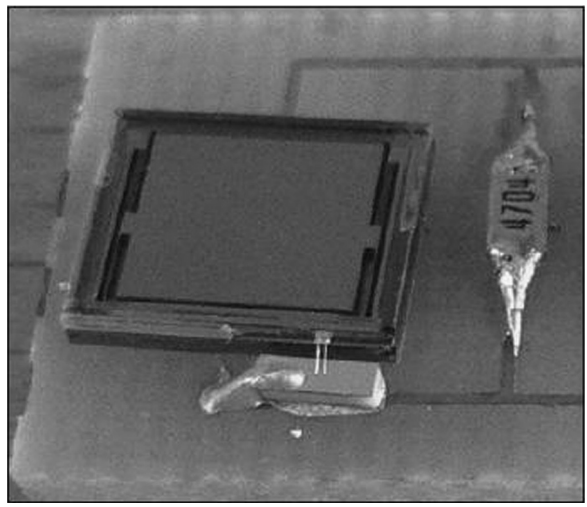

3.19 View of vibration energy harvester mounted on test PCB with load resistor.

Thus, the harvested average output power from tangential accelerations might be in the range of 3 to 5 μW and therefore feasible for sending an optimized TPMS protocol. However, no series production of TPMS utilizing energy harvesters has been seen so far. Several technical challenges as well as cost targets must be met before energy harvesters will replace the standard coin cell battery.

3.6 Future TPMS applications

3.6.1 Commodity – reduction of system costs

With the mandatory legal regulation of TPMS in the US market and the issued European regulation mandatory for all new vehicles in 2014, TPMS has become a commodity product. Thus, the car manufactures cannot sell TPMS as an additional high margin supplement; rather they are necessary to fulfill legal

© Woodhead Publishing Limited, 2013

requirements. Therefore, the additional systems costs for implementation in standard cars must be as small as possible. Strong annual system cost reduction at the IC, module and system levels are expected.

In order to reduce the systems costs, all parts of TPMS systems are under constant cost-down evaluation:

- integration of TPMS RF receiver with RF Remote Keyless functionality;
- reduction of auto localization costs;
- smaller TPMS modules with smaller battery size;
- lower cost valve designs;
- combination or reuse with ABS/ESC infrastructure.

Besides the cost reduction, future TPMS systems might also migrate into the rubber tire. TPMS for trucks, which will be attached to the inner liner of the tire, are currently being developed. Several TPMS providers are working on solutions in the direction of the so-called 'intelligent tire', where, besides the pressure signal, additional parameters such as load detection and tire wear are provided.

3.6.2 Integration into the tire

As discussed in the previous section, TPMS providers are currently working on in-tire solutions for truck applications based on battery powered sensors. For truck tires, the weight limitations for additional parts are not as strict as for light vehicles. For light vehicles, the weight limitation is a maximum of 10 g, otherwise the localized weight cannot be compensated and vibrations will occur. The weight of a typical TPMS module is in the order of 20 to 40 g, thus smaller batteries or new power sources must be used in order to fulfill these requirements.

For the integration of the TPMS electronics with the tire, several known requirements must be met:

- maximum weight for the complete module is in the range of maximum of 10 g;
- shock robustness against high acceleration forces of up to 4000 g;
- reliable integration process of module with the tire.

However, major benefits must be realized in order to switch the established TPMS value and logistics chain for light vehicles into this direction. The additional parameters, which might be obtained from integrated TPMS modules, are:

- measurement of the load condition of individual tire;
- ID number of tire for logistics tracking;
- revolution counter/condition of tire wear;
- increased information about the friction coefficient;
- tire temperature.

© Woodhead Publishing Limited, 2013

3.7 Conclusion

The implementation of TPMS systems into new light vehicles is increasing because of mandatory legal regulations. Most of these regulations allow for different technologies, but direct TPMS systems are superior due to improved pressure accuracy and detection time. However, indirect TPMS might gain a market share due to overall lower system costs. MEMS-based pressure sensors are commonly used in this application; in addition, one- and two-axis accelerometers are implemented, to allow motion detection as well as a localization of the individual TPMS module. Since direct TPMS systems are wireless sensor systems, a local power source is needed. So far, Li-ion batteries are used, but in order to increase the overall lifetime, energy harvesting concepts are discussed. Using mechanical vibrations from the tire might be feasible, but for MEMS-based harvesters, several challenges must still be solved prior to successful implementation. The integration of TPMS into the tire for light vehicles is under evaluation; however, major benefits in cost position, feature set and standardization must be realized before a significant number of r/m based TPMS will be replaced.

3.8 References

Apollo Project (2001), *Intelligent Tyre for Accident-free Traffic*. Available from: http://virtual.vtt.fi/virtual/proj3/apollo/deliverables/apollo_final%20report.pdf (accessed 17 June 2011).

ARIB (2007), *Telecontrol and Data Transmission Radio Equipment for Specified Low Power Radio Station*, Standard T93, 315 MHz-Band Telemeter, Japan, Association of Radio Industries and Businesses.

Bustillo J M, Howe R T and Muller R S (1998), 'Surface micromachining for micro-electro mechanical systems', *Proc IEEE*, 86(8), 1552–1574.

Czarnocki W S and Schuster J P (1999), *The Evolution of Automotive Pressure Sensors*. Available from: http://www.sensorsmag.com/sensors/pressure/the-evolution-automotive-pressure-sensors-844 (accessed 17 June 2011).

Eaton W P and Smith J H (1997), 'Micro machined pressure sensors: review and recent developments', *Smart Mater Struct*, 6, 530–539.

Eaton W P, Smith J H, Monk D J, Brien G O and Miller T F (1998), 'Comparison of bulk- and surface micromachined pressure sensors', *Proc SPIE*, 3514, 431.

ECE, UN/ECE (2010), *Regulation No 64 of the Economic Commission for Europe of the United Nations (UN/ECE) – Uniform provisions concerning the approval of vehicles with regard to their equipment which may include: a temporary-use spare unit, run-flat tyres and/or a run-flat system, and/or a tyre pressure monitoring,* Regulation 64 of the Inland Transport Committee, Geneva, UN/ECE.

Elwenspoek E and Jansen H (1998), *Silicon Micromachining*, Cambridge UK: Cambridge University Press.

ETSI (2010), *Electromagnetic compatibility and Radio spectrum Matters (ERM); Short Range Devices (SRD); Radio equipment to be used in the 25 MHz to 1000 MHz frequency range with power levels ranging up to 500 mW; Part 1: Technical characteristics and test methods*, standard EN 300 220–1 V2.3.1, France: European Telecommunications Standards Institute.

© Woodhead Publishing Limited, 2013

FCC (2007), *Design Requirements for Short Range Transmitters*, Title 47 of the Code of Federal Regulations, Part 15: Radio Frequency Devices, USA: Federal Communications Commission.

Fischer M (2003), *Tire Pressure Monitoring*, vol. 243, Die Bibliothek der Technik, Verlag Moderne Industries.

Flatscher M, Dielacher M, Lentsch T, Matischek R, Prainsack J, *et al.* (2010), 'Bulk acoustic wave (BAW) based transceiver for an in-tire-pressure monitoring sensor node', *J Solid States Circ*, 45(1). IEEE.

Halvorsen E (2008), 'Energy harvesters driven by broadband random vibrations', *J Microelect Syst*, 17, 1061.

Halvorsen E, Westby E R, Husa S, Vogl A, Østbø, N P, *et al.* (2009), 'An electrostatic energy harvester with electret bias', *Proc Transducers*, 1381, 1381–1384.

Infineon Technologies AG (2004), *Halbleiter*. Munich: Publicis Corporate Publishing, pp. 235–242.

ISO (2006), *Road Vehicles – Safety enhancement in conjunction with the tyre inflation pressure monitoring*, Standard 21750 of the International Organization for Standardization, Geneva: ISO.

Löhndorf M, Kvisteroey T and Lange T (2007a), *Intelligent low-power management and concepts for battery-less direct Tire Pressure Monitoring Systems (TPMS)*, Advanced Microsystems for Automotive Applications (AMAA), Berlin: Springer.

Löhndorf M, Kvisteroey T, Westby E and Halvorsen E (2007b), *Evaluation of Energy Harvesting Concepts for Tire Pressure Monitoring Systems*, Proceedings of Power MEMS, Munich.

MIC (2007), *Ordinances and Technical Standards for Radio Waves*; Notice No. 2007–63, Part 13: Technical Standards for Radio Equipments, Radio Research Laboratory, Korea: Ministry of Information and Communication.

NHTSA (2005), *Federal Motor Vehicle Safety Standards; Tire Pressure Monitoring Systems; Controls and Displays*, docket no. NHTSA 2000–8572 of the National Highway Traffic Safety Administration, USA: Department of Transportation.

Robert Bosch GmbH (2007), *Autoelektrik/Autoelektronik*. Vieweg, pp. 324–326.

Roundy S, Wright P K and Rabaey J (2003), 'A study of low level vibrations as a power source for wireless sensor nodes', *Comp Comm*, 26, 1131–1144.

Shaw M, Ziglioli F, Combi C and Baldo L (2008), 'Package design of pressure sensors for high volume consumer applications', *IEEE Electronic Components and Technology Conference*, IEEE, pp. 834–840.

© Woodhead Publishing Limited, 2013

4

MEMS pressure and flow sensors for automotive engine management and aerospace applications

D. SPARKS, Hanking Electronics Ltd, China

DOI: 10.1533/9780857096487.1.78

Abstract: Micromachined pressure and flow sensors for automotive and aerospace applications are covered in this chapter. MEMS design, fabrication and packaging are explored for these applications. Both new and developing MEMS sensors for high temperature, high pressure subsystems and related fuel quality sensors are included in this review.

Key words: pressure sensor, flow sensor, MEMS, fuel quality.

4.1 Sensors used in system and engine management

MEMS related, automotive sensor-based engine management started in 1979 in an effort to reduce tailpipe emissions (Eddy and Sparks, 1998). A microprocessor-based engine control module was utilized to control the air-to-fuel ratio fixed at the stoichiometric point. In this manner, the catalytic converter can effectively reduce the amount of unburned fuel. This new technology enabled the automobile companies to comply with new government mandates associated with automotive pollution control and fuel efficiencies. The engine control module in these new systems could not operate effectively without sensors providing feedback. Both air input and exhaust output sensors were needed. Stabilized zirconia oxygen sensors were employed in the exhaust. These electroceramic sensors have to be heated to above 400°C to allow for mobile ion transport and provide accurate oxygen concentration data. The hot exhaust provides the heat source for the sensor. At the engine inlet, two types of sensing approaches were undertaken: direct mass air flow measurement and indirect air flow measurement using air density plus temperature measurements. Figure 4.1 shows examples of both a hot-wire mass air flow (MAF) sensor (top) and a manifold absolute pressure (MAP) sensor (bottom). The platinum hot-wire (Fig. 4.1) of these early models extends across the entire length of the air intake hose. The black plastic packaged MAP sensor (Fig. 4.1), has generally been a piezoresistive pressure sensor, although capacitive pressure sensors have been utilized in a few cases. The MAP sensor diaphragm is sealed above a vacuum (absolute) reference microcavity. The pressure sensor is connected to the air intake line via a plastic port built into the sensor package and a tube. By estimating air density, the MAP sensor is used to infer mass air flow into the engine.

The initial MAF sensors were larger, used platinum wires and so were more expensive than the smaller MEMS-based MAP sensors. By using the air pressure

© Woodhead Publishing Limited, 2013

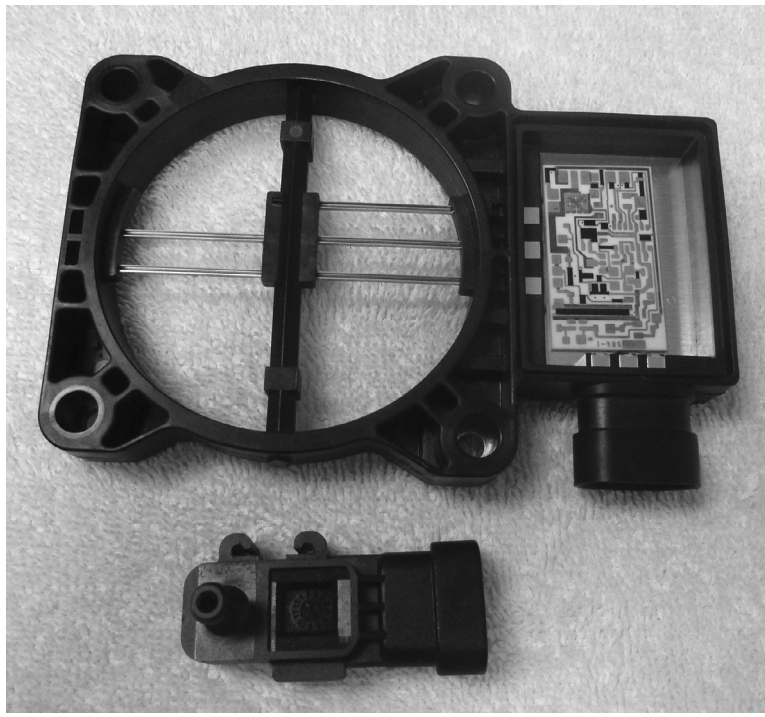

4.1 An automotive MAF (top) and MAP sensor (bottom).

and temperature along with engine speed, a good estimate of the mass air flow into the engine could be obtained. The MAP sensors used micromachined silicon pressure sensors, one of the first high-volume applications for these MEMS devices. The size and cost advantage resulted in millions of these sensors being produced annually in short order.

Other pressure sensors found their way into the automobile over the years to improve engine function. Silicon pressure sensors are employed to measure barometric pressure, exhaust gas pressure and the pressure of turbochargers. Barometric absolute pressure (BAP) sensors are used in vehicles that rely on direct mass airflow measurements primarily for altitude compensation (Czarnocki and Schuster, 1999). The same piezoresistive pressure sensors used in MAP applications are also used in closed-loop exhaust gas recirculation (EGR) systems. The pressure sensors assist in controlling the EGR flow, sending a portion of the exhaust gas to the engine cylinder. In spark controlled combustion engines, the exhaust gas displaces some of the combustible material, which is used to reduce NO_x emissions. While this does reduce the combustion rate, spark timing is adjusted to compensate. In diesel engines, the EGR system uses the exhaust gas to replace excess oxygen in the pre-combustion mix. Turbochargers use an exhaust

© Woodhead Publishing Limited, 2013

gas driven turbine to increase the pressure of air entering the engine, to create more power and overcome problems with driving at high altitudes, so also require a pressure sensor.

In addition to absolute pressure sensors and flow sensors, differential pressure sensors are employed in vehicles. Highly sensitive differential piezoresistive pressure sensors are used extensively to detect leaks in fuel systems to reduce evaporative emissions of gasoline. Silicon and in some cases ceramic or stainless steel pressure sensors, most often differential (Yamazaki *et al.*, 1985; Dunbar and Sagar, 2000; Sippola and Ahn, 2006) have been used to measure oil, transmission, hydraulic, cylinder, coolant and brake lines.

While many first-generation automotive and aerospace sensors will not use MEMS technology, high volume cost pressures often force a changeover to MEMS devices in subsequent generations. MEMS offer smaller size, lower weight, often higher reliability and fewer discrete subcomponents. Using silicon wafer fabrication techniques enables thousands of sensors to be produced in each manufacturing lot, and in some cases on each wafer. This drives down the cost of the sensing elements and is the main reason why the MEMS technology often prevails in the marketplace.

4.1.1 Automotive and aircraft sensor networks

MEMS sensors are increasingly being used as part of a vehicle-wide sensor bus network (Sparks *et al.*, 1999). System-wide multiplexing in automobiles began in the 1980s, initially for simple diagnostics but then to reduce wire harness cost and weight. Eventually the benefits to reducing subsystem costs by sharing sensor and actuator data between engine, braking, transmission and safety systems accelerated the use of in-vehicle networks for automobiles, trucks and aircraft. The various automobile manufacturers began with slower serial bus protocols such as VAN (vehicle area network), J1850 and ISO 9141-2. Many automotive manufacturers migrated to the CAN (controller area network) protocol, which is used in many other industries. Customized CAN chips are commonly integrated into sensing and actuating systems. Aircraft control systems also use CAN, as well as time triggered protocol (TTP) and avionic full-duplex (AFDX), ARINC 429 and 664 (Aeronautical Radio Incorporated) and MIL-STD-1553 multiplexing protocols (Glass, 2007). Sensor module designers for automotive and aircraft must take this digital output mode into consideration.

Access to the network can be obtained by providing a sensor, a processor, protocol controller and transceiver. These additional electronics can be provided by several ICs or a single network chip. While this raises the cost of the sensor, now a sensor node on the bus, it enables other subsystems to utilize the sensor data, potentially lowering the overall system cost.

As an example, a braking system algorithm may require information from a steering wheel position sensor, brake fluid pressure sensors, angular rate

© Woodhead Publishing Limited, 2013

(gyroscope) sensors and wheel speed sensors (Sparks *et al.*, 1997). This sensor data is used to assist the driver in maintaining control under icy road conditions. The sensor data may be employed by other systems, such as navigation, adaptive cruise control, air bag deployment and tire pressure monitoring modules. The number of sensors in an automobile can exceed 50 to 60, which adds to the cost of the product. Aircraft use a variety of sensors, such as hydraulic pressure sensors, temperature sensors and level sensors. By making the data of one sensor available to multiple subsystems, both cost and weight can be reduced. Central multi-sensor modules have been used to more efficiently utilize a vehicle-wide databus and eliminate redundant sensors (Sparks *et al.*, 1999).

The term 'virtual sensor' is often used to describe a subsystem that is using the sensor databus to help control the performance of the subsystem. This parameter may have utilized a separate sensor in older vehicle models, but is now sensor-free because of data obtained from the system network bus. Barometric pressure can be used in aircraft for altitude measurement, to improve engine performance and enhance cabin comfort. In some cases, direct sensing data is not used, but a parameter is inferred from information and an algorithm. Of course, this type of virtual sensor using inferred data is not as accurate as a direct measurement, but it is less expensive. For example, tire inflation has been inferred using tire speed comparison, although a more expensive pressure sensor in each tire would provide a more accurate assessment of tire pressure. At the system level, the cost to performance trade off must be taken into account, to justify the use of direct sensor measurement or employing a virtual sensor.

4.2 The MEMS design process

A new MEMS design generally starts with finite element modeling of active elements (Sparks *et al.*, 2000). For pressure sensors, the diaphragm deflection as a function of pressure is key, as is the location of stress maxima. Flow sensors most often use mechanical modeling as well as computational fluid dynamics (CFD).

Design rules that are generated from a fully characterized process are important for quick, successful development of a microsensor. Special test structures that examine the yield of the linewidths and lateral and vertical spacings between traces of the same layer and other relevant layers are needed. For example, the spacing between parallel metal traces, often concentric circles or squares as well as long meandering traces, is varied and then tested for electrical shorts. For multilayered conductors, meandering or serpentine traces will be run under and over other layers, such as polysilicon and metal layers. Again these structures will be tested for short circuits or open circuits. Open circuits denote that the design linewidth is too narrow for the process. Short circuits may indicate that the spacing rule is too aggressive, that the dielectric layer is too thin or that better planarization is needed for the process. These types of test structures have been used for decades with integrated circuits (ICs) and adapted by MEMS processes. New test structures

© Woodhead Publishing Limited, 2013

are required for MEMS processes due to the unique features of micromachined structures and surface topographies. The process capabilities of each step and layer of the MEMS process and how it affects the electrical and mechanical structure must be fully understood and layer dimensions adjusted to maximize yield, reliability and device performance.

The same test structures, or a simplified version of these test structures that were used to characterize a process, are also used to monitor the process during manufacturing. Electrical test structures for short circuits, open circuits, resistances and active device parameters will be placed in saw streets on the wafers or located on a few select places across a wafer. These devices can be tested during processing to ensure the quality of the wafer and/or tested at the completion of wafer processing. Correlation between the test device results and the actual device performance can be used to reject or accept an entire wafer. The test results will also be used to adjust the wafer fabrication process to optimize the yield. With both finite element modeling and process based design rules and alignment keys between levels, the MEMS mask design can now be generated.

4.2.1 MEMS fabrication

Silicon fabrication steps that are most often used with pressure and flow sensors include wet and dry silicon etching, wafer-to-wafer bonding and the standard processing steps used with both ICs and MEMS wafers.

The traditional planar IC fabrication steps often used by MEMS sensors include thermal oxidation, dopant diffusion, photolithography, chemical vapor deposition (CVD) of insulating oxide and nitride films, as well as doped polysilicon films and oxide etching and metallization (Wolfe and Tauber, 1986).

The unique MEMS processes include those that produce 3-D structures. Pressure sensors and many thermal-based flow sensors use thinned diaphragms. For pressure sensors, these diaphragms flex in response to pressure, while for thermal sensors they are thinned to reduce heat loss. Wafer-to-wafer bonding is employed to form a reference vacuum behind the diaphragm of an absolute pressure sensor. Bonding is also used to better mechanically or thermally isolate the active sensing elements from the package. The most common wafer bonding processes used in pressure and flow sensors include anodic, fusion and reflowed glass bonding, although other bonding methods, such as eutectic and solder bonding, have been used (Albaugh, 1991; Schmidt, 1998; Sparks *et al.*, 2001). Anodic bonding requires both high temperature (300–450°C) and an applied voltage to move sodium ions in the borosilicate glass. Silicon-to-silicon fusion bonding requires very flat surfaces and often high temperature annealing (>900°C). The glass reflow process uses a lead borosilicate glass that melts at around 400°C.

Wet silicon etching with ethylene diamine pyrocatechol (EDP), potassium hydroxide (KOH) and tetramethylammonium hydroxide (TMAH) is used to form diaphragms. Etch stops, such as highly doped P-type silicon or a buried oxide

© Woodhead Publishing Limited, 2013

layer, are often used to control the thickness of the diaphragm. The wet etch rate varies according to the crystallographic orientation of the silicon. This crystallographic etch rate dependence results in angled sidewalls. Deep reactive ion etching (DRIE) or plasma etching is used to produce vertical sidewalls. This is accomplished by an alternating etch/deposit process, which passivates the sidewalls while etching vertically into the silicon.

Figure 4.2 shows an abbreviated process flow example for a piezoresistive absolute pressure sensor (Tufte and Long, 1962; Shankland, 1991; Baney *et al.*, 1997). The basic steps are similar for many MEMS devices. The process starts with a (100) oriented silicon wafer that is polished on both sides, allowing for patterning of the front and back, which is a unique requirement for MEMS wafers versus traditional IC wafers. The wafer is oxidized to form an etch mask and eventually patterns the diffused silicon resistors that form the Wheatstone bridge. Photoresist is used to mask the areas for the resistors. Boron ions are implanted into the silicon, generally through a thin oxide layer. The boron implant is thermally activated and diffused into the silicon. Next, a mask for the contacts between the P-type silicon resistors and metal runners are opened up using photolithography and hydrofluoric acid etching. A metal layer is sputtered or evaporated onto the wafer and then another mask is used to pattern the metal layer. A CVD passivation layer, such as silicon oxide or nitride, is then applied to cover the metal runners. Next, the back side of the wafer is patterned, by aligning where the cavity walls will intersect with the piezoresistors. Infrared alignment, which can see through a silicon wafer, is often employed for this step. The silicon is then etched through the majority of the wafer, leaving behind a relatively thin

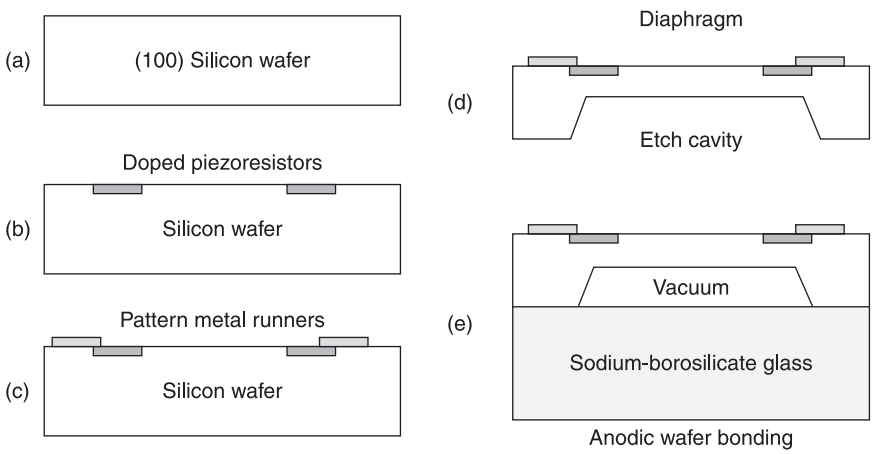

4.2 The MEMS fabrication steps for making a silicon absolute piezo-resistive pressure sensor: (a) (100) silicon wafer polish and oxidation; (b) ion implant the P-type resistors; (c) metallization and passivation; (d) cavity etching; (e) wafer-to-wafer bonding in vacuum.

© Woodhead Publishing Limited, 2013

silicon diaphragm. The diaphragm thickness is determined by timing, using a highly doped selective etch stop, oxide layer or pn junction electrochemical etch stop. Vacuum wafer-to-wafer bonding is then employed to form the reference vacuum behind the silicon diaphragm. Anodic bonding requires a polished silicon surface, with the oxide etch mask removed and a sodium doped glass with a similar expansion coefficient to silicon. Borosilicate glass is used for this wafer. Finally, the bond pads must be opened through the passivation layer to enable wire bonding from the sensor element to the IC or circuit board.

Figure 4.3 shows how this basic MEMS wafer process flow can be altered to produce a variety of pressure and flow sensors. Figure 4.3(a) shows the absolute pressure sensor previously described. Alternative process and design steps include using a reflowed glass to bond the silicon device wafer to an underlying silicon or glass wafer without the high voltage or surface smoothness required for anodic bonding. Figure 4.3(b) illustrates how a differential pressure sensor can be made. The hole through the glass wafer enables back-side sensing. The thickness of this glass is often increased to provide improved stress release from the package that the chip is mounted to. Figure 4.3(c) illustrates a surface micromachined absolute pressure sensor. The vacuum reference can be made by silicon direct fusion bonding of two polished silicon wafers. The top wafer is then thinned back to the diaphragm thickness by polishing and/or etching. Circuits can be fabricated on this thinned silicon surface; however, temperatures in excess of 700°C can lead to plastic deformation of the silicon diaphragm. Surface micromachined pressure sensors can also be made using polysilicon as well as silicon-on-insulating (SOI)

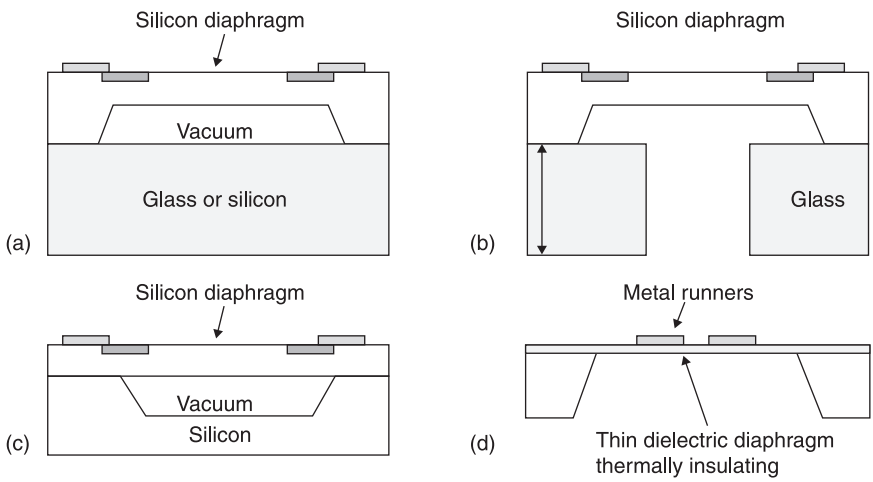

4.3 Four different MEMS structures: (a) absolute pressure sensor; (b) differential or back-side sense pressure sensor; (c) surface micromachined absolute pressure sensor; (d) thermal or hot-wire flow sensor using an insulating.

© Woodhead Publishing Limited, 2013

wafers (Gridehin, 1995). Both of these processes require the etching of a sacrificial layer, generally oxide, and then sealing of small holes with a CVD film (Chang-Chien and Wise, 2002).

Finally, Fig. 4.3(d) illustrates how a thin-film hot-wire flow sensor is made (Huijsing *et al.*, 1982; Lambert and Harrington, 1986). The cross-sectional structure is similar to the pressure sensor; however, instead of a silicon diaphragm, a dielectric diaphragm is used. The dielectric (oxide or nitride layer) film is a better thermal insulator than silicon, which better isolates the heated metal runners from the thicker portion of the MEMS chip. Wet or dry etching of the underlying silicon substrate frees this insulating diaphragm.

Both absolute piezoresistive and capacitive pressure sensors, as well as resonant Coriolis mass flow and density sensors, have recently incorporated getters (Esashi *et al.*, 1998; Sparks *et al.* 2003, 2010) to reduce trapped water vapor, oxygen and nitrogen in the reference vacuum cavity. The getters absorb gases that would otherwise degas from the cavity sidewalls at high temperatures and then slowly adsorb at cold temperatures, resulting in a temperature sensitivity error over the life of the part, during different seasons and engine conditions. Aerospace MEMS applications have lead to the adoption of getter technology, due to their tighter accuracy requirements. Unlike wafer-bonded devices, CVD-sealed surface micromachined absolute pressure sensors do not require getters, since they are sealed at high temperature and the reactant products primarily generate hydrogen, which diffuses into the silicon sidewalls of the microcavity during annealing.

One process for making a piezoresistive pressure sensor on a stainless steel, media compatible diaphragm (Yamazaki *et al.*, 1985) is shown in Fig. 4.4. The thimble-shaped steel diaphragm is first machined and then, as shown on the left of Fig. 4.4, a silicon dioxide layer is deposited onto the top surface of the steel

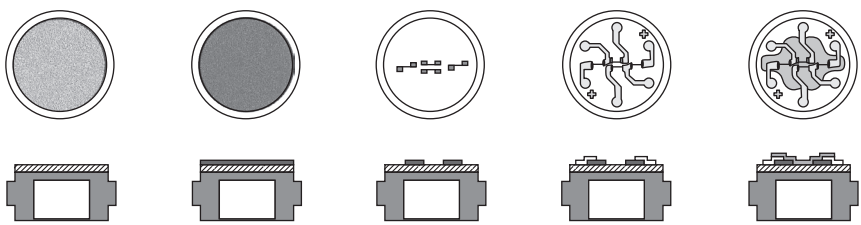

4.4 The process fabrication steps for a polysilicon Wheatstone bridge on stainless steel.

© Woodhead Publishing Limited, 2013

diaphragm. This is followed by the CVD deposition of doped polysilicon. The sensing element is now placed in a tray, sprayed with photoresist and then exposed and developed to allow for the patterned etching of the polysilicon layer. As in the case of the silicon pressure sensor, the resistors are aligned with the edge of the diaphragm. A shadow mask is then used to sputter the metal runner and bond pad pattern. Finally, another shadow mask is aligned to the metal pattern and a silicon nitride passivation is deposited over the polysilicon Wheatstone bridge and most of the metal runners.

4.3 Pressure sensors

MEMS-based pressure sensors represent a billion dollar market, of which automotive sensors make up 40% and aerospace pressure sensors make up around 10% (Castellano, 2010). Hundreds of millions of MEMS pressure sensors have been used by the automotive and aerospace industries in the past four decades (Baney *et al.*, 1997; Eddy and Sparks, 1998; Czarnocki and Schuster, 1999). Air intake is perhaps the best known pressure sensor application in automobiles, but these sensors are also used for reading barometric pressure, in turbochargers and exhaust lines (Wesson *et al.*, 1991; Eddy and Sparks, 1998; Culliname and Strange, 1999; Czarnocki and Schuster, 1999; Ueno *et al.*, 2008). High pressure sensor applications include braking, hydraulic and transmission fluid, air conditioning, diesel fuel injection and cylinder pressure. Piezoresistive pressure sensors have by far been the most common technology employed in these applications; however, capacitive pressure sensors have seen widespread use and even optical pressure sensors have been developed for use in high temperature conditions. Pressure sensors have not been restricted to silicon; either both stainless steel diaphragms and ceramic exposed surfaces have been used in applications with corrosive fluid, especially when sensing high pressure is required.

Pressure sensors, as well as temperature and acceleration sensors, have been used to monitor high temperature turbine engines, high-speed combustors and other aerospace propulsion applications (Przbylko, 1998). In these applications, high frequency pressure and temperature variations can be caused by turbine blade-row interactions, combustion instabilities and unstable aerodynamic phenomena. Dynamic pressure measurement in the compressor is used to detect instabilities that are precursors to surge or rotating stall. Turbine engines experience temperatures of 1300 to 1400°C, while supersonic combustors go up to 2000°C and rocket engines up to 3000°C. Pressure measurements in these high temperature environments are made through a special sensing port, which separates the sensor from the extreme temperatures. However, for high frequency applications, it is important to reduce the distance between the sensor and high temperature area. In some cases, a flush diaphragm may be used to expose the sensor element directly to the high temperature cavity where the pressure fluctuation is occurring. Traditional MEMS sensors used in the automotive

© Woodhead Publishing Limited, 2013

industry will not function in these harsh environments. This section will examine the different aspects of pressure sensing in the automotive and aerospace markets.

4.3.1 Piezoresistive pressure sensors

Piezoresistive pressure sensors generally use a Wheatstone bridge configuration, in which four silicon resistors are placed at points of maximum deflection of a thinned diaphragm (Tufte and Lang, 1962; Shankland, 1991). The conductivity of the doped silicon changes due to mechanical stress. Usually these resistors are boron doped, P-type single crystal silicon, although polycrystalline silicon resistors are used in some applications. Hundreds of thousand of sensors are made on each silicon wafer. These sensing elements are not strain gauges, merely changing resistance as the element is stretched or compressed; they actually change due to the charge carriers associated with the energy minima of the conduction band and effective mass of the carriers in the semiconducting crystal lattice. The crystallographic orientation of the wafer and hence the diaphragm affects the gauge factor, and as a result (100) oriented wafers are used to maximize the piezoresistive effect. The gauge factor of a single crystal silicon piezoresistor is often 50 to 100 times greater than that which a simple metal strain gauge would possess. These sensors are well suited for the –40 to 125°C automotive environment. Higher temperatures required the use of polycrystalline silicon or silicon carbide (Wu *et al.*, 2001) for the active elements.

Polycrystalline silicon piezoresistors (Gridehin *et al.*, 1995) tend to have lower gauge factors than their single crystal counterparts. On the positive side, polycrystalline piezoresistors can perform at higher temperatures, since there are no leakage currents related to the pn junction found in single crystal piezoresistors. These sensors are often used at or above 150°C. The wafers are annealed to diffuse the boron into the wafer at an optimum depth. The polycrystalline resistors are generally deposited on an insulating oxide or nitride layer. The polysilicon resistors can be deposited doped or an implant can be employed to better control the uniformity of the resistance across the wafer. Both single crystal and polysilicon resistors need to be covered by an insulating layer, which is generally thermally grown silicon dioxide. Other layers may be used, such as chemical vapor deposited (CVD) silicon dioxide or silicon nitride layers. Thick insulating layers are generally avoided, since they can adversely affect the performance of the device over temperatures due to thermomechanical stress. These sensors have been integrated with circuitry on the same chip to amplify, compensate and process the pressure signals (Maseeh *et al.*, 1992; Obermeier *et al.*, 1995; Sun *et al.*, 2009).

The piezoresistors are generally positioned on a square diaphragm so the opposing resistors are of the same shape and orientation, while those to the right or left are positioned orthogonally to each other. With this bridge design, the resistance of the orthogonal piezoresistors varies in opposite directions with

© Woodhead Publishing Limited, 2013

respect to uniform diaphragm deformation, while those opposing each other change in the same direction. Finite element modeling is often performed on the MEMS diaphragm to determine the optimal position for the piezoresistors and the optimum shape of the four resistors and to add or vary any desired bridge offsets. The maximum deflection is often just a few microns from the edge of the diaphragm around its perimeter, generally centered on each side. Thicker boss areas have been employed in the central region of the diaphragm and piezoresistors can be placed at the edges of the bosses.

An additional resistor network may be included to enable the Wheatstone bridge offset to be trimmed during wafer testing. This trim network will be placed in a thick area of the MEMS chip, so that it is not sensitive to pressure changes. Metal bond pads used to link the MEMS chip to the electronics or package will also be placed in the thicker perimeter portion of the chip.

4.3.2 Capacitive pressure sensors

Capacitive pressure sensors have been around for decades (Zhang and Wise, 1994; Baney *et al.*, 1997; Sun *et al.*, 2009) but have not achieved the high volumes that piezoresistive pressure sensors have. Relatively low sensitivity, and in some cases high parasitic capacitances, have slowed the adoption of the capacitive pressure sensor. These sensors are essentially two parallel plates, separated by a gap that varies with pressure. The area of the diaphragm, plate gap and diaphragm thickness are the first-order design parameters controlling the performance of a capacitive pressure sensor. The diaphragm shape over pressure stops and the design of bosses (Zhang and Wise, 1994) are secondary features that affect the sensitivity and reliability of capacitive pressure sensors.

Silicon and ceramic capacitive pressure sensors have been used in automotive applications. Ceramic pressure sensors have been used in high pressure and air conditioning applications. Structurally, these ceramic sensors are more related to hybrid microelectronics and co-fired ceramic substrates than silicon micromachining. Touch-mode silicon capacitive pressure sensors have also seen use (Baney *et al.*, 1997). Touch-mode sensors have a linear output region and also a built-in overpressure stop to prevent diaphragm breakage during high pressure transients. The advantages of capacitive pressure sensors over piezoresistive pressure sensors include lower current/power consumption, less complex temperature and packaging stress compensation requirements. Touch-mode sensors have higher burst pressures. The disadvantages of capacitive pressure sensors include sensitivity to lower electrostatic discharge (ESD) voltages, and higher cost due to lower manufacturing volumes.

Touch mode capacitive pressure sensors have also been made using silicon carbide (Young *et al.*, 2004). Structurally, the design of this device is the same as the silicon sensor described previously, with the exception of the diaphragm. To enable high temperature operations of 200 to 400°C, a 3C-SiC diaphragm was

© Woodhead Publishing Limited, 2013

formed using CVD thin film techniques on top of a silicon wafer. To function as a practical device, this high temperature sensing element must be combined with electronics using interconnections that can also operate at these extreme temperatures. SiC circuits have been developed for this temperature range (Neudeck *et al.*, 2002; Wang and Ko, 2005).

4.3.3 Fiber optic pressure sensors

Conventional fiber optic pressure sensors have seen use up to 600°C (Murphy *et al.*, 1991; Wagner *et al.*, 1994; Xiao *et al.*, 1997). They have been applied to cylinder monitoring and aerospace applications. By using a sapphire-based fiber optic sensor, temperatures as high as 900°C can be monitored. These types of high temperature sensors are used intensively in heavily instrumented validation engines. Special active cooling may be required for these test devices.

The transducing mechanism employed by most fiber optic pressure sensors is based on the extrinsic Fabry–Perot interferometer (Murphy *et al.*, 1991; Wagner *et al.*, 1994; Xiao *et al.*, 1997). These sensors use a distance measurement method based on the formation of a Fabry–Perot cavity between the polished end face of an optic fiber and a reflective surface. For pressure sensors, this reflective surface is a flexible diaphragm. Light passes through the fiber and part of it is reflected off the fiber/air interface, while the remaining light goes through the air gap to the reflective diaphragm surface. The light reflects off the diaphragm and then back to the fiber, where it interferes constructively or destructively based on the length traveled. The resulting light goes to the detector. Here the signal is demodulated to produce the distance measurement, which is proportional to pressure.

Micromachined silicon carbide (SiC) and diamond films (Okojie *et al.*, 1997; Ziermann *et al.*, 1997) have been used as the diaphragm material. Traditional silica fiber has been replaced with sapphire to further boost the operating temperature of the sensor. The combination of a MEMS SiC diaphragm and sapphire fiber can boost the operating temperature up to 1100°C. While fiber optic pressure sensors, monitoring the high temperature diaphragm deflection, can operate in harsh environments, their costs rarely justify applications beyond the engine development testing laboratory.

4.4 Flow sensors

4.4.1 Differential pressure flow sensors

Differential pressure sensors operate on the general principle that the pressure drop across the meter is proportional to the square of the flow rate. Multiple pressure sensors, covered earlier in the chapter, are used to measure this pressure differential. The mechanical part of the sensor is used to produce the pressure differential, while the electrical part of the sensor measures the pressure difference.

© Woodhead Publishing Limited, 2013

4.5 A jet mounted pitot tube.

Pitot tubes, used extensively in aerospace applications (Figs. 4.5 and 4.6) are the most common differential pressure sensor used for air flow measurements.

A pitot tube uses two tubes or split tubes to measure a differential pressure. The first tube measures the static pressure and is usually mounted into the pipe wall (Fig. 4.6). The figure illustrates how the pitot-static tube, or Prandtl tube, functions. The second or central tube measures the impact pressure. The faster the aircraft is moving, the higher the impact pressure. The differential pressure between the impact and static pressure is measured with this sensor. A silicon pressure sensor diaphragm or thin steel diaphragm with a strain gauge is generally used in this device. The flow rate or air speed is proportional to the square root of the difference between the static and impact pressure divided by the air density. This sensor does not work well at low velocities, since a differential pressure is being monitored. Supersonic shock waves can also require correction factors to obtain an accurate air velocity measurement. Icing and particulates must also be taken into account with these exposed tube channels.

© Woodhead Publishing Limited, 2013

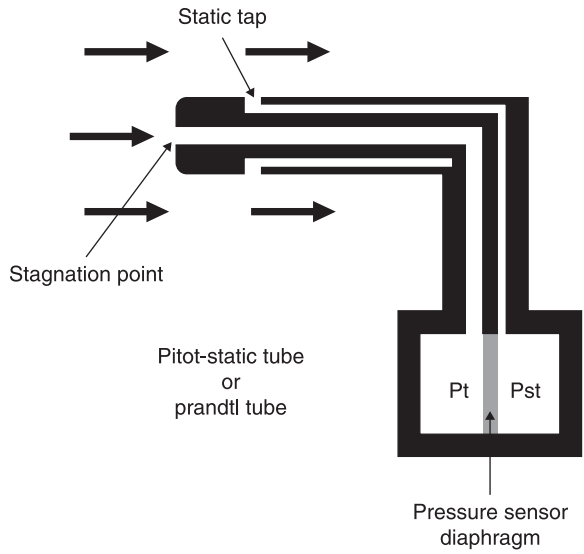

4.6 A schematic diagram of the pitot-static or prandtl tube.

4.4.2 Hot wire flow sensors

Thermal anemometers, or hot wire flow sensors, measure the flow rate by monitoring the amount of heat removed from a surface using one or more simple temperature sensors. They have found wide use in the automotive industry for monitoring the air intake of the engine.

One of the simplest hot wire sensors is the Pirani gauge or thermal conductivity device. The Pirani gauge is made up of a single wire or metal strip. The resistance of the wire is a function of the pressure of a specific, stagnant gas surrounding the wire. This device is used to measure pressure or gas concentration in binary mixes, not flow, and has found widespread use with vacuum systems as a pressure gauge, but has not been commonly used in automotive and aerospace applications.

The hot wire flow sensor (Huijsing *et al.*, 1982; Lambert and Harrington, 1986; Foss *et al.*, 2005; Shmid *et al.*, 2008) operates on a similar principle, in which the surrounding fluid interacts with a hot wire of the thin metal film. The cooling effect of a single wire can also be used to determine the flow rate of the fluid passing over the hot wire. A single wire cannot indicate the direction of the flow, but this was not an issue with the early hot-wire flow sensors used in automotive applications for air intake. The calibration coefficients of this type of sensor also depend on the type of fluid flowing over the hot wire. In industrial applications, different coefficients are used for different gases. For the air intake application, this is generally not an issue, although large differences in humidity affect the accuracy of the sensor.

© Woodhead Publishing Limited, 2013

By employing multiple wires or thin films, the flow rate and direction can be measured. This is useful in four-cylinder engines where reverse pulsations, also called backflow, occur under heavy load. The backflow frequency can be 100 Hz, requiring special flow sensors. Figure 4.7 illustrates a bi-directional thin-film mass air flow sensor designed for this fast pulsating automotive flow sensor application (Lambert and Harrington, 1986). The central wire or metal strip is heated, while the two outer wires are thin film temperature sensors. These thin film temperature sensors are just 20 to 50 microns from the heated metal strip. A thermally insulating substrate is used to improve thermal response time. A bypass sensor design also improved the performance of the sensor. As is illustrated in Fig. 4.7, as air flows in one direction the downstream temperature sensor heats up more than the upstream temperature sensing strip. This allows for bi-directional sensing capability.

Thin film hot thin film flow sensors have also been applied to fuel injections systems (Shmid *et al.*, 2008). Figure 4.8 shows an example of a thin film hybrid co-fired ceramic flow sensor built into a fuel injector. The resistance change in a Wheatstone bridge is monitored as an indicator of fuel flow rate. This has been used in common rail direct diesel fuel injectors operating at pressures as high as 1350 bar. Flow rate response times of 0.3 to 1.5 ms could be detected, providing direct information on the hydraulic status of the interior of the fuel injector nozzles.

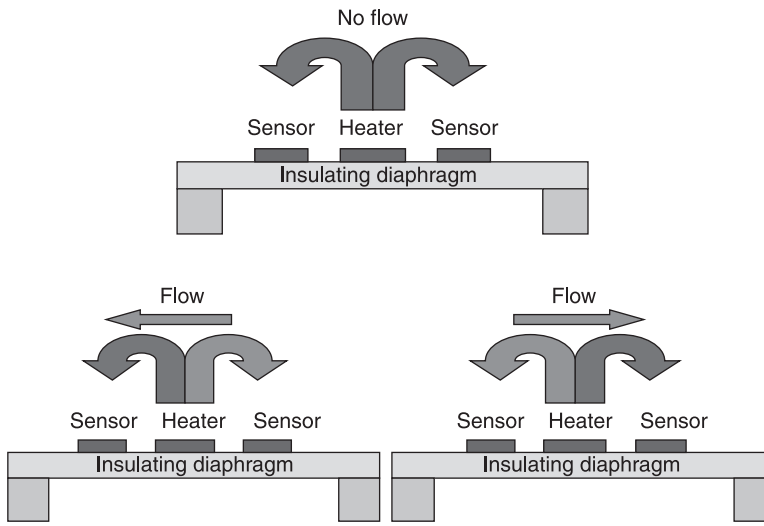

4.7 A bidirectional thin-film thermal anemometer under no flow (top) and directional flow conditions (bottom).

© Woodhead Publishing Limited, 2013

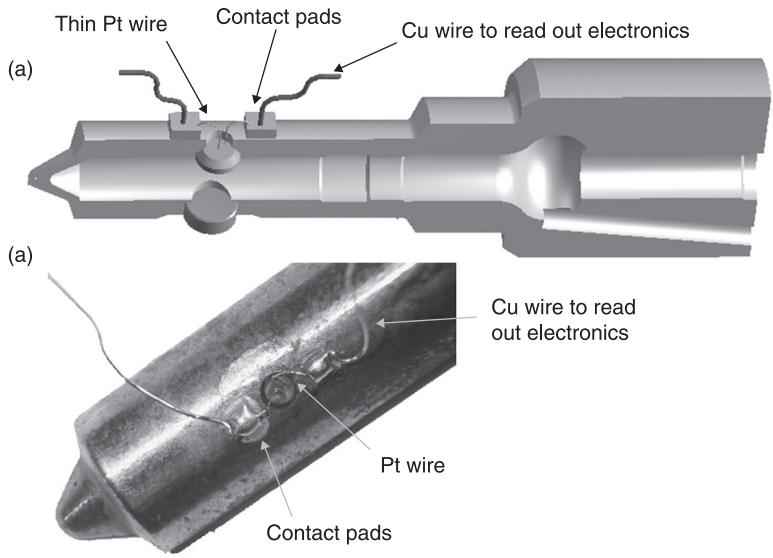

4.8 (a, b) Hybrid ceramic hot wire flow sensor integrated into a fuel injector (Shmid, 2008).

4.4.3 Coriolis mass flow sensors

Conventional steel Coriolis mass flow sensors have been commercially available for over 30 years. Micromachined versions of this flow sensing technology have been developed (Enoksson *et al.*, 1997; Smith *et al.*, 2009). The mass flow rate going through the resonating tube is directly proportional to the twisting angle and inversely proportional to the resonance frequency. The density of the fluid in the tube is inversely proportional to the square of the resonance frequency.

At the core of the MEMS sensor (Fig. 4.9), is a C-shaped, vacuum-sealed resonating silicon microtube. Figure 4.10 is a schematic diagram of this sensor. The fabrication process uses a combination of plasma and wet etching, photolithography, along with various types of wafer-to-wafer bonding to form the microfluidic chips (Smith *et al.*, 2009).

The doped silicon tube is anodically bonded to a metallized Pyrex wafer. Holes for the passage of fluid are predrilled into the Pyrex wafer. The metal pattern on the Pyrex forms capacitor plates, feedthroughs, electrical runners, a temperature sensor and silicon contacts.

A capping wafer, generally either silicon or glass, was patterned and etched to form both a cavity that encloses the active micromachine and opens up access to the electrical bond pads. At this point, the thin film getter was applied and patterned on the top portion of the cavity (Fig. 4.10).

© Woodhead Publishing Limited, 2013

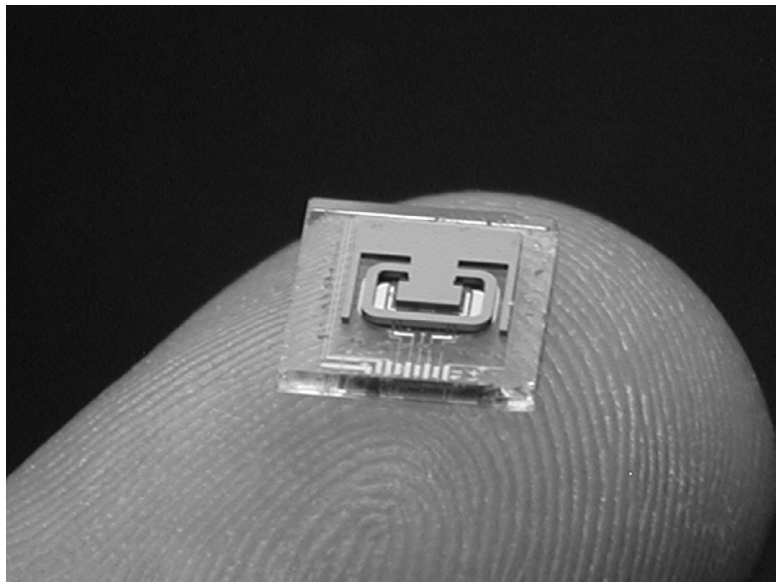

4.9 The MEMS chip and resonating microtube.

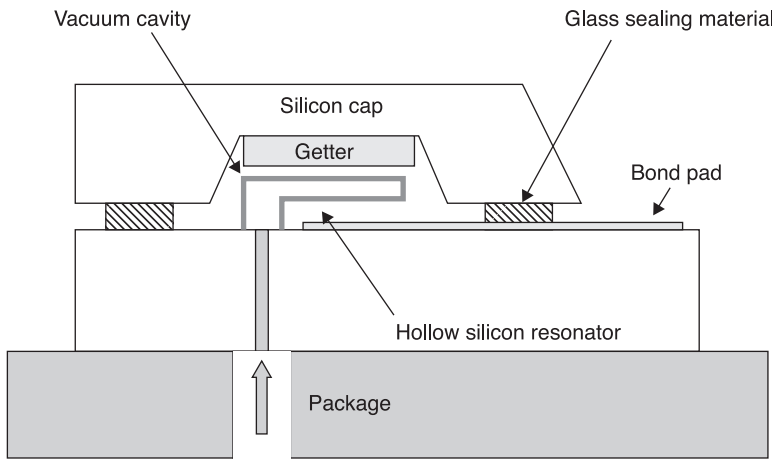

4.10 Cross-section of the vacuum packaging and gettering approach.

The microtube is driven into resonance electrostatically and its motion sensed capacitively using metal electrodes under the tube and accompanying electronic circuits connected to the MEMS chip via wire bonding. This device cannot only measure true mass flow but also other fluid parameters such as density and binary chemical concentration, which make it attractive to vehicular applications.

© Woodhead Publishing Limited, 2013

4.5 Concentration, density and fuel quality sensors

The addition of ethanol to gasoline has become more common, as has the availability of E85 (85% ethanol) fuel and compatible vehicles. Due to fuel line corrosion and changes in engine management for high alcohol fuels, special vehicle manufacturing is required to utilize this type of fuel. The air to fuel ratio, timing and compression ratio needs to be adjusted when using ethanol to maximize fuel efficiency, reduce tail pipe emissions and avoid engine damage. Ethanol concentration sensors were employed on many of the original flex-fuel vehicles. These were usually capacitive frequency-based sensors that monitored the change in the dielectric constant of the fuel when ethanol was added (Fig. 4.11). These sensors have problems with water contaminated fuel and are relatively large and expensive.

In several cases, virtual sensor software algorithms have been developed to replace the concentration sensor (Fig. 4.11). This virtual sensor uses the oxygen

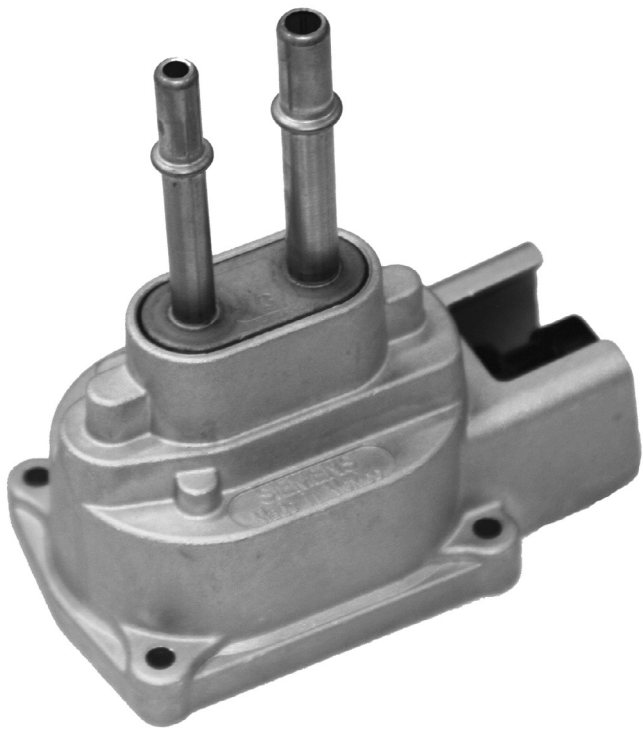

4.11 An automotive ethanol concentration sensor based on measurement of the fuel's dielectric constant.

© Woodhead Publishing Limited, 2013

sensor in the exhaust line. The oxygen sensor output is monitored while all other emission systems are temporarily halted. While not as accurate as a direct measurement, this does eliminate the need for a dedicated fuel concentration sensor. If a Coriolis mass flow sensor is employed to monitor fuel, its density output can be used to directly and accurately measure the ethanol/gasoline concentration.

Density measurements have long been used to monitor petrochemical distillation. The density of the petrochemicals decrease moving up the distillation column. Measuring the density or specific gravity of biodiesel has been reported as the preferred method of blending biodiesel fuel for both accuracy and ease of use (Clark, 1999; Duban and Turner, 2006). Table 4.1 shows the published biodiesel (Tat and Gerpen, 2002) and measured gasoline, E85 and diesel fuel density ranges. Because of differing refining and fuel blending processes, the density of commercial fuels will vary within a range. Table 4.1 shows that a density measurement is able to distinguish the type of fuel with a high degree of accuracy. The table also shows that density can be used to detect water and air bubbles in fuel or lubricants. Water contamination can be a problem with pipe transport and tank storage. Trapped water at the bottom of a fuel tank can be detected easily via density. Figure 4.12 shows how this sensor can be used to measure ethanol in gasoline concentration.

Table 4.1 Density ranges of various liquids and fluids

Fuel/Fluid	Density range (gm/cc)
Air	0.00122
Gasoline	0.725–0.775
E85	0.775–0.782
Ethanol	0.7856
Butanol	0.8095
Fisher–Tropsch 'diesel'	0.784–0.801
Diesel	0.822–0.860
Biodiesel	0.860–0.900
Water	0.99904

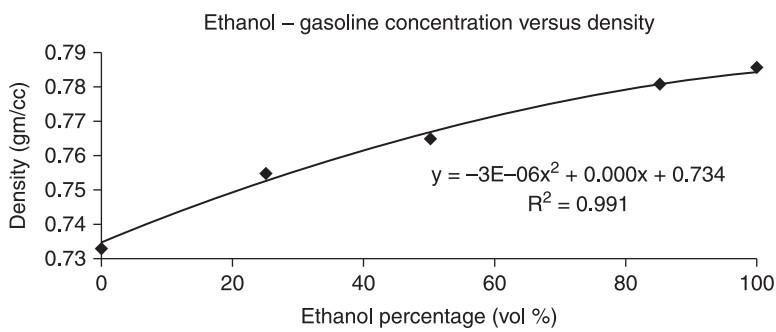

4.12 The density plot for ethanol–gasoline at 25°C.

© Woodhead Publishing Limited, 2013

One potential long-term solution to the US dependence on Middle Eastern oil imports is the development of Fisher–Tropsch (FT) fuels. These liquid fuels are produced from hydrocarbon feedstock such as coal, natural gas or oil shale. The US military has taken the lead in this area, with a long-term goal on replacing 75% of the oil imports by 2025 (Frame 2004; Harrison, 2006). These reserves offer the equivalent oil reserve of 2.3 trillion barrels, more than three times the Middle East oil reserves. The main measurable difference between FT fuel and petrochemical fuel is density.

To become a widely adopted measurement technology, the method must not only be capable of accurately monitoring a parameter, but must do so in an economic manner. The resonating microtube shown in Fig. 4.9 has been used to make this type of fuel density measurement (Sparks, 2010) and is being developed for automotive and aerospace fuel applications. Its mass and size are low enough to enable in-wing, redundant monitoring of fuel quality in aircraft.

4.6 Sensor signal conditioning

The raw output of a pressure sensor element exhibits a wide, often non-linear, variation of parameters over temperature and pressure. Piezoresistive sensors are well-known for a strong temperature output variation of the Wheatstone bridge offset and pressure sensitivity (Shankland, 1991). These parameters vary across a wafer and from wafer batch to batch.

Sensor signal conditioning in the 1980s was accomplished using analog circuits on a fiberglass printed circuit board (PCB), often with laser trimming of hybrid resistors and thermistors network, which was also mounted on the PCB along with off-the-shelf bipolar IC devices. The trimming of thermistors and resistors adjusts both the sensor's bridge offset and temperature variation. The subsequent generation of conditioning devices was placed on a hybrid ceramic circuit board and the ICs were soldered to this hybrid substrate. This greatly improved the reliability of the pressure sensing module and reduced its size.

The automotive industry is constantly driving down component costs so an increasing amount of the signal conditioning circuitry and trim network was consolidated into application specific ICs or ASICs (application-specific integrated circuits). The ASICs are customized by automotive companies or their direct suppliers for the wide temperature range (−40 to 125°C), electromagnetic fields and even the specific pressure sensor element used in the automotive environment. The first-generation ASICs were bipolar designs. On-chip network trimming was often accomplished by blowing aluminum fuses or Zener diodes that were placed on the ASIC or the separate pressure sensor chip. Two chips, an ASIC and MEMS pressure sensor, are most commonly used in automotive applications (Fig. 4.13). Integrating the pressure sensor and some of the signal conditioning circuits onto one chip (Maseeh *et al.*, 1992) began in the 1990s. The use of CMOS and BiCMOS ASICs allowed electrically programmable memory (EPROM) to be employed for

© Woodhead Publishing Limited, 2013

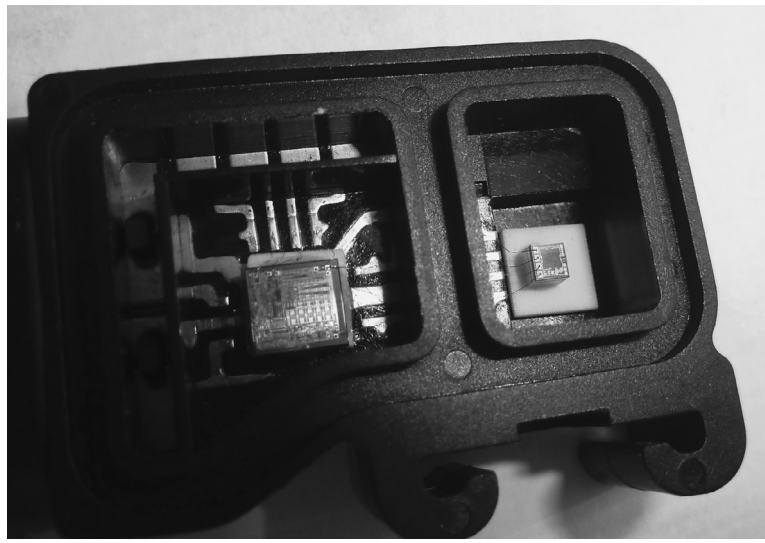

4.13 An automotive MAP package showing the ASIC and MEMS pressure sensor.

calibrating both piezoresistive and capacitive pressure sensors. EPROM greatly reduced the chip area and hence cost over older fuse and Zener diode trim networks. As with bipolar signal conditioning circuits, single chip or monolithic sensors with CMOS circuits were also developed (Sun *et al.*, 2009), although the cost effectiveness of this approach for pressure sensors is still under debate and varies with the semiconductor processing and packaging capability and yields of the manufacturer. Absolute polysilicon and SOI surface pressure sensors can be sealed via CVD of silicon or oxide films, which makes small integrated pressure sensors attractive.

Packaging and media compatibility issues also determine if a single chip pressure sensor can be used. Absolute pressure sensors must be coated to protect the small metal runners from corrosion, and leakage paths and CMOS devices from sodium related voltage shifts. The coatings, often silicones or parylene-based, must not harden with time, chemical exposure or coating, to prevent the diaphragm sensitivity from drifting or initiating output hysteresis. In the automotive environment over the course of 10 years, this can present an almost impossible task for a pliable organic protective coating. Single chip differential pressure sensors, where the media only makes contact with the back side of the diaphragm, is more forgiving to air pressure applications. Liquid media exposure to the adhesive or solder used to attach the silicon sensor to the package is the weak point for one or two chip pressure sensors. This is often the reason why steel diaphragms are used for differential pressure sensors.

© Woodhead Publishing Limited, 2013

4.7 Packaging MEMS sensors for harsh environments

Unlike motion sensors, all pressure and flow sensors are exposed to the media of interest. Packaging is the key system ingredient enabling a sensor to interface with a potentially aggressive environment (Sparks, 2001; Monajemi *et al.*, 2008). Protection of the sensing element starts at the chip level. For pressure sensors, back-side sensors and/or stainless steel diaphragms offer protection from the most corrosive ambients. For silicon absolute pressure sensors, silicon nitride or oxide passivation films form the initial protective layer. Special metal layers, such as gold and platinum, can be employed to prevent corrosion of bond pads and metal runners. Parylene and silicone coatings also are used to protect the circuit side of a MEMS or IC chip.

Chip attachment must also take thermomechanical stress into account. Both the adhesive and underlying substrate, which the silicon chip is attached to, can adversely affect the accuracy and reliability of the sensor. Efforts are made to match the expansion coefficients of the silicon or silicon/glass MEMS chip with the substrate. Thick Pyrex glass wafers have been bonded to the silicon wafers to assist in buffering the sensor from packaging stress. Inserts in the plastic packages of glass, Kovar or ceramic are also used to buffer the thermomechanical stresses encountered with plastic packages often used in high-volume, low-price, automotive applications. Softer adhesives can also assist in buffering this stress. Media compatibility must also be taken into account in the package design, if corrosive liquids or gases are to come into contact with the back of the silicon diaphragm. For front-side air contact, silicon gels or parylene films are often used to coat the silicon chip and its wirebonds to provide a low cost protective barrier. The protective barrier must be compliant over the temperature range of use and life of the part, to prevent it from degrading the accuracy of the sensor. For very aggressive environments, the MEMS chip is often immersed in a silicone liquid with a corrugated stainless steel diaphragm protecting it from the fluid, while still transferring the pressure changes encountered.

Thermal design issues are critical when fabricating a hot wire flow sensor. Like the pressure sensor, design and thermal isolation of a thin film thermal anemometer begins at the chip level. Insulating dielectric thin films such as silicon oxide, nitride or ceramics are used to physically support the heated metal runners. Mounting of the MEMS chip onto the package must also take thermal isolation into account. As mentioned previously, for extreme engine related aerospace sensing devices, traditional sensing elements made of silicon cannot be employed. Silicon carbide, sapphire and diamond are the materials of choice for pressure and flow sensors.

Mechanical package design is the next level of protection for a microsystem. This portion of the packaging process can often be the most expensive material component cost of the entire system, particularly for aerospace applications. In aircraft applications, reliability has the highest priority in package design. Aerospace was one of the first markets to adopt MEMS pressure sensors; however,

© Woodhead Publishing Limited, 2013

it was the automotive market that transformed this technology into high-volume, low-cost products.

Pressure sensors are essentially strain gauges. As such, they can pick up package related stresses during temperature gradients or transient as well as from mechanical mounting. Modeling of the package and sensor to detect such potential interactions over temperature and feasible mechanical stress is an important aspect of the system design process. No product development process is complete without a comprehensive reliability testing packaged device over time, temperature and pressure. Vibration, shock, drop, temperature cycling, high and low temperature storage, ESD, electromagnetic coupling and combinations of some of these conditions are required prior to field testing. Output drift and hysteresis of statistically significant batches of parts are needed to arrive at an optimum final package design and manufacturing process.

The first MAP pressure sensors were silicon piezoresistive pressure sensors coupled with hybrid ceramic circuits. After a decade, ICs replaced the hybrid circuits for processing the pressure sensor signal. Unlike the aerospace market, which used stainless steel or other metals as its sensor packaging material, the cost pressures of the automotive market required plastic packaging. The expansion coefficient of plastic, even filled plastic, is higher than silicon. Mounting silicon pressure sensors directly to plastic, especially differential pressure sensors, results in sensor inaccuracies over the wide temperature range of the automotive environment. For under-the-hood applications, the sensor must operate accurately between −40 and 125°C. If mounted to the engine, the upper temperature limit goes up to 150°C or higher. MAP sensors are exposed to air, fuel vapors and various hydrocarbons. As is shown in Fig. 4.14, the silicon piezoresistive pressure sensor is attached to the package. The schematic diagram of the sensing element is shown in Fig. 4.3(c). Wirebonding connects the four bond pads on the MEMS chip to the gold plated copper lead frame tabs. This metal lead frame goes through the walls of the plastic package. A simple coating of the silicon diaphragm with silicone or parylene is sufficient to protect the aluminum bond pads, which are the most likely element to corrode in a hot, moist atmosphere. This organic protective coating also maintains its elasticity, which insures good pressure accuracy over the life of the part.

Fuel vapor pressure sensors were another automotive application that appeared in the 1990s. This application uses a differential silicon pressure sensor and the die attach adhesive must be resistant to gasoline vapors. It monitors a tighter, lower pressure change than the MAP sensor and so can be more adversely affected by packaging stress problems than the MAP sensor.

High pressure sensor applications are also seeing use in the automotive and aerospace markets for monitoring oil, fuel, air conditioning fluid, transmission hydraulic and brake fluid. Silicon can be etched by fluorocarbons used in air conditioning systems and most die attach adhesives can be weakened over time at the high end of the automotive temperature ranges and are not appropriate for

© Woodhead Publishing Limited, 2013

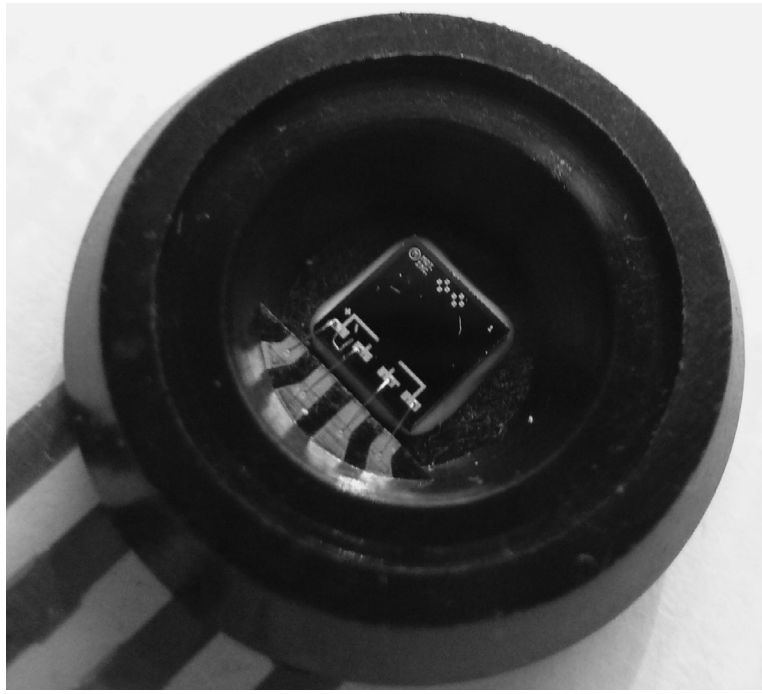

4.14 A plastic packaged silicon pressure sensor.

high pressures. The first pressure sensors used in this market were ceramic capacitive devices.

Stainless steel pressure transmitters have also been employed in harsh environments. These sensors use a corrugated, flexible stainless steel diaphragm that transmits the pressure to the silicone oil. The silicon pressure sensor is immersed in the silicone oil and the pressure of the silicone oil is transmitted to the silicon diaphragm. These sensors have been used in aerospace applications associated with hydraulic systems, but their cost has generally been too high for automotive applications.

As was outlined in the section on MEMS processing, stainless steel diaphragms have been coupled with polysilicon Wheatstone bridges. Wirebonding is used to connect the metal bond pads linked to the polysilicon sensor elements to the electronics via a lead frame, that are contained in the package (Fig. 4.15). A plastic or thin metal cover often protects the electronics. Like the lower priced all-plastic packages for automotive applications (Fig. 4.14), this cover must protect the electronics from the hot, humid under-hood environment and provide splash protection for 5 to 10 years. High pressure fluid ports for aerospace and some automotive sensors are often threaded, as indicated at the bottom right of Fig. 4.15.

An electrical connector (Fig. 4.16), on the sensor housing must also mate with the standard automotive or aerospace cable connector without allowing moisture

© Woodhead Publishing Limited, 2013

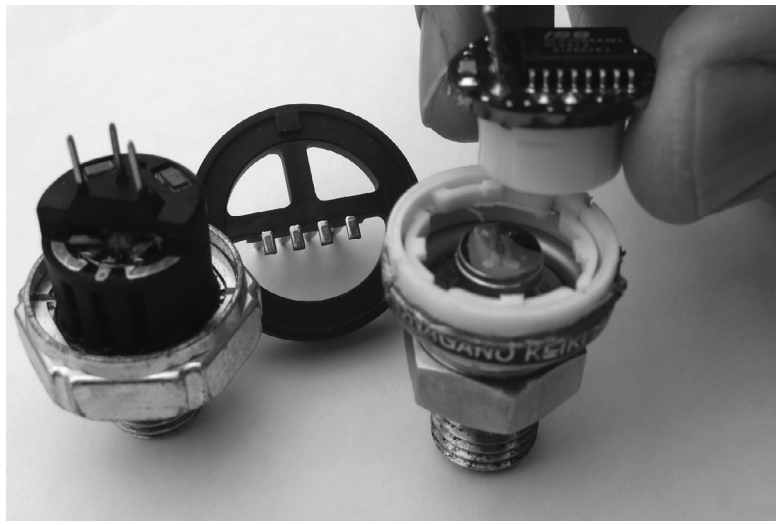

4.15 The interior construction of stainless steel diaphragm pressure sensors.

4.16 Three pin connector on an automotive MAP sensor.

© Woodhead Publishing Limited, 2013

to short out the sensor wiring. This 3-pin connector has a keying feature molded into the plastic to prevent reverse connection of the wiring. In addition to moisture ingress, electromagnetic coupling through the wire harness is a potential package problem, which often requires a circuit design solution integrated with package alterations. A system level approach to design and validation testing must extend from the MEMS chip, through the electronics, and mechanical housing all the way to the connector and wire harness.

4.8 Conclusion and future trends

For automotive sensors, cost is a big driver in future designs. Improved signal processing will enable more information to be obtained from the existing sensing elements, and system-level software techniques will be used along with virtual sensing method. Pressure sensing elements will continue to decrease in size to lower the cost of the elements. Aerospace sensors will be employed in locations hitherto used only on testing stands. The high temperature requirement for aerospace and some automotive applications will require the use of more exotic materials, such as silicon carbide and diamond film in the transducers.

4.9 References

Albaugh K (1991), 'Electrode phenomena during anodic bonding of silicon to sodium borosilicate glass', *J Electrochem Soc*, 138, 3089–3093.

Baney W, Chilcott D, Huang X, Long S, Siekkinen J, *et al.* (1997) 'A comparison between micromachined piezoresistive and capacitive pressure sensors', *Proc of the Fall SAE Conf*, 973241, 61–65.

Castellano R (2010), 'MEMS packaging', *Wafer Device Pack Intercon*, 1, 10–11.

Chang-Chien P and Wise K (2002), 'A barometric pressure sensor with integrated reference pressure control using localized CVD', in *Solid-State Sensor, Actuator and Microsystem Workshop*, Hilton Head, SC, pp. 90–93.

Clark N (1999), 'On-road use of Fischer-Tropsch diesel blends', SAE, Paper No. 1999-01-2251.

Culliname W and Strange R (1999), 'Gas turbine engine validation instrumentation measurements, sensors, and needs', *SPIE Conference on Harsh Environment Sensors*, SPIE, vol. 3952.

Czarnocki W and Schuster J (1999), 'The evolution of automotive pressure sensors', *Sensors*, 16, 52–65.

Duban J and Turner R (2006), 'On farm methods of biodiesel blend detection', *2006 ASABE Annual International Meeting*, Paper No. 0066239.

Dunbar M and Sager K (2000), 'A novel media-compatible pressure sensor for automotive applications', *Sensors*, 17, 28–34.

Eddy D and Sparks D (1998), 'Application of MEMS technology in automotive sensors and actuators', *Proc IEEE*, 86, 1747–1755.

Enoksson P, Stemme G and Stemme E (1997), 'A silicon resonant sensor structure for Coriolis mass-flow measurements', *J MEMS*, 6, 119–125.

© Woodhead Publishing Limited, 2013

Esashi M, Sugiyama S, Ikeda K, Wang Y and Miyashita H (1998), 'Vacuum-sealed silicon micromachined pressure sensors', *Proc IEEE*, 86, 1627–1632.
Foss J, Lawrenz A and Norcock M (2005), 'Temperature and flow rate measurement with a thermal transient anemometer', *SAE* 2005-01-2030.
Frame E (2004), 'Alternative fuels: assessment of Fisher–Tropsch fuel for military use in 6.5 L diesel engine', *SAE Trans*, 113, 1826–1842.
Glass M (2007), 'Buses and networks for contemporary avionics', *AeroTech Congress*, SAE 2007-09-17.
Gridehin V, Lubimsky V and Sarina M (1995), 'Piezoresistive properties of polysilicon films', *Sens Actuat A*, 49, 67–72.
Harrison W, (2006) 'The role of Fischer–Tropsch fuels for the US military,' *AFRL*-06-0078.
Huijsing J, Schuddemat J and Verhoef W (1982), 'Monolithic integrated direction sensitive flow sensor', *IEEE Tran Elect Dev*, ED-29, 133–138.
Lambert D and Harrington C (1986), 'An air flow sensor based on interface thermal wave propagation', *J Appl Phys*, 59, 59–66.
Maseeh F, Joseph J, Madou M (1992), 'Feasibility and practicality of monolithic sensors', *Sensors*, 9, 31–35.
Monajemi P, Ayazi F and Sparks D (2008), 'MEMS packaging', in R Tummala, *System-On-Package*, Ch. 9, New York: McGraw Hill, pp. 503–540.
Murphy K, Fogg B, Wang G and Vengsarkar A (1991), 'Sapphire fiber interferometer for microdisplacement at high temperature', *Proc of SPIE*, 1566, Boston, MA.
Neudeck P, Okojie R and Chen L (2002), 'High temperature electronics – a role for wide bandgap semiconductors?' *Proc IEEE*, 90, 1065–1076.
Obermeier E, Hein S, Schlichting V, Hammerschmidt D, Schnatz F, *et al.* (1995), 'A smart pressure sensor with on-chip calibration and compensation capability', *Sensors*, 12, 20–24.
Okojie R, Ned A and Kurtz A (1997), 'Operation of a (6H)-SiC pressure sensor at 500°C', *Transducers'97, IEEE*, 4D2.03, 1407–1409.
Przbylko S (1998), '*MEMS for aircraft engines*,' DARPA ELTO MEMS for Harsh Environment Workshop.
Schmidt M (1998), 'Wafer-to-wafer bonding for microstructure formation', *Proc IEEE*, 86, 1575–1582.
Shankland E (1991), 'Piezoresistive silicon pressure sensors', *Sensors*, 8, 22–26.
Shmid U, Krotz G and Schmitt-Landsiedel D (2008), 'A volumetric flow sensor for automotive injection system', *J Micromech Microeng*, 18, 045006.
Sippola C and Ahn C (2006), 'A thick film screen-printed ceramic capacitive pressure microsensor for high temperature applications', *J Micromech Microeng*, 16, 1086–1091.
Smith R, Sparks D, Riley D and Najafi N (2009), 'A MEMS-based Coriolis mass flow sensor for industrial applications', *IEEE Trans Indust Elect*, 56, 1066–1071.
Sparks D, Zarabadi S, Johnson J, Chia M, Jiang G, *et al.* (1997), 'CMOS integrated surface micromachined angular rate sensor for automotive applications', *Transducers '97*, 3B1.04, 851–853.
Sparks D, Noll T, Agrotis D, Betzner T and Gschwend K (1999), 'Multi-sensor modules with data bus communication capability', *Auto Eng*, 107, 37–38.
Sparks D, Bifano T and Malkani D (2000), 'Operation and design of MEMS/MOEMS devices', in P. Rai-Choudhury (Ed.), *MEMS and MOEMS Technology and Applications*, SPIE, Ch. 2, 47–108.

© Woodhead Publishing Limited, 2013

Sparks D (2001), 'Packaging of microsystems for harsh environments,' *IEEE Instrum Meas Mag*, 4, 30–33.

Sparks D, Queen G, Weston R, Woodward G, Putty M, *et al.* (2001), 'Wafer-to-wafer bonding of nonplanarized MEMS surfaces using solder', *J Micromech Microengr*, 11, 630–634.

Sparks D, Massoud-Ansari S and Najafi N (2003), 'Chip-level vacuum packaging of micromachines using nanogetters', *IEEE Trans Adv Packaging*, 26, 277–282.

Sparks D (2010), 'Thin film getters: from vacuum tubes to wafer Scale MEMS packaging', *Wafer Dev Pack Intercon*, 1, 19–22.

Sparks D, Smith R, Riley D, Tran N, Patel J, *et al.* (2010) 'Monitoring and blending biofuels using a microfluidic sensors', *J ASTM Int*, 7(8), 111–122.

Sun C, Wang C, Tsai M, Hsieh H and Fang W (2009), 'Monolithic integration of capacitive sensors using a double-side CMOS MEMS post process', *J Micromech Microeng*, 19, 015023, 9.

Tat M and Gerpen J (2002), 'Physical properties and composition detection of biodiesel fuel blends', *Proc 2002 ASAE Intl Mtg*, Paper No. 026084.

Tufte O and Long G (1962), 'Silicon diffused element piezoresistive diaphragm,' *J Appl Phys*, 33, 3322–3330.

Ueno M, Izumi T, Watanabe Y, Baba H, (2008) 'Exhaust gas pressure sensor', *SAE* 2008-01-00907.

Wagner D, Frankenberger J and Deimel P (1994), 'Optical pressure sensors using two Mach-Zehnder interferometers for the TE and TM polarization', *J Micromech Microeng*, 4, 35–39.

Wang R and Ko W (2005), 'Silicon-carbide MESFET-based 400C MEMS sensing and data telemetry', *IEEE Sensors J*, 5, 1389–1394.

Wesson L, Cabato N, Pine N and Bird V (1991), 'Fiber optic pressure sensor system for gas turbine engine control', *SPIE Proc* 1307, DOI 10.1117/12 24746.

Wolfe S and Tauber R (1986), *Silicon Processing for the VLSI Era*. Sunset Beach, CA: Lattice Press.

Wu C, Stefanescu S, Kuo H, Zorman C and Mehregany M (2001), 'Fabrication and testing of single crystalline 3C-SiC piezoresistive pressure sensors', *Proceedings of the 11th International Conference on Solid State Sensors and Actuators*, pp. 514–517.

Xiao Z, Engstrom O and Vidovic N (1997), 'Diaphragm deflection of silicon interferometer structures uses as a pressure sensor', *Sens Actuat A*, 58, 99–107.

Yamazaki M, Miyazawa K, Nakao M, Kamimura K, Onuma Y, *et al.* (1985), 'Pressure sensors prepared with heavily boron doped polycrystalline silicon films by plasma assisted chemical vapor deposition', *Proceedings of the 5th Sensor Symposium*, pp. 153–157.

Young D, Du J, Zorman C and Ko W (2004), 'High-temperature single crystal 3C-SiC capacitive pressure sensor', *IEEE Sensors J*, 4, 464–470.

Zhang Y and Wise K (1994), 'An ultra-sensitive capacitive pressure sensor with a bossed dielectric diaphragm', Hilton Head, SC: Transducers Research Foundation, pp. 205–208.

Ziermann R, Berg J, Reichert W, Obermeier E, Mickhoff M, *et al.*. (1997), 'A high temperature pressure sensor with b-SiC piezoresistors on SOI substrates', *Transducers '97, IEEE*, 4D2.04, 1411–1414.

© Woodhead Publishing Limited, 2013

5

RF MEMS for automotive radar sensors

J. OBERHAMMER, N. SOMJIT, U. SHAH
and Z. BAGHCHEHSARAEI,
KTH Royal Institute of Technology, Sweden

DOI: 10.1533/9780857096487.1.106

Abstract: Radio-frequency micro-electromechanical systems (RF MEMS) devices and circuits have attracted interest in applications such as car radar systems, particularly in the 76 to 81 GHz frequency band, due to their near-ideal signal performance and compatibility with semiconductor fabrication technology. This chapter gives an introduction to state-of-the-art car radar sensors and architectures, describes the most commonly engaged RF MEMS components and circuits, and gives examples of RF MEMS-based automotive radar prototypes.

Key words: radio-frequency micro-electromechanical systems (RF MEMS), car radar, automotive radar, phase shifter.

5.1 Introduction

Automotive safety is evolving from passive systems such as airbags and seat belts to the use of active sensors for collision avoidance. The competing technologies to achieve the active vehicular surround sensing functions include radar, Lidar, ultrasonic and video cameras (Dariu *et al.*, 2001). Automotive radar is one of the leading technologies, owing to its weather independence and high information content, including range and speed detection, when compared to many alternative sensors, especially visual sensors. Additional information from the radar signal, for example angle of targets, can be extracted using advanced techniques. Automotive radar has been under development since the mid-1960s. The first applications using automotive radar were adaptive cruise control and collision warning systems. The collision warning systems were successfully introduced in the USA in the 1990s, with Greyhound installing more than 1600 radar systems in their buses, resulting in reduction of accidents by 21% in 1993, compared to the previous year (Schneider, 2005). Radar-based autonomous cruise control (ACC) systems were first introduced in the Mercedes S class series in 1999 (Wenger, 2005). Additional safety functions, such as pre-crash sensing and collision mitigation using active brake assist, is also offered in 77 GHz radar sensor, providing much higher braking forces for deceleration when a threatening situation arises (Schneider, 2005; Wenger, 2005).

Frequency regulation is an important aspect of any commercially functioning radar and the same is true for automotive radar. The 76 to 77 GHz band was regulated in the 1990s and now is allocated for Intelligent Transport Services

© Woodhead Publishing Limited, 2013

(ITS) in Europe, North America and Japan (Schneider, 2005). The Federal Communications Commission (FCC) regulated ultra-wide band (UWB) for the North American market in 2002. For the automotive UWB short-range radar (SRR) systems, the FCC allocated the band 22 to 29 GHz (Schneider, 2005). Because of the strong objections of the telecom industry and Earth observation institutions, considerable effort was dedicated to finding a compromise and hence to enable automotive UWB radar systems. In January 2005, it was decided by the European Commission to allocate the frequency band of 21.625 to 26.625 GHz for UWB SRR for automotive applications, on a temporary basis from July 2005 to 30 June 2013. It is expected that in eight years, work will be done towards the introduction of inexpensive SRR sensors operating at a new frequency, without impairing other commercial, scientific or military systems and services. Hence, in March 2004, the European Commission allocated the frequency range 77 to 81 GHz for UWB SRR with permitted usage from 2005 onwards. Anticipating the allocation of this band also in Japan and North America, the SRR suppliers will probably shift their UWB developments from 24 to 79 GHz in the medium term.

5.1.1 Sensor types and architecture

The automotive radar sensor can be divided in two categories; short-range radar (SRR) and long-range radar (LRR). The combination of both these types of radar provides valuable data for advanced driver assistance systems. The combination of SRR and LRR can be seen in Fig. 5.1, where LRR can track 3 motorway lanes over a distance of up to 150 m and SRR uses an angle of 80° to monitor the immediate area up to 30 m (Wenger, 2005).

Short-range radar (SRR)

For short-range applications, UWB sensors are preferred because of their low-cost perspective and their high resolution in range. Since these sensors do not

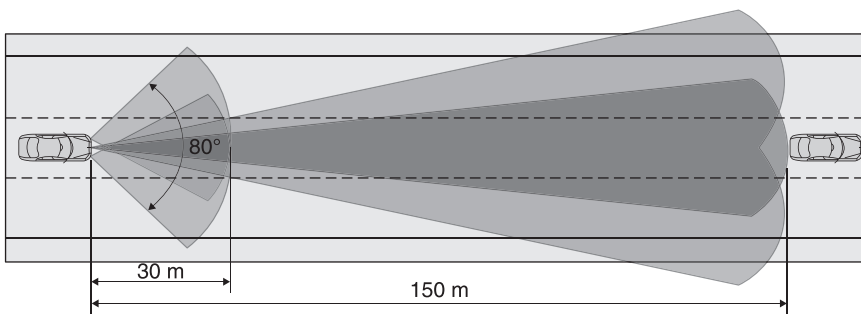

5.1 Combination of LRR and SRR for advanced safety features (Dariu *et al.*, 2001).

© Woodhead Publishing Limited, 2013

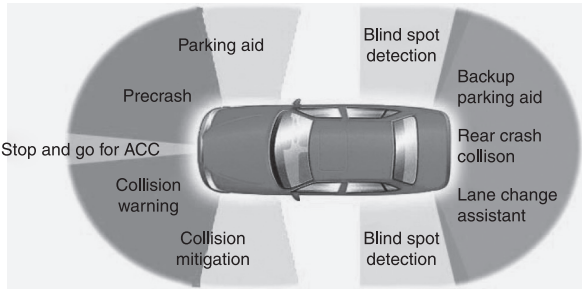

5.2 Applications using SRR (Dariu *et al.*, 2001).

require long-range capability, lower frequencies are preferred (Schneider, 2005). The applications of SRR are shown in Fig. 5.2, which include (Wenger, 2005):

1. ACC support with Stop and Go functionality;
2. collision warning;
3. collision mitigation;
4. blind spot monitoring;
5. parking aid (forward and reverse);
6. lane change assistant;
7. rear crash collision warning.

Long-range radar (LRR)

The automotive LRR functions at 77 GHz to access blind areas in front of the automobile. This sensor provides information about the traffic situation in front of the vehicle, making it possible to react to altered traffic conditions. This radar is the fundamental part of the ACC with active brake assist. In contrast to the smooth deceleration capability of the ACC, the active brake assist provides much higher braking forces for deceleration (Schneider, 2005). LRRs measure range, angle and relative radial velocity of multiple targets, by using multi-beam antenna systems.

Radar sensors for automotive applications are typically divided into two categories, continuous wave (CW) radar and pulse radar.

Continuous-wave radar

Continuous-wave (CW) radar transmits and receives at the same time. The transmitter generates a continuous sinusoidal oscillation at frequency, f_t, which is radiated by the antenna. On reflection by a moving target, the transmitted signal is shifted by the Doppler effect by an amount of f_d. It is also possible to measure the range using a CW radar system by frequency modulation or digital modulation techniques such as phase-shift keying (PSK). A systematic variation of transmitted

© Woodhead Publishing Limited, 2013

frequency or phase places a unique time stamp on the transmitted wave at every instant. By measuring the frequency or phase of the received signal, the time delay between transmission and reception can be measured and therefore the range can be measured (Koen and Van Caekenberghe, 2007):

$$R = c\frac{T}{2}\frac{\Delta f}{f_2 - f_1} \quad [5.1]$$

where c is the speed of light, f is the difference between transmitted and received signal, f_2 is the maximum transmitted frequency, f_1 is the minimum transmitted frequency and T is the period between f_1 and f_2, and the velocity is given by (Koen and Van Caekenberghe, 2007):

$$v = \frac{dR}{dt} \quad [5.2]$$

Pulse radar

The pulse Doppler radar has the advantage to detect small amplitude moving target returns against a large amplitude cluttered background. Pulse-delay ranging is based on the measurement of the time delay between the transmitted pulse and the received echo (Koen and Van Caekenberghe, 2007):

$$R = c\frac{\Delta T}{2} \quad [5.3]$$

where c is the speed of light and T is the time difference between transmitted and received pulse and echo. The velocity is related to the Doppler frequency shift between the transmitted pulse and received echo (Koen and Van Caekenberghe, 2007):

$$v = \frac{f_d \lambda_o}{2} \quad [5.4]$$

where f_d is the Doppler frequency shift and λ_o is the free space wavelength at the center frequency. Pulse-Doppler radars are half duplex, meaning that they either transmit or receive, which results in high isolation between the transmitter and receiver, thus increasing the dynamic range of the receiver and the range detection of the radar. The disadvantage of this system is the existence of a blind zone given by (Koen and Van Caekenberghe, 2007):

$$R_b = c\frac{(\tau_p + t_s)}{2} \quad [5.5]$$

where τ_p is the pulse width and t_s is the switching time of the transmit and receive switch, if applicable. Pulse-Doppler radar systems are therefore better suited for long-range detection, whereas FMCW radar is better suited for short-range detection (Koen and Van Caekenberghe, 2007).

© Woodhead Publishing Limited, 2013

5.1.2 Requirements for car radar sensors

The acquisition parameters for high resolution LRR data are (Wenger, 2005):

- center frequency 76.5 GHz;
- maximum field of view ±10°;
- azimuth beamwidth 1°;
- elevation beamwidth 5°;
- range resolution 1 m;
- velocity resolution 1 km/h;
- system sensitivity −20 dBm at 150 m.

Typical specifications for a 79 GHz SRR sensor are (Wenger, 2005):

- frequency 79 GHz;
- bandwidth 4000 MHz;
- maximum field of view ±80°;
- range 30 m;
- range accuracy ± 5 cm;
- bearing accuracy ±5°.

5.2 Radio-frequency (RF) MEMS components for automotive radar

5.2.1 RF MEMS switches and tunable capacitors

Radio-frequency (RF) MEMS switches and tunable capacitors are the principal components of most RF MEMS circuits and devices, such as phase shifters (Barker and Rebeiz, 2000), reconfigurable antennas and matching circuits (Brown, 1998; Ulm *et al.*, 2003), and beam steering applications (Brown, 1998; Schoebel *et al.*, 2005; Sterner *et al.*, 2009), which are suitable for automotive radar applications.

Low insertion loss, high signal linearity, high isolation, near-zero power consumption, large bandwidth of RF MEMS switches, high tuning range, low series resistance and high linearity of mechanically tunable capacitors are the advantages of these components as compared to their semiconductor equivalents. As their semiconductor counterparts, they can be fabricated in large volume parallel processes on semiconductor wafers, resulting in high product uniformity, potentially very low cost and ease of integration/assembly with semiconductor components and systems. However, they suffer from reliability issues, low switching or actuation speed, low number of cycles corresponding to lifetime, low power handling capabilities or limited hot switching in high power applications; and most of them require complex fabrication and integration processes in non-standardized process flows (Oberhammer, 2004).

Electrostatic actuation is the most widely used because of the near-zeroactuation power consumption, simple design and fabrication, well-developed theory,

© Woodhead Publishing Limited, 2013

maximum force in the contact position, pull-in hysteresis for robustness and good integration compatibility with IC technology.

In general, RF MEMS switches can be categorized by the nature of the switching mechanism (metal-contact or capacitive contact), and the usage on a circuit level (series or shunt configuration). The most commonly used embodiments are electrostatically actuated metal-contact series switches and electrostatically-actuated capacitive shunt switches, schematically illustrated in Fig. 5.3, and shortly summarized in the following:

- *Electrostatically actuated series switch with metal contacts*: a cantilever or membrane with a metal contact bar opens or closes the signal line by a metal-to-metal direct ohmic contact. Switches of this category are normally off. The ohmic contact characteristic of this switch type makes it capable of switching DC to RF signals of up to 100 GHz, but they normally suffer from low isolation at high frequencies because of up-state capacitance and substrate wave coupling. The metal contact physics is complicated and large-force actuators must be employed for high reliability. Lifetime is limited by contact degradation, and these switches typically fail in short-circuit by the metal contacts getting stuck, the most mature designs surviving billions to trillions of switching cycles.
- *Electrostatically actuated capacitive shunt switches*: these consist of a metal bridge or membrane connected to RF ground and moving vertically above the signal line, which is isolated by a thin dielectric film. The switch is normally in

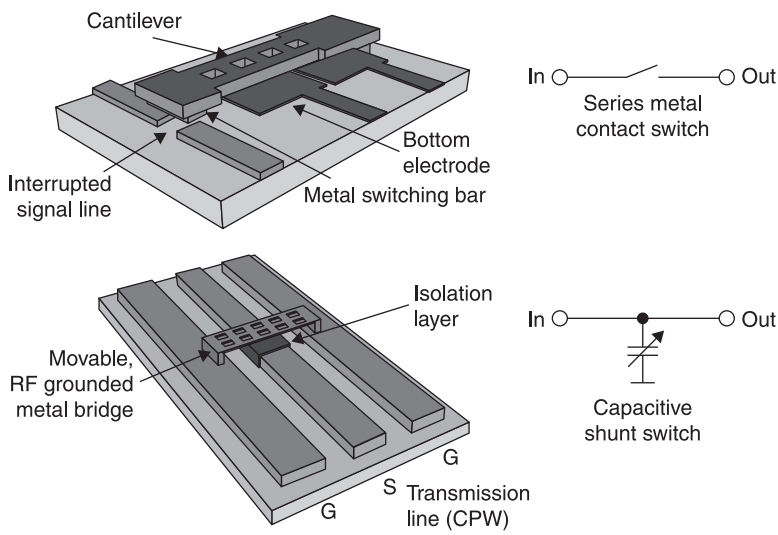

5.3 The two most commonly used electrostatically actuated MEMS switch types (Oberhammer, 2004).

© Woodhead Publishing Limited, 2013

the up position (on-state), where the signal freely propagates. In the down-state, the bridge capacitively short-circuits the signal line to the RF ground (off-state). Due to its capacitive nature, this switch type is not suitable for low frequency signals and is mostly used in applications above 10 GHz. Its performance is limited by the down-state parasitic inductance. The main reliability factor is the dielectric charging of the isolation layer, which results in non-reproducible actuation, or even in failure of the switch to open the signal line.

As an example, an inline DC-contact MEMS series switch (Thanh *et al.*, 2009), developed for V band applications (50–75 GHz), is shown in Fig. 5.4. Table 5.1 gives an overview of MEMS switches, mainly designed for W-band (75–110 GHz), thus suitable for 76 to 81 GHz automotive radar.

Another RF MEMS component of importance is tunable capacitors. In MEMS-based tuning circuits, either MEMS-switched capacitor banks or electromechanically tunable capacitors are used. The capacitance can be tuned either by varying the gap between parallel plates or by changing the overlapping area between a fixed and a moving electrode. An example of the latter concept, such as area tuning capacitors, is a comb-drive tunable capacitor which, however, is not suitable for higher GHz frequencies because of limited Q-factors. Actuators tuning the gap between two parallel plates are similarly built to RF MEMS capacitive shunt switches. However, instead of keeping the suspended part either in the down-state or up-state, it is possible to tune the position of the capacitive membrane in analog mode, and thus the capacitive loading of the line, which results in very high Q factors and thus suitability for W-band applications. However, the limited tuning range and non-linearity effects of analog tuning have rendered tunable capacitors less suitable for W-band circuits as compared to MEMS-switched capacitive loads.

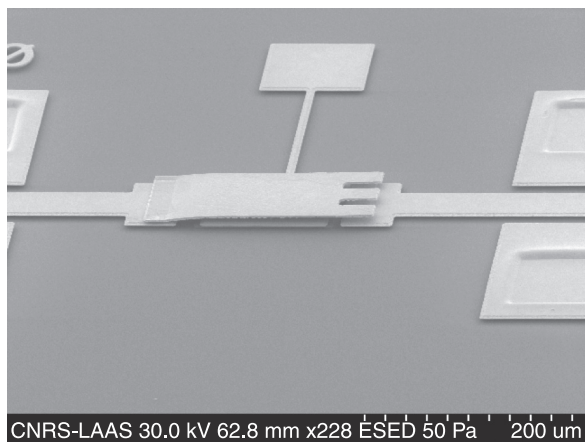

5.4 An in-line DC-contact MEMS series switch (Thanh *et al.*, 2009).

© Woodhead Publishing Limited, 2013

Table 5.1 Comparison of RF MEMS switches

Device	Frequency band	Actuation voltage (V)	On/off speed (μs)	Insertion loss (dB)	Isolation (dB)	Reference
DC-contact series switch	V-band	80	0.3 and 0.16	1.94 at 60 GHz	14.79 at 60 GHz	Thanh *et al.* (2009)
Capacitive series switch	W-band	–	15	0.3 at 50–100 GHz	17 at 76.5 GHz	Stehle *et al.* (2008)
T-match capacitive shunt switch	W-band	30	–	0.25 ± 0.1	20 at 80–110 GHz	Rizk *et al.* (2001)
π-match capacitive shunt switch	W-band	30	–	0.4 ± 0.1 at 90 GHz	30–40 at 75–110 GHz	Rizk *et al.* (2001)
Longitudinal coplanar shunt switch	W-band	25	–	0.3 at 75–100 GHz	30 at 77–94 GHz	Ulm *et al.* (2003)
T-match and π-match capacitive shunt switch on quartz substrate	W-band	40	–	0.2–0.5	25 over the W-band	Rizk and Rebeiz (2004)
Metal-to-metal contact shunt switch	DC to 100 GHz	22	0.5 with 40 V bias in g voltage	1 at 75 GHz, 1.4 at 100 GHz	22 at 100 GHz	Mercier *et al.* (2004)
DC contact series switch	1–40 GHz and W-band	39	45	036 at 77 GHz	17.3 at 77 GHz	Ghodsian *et al.* (2008)

© Woodhead Publishing Limited, 2013

Examples of a MEMS-tunable W-band capacitor for beam steering applications are demonstrated in Sterner *et al.* (2009) and Chicherin *et al.* (2010a). The tunable varactors are composed of metal patches suspended with four folded flexures above the fixed electrode. The gap can be tuned gradually from the initial distance of 1.0 to 0.4 μm, with an actuation voltage below 35 V.

5.2.2 MEMS phase shifters

Phase shifters are widely employed in radar systems based on phased antenna arrays. MEMS technology offers lower insertion loss, higher linearity over a large bandwidth and lower power consumption as compared to solid-state technology. Ferrite-based phase shifters have good performance, but cannot be easily integrated and are more expensive in fabrication as compared to MEMS technology.

Three main types of MEMS phase shifters have been presented in the literature to date:

1. MEMS-switched true-time delay-line (TTD) phase shifter networks (Stehle *et al.*, 2008);
2. distributed MEMS transmission line (DMTL) phase shifters (Ulm *et al.*, 2003); and
3. a novel concept based on tuning the loading of a 3-D micromachined transmission line by a dielectric block placed on top of the line, which is vertically moved by MEMS actuators (Somjit *et al.*, 2009).

A discussion of each of these types with examples is provided in the following:

MEMS-switched true-time delay (TTD) phase-shifter networks

MEMS-switched TTD phase shifters consist of various phase shifter sections in a cascade arrangement. MEMS switches are employed in different lines to switch the linelength of the signal, resulting in different phase shifts. Since RF MEMS switches are used to switch between different paths, this kind of phase shifter inherits all the advantages of RF MEMS switches, resulting in excellent performance. However, they are not suitable for millimeter wave frequency, including W-band, because the performance of multiple switches and the necessary lengths of the transmission line degrade the performance (Somjit *et al.*, 2009).

Stehle *et al.* (2008) describe a phase shifter consisting of a 45° loaded-line phase shifter element, a 90° as well as a 180° switched-line phase shifter element, resulting in 3-bit RF MEMS phase shifter. For the complete device, return loss was better than −12 dB and the insertion loss was −5.7 dB at 76.5 GHz.

Design equations for a MEMS switched TTD phase shifter comprised of impedance-matched slow-wave unit cells with the optimization goal to maximize the figure-of-merit $\Delta\varphi$/dB are presented by Lakshminarayanan *et al.* (2007). To

© Woodhead Publishing Limited, 2013

verify the equations, 1-bit phase shifters were implemented by a cascading number of unit cells corresponding to various maximum design frequencies. The phase shifter with maximum frequency of 110 GHz showed an insertion loss of about 2.65 dB, measured $\Delta\varphi$/dB of 150°/dB and return loss below −19 dB.

Distributed MEMS transmission line phase shifters

The second type, distributed MEMS transmission line (DMTL) phase shifters, is based on periodically loading the transmission line with capacitive MEMS bridges to vary the line capacitance. Consequently, the propagation coefficient of the line and the signal phase between the input and the output of the phase shifter are altered. Varying the capacitance of the line, in addition to changing the propagation coefficient, changes the line impedance. This effect imposes another limitation on the maximum usable capacitance ratio, in addition to those required by the switch design parameters, according to the acceptable mismatch. The capacitance ratio is reported to be limited to approximately 1.3 to 1.6 in (Ulm *et al.*, 2003).

In general, DMTL phase shifters have excellent performance in the millimeter-wave regime in comparison to TTD phase shifters. However, there are some disadvantages to take into consideration. Capacitive MEMS bridges incorporated in DMTL phase shifters are composed of thin metal bridges that cannot handle large induced current densities at high RF power, because of limited heat conductivity to the substrate due to their suspension above the substrate. This results in reliability issues due to buckling (plastic deformation) or even melting of the thin metal layer. In addition, thin gold bridges, as employed in both types of MEMS phase shifters, are subject to drastically losing their elastic behavior, even at slightly elevated temperatures of just around 80°C, resulting in decreased reliability (Somjit *et al.*, 2009).

It is also possible to load the transmission line digitally by employing fixed capacitances, which can be switched to load the line. This alternative method provides the capability of increasing the capacitance ratio, which is more suitable in millimeter-wave regimes (Ulm *et al.*, 2003).

Barker and Rebeiz (2000) presented design and optimization of DMTL phase shifters for U-band and W-band, with analog tuning capability of the bits on quartz substrate. The W-band DMTL phase shifter consisted of 48-bridge DMTL elements with pull-down voltage of just over 26 V and corresponding capacitance ratio of 1.15. Measured phase shift per decibel loss was 70°/dB from 75 to 110 GHz. Average measured insertion loss was −2.5 dB and return loss was −11 dB at 94 GHz.

Hung *et al.* (2003) demonstrated a low-loss distributed 2-bit W-band MEMS phase shifter on glass substrate (Fig. 5.5). Each unit cell of this phase shifter consists of a MEMS bridge and the sum of two MAM capacitors, which were fabricated using the cross-over between the MEMS bridge and the CPW ground plane. Since the simulated phase shift of the unit cell was about 1.2° at 80 GHz, a

© Woodhead Publishing Limited, 2013

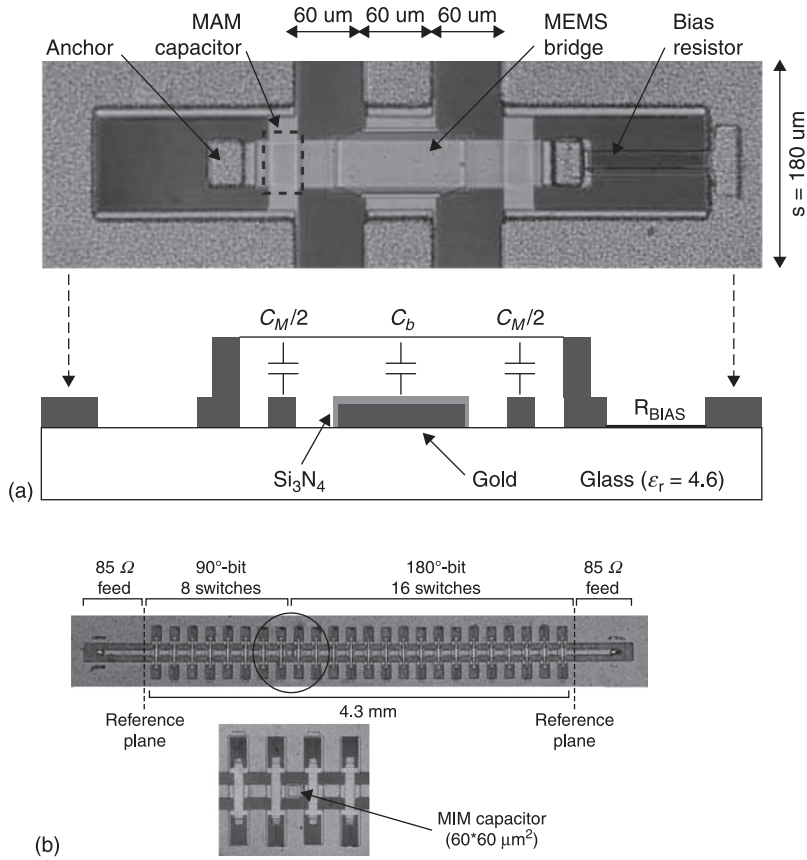

5.5 A low-loss distributed 2-bit W-band MEMS DMTL phase shifter: (a) single cell with its corresponding profile; (b) entire 2-bit DMTL phase shifter composed of 24 switches (Hung *et al.*, 2003).

90° section with 8 switches and a 180° degree section with 16 switches were cascaded. Phase shifts of 0, 89.3, 180.1 and 272° were measured at 81 GHz, which were close to the designed frequency and phase shifts. Return loss was better than −11 dB, the average insertion loss was −2.2 dB and the phase error was equal to ±2°. The worst insertion loss was measured as −2.9 dB at 94 GHz.

MEMS tunable dielectric-block loaded-line phase-shifter

The third type of MEMS phase shifters was presented by Somjit *et al.* (2009) and is based on tuning the loading of a 3-D micromachined transmission line by a dielectric block placed on top of the line and moved by MEMS actuators (Fig. 5.6). The single cell of this phase shifter consisted of a high-resistivity monocrystalline silicon block placed upon and loading a 3-D high-impedance micromachined

© Woodhead Publishing Limited, 2013

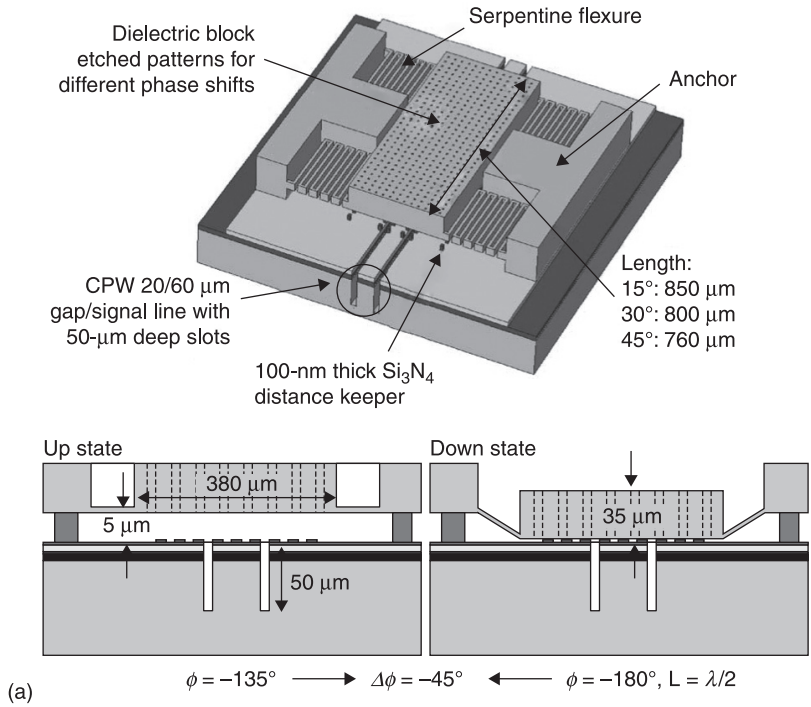

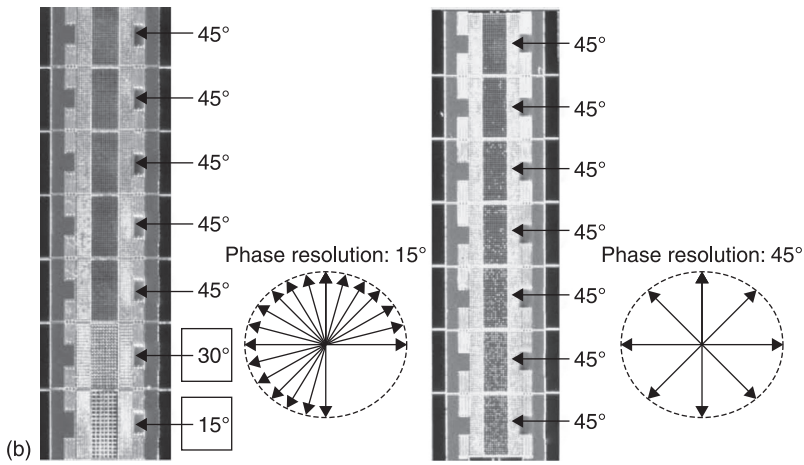

5.6 Binary-coded 4.25-bit W-band monocrystalline-silicon MEMS multistage dielectric-block phase shifters: (a) working principle of a single stage of the phase shifter, (b) microscopic pictures of fabricated seven-stage phase shifters (Somjit *et al.*, 2009).

© Woodhead Publishing Limited, 2013

coplanar waveguide (CPW). The relative phase shift was achieved by vertically moving the dielectric block above the transmission line by electrostatic actuation, which resulted in different propagation constants of the microwave signal, depending on the vertical displacement of the dielectric block. Periodic patterns were etched into the dielectric block, and the ratio of the etched to the unetched area made it possible to artificially tune the macroscopically effective dielectric constant of each individual block. By cascading multiple stages of such unit cells, a binary coded 15° + 30° + 5° × 45° phase shifter was implemented. At the design frequency of 75 GHz, maximum return and insertion loss were −17 and −3.5 dB, respectively, which corresponded to a loss of −0.82 dB/bit, and a phase shift efficiency of 71.1°/dB and 490.02°/cm. This phase-shifter type was found to be linear with a third-order intercept point IIP3 of 49.27 dB (Somjit *et al.*, 2009). Also, as this concept does not employ any thin metallic bridges, which limit the current and thus the power handling of conventional MEMS TTD and DMTL phase-shifters, the power handling is effectively only limited by the heat-sink capability of the transmission line itself, that is not by the MEMS part. A comparable study found that even at 40 dBm power at 75 GHz, the hottest spot on this phase-shifter design has only increased by 30°C, which is 10 to 20 times less than for conventional MEMS TTD and DMTL phase-shifter designs (Somjit *et al.*, 2011).

To summarize this section on RF MEMS phase shifters, a comparison among several W-band phase shifters is provided in Table 5.2. Most data is reproduced from Somjit *et al.* (2009), with some additions.

5.2.3 MEMS oscillators

Resonators can be classified into two types, electromagnetic wave resonators and electromechanical or (electro)acoustic wave resonators, based upon their principle of operation. Since the second type is mostly based on mechanical resonation, they are not usable in high frequency applications. Among various resonators of the first type, cavity and dielectric resonators can be used at millimeter-wave frequencies, with Q-factors above 500. Since dielectric resonators consist of a piece of higher density material, generally their size is smaller in comparison to air-filled cavity resonators (De Raedt *et al.*, 2003).

Micromachining (MEMS) technology can be employed to enhance the performance of resonators at higher frequencies or to add the tuning capability. However, most of the resonators investigated in the literature, for millimeter-wave regime, are mainly measured for the resonance frequency below 60 GHz (Guillon *et al.*, 1999; Ocket *et al.*, 2006) and just a few are demonstrated for W-band.

Dancila *et al.* (2010) presented a variable-sized MEMS-based Faraday cage, used to tune the resonant frequency of a silicon micromachined cavity resonator (Fig. 5.7). An electrostatically tunable micro-electromechanical cantilever array,

© Woodhead Publishing Limited, 2013

Table 5.2 Comparison among several W-band RF MEMS phase shifters (Somjit, 2009)

Reference	Stehle *et al.* (2008)	Rizk and Rebeiz (2003a)	Rizk and Rebeiz (2003b)	Lakshminarayanan and Weller (2007)	Hung *et al.* (2004)	Barker and Rebeiz (2000)	Hung *et al.*. (2003)	Somjit *et al.* (2009)
type	Loaded line and switched line	Switched line	Switched line and reflect line	TTD	DMTL	DMTL	DMTL	Loaded line with dielectric-block
Substrate	Si	Quartz	Quartz	Quartz	Glass	Quartz	Glass	Si
Nominal frequency f_n (GHz)	76.5	90	80	110	78	94	81	75
Number of bits	3	1	2	1	3	analog	2	4.25
Config. possibilities	8	2	4	2	8	analog	4	19
Max. $\Delta\varphi$ of f_n $(^o)$	315	180	282	410	315	170	272	270
Max. IL of f_n (dB)	≥5.8	≥2.5	≥6.1	≥2.65	≥3.2	≥2.5	>2.2	≥3.5
Max. IL/bit of $f_n\left(\frac{dB}{bit}\right)$	–1.93	–2.5	–3.05	–2.65	–1.07	–	–1.1	–0.82
Max. $\Delta\varphi$ loss of $\left(^{\circ}\frac{\square}{dB}\right)$	55.26	85.71	70.5	150	95.75	70	–	71.05
Max. $\Delta\varphi$/loss $\left(^{\circ}\frac{\square}{dB}\right)$	–	32.85	–	–	83.3	–	–	98.3
Max. RL of f_n (dB)	≤12	≤12	≤9.5	≤19	≤12	≤11	≤11	≤17
Max. IL at W (dB)	≥8	≥6	≥7	–	≥6	≥2.7	≥2.9	≥4.1
Max. RL at W (dB)	≤7.5	≤3	≤9	≤19	≤9	≤10	≤11	≤12

© Woodhead Publishing Limited, 2013

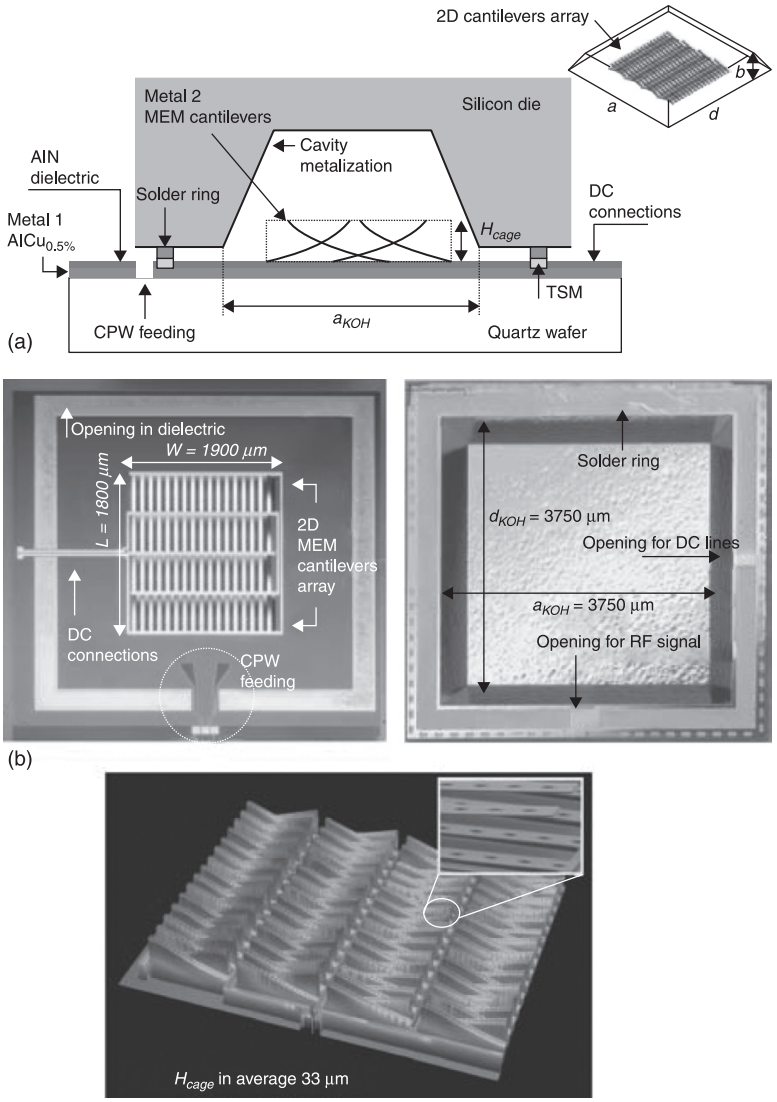

5.7 A MEMS variable Faraday cage as tuning element for integrated silicon micromachined cavity resonators: (a) cross-section of the MEMS tunable cavity resonator, (b) bottom part, top part and plot of the 2-D MEM cantilever array implementing the Faraday cage (Dancila *et al.*, 2010).

© Woodhead Publishing Limited, 2013

which forms a Faraday cage, incorporated in the cavity could change the resonance frequency of the resonator by influencing the electromagnetic field inside the cavity resonator. The dimension of the cavity resonator designed for the resonance frequency of 60 GHz was 3844 × 3844 × 440 μm. MEMS cantilevers could be actuated gradually from 0 to 30V. The measured unloaded and loaded quality factors were 55 and 48, respectively, which were low because of the reported flaw in the metallization of the cavity resonator.

5.3 Examples of RF MEMS-based automotive radar front-end technology

In this section, concepts, implementations and advantages of two RF MEMS-based radar front-ends for automotive applications are discussed. These MEMS automotive-radar front-ends were developed at the University of Michigan (USA) (Van Caekenberghe and Sarabandi, 2006; Van Caekenberghe, 2009) and Robert Bosch GmbH (Germany) (Ulm *et al.*, 2003; Schobel *et al.*, 2005).

5.3.1 The University of Michigan 38-GHz RF MEMS car-radar front-end

A 38-GHz high-pulse repetition frequency (HPRF) mono-pulse Doppler-radar front-end was developed at the University of Michigan by Van Caekenberghe and Sarabandi (2006) and Van Caekenberghe (2009), for a long-range automotive radar applications, such as pre-crash detection and ACC. The radar front-end is based on an RF MEMS electronically scanned array (ESA) design and low-loss MEMS time-delay units (TDU), which offer cost and performance advantages over the other technologies. A maximum radar range up to 150 m and a resolution of 1.5 m are obtained from this design. The scanning angle resolution for this car radar is ±11° in the Azimuth plane, with an angular deviation of ±2.5° from an amplitude mono-pulse tracking, as compared to the scanning angle. This front-end was optimized for 38 GHz; however, it can be scaled to 77 GHz to match the ITU-R recommendations (Van Caekenberghe and Sarabandi, 2006). The front-end concept of the RF MEMS-based HPRF automotive radar is shown in Fig. 5.8.

As shown in Fig. 5.8, the radar front-end consists of a T/R module, an IF impulse processor and two passive sub-arrays, which are individually connected to the T/R module. In the transmitting mode, a transmitted signal is fed to the transmitter module via an IF impulse processor, while the received signal is separated and fed to the sum and the Azimuth-different channels to correct the angular errors. The radiation patterns of the transmit and receive modules are shown in Figs. 5.9(a) and 5.9(b), respectively. Two passive sub-arrays, as the key units, are composed of 16-dB-gain 64 elements of microstrip antennas optimized at 38 GHz. The line antenna arrays fed through a slotted aperture from a microstrip

© Woodhead Publishing Limited, 2013

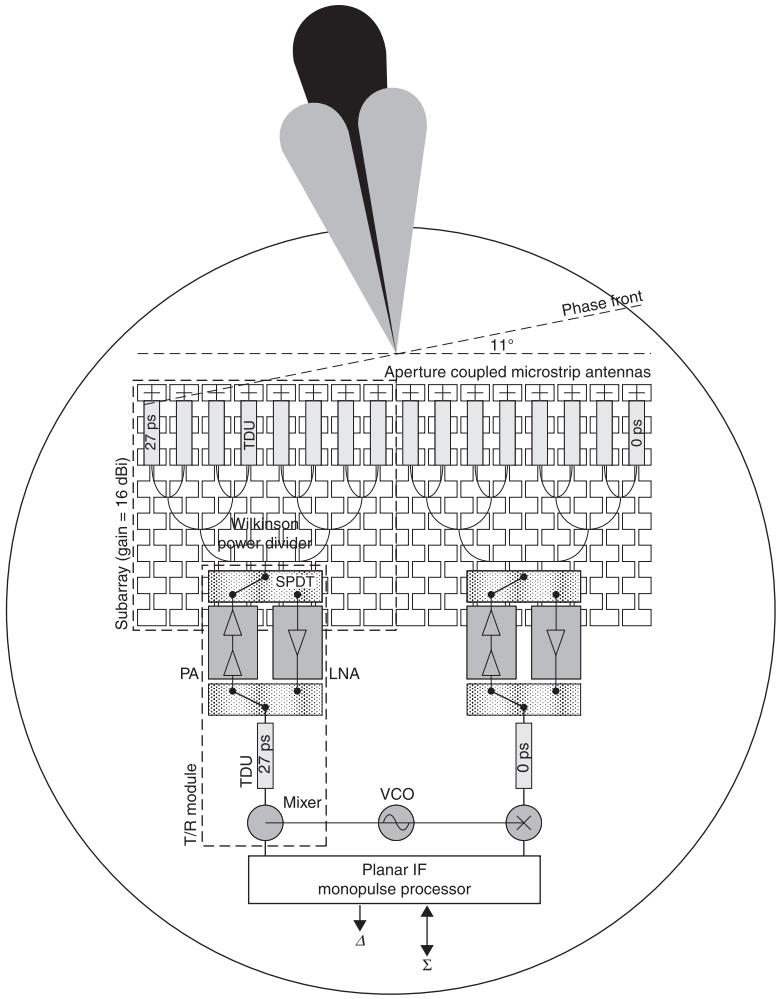

5.8 A complete 38-GHz RF MEMS-based front end of a HPRF mono-pulse Doppler-radar at the University of Michigan (Van Caekenberghe and Sarabandi, 2006).

corporative feed network consist of Wilkinson power dividers and grounded coplanar waveguide (GCPW) TDUs, which are analog DMTLs and each line is loaded with 60 elements of RF MEMS varactor. This design offers a low-loss and wideband device, with a good power handling capability at 38 GHz.

The front-end module was fabricated on a 6-inch fused silica wafer and a Rogers TMM3 substrate using wafer-scale monolithic tile construction. The fused silica wafer contains two passive sub-arrays, which are the MEMS TTD feed networks coupled to microstrip antenna arrays fabricated on the Rogers substrate. Apart from the microstrip antenna arrays, the other modules were fabricated in a

© Woodhead Publishing Limited, 2013

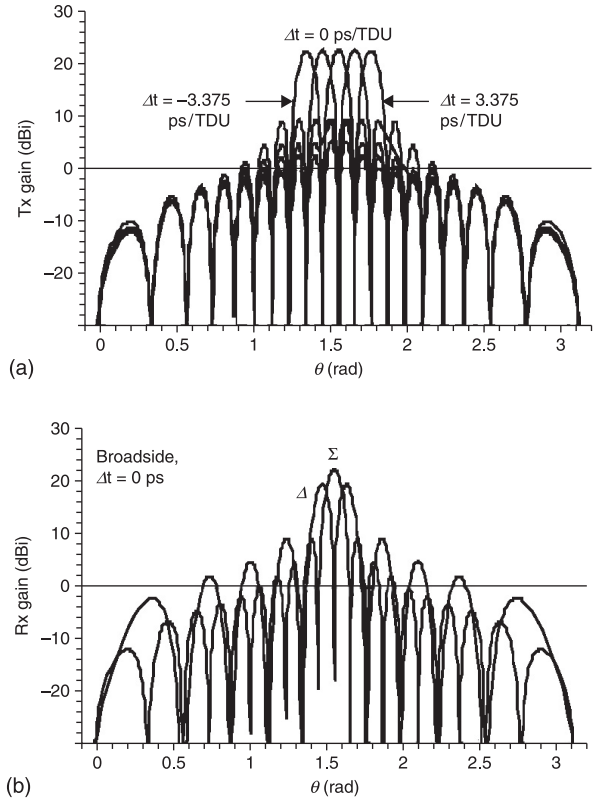

5.9 Radiation characteristic of the transmit (a) and receive (b) mode of the 38-GHz high-pulse repetition frequency (HPRF) mono-pulse Doppler-radar (Van Caekenberghe and Sarabandi, 2006; Van Caekenberge, 2009).

class-100 cleanroom with a wafer-scale RF MEMS process with SiCr integrated thin-film resistors and high-resistivity bias lines.

5.3.2 Robert Borsch 77-GHz automotive-radar front-end

Schoebel *et al.* (2005) at Robert Bosch GmbH developed two designs for 77-GHz analog-beam-forming automotive radar front-ends. The first approach was based on a MEMS single-pole-multi-throw switch, which is employed to select one of several beams of a planar Rotman lens, which then feeds branches of a patch-antenna array. The second approach was a more conventional patch-antenna array beam-steering concept, where RF MEMS phase shifters, fed via a Wilkinson power divider, were used to configure the phase distribution of the signals of the antenna array (Ulm *et al.*, 2003; Schoebel *et al.*, 2005). These designs offer better performance, ease of design and low manufacturing costs in comparison to

© Woodhead Publishing Limited, 2013

the other millimeter-wave technology. These two 77-GHz RF MEMS-based automotive-radar concepts are shown in Fig. 5.10.

For the first design, an automotive radar front-end implemented with RF MEMS phase shifters with less than 3 bits and a patch antenna array was investigated. The distance between each antenna element was a half-wavelength, as compared to the wavelength in free space. Therefore, fixed scanning beams of 0, ±14.5, ±30 and ±48.6° from the boresight axis are obtained from this design. The beam for mrf is implemented by constructing 3 stages of a 2-port Wilkinson power divider with an employment of a 20-dB Chebyshev pattern. RF MEMS stub-loaded-line phase shifters employed in this automotive radar design is based on MEMS capacitive shunt switches, offering a 90 and 180° phase shift and less than 4° phase tolerance. This phase shifter exhibits a very wide bandwidth, which is suitable for ultra-wideband (UWB) applications.

The second alternative design consists of a Rotman lens and a single-pole–quadruple-throw (SP4T) switch. This design is straightforward and offers a complete symmetrical device, exhibiting a uniform loss for all scan beams. The numbers of the scan angle reduces to 4, pointing to ±6 and ±18° from boresight axis. The Rotman lens was implemented by microstrip technology and the body of the lens is designed as a parallel-plate waveguide with microstrip feeding. The Rotman lens with patch antenna and waveguide interconnects are realized on a

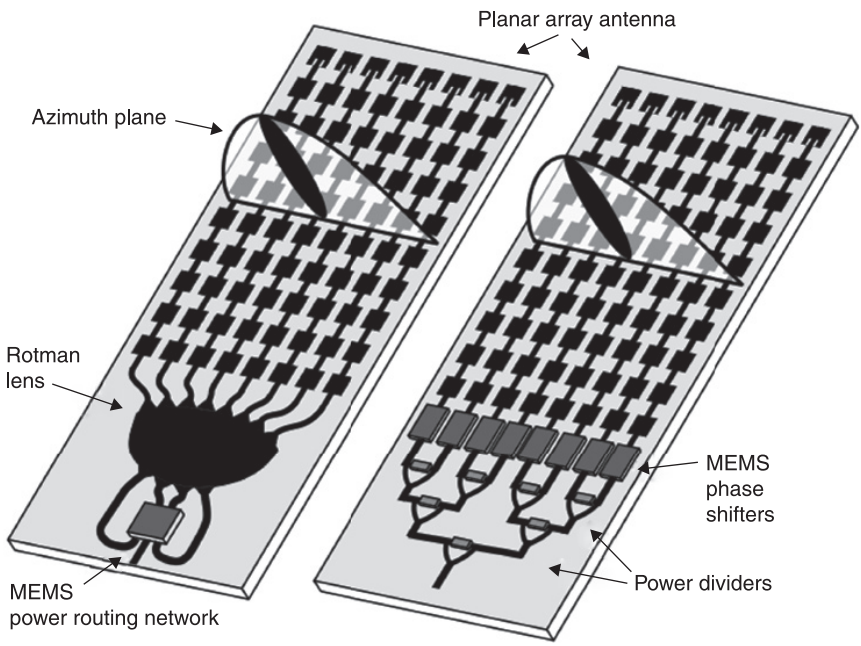

5.10 Two 77-GHz RF MEMS automotive-radar front ends from Robert Bosch GmbH (Schoebel *et al.*, 2005). The designs are based on Rotman lens (left) and MEMS phase shifters (right).

© Woodhead Publishing Limited, 2013

5-mil Ro3003 substrate. The SP4T switch is designed based on capacitive-shunt single-pole–double-throw (SP2T) switch design. The SP2T switch offers an insertion loss of 1.8 dB at 77 GHz. Figure 5.11 shows the fabricated MEMS automotive radar based on Rotman lens and SP4T switch. The radiation pattern of the design with Rotman lens and the antenna array is shown in Fig. 5.12, in

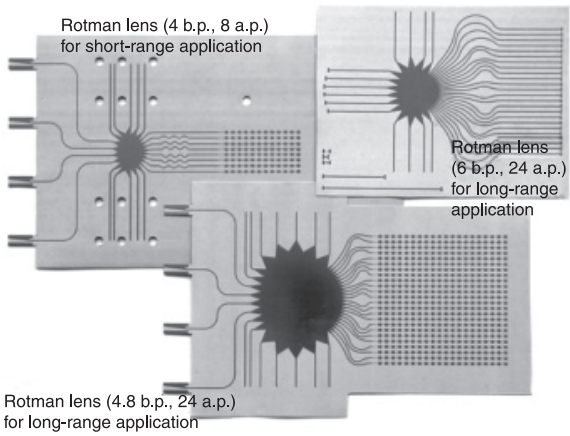

5.11 77-GHz MEMS automotive radar realized by RFMEMSSP4T switch and Rotman lens (Schoebel *et al.*, 2005).

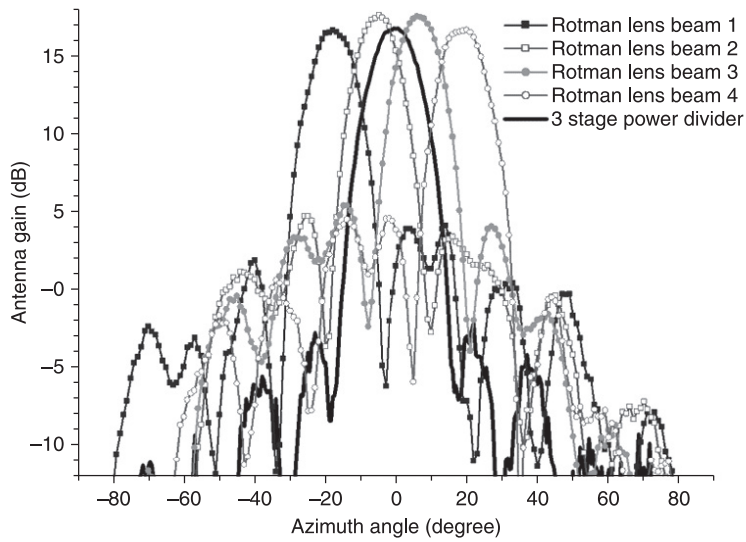

5.12 Radiation characteristics of the 77-GHz MEMS automotive radar based on Rotman lens with microstrip antenna array compared with the alternative design implemented with MEMS phase shifters, three-stage Wilkinson power divider and the microstrip antenna array (Schoebel *et al.*, 2005; Ulm *et al.*, 2003).

© Woodhead Publishing Limited, 2013

comparison to the three-stage Wilkinson power divider and MEMS phase shifters, with the same microstrip antenna array.

5.4 Unconventional MEMS radar beam steering technologies

5.4.1 MEMS tunable reflective microwave surfaces

MEMS tunable high-impedance surface (HIS) have been used by several research teams (Sterner *et al.*, 2009a,b; Chicherin *et al.*, 2010a,b,c) for designing low-loss analog-type phase shifters. HIS, consisting of electrically small MEMS varactors placed on a dielectric substrate with the ground plane shown in Fig. 5.13, was used to achieve tunability of the effective surface input impedance. Since the size of the MEMS varactors is much smaller than the wavelength of the field above the structure, its electromagnetic response can be described in terms of the effective surface impedance. The array of MEMS varactors provides capacitive response to the electromagnetic field above the structure, and the grounded dielectric below provides an inductive response. Consequently, the structure possesses resonant properties, and at the resonance frequency its impedance becomes very high. When bias voltage is applied to the MEMS varactors, the

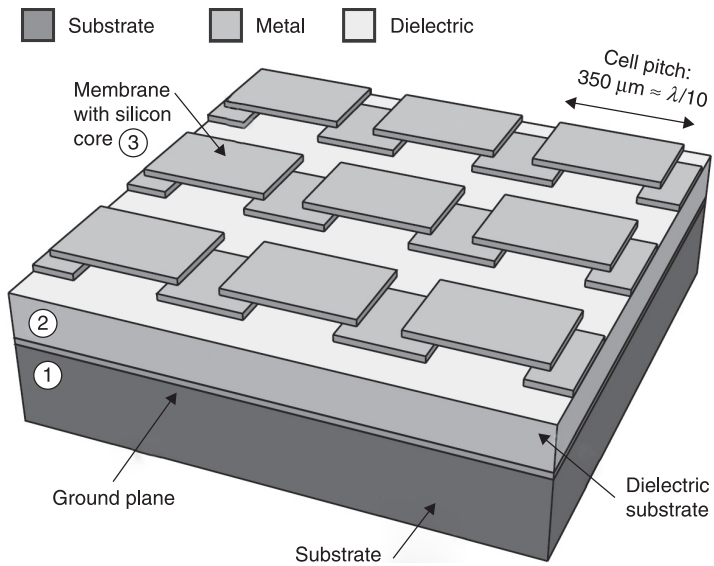

5.13 Periodic high-impedance metamaterial surface, composed of a low-loss dielectric substrate (2) integrated with a silicon substrate (1) and a transferred monocrystalline silicon membrane (3) (Sterner *et al.*, 2009).

© Woodhead Publishing Limited, 2013

gap of the MEMS varactors decreases, thereby increasing the effective capacitance of the structure and hence changes the effective surface impedance. This effects the phase of the reflection coefficient or propagation constant of the field reflecting from the structure or propagating above it, which can be used in beam steering and phase shifting applications. Electronic beam steering is achieved by inducing a gradient of the effective surface impedance throughout of the HIS, by applying different bias voltages to the different rows of elements of the structure (Fig. 5.14). Effectively, this allows tuning the phase of the reflection coefficient in different sections of the HIS, which affects the direction of the reflecting beam.

Reflection-type analog phase shifters can be obtained by placing the MEMS tunable HIS as a back-short of the rectangular metal waveguide in order to control the reflection phase. The fabricated MEMS-based HIS was placed as back-short of the rectangular metal waveguide WR-10 measuring S_{11}. As soon as the MEMS varactors are actuated, the reflection phase decreases, creating an analog tunable reflection type phase shifter. Transmission type analog phase shifters can be obtained by introducing MEMS tunable HIS in waveguide structures, in order to affect the phase factor of the propagation constant. The HIS can be placed adjacent to a dielectric rod waveguide at a distance *d* (Fig. 5.15). Changing the effective impedance of the HIS by applying different bias voltage to all MEMS varactors of the structure changes dramatically the phase at Port 2 of the waveguide, where the operation frequency is close to the resonance frequency. The phase shift is proportional to the length of the HIS.

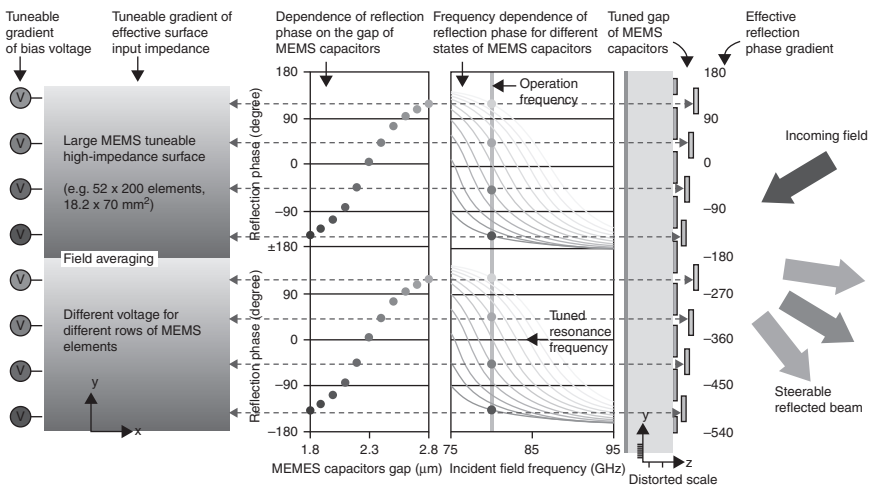

5.14 MEMS-based HIS with induced tunable gradient of the effective surface impedance for electric beam steering (Chicherin *et al.*, 2011).

© Woodhead Publishing Limited, 2013

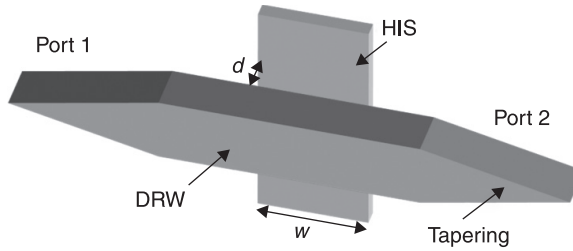

5.15 Phase shifter based on a dielectric rod waveguide (DRW) with an adjacent MEMS tuneable high-impedance surface (HIS) of a width, *w*, at a distance, *d* (Chicherin *et al.*, 2010a).

5.4.2 MEMS steerable leaky-wave antennas

The leaky-wave antenna (LWA), presented in Zvolensky *et al.* (2011), comprises a right-left-handed transmission line, where a microstrip is used as the right-handed transmission line and the left-handed loading comprises series reconfigurable MEMS capacitors and shunt narrow strip inductors. Microstrip, as a right-handed (RH) transmission line, offers two main advantages, ease and low-cost fabrication and suitability for MEMS implementation. Tunable MEMS capacitors are connected in series and shunt inductors are built, in the initial design, from thin strip lumped inductors, resulting in a transmission line circuit of distributed resonance element along the line. The resulting antenna is built from such cascaded unit cell resonators (Fig. 5.16). The length of the unit cell, just a fraction of the wavelength, makes the transmission line effectively homogenous.

In Fig. 5.17, scattering parameters (obtained from EM simulation software) of a single unit cell are shown. It is supposed that the scattering of one unit cell (in the case of a balanced unit cell) is enough to determine the main resonance frequency of the structure composed of such cells.

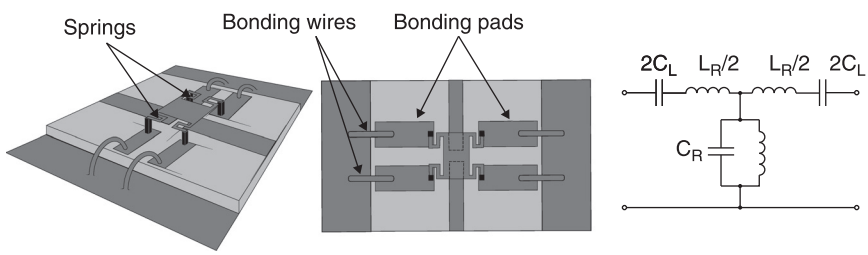

5.16 Unit cell of a MEMS-tunable leaky-wave antenna, and its equivalent lumped element circuit (Zvolensky *et al.*, 2011).

© Woodhead Publishing Limited, 2013

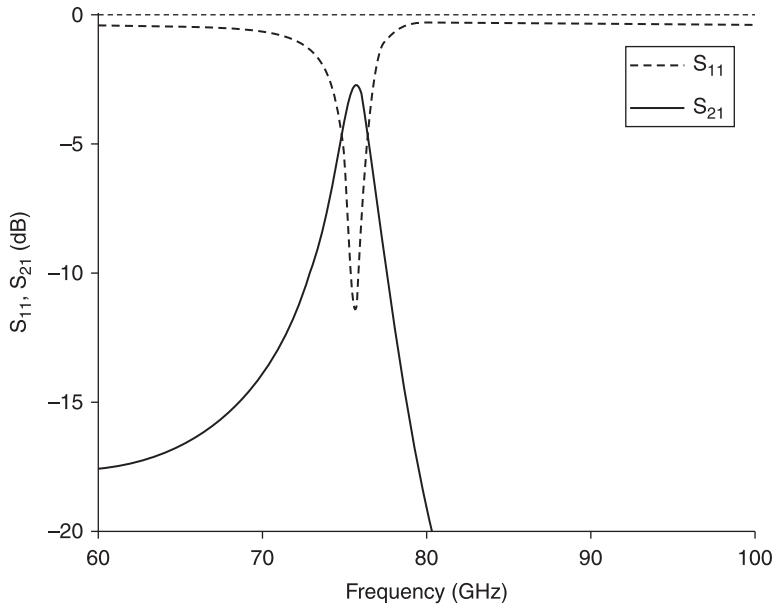

5.17 Simulated scattering parameters of a single unit cell of a leaky-wave antenna (Zvolensky *et al.*, 2011).

Figure 5.18 shows a scanning-electron microscopy (SEM) picture of a micromachined tuneable LWA, comprising 30 sequentially cascaded unit cells.

5.4.3 Mechanically driven antenna platform

A single antenna platform steered by an external magnetic field where a monolithic microwave integrated circuit (MMIC) and capacitors are vertically integrated has been shown by Kim *et al.* (2011). The electrical steering scheme using phase shifters is already mature and shows a fast scan speed. However, it requires a number of phase shifters and power amplifiers to obtain a large scan angle, resulting in bigger and more expensive systems. A mechanical steering antenna can radiate the beam directly, and it has a constant RF gain at any scan angle. The absence of multiple phase shifters and amplifiers, even at large scan angles, makes the mechanical beam steering antenna smaller in size and more efficient in RF capability. The required deflection of the antenna in Kim *et al.* (2011) is over 1.3 mm. A schematic of the RF antenna and steering method is shown in Fig. 5.19.

The antenna consists of two pairs of mechanical springs made of BCB with a thickness of 40 μm. Two metal-insulator-metal (MIM) capacitors are implemented by conventional micromachining and are vertically flip chip bonded to the suspended antenna substrate. Currents with the same magnitude and the same direction flow through a pair of adjacent coils under the movable antenna substrate and generate the driving magnetic force. When the current flows through two

© Woodhead Publishing Limited, 2013

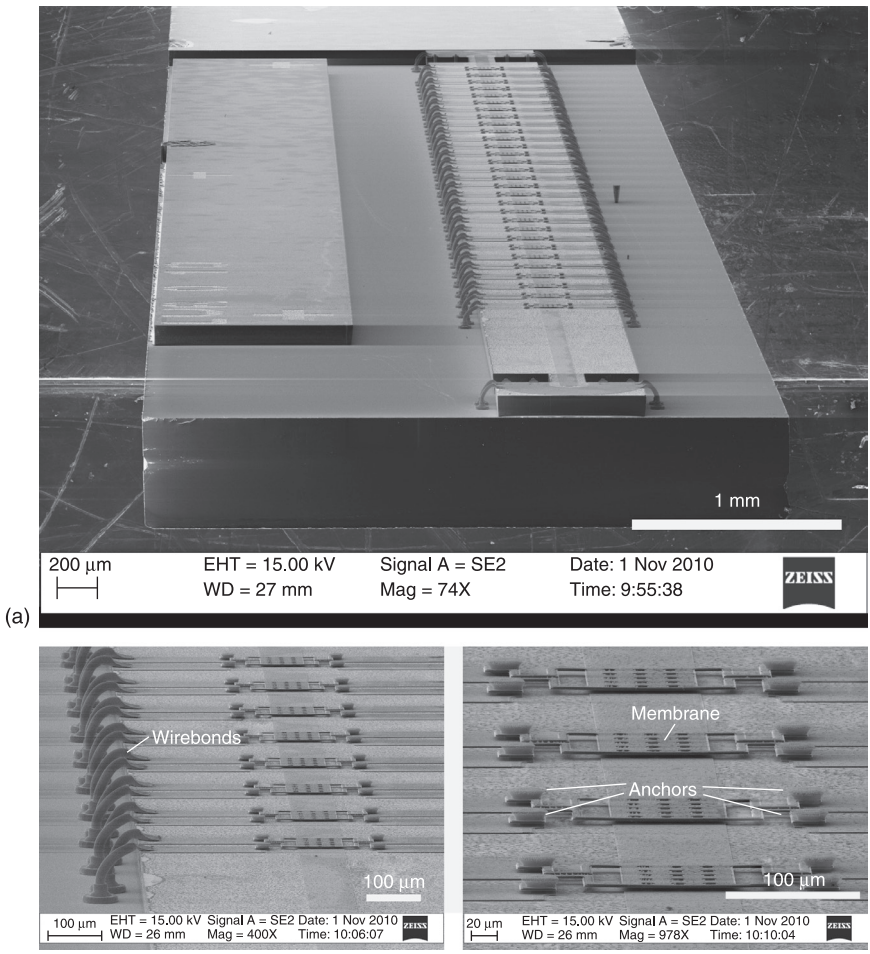

5.18 SEM images of fabricated leaky-wave antennas: (a) the whole chip with a 30 element array; (b) close-up of the wire bonds connecting the membranes to the ground plane (c) close-up of the membranes with springs and anchors (Zvolensky *et al.*, 2011).

pairs of coils, the magnetic field is exerted to the nickel underneath the silicon substrate and the plate rotates. The average tilting angles are 5.4, 8.2, 13.4 and 18.3°, respectively, when the applied currents are 200, 300, 400 and 500 mA in the H-plane. The average tilting angles are 4.7, 6.8, 12.1 and 17.7° in the E-plane. The measured radiation beam patterns and tilting angles are depicted in Fig. 5.20. The beam radiation pattern shifts, originating from the rotation at the angles of −14, 0 and +18° in the H-plane and the beam patterns at −18, −12, 0, +12 and +16° in the E-plane are shown in Fig. 5.20.

© Woodhead Publishing Limited, 2013

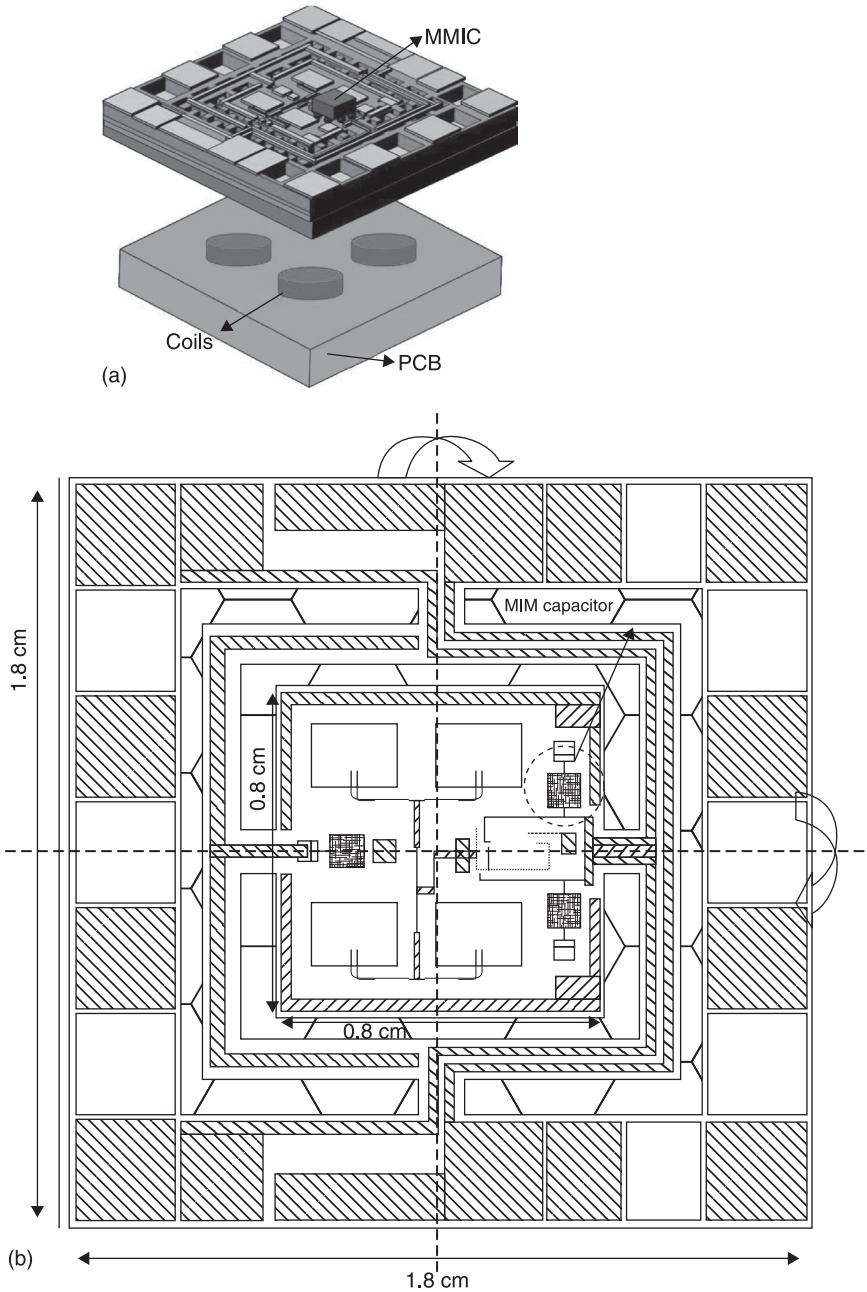

5.19 Micro-mechanically driven antenna platform: (a) schematic view of the proposed RF antenna; (b) design layout (Kim *et al.*, 2011).

© Woodhead Publishing Limited, 2013

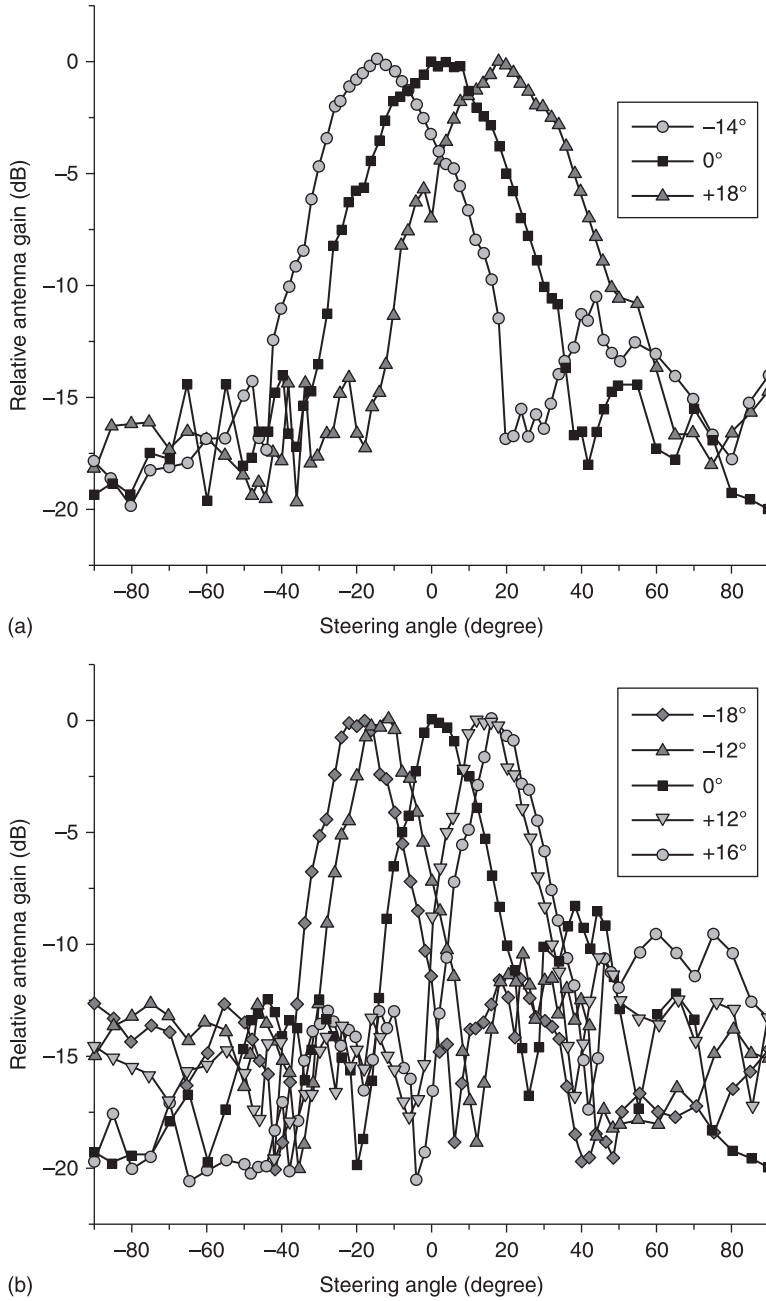

5.20 Radiation beam pattern of the mechanically tilted RF antenna actuated by magnetic field: (a) H-plane; (b) E-plane (Kim *et al.*, 2011).

© Woodhead Publishing Limited, 2013

5.4.4 MEMS reconfigurable Vee-antennas

In Chiao *et al.* (1999), a planar antenna structure is dynamically reconfigured to steer the radiation beam or change the shape of the beam using electrically-controlled microactuators. Figure 5.21 show the concept and the cross-section of the reconfigurable Vee-antenna, respectively.

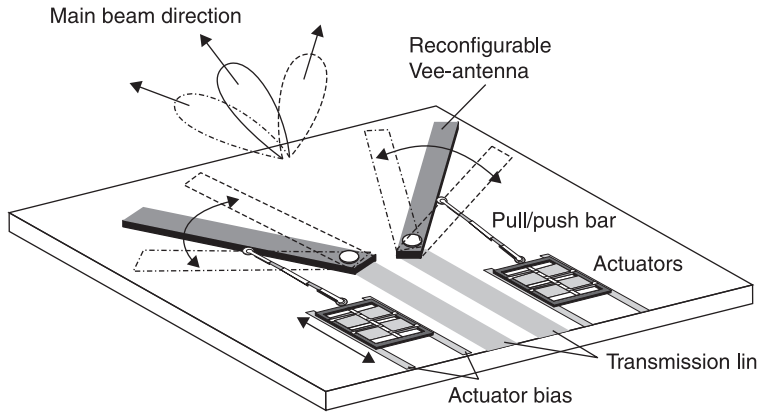

5.21 Concept of micro-mechanically reconfigurable Vee-antenna (Schoebel *et al.*, 2005).

The antenna arms of the Vee-antenna are moved through pulling or pushing by microactuators. One end of the antenna arm is held by a fixed rotation hinge locked on the substrate, which allows the arm to rotate with the hinge as the center of a circle. Both antenna arms were rotated by 30 and 45° in the same direction, while the Vee-angle was kept at 75°. Figure 5.22 shows that the main beams shift by 30 and 48°. It also shows that the first null shifts from 35 to 15° for the 30°-steering and from 35 to 0° for the 45°-steering.

5.5 Conclusion

RF MEMS is a very interesting technology for 76 to 81 GHz automotive radar, mainly because of the near-ideal signal properties of RF MEMS devices, such as switches and phase shifters. Various RF MEMS components and demonstrators for RF MEMS-based automotive radar have been presented, and alternative beam-steering technologies enabled by micro-electromechanical tuneable components are summarized in this chapter. Developing RF MEMS components to market maturity still requires a major effort, especially as it is difficult to overcome reliability problems such as contact stiction or dielectric charging of isolation layers, and to realize low-cost packaging methods, which provide with package hermeticity and good RF feedthroughs. A handful of companies have

© Woodhead Publishing Limited, 2013

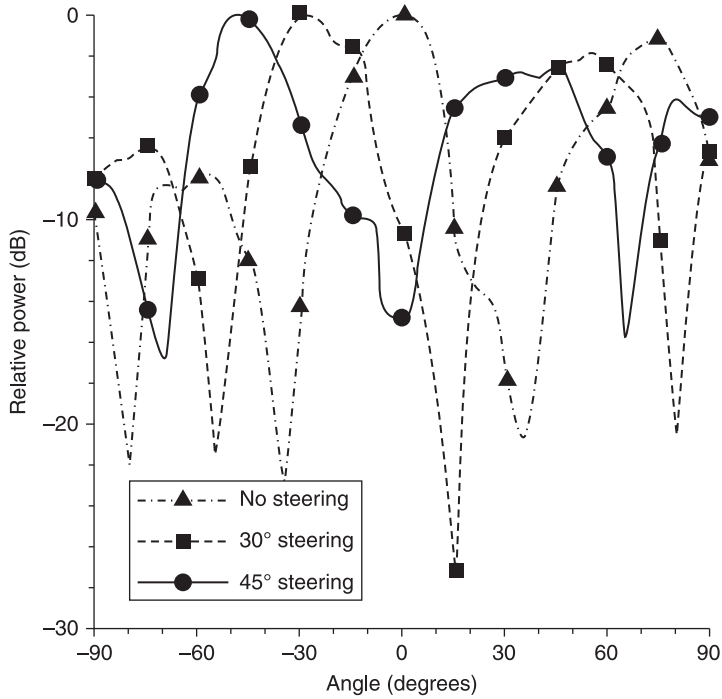

5.22 E-plane beam-steering patterns for a 17.5 GHz MEMS reconfigurable Vee-antenna (Schoebel *et al.*, 2005).

succeeded in developing reliable RF MEMS components and circuits, which are fulfilling customer specifications both in electrical performance and in reliability requirements. Switches, for instance, already exceed the lifetime of mechanical RF relays by a factor of 100. For the low-power requirements of automotive radar of 1 to 10 mW, state-of-the-art RF MEMS components are able to fulfill the reliability requirements. No RF MEMS-based car radars are on the market yet, but various RF MEMS components, mainly switches and circuits, for instance antenna matching networks, have reached maturity and are commercially offered.

5.6 References

Barker N S and Rebeiz G M (2000), 'Optimization of distributed MEMS transmission-line phase shifters-U-band and W-band designs', *IEEE Trans Microw Theory Tech*, 48(11), 1957–1966.

Brown E R (1998), 'RF-MEMS switches for reconfigurable integrated circuits', *IEEE Trans Microw Theory Tech*, 46(11), 1868–1880.

Chiao J C, Fu Y, Chio J M, DeLisio M and Lin L Y (1999), 'MEMS reconfigurable antenna', in *IEEEMTT-S International Microwave Symposium*, June, pp. 1515–1518.

Chicherin D, Sterner M, Oberhammer J, Dudorov S, Åberg J, *et al.* (2010a), 'Analog type millimeter wave phase shifters based on MEMS tunable high-impedance surface in

© Woodhead Publishing Limited, 2013

rectangular metal waveguide', *IEEE International Microwave Symposium 2010*, Anaheim, CA, 23–28 May, pp. 61–64.

Chicherin D, Sterner M, Oberhammer J, Dudorov S, Lioubtchenko D, *et al.* (2010b), 'MEMS based high-impedance surface for millimetre wave dielectric rod waveguide phase shifter', *Proc IEEE European Microwave Conference 2010*, Paris, France, 26 September–1 October, pp. 950–953.

Chicherin D, Sterner M, Oberhammer J, Dudorov S, Lioubtchenko D, *et al.* (2010c), 'MEMS tunable metamaterials surfaces and their applications', *Proceedings of the IEEE Asia Pacific Microwave Conference 2010*, Yokohama, Japan, 7–10 December, pp. 239–242.

Dancila D, *et al.* (2010), 'A MEMS variable Faraday cage as tuning element for integrated silicon micromachined cavity resonators', *Proceedings of the IEEE Micro Electro Mechanical Systems*, 24–28 January, pp. 723–726.

De Raedt W, Beyne E, and Tilmans H A C (2003), 'MEMS for wireless communications: from RF-MEMS components to RF-MEMS-SiP', *J Micromech Microeng*, 13(4), 139–163.

Gavrila M K, Dariu M and Ulrich L (2001), 'A multi-sensor approach for the protection of vulnerable traffic participants – the PROTECTOR project', *Proceedings of the IEEE Instrumentation and Measurement Technology Conference*, Budapest, Hungary, 21–23 May.

Ghodsian B, Bogdanoff P and Hyman D (2008), 'Wideband DC-contact MEMS series switch', *IETMicro and Nano Letters*, 3(3), 66–69.

Guillon B, *et al.* (1999), 'Design and realization of high Q millimeter-wave structures through micromachining techniques', *Proc IEEE Intern Microw Symp*, 4, 1519–1522.

Hung J J, Dussopt L, and Rebeiz G M (2003), 'A low-loss distributed 2-bit W-band MEMS phase shifter', *Proc IEEE/EuMA Microwave Conference 2003*, October, pp. 983–985.

Hung J J, Dussopt L, and Rebeiz G M (2004), 'Distributed 2- and 3-bit W-band MEMS phase shifters on glass substrates', *IEEE Trans Microw Theory Tech*, 52(2), 600–606.

Kim Y, Kim N G, Kim J M, Lee S H, Kwon Y-W, *et al.* (2011) '60-GHz full MEMS antenna platform mechanically driven by magnetic actuator', *IEEE Trans Ind Elect*, 58(10), 4830–4836.

Koen A P and Van Caekenberghe A (2007), 'RF MEMS Technology for Millimeter-Wave Radar Sensors', PhD Dissertation, University of Michigan.

Lakshminarayanan B and Weller T M (2007), 'Optimization and implementation of impedance-matched true-time-delay phase shifters on quartz substrate', *IEEE Trans Microw Theory Tech*, 55(2), 335–342.

Mercier D *et al.* (2004), 'A DC to 100 GHz high performance ohmic shunt switch', *Proc IEEE Int Microw Symp Dig*, 3, 1931–1934.

Oberhammer J (2004), 'Novel RF MEMS switches and packaging concepts', PhD dissertation, KTH Royal Institute of Technology, Stockholm.

Ocket I, Nauwelaers B, Carchon G, Jourdain A and De Raedt W (2006), '60 GHz Si micromachined cavity resonator on MCM-D', *Proc Topical Meeting on Silicon Monolithic Integrated Circuits in RF Systems*, 18–20 January, p. 4.

Rizk J B and Rebeiz G M (2003a), 'W-band microstrip RF-MEMS switches and phase shifters', *Proc IEEE MTT-S International Microwave Symposium*, vol. 3, 8–13 June, pp. 1485–1488.

Rizk J B and Rebeiz G M (2003b), 'W-band CPWRFMEMS circuits on quartz substrates', *IEEE Trans Microw Theory Tech*, 51(7), 1857–1862.

Rizk J, Tan G L, Muldavin J B and Rebeiz G M (2001), 'High-isolation W-band MEMS switches', *IEEE Microw Wireless Comp Lett*, 11(1), 10–12.

© Woodhead Publishing Limited, 2013

Schneider M (2005), 'Automotive radar – status and trends', *Proceedings of the German Microwave Conference GeMiC*, Ulm, Germany, April, pp. 144–147.

Schoebel J, Buck T, Reimann M, Ulm M, Schneider M, *et al.* (2005), 'Design considerations and technology assessment of phased-array antenna systems with RF MEMS for automotive radar applications', *IEEE Trans Microw Theory Techs*, 53(6), 1968–1975.

Somjit N, Stemme G and Oberhammer J (2009), 'Binary-coded 4.25-bit-band monocrystalline–silicon MEMS multistage dielectric-block phase shifters', *IEEE Trans Microw Theory Tech*, 57(11), 2834–2840.

Somjit N, Stemme G and Oberhammer J (2011), 'Power handling analysis of high-power W-band all-silicon MEMS phase shifters', *IEEE Trans Elect Dev*, 58(5), 1584–1555.

Stehle A, *et al.* (2008), 'RF-MEMS switch and phase shifter optimized for W-band', *IEEE/EuMA European Microwave Conference*, 27–31 October, pp. 104–107.

Sterner M, Stemme G and Oberhammer J (2009a), 'Wafer counter-bonding for integrating CTE-mismatched substrates and its application to MEMS tuneable metamaterials', *Proc IEEE TRANSDUCERS 2009*, Denver, CO, 22–25 June, pp. 1722–1725.

Sterner, M, Chicherin, D, Räisänen A V, Stemme, G and Oberhammer J (2009b), 'RF MEMS high-impedance tuneable metamaterials for millimeter-wave beam steering', *Proc IEEE Micro Electro Mechanical Systems*, Sorrento, Italy, 25–29 January, pp. 896–899.

Thanh M V, *et al.* (2009), 'Fabrication and characterization of RF-MEMS switch in V-band', *IEEE Asia-Pacific Microwave Conference*, 7–10 December, 202–205.

Ulm M, Schobel J, Reimann M, Buck T, Dechow J, *et al.* (2003), 'Millimeter-wave micro-electro-mechanical (MEMS) switches for automotive surround sensing systems', *Proc 2003 Topical Meeting on Silicon Monolithic Integrated Circuits in RF Systems*, 9–11 April, pp. 142–149.

Van Caekenberghe K (2009), 'RF MEMS technology for radar sensors', *International Radar Conference – Surveillance for a Safer World*, pp. 1–6.

Van Caekenberghe K and Sarabandi K (2006), 'Monopulse-doppler radar front-end concept for automotive applications based on RF MEMS technology', *Proceedings of the IEEE International Conference on Electro/information Technology*, pp. 1–5.

Wenger J (2005), 'Automotive radar – status and perspective', *Compound Semiconductor Integrated Circuits Symposium 2005*, Palm Springs, CA, October.

Zvolensky T, Chicherin D, Räisänen A, Simovski C, Sterner M, *et al.* (2011), 'Leaky-wave antenna at 77 GHz', *Proceedings of the IEEE/Eu MA European Microwave Conference 2011*, Manchester, UK, 9–14 October, pp. 1039–1042.

© Woodhead Publishing Limited, 2013

6

MEMS for passenger comfort in vehicles

S.J. LEE, San Jose State University, USA

DOI: 10.1533/9780857096487.1.137

Abstract: This chapter discusses the use of MEMS devices and related transducers for assessing and enhancing automotive passenger comfort. The chapter is organized in terms of various aspects including seating, climate, visual comfort and auditory comfort. Examples and working principles of relevant transducers are presented for each category. Transducers for passenger comfort are less commonplace than well-established MEMS devices such as pressure sensors in tires and inertial sensors for vehicle dynamics. Accordingly, this chapter reviews a broad variety of research developments, illustrating the diverse potential for MEMS in the area of passenger comfort.

Key words: MEMS, passenger comfort, smart seating, automotive sensors, climate control.

6.1 Introduction

Micro-electromechanical systems (MEMS) technology is used in a wide variety of modern automotive sensors (Eddy and Sparks, 1998; Fleming, 2008; Marek, 2011). MEMS transducers address functions related to safety, vehicle dynamics, engine performance (Igarashi, 1986) and subsystem communications. The most well-known MEMS devices for automotive applications are inertial sensors (e.g. accelerometers and gyroscopes) and pressure sensors. The functional transducer component (not including power sources and electronic signal processing) typically occupies less than 1 mm^3 of space. Such small devices are particularly favorable for vehicle applications because of low power consumption, high sensitivity, fast response and negligible payload.

This chapter focuses on MEMS for passenger comfort, to illustrate various ways in which MEMS devices are used – or potentially may be used – to provide and enhance passenger comfort. For more detail on each type of device, there are several more comprehensive sources that provide thorough descriptions of specific design principles and fabrication methods (Kovacs, 1998; Hsu, 2008; Madou, 2011).

6.1.1 Scope

The Oxford Dictionary defines *comfort* as 'a state of physical ease and freedom from pain or constraint' (Oxford University Press, 2012). From an engineering problem-solving perspective, it may be more convenient to consider a working definition of *discomfort*. Discomfort can be expressed as a state of physical

© Woodhead Publishing Limited, 2013

difficulty or sense of pain, over-constraint, fatigue or other unpleasant condition. MEMS technologies offer a variety of ways to sense conditions that lead to discomfort, and thereby provide the opportunity to address the problems with engineered solutions. So a good starting question is, 'What are some causes of passenger discomfort?' Below are some specific examples:

- soreness and fatigue in muscles and joints;
- temperature or humidity that is too high or too low;
- eye strain;
- noise, both external and internal to the vehicle.

Accordingly, this chapter is organized in terms of various aspects of comfort including seating, climate (i.e. temperature and humidity), visual comfort and auditory comfort. Examples of relevant transducers are discussed for each of these categories, as well as a few additional concerns related to ergonomics for the driver. The chapter reviews several proof-of-concept devices and research developments, illustrating the diverse potential of MEMS for passenger comfort. The word 'passenger' in this chapter will include both drivers and non-driving passengers, and will be considered synonymous with the word 'rider'. The driver, of course, bears additional responsibilities of awareness, decision-making and vehicle control.

Cruise control (i.e. automatic regulation of a designated speed) is a ubiquitous comfort feature in modern cars. Some implementations of cruise control use MEMS inertial sensors to determine speed (Jairam, 2008). Going beyond cruise control, emerging technologies for *autonomous* vehicle control (e.g. including steering and acceleration) may also involve MEMS technologies, in particular for radar (Bloecher *et al.*, 2009; Fleming, 2012) and radio-frequency communications (Yao, 2000). However, the scope of 'comfort' in this chapter will not be so broad as to include autonomous driving, automatic parking or even cruise control. Autonomous vehicle control is a major topic in and of itself, with typically greater emphasis on software and intelligent decision making than on the particular sensors used (Veres *et al.*, 2011). Also not discussed directly are the different types of radio frequency (RF) MEMS devices, which are often used in wireless communications. Such devices, including switches, varactors and inductors, are discussed more thoroughly elsewhere in this book and in sources specific to RF MEMS (Rebeiz, 2003). However, one emerging way in which RF-based communication supports vehicle comfort is by storing and transmitting individual preferences for seat configuration and climate settings on the ignition key used by each driver.

Although narrowly defined as 'electromechanical', this chapter discusses MEMS in a more liberal sense, including microscale transducers that are not necessarily electromechanical *per se*. Examples include sensors and actuators based on thermoelectric, electrochemical, electrochromic and electrofluidic transduction principles.

© Woodhead Publishing Limited, 2013

6.1.2 Role of MEMS in passenger comfort

If the intent of MEMS technology is to provide or enhance passenger comfort, a fundamental question is how to express or quantify the level of passenger comfort. There is no universally correct answer. Not only is comfort multifaceted (e.g. seating vs. climate), but it is also unique to individual preferences. There are also fundamental aspects of passenger comfort, such as raw legroom and headroom that cannot be solved in any practical way by microscale transducers.

One important realization is that comfort is a psychophysical process. Ultimately the passenger plays the most critical role in evaluating whether or not conditions are comfortable. Consequently, the best way to achieve comfort may simply be to provide relevant information so that passengers and vehicle designers can make informed decisions. One example of quantifying comfort has been to define a ride discomfort index (RDI) that is empirically based on velocity fluctuations (Wang *et al.*, 2001). In the case of temperature, an expression of comfort is the predicted mean vote (PMV), for which a larger population is expected to reach convergence of perceived comfort (Fanger, 1973). However, regardless of the comfort index, the passenger should have an appropriate means of making adjustments.

Figure 6.1 shows a conceptual illustration of a comfort feedback loop, to present a contextual framework for the role of MEMS. A desired condition for comfort is prescribed, presumably by the passenger. In the feed-forward direction, this preferred condition is fed to some type of actuator that alters the 'system', which may be the passenger, a seat, a window, the cabin or some combination of any of the above. The effect of the appropriate actuator leads to a condition that may or may not be sufficiently close to the desired comfort level. In the feedback direction, some type of sensor measures the resulting condition. A comparison is made between the desired and measured conditions, and a next appropriate change is made if needed.

Figure 6.1 also serves to highlight a basic distinction among MEMS transducers. Transducers may be categorized as either *sensors* or *actuators*. Sensors convert some physical input condition (strain, pressure, temperature, luminance, etc.) into

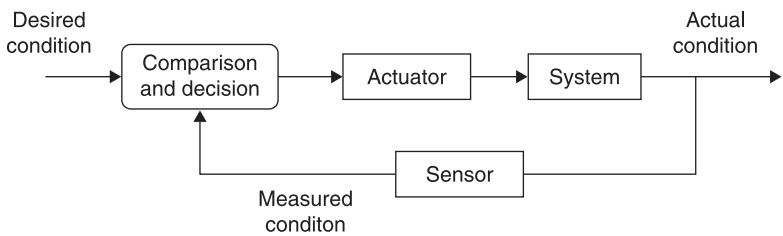

6.1 Conceptual illustration of a comfort feedback loop with sensor, decision-maker and actuator.

© Woodhead Publishing Limited, 2013

an electrical output signal. Conversely, actuators respond to an input signal (typically electrical) by producing some physical change. As a broad generalization, the most fitting role of MEMS for passenger comfort lies with sensing rather than actuating. In most cases, the appropriate action or adjustment would still be determined by the passenger. MEMS devices are often poorly suited for use as actuators, because necessary changes to the macroscopic world (e.g. seat position, air flow, etc.) require orders of magnitude of more power than can be generated by microscale devices.

There is a wide variety of automotive sensors (Fleming, 2001) for measuring such variables as acceleration, pressure, force, temperature, humidity, air flow, sound level, light intensity and other physical conditions. The remainder of this chapter focuses primarily on presenting examples of how sensing of such variables can contribute to various aspects of passenger comfort. As seen in the examples, most MEMS devices do not provide comfort as actuators, but instead provide relevant sensor output to passengers and vehicle designers. In most cases, the passenger remains predominantly responsible for making adjustments that would provide greater comfort.

Each of the following sections begins with a question regarding what determines comfort for the respective topic. Often there will be more than one answer, and so it may be easier to query in terms of what causes discomfort. Specific examples are then surveyed for each section.

6.2 Seating

Riding in an automobile generally means being in a seated position, sometimes for long durations. Consequently, seating tends to be a first concern when considering passenger comfort. What might cause seating discomfort? Holding the body in a posture that causes muscle strain is one cause. Poorly distributed pressure on the body is another cause. A third common cause of discomfort is the transmission of vehicle vibration to the body. Since pressure (or spatial distribution of force) and vibration are key concerns for seating, MEMS pressure sensors (Eaton and Smith, 1997) and accelerometers (Biswas *et al.*, 2007) are highly relevant microsensors for addressing these concerns.

The concept of an 'intelligent' car seat implies that sensors in the seat can detect sub-optimal pressure distribution and vibration conditions, and can *automatically* take appropriate corrective action. The challenge lies in knowing what the appropriate corrective action is. Relatively simple devices, such as microfabricated pressure sensors, strain gauges or force-sensitive resistors can be used for weight sensing. Weight sensing can in turn be used for the convenience of rider-specific custom setting (e.g. distance from steering wheel, headrest height, mirror angle), but the actuation of such custom settings typically still requires macroscopic actuators (e.g. conventional electromagnetic motors).

© Woodhead Publishing Limited, 2013

Much of the published work involving MEMS for vehicle seating comfort focuses on the use of sensors during design, research and development. To provide quantitative data for seat design, MEMS pressure sensors have been used to determine the spatial distribution of body weight resulting from interfacing with car seats (Voisin *et al.*, 1998). While characteristic pressure distribution maps can be correlated with a sense of human comfort, such correlations still depend on expression of subjective human judgment (Tada *et al.*, 1998). A commercial example of arrayed sensors useful for such studies is the CONFORMat system shown in Fig. 6.2. The array is comprised of thin-film electrodes and force-sensitive resistors integrated within a flexible substrate (Tekscan, Inc. South Boston, MA).

Seating comfort cannot solely be parameterized by pressure distribution, because it is also determined by a combination of factors including posture and anthropometric parameters (Yamazaki, 1992). Accordingly, a more comprehensive understanding of how to support comfortable posture necessitates additional information, such as might be gained from complementary optoelectronic systems (Andreoni *et al.*, 2002) that track body posture.

There are at least four standards that provide expressions of anticipated comfort, based on engineering variables associated with power, amplitude and frequency. These methods have been shown to have reasonably good correlation with subjective assessments of comfort (Els, 2005). Having such standards is

6.2 Sensor array with thin-film electrodes to map force-sensitive resistance on automobile seats (courtesy of Tekscan, Inc.).

© Woodhead Publishing Limited, 2013

particularly useful for screening the relative influence of many input factors in an objective manner (Mastinu *et al.*, 2010). Ride comfort has also been studied in terms of subjective assessment by passengers during vehicle motion, and has been correlated to quantitative metrics based on directional accelerations and vibration (Wang *et al.*, 2001). Accordingly, accelerometers are invaluable for correlating ride comfort with vehicle dynamics (Juranek and Kulhanek, 2011). Accelerometers can be placed at various locations, including footrest, seat base, seat and backrest, to distinguish frequency-dependent attenuation and predicted discomfort level (Nahvi *et al.*, 2009). However, a complicating factor is that the intensity of vibration experienced by a passenger varies depending on posture (Cucuz, 1994).

The use of sensors that are outfitted onto car seats is a relatively straightforward strategy, but other approaches have also been used. For example, an instrumented dummy has been used to measure actual accelerations on a simulated human body rather than on the seat (Pennati *et al.*, 2009). Interestingly, invasive studies have also been conducted using MEMS pressure sensors surgically implanted to measure pressure in the spinal discs of human passengers (Zenk *et al.*, 2012).

6.3 Climate control

In vehicle applications, 'climate' typically refers to temperature and humidity, and to some extent air quality as well. What might cause climate discomfort? The most routine cause is equilibrium of cabin conditions with respect to the surrounding environment. That is, very warm weather normally means that the temperature inside the vehicle will be uncomfortably hot, and very cool weather normally means that the temperature inside the vehicle will be uncomfortably cold. Climate comfort is important also because it has been shown that cabin temperature can affect driver vigilance and corresponding driving safety (Norin and Wyon, 1992).

Microsensor technology – although typically not 'electromechanical' *per se* – offers diverse sensor options for climate sensing (Kimura, 2009). There are numerous temperature measurement principles that can be used in transducers for climate sensing. Some examples of different sensing principles include the thermoelectric Seebek effect, temperature-dependent resistance, mismatch of thermal expansion, fluid volume expansion, temperature-dependent semiconductor band gap and thermal radiation (Childs *et al.*, 2000). One or more of these principles can effectively be incorporated in microfabricated temperature sensors made by the processes of doping, thin-film deposition and etching.

To change the cabin environment, sensor output can be used for automatic temperature regulation via closed-loop feedback control. The actuation hardware typically involves heaters, fans and air conditioning systems. While the regulation

© Woodhead Publishing Limited, 2013

of a specified temperature set-point can readily be automated, interpretation is still highly dependent on individual preferences, because thermal comfort involves physiological and psychological considerations (Rutkowski, 2010; Alahmer *et al.*, 2011). Although not necessarily microsensor-based, one novel approach to acquiring sensory data automatically has been to use non-contact infrared detectors to measure skin temperature of vehicle occupants (Wei and Dage, 1995).

However, effectively providing temperature comfort involves more than just measuring temperatures and altering heating or air conditioning. In fact, two of the most uncomfortable scenarios related to riding in a car occur immediately upon entry, even before climate control systems are even powered. The temperature inside of a *parked* car is strongly determined by equilibrium with its environment. So the inside temperature on a hot day will inevitably be uncomfortably warm. To address this fundamental problem, so-called 'smart windows', based on liquid crystal or electrochromic phenomena, can play a useful role in attenuating the solar radiation that is transmitted through window glass (Lynam, 1990; Jaksic and Salahifar, 2003). This has practical benefits, not only for passenger comfort but also for energy efficiency, because less energy will be needed for active temperature control by air conditioning.

Air quality is another factor related to climate, and air composition can be measured effectively by thin-film microsensors. One aspect of air quality involves the presence or absence of unpleasant odors, as might be caused by cigarette smoke or farm manure. What is deemed unpleasant is subject to human interpretation. For example as an air freshener may cause strong olfactory sensation yet not be considered unpleasant. Microfabricated metal-oxide gas sensors have been proven to have sensitivity that can be well correlated to human opinion of discomfort level (Blaschke *et al.*, 2006). Having this detection capability could automate response actions such as adjusting a fresh-air vane or increasing forced air flow rate.

Small size, high sensitivity and low power consumption are some of the merits of microsensors for regulating vehicle climate. A benefit of the small size and low cost of microsensors is the ability to facilitate multi-zone climate preferences with several sensors distributed throughout different parts of the passenger cabin (Lexus, 2012). Also, during the design of heating, ventilation and air conditioning (HVAC) systems for vehicles, mannequins can also be outfitted with a multitude of sensors to measure temperature, humidity and air flow (Cisternino *et al.*, 1997). Another important merit of microsensors is the ability to integrate multiple measurements such as temperature, pressure and relative humidity in a single device (Johari and Pryputniewicz, 2003). Figure 6.3 shows an example of integrating temperature and humidity on a silicon chip for indoor comfort sensing (Kang *et al.*, 1997). A similar approach by the same authors was also used for air flow sensing, based on unbalanced bridge output of temperature-sensitive resistors in response to air flow.

© Woodhead Publishing Limited, 2013

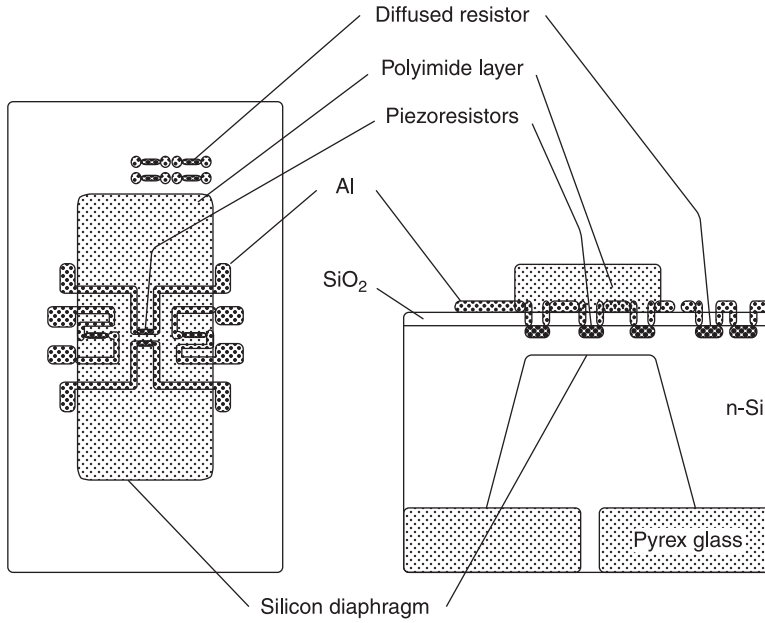

6.3 Microfabricated sensors for measuring temperature and humidity using principles of temperature-sensitive resistance and hygroscopic expansion (image reproduced from Kang (1997), with corresponding author's permission).

6.4 Visual comfort

What are factors that might cause visual discomfort? Answers to this question can be categorized into different concerns. One source of discomfort is glare from external sources, such as headlights from other vehicles at night, bright sunlight or low-incidence sunlight near dawn and dusk. A different aspect of visual comfort is instrument panel clarity. MEMS solutions address these concerns in two primary ways, with light-sensitive windows and mirrors and with novel display technologies.

So-called 'smart windows' are responsive to stimuli, typically based on the absence, presence or strength of an electric field on conductive coatings. There are several different operating principles, such as liquid crystal displays, suspended particles and electrochromic materials. Figure 6.4 illustrates two different principles for electrochromic devices (Granqvist *et al.*, 1998). Electrochromic materials have been used in rearview mirrors to provide automatic dimming.

Within the passenger cabin, optical sensing using either photovoltaic or photodiode principles can be used to automate lighting, particularly at twilight transitions (Butler, 1999). When external ambient lighting dims, backlit gauges and other instrument panel displays can be programmed to illuminate automatically.

© Woodhead Publishing Limited, 2013

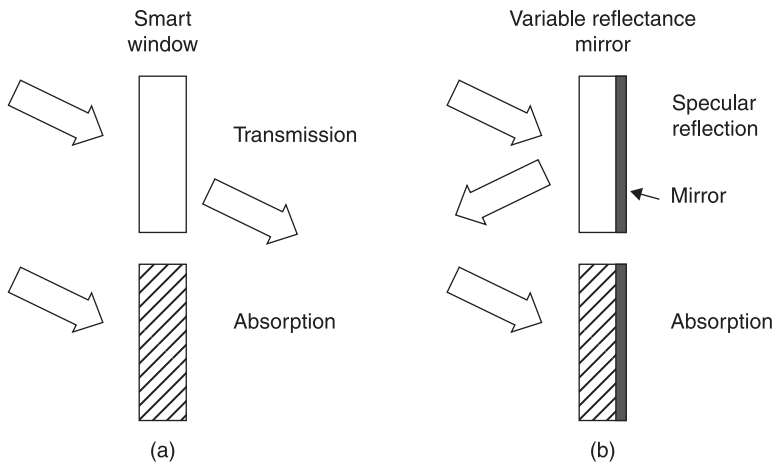

6.4 Electrochromic behavior: (a) for smart windows; (b) smart mirrors (reprinted from Granqvist *et al.* (1998), with permission from Elsevier).

Although not presently commonplace in automotive displays, reflective electronic displays present an emerging area of display technology (Heikenfeld *et al.*, 2011). Reflective displays can reduce eye strain because images are not produced by emissive energy, in contrast to light-emitting diode (LED) displays, for example. These technologies are gaining popularity in other consumer markets, and for 'e-reader' devices in particular, but may have growth potential in automotive applications because of the ability to have low-power displays that maintain high image contrast even in bright daylight. Some of these 'e-display' approaches use electrophoretic inks or particles, but one approach that is directly based on MEMS actuation is the 'Mirasol' device (Bita, 2008). Mirasol displays are based on a bistable interferometric modulator that alters the geometry of an optical cavity, thereby controlling which wavelengths are amplified or diminished for viewing.

6.5 Auditory comfort

With respect to auditory inputs, unwanted noise is the most obvious cause of passenger discomfort. Common sources of noise that can be transmitted to the passenger cabin are engine transmission and tire contact with the road (Junoh *et al.*, 2011). To address the problem of unwanted noise, the role of transducers is two-fold, first to measure the noise and second (if possible) to cancel it. As is the case with passenger seating, much of the benefit of sensors is gained during vehicle design and development stages. Sound measurement, especially in a testing facility, does not necessarily require microscale transducers, but several

© Woodhead Publishing Limited, 2013

MEMS microphone designs have been developed. MEMS microphones generally involve a deformable membrane or diaphragm. However, sensing principles vary widely and, for example, may be based on piezoelectric behavior (Lee and Lee, 2008), capacitive sensing (Elko, 2005; Leinenbach *et al.*, 2010) or electromagnetic induction (Horng *et al.*, 2010).

As originally presented in Fig. 6.1, MEMS transducers excel in the sensing function. However, they generally lack the macroscopic power needed to perform most actuation duties. MEMS microphones can be distributed with relative ease throughout a passenger cabin, but in demonstrated cases of active noise reduction, the aid of conventional (i.e. macroscopic) loudspeaker devices is generally needed (Bravo and Cobo, 2002). One prospective opportunity for improving auditory comfort is the use of 'smart materials' in semi-active noise cancellation schemes (Alves *et al.*, 1994; Strock, 1995).

6.6 Conclusion and future trends

Ergonomics in any context is focused on task performance, in a way that is efficient, safe and comfortable. The most fundamental task for an automobile driver is control of the vehicle, but MEMS devices have future opportunities for making some of those tasks more efficient, safe and comfortable. For example, some vehicles provide adaptive headlights that turn with the car to illuminate what is immediately ahead. Altering the distribution of light energy can be achieved by MEMS mirror devices, not only for lateral turning but also switching from low-beam to high-beam from a single optical system (Hung *et al.*, 2010).

A broader challenge for comfort in future years may well depart from traditional concerns such as seating, climate, lighting and noise. Technological advances continue to be made with features related to proximity sensing, satellite navigation systems, heads-up displays (Hedili *et al.*, 2012) and even health monitoring (D'Angelo *et al.*, 2010). This 'information overload' may shift some attention toward psychological aspects in greater proportion relative to physiological concerns. Issues for driver and passenger comfort may involve finding solutions with more intuitive user interfaces (Kirby and Guerrero, 2009) and fewer mental concerns (Hilton, 2006), as the ability to gather various sensory inputs continues to expand.

6.7 References

Alahmer A, Mayyas A, Mayyas A A, Omar M A and Shan D (2011), 'Vehicular thermal comfort models; a comprehensive review', *App Therm Eng*, 31(6–7), 995–1002.

Alves G S, Shoureshi R, Knurek T and Ogundipe L (1994), 'Active vibro-acoustic control of automotive vehicles', *Proceedings of the 1994 International Mechanical Engineering Congress and Exposition*, 6–11 November, Chicago, IL: ASME, pp. 51–56.

© Woodhead Publishing Limited, 2013

Andreoni G, Santambrogio G C, Rabuffetti M and Pedotti A (2002), 'Method for the analysis of posture and interface pressure of car drivers', *App Ergo*, 33(6), 511–522.

Biswas K, Sen S and Dutta P K (2007), 'MEMS capacitive accelerometers', *Sensor Lett*, 5(3–4), 471–484.

Bita I (2008), 'Mirasol displays: Technology and manufacturing of interferometric MEMS on large area glass substrates', *15th International Display Workshops, IDW '08*, 3–5 December, Niigata, Japan: Institute of Image Information and Television Engineers, pp. 89–92.

Blaschke M, Tille T, Robertson P, Mair S, Weimar U, *et al.* (2006), 'MEMS Gas-sensor array for monitoring the perceived car-cabin air quality', *Sens J, IEEE*, 6(5), 1298–1308.

Bloecher H L, Dickmann J and Andres M (2009), 'Automotive active safety and comfort functions using radar', *Ultra-Wideband, 2009*. ICUWB, IEEE International Conference, p. 490.

Bravo T and Cobo P (2002), 'A demonstration of active noise reduction in a cabin van', *Acta Acustica united with Acustica*, 88(4), 493–499.

Butler W (1999), 'Multi-function electro-optical sensor for lighting and climate control automation in automotive and off-road vehicles', *Proceedings of SENSORS EXPO*, 4–6 May, Peterborough, NH: Helmers Publishing, pp. 183–190.

Childs P R N, Greenwood J R and Long C A (2000), 'Review of temperature measurement', *Rev Sci Instrum*, 71(8), 2959–2978.

Cisternino M, Malvicino C and Palazzetti M (1997), 'The thermal perception – an instrument device to measure the dry thermal comfort based on a smart hot film sensor', *Proceedings of 2nd Italian Conference on Sensors and Microsystems, Singapore*, 3–5 February, pp. 307–311.

Cucuz S (1994), 'Evaluation of ride comfort', *Int J Veh Des*, 15(3–5), 318–325.

D'Angelo L T, Parlow J, Spiessl W, Hoch S and Luth T C (2010), 'A system for unobtrusive in-car vital parameter acquisition and processing', *4th International Conference on Pervasive Computing Technologies for Healthcare*, IEEE, pp. 1–7.

Eaton W P and Smith J H (1997), 'Micromachined pressure sensors: review and recent developments', *Smart Mat Struct*, 6(5), 530–539.

Eddy D S and Sparks D R (1998), 'Application of MEMS technology in automotive sensors and actuators', *Proc IEEE*, 86(8), 1747–1755.

Elko G W, Pardo F, López D, Bishop D and Gammel P (2005), 'Capacitive MEMS microphones', *Bell Labs Tech J*, 10(3), 87–198.

Els P S (2005), 'The applicability of ride comfort standards to off-road vehicles', *J Terramech*, 42(1), 47–64.

Fanger P O (1973), 'Assessment of man's thermal comfort in practice', *Brit J Indust Med*, 30(4), 313–324.

Fleming B (2012), 'Recent advancement in automotive radar systems', *IEEE Veh Tech Mag*, 7(1), 4–9.

Fleming W J (2001), 'Overview of automotive sensors', *IEEE Sens J*, 1(4), 296–308.

Fleming W J (2008), 'New automotive sensors – a review', *IEEE Sens J*, 8(11), 1900–1921.

Granqvist C G, Azens A, Hjelm A, Kullman L, Niklasson G A, *et al.* (1998), 'Recent advances in electrochromics for smart windows applications', *Solar Energy*, 63(4), 199–216.

Hedili M K, Freeman M O and Urey H (2012), 'Microstructured head-up display screen for automotive applications', *Proc SPIE*, 8428, 84280X.

© Woodhead Publishing Limited, 2013

Heikenfeld J, Drzaic P, Yeo J and Koch T (2011), 'Review paper: a critical review of the present and future prospects for electronic paper', *J Soc Info Disp*, 19(2), 129–156.

Hilton J (2006), 'Fewer buttons – more comfort and convenience', *Auto Indust AI*:http://www.ai-online.com

Horng R, Chen K, Tsai Y, Suen C and Chang C (2010), 'Fabrication of a dual-planar-coil dynamic microphone by MEMS techniques', *J Micromech Microeng*, 20(6), 065004.

Hsu T (2008), *MEMS and Microsystems – Design, Manufacture, and Nanoscale Engineering, Second Edition*, Hoboken, NJ: John Wiley and Sons.

Hung C, Fang Y, Huang M, Hsueh B, Wang S, *et al.* (2010), 'Optical design of automotive headlight system incorporating digital micromirror device', *App Optics*, 49(22), 4182–4187.

Igarashi I (1986), 'New technology of sensors for automotive applications', *Sens Act*, 10(3–4), 181–193.

Jaksic N I and Salahifar C (2003), 'A feasibility study of electrochromic windows in vehicles', *Solar Energ Mat Solar Cells*, 79(4), 409–423.

Jairam S, Lata K, Roy S K and Bhat N (2008), 'Formal verification of a MEMS-based adaptive cruise control system', *NSTI Nanotechnology Conference and Trade Show*, Boston, MA, pp. 611–614.

Johari H and Pryputniewicz R J (2003), 'MEMS Sensors for temperature, pressure, and relative humidity measurements', *2003 International Symposium on Microelectronics*, 18–20 November, Boston, MA, SPIE, pp. 739–744.

Junoh A K, Muhamad W Z A W, Nopiah Z M, Nor M J M, Ariffin A K, *et al.* (2011), 'A study on the effects of tyre to vehicle acoustical comfort in passenger car cabin', *Computer Research and Development (ICCRD), 2011 3rd International Conference*, pp. 342–345.

Juranek M and Kulhanek J (2011), 'The use of MEMS accelerometers for measurement of driver seat comfort', *Carpathian Control Conference (ICCC), 12th International*, pp. 172.

Kang J, Kim Y, Kim H, Jeong J and Park S (1997), 'Comfort sensing system for indoor environment', *Solid State Sensors and Actuators, 1997. TRANSDUCERS '97 Chicago, International Conference*, pp. 311–314.

Kimura, M (2009), 'Micro temperature sensors and their applications to MEMS thermal sensors', *Third International Conference on Sensing Technology, ICST 2008*, 30 November–3 December, Tainan, Taiwan: Berlin and Heidelberg: Springer Verlag, pp. 309–326.

Kirby E and Guerrero R (2009), 'Smart touch sensing places the power of the microprocessor at your fingertips', *SAE Int J Pass Cars – Electron Elect Syst*, 2(1), 159–162.

Kovacs G T A (1998), *Micromachined Transducers Sourcebook*, Boston, MA: McGraw Hill.

Lee W S and Lee S S (2008), 'Piezoelectric microphone built on circular diaphragm', *Sens Actuat, A: Physical*, 144(2), 367–373.

Leinenbach C, Van Teeffelen K, Laermer F and Seidel H (2010), 'A new capacitive type MEMS microphone', *23rd IEEE International Conference on Micro Electro Mechanical Systems, MEMS*, Hong Kong, China, pp. 659–662.

Lexus (2012), 'Lexus Introduces 2013 LX 570 Luxury Utility Vehicle at North American International Auto Show' (News Release), Toyota Motor Sales, USA, Inc. Available from: http://pressroom.lexus.com/releases/ (accessed March 2012).

Lynam N R (1990), 'Smart windows for automobiles', *SAE International Congress and Exposition*, 26 February–2 March, Detroit, MI, p. 900419.

© Woodhead Publishing Limited, 2013

Madou M J (2011), *Fundamentals of Microfabrication and Nanotechnology, Third Edition*, Boca Raton, FL: CRC Press.

Marek J (2011), 'Automotive MEMS sensors – Trends and applications', *2011 International Symposium on VLSI Technology, Systems and Application (VLSI-TSA)IEEE*, Piscataway, NJ, 25–27 April, p. 2.

Mastinu G, Gobbi M and Pennati M (2010), 'Theoretical and experimental ride comfort assessment of a subject seated into a car', *SAE Int J Pass Cars – Mech Syst*, 3(1), 607–625.

Nahvi H, Fouladi M H and Mohd Nor M J (2009), 'Evaluation of whole-body vibration and ride comfort in a passenger car', *Int J Acoust Vib*, 14(3), 143–149.

Norin F and Wyon D P (1992), 'Driver vigilance – the effects of compartment temperature', *International Congress and Exposition*, 24–28 February, SAE, Detroit, MI, p. 7

Oxford University Press (2012), Available from: http://oxforddictionaries.com/definition/comfort/ (accessed April 2012).

Pennati M, Gobbi M. and Mastinu G (2009), 'A dummy for the objective ride comfort evaluation of ground vehicles', *Veh Syst Dynam*, 47(3), 343–362.

Rebeiz G M (2003), *RF MEMS Theory, Design, and Technology*, Hoboken, NJ: John Wiley and Sons, Inc.

Rutkowski P M (2010), 'Thermal comfort modeling of cooled automotive seats', *SAE Int J Pass Cars – Mech Syst*, 3(1), 523–532.

Strock H B (1995), 'Smart materials systems: emerging automotive applications', *Mat Tech*, 10(7–8), 159–162.

Tada M, Sekiguchi S, Nisimatsu T and Toba E (1998), 'Measurement and evaluation of sitting comfort of automotive seat', New York: 98CH36222, *IEEE*, 18–21 May, pp. 316.

Veres S M, Molnar L, Lincoln N K and Morice C P (2011), 'Autonomous vehicle control systems – a review of decision making', in *Proceedings of the Institution of Mechanical Engineers. Part I: J Syst Contr Eng*, 225(3), 155–195.

Voisin A, Bombardier S, Levrat E and Bremont J (1998), 'Sensory features measurement of the under-thigh length of car seat', Part 2, 4–9 May, Anchorage, AK: IEEE, pp. 1589.

Wang F, Ma N and Inooka H (2001), 'A driver assistant system for improvement of passenger ride comfort through modification of driving behaviour', *Advanced Driver Assistance Systems, 2001. ADAS. International Conference on (IEEE Conf Publ No 483)*, pp. 38–42.

Wei K C and Dage G A (1995), 'An intelligent automotive climate control system', *Intelligent Systems for the 21st Century IEEE*, New York, 22–25 October, pp. 2977–2982.

Yamazaki N (1992), 'Analysis of sitting comfortability of driver's seat by contact shape', *Ergonomics*, 35(5–6), 677–692.

Yao J J (2000), 'RF MEMS from a device perspective', *J Micromech Microeng*, 10(4), 9–38.

Zenk R, Franz M, Bubb H and Vink P (2012), 'Technical note: Spine loading in automotive seating', *App Ergon*, 43(2), 290–295.

© Woodhead Publishing Limited, 2013

7

MEMS devices for active drag reduction in aerospace applications

J. F. MORRISON, Imperial College, London UK

DOI: 10.1533/9780857096487.2.153

Abstract: This chapter summarises the requirements and challenges for feasible control to effect drag reduction in the transport sector, focusing primarily on aerospace applications. Key concepts such as the delay of separation, laminar flow control, turbulent skin-friction reduction and base-pressure recovery are reviewed, as their basic understanding is a prerequisite to effective control for drag reduction. Similarly basic open- and closed-loop control concepts are introduced. Practical schemes require sensing and actuation applied on integral, load-bearing surfaces only. Devices for skin-friction reduction, separation delay (from curved surfaces) and base-pressure recovery are discussed, distinguishing between applications for which MEMS are appropriate and those for which a single large-scale actuator is more likely to be suitable.

Key words: surface pressure, skin friction, dimples, pulsed jets, electro-active polymers.

7.1 Introduction

Aerodynamic drag arises principally through either the change in static pressure across a body moving in a fluid, or the effect of the 'no-slip' condition (the requirement that the relative velocity between the fluid and the surface of the body is zero), which generates a viscous shear stress. The relative size of these two depends on the body shape: a 'bluff' body generates pressure drag that is much larger than skin-friction drag. Alternatively, on a streamlined body (i.e. an aircraft wing), the frictional drag is much larger component. Both types of drag have their origins in the formation of a boundary layer that supports the viscous shear stress. The boundary layer can be either laminar or turbulent, the viscous drag of the latter being about four or five times that of the former. There is, therefore, considerable benefit in being able to delay transition onset, which is determined by many factors, including the nature of free-stream disturbances, surface roughness and Reynolds number, Re – the ratio of inertial forces to viscous forces, $u\ell/\nu$, where u and ℓ are velocity and lengthscales, respectively, of the fluid motion and ν is the kinematic viscosity. At low disturbance levels, the initial disturbance, in the form of Tollmien–Schlichting (TS) waves, has a linear origin and starts to amplify beyond a critical Reynolds number. An alternative to this 'modal' growth is the more practically relevant 'bypass' scenario, which prevails in conditions of background turbulence above 1% of the mean flow speed, or when wall-roughness

© Woodhead Publishing Limited, 2013

effects are appreciable. Under these conditions, which are ubiquitous to engineering flows, transition can take place at sub-critical Reynolds numbers, thus *bypassing* the natural route to boundary layer turbulence. Bypass transition is preceded by the amplification of boundary layer streaks, or Klebanoff distortions. The streaks can amplify to levels of 10 to 15% of the free stream velocity, when the background noise is about 3%.

Turbulent boundary layers are significantly more complicated where the random, turbulent motion, which for most applications satisfies the non-linear Navier–Stokes equations, may be characterized by a Reynolds decomposition, wherein Reynolds-averaging gives rise to Reynolds stresses. Strictly, these are not stresses (although the fluid can still sustain a viscous stress, unlike a solid, a stressed fluid moves), rather they are momentum fluxes arising from turbulent motion alone. Modeling of Reynolds stresses allows a closed-form solution of the Reynolds-Averaged Navier–Stokes (RANS) equations. Substituting this decomposition into the Navier–Stokes equation and applying Prandtl's boundary layer approximations (Morrison, 2010) gives:

$$U\frac{\partial U}{\partial x}+V\frac{\partial U}{\partial y}=-\frac{1}{\rho}\frac{dp}{dx}-\frac{\partial\overline{uv}}{\partial y}+\nu\frac{\partial^2 U}{\partial y^2} \qquad [7.1]$$

where x, y are the stream-wise and wall-normal Cartesian directions, respectively, and U, u and V, v are the corresponding mean, fluctuating velocity components. The non-linearity of the convective terms (e.g. $U\partial U/\partial x$) gives rise to products of the fluctuating velocity components, which on averaging lead to the Reynolds stresses (here, $\overline{uv}$). Gradients of Reynolds stresses constitute the turbulent momentum flux: their non-appearance in the corresponding equation for a laminar boundary layer:

$$U\frac{\partial U}{\partial x}+V\frac{\partial U}{\partial y}=-\frac{1}{\rho}\frac{dp}{dx}+\nu\frac{\partial^2 U}{\partial y^2}, \qquad [7.2]$$

explains the principle physical differences between the drag-producing properties of laminar and turbulent boundary layers.

This is further complicated by the fact that, owing to the non-linearity of the equations, a modification of the boundary conditions does not lead to a proportional response across all terms; the turbulence does not change in proportion to a change in the mean rate of strain. As a result, many boundary layers of practical interest are more complicated than those described by Reynolds-number similarity alone. These often include such effects as sudden changes in surface condition, large surface curvature, or shear-layer interactions such as those at a wing-body junction, or at the wing trailing edge. Generically, these complicated boundary conditions give rise to 'complex flows' in which the effects of these additional boundary conditions are not easily predicted by standard calculation methods

© Woodhead Publishing Limited, 2013

(Morrison, 2005). However, those boundary layers that conform to Prandtl's boundary-layer approximation (Morrison, 2010) are readily predicted by standard RANS solvers or by large-eddy simulation (LES) codes, without the need for additional modeling.

In terms of drag reduction, the delay of transition is amenable to control by arrays of discrete sensors and actuators. Active control of turbulent boundary layers is more challenging; present progress is focused on non-realizable computational approaches. Here we offer a pragmatic, cross-sectorial approach to active drag reduction, focusing on the sensors and actuators (using, not exclusively, MEMS), which are most likely to offer measurable improvements to energy efficiency through either a reduction in skin friction or control of separation. The approach stems from the recognition that effective flow control requires an understanding of the important drag-producing mechanisms, knowledge of control theory and its concepts, and knowledge of the advantages and limitations of candidate sensors and actuators. For effective drag reduction, MEMS technology cannot be considered in isolation. Control schemes based on physical reasoning are more likely to offer efficient reduced-order control models of processes involving a large number of degrees of freedom than those that do not.

Within the transport sector, examination of the relative sources of energy consumption is illuminating. Stern (2006) clearly identifies the automotive sector as the dominant source of CO_2 emissions (Fig. 7.1). The overall CO_2 contribution from the automotive sector (shown here as ~76%) is very close to both the IEA Statistics (2010) from the OECD and those reported in International Energy Outlook (2010) from the US DOE. Therefore the need for significant reductions

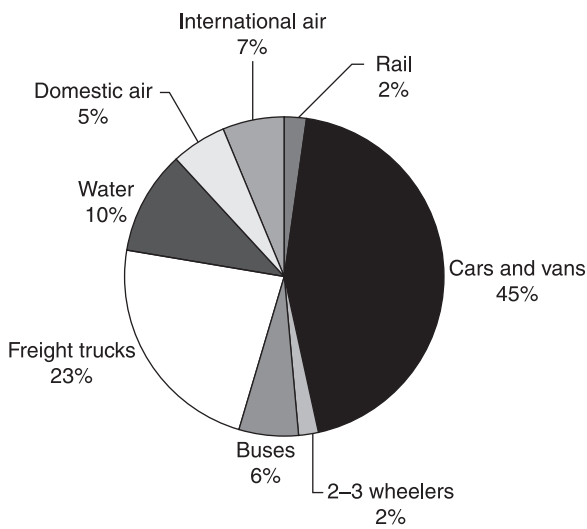

7.1 Transport CO_2 emissions by mode in 2000 (Stern, 2006).

© Woodhead Publishing Limited, 2013

in transport emissions by technological innovation is undeniable. Moreover, new approaches to the reduction of aerodynamic drag are complementary to other technologies (e.g. electric motors, batteries, lightweight structures, energy management strategies), which presently offer a better return on investment (Technology Strategy Board, 2010). Significant drag reductions are possible by addressing specific phenomena relating to both internal and external flow fields (Hucho and Sovran, 1993): here we focus on active drag reduction techniques for the latter, in particular the single largest contribution, pressure drag.

Stern (2006) also identifies air travel as contributing 12% emissions within the transport sector (or 2–3% overall), and within the aerospace sector, the need for drag reduction is driven rather more by regulatory requirements and the perception that air travel is the fastest growing transport sector. The Advisory Council for Aeronautics Research in Europe (ACARE) has recently published new targets for emissions for 2050 (European Commission, 2011). Relative to the capabilities of typical new aircraft in 2000, 2050 technologies and procedures are expected to provide a 75% reduction in CO_2 emissions per passenger kilometer and a 90% reduction in NO_x emissions. The perceived noise emission from aircraft is to be reduced by 65%. Drag reduction for aircraft is more challenging; ignoring the small contributions from excrescence drag and wave drag, most of the drag arises from pressure ('lift-dependent') drag and friction drag. It is the last component that offers the largest potential from drag reduction (Goldhammer and Vijgen, 2009) and is therefore the focus of much recent research. Roughly half of friction drag is generated by the wings, and half by the fuselage. In the case of the wings, natural laminar flow control (NLFC) has been a fruitful area of development with no concomitant penalties in terms of weight. Saric *et al.* (2011) are developing the application of discrete roughness elements to delay the onset of modal transition. However, hybrid laminar flow control (HLFC) involves active, steady suction near the leading edge to control leading-edge contamination and cross-flow instabilities. Therefore this technique leads to additional penalties associated with both weight and power.

There is the potential for greater drag (and power) reductions using active devices with feedback control, where the effectiveness of a particular form of actuation can be optimized and the duty cycle of actuators minimized. Chapters contributed in Leschziner *et al.* (2011) provide a recent review of active technologies appropriate for either transition delay (Erdmann *et al.*, 2011), for turbulent skin-friction reduction (Choi *et al.*, 2011; Kim, 2011; Quadrio, 2011), separation control using pulsed jets (Colonius and Williams, 2011; Glezer 2011) and plasma actuators (Choi *et al.*, 2011; Corke *et al.*, 2011). Spalart and Mclean (2011) provide an up-to-date, industrial perspective that emphasises the need for realistic estimates of power consumption and system weight. Current work involving physical demonstrations of feedback control (Li and Gaster, 2006; Erdmann *et al.*, 2011) has inevitably focused on the (linear) cancellation of TS waves rather than the less tractable problem of turbulent skin-friction reduction.

© Woodhead Publishing Limited, 2013

LaGraff *et al.* (2010) provide an overview that attempts to address the even more demanding requirements for control of turbomachinery flows.

For the control of turbulence, some knowledge of the energy cascade and its scaling is required; the rate of dissipation of turbulence kinetic energy (per unit mass), $\varepsilon = u^3/\ell$, is determined by the inertial timescale, ℓ/u, except in the final stages when it is determined by the corresponding viscous timescale, ℓ^2/ν, where the ratio of these is:

$$\mathrm{Re} = u\ell/\nu = \frac{\ell/u}{\ell/\nu} \qquad [7.3]$$

while the Kolmogorov scales are measures of the smallest, dissipating scales of motion, the dissipation rate itself being set by the inertial scales. An unavoidable concomitant of Reynolds-number scaling is the ratio of the energy-bearing lengthscale, ℓ, to that of the Kolmogorov lengthscale:

$$\eta = \left(\nu^3/\varepsilon\right)^{\frac{1}{4}}, \text{ is } \left(\ell/\eta\right)^3 \propto \mathrm{Re}^{\frac{9}{4}} \qquad [7.4]$$

for 3-D flow. Thus, even at small Reynolds numbers (say $\mathrm{Re} \approx 10^4$), the required resolution for sensors and actuators is prohibitively large. The situation is mitigated to some extent by the turbulence dissipation rate reaching a maximum at approximately 10η and that near-wall turbulence is populated by quasi-streamwise vortices that are several thousands wall units in length. However, there is a clear need for a dense array of MEMS devices sufficiently miniaturized and with a high frequency response. Carpenter *et al.* (2007) estimate that for an Airbus A340–300 at cruise conditions, 10^9 actuators would be required for drag reduction on the fuselage. Such requirements lead inexorably to the need for distributed and hierarchical processing of information, but even then, practical considerations mean that viable drag reduction is more likely to be achieved by emerging technologies that can offer a paradigm shift. It is the view of the author that a physical understanding of the dominant drag-producing processes in wall turbulence is a prerequisite for such technologies to be effective.

7.1.1 Drag reduction: contrasting perspectives

In the case of surface friction generated by turbulent flow, the arguments above may make a MEMS-based approach to drag reduction unfeasible. Moreover, much of our understanding of near-wall turbulence in based on kinematic observations at low Reynolds numbers (Robinson, 1990). An approach to wall-based control will have to involve an understanding of the dynamical relationship between the forcing and the boundary-layer response; typically this will involve design of a low-order estimator (Jones *et al.*, 2011), but such an approach models only the uncontrolled flow and there is not necessarily a guarantee that the model remains accurate once the loop is closed.

© Woodhead Publishing Limited, 2013

Kim (2011) highlights the importance of linear mechanisms in wall turbulence and therefore of linear optimal control theory to drag reduction. A linear system is observable if it is possible to determine its state through measurements of input and output. Kim and Bewley (2007) illustrate the significant challenges in observing wall turbulence through wall-based sensing alone. Sharma *et al.* (2011) have recently proposed a linear control scheme, which obviates the need for an explicit estimator. Linear effects have received some attention since Batchelor and Proudman's seminal work on rapid distortion theory (RDT). Our perspective comes from linear control of turbulent channel Direct Numerical Simulations (DNS) with full-field forcing (Sharma *et al.*, 2011). For a finite or periodic domain, the Reynolds–Orr equation shows that only linear disturbances are responsible for changes in the total disturbance energy. The results have been interpreted in terms of Landahl's (1977) theory, based on the Orr–Sommerfeld–Squire (OSS) equations for a turbulent base flow with non-linear source terms comprising Reynolds stresses. Figure 7.2a shows the response to forcing of the u-component velocity compared to the more rapid response of the v-component velocity and pressure (Fig. 7.2b). This occurs because the shear interaction timescale is considerably shorter than either the viscous or turbulence timescales, so that the Reynolds stresses are less effective. Shear interaction is a linear RDT approximation embodied in the OSS equations, which is governed by the v-component, which is related to the pressure via the linear 'fast' source term in the Poisson equation for pressure fluctuations. Batchelor and Townsend (1956) have shown that pressure-gradient fluctuations drive the momentum field, appearing as spikes in the instantaneous mean-square acceleration. We have also shown that first they reach

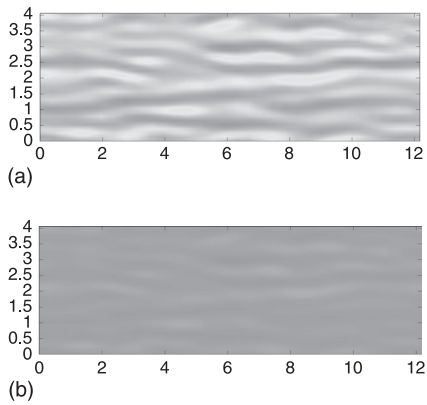

7.2 Instantaneous contours of (a) streamwise velocity and (b) pressure at $y^+ = 20$ at $t = 10$. Both pressure and v-component decay more quickly than horizontal velocity components: $y^+ = 20$ is location of maximum forcing and corresponds to peak in mean-square pressure gradient.

© Woodhead Publishing Limited, 2013

a maximum at $y^+ = 20$, and second, the forcing is at a maximum at the same location. This explains why the linear controller is effective, even though it is operating on the *v*-component alone. Landahl's (1977) theory also provides a 'wave-guide' model of the viscous sublayer, in which the least dispersive components are those of the *v*-component and pressure fields. Clearly, understanding these linear mechanisms and the extent to which they are local to the wall has a significant bearing on potential drag-reduction strategies. Understanding the mechanisms of sublayer waves would provide guidance on potential designs of compliant surfaces for turbulent drag reduction. For active, linear control, a fundamental appreciation of the shear-interaction timescale is a prerequisite and pressure is a key component to inner-outer interaction (Morrison, 2007). Our understanding of the drag-producing properties of 'coherent' structures is still in its infancy and without this, the feasibility of wall-based active control cannot be assessed.

Whether drag reduction by separation control is best achieved by arrays of multiple sensors and actuators or by a single actuator (probably controlled by multiple sensors) is once again determined by a fundamental understanding of the physical phenomena to be controlled. Separation fundamentally takes two forms – both relevant to the aerodynamics of aircraft and road vehicles, but one very different to the other. In one, separation occurs from a salient edge that defines the point of separation. It also suggests that any control of the separation process may only be through direct wake modification and in particular, its rate of growth or entrainment. This acknowledgement greatly constrains the form of actuation that can be effective. The less important process of separation from a curved surface presents an altogether different set of challenges; the separation is inherently unsteady and therefore the position of separation is time-dependent. Moreover, the separation is likely to be 3-D, even when the surface can be described by a 2-D coordinate system. This makes the separation process a rich field of dynamical processes, essentially describable by a number of 'critical points', a node, focus or saddle point – singular points in the instantaneous surface streamline pattern determined by the eigenvalues of the continuity equation (Tobak and Peake, 1982).

For the delay of separation from a continuous surface, some general rules can be helpful:

- The main objective should be to manage a local change in vorticity to improve the global distribution as much as possible, rather than trying to eliminate a shed vortex once formed.
- All streamlines pass through singular points, therefore affect change in vorticity at singular points (e.g. nodes, saddles, foci) of instantaneous streamlines.
- Moreover, the numbers of nodes and saddles conform to simple topological rules (Foss, 2007). Therefore the removal of say, a saddle point will lead to the elimination of a corresponding node.

© Woodhead Publishing Limited, 2013

- The fewer the number of saddles and nodes the better. A larger number suggests a more complicated flow structure and higher flow losses.
- Use unsteady generation of vorticity: the non-linearity of the interaction between the forcing and the flow will lead to a net streaming effect.

Dynamical similarity and the description of vortex shedding frequency, f, by a non-dimensional quantity, a Strouhal number:

$$S = fD/U_{\infty} \qquad [7.5]$$

illustrates a minimum requirement for some form of sensing and a simple form of feedback control.

The simple pragmatic requirement that sensors and actuators should be robust means that they should be integrated into a surface on or about which the drag is to be reduced. Therefore previous work has tended to focus on the measurement of surface pressure and/or surface shear stress. In Section 7.2, we briefly review different types of wall sensor, with a view to incorporating some form of feedback control. This offers several advantages; change in speed will invariably imply a change in frequency. Robust control will offer further advantages in terms of rejecting the influence of exogenous disturbances (e.g. gusts) and optimizing the efficiency of actuators. The latter is especially important in terms of maximizing the efficiency of the actuation process as a whole. Clearly there is little to be gained in reducing drag without a corresponding increase in energy efficiency. In Section 7.3, we identify fundamental surface mechanisms that may be used to inform the minimum requirements of any actuator design.

7.2 Surface sensors

An estimate may be made of the ratio of root-mean-square pressure fluctuations to skin-friction fluctuations:

$$\sqrt{\overline{p^2}/\overline{\tau_w^2}} \qquad [7.6]$$

which, at laboratory Reynolds numbers ($\mathrm{Re} \approx 10^4$), is approximately 10, rising to about 20 at flight conditions, $\mathrm{Re} \approx 10^7$. This scaling indicates that measurements of surface pressure are easier to make; however, pressure is the integral of the velocity field, and is therefore a global variable. As such, without clear physical understanding, the use of surface pressure (see above) as part of a distributed control system may be more difficult to implement. However, one or more components of the surface skin friction are more obvious quantities and therefore may be more attractive (Naguib *et al.*, 2010; Jones *et al.*, 2011).

Skin friction sensors are of two basic types: the surface shear stress can be measured directly or indirectly. Indirect measurements usually involve the rate of forced convective heat loss from a small sensor. Direct measurement involves an understanding of the scaling of basic types of force (Trimmer and Stroud, 2002)

© Woodhead Publishing Limited, 2013

which, for a length, L, will scale as L^n. For surface tension, electrostatic, magnetic and gravitational forces, n = 1, 2, 3 and 4 respectively. Therefore, micron-sized devices will be dominated by surface tension forces and is the reason why a MEMS floating element gauge will not work. A fluid-based device is likely to be impractical. For these reasons, direct measurement of surface forces is more likely to be achieved by an electrostatic mechanism. Naughton and Sheplak (2002) provide a comprehensive overview of almost all known techniques for the measurement of mean and time-dependent surface shear stress. Focusing on those techniques that can measure the latter (as well as the former) and ruling out floating element techniques, we shall discuss indirect, thermal techniques as well as direct techniques of the surface-fence type.

7.2.1 Skin friction sensors

Thermal methods of surface friction can lead to difficulties related to loss of heat to the substrate, which have the effect of increasing the effective size of the sensor and therefore to its thermal mass. This in turn leads to a degradation of the frequency response (Goldstein, 1996). Figure 7.3 shows how the sensor, either a film or a wire, works and shows its basic problem, namely that the heat flux from the element, Q_w, passes into the substrate, Q_s as well as to the air, Q_f, such that $Q_w = Q_s + Q_f$. The effect of the heat conduction into the substrate is to increase the effective length of the sensor in x, $L_{eff} \gg L$. L_{eff} is not known, nor would an analytical solution be straightforward, and therefore all gauges have to be calibrated

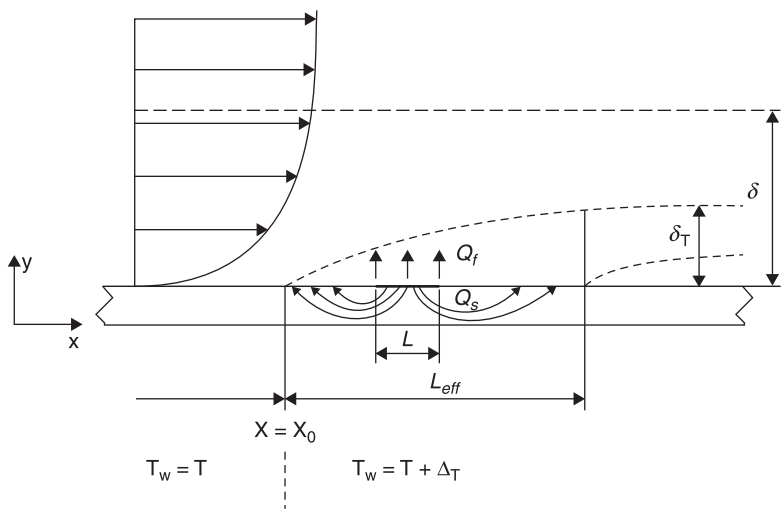

7.3 Heat loss from a wall-mounted, thermal sensor, width, L, with effective sensor length, L_{eff}, and giving rise to thermal boundary layer with thickness, δ^T.

© Woodhead Publishing Limited, 2013

individually. For a rectangular element flush with the wall, the steady state solution for the heat flux in the 2-D plane is given by:

$$\frac{Q_w}{\Delta T} \propto \left(\frac{\rho C_p k_f^2}{\mu L} \right)^{\frac{1}{3}} \tau_w^{\frac{1}{3}} \qquad [7.7]$$

where k_f is the thermal conductivity of the fluid. Obviously, the power supplied by the anemometer matches the total heat loss by the sensor, and since the thermal properties of the fluid change little with temperature, $E^2 \propto \tau_w^{\frac{1}{3}}$, where E is the voltage of a constant temperature anemometer. Empirically, we have:

$$E^2 = A + B\tau_w^{\frac{1}{3}}, \qquad [7.8]$$

where A and B are found by calibration. The cooling effect of the fluid flow by forced convection will be increased by the presence of turbulence, which provides additional heat flux. If the unsteadiness of the turbulence is not too great, Eq. 7.8 may be used for turbulent flow, where the variables are now taken to be time-averaged quantities. Since the heat loss to the substrate increases the effective size of the sensor, the effect of the turbulence becomes more pronounced as Q_s increases. Therefore the difference between the constants in laminar and turbulent calibrations is a measure of the thermal conductivity of the substrate; the higher k_s, the greater the difference in the constants for the two calibrations. Improvements to this basic design involve minimizing Q_s, either by making the thermal conductivity of the substrate as small as possible, or by using a small air cavity directly beneath the sensor, since air has a low value of k_f. Pesce and Morrison (2004) have used arrays of surface-mounted hot wires for the detection of near-wall quasi-streamwise vortices in a 2-D turbulent boundary layer. By using pairs of sensors, each at 45° to the mean skin-friction vector, both components of the fluctuating skin friction could be measured. They showed that the fluctuating spanwise component could be used to educe quasi-stream-wise vortices, even though the flow is turbulent. Such sensors are straightforwardly fabricated by standard MEMS fabrication techniques in which the thermal sensor is embedded as a film in the substrate. Löfdahl and Gad-el-Hak (2002) report work performed in the mid-1990s, in which a sensor of 5:1 aspect ratio showed some directional sensitivity. However, robustness and miniaturization, while still retaining sensitivity, remain key issues.

Fernholz *et al.* (1996) have extended the surface-fence concept, which has been used for direct, mean surface-friction measurements for some time; the technique effectively uses Eq. 7.1 when applied to the linear sublayer (i.e. close to the surface, the effects of convection and the Reynolds stresses are small), so that:

$$dp/dx = d\tau/dy \qquad [7.9]$$

© Woodhead Publishing Limited, 2013

where the viscous shear stress:

$$\tau = v\partial U/\partial y \qquad [7.10]$$

For fluctuation skin-friction measurements, a small fence is pinned to the substrate via miniaturized strain gauges. In doing so, the design builds on existing technology and the use of a Wheatstone bridge circuit to provide a near-linear device. However, in order to be sufficiently sensitive, it has to be large, $O(10)$ mm. Therefore, the frequency response is modest (<3 kHz) and second-order calibration terms become necessary for large amplitudes in surface stress when inertial effects become significant. While some progress was made up until about 2000 using silicon-based devices (Löfdahl and Gad-el-Hak, 2002), it seems likely that newer technologies, such as fiber Bragg gratings (FBG), may offer better prospects. The Bragg wavelength is sensitive to both temperature and strain, the latter being induced by either pressure or shear stress (Chehura *et al.*, 2009). While such devices are robust, the potential frequency response of such devices is unknown.

Another direct technique that shows promise is the micro-pillar technique (Brücker *et al.*, 2005; Große and Schröder, 2008, 2009), in which elastomer polydimethylsiloxane (PDMS) polymers are molded onto a substrate. Figure 7.4 shows pillars of typical diameter 15 to 45 μm, with length-to-diameter ratios of 15:25 in the linear sublayer; the local shear stress is, to a first approximation, proportional to the pillar displacement, which can be measured using standard optical techniques and a high-speed camera. Brücker *et al.* (2007) have examined the effects of non-linearity and the dynamic response. Große and Schröder (2008, 2009) have examined manufacturing issues and the sensitivity to the wall-normal

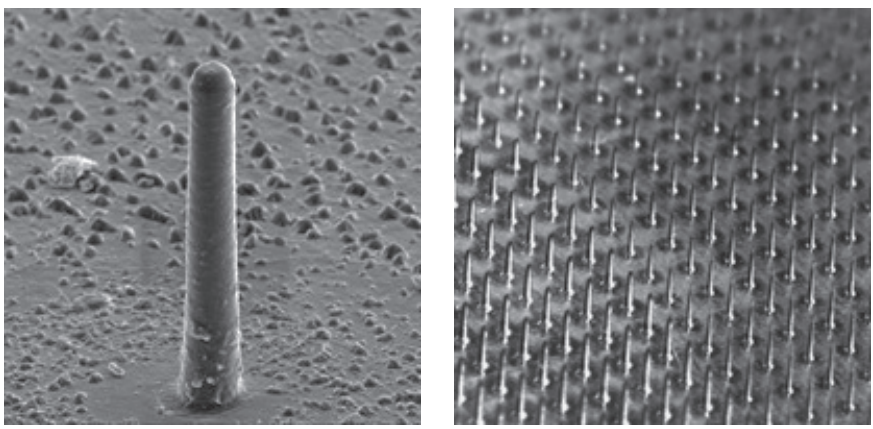

7.4 SEM images of (a) a single micro pillar; (b) pillar array. Typical pillar diameter = 20 μm; length-to-diameter ≈ 15–25 (Große and Schröder, 2009).

© Woodhead Publishing Limited, 2013

pressure gradient and to pressure-gradient fluctuations, which are of the same order as the viscous stress fluctuations in the sublayer. To date, micro-pillar measurements have been used to provide measurements of instantaneous wall shear stress in channel flow with polymer additives (Nottebrock *et al.*, 2011). However, there is significant scope for development of the technique in which the pillar displacements are measured by an embedded resistance or capacitance. Such an advance would be a key step toward wall-based control of turbulent flow and obviate the need for external laser-based measurement.

7.2.2 Surface pressure transducers

The basis of many pressure transducers is a flexible membrane that is deformed by a differential pressure to provide a direct measurement. An accurate estimate of the membrane deflection is the key to producing a workable device. Changes in either the resistive, capacitive or piezoelectric properties of the membrane can be used to estimate the deflection (Löfdahl and Gad-el-Hak, 2002). The resistive approach is generally based on applying a strain gauge to the membrane (Kälvesten *et al.*, 1994, 1996). As this membrane deforms on bending, one side of the surface is strained in tension. A strain gauge applied to the surface of the membrane can detect these changes in length (Fig. 7.5). Kälvesten and Stemme (1996) describe measurements beneath a turbulent boundary layer. While this method works well on larger devices, miniaturization greatly reduces the change in resistance of the strain gauges. In turn, this can be made larger by using finer strain gauges; however, then resistive heating becomes problematic. Moreover, the requirement of a solid substrate, on which to apply the resistive track of the strain gauge, forces the use of stiffer substrates, thus limiting sensitivity. The diaphragm in Fig. 7.5

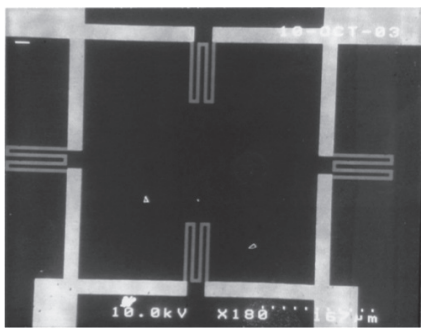

(a)

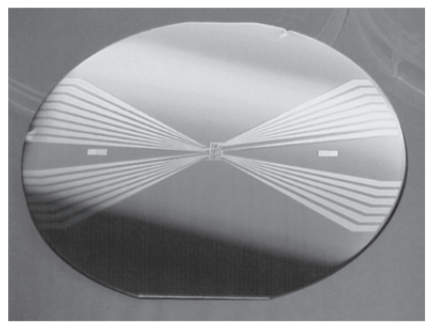

(b)

7.5 Silicon nitride pressure sensor: (a) SEM image of single SiN diaphragm (400 μm square) with four Pt resistance strain gauges, of which two are for reference and built into substrate; (b) wafer holding an array for measurements of surface pressure gradient.

© Woodhead Publishing Limited, 2013

is made using silicon nitride. Piezoelectric devices make use of the piezoelectric effect, the tendency of certain materials to accumulate charge in response to applied mechanical strain. A thin membrane of a piezoelectric material, when deformed by an applied pressure, will produce a measurable current. Again this method works well on larger devices but, due to the high Young's modulus of piezoelectric materials and the small currents that are produced, the ability to miniaturize such devices is limited.

Our current work (Potter *et al.*, 2011) focuses on using a capacitance-based approach to measure the deflection of a flexible membrane. Such a device typically offers a sensitivity of about 10 times that of a resistance transducer of similar size. A pair of separated, parallel, conductive plates has a capacitance given by:

$$C = \frac{\varepsilon_0 \varepsilon_r A}{d} \qquad [7.11]$$

where A is the area of the plates and d is the perpendicular separation. The capacitance of the unit varies as the separation of the plates changes (Fig. 7.6a). By constructing a transducer that consists of a conductive, flexible membrane, in close proximity to a conductive back plate, a basic capacitance device is formed. To prevent shorting if the two plates come together, an insulation layer is included on the base plate. This design is shown in Fig. 7.6b; use of a curved cavity provides greater sensitivity, in that the transducer is always operating in the so-called 'touch-down' mode. The inclusion of the insulating layer modifies the capacitance so that the distance between the plates is not constant; then the capacitance is determined from integration:

$$C = \int_0^r \frac{\varepsilon_0 \varepsilon_a \varepsilon_m}{\varepsilon_a t + \varepsilon_m (g - Z(r))} dA \qquad [7.12]$$

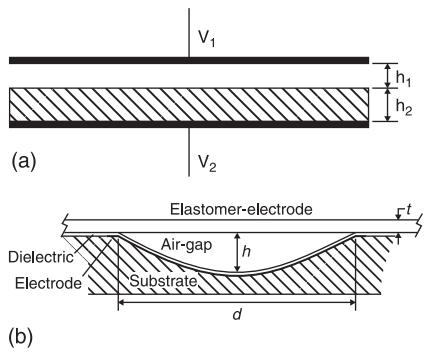

7.6 (a) Capacitance transducer function $C = \dfrac{\varepsilon_0 \varepsilon_{r1} \varepsilon_{r2} A}{\varepsilon_{r1} h_2 + \varepsilon_{r2} h_1}$; (b) transducer design.

© Woodhead Publishing Limited, 2013

where *Z(r)* is the deformation of the top membrane as a function of radius and *g* is the initial separation. The capacitor is biased with a low voltage (~3 V) to ensure operation in touch-down mode and the change in stored charge is measured as the capacitance changes. The current generated through a resistor permits amplification of the voltage change through an op-amp. Inclusion of the device in a multi-vibrator circuit allows the capacitance change to be estimated by frequency modulation, while its inclusion in a low-pass filter circuit provides a simple transfer function based on a low-pass filter. The membrane is presently made of a silicone layer spun-coated to ensure uniform thickness. A thin layer of gold is then deposited to provide the top electrode. Prototype sensors have been made by standard micro-fabrication techniques, and therefore these types of devices are straightforwardly miniaturized, the limit to size being determined by the resolution capabilities of, for example, the DRIE technique.

A particular focus of this work is the measurement of surface pressure gradients (Andreopoulos and Agui, 1996; Klewicki *et al.*, 2008), where estimates of the surface vorticity flux, σ, may be made. There are two components given by:

$$\sigma_z = -\nu \left.\frac{\partial \omega_z}{\partial y}\right|_s = -\nu \left.\frac{\partial}{\partial y}\left(\frac{\partial v}{\partial x} - \frac{\partial u}{\partial y}\right)\right|_s = \nu \left.\frac{\partial^2 u}{\partial y^2}\right|_s = \frac{1}{\rho}\left.\frac{\partial p}{\partial x}\right|_s \qquad [7.13]$$

$$\sigma_x = -\nu \left.\frac{\partial \omega_x}{\partial y}\right|_s = -\nu \left.\frac{\partial}{\partial y}\left(\frac{\partial w}{\partial y} - \frac{\partial v}{\partial z}\right)\right|_s = -\nu \left.\frac{\partial^2 w}{\partial y^2}\right|_s = \frac{1}{\rho}\left.\frac{\partial p}{\partial z}\right|_s . \qquad [7.14]$$

Andreopoulos and Agui (1996) use measurements of σ to estimate the time-dependent wall shear stress. The low-pass filter design of the pressure transducer lends itself to the use of a differential bridge, which measures pressure differences directly. Remaining challenges involve retaining sufficient sensitivity while making the device as small as possible. At present, the diaphragm diameter is 650 μm; Potter *et al.* (2011) provide further details.

7.3 Actuators

At high Reynolds numbers (e.g. on an aircraft), the scaling laws described in Section 7.1 suggest that actuator responses will need to be fast and provide a large force. Conversely, required amplitudes are likely to be small; however, an actuator moving harmonically at small amplitude will be required to provide a large force, since the acceleration is proportional to frequency squared. Huber *et al.* (1997) have identified important performance characteristics, which are presented in graphical form for ease of comparison. Various factors are considered (e.g. stress vs. strain and output power density vs. frequency); inspection of these clearly identifies piezoelectric devices as being the most suitable for aerospace applications. Piezoelectric polymers also offer much larger strain in comparison

© Woodhead Publishing Limited, 2013

to silicon-based piezoelectrics. Bell *et al.* (2005) construct performance maps as well as emphasise the importance of integrating multiple devices (both sensors and actuators) onto a single chip.

Cattafesta and Sheplak (2011) provide a comprehensive, recent overview of actuators, their comparison and modeling, with an emphasis on aerodynamic applications. Actuator requirements for feedback control are also considered; while resonance is an important feature (i.e. it makes a device very efficient), its consequences (non-linear behavior and π phase shifts) have to be considered carefully. Their principal focus is on the zero-net-mass-flux jet (ZNMF or 'synthetic' jet) and the plasma actuator.

The ZNMF actuator has received much attention since the work of Glezer and Amitay (2002). It was originally introduced by Ingard (1953), but since then has been applied to many flow-control problems. The ZNMF jet is usually generated by a piezoelectric diaphragm driven at its resonant frequency and forming the lower edge of a cavity (Fig. 7.7). The cavity volume is then adjusted such that the diaphragm resonance frequency matches that of the Helmholtz resonance of the cavity. The devices are therefore very efficient and can provide large blowing velocities. The diaphragm is usually driven harmonically so that the net mass flux is zero (hence the term 'synthetic').

The synthetic jet is made a variable frequency device by amplitude modulation of the resonance frequency (typically of the order of 10 kHz). For aerodynamic applications at low frequency, the modulating frequency is varied from 10 Hz up to 1 kHz and it is the modulating frequency that provides the aerodynamic control while the resonance frequency is the carrier. While the devices are massless, in the sense that the mass efflux during the blowing part of the cycle is matched by that sucked back into the cavity during the suction part of the cycle, it is important to

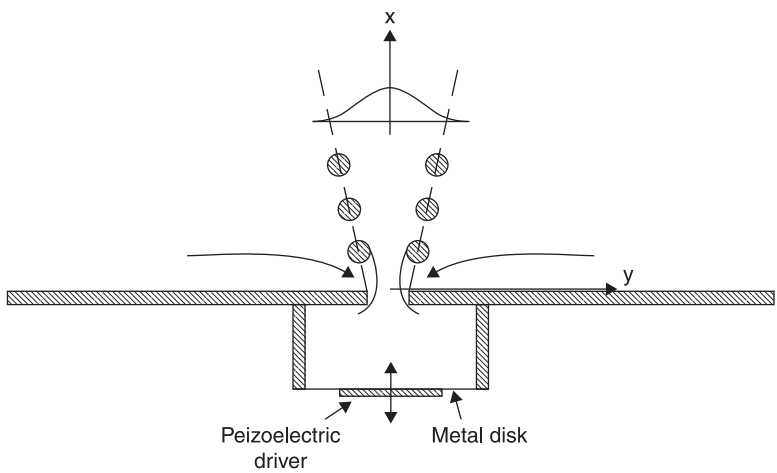

7.7 Basic design of zero-net-mass-flux 'synthetic' jet.

© Woodhead Publishing Limited, 2013

note that they are capable of providing considerable momentum flux or force by the non-linear coupling of the jet motion to that of the oncoming air stream. It is also important to note that this coupling occurs outside of the body, so that the momentum flux is generated away from the body and not on it. Therefore a synthetic jet does not itself place an additional load on the body on which it is mounted. Cattafesta and Sheplak (2011) consider design criteria using lumped-element modeling.

Dielectric barrier discharge (DBD) is the most common technique for introducing a body force into the working fluid (normally air) by plasma actuation. It is a popular technique because it has no moving parts, provides a fast response and can be easily implemented. On a surface, the actuator comprises two electrodes separated by a dielectric layer. The plasma is generated by a large voltage (order of kV) at high frequency (order of kHz), causing local ionization around the exposed electrode. The electrons travel from the exposed electrode to the dielectric so that its charge builds up. During the subsequent half-cycle, electrons return from the dielectric to the exposed electrode, near which regions of net charge density appear. As a result, the electric field exerts a force on the plasma. Cattafesta and Sheplak (2011) compare ZNMF and DBD actuation; in the context of drag reduction, energy consumption of these devices is clearly important (Spalart and McLean, 2011). Power efficiency studies are few; Jolibois and Moreau (2009) note peak electromechanical single DBD efficiencies of about 0.1%. An estimate of the drag reduction necessary for a large aircraft at cruise (i.e. Mach 0.8) using DBD is chastening. Assuming a typical DBD actuator power consumption of 50 Wm^{-1} (or 3.5 kWm^{-2}), a turbulent drag reduction of about 40% is required to balance the actuator power requirement.

7.3.1 Pulsed massless jets

Many devices are not necessarily resonant, especially if they are still undergoing fundamental studies for tailoring to a particular problem over a range of forcing frequencies. Our own work involves the application of an axisymmetric jet of variable frequency and amplitude to force a wake immediately below the point of separation on an axisymmetric bluff body (Fig. 7.8), in which the free stream flows in the *x*-direction (Qubain *et al.*, 2012). For direct-wake control, MEMS devices are not appropriate and here a speaker mounted inside the body functions as a zero-net-mass-flux device where the wake is affected directly by the pulsed jet. The base flow has several naturally appearing modes, which are (in order of increasing frequency) bubble pumping, helical and shear-layer instability. However, the most interesting phenomenon appears when the wake is forced at very high frequencies, where the internal shear layer generated acts as a 'virtual spoiler' and the base pressure rises by as much as 45% (Fig. 7.9). It appears that there is a form of resonance between a range of naturally occurring frequencies and wavelengths in the wake. A strict resonance condition requires a matching of both; the turbulence

© Woodhead Publishing Limited, 2013

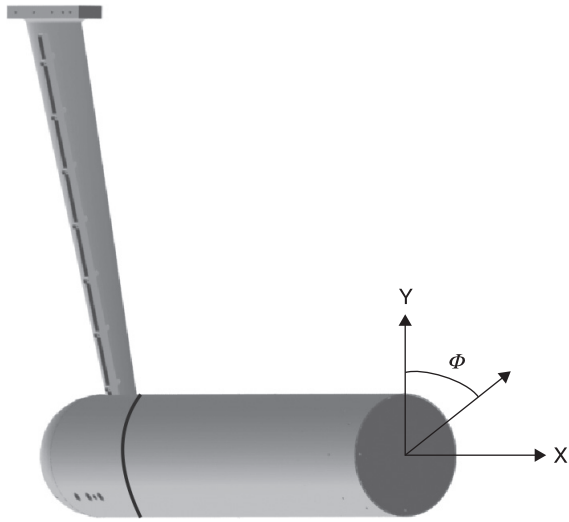

7.8 Projection of axisymmetric model with sting: free stream in *x*-direction.

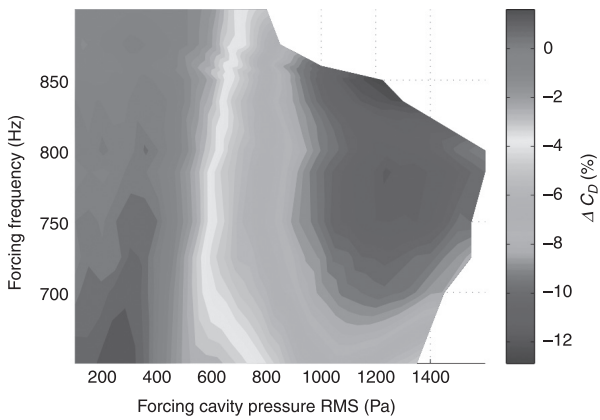

7.9 Drag coefficient map for axial harmonic forcing.

comprises a broad convective ridge in which frequency alone does not distinguish large eddies moving quickly from small eddies moving slowly.

7.3.2 Dimples

Dimples are an example in which the application of arrays of MEMS devices is appropriate is separation from a curved surface, where it is not known, *a priori*,

© Woodhead Publishing Limited, 2013

where the separation point is likely to be. The straightforward extension of static dimples used as efficient vortex generators to a generalized flexible surface capable of time-dependent motion greatly increases the range of application. Conceptually, such a surface for skin-friction reduction could be composed of either an array of discrete dimple actuators or a generalized deformable surface; so far this problem has been approached numerically (Koberg, 2007). Lambert and Morrison (2006) have performed fundamental studies of discrete actuators executing harmonic motion, such that the upmost part of the cycle brings the dimple face flush with the adjacent surface. Udovidchik and Morrison (2006) have used discrete dimple actuators to delay both laminar and turbulent separation. The fundamental aspects are well described by the vorticity flux:

$$\sigma = \nu(\mathbf{n}\cdot\nabla\mathbf{w})\big|_s \qquad [7.15]$$

where **n** is the unit-normal vector (pointing out of the fluid) and **w** is the vorticity vector. Wu and Wu (1996) and Wu *et al.* (2006) have derived the vorticity-flux equation for a moving surface of arbitrary shape, for which Eq. 7.15 becomes:

$$\sigma = \boldsymbol{n}\times\boldsymbol{a} + \boldsymbol{n}\times\frac{\nabla p}{\rho} - \left(\boldsymbol{n}\times\frac{\tau_w}{\rho}\right)\cdot\nabla_\pi\boldsymbol{n} - \boldsymbol{n}\left(\boldsymbol{n}\cdot\left(\nabla\times\frac{\tau_w}{\rho}\right)\right) \qquad [7.16]$$

On the right-hand side, the first three terms represent the generation of vorticity flux by surface acceleration, **a**, pressure gradient and surface curvature, respectively ('ascending mechanisms'). The curvature tensor is $\mathbf{K} = -\nabla_\pi\mathbf{n}$, with ∇_π being the tangential component of the nabla operator. The last term of the equation, the shear-stress gradient, is the 'upturning mechanism' (Wu and Wu, 1996), which is a viscous diffusion term that creates wall-normal vorticity as a consequence of the solenoidal condition. Lambert and Morrison (2006) show that there are distinct differences arising from the details of dimple geometry; in particular, sharp corners at which the curvature term becomes infinite are sources of very large vorticity flux that dominate all the other sources. This term in Eq. 7.10 will become significant as soon as the moving surface moves down and it will dominate throughout the cycle; this therefore reduces the effectiveness of any control. It is for this reason that smooth-edged dimples are preferred. Using a simple mass conservation argument, Lambert and Morrison (2006) show that the penetration depth, L_D/D, as a fraction of the orifice diameter is $O(0.1)$ for a dimple, but $O(10)$ for a synthetic jet. This suggests that the vorticity flux generated by a dimple remains much closer to the wall than that generated by a synthetic jet. Arguably therefore, a dimple is more efficient for control of separation from a curved surface (Udovidchik and Morrison, 2006) than a synthetic jet, while the opposite is true for wake control (Qubain *et al.*, 2012).

In terms of addressing the long-term goal of developing a 'smart' skin for skin-friction reduction, our own work has investigated the suitability of using electro-active polymers (EAP) for actuators in the form of either discrete dimples or as a

© Woodhead Publishing Limited, 2013

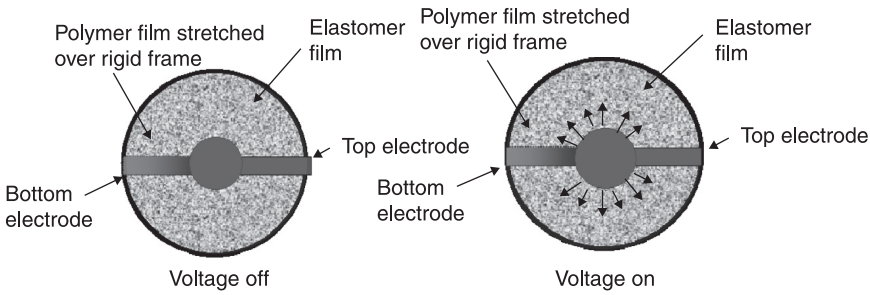

7.10 Circular EAP actuator.

continuous surface (Morrison *et al.*, 2006). In either case, the boundary layer response may be described by Eq. 7.16. Dearing *et al.* (2007, 2010) have developed EAP as the basis of actuation (Fig. 7.10), in which a voltage of variable frequency is applied to the EAP, which may be regarded as a flexible capacitor comprising an elastomer dielectric, of thickness typically 100 μm sandwiched between two compliant electrodes. On application of an electric field (typically 100 MV/m), electrostatic attraction between the two oppositely charged electrodes causes a mechanical compression in the thickness direction, while the repulsion of like charges on the same electrode causes the surface to expand. The driving force for actuation, the electrostatic pressure, P, is given by Maxwell's equation (for a constant electric field across the electrodes):

$$P = \varepsilon_0 \varepsilon_r \frac{V^2}{z_0^2}, \qquad [7.17]$$

where ε_0 is the permittivity of free space, ε_r is the relative permittivity of the dielectric, V is the applied voltage and z_0 is the undeformed elastomer thickness. Bonding of EAP onto a silicon wafer (Fig. 7.11) allows the formation of dimples in which in-plane expansion of the polymer leads to out-of-plane buckling (Dearing *et al.*, 2010). Requirements for control of a turbulent boundary layer suggest that the actuators need to be 10 to 1000 μm in size, and in the present work, actuation is effected with out-of-plane displacements of approximately 10% of their diameter. Further development is required to assess the non-linear transfer function; while buckling readily provides large amplitudes, it makes the response difficult to predict. Dearing *et al.* (2010) show how the phase of the displacement response to the applied voltage varies with frequency.

While EAP offers many advantages, in terms of large in-plane strains and low power consumption, it also presents challenges in terms of repeatability (hysteresis, Mullin's effect), viscoelastic effects and frequency response. Potter *et al.* (2011) present a theoretical model for predicting the behavior of EAP actuators. It takes the form of an array of masses with the interconnecting forces derived using Hooke's law coupled with an electrostatic force. Forming the model in this way

© Woodhead Publishing Limited, 2013

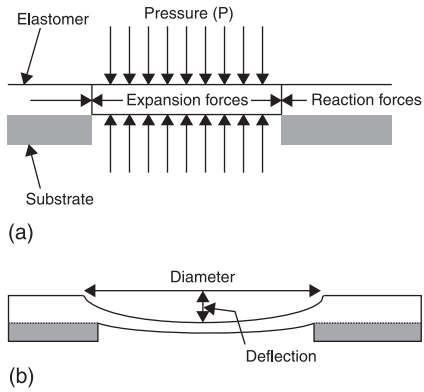

7.11 Formation of active dimple through buckling: (a) forces; (b) buckling.

allows the response of actuators of various sizes and pre-strains to be simulated with a range of electrode designs. It has been validated for a series of Nusil MED4905 polydimethylsiloxane actuators with variable electrode designs. By comparing the positions of grid nodes on a deformed specimen to those on the undeformed one, the model was shown to work well. Gouder (2011) has attempted to use EAP to generate surface waves and replicate the simulations of Quadrio (2011); owing largely to the forces generated in the surface and the day-to-day variations in the material behavior, this has not met with success.

Ink-jet printing offers a paradigm shift for fabrication, which is otherwise expensive and time-consuming (Arthur *et al.*, 2006). Moreover, ink-jet printing is consistent with the use of graphite-based electrodes, and also with the incorporation of carbon nanotubes, which can be made to be both conducting and semi-conducting. Given the sensing capabilities of EAP, a monolithic EAP-based 'intelligent' surface for active flow control becomes a real possibility (Morrison *et al.*, 2006). However, attempts at ink-jet printing have not proved successful owing largely to the high viscosity of EAP, even when oil-based silicones are replaced with water-based polymers. Other forms of printing (e.g. contact printing) are being investigated and much work is required to determine an optimum type of polymer.

7.4 Conclusion and future trends

A pragmatic vision for the application of MEMS technology to drag reduction in both aerospace and automotive sectors has been proposed. A fundamental understanding of the basic physical processes drives the approach; for skin-friction reduction, owing to the prohibitive requirements for resolution and density, arrays of micron-sized devices are not considered feasible. However, the prospects for linear wall-based feedback control appear to be promising. We

© Woodhead Publishing Limited, 2013

have also demonstrated that a single-actuator system (with multiple pressure sensors) may well provide a practical system for the recovery of base pressure on such bluff bodies as cars and trucks. Owing to the nature of separation from curved surfaces, where the separation point fluctuates in time and is subject to even minor changes in boundary conditions, there is scope for the development of separation control techniques that do make use of multiple sensor and actuator systems. In the shorter term, separation control is more likely to lead to demonstrable drag reductions than the more challenging problem of skin-friction reduction. New technologies involving the development of robust fast, high force materials are required. EAP is promising but requires significant development for higher forces.

7.5 Acknowledgements

I am indebted to many colleagues and students, past and present, with whom I have had the privilege to work and whose work appears both here and in the papers referenced. They are Graham Arthur, Dave Birch, Alexander Bismarck, Stella Dearing, Kevin Gouder, Kingsley Ho, Lorenzo Iannucci, Phil Lavoie, Beverley McKeon, Anthony Oxlade, Giuseppe Pesce, Mark Potter, Ala Qubain. I am grateful to Ferrari S.p.A. and to EPSRC (grants GR/L90989/01, GR/S20994, EP/C535847, EP/F004435/1, EP/G023530, EP/I005684) for financial support.

7.6 References

Andreopoulos J and Agui J H (1996), 'Wall-vorticity flux dynamics in a two-dimensional turbulent boundary layer', *J Fluid Mech*, 309, 45–84.

Arthur G G, McKeon B J, Dearing S S, Morrison J F and Cui Z (2006), 'Manufacture of micro-sensors and actuators for flow control', *Microelect Eng*, 83, 1205–1208.

Batchelor G K and Townsend A A (1956), 'Turbulent diffusion', in G K Batchelor and R M Davis (Eds.), *Surveys in Mechanics*, Cambridge, UK: Cambridge University Press, pp. 352–399.

Bell D J, Lu T J, Fleck N A and Spearing S M (2005), 'MEMS actuators and sensors: observations on their performance and selection for purpose', *J Micromech Microeng*, 15, S153–S164.

Brücker C, Spatz J, Schröder W (2005), 'Feasibility study of wall-shear stress imaging using microstructured surfaces with flexible micropillars', *Exp Fluids*, 39, 464–474.

Brücker C, Bauer, D and Chaves H (2007), 'Dynamic response of micro-pillar sensors measuring fluctuating wall-shear-stress', *Exps Fluids*, 42, 737–749.

Carpenter P W, Kudar K L, Ali R, Sen P K and Davies C (2007), 'A deterministic model for the sublayer streaks in turbulent boundary layers for application to flow control', *Phil Trans R Soc A*, 365, 2419–2441.

Cattafesta L N and Sheplak M (2011), 'Actuators for active flow control', *Ann Rev Fluid Mech*, 43, 247–272.

Chehura E, James S W, Lawson N, Garry K P and Tatam R P (2009), 'Pressure measurements on aircraft wing using phase-shifted fibre Bragg grating sensors', *Proc SPIE*, 7503, 750334.

© Woodhead Publishing Limited, 2013

Choi K. S, Jukes T and Whalley R (2011), 'Turbulent boundary-layer control with plasma actuators', in M Leschziner, H Choi and K Choi (Eds.), 'Flow-control approaches to drag reduction in aerodynamics: progress and prospects', *Phil Trans R Soc A*, 369, 1443–1458.

Colonius T and Williams D R (2011), 'Control of vortex shedding on two- and three-dimensional aerofoils', in M Leschziner, H Choi and K S Choi (Eds.), 'Flow-control approaches to drag reduction in aerodynamics: progress and prospects', *Phil Trans R Soc A*, 369, 1525–1539.

Corke T C, Bowles P O, He C and Matlis E H (2011), 'Sensing and control of flow separation using plasma actuators', in M Leschziner, H Choi and K S Choi (Eds.), 'Flow-control approaches to drag reduction in aerodynamics: progress and prospects', *Phil Trans R Soc A*, 369, 1459–1475.

Dearing S S, Morrison J F and Iannucci L (2010), 'Electro-active polymer (EAP) "dimple" actuators for flow control: design and characterisation', *Sens Actuat A*, 157, 210–218.

Dearing S S, Lambert S and Morrison J F (2007), 'Flow control with active dimples', *Aeronaut J*, 111(1125), 705–714.

Erdmann R, Pätzold A, Engert M, Peltzer I and Nitsche W (2011), 'On active control of laminar-turbulent transition on two-dimensional wings', in M Leschziner, H Choi and K S Choi (Eds.), 'Flow-control approaches to drag reduction in aerodynamics: progress and prospects', *Phil Trans R Soc A*, 369, 1382–1395.

European Commission (2011), 'Flightpath 2050 Europe's Vision for Aviation', *Report of the High Level Group on Aviation Research*. Available from http://www.acare4europe.org/html/documentation.asp (accessed 28 April 2011).

Fernholz H H, Janke G, Schober M, Wagner P M, Warnack D (1996), 'New developments and applications of skin-friction measuring techniques', *Meas Sci Technol*, 7, 1396–1409.

Foss J F (2007), 'Topological considerations in fluid mechanics measurements', in C Tropea, A L Yarin and J F Foss (Eds.), *Handbook of Experimental Fluid Mechanics*, Ch. 13, Berlin, Heidelberg: Springer, pp. 909–918.

Glezer A (2011), 'Some aspects of aerodynamic flow control using synthetic-jet actuation', in M Leschziner, H Choi and K S Choi (Eds.), 'Flow-control approaches to drag reduction in aerodynamics: progress and prospects', *Phil Trans R Soc A*, 369, 1476–1494.

Glezer A and Amitay M (2002), 'Synthetic jets', *Ann Rev Fluid Mechs*, 34, 503–529

Goldhammer M and Vijgen P (2009), 'The next decade in commercial aircraft aerodynamics – a Boeing perspective', in *KATnet II Conference on Key Aerodynamic Technologies*, Bremen, Germany, 12–14 May.

Goldstein R J (1996), *Fluid Mechanics Measurements, Second Edition*. Washington DC and London: Taylor and Francis.

Gouder K (2011), 'Turbulent friction drag reduction using electroactive polymer surfaces', PhD thesis, Imperial College, London.

Große S and Schröder W (2008), 'Dynamic wall-shear stress measurements in turbulent pipe flow using the micro-pillar shear-stress sensor MPS^{3}', *Int J Heat Fluid Flow*, 29, 830–840.

Große S and Schröder W (2009), 'The micro-pillar shear-stress sensor MPS^3 for turbulent flow', *Sensors*, 9, 2222–2251.

Huber J E, Fleck N A and Ashby M F (1997), 'The selection of mechanical actuators based on performance indices', *Proc Soc A*, 453, 2185–2205.

Hucho W H and Sovran G (1993), 'Aerodynamics of road vehicles', *Ann Rev Fluid Mech*, 25, 485–537.

© Woodhead Publishing Limited, 2013

IEA Statistics (2010), *CO_2 Emissions from Fuel Combustion 2010*, International Energy Agency, US Energy Information Administration, Washington, DC: OECD Publishing.
Ingard U (1953), 'On the theory and design of acoustic resonators', *J Acoustic Soc Amer*, 25, 1037–1061.
International Energy Outlook (2010), 'US Energy Information Administration', Report No. DOE/EIA-0484(2010).
Jolibois J and Moreau E (2009), 'Enhancement of the electromechanical performances of a single dielectric barrier discharge actuator', *IEEE Trans Dielectr Electr Insul*, 16, 758–767.
Jones B L, Kerrigan E C, Morrison J F and Zaki T (2011), 'Flow estimation of boundary layers using DNS-based wall shear information', *Int J Control*, 84, 1310–1325.
Kälvesten E, Löfdahl L and Stemme G (1994), 'A small-size silicon microphone for measurements in turbulent gas flows', *Sens Actuat A*, 45, 103–108.
Kälvesten E and Stemme G (1996), 'Small silicon pressure transducers for space-time correlation measurements in a flat plate boundary layer', *J Fluids Eng*, 118, 457–463.
Kälvesten E, Vieider C, Löfdahl L and Stemme G (1996), 'An integrated pressure-flow sensor for correlation measurements in turbulent gas flows', *Sens Actuat A*, 52, 51–58.
Kim J (2011), 'Physics and control of wall turbulence for drag reduction', in M Leschziner, H Choi and K S Choi (Eds.), 'Flow-control approaches to drag reduction in aerodynamics: progress and prospects', *Phil Trans R Soc A*, 369, 1396–1411.
Kim J and Bewley T R (2007), 'A linear systems approach to flow control', *Ann Rev Fluid Mech*, 39, 383–417.
Klewicki J C, Priyadarshana P J A and Metzger M M (2008), 'Statistical structure of the fluctuating wall pressure and its in-plane gradients at high Reynolds number', *J Fluid Mech*, 550, 185–205.
Koberg H (2007), 'Turbulence control for drag reduction with active wall deformation', PhD thesis, Department of Aeronautics, Imperial College.
LaGraff J E, Povinelli L A, Gostelow J P and Glauser M (2010), '2009 Workshop on flow physics and control for internal and external aerodynamics', NASA/CP–2010-216112.
Lambert S and Morrison J F (2006), 'Fundamental studies of active dimples', *AIAA-2006-3182*.
Landahl M T (1977), 'Dynamics of boundary layer turbulence and the mechanism of drag reduction', *Phys Fluids*, 20(10), S55–S63.
Leschziner M, Choi H and Choi K S (Eds.) (2011), 'Flow-control approaches to drag reduction in aerodynamics: progress and prospects', *Phil Trans R Soc A*, 369, 1940.
Li Y and Gaster M (2006), 'Active control of boundary layer instabilities', *J Fluid Mech*, 550, 185–205.
Löfdahl L and Gad-el-Hak M (2002), 'Sensors and actuators for turbulent flows', in M Gad-el-Hak, *The MEMS Handbook*, Ch. 26, Boca Raton, FL: CRC Press, pp. 26–1–26–77.
Morrison J F (2005), 'Boundary layers under strong distortion: an experimentalist's view', in G F Hewitt and J C Vassilicos (Eds.), *Prediction of Turbulent Flows*. Royal Academy of Engineering, Cambridge, UK: Cambridge University Press.
Morrison J F (2007), 'The interaction between inner and outer regions of turbulent wall-bounded flow', *Phil Trans R Soc A*, 365, 683–698.
Morrison J F (2010), 'Turbulent boundary layers', in R Blockley and W Shyy (Eds.), *Encyclopedia of Aerospace Engineering*. New York and Chichester UK: John Wiley and Sons Ltd.
Morrison J F, Dearing S S, Arthur G G, McKeon B J and Cui Z (2006), 'Fluid flow control using boundary layer control', Geneva: World Intellectual Property Organisation.

© Woodhead Publishing Limited, 2013

Naguib A M, Morrison J F and Zaki T (2010), 'On the relationship between the wall-shear-stress and transient-growth disturbances in a laminar boundary layer', *Phys Fluids*, 22, 054103.

Naughton J W and Sheplak M (2002), 'Modern developments in shear-stress measurement', *Prog Aerosp Sci*, 38, 515–570.

Nottebrock B, Große S and Schröder W (2011), 'Development of a shear-stress sensor to analyze the influence of polymers on the turbulent wall-shear stress', *J Phys Condens Matt*, 23, 184121.

Pesce G and Morrison J F (2004), 'A wall-shear-stress based algorithm for the control of turbulent wall flow', in H I Anderson and P A Krogstad (Eds.), *Advances in Turbulence X*. Barcelona: CIMNE.

Potter M, Gouder K and Morrison J F (2011), 'A numerical model for electro-active polymer actuators with experimental validation', *Sens Actuat A Phys*, 170, 121–130.

Quadrio M (2011), 'Drag reduction in turbulent boundary layers by in-plane wall motion', in M Leschziner, H Choi and K S Choi (Eds.), 'Flow-control approaches to drag reduction in aerodynamics: progress and prospects', *Phil Trans R Soc A*, 369, 1428–1442.

Qubain A, Oxlade A and Morrison J F (2012), 'Active control of an axisymmetric, turbulent wake', Submitted, *J Fluid Mech.*

Robinson S K (1991), 'Coherent motions in the turbulent boundary layer', *Ann Rev Fluid Mechs*, 23, 601–639.

Saric W S, Carpenter A L and Reed H L (2011), 'Passive control of transition in three-dimensional boundary layers, with emphasis on discrete roughness elements', in M Leschziner, H Choi and K S Choi (Eds.), 'Flow-control approaches to drag reduction in aerodynamics: progress and prospects', *Phil Trans R Soc A*, 369, 1352–1364.

Sharma A S, Morrison J F, McKeon B J, Limebeer D J N, Koberg W H, *et al.* (2011), 'Relaminarisation of turbulent channel flow with globally stabilising linear feedback control', *Phys Fluids*, 23, 125105.

Spalart P R and McLean J D (2011), 'Drag reduction: enticing turbulence, and then an industry', in M Leschziner, H Choi and K S Choi (Eds.), 'Flow-control approaches to drag reduction in aerodynamics: progress and prospects', *Phil Trans R Soc A*, 369, 1556–1569.

Stern N (2006), 'Stern Review on the economics of climate change'. Available from: http://webarchive.nationalarchives.gov.uk/+/http:/www.hm-treasury.gov.uk/independent_reviews/stern_review_economics_climate_change/stern_review_report.cfm (accessed 21 April 2011).

Technology Strategy Board (2010), 'Automotive technologies: the UK's current capability'. Available from: http://www.innovateuk.org/_assets/pdf/corporate-publications/automotive%20tech%20summary.pdf (accessed 21 April 2011).

Tobak M and Peake D J (1982), 'Topology of three-dimensional separated flows', *Ann Rev Fluid Mech*, 14, 61–85.

Trimmer W and Stroud R H (2002), 'Scaling of micromechanical devices', in M Gad-el-Hak *The MEMS Handbook*, Ch. 2, Boca Raton: CRC Press, pp. 2-1–2-9.

Udovidchik N and Morrison J F (2006), 'Investigation of active dimple actuators for separation control', *AIAA-2006-3190*, Third AIAA Flow Control Conference, San Francisco, 5–8 June.

Wu J-Z and Wu J M (1996), 'Vorticity dynamics on boundaries', *Adv in Appl Mech*, 32, 119–275.

Wu J-Z, Ma H-Y and Zhou M-D (2006), *Vorticity and Vortex Dynamics*, Berlin, Heidelberg: Springer.

© Woodhead Publishing Limited, 2013

8

MEMS inertial navigation systems for aircraft

Y. DONG, Colibrys SA, Switzerland

DOI: 10.1533/9780857096487.2.177

Abstract: This chapter discusses MEMS accelerometers and gyroscopes and how inertial navigation systems (INS) are used with these sensors for aircraft. The chapter first reviews MEMS sensors and the limitations of MEMS inertial sensors to be embedded in INS, then discusses INS and the integration of INS with global positioning systems (GPS); it provides background on the use of sensor fusion and a Kalman filter to aid INS, and presents the challenges and trends of MEMS INS for aircraft.

Key words: accelerometers, aerospace, GPS, gyroscopes, inertial navigation, MEMS.

8.1 Introduction

The most important parameters of MEMS inertial sensors for aerospace applications are their bias instability and noise level, size and cost. However, perhaps above all, reliability of MEMS inertial sensors over lifecycles imposes far more stringent requirements and constraints on aerospace applications than automotive and consumer applications (Schadow, 2003). In the harsh aviation environment, MEMS inertial sensors need resilience to cosmic particle radiation, immunity to inevitable electromagnetic interference, extreme shock survivability, excellent stability under post-vibration and shock, and precise repeatability for thermal compensation in a high operating temperature range (–55 to 125°C).

Aircraft are usually referred to as vehicles, such as propeller or jet airplanes, helicopters, unmanned aerial vehicles (UAVs), cruise missiles, etc., which use aerodynamics as the primary lift to counter the force of gravity and are able to fly by being supported by the air. Navigation is the determination process of position and direction and guidance of a vehicle from one place to another. Among modern navigation techniques, inertial navigation is a typical dead-reckoning navigation technique. The operation of inertial navigation systems (INS) depends upon Newton's laws of classical mechanics. An INS consists of an inertial measurement unit (IMU) and a digital computer. The inertial sensors referred to here are gyroscopes and accelerometers. Gyroscopes measure angular rotation with respect to inertial space. Rate gyroscopes measure rotation rate, and integrating gyroscopes (whole-angle gyroscopes) measure rotation angle. Accelerometers measure linear acceleration with respect to inertial space. A six degree-of-freedom (DoF) inertial sensor assembly (ISA) comprises three-orthogonal gyroscopes and three-orthogonal accelerometers. Figure 8.1 shows the relationship among the ISA, IMU and INS.

© Woodhead Publishing Limited, 2013

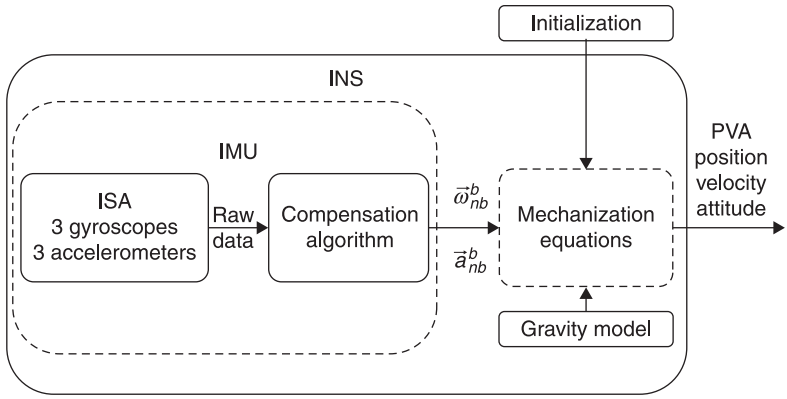

8.1 The relationship among ISA, IMU and INS.

Three-orthogonal gyroscopes measure angular rotations about three perpendicular axes (pitch, yaw and roll), while three-orthogonal accelerometers measure axial accelerations about translation in three perpendicular axes (x, y and z). All these six axis motions are freely independent of each other (Fig. 8.2).

Under all weather global operation, based on the initial information about aircraft, an INS can derive the aircraft's attitude, velocity and position. INS is the only and completely self-contained navigation format, which does not require external references. However, a major disadvantage of inertial navigation is that the estimation errors of the process are accumulative. The global positioning system (GPS) is a space-based global navigation satellite system (GNSS) that provides location and time information in all weathers, anywhere on or near the

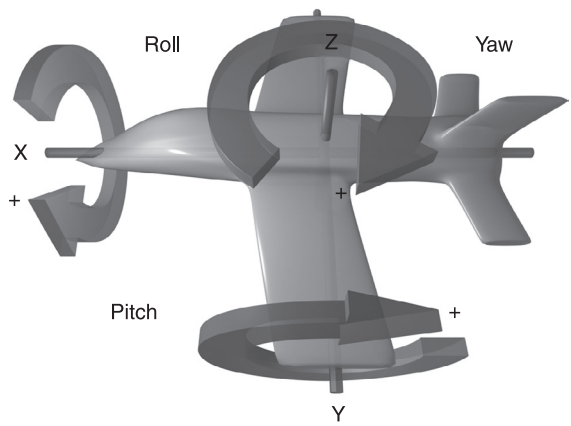

8.2 Roll, yaw and pitch axis definition for an airplane.

© Woodhead Publishing Limited, 2013

Earth. GPS seems an ideal navigation solution for aircraft; however, due to signal blockages under certain environmental conditions, GPS cannot provide continuous navigation. MEMS integrated navigation systems (Aggarwal *et al.*, 2010), which integrate the signals from GPS and INS, provide reliable accurate long-term continuous navigation capability. Such an integrated navigation system solves both the problems of the satellite's signal unavailability or unreliability and INS error accumulation.

8.1.1 Gimbaled stable platform mechanization

In a gimbaled IMU, the gyros and accelerometers are isolated from vehicle angular movements by means of gimbals. A gimbaled IMU is in fact a gyro stabilized platform. A gimbal assembly and torque motors use resolvers, slip rings, bearings, etc. to control the platform, to maintain the inertial reference frame locally level or stable. Figure 8.3 illustrates the gimbaled INS (IEEE Std 1559-2009, 2009).

The original INS was implemented using the stable platform mechanization. The aircraft travels over a spherical surface and thus the direction of the gravity vector changes with its position. The Earth rotates on its axis and thus the direction of the gravity vector changes with time. A platform is mounted on gimbals to keep accelerometers horizontally aligned with the surface of the Earth, such that it is mechanically isolated from aircraft attitude; therefore accelerometers do not sense

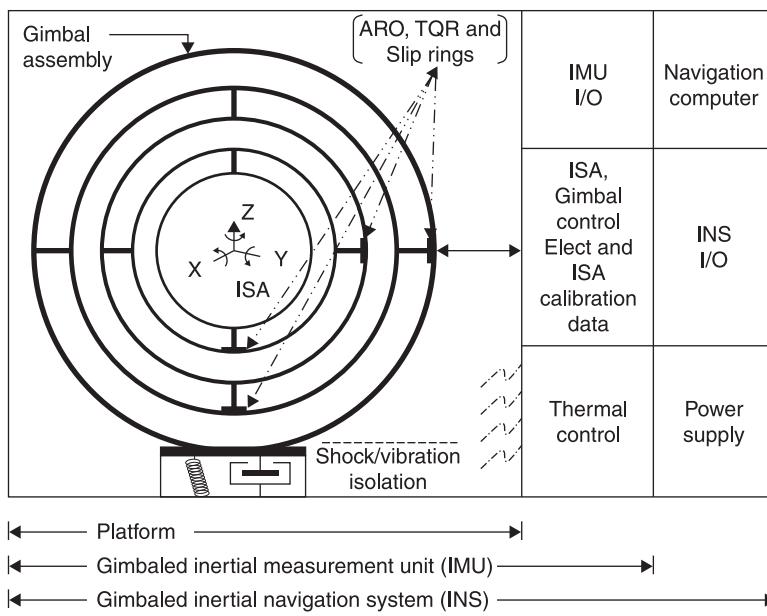

8.3 Gimbaled inertial navigation system (IEEE Std 1559-2009, 2009).

© Woodhead Publishing Limited, 2013

the gravity vector. The gyroscopes sense platform rotation in any of the three axes and then send a correction signal to the pivot motors, which then rotate the relevant gimbals to maintain the platform at the correct attitude. However, gimbaled INS has critical issues with cost and reliability. Due to numerous precisely moving mechanical parts, maintenance is very expensive.

8.1.2 Strapdown systems technology

The main problem for an INS is to separate the vehicle acceleration from the effect of gravity on the accelerometers. In a gimbaled platform, this is done by maintaining the accelerometers perpendicular to the gravity vector, which allows the INS to ignore the effect of gravity. Another approach is to keep track of the gravity vector and subtract its effect from the outputs of the accelerometers. In a strapdown IMU, all inertial sensors are rigidly fixed or 'strapped down' to the chassis of the IMU and hence to the aircraft (body frame) without mechanical movement. Figure 8.4 illustrates the strapdown INS (IEEE Std 1559-2009, 2009).

Three gyroscopes are used to keep track of the orientation between the accelerometer axis and the gravity vector. This is an analytical or computational mechanization; in fact, a *mathematical* platform replaces the mechanical gimbaled inertial platform. Strapdown INS has great advantages of immediate detection of body rates and accelerations, fewer moving parts and potential redundancy.

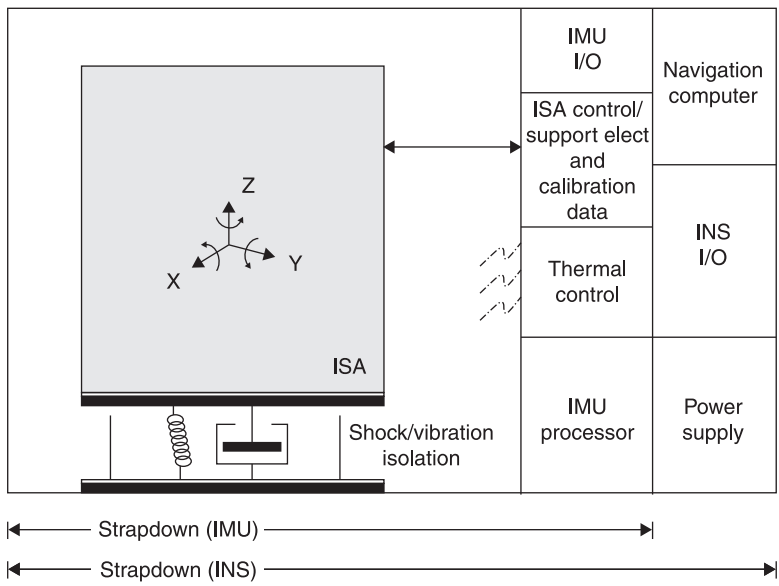

8.4 Strapdown inertial navigation system (IEEE Std 1559-2009, 2009).

© Woodhead Publishing Limited, 2013

8.1.3 Inertial reference frame

Aircraft naturally choose the Earth as an inertial frame. However, the Earth's rotation cannot be neglected and also the Earth is not a perfectly round geometrical object in 3-D space. Aircraft need navigation parameters with respect to the Earth. It is necessary to express vectors in different coordinate frames. This requires the rotation matrix, which relates coordinates and unit vectors in one frame to those in another frame. The IMU inertial signals need coordinate transformations between different coordinate reference frames to determine an aircraft's attitude and position. The choice of navigation frame is also known as mechanization. A strapdown mechanization (Dorobantu and Gerlach, 2004) in the *e*-frame is shown in Fig. 8.5.

Earth-centered inertial (ECI) frame (denoted by the symbol i)

i is originated at the center of mass of the Earth and oriented with respect to the Earth's spin axis and the stars.

Earth-centered Earth-fixed (ECEF) frame (denoted by the symbol e)

e is originated at the center of the mass of the Earth. ECEF can be defined in Cartesian (x, y and z in meters) or spherical (latitude L, longitude λ and altitude h) coordinates. Its axes are aligned with the international reference pole (IRP) and international reference meridian (IRM), which are fixed with respect to the surface of the Earth.

Navigation frame (denoted by the symbol n)

n is a local geographic frame, which is thought to be located at the surface of the Earth, directly beneath the vehicle and has its origin at the location of the INS.

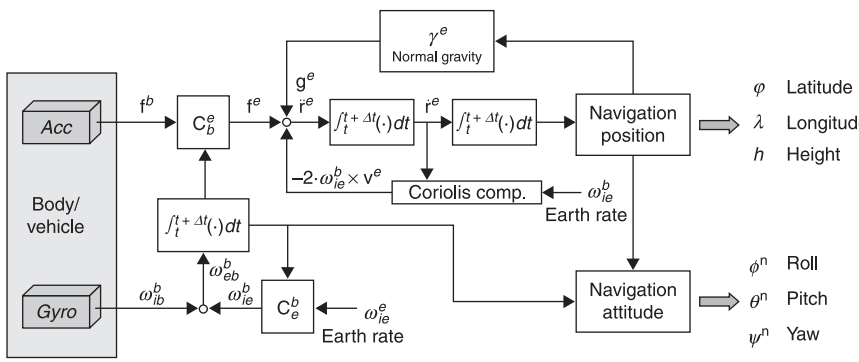

8.5 Strapdown mechanization in the *e*-frame (Dorobantu and Gerlach, 2004).

© Woodhead Publishing Limited, 2013

Axes are aligned in the directions of north, east and down (NED), with the *x*-axis pointing north, the *z*-axis pointing vertically down, and with the last completing the right-hand coordinate frame *y*-axis pointing east. The frame is tangental to the Earth's surface but translated to the center of the Earth. The vertical *z*-axis is normal to the Earth's surface and the *x*- and *y*-axes are level. The turn rate of the navigation frame with respect to the Earth-fixed frame is often referred to as the transport rate.

Local frame (denoted by the symbol l)

l is thought to be the same as navigation frame, except that axes are aligned in the directions of east, north and up (ENU), with the *x*-axis pointing east, the z-axis pointing vertically up, and with the last completing the right-hand coordinate frame, the *y*-axis pointing north. The *y*-axis makes wander angle α with respect to true north, to overcome a singularity at the north or the south poles.

Body frame (denoted by the symbol b)

b is fixed to the casing of the IMU, which is attached to the aircraft. The axes of the body frame are known as roll, pitch and yaw. The body frame is centered in the body of the vehicle (usually at the center of gravity). The body frame is essential in navigation because it describes the object that is navigating. All strapdown inertial sensors measure the motion of the body frame, with respect to a generic inertial frame.

8.1.4 Navigation equations

In order to compute the navigation solution, the inertial sensor signals must be transformed to a unified point of the reference frame. The orientation, or attitude, of an INS relative to the global frame of reference is tracked by 'integrating' the angular velocity signal obtained from the system's rate-gyroscopes. In order to specify the orientation of an INS, one of several attitude representations must be used. All frames are Earth-centered, hence coordinate frame conversions can be implemented by matrices rotation. Common representations include Euler angles, quaternions and direction cosine matrix.

Direction cosine matrix (DCM)

The direction cosine matrix, representing the attitude of the body frame relative to the reference frame, is specified by a 3 × 3 rotation matrix $\boldsymbol{C}$, the columns of which represent unit vectors in the body axes projected along the reference axes. Here, C_i^j is the rotation matrix transforming r from frame $\boldsymbol{i}$ to frame $\boldsymbol{j}$. C_b^n is written here in component form as:

© Woodhead Publishing Limited, 2013

$$C_b^n = \begin{bmatrix} c_{11} & c_{12} & c_{13} \\ c_{21} & c_{22} & c_{23} \\ c_{31} & c_{32} & c_{33} \end{bmatrix} \quad [8.1]$$

The element in the ***i***th row and the ***j***th column represents the cosine of the angle between the ***i***-axis of the reference frame and the ***j***-axis of the body frame.

For a vector $\boldsymbol{r}^i$ defined in frame ***i***, may be expressed in reference frame ***j*** by pre-multiplying the vector by the direction cosine matrix $\boldsymbol{C}_i^j$ as:

$$\boldsymbol{r}^j = C_i^j \boldsymbol{r}^i \quad [8.2]$$

Equation 8.2 shows the local acceleration is to be computed using direction cosine matrix C_b^n, which is derived from gyro-sensed body rates.

Propagation of direction cosine matrix with time can be expressed as:

$$\dot{\boldsymbol{C}}_b^n = \boldsymbol{C}_b^n \boldsymbol{\Omega}_{nb}^b = -\boldsymbol{\Omega}_{nb}^b \boldsymbol{C}_b^n \quad [8.3]$$

The rate of change of $\dot{\boldsymbol{C}}_b^n$ represents the turn rate of the ***b***-frame with respect to the ***n***-frame expressed in body axes. $\boldsymbol{\Omega}_{nb}^b$ is the relative angular velocity between the ***b***-frame and the ***n***-frame, and the angular velocity is expressed in the ***b***-frame: where $\Omega_{nb}^b = \begin{pmatrix} 0 & -\omega_z & \omega_y \\ \omega_z & 0 & -\omega_x \\ -\omega_y & \omega_x & 0 \end{pmatrix}$ is the skew-symmetric matrix format of the angular rate vector $\omega_{nb}^b = \begin{bmatrix} \omega_x & \omega_y & \omega_z \end{bmatrix}^T$.

Equation 8.3 is linear and very simple, but the main disadvantage is that it has too many elements to be integrated and this leads to computational burden.

Euler angles

A transformation from one coordinate frame to another can be carried out as three successive rotations about different axes. For instance, a transformation from reference axes to a new coordinate frame may be expressed mathematically as three separate direction cosine matrices as:

$$\text{rotation through angle } \varphi \text{ about } x\text{-axis, } C_1 = \begin{bmatrix} 1 & 0 & 0 \\ 0 & \cos\varphi & -\sin\varphi \\ 0 & \sin\varphi & \cos\varphi \end{bmatrix} \quad [8.4]$$

$$\text{rotation through angle } \theta \text{ about } y\text{-axis, } C_2 = \begin{bmatrix} 1 & 0 & 0 \\ 0 & \cos\varphi & -\sin\varphi \\ 0 & \sin\varphi & \cos\varphi \end{bmatrix} \quad [8.5]$$

© Woodhead Publishing Limited, 2013

$$\text{rotation through angle } \psi \text{ about } z\text{-axis, } C_3 = \begin{bmatrix} 1 & 0 & 0 \\ 0 & \cos\varphi & -\sin\varphi \\ 0 & \sin\varphi & \cos\varphi \end{bmatrix} \qquad [8.6]$$

Thus, a transformation from body to reference axes may be expressed as:

$$\begin{aligned} C_b^n &= \left(C_n^b\right)^T = C_1^T C_2^T C_3^T \\ &= \begin{bmatrix} \cos\psi & -\sin\psi & 0 \\ \sin\psi & \cos\psi & 0 \\ 0 & 0 & 1 \end{bmatrix} \begin{bmatrix} \cos\theta & 0 & \sin\theta \\ 0 & 1 & 0 \\ -\sin\theta & 0 & \cos\theta \end{bmatrix} \begin{bmatrix} 1 & 0 & 0 \\ 0 & \cos\varphi & -\sin\varphi \\ 0 & \sin\varphi & \cos\varphi \end{bmatrix} \\ &= \begin{bmatrix} \cos\psi\cos\theta & -\sin\psi\cos\varphi + \cos\psi\sin\theta\sin\varphi & \sin\psi\sin\theta + \cos\psi\sin\theta\cos\varphi \\ \sin\psi\cos\theta & \cos\psi\cos\varphi + \sin\psi\sin\theta\sin\varphi & -\cos\psi\sin\varphi + \sin\psi\sin\theta\cos\varphi \\ -\sin\theta & \cos\theta\sin\varphi & \cos\theta\cos\varphi \end{bmatrix} \end{aligned} \qquad [8.7]$$

where ψ, θ and φ are referred to as the Euler rotation angles.

This is the direction cosine matrix given by Eq. 8.7, expressed in terms of Euler angles. This type of representation is popular because of the physical significance of the Euler angles, which correspond to the angles that would be measured by angular pick-offs between a set of three gimbals in a stable platform INS.

The body-fixed angular velocity vector, $[\omega_x, \omega_y, \omega_z]^T$, is related to the propagation of Euler angles with time $\dot{\psi}$, $\dot{\theta}$ and $\dot{\varphi}$ determined as follows:

$$\begin{bmatrix} \dot{\varphi} \\ \dot{\theta} \\ \dot{\psi} \end{bmatrix} = \begin{bmatrix} 1 & \sin\varphi\tan\theta & \cos\varphi\tan\theta \\ 0 & \cos\varphi & -\sin\varphi \\ 0 & \dfrac{\sin\varphi}{\cos\theta} & \dfrac{\cos\varphi}{\cos\theta} \end{bmatrix} \begin{bmatrix} \omega_x \\ \omega_y \\ \omega_z \end{bmatrix} \qquad [8.8]$$

However, heading, pitch and roll, are not suitable for a strapdown system, because the solution of the $\dot{\varphi}$ and $\dot{\psi}$ equations contain trigonometric terms with singularities when $\dot{\theta} = \pm 90°$.

Quaternion method

For quaternion attitude representation, quaternion $\boldsymbol{q}$ is a quadruple of real numbers, $q = q_1 + q_2\boldsymbol{i} + q_3\boldsymbol{j} + q_4\boldsymbol{k}$. The transformation from one coordinate frame to another may be effected by a single rotation about a vector μ defined with respect to the reference frame. Only one more in number than the minimum number required three components define the axis of rotation, the first one – the amount of rotation numerically stable characteristics can be converted to direction cosines and Euler angles preferred for strapdown systems. The quaternion, denoted here by the symbol q, is a four element vector, the elements of which are functions of this vector and the magnitude of the rotation:

© Woodhead Publishing Limited, 2013

$$
\begin{aligned}
q_1 &= \cos\left(\frac{\mu}{2}\right) \\
q_2 &= \cos\alpha \sin\left(\frac{\mu}{2}\right) = \frac{\mu_x}{\mu}\sin\left(\frac{\mu}{2}\right) \\
q_3 &= \cos\beta \sin\left(\frac{\mu}{2}\right) = \frac{\mu_y}{\mu}\sin\left(\frac{\mu}{2}\right) \\
q_4 &= \cos\gamma \sin\left(\frac{\mu}{2}\right) = \frac{\mu_z}{\mu}\sin\left(\frac{\mu}{2}\right)
\end{aligned}
\qquad [8.9]
$$

where μ_x, μ_y, and μ_z are the components of the angle vector μ, and μ the magnitude of μ. The magnitude and direction of μ are defined in order that the reference frame may be rotated into coincidence with the body frame by rotating about μ through an angle μ.

A vector r^b defined in body axes may be expressed in reference axes as r^n, using the quaternion for vector transformation directly:

$$
\begin{aligned}
r^n = qr^b q^* &= \begin{bmatrix} q_1 \\ q_2 \\ q_3 \\ q_4 \end{bmatrix} \begin{bmatrix} 0 \\ r_i \\ r_j \\ r_k \end{bmatrix} \begin{bmatrix} q_1 \\ -q_2 \\ -q_3 \\ -q_4 \end{bmatrix} \\
&= \begin{bmatrix} q_1^2+q_2^2-q_3^2-q_4^2 & 2(q_2q_3-q_1q_4) & 2(q_2q_4+q_1q_3) \\ 2(q_2q_3+q_1q_4) & q_1^2-q_2^2+q_3^2-q_4^2 & 2(q_3q_4-q_1q_2) \\ 2(q_2q_4-q_1q_3) & 2(q_3q_4+q_1q_2) & q_1^2-q_2^2-q_3^2+q_4^2 \end{bmatrix} r^b
\end{aligned}
\qquad [8.10]
$$

Propagation of quaternion q with time is in accordance with the following:

$$
\dot{\boldsymbol{q}} = \frac{1}{2}[\Omega_b]\boldsymbol{q} - \frac{1}{2}[\Omega_n]\boldsymbol{q} = \frac{1}{2}\begin{pmatrix} q_1 & -q_2 & -q_3 & -q_4 \\ q_2 & q_1 & -q_4 & q_3 \\ q_3 & q_4 & q_1 & -q_2 \\ q_4 & -q_3 & q_2 & q_1 \end{pmatrix}\begin{pmatrix} 0 \\ \omega_x \\ \omega_y \\ \omega_z \end{pmatrix} \qquad [8.11]
$$

where Ω_b and Ω_n are skew-symmetric matrices containing the rotation rates of the body-fixed frame with reference to inertial frame in body-fixed coordinates.

Navigation equations

Basic strapdown navigation equations need to compute attitude, velocity and position. In this section, direction cosines representation will be used to derive an

© Woodhead Publishing Limited, 2013

algorithm for tracking the attitude. Similar derivations, using both Euler angles and quaternions, can be found in Titterton and Weston (2005).

The two most important DCMs in a coordinate frame conversion for aircraft are:

1. *body frame to local frame*: C_b^l, also called body frame to navigation frame and notated as $\boldsymbol{C}_b^n$, which yields attitude about Euler angles for roll, pitch and yaw:
2. *local frame to Earth frame*: $\boldsymbol{C}_l^e$, which determinates the position of aircraft. Local level frame changes its orientation with respect to the Earth's center, in order to maintain local level with respect to the Earth's surface.

The relations between operational inertial-frame, earth-frame, navigation-frame and body-frame (Dorobantu and Gerlach, 2004) are illustrated in Fig. 8.6. Three differential equations are described below:

1. Equation for body to local level transformation: C_b^l – the direction cosine matrix from body-fixed coordinates (*b*-frame) to local coordinates (*l*-frame), which determines attitude and can vary rapidly:

$$\dot{C}_b^l = C_b^l \Omega_{ib}^b - \left(\Omega_{el}^l + \Omega_{ie}^l\right) C_b^l \qquad [8.12]$$

- Ω_{ib}^b is rotational rate of aircraft in body coordinates;
- Ω_{ie}^l is Earth rate in local level coordinates;
- Ω_{el}^l is transport rate in local level coordinates.

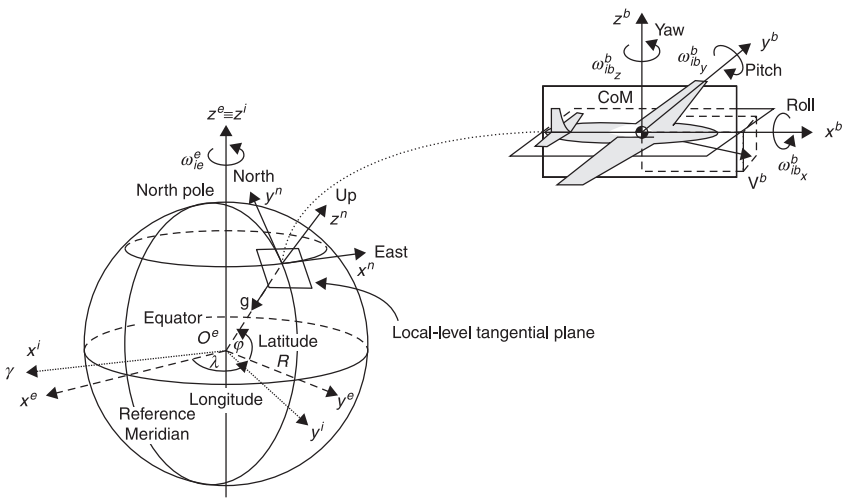

8.6 Relations between operational inertial-, earth-, navigation- and body-frames (Dorobantu and Gerlach, 2004).

© Woodhead Publishing Limited, 2013

All the Ω matrices represent rotation vector cross products in skew-symmetric matrix format.

Transport rate is the rotational rate of the aircraft due to motion over the surface of the Earth. Ω_{ib}^{b} is total inertial angular rate sensed by gyros and includes effects of transport rate Ω_{el}^{l} and Earth rate Ω_{ie}^{l}, which effects have to be subtracted.

2. An accelerometer can only sense the deviation from freefall and can never measure gravitational acceleration (the difference between aircraft acceleration and gravity). In navigation equations, accelerometers need correction by adding the local gravitational acceleration g. The velocity rate equation is given by:

$$\dot{v}^{l} = C_{b}^{l} a^{b} - \left(\Omega_{el}^{l} + 2\Omega_{ie}^{l}\right) v^{l} + g^{l} \qquad [8.13]$$

where a^b is specific force sensed by accelerometers in body coordinates g^l is the local gravity vector, which includes the combined effects of the mass attraction of the Earth (g) and the centripetal acceleration caused by the Earth's rotation ($g^l = g - \omega_{ie} \times \omega_{ie} \times R_e$). $v_e^n = [v_N \; v_E \; v_D]^T$ represents velocity with respect to the Earth, expressed in the local geographic frame NED.

ω_{ie} is the Earth rotation vector, expressed as:

$$\omega_{ie}^{n} = \left[\omega_e \cos L \quad 0 \quad \omega_e \sin L\right]^T \qquad [8.14]$$

where ω_e is the Earth's rotation rate; L is the geodetic latitude and λ the longitude. ω_{en} is the angular rate of the navigation frame relative to the Earth fixed frame, the transport rate and given by:

$$\omega_{en}^{n} = \left[\dot{\lambda}\cos L \quad -\dot{L} \quad -\dot{\lambda}\sin L\right]^T \qquad [8.15]$$

$$\begin{bmatrix} \dot{v}_N \\ \dot{v}_E \\ \dot{v}_D \end{bmatrix} = C_b^n \begin{bmatrix} a_x \\ a_y \\ a_z \end{bmatrix} + \begin{bmatrix} 0 & -(2\omega_e + \dot{\lambda})\sin L & \dot{L} \\ (2\omega_e + \dot{\lambda})\sin L & 0 & (2\omega_e + \dot{\lambda})\cos L \\ -\dot{L} & -(2\omega_e + \dot{\lambda})\cos L & 0 \end{bmatrix} \begin{bmatrix} v_N \\ v_E \\ v_D \end{bmatrix} + g_l^n \qquad [8.16]$$

The Earth's rate ω_e = 15.041067°/h, the Earth's semi-major axis R_e = 6378.1371 km, and the Earth's ellipticity $\boldsymbol{e} \approx 1/298$. Latitude L, longitude λ and height h above the surface of the Earth are given by:

$$\dot{L} = \frac{v_N}{(R_N + h)}$$

$$\dot{\lambda} = \frac{v_E}{(R_E + h)\cos L}$$

$$\dot{h} = -v_D \qquad [8.17]$$

© Woodhead Publishing Limited, 2013

where $R_E = \dfrac{R_e}{\sqrt{1-e^2\sin^2 L}}$, $R_N = \dfrac{R_e\left(1-e^2\right)}{\sqrt[3]{1-e^2\sin^2 L}}$, the mean radius $R_0 = \sqrt{R_N R_E}$.

3. Position rate equation (transport rate equation)
   For local level to the Earth for position DCM, C_l^e determines the position and is slowly varying relative to attitude dynamics:

$$\dot{C}_l^e = C_l^e \Omega_{el}^l \tag{8.18}$$

Strapdown error equations

An error operator can be defined as $\delta A = \hat{A} - A$, where $\hat{A}$ is a measured value (or estimated value, or some computed value) and A is the true value. Error operator satisfies $\delta(AB) = \delta A \cdot B + A \cdot \delta B$. Applying error operator to the three differential equations yields three error equations:

$$\delta\dot{C}_b^n = \delta C_b^n \Omega_{ib}^b + C_b^n \delta\Omega_{ib}^b - \left(\delta\Omega_{en}^n + \delta\Omega_{ie}^n\right) C_b^n - \left(\Omega_{en}^n + \Omega_{ie}^n\right)\delta C_b^n \tag{8.19}$$

$$\delta\dot{\upsilon}^n = \delta C_b^n a^b + C_b^n \delta a^b - \left(\delta\Omega_{en}^n + 2\delta\Omega_{ie}^n\right)\upsilon^n - \left(\Omega_{en}^n + 2\Omega_{ie}^n\right)\delta\upsilon^n - \delta g^n \tag{8.20}$$

$$\delta\dot{C}_n^e = \delta C_b^e \Omega_{en}^n + C_b^e \delta\Omega_{en}^n \tag{8.21}$$

By introducing $\phi^n = \begin{bmatrix}\phi_x^n & \phi_y^n & \psi_z^n\end{bmatrix}^T$, and a small angular position angle error $e^n = \begin{bmatrix}e_x^n & e_y^n & e_z^n\end{bmatrix}^T$, the attitude error Eq. 8.21 can be rewritten as:

$$\dot{\phi}^n = -\left(\Omega_{en}^n + \Omega_{ie}^n\right)\phi^n - C_b^n \delta\omega_{ib}^b + \Omega_{ie}^n e^n + \delta\omega_{en}^n \tag{8.22}$$

where

$$\delta\omega_{en}^n = \frac{1}{R_e}\left(u_R^n \times \delta\upsilon^n\right) - \frac{\delta h}{R_e^2}\left(u_R^n \times \upsilon^n\right) + \delta\rho_R u_R^n \tag{8.23}$$

$$\begin{aligned}\delta\dot{\upsilon}^n = {} & a^b \times \phi^n + C_b^n \delta a^b - \left(\Omega_{en}^n + 2\Omega_{ie}^n\right)\delta\upsilon^n \\ & - \left(\delta\omega_{en}^n - 2e^n\omega_{ie}^n\right)\upsilon^n - \frac{2g\delta h}{R_e}u_R^n - \delta g^n\end{aligned} \tag{8.24}$$

The equation for the position angle error e^n itself is:

$$\dot{e}^n = -\Omega_{en}^n e^n + \delta\omega_{en}^n \tag{8.25}$$

Further simplification using telescope pointing angle error, $\psi^n = \phi^n - e^n$:

$$\Delta\dot{R}^n = \delta\upsilon^n - \Omega_{en}^n \Delta R^n \tag{8.26}$$

© Woodhead Publishing Limited, 2013

$$\delta\dot{v}^n = C_b^n \delta a^b + a^b \psi^n - \frac{g}{R_e}\Delta R_H^n - \left(2\omega_{ie}^n + \omega_{en}^n\right)\delta v^n - \left(\delta\omega_{en}^n - 2e^n\omega_{ie}^n\right)v^n + \frac{2g\delta h}{R_e}u_R^n + \delta g^n \quad [8.27]$$

The equation for the telescope pointing angle errors:

$$\dot{\psi}^n = -\left(\Omega_{ie}^n + \Omega_{en}^n\right)\psi^n - C_b^n \delta\omega_{ib}^b \quad [8.28]$$

8.2 Microfabrication

There are two typical types of micromachining processes to fabricate MEMS sensors, surface micromachining and bulk micromachining. Silicon-based technology has become the mainstream technology, because silicon MEMS can be fabricated in batches and are compatible with integrated circuit (IC) technology.

Surface micromachined sensors have high mechanical noise due to a small proof mass, which has only several micrometers of the deposition thickness. Moreover, the suspension system fabricated in polycrystalline silicon suffers from elastic hysteresis and residual stress, which lead to sensitivity drift. Surface micromachining cannot meet the precision and accuracy requirements for INSs. However, surface micromachining uses compatible complementary metal-oxide-semiconductor (CMOS) processes and can monolithically integrate electronics on the same chip to reduce parasitic capacitance and series resistance.

Bulk micromachined sensors have a large proof mass, which can be fabricated by deep reactive-ion etching (DRIE) and multiple layers can be combined by bonding, thus very low stresses can be achieved by mono-crystalline bulk silicon.

One of the most widely-used micromachining processes is fabrication with SOI (silicon-on-insulator) wafers. This kind of structure provides reliable electrical insulation, excellent etching stop and sacrificial layer functions; therefore, it increases the fabrication accuracy, process simplicity and device performance. MEMSCAP 10 μm/25 μm SOIMUMPs (MEMSCAP, 2011), TRONICS 60 μm SOI-HARM (Tronics, 2011) and X-fab 15 μm SOI (X-fab, 2011) are commercially available SOI processes.

However, MEMS processes are still restricted by the current planar process and DRIE aspect ratio limitation, which leads to slow progress in reducing micromachining tolerance to obtain a precise sensing element at arbitrary silicon thickness.

8.2.1 MEMS inertial sensors

The gyroscopes (Armenise, 2010) commonly used in today's IMUs include high-performance mechanical spinning mass gyroscopes, ring laser gyroscopes (RLGs), fiber optic gyroscopes (FOGs) and hemispherical resonator gyroscopes

© Woodhead Publishing Limited, 2013

(HRGs). Spinning mass gyroscopes are classic mechanical gyroscopes, which operate on the principle of conservation of angular momentum and precession, but they are sensitive to shock and time-consuming to start up. Both RLGs and FOGs operate on the principle of the Sagnac effect. RLGs are revolutionary products for modern INSs, which have advantages over spinning mass gyros; they are more rugged, have a large dynamic range, good linearity and a short warm-up time. HRGs are the most successful vibratory gyroscopes, which operate on the principle of elastic wave precession. All navigation-grade gyros to date have been large; in fact, the sensitivity of spinning mass gyros and RLGs are a direct function of their size. For the current navigation systems, macromechanical or optical inertial sensors are still too expensive and also expensive to maintain due to relatively high failure rates. Typical accelerometer and gyro biases, for different grades of IMU, are listed in Table 8.1.

Figures 8.7 and 8.8 show the state-of-the-art performance of accelerometers and gyroscopes for different applications, respectively.

So far, MEMS inertial sensors have struggled to approach tactical-grade quality (Barbour *et al.*, 2011). For navigation-grade MEMS inertial sensors in aerospace applications, there is a need to achieve not only the static parameters such as bias instability, scale factor and noise level, but also dynamic parameters such as g-sensitivity, vibration rectification error and non-linearity, and resilience to large overload and high shock. Packaging for aerospace quality MEMS is even more critical for high precision under harsh environments, due to the cost and most of the device failures. Selecting reliable packaging structure and materials, proper release of the die-attachment-induced stress, and achieving extremely stable vacuum wafer-to-wafer bonding are still among obstacles to achieving these goals.

For supersonic aircraft, MEMS inertial sensors need be characterized in acoustically harsh environments. Dean *et al.* (2011) have demonstrated that high-power high-frequency content acoustic noise can be transmitted into the MEMS device through the device package. Acoustic energy frequency components in the vicinity of the resonating microstructure natural frequency can disturb mechanical proof mass motion, which yields a corrupted angular rate measurement.

Table 8.1 Typical accelerometer and gyro biases for different grades of IMU

	Gyro bias	Accelerometer bias
IMU grade	°/h	μg
Marine	0.001	10
Aviation	0.01	3–10
Intermediate	0.1	100–1000
Tactical	1–10	1000–10000
Automotive	10–100	10000

© Woodhead Publishing Limited, 2013

© Woodhead Publishing Limited, 2013

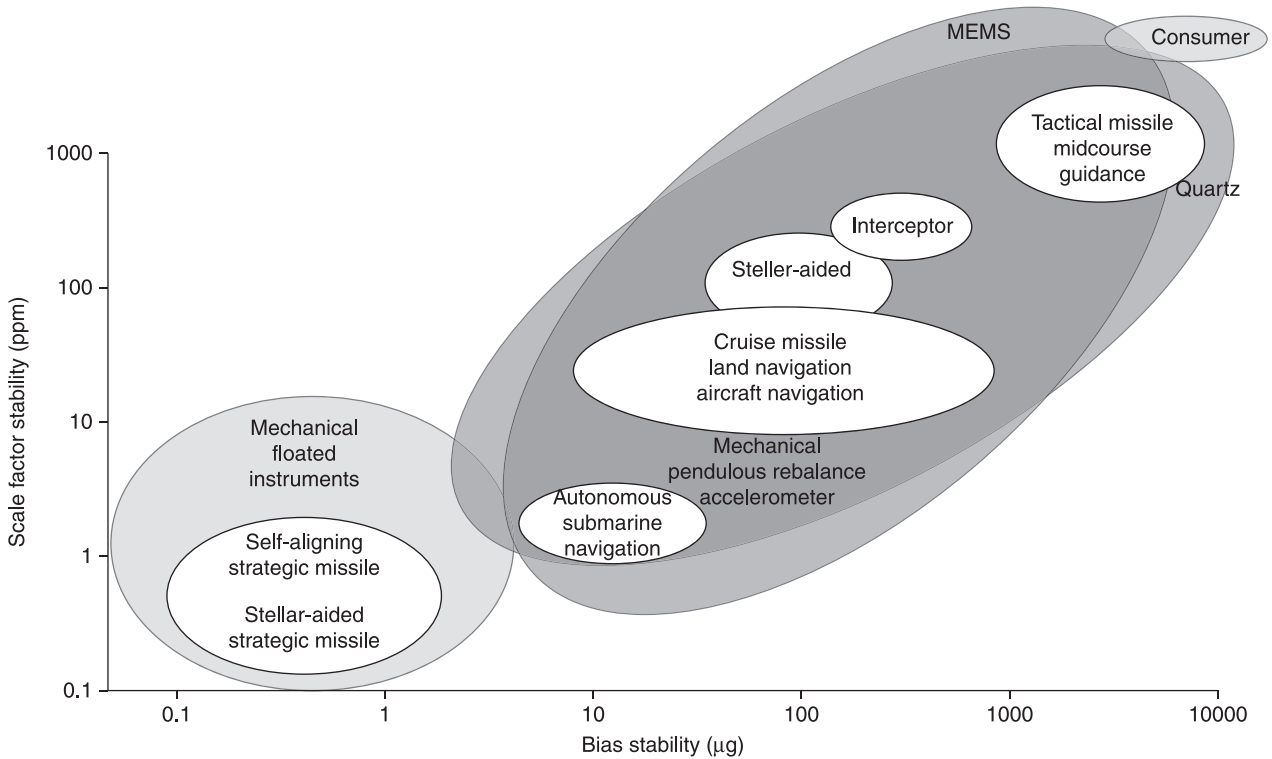

8.7 Current accelerometer technology applications (Schmidt, 2011).

© Woodhead Publishing Limited, 2013

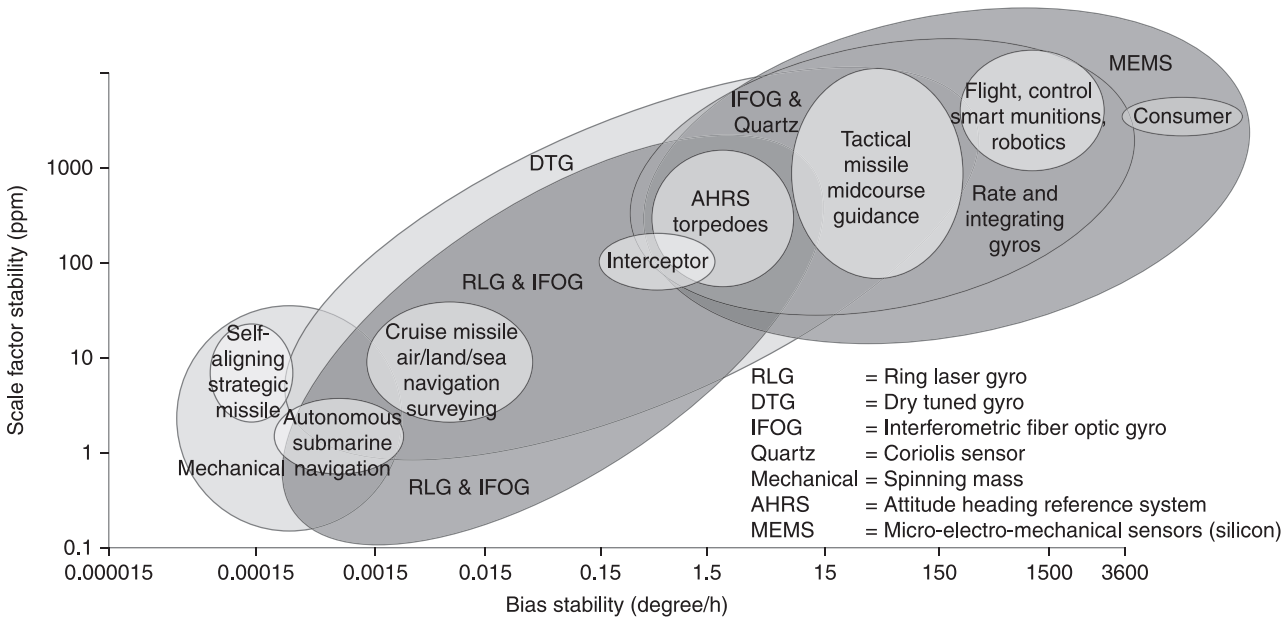

8.8 Current gyro technology applications (Schmidt, 2011).

MEMS accelerometers

The principle of operation for MEMS accelerometers can be described as a simplified second-order mass-damper-spring system (Beeby *et al.*, 2004). In order to make an ultra-high precision and stable MEMS accelerometer, there are three key technical issues to be addressed: a highly stable MEMS sensing element, an excellent assembly and packaging technology and very high-quality electronics. Here, an example is illustrated by Colibrys' ultra-high precision MEMS accelerometer (Dong *et al.*, 2011).

All single-crystal silicon wafers are used to fabricate the microstructure to reduce residual stress during DRIE, high temperature silicon fusion bonding and packaging phases. The capacitive device is based on the out-of-plane 3-stack silicon wafer structure, which is constituted of a proof mass with a thickness of 500 μm and a gap of 2 μm. The die attach stress during packaging is crucial to long-term stability and thermal behavior. A 5th-order sigma-delta ($\Sigma\Delta$) closed-loop regulation (Fig. 8.9), has been designed for this application, instead of using traditional analog closed-loop control. System level parameters need a comprehensive optimization to obtain an optimal mechanical proof-mass servo position and therefore reduce the effects from voltage reference flicker noise.

In the ($\Sigma\Delta$) loop, under overload conditions, the digital integrators start to saturate, and by observing the statistics of output bitstream, overload detection is implemented and triggers a soft reset by resetting the numerical integrators. The loop stability can be automatically recovered. Figure 8.10 shows the loop automatic recovery within 0.7 ms after 6000 g shock (half sine period 1 ms). Long-term stability drift measurements over 1 hour are demonstrated in Fig. 8.11, in which values are as good as the peak-peak value of ±15 μg (±1 ppm) without temperature compensation.

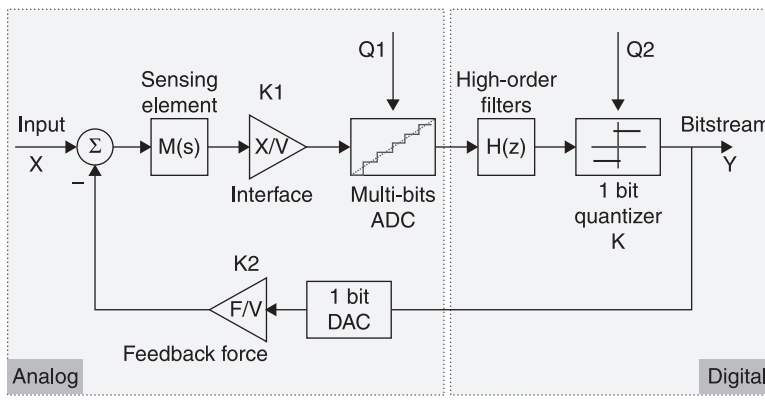

8.9 A mixed-signal high-order sigma-delta dual-quantization loop (Dong *et al.*, 2011).

© Woodhead Publishing Limited, 2013

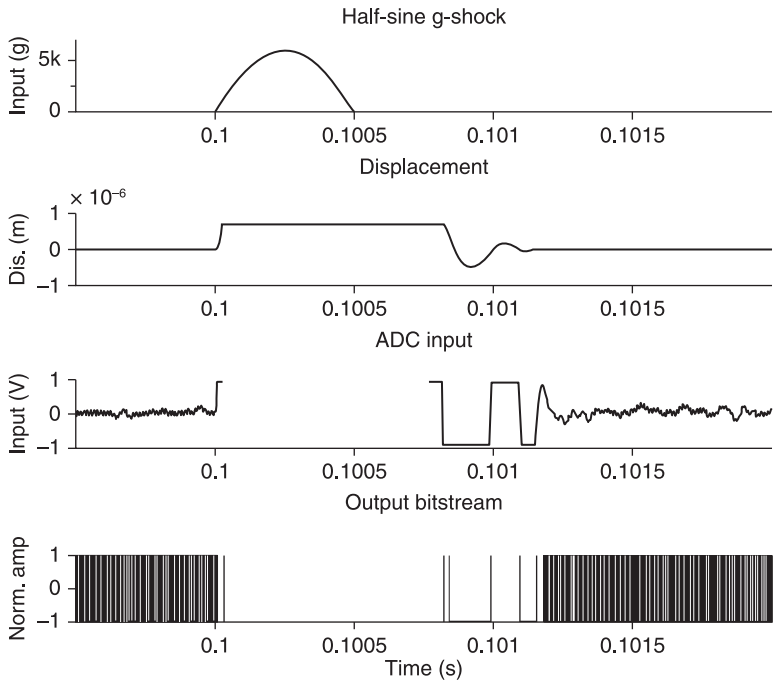

8.10 System dynamics after 6000 g shock (half sine period 1 ms). With overload detection, the loop can automatically recover within 0.7 ms (Dong *et al.*, 2011).

A performance comparison is given between the MEMS sensors and Honeywell's Q-Flex sensors (Honeywell, 2005). The state-of-the-art navigation standard QA-2000 and QA-3000 closed-loop accelerometers are fabricated with expensive quartz technology, but they are the highest performance inertial navigation grade accelerometers available (Table 8.2).

Capacitive-based MEMS accelerometers have been the most widely commercialized due to the operational simplicity of the device and available fabrication methods. However, optical MEMS inertial sensors can achieve even super sensitivity over that of a tunneling transducer and stability exceeding those of current capacitive accelerometers (Waters and Jones, 2007). The concept involves the integration of a Fabry–Perot interferometer and a photodiode on silicon substrate using surface and bulk micromachining techniques, resulting in a compact device with minimal parasitic elements. This optical MEMS accelerometer operates with closed-loop electronics and has good long-term stability below 10 μg with a 10 V/g scale factor for integration times up to 1000 seconds.

© Woodhead Publishing Limited, 2013

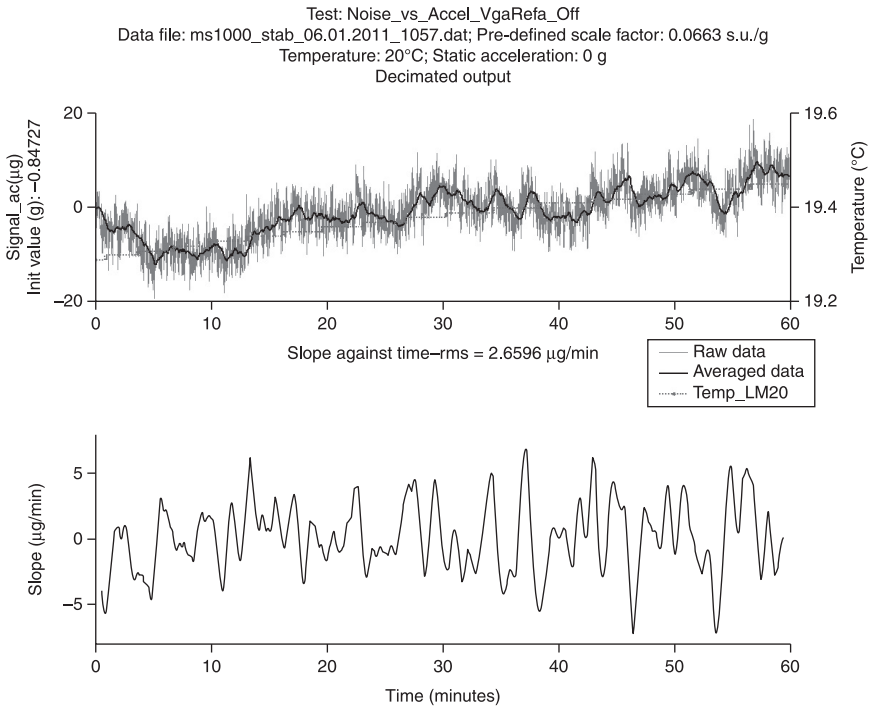

8.11 Bias stability peak-peak value is ±15 μg over 1 h (Dong *et al.*, 2011).

Table 8.2 Comparison between Colibrys MEMS accelerometer and Honeywell QA2030

Parameters	Colibrys Aida-15	Honeywell QA2000-30	Unit
Full input range	15	60	*g*
Noise level	1	3	μg/√Hz
Bandwidth (BW)	500	500	Hz
Dynamic range (1 Hz BW)	22.2	24.2	bit
Bias stability (24 h)	0.1	0.1	mg
Non-linearity VRE	<10	<20	$\mu g/g^2$
Bias temperature coefficient	200	<30	μg /°C
Scale factor temperature coefficient	40	180	ppm/°C
Shock resistance	4000	250	g
Power consumption	100	480	mW
Signal output	Digital	Analog	

© Woodhead Publishing Limited, 2013

MEMS gyroscopes

MEMS vibratory gyroscopes (IEEE Std 1431-2004, 2004; Acar and Shkel, 2009) are based on the principle of the Coriolis Effect, which is caused by the rotation of the object and the inertia of the mass experiencing the effect. The magnitude and direction of the Coriolis acceleration is given by:

$$\vec{F}_{Coriolis} = -2m\vec{\Omega} \times \vec{v} \qquad [8.29]$$

where m is the mass of the object, v is the velocity of the object in the rotating system, and Ω is the angular velocity vector, which has magnitude equal to the rotation rate. ω. and is directed along the axis of rotation of the rotating reference frame.

Usually the mechanical proof mass is excited by the electrostatic drive forces along drive direction to its resonant frequency at constant amplitude of oscillation. The sense direction is orthogonal to the drive direction. If there is rotation applied to the object, the Coriolis force is induced from the energy transfer from drive mode to sense mode, and the resulting displacement of the sensing element can be detected by electrical or optical approaches. As shown in Fig. 8.12, a vibratory rate gyroscope can be typically described as a two DoF mass-spring-damper dynamic system:

$$\begin{aligned} m\ddot{x} + c_x\dot{x} + k_x x &= F_{drive}\sin\omega t \\ m\ddot{y} + c_y\dot{y} + k_y y &= 2m\Omega\dot{x} \end{aligned} \qquad [8.30]$$

where Ω is the angular velocity of the coordinate frame associated with the gyroscope, m is the mass, c_x and c_y are damping coefficients, k_x and k_y are stiffness

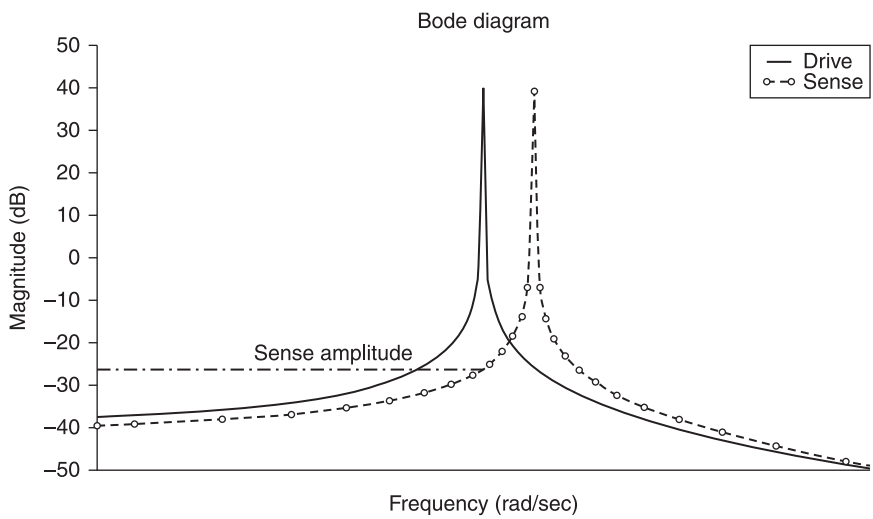

8.12 A vibratory gyroscope can be viewed as a combination of a 1-DoF drive-mode resonator and a 1-DoF sense-mode resonator.

© Woodhead Publishing Limited, 2013

coefficients, and F_{drive} is externally driven force to the mass with respect to the reference coordinate frame.

MEMS vibratory gyroscopes can be classified into two main categories, angle gyroscopes and rate gyroscopes (Shkel, 2006). Angle gyroscopes, also called rate integrating gyroscopes, measure orientation angles directly, while rate gyroscopes measure the angular velocity, or the rate of rotation of an object. So far, most implemented MEMS vibratory gyroscopes have been rate gyroscopes.

MEMS angular rate gyroscopes can operate in either mode-matching or split-mode conditions. Under mode-matching operating conditions, the sense mode is designed to have the same resonant frequency as the drive mode. Hence, the rotation-induced Coriolis signal is amplified by the mechanical quality factor of the sense mode (Ezekwe and Boser, 2008).

It is highly desirable to operate a gyroscope in a vacuum and match the resonance frequencies of the drive and sense modes. Mode-matching silicon gyroscopes with Q of 100 000 have been demonstrated to provide sub-degree-per-hour bias stability (Zaman *et al.*, 2008). However, mode matching of a high-Q rate gyroscope typically limits the open-loop sense-mode range to below 50°/s and rate bandwidth to 1 Hz.

INSs, especially for a strapdown system, require both high dynamic range and high bandwidth to accurately and quickly measure directional changes in such moving objects. Moreover, mode-matching gyroscopes are highly susceptible to the instability of the resonance condition under ambient conditions, and also ambient conditions increase quadrature coupling, which degrades the stability and robustness of the gyroscope against environmental variations. A promising approach with the mode-matching principle is to operate the gyroscope at a very high resonant frequency of 1 to 10 MHz, using a relatively low-Q gyroscope and very small capacitive gap sizes (~200 nm) (Sung *et al.*, 2010).

In the split-mode condition, the drive and sense modes have two different resonant frequencies. Since there is no quality factor amplification, gyroscopes operating in a split-matching configuration offer lower sensitivity. Split-mode configuration is more common in applications where high robustness is required. A good compromise is to utilize two DoF sense modes to achieve a flat gain region, and the resulting wide bandwidth yields a robust operation against environmental variations (Sahin *et al.*, 2009; Schofield *et al.*, 2011).

A large number of current MEMS gyroscope designs are based on capacitive drive and sense electrodes, whereby the drive and sense resonant frequencies are closely matched. The matching of the drive and sense resonant frequencies, along with methods to increase the mechanical Q of both drive and sense axis, act to increase the sense-axis coupling to the Coriolis force, thereby allowing for smaller angular resolution.

One of the major limitations of MEMS gyroscopes is the mechanical cross-coupling between the drive and sense modes. The dominant quadrature error source comes from the imbalances in mechanical springs, which arise due to poor

© Woodhead Publishing Limited, 2013

manufacturing tolerances relative to the minimum feature size during microfabrication processes. The amount of this coupling can be as high as 1000 °/s. Although it is possible to suppress the offset caused by unwanted mechanical coupling by more than two orders of magnitude using phase-sensitive detection, it still cannot be annulled completely and is still a dominant factor limiting the operating range, scale-factor linearity and bias instability. A mode-decoupled gyroscope structure is shown in Fig. 8.13 (Alper*et et al.*, 2008).

An electrostatic quadrature cancellation method (Tatar *et al.*, 2011) is applied to a fully decoupled MEMS gyroscope, to demonstrate the extent of performance improvement by cancellation of this error. Figure 8.14 shows a conceptual view of the quadrature cancellation electrodes. The capacitive electrode configuration (C1, C2, C3 and C4) generates an electrostatic quadrature annulling force in response to a quadrature motion. It has been experimentally shown that the bias instability and angular random walk (ARW) of a fully-decoupled MEMS gyroscope improve up to 10 times with quadrature annulling, reaching down to 0.91 °/hr and 0.034 °/√hr, respectively.

In contrast to rate measuring MEMS gyroscopes, rate integrating gyroscopes can directly measure absolute angles of rotation and eliminate integrating this derivative rate signal to provide an absolute angle, therefore the long-term precision, such as bias instability and ARW, are considerably improved.

Angle gyroscopes work on the same principles as a Foucault Pendulum. A lumped mass-spring system is allowed to freely oscillate and input rotation induced Coriolis force causes the line of oscillation to precession. Through detection of the position and velocity of the mass at any point in time, the precession angle can be instantly identified, which is proportional to the angle of rotation.

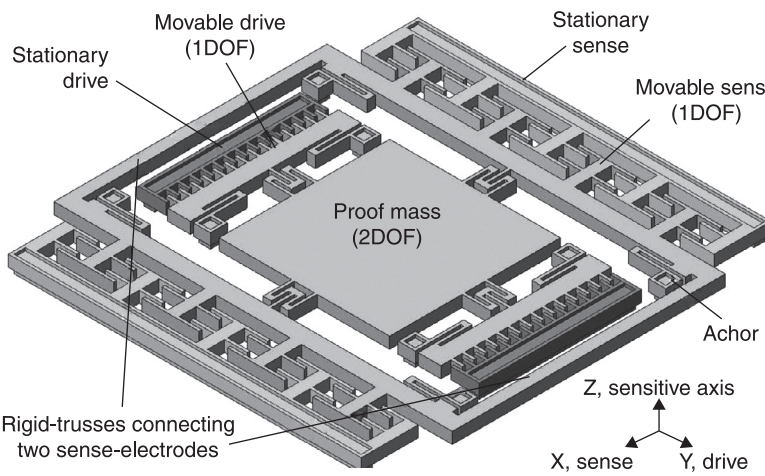

8.13 3-D model of the mode-decoupled gyroscope structure (Alper, 2008).

© Woodhead Publishing Limited, 2013

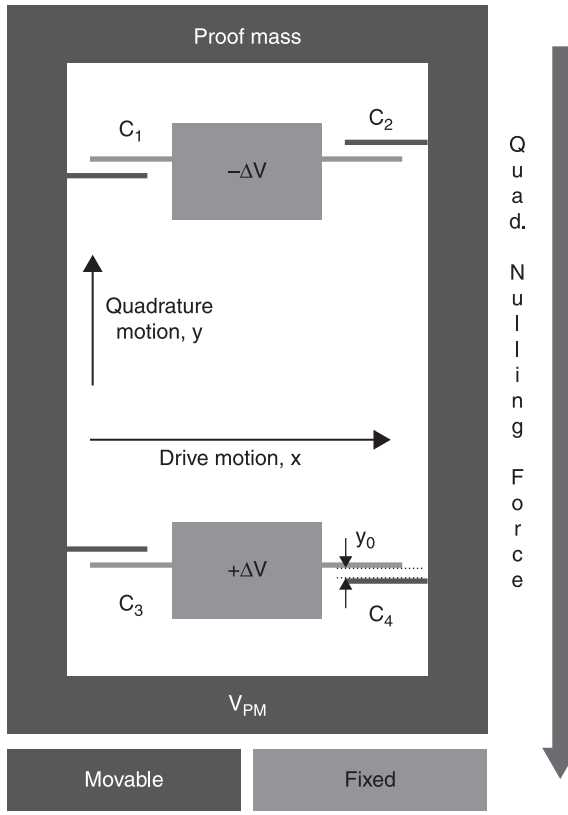

8.14 A conceptual view of the quadrature cancellation electrodes (Tatar, 2011).

An ideal angle gyroscope is a 2-D isotropic mass-spring system, which assumes isotropic stiffness and negligible damping:

$$m\ddot{x} + kx + 2m\Omega\dot{y} = 0$$
$$m\ddot{y} + ky - 2m\Omega\dot{x} = 0 \qquad [8.31]$$

A chip-scale Foucault pendulum was reported using silicon microfabrication processes (Prikhodko *et al.*, 2011) (Figs. 8.15 and 8.16). The 2-D pendulum consists of four small proof masses of a few hundred micrometers wide, which sit at the meeting point of two silicon springs that are at right angles to each other. As the precisely balanced structure spins, the direction of the vibration energy precesses in the same way as a swinging pendulum. The gyroscope operates with a bandwidth of 100 Hz and has a wide dynamic range of 450 °/s, which greatly relaxes both the bandwidth and range constraints of MEMS rate gyroscopes.

© Woodhead Publishing Limited, 2013

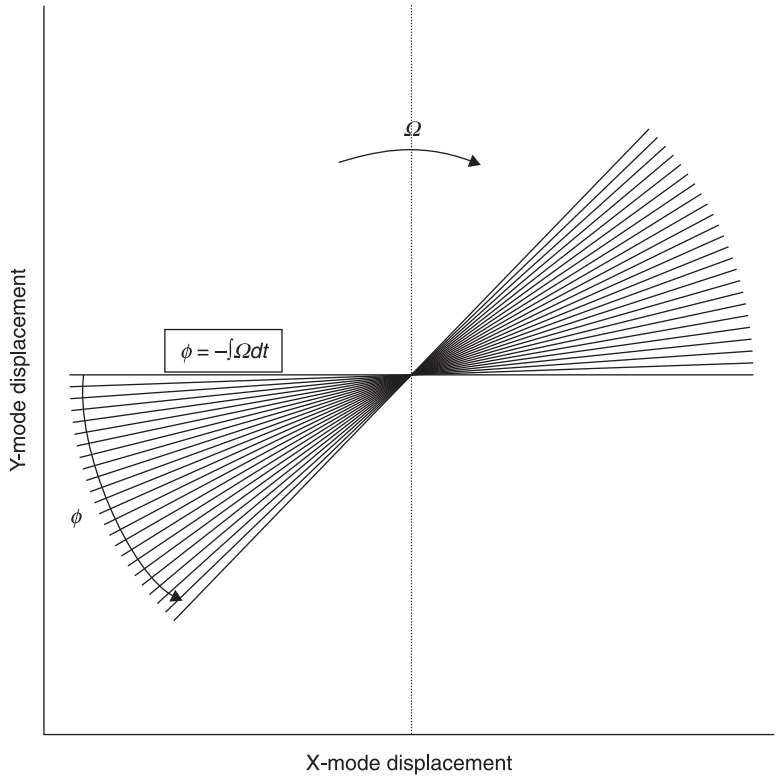

8.15 Whole-angle mode: the orientation reference remains fixed in the inertial space, enabling angle detection (Prikhodko *et al.*, 2011).

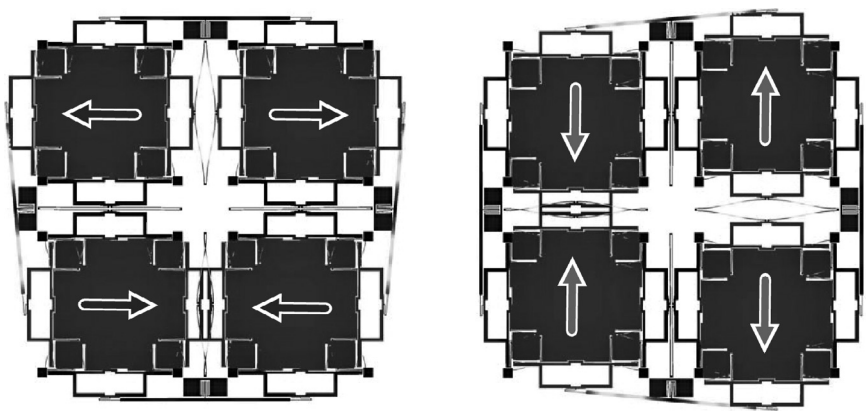

8.16 Degenerate, anti-phase *x*- and *y*-vibratory modes of dynamically balanced quad mass gyroscope, modeling (Prikhodko *et al.*, 2011).

© Woodhead Publishing Limited, 2013

For MEMS vibratory gyroscopes, there is not only the strong mechanical coupling, but also strong electrical coupling (capacitive cross-talk) between the drive and sense modes, which can in turn impact the angular resolution and bias instability. Optical MEMS gyroscopes can effectively decouple the electrical coupling by optical sensing of the Coriolis force and have the potential to reach navigation-grade performance. The electro-optical MEMS design (Waters *et al.*, 2010) eliminates the capacitive cross-talk signals between the drive mode and sense mode. A dual crystalline silicon spring fabrication approach, along with a large drive mass and small sense mass, is designed to enhance Coriolis displacement. An optical Fabry–Perot interferometric approach is used to increase mechanical displacement sensitivity. Expected performance are bias instability <0.01 °/hr and ARW <0.001 °/√hr.

Closed-loop MEMS inertial sensors

So far, most MEMS inertial sensors operate with an open-loop configuration. For an open-loop sensor, using current micromachining processes, the typical tolerance of damping and stiffness could vary within ±20% of their nominal values. The mechanical spring constant is a function of the material properties and temperature. Mechanical springs suffer from bonding and packaging stress. The stability drift of an open-loop MEMS inertial sensor is almost only dependent on the mechanical control of these mechanical parameters. Typically, open loop sensors have ±100 ppm stability, 0.1 to 1% linearity and 12- to 16-bit resolution.

Most precision macromechanical inertial sensors use a force-rebalance control strategy to increase the dynamic range, linearity and bandwidth. MEMS sensors are manufactured at sub-millimeter scales, at which scale electrostatic forces are significant. Electrostatic or piezoelectric forcing is used in most MEMS sensors. Vibration frequencies also scale up as size shrinks, and this makes vibratory Coriolis gyroscopes effective at MEMS scales. Closed-loop sensors regulate the proof mass motion in a nearly null position and the inertia is compensated for by feedback forces, and thus the performance is mostly determined by feedback, such as electrostatic force generated by high stability voltage. Therefore, the sensitivity and bias to manufacturing tolerances can be considerably reduced. Closed-loop sensors will cover the stability of ±1 to 10 ppm, the linearity of ±1 to 10 ppm and the resolution range of 20 to 24 bits and beyond.

However, unlike macromechanical systems, where the implementation of the feedback is relatively simple, in the MEMS case, the feedback design is problematic due to fast actuator dynamics (Borovic *et al.*, 2005). Analog closed-loop schemes suffer from electrostatic pull-in problems, in which electrostatic forces can lead the proof mass to latch onto one set of electrodes. In the last 10 years, a closed-loop force feedback control scheme, with ($\Sigma\Delta$) modulation, has become very attractive for capacitive micromachined inertial sensors (Petkov and Boser, 2005; Dong *et al.*, 2007; Raman *et al.*, 2009; Lapadatu *et al.*, 2010), which is an effective closed-loop approach to improve the robustness, bandwidth,

© Woodhead Publishing Limited, 2013

dynamic range and long-term stability. One-bit ($\Sigma\Delta$) electrostatic feedback means the digital MEMS sensors have a nearly perfect linearity.

8.2.2 Noise characteristics in MEMS inertial sensors

The noise characteristics of MEMS inertial sensors can be categorized into two parts:

1. *deterministic (or constant) errors*: which can be determined by calibration; and
2. *stochastic variations (random noises)*; which should be modeled as a stochastic process and include the Kalman filter state vector.

Understanding of stochastic variations in MEMS inertial sensors is of significant importance for the development of optimal estimation algorithms for inertial navigation.

Allan variance and power spectral density (PSD)

Two main parameters, representing the quality of inertial sensors, are the ARW and the bias instability for gyroscopes, and the velocity random walk (VRW) and bias instability for accelerometers. These two parameters can be obtained by the Allan variance (AVAR) method or by PSD.

The AVAR analysis is a time-domain method of analyzing a time sequence to pull out the intrinsic noise in the system as a function of the averaging time, which can evaluate the real performance of MEMS inertial sensors in relation to the effects of bias instability, ARW and rate random walk (RRW):

- *Step 1: data collection*: sample the bias data from sensor at interval T_s to obtain a long sequence of consecutive N-point data;
- *Step 2: data clustering*: divide the N-point data into K clusters, with each cluster having the length of M-point data:

$$\underbrace{\omega_1, \omega_2, \cdots, \omega_M}_{i=1}, \underbrace{\omega_{M+1}, \omega_{M+2}, \cdots, \omega_{2M}}_{i=2}, \cdots \underbrace{\omega_{N-M+1}, \omega_{N-M+2}, \cdots, \omega_N}_{i=k} \quad [8.32]$$

- *Step 3: data averaging*: average the data in each cluster:

$$\bar{\omega}_k(M) = \frac{1}{M}\sum_{i=1}^{M} \omega_{(k-1)M+i} \quad [8.33]$$

  $k = 1, 2, \ldots K$.
- *Step 4: calculate variance*: take the difference in average between successive clusters. There must be enough data for at least nine bins, otherwise the results obtained begin to lose their significance. The AVAR is defined as the mean value of the square of the difference of adjacent time averages from a time series as a function of averaging time $\tau = mT_s$ and is expressed as:

© Woodhead Publishing Limited, 2013

$$\sigma^2_{Allan}(\tau) = \frac{1}{2}\left\langle \left(\bar{\omega}_{k+1}(m) - \bar{\omega}_k(m)\right)^2 \right\rangle = \frac{1}{2(K-1)} \sum_{k=1}^{K-1} \left[\bar{\omega}_{k+1}(M) - \bar{\omega}_k(M)\right]^2 \quad [8.34]$$

where $\langle \cdot \rangle$ represents the whole data average.

The above equation is only valid for rate gyroscopes, and for integrating (angular) gyroscopes will be modified as:

$$\sigma^2_{Allan}(\tau) = \frac{1}{2}\left\langle \left(\bar{\omega}_{k+1}(m) - \bar{\omega}_k(m)\right)^2 \right\rangle = \frac{1}{2\tau^2(N-2m)} \sum_{k=1}^{N-2m} \left[\theta_{k+2m} - 2\theta_{k+m} + \theta_k\right]^2 \quad [8.35]$$

where output angle signal θ_k is sampled at $t_k = kT_s$ and the average angular rate is:

$$\bar{\omega}_{k+1}(m) = \frac{\theta_{k+m} - \theta_k}{\tau}.$$

A typical Allan plot for gyroscopes is shown in Fig. 8.17, in which the values of the root AVAR are plotted against the averaging interval, τ, in log-log form. Different types of random processes cause slopes with different gradients to appear on the plot and also are correlated with different averaging times, and therefore correspond to different locations on the Allan plot. The basic noise terms are ARW, RRW, bias instability, quantization noise and drift rate ramp. In addition, the sinusoidal noise and exponentially correlated noise can also be identified on the plot.

As shown in Fig. 8.17, the thermo-mechanical white noise (or electronic white noise) is characterized on the AVAR plot as a slope with gradient −1/2. The random walk measurement for this white noise, such as the ARW for gyros and VRW for accelerometers, can be obtained directly by reading the slope line at $\tau = 1$.

Bias instability is due to low frequency bias fluctuations, which are characterized by 1/f noise or flicker noise spectrum. Bias instability appears on the plot as a

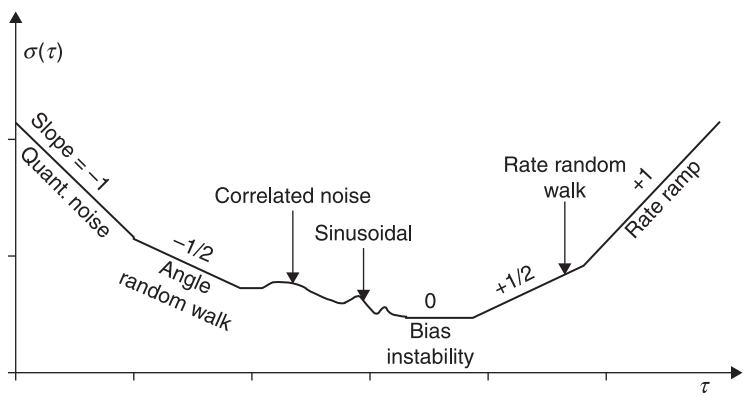

8.17 Sample plot of Allan variance analysis results (IEEE Std 952-1997, 1997).

© Woodhead Publishing Limited, 2013

plateau around the minimum. The flat region of the plot can be examined to estimate the limit of the bias instability, as well as the cutoff frequency of the underlying flicker noise.

The RRW indicates that the random walk is represented by a slope of +1/2 on the AVAR plot. The magnitude of this noise, K, can be read off the slope line at $\tau = 3$.

Integrated noise results in zero-mean random walk with standard deviation that grows with time as $\sigma_\theta = \sigma\sqrt{T_s t}, ARW = \sigma_\theta$ (1) (°/√h) or (°/√s). It can be thought of as the variation (or standard deviation), due to noise, of the result of integrating the output of a stationary gyro over time.

The noise terms, including quantization noise, rate ramp, exponentially correlated noise and sinusoidal noise, as shown in the AVAR plot, are not discussed here for reasons of simplicity. Readers can refer to IEEE Std 952-1997 (1997) for detailed descriptions.

Spectrum analysis is a frequency domain approach, which is the most commonly used representation of the spectral decomposition of a time series. It is a powerful tool for analyzing or characterizing data and stochastic modeling. Noise can also be defined as a function of frequency using a PSD. In these cases, the noise specification will be a noise density in °/s/√Hz that describes the output noise as a function of the bandwidth of the sensors. The relationship between the AVAR and the two-sided PSD is given by:

$$\sigma^2_{Allan} = 4\int_0^\infty PSD_\omega(f)\frac{\sin^4(\pi f\tau)}{(\pi f\tau)^2}df \qquad [8.36]$$

The filter transfer function $\frac{\sin^4(\pi f\tau)}{(\pi f\tau)^2}$ is applied on $PSD\omega\,(f)$ due to the process of the data clustering and averaging during computation of the AVAR.

Converting ARW and PSD noise values is expressed as:

$$ARW\left(\left/\sqrt{hr}\right.\right) = \frac{1}{60}\sqrt{PSD\left(\left(\left/\sqrt{hr}\right.\right)^2 \Big/_{Hz}\right)} \qquad [8.37]$$

A good summary is given in Trusov (2011) to classify three main random noises (white noise, pink noise and white accumulation noise) as applied to rate gyroscopes.

Bias

Bias is the average over a specified time of output signal measured at specified operating conditions that have no correlation with input signals. Bias instability is the random variation in the bias as computed over specified finite sample time and averaging time intervals. This non-stationary (evolutionary) process is characterized by a $1/f$ spectrum due to flicker noise, which when the effects are observed at low frequencies and at high frequencies, white noise is more dominant

© Woodhead Publishing Limited, 2013

over flicker noise. The gyro bias is typically expressed in degree per hour (°/h) and the accelerometer bias is expressed in (m/s^2, g).

Bias models in both gyros and accelerometers can be further broken down into several components:

1. *Constant bias*: the signal output from the rate gyroscope when it is not experiencing any rotation. It essentially represents a rotational velocity in degrees per second (°/s). The constant bias from turn-on to turn-on can be calibrated from the output.
2. *Bias instability*: in-run bias drift refers to the additive error in a gyroscope's output with stochastic characteristics. It cannot be calibrated out, but can be characterized in terms of variance, which can be modeled as a random constant. It represents the best bias stability that could be achieved for a given gyro, assuming that bias averaging takes place at the interval defined at the AVAR minimum.
3. *Bias variation over temperature*: the ambient temperature has an effect on the bias, and performance parameters are only relevant with the specified operating temperature range. It is possible to improve the gyro bias performance dramatically by calibration with an internal temperature sensor to aid this process.

Scale factor

The nominal scale factor of a MEMS inertial sensor describes the basic transfer function of the device. It is the measure of the gradient of the best straight line that can be fitted by the method of least squares to the expected sensor output signal, against input inertial signal over the full dynamic range at room temperature. Scale factor stability means the variation of scale factor with temperature and its repeatability, which is typically given in the unit of parts-per-million (ppm). The scale factor temperature coefficient (ppm/°C) is the maximum deviation of the scale factor under variable external temperature conditions.

Misalignment

Axes misalignment is a mechanical mounting error with a unit of milli-radians, which results from the imperfect non-orthogonality of the sensor triad in the INS body frame. The sensor output signals have couplings or interactions due to the misalignment. Axes misalignment can, in general, be compensated or modeled in the INS error equation.

Cross-axis response

Cross-axis response refers to the sensor output that occurs when the device is presented with a stimulus that is vertically orthogonal to the sense axis.

© Woodhead Publishing Limited, 2013

Misalignment and cross-axis response are often difficult to distinguish, particularly during testing and calibration.

Gyroscopes' g-sensitivity

Gyroscopes' g-sensitivity (with units of °/h/g) refers to gyroscopes that are sensitive to acceleration, primarily due to the device mass asymmetry, in which the imbalance is induced by imperfections caused by the microfabrication process, but it is linear in acceleration.

g^2-sensitivity

g^2-sensitivity (with units of °/h/g^2), also called acceleration-squared drift rate, is the anisoelastic effects of mismatches in the stiffness of the springs supporting the sensing element.

Alignment and gyrocompassing

INS needs the direction of the gravity vector. The outputs of the accelerometers are proportional to the direction cosines of the gravity vector. If the roll and pitch angles are φ and θ, respectively:

$$\begin{aligned} a_x &= g \sin \theta \\ a_y &= g \sin \varphi \cos \theta \\ a_z &= g \cos \varphi \cos \theta \end{aligned} \qquad [8.38]$$

therefore:

$$\varphi = \sin^{-1}\left(\frac{a_x}{g}\right) \text{ and } \theta = \sin^{-1}\left(\frac{a_y}{g\cos\varphi}\right)$$

During alignment, the gyros on the *x*- and *y*-axes give a direct readout of the two platform rates required for gyrocompassing.

Gyrocompassing is the concept of north-seeking by measuring the direction of the Earth's axis of rotation relative to inertial space. Gyrocompassing seeks geographic (true) north instead of magnetic north and also is unaffected by the ferromagnetic environment and thus can be used near the Earth's magnetic poles, where a magnetic compass is useless. The Earth's rotation is measured by means of gyros. The rotation of the platform to keep it level is used to determine the direction of true north relative to the platform heading. Thus, the Earth's rotation rate and the heading can be calculated at a maximum when the sensitive axis points to the north and zero when it points to the east.

© Woodhead Publishing Limited, 2013

Schuler tuning

Due to the Earth's rotation, to compensate for travel over the surface of the Earth, the platform must be rotated. This is like pulling a pendulum off center and letting it go, a phenomenon known as Schuler oscillation:

$$\omega = \sqrt{\frac{g}{R}} \qquad [8.39]$$

where R is the radius of the Earth. The period of this oscillation is 84 minutes.

Coning error and sculling error

If there are simultaneous angular oscillatory motions of equal frequency in orthogonal axes, the conical (or near conical) motion will be induced in the third orthogonal axis. Coning error relates specifically to the gyroscope angle measurement. However, sculling error results from combinations of angular and linear oscillatory motions of equal frequency in orthogonal axes (sculling motion), which is a rectification error relating to the accelerometer velocity measurement. These integration-related errors can be particularly detrimental to a strapdown navigation system. To reduce the errors, a high sampling rate should be applied to inertial signals and the INS needs a proper compensation algorithm (Titterton and Weston, 2005).

INS carouseling

Carouseling involves continuous rotation of an ISA about two orthogonal axes in inertial space, to reduce navigation errors due to bias errors. MEMS INS carouseling scheme can make high-accuracy applications possible, such as gyrocompassing (Iozan *et al.*, 2010). Johnson *et al.* (2010) demonstrated the carouseling of the MEMS ISA in significantly reducing azimuth error covariance. In-run bias stability of 0.03 °/hr and ARW of 0.002 °/rt(hr) have been achieved.

8.3 Integrated inertial navigation systems (INS) with global positioning system (GPS)

A major disadvantage of inertial navigation is that the estimation process is error cumulative and oscillates with an 84-minute Schuler's period. Furthermore, MEMS inertial sensors exhibit high drift rates and thus are not suitable for stand-alone navigation. MEMS INS should be effectively used in combination with other navigation aids to provide reliable navigation capability under virtually any conditions.

GPS is such an effective aiding method, consisting of a constellation of 24 satellites in 6 orbital planes, with 4 satellites in each plane. Position and velocity of aircraft are determined by the time-of-flight of an RF signal from four or more satellites to their receiving antenna. However, due to signal blockages under

© Woodhead Publishing Limited, 2013

certain environmental conditions, GPS cannot provide continuous navigation. In order to solve the satellite's signal unavailability or unreliability, GPS integrated with MEMS INS is a low-cost navigation system.

8.3.1 INS and GPS complementary characteristics

The integration of GPS and MEMS INS has perfectly complementary operational characteristics, and thus provides accurate and robust determination of both position and attitude of aircraft over a stand-alone GPS or stand-alone MEMS INS navigation. For example, GPS has a very low sampling rate of about 1 Hz, while the MEMS INS has a high sampling rate of about 100 Hz.

GPS have high enough accuracy and stability over time to provide accurate estimation of aircraft positions. GPS aiding of INS is an effectively continuous approach to stabilize and bound the INS errors. INS is self-contained and offers high short-term accuracy. The GPS-aided INS or INS-aided GPS has immunity to GPS outages and reduced ambiguity searching time, and more importantly, the integration can give continuous attitude solution of aircraft. A Kalman filter is often used to help blend the GPS measurements with the INS outputs in an optimal way.

8.3.2 Kalman filter

The Kalman filter is a set of mathematical equations that provides an efficient recursive means to estimate the state of a process, in a way that minimizes the mean of the squared error. The Kalman filter is used to integrate INS with GPS in coupled systems, which use the best characteristics of each.

The Kalman filter produces estimates of the true values of measurements and their associated calculated values by predicting a value, estimating the uncertainty of the predicted value, and computing a weighted average of the predicted value and the measured value. The Kalman filter estimates a process by using a form of feedback control: the filter estimates the process state at some time and then obtains feedback in the form of noisy measurements. The error dynamics of an INS can be described by the following linear discrete-time dynamic system:

$$\text{System model:} \quad x_k = \Phi_{k-1}^{k} x_{k-1} + w_k$$

$$\text{Measurement model:} \quad z_k = H_k x_k + v_k$$

where x_k is the error-state vector of the system at time t_k, Φ_{k-1}^{k} the state-transition matrix that maps the error states from time t_{k-1} to t_k, w_k represents input process white-noise, H_k is the measurement matrix that relates the measurements to the states of the system, and v_k represents the output measurement white noise.

Predictions using state dynamics are responsible for projecting forward the current state and error covariance estimates to obtain the *a priori* estimates for the next time step. Correction using measurement data are responsible for incorporating a new measurement into the *a priori* estimate to obtain an improved *a posteriori* estimate.

© Woodhead Publishing Limited, 2013

Discrete Kalman filter time update equations are given by:

State extrapolation (predicted estimate): $\hat{x}_{k|k-1} = \Phi^{k}_{k-1}\hat{x}_{k-1|k-1}$

Error covariance extrapolation: $P_{k|k-1} = \Phi^{k}_{k-1}P_{k-1|k-1}\left(\Phi^{k}_{k-1}\right)^{T} + Q_{k-1}$

Discrete Kalman filter measurement update equations are given by:

Estimate correction using Kalman gain: $K_k = P_{k|k-1}H_k^T(H_kP_{k|k-1}H_k^T + R_k)^{-1}$

State estimate update (corrected estimate): $\hat{x}_{k|k} = \hat{x}_{k|k-1} + K_k(z_k - H_k\hat{x}_{k|k-1})$

Error covariance update: $P_{k|k} = (I - K_kH_k)P_{k|k-1}$

where:

- $\hat{x}_{k|k-1}$ state estimate extrapolated to t_k, but prior to the measurement;
- $\hat{x}_{k-1|k-1}$ state estimate at t_{k-1}, after the measurement;
- $P_{k-1|k-1}$ *a priori* estimation error covariance at t_{k-1}, but updated after the measurement;
- $P_{k|k-1}$ *a posteriori* estimation error covariance extrapolated to t_k, but prior to the measurement;
- R_k is the process white noise covariance matrix, assumed as constant;
- Q_{k-1} is the measurement white noise covariance matrix, assumed as constant.

8.3.3 INS error model using Kalman filter

The canonical nine-state Kalman filter includes:

- 3 position errors: ΔR_x, ΔR_y, ΔR_z derived from δC^e_n;
- 3 velocity errors: ΔV_x, ΔV_y, ΔV_z derived from δv^n;
- 3 attitude errors: ϕ_x, ϕ_y, ψ_z derived from δC^n_b;

where ϕ_x and ϕ_y are known as the tilt errors and ψ_z is known as the azimuth error.

The canonical nine states are not enough, as they only characterize the inertial error dynamics. The nine-state Kalman filter does not help characterize the dynamics of aiding sensor errors, such as Doppler bias and GPS receiver clock errors; moreover, they also do not estimate inertial instrument drifts such as bias drift or scale factor errors.

The Kalman filter describes the INS psi-angle error model (Benson, 1975; Bar-Itzhack and Berman, 1988):

$$\delta\dot{v} = -(\omega_{ie} + \omega_{in}) \times \delta v + \nabla - \delta\psi \times f + \delta g$$

$$\delta\dot{r} = -\omega_{en} \times \delta r + \delta v$$

$$\delta\dot{\psi} = -\omega_{in} \times \delta\psi + \varepsilon$$

© Woodhead Publishing Limited, 2013

For example, a 24-state INS model may include the following variables:

$$\mathbf{x}_{Nav} = [\delta r_N, \delta r_E, \delta r_D, \delta v_N, \delta v_E, \delta v_D, \delta\psi_N, \delta\psi_E, \delta\psi_D]^T$$
$$\mathbf{x}_{ACC} = [\nabla_{bx}, \nabla_{by}, \nabla_{bz}, \nabla_{fx}, \nabla_{fy}, \nabla_{fz}]^T$$
$$\mathbf{x}_{Gyro} = [\varepsilon_{bx}, \varepsilon_{by}, \varepsilon_{bz}, \varepsilon_{fx}, \varepsilon_{fy}, \varepsilon_{fz}]^T$$
$$\mathbf{x}_{Grav} = [\delta g_N, \delta g_E, \delta g_D]^T$$

where δv, δr and $\delta\psi$ are the velocity, position and attitude error vectors, respectively; ∇ is the accelerometer error vector; δg is the error in the computed gravity vector; ε is the gyro drift vector; subscript b stands for bias; f is the scaling factor; N is north; E is east; and D is down.

The non-linear Kalman filter state equation (Grejner-Brzezinska, 2007) is given by:

$$\begin{bmatrix} \dot{r}^e \\ \dot{v}^n \\ \dot{q} \\ \Delta\dot{f}^b \\ \Delta\dot{g}^b \\ \Delta\dot{\omega}_{ib}^b \\ \Delta\dot{\Phi}_{GPS} \end{bmatrix} = \begin{bmatrix} C_n^e v^n \\ -(\omega_{ie}^n + \omega_{en}^n) \times v^n + C_b^n f^b - C_b^n \Delta f^b + g_c^n - \Delta g \\ 0.5\left(\Omega_b - \Delta\Omega_b - \Omega_n\right) q \\ \text{error model for } \Delta f^b \\ \text{error model for } \Delta g^n \\ \text{error model for } \Delta\omega_{ib}^b \\ \text{error model for } \Delta\Phi_{GPS} \end{bmatrix} \quad [8.40]$$

For example, a 25-state INS model may include the following variables:

$$\mathbf{X}_{Nav} = [r_X, r_Y, r_Z, v_N, v_E, v_D, q_0, q_1, q_2, q_3]^T$$
$$\mathbf{X}_{Acc} = [\nabla_{bx}, \nabla_{by}, \nabla_{bz}, \nabla_{fx}, \nabla_{fy}, \nabla_{fz}]^T$$
$$\mathbf{X}_{Gyro} = [\varepsilon_{bx}, \varepsilon_{by}, \varepsilon_{bz}, \varepsilon_{fx}, \varepsilon_{fy}, \varepsilon_{fz}]^T$$
$$\mathbf{X}_{Grav} = [\delta g_N, \delta g_E, \delta g_D]^T$$

where v, r and q are the velocity, position and quaternion (attitude), respectively; ∇ is the accelerometer error vector; δg is the error in the computed gravity vector; ε is the gyro drift vector; subscript b stands for bias; f scaling factor; N is north; E is east; and D is down.

8.3.4 Application of the Kalman filter to aided INS

For a GPS/INS integrated system, the system performance is dependent on the level at which the signals are combined. Integration architectures have loosely coupled, tightly coupled and deeply coupled configurations.

© Woodhead Publishing Limited, 2013

INS/GPS loosely coupled architecture

In the loosely coupled GPS/INS system (Fig. 8.18), the INS and GPS generate navigation solutions independently and redundantly. The first GPS Kalman filter estimates the parameters of position, velocity, acceleration, clock bias and clock drift. INS provides position, velocity, acceleration, attitude and attitude rate. The second integrated Kalman filter is then applied to integrate the GPS and inertial solutions to generate an optimal navigation solution of position, velocity and attitude corrections.

The features of this scheme include:

- GPS bounds INS error drifts;
- INS bridges GPS short duration outages; and
- the integration Kalman filter includes calibration and alignment estimates that provide in-flight improvement of the INS calibration and alignment.

However, a loosely-coupled scheme has limited applications, because it requires at least four GPS satellites in view. Furthermore, a MEMS based INS is not suitable to use in a loosely-coupled scheme, since the performance of the integrated system heavily depends on that of INS during GPS outages.

INS/GPS tightly coupled architecture

Figure 8.19 shows the architecture of the tightly coupled integration. In this centralized scheme, a single Kalman filter is employed to integrate both raw GPS observations and INS measurements to offer a single navigation solution. The pseudo-range and Doppler delta range measurements from the GPS receiver are incorporated directly into the navigation estimate, and the position and velocity from the INS are used by the GPS receiver to reduce the tracking loop bandwidth

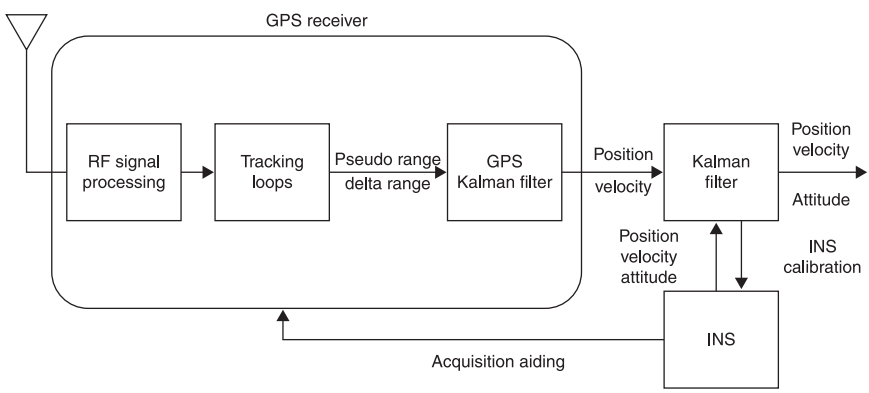

8.18 GPS-INS loosely coupled approach (Schmidt and Phillips, 2011).

© Woodhead Publishing Limited, 2013

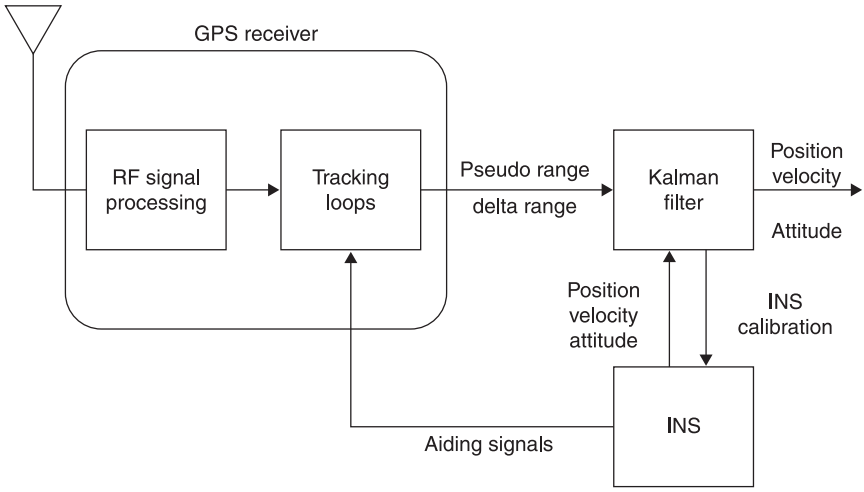

8.19 GPS-INS tightly coupled approach (Schmidt and Phillips, 2011).

(jamming resistance) and keep reliable tracking under high dynamics. The integration allows use of GPS measurements from less than four satellites and offers superior performance compared to the loosely coupled mode.

INS/GPS deeply coupled architecture

Figure 8.20 shows the architecture of a deeply integrated INS/GPS navigation system. In the deeply integrated architecture, a non-linear adaptive filter is

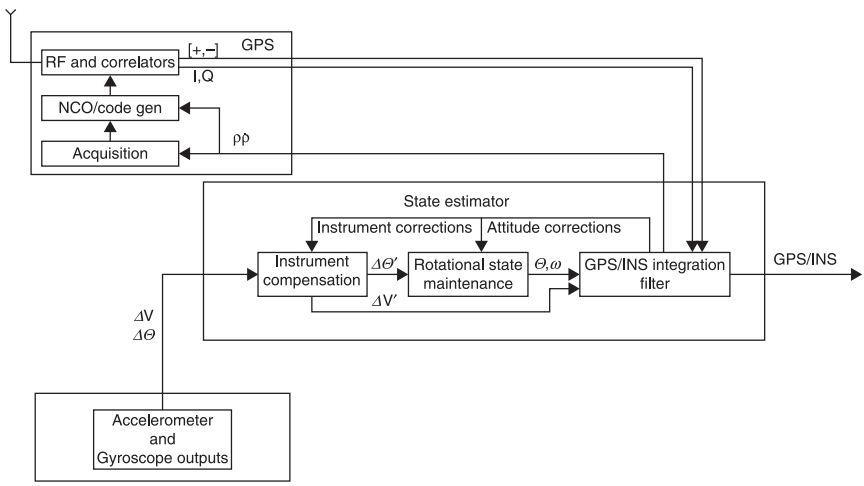

8.20 INS-GPS deeply coupled architecture (Schmidt and Phillips, 2011).

© Woodhead Publishing Limited, 2013

employed to search the optimum (minimum-variance) estimation for each component of the multidimensional navigation state vector, which is derived directly from the dynamical models, measurement models and noise models. Filter gains continuously adapt to changes in the jammer/signal (J/S) environment, and the error covariance propagation is driven directly by measurements to enhance robustness under high jamming conditions.

Deeply integrated architectures significantly improve the signal to noise ratio (SNR) of the GPS system. For navigators using GPS only, navigation errors will be reduced significantly by using algorithms that approximate the minimum-variance solutions at high J/S. The scheme is widely in use for anti jamming and blocking of GPS signals in defense applications.

Most importantly, a low-cost MEMS INS can be used in the deeply integrated approach, due to its excellent sensor calibration capability and this reduces the MEMS sensor performance requirements.

8.3.5 MEMS inertial measurement unit (IMU) and MEMS INS/GPS for aerospace applications

As long as a GPS signal is available, MEMS inertial sensors are acceptable for integrated navigation. Significant effort continues to be put into improving the performance of MEMS sensors to reach tactical grade or better to reduce the reliance on GPS. So far there are very few suppliers available to provide the tactical grade MEMS IMUs and MEMS INS/GPS systems. Draper Laboratory developed the world's highest performance MEMS IMU. Table 8.3 presents a summary of the highest published performance attained to date on an all-silicon MEMS IMU (Barbour *et al.*, 2011).

The most successful silicon MEMS IMUs for military/aerospace applications are Honeywell's HG1930/HG1940, which are gun-hard, low-cost MEMS IMU for the most demanding projectile guidance requirements. The key parameters of

Table 8.3 DARPA MEMS IMU

Parameter	Gyros	Accelerometers
Bias turn-on repeatability	3 °/h	2 mg
Bias in-run stability	5 °/h	1 mg
Bias drift	5 °/h	2 mg
Scale factor turn-on repeatability	70 ppm	125 ppm
Scale factor in-run stability	100 ppm	600 ppm
Axis misalignment	1 mrad	1 mrad
Input axis repeatability	0.2 mrad	0.2 mrad
Maximum input range	1000 °/s	45 g
Bandwidth	150 Hz	100 Hz
Angle random walk	0.05 °/√h	0.02 m/s/√h

© Woodhead Publishing Limited, 2013

HG1930 are shown in Table 8.4 (Honeywell, 2006). Integrated Guidance Systems LLC made further progress by the introduction of the MEMS-based IGS-2xx series, an ultra tightly coupled INS-GPS system for projectiles and small unmanned platforms. These robust anti-jam INS-GPS provide less than 5 m circular error probability of (CEP) GPS-aided accuracy (IGS, 2007).

Atlantic Inertial Systems (AIS) developed the SiIMU02 and SiIMU04 MEMS IMUs, as well as the SiNAV MEMS INS/GPS integrated navigation systems, based on ultra-tightly coupled architecture. The key parameters of SiIMU02 and SiNAV are summarized in Table 8.5 (AIS, 2010a) and Table 8.6 (AIS, 2010b), respectively.

Table 8.4 Honeywell HG1930 MEMS IMU

Gyro input range	±1440 °/s
Gyro rate scale factor	300 ppm, 1σ
Gyro rate bias	20 °/h, 1σ turn on – turn on 20 °/h, 1σ in run stability
Angular random walk	0.15 °/h max
Accelerometer range	±30 g
Accelerometer scale factor accuracy	700 ppm, 1σ
Accelerometer bias	4 mg, 1σ
Accelerometer linearity	30 ppm, 1σ
Operating temperature range	–55 to 85°C
Power	<3 watts
Weight	<0.35 lbs
Volume	<4 cubic in.
Dimension (in.)	2.0 diam. × 1.3 ht.

Table 8.5 AIS SiIMU02 MEMS IMU

Performance	Angular	Linear
Measurement range	±9000 °/s Axis 1 ±500 °/s Axis 2 and 3 (to ±14,000 °/s Axis 1, 2 and 3)	±15 g to ±100 g Axis 1, 2 and 3
Bias repeatability	<100 °/hr 1σ	<10 mg 1σ
Bias instability	<6.0 °/hr	<0.5 mg
Random walk	<0.5 °/ hr	<0.5 m/s/ hr
Scale factor repeatability	<500 ppm 1σ (±1000 °/s rate range)	<1500 ppm 1σ
	Power consumption <3.75 W (+5 V DC) Mass <210 gram	

© Woodhead Publishing Limited, 2013

Table 8.6 AIS SiNAV MEMS INS/GPS

Free inertial	Angular	Linear
Measurement range	±600 to ±14 000°/s	±15 to ±100g
	Navigation Availability of GPS	
Steady-state, assuming:		GPS outage for 30 seconds
Attitude	<0.1° rms	<0.12° rms
Heading	<0.15° rms	<0.18° rms
Velocity	<0.1 m/s rms	<0.4 m/s
Position	<10 m	<30 m
	Power Consumption <8W (+5V DC)	
	Mass <400 gram	

Systron Donner Inertial (SDI) developed the SDI500 tactical MEMS IMU and also has the SDN500 tightly coupled integrated GPS/INS system (SDI, 2011). These devices have extremely low noises, but they are fabricated with quartz technology.

Ten-minute simulations of a future precision MEMS IMU (3-axis accelerometers with 10 μg bias and 3-axis gyroscopes with 0.1 °/hr bias and 0.01 °/√hr ARW) are illustrated in Figs. 8.21 and 8.22, respectively.

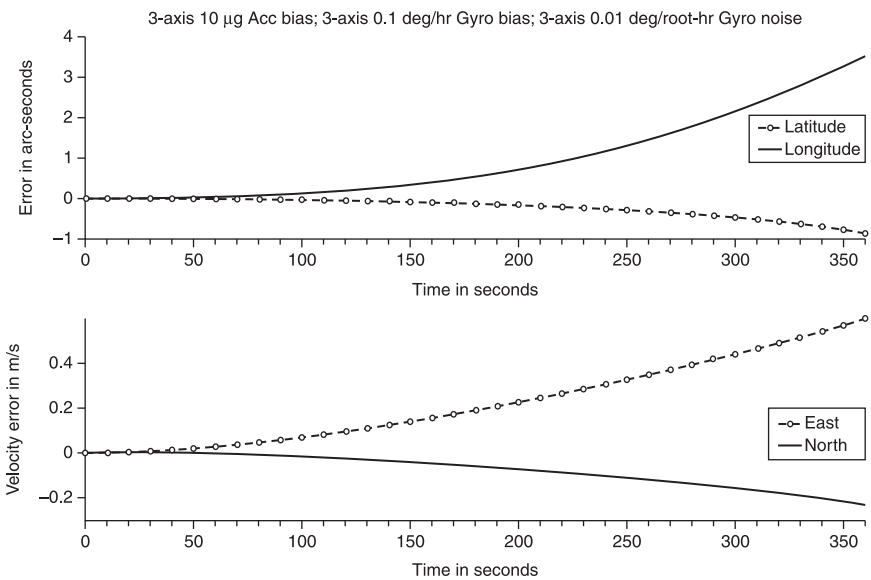

8.21 Position and velocity errors using INS simulations (GPSoft, 2011) with 3-axis accelerometers (10 μg bias) and 3-axis gyroscopes (0.1 °/hr bias; 0.01 °/√hr ARW).

© Woodhead Publishing Limited, 2013

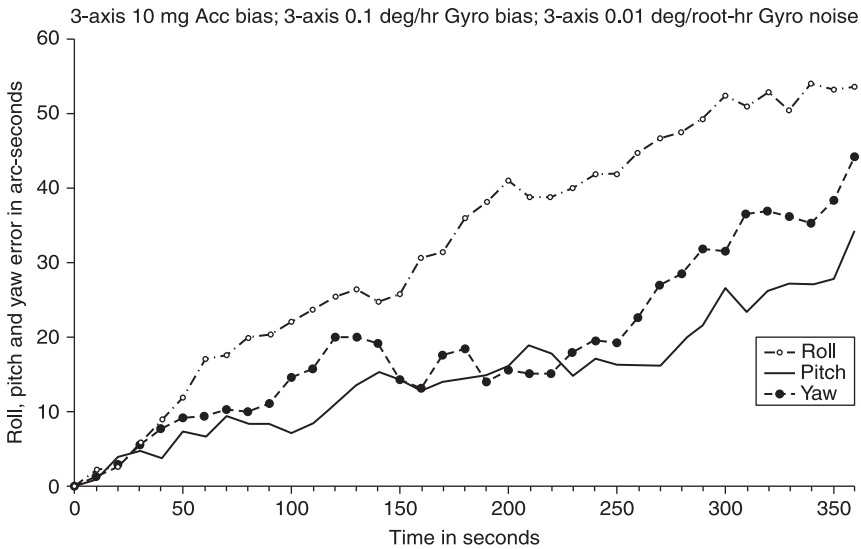

8.22 Attitude errors using INS simulations (GPSoft, 2011) with 3-axis accelerometers (10 μg bias) and 3-axis gyroscopes (0.1 °/hr bias; 0.01 °/√hr ARW).

In addition to the GPS/INS integrated navigation systems, integrated navigation systems should take advantage of sensor fusion with miniature augmentation sensors, such as MEMS barometers, MEMS magnetometers, MEMS precision clocks, velocity sensors and optical sensors to augment the accuracy of the MEMS INS (Hopkins *et al.*, 2011).

8.4 Conclusion and future trends

Inertial navigation as a pure, stand-alone technique, may ultimately disappear; however, integrated (GPS, secondary sensor fusion) navigation systems will continue to increase in sophistication, and will continue to require inertial data as an essential ingredient (King, 1998).

Development efforts are still needed to further explore pushing the tolerance limitations of the microfabrication processes and apply new physical sensing principles to improve the precision and accuracy of MEMS inertial sensors. In the future, with the improvement of precision and accuracy of MEMS inertial sensors (the bias stability about 0.01°/h and scale factor stability about 10 ppm for MEMS gyros, the bias stability about 1 μg and scale factor stability about 1 ppm for MEMS accelerometers), integrated navigation systems will eventually provide a low-cost and continuously reliable long-term navigation solution for aircraft.

© Woodhead Publishing Limited, 2013

8.5 References

Acar C and Shkel A (2009), *MEMS Vibratory Gyroscopes: Structural Approaches to Improve Robustness*, New York: Springer.

Aggarwal P, Syed Z, Noureldin A and El-Sheimy N (2010), *MEMS-Based Integrated Navigation*, Norwood, USA: Artech House Publishers.

AIS (2010a), SiIMU02 datasheet, *Atlantic Inertial Systems*. Available from: http://www.siliconsensing.com/wp-content/uploads/downloads/2010/08/SiIMU02-datasheet.pdf (accessed 28 November, 2011).

AIS (2010b), SiNAV datasheet, *Atlantic Inertial Systems*. Available from: http://www.atlanticinertial.com/uploads/pdfs/4237-SiNavlow.pdf (accessed 28 November 2011).

Alper S E, Temiz Y and Akin T (2008), 'A compact angular rate sensor system using a fully decoupled silicon-on-glass MEMS Gyroscope', *J Microelectromech Syst*, 17(6), 1418–1429.

Anthony Lawrence (1998), *Modern Inertial Technology: Navigation, Guidance, and Control, Second Edition*, New York: Springer.

Armenise M N, Ciminelli C, Dell'Olio F and Passaro V M N (2010), *Advances in Gyroscope Technologies*, Berlin/Heidelberg: Springer-Verlag.

Barbour N, Hopkins R and Kourepenis A (2011), 'Inertial MEMS Systems and Applications', *Low-Cost Navigation Sensors and Integration Technology RTO-EN-SET-116(2011)*, NATO Research and Technology Organisation. Available from: http://www.rto.nato.int (accessed 30 July 2011).

Bar-Itzhack I Y and Berman N (1988), 'Control technical approach to inertial navigation systems', *J Guidance*, 11(3), 237–245.

Beeby S P, Ensel G and Kraft M (2004), *MEMS Mechanical Sensors*, Norwood, USA: Artech House Publishers.

Benson D O (1975), 'A comparison of two approaches to pure-inertial and Doppler-inertial error analysis', *IEEE Trans Aerosp Elect Syst*, 11(4), 447–455.

Borovic B, *et al.* (2005), 'Open-loop versus closed-loop control of MEMS devices: choices and issues,' *J Micromech Microeng*, 15, 1917–1924.

Dean R N, Castro S T, Flowers G T, Roth G, Ahmed A, *et al.* (2011), 'A characterization of the performance of a MEMS gyroscope in acoustically harsh environments', *IEEE Trans Ind Elect*, 58(7), 2591–2596.

Dong Y, Kraft M and Redman-White W (2007), 'Micromachined vibratory gyroscopes controlled by a high-order bandpass sigma-delta modulator', *IEEE Sens J*, 7(1), 59–69.

Dong Y, Zwahlen P, Nguyen A M, Frosio R and Rudolf F (2011), 'Ultra-high precision MEMS accelerometer', *The 16th International Conference on Solid-State Sensors, Actuators and Microsystems (TRANSDUCERS'2011)*, Beijing, China, 5–9 June, 2533–2536.

Dorobantu R and Gerlach C (2004), '*Investigation of a navigation-grade RLG SIMU type iNAV-RQH*', IAPG/FESG 16, Institut für Astronomische und Physikalische Geodäsie, Technische Universität Munich.

Ezekwe C D and Boser B E (2008), 'A mode-matching ΣΔ closed-loop vibratory gyroscope readout interface with a 0.004 °/s/√Hz noise floor over a 50 Hz band', *IEEE J Solid-St Circ*, 43(12), 3039–3048.

GPSoft (2011), Inertial Navigation System (INS) Toolbox for MATLAB. Available from: http://www.gpsoftnav.com/inertial.html (accessed 30 July 2011).

Grejner-Brzezinska D A (2007), 'Integrated GPS/INS System in Support of Direct Geo-referencing', Lecture note, The Ohio State University. Available from: http://www.cfm.ohio-state.edu/research/AIMS/Lecture1.ppt (accessed 28 November 2011).

© Woodhead Publishing Limited, 2013

Honeywell (2005), Q-Flex® QA-2000 accelerometer datasheet. Available from: http://www51.honeywell.com/aero/common/documents/myaerospacecatalog-documents/MissilesMunitions-documents/QA2000_DataSheet.pdf (accessed 28 November 2011).

Honeywell (2006), HG1930 datasheet. Available from: http://www51.honeywell.com/aero/common/documents/myaerospacecatalog-documents/Missiles-Munitions/HG1930_Datasheet.pdf (accessed 28 November 2011).

Hopkins R E, *et al.* (2011), 'Miniature augmentation sensors for integrated inertial/GPS based navigation applications', *Low-Cost Navigation Sensors and Integration Technology RTO-EN-SET-116(2011)*, NATO Research and Technology Organisation. Available from: http://www.rto.nato.int (accessed 28 November 2011).

IEEE Std 952-1997 (1997), *IEEE standard specification format guide and test procedure for single axis interferometric fiber optic gyros*, the IEEE/AESS Gyro and Accelerometer Panel.

IEEE Std 1431-2004 (2004), *IEEE Standard Specification Format Guide and Test Procedure for Coriolis Vibratory Gyros*, the IEEE/AESS Gyro and Accelerometer Panel.

IEEE Std 1559-2009 (2009), *IEEE Standard for Inertial Systems Terminology*, the IEEE/AESS Gyro and Accelerometer Panel.

IGS (2007), IGS-2xx series datasheet, Integrated Guidance Systems. Available from: http://www.igsllc.com/docs/IGS-2xx.pdf (accessed 28 November 2011).

Iozan L I, *et al.* (2010), 'North finding system using a MEMS gyroscope', *The European Navigation Conference on Global Navigation Satellite Systems 2010*, Braunschweig, Germany, 19–21 October.

Johnson B R, Cabuz E, French H B and Supino R (2010), 'Development of a MEMS gyroscope for northfinding applications', *2010 IEEE/ION Position Location and Navigation Symposium (PLANS)*, 4–6 May, Indian Wells, CA, 168–170.

King A D (1998), 'Inertial navigation – forty years of evolution', *GEC REVIEW*, 13(3), 140–149.

Lapadatu D, Blixhavn B, Holm R and Kvisteroy Terje (2010), 'SAR500 – A high-precision high-stability butterfly gyroscope with north seeking capability', *2010 IEEE/ION Position Location and Navigation Symposium (PLANS)*, 4–6 May, Indian Wells, CA, 6–13.

MEMSCAP (2011), 1SOIMUMPs. Available from: http://www.memscap.com/en_mumps.html (accessed 28 November 2011)

Petkov V P and Boser B E (2005), 'A fourth-order ΣΔ interface for micromachined inertial sensors', *IEEE Solid-St Cirs*, 140(8), 1602–1609.

Prikhodko I P, Zotov S A, Trusov A A and Shkel A M (2011), 'Foucault pendulum on a chip: angle measuring silicon MEMS gyroscope', *Proceedings of IEEE 24th International Conference on Micro Electro Mechanical Systems (MEMS)*, Cancun, Mexico, 23–27 January, 161–164.

Raman J, Cretu E, Rombouts P and Weyten L (2009), 'A closed-loop digitally controlled MEMS gyroscope with unconstrained sigma-delta force-feedback', *IEEE Sens J*, 9(3), 297–305.

Sahin K, Sahin E, Alper S E and Akin T (2009), 'A wide-bandwidth and high-sensitivity robust microgyroscope', *J Micromech Microeng*, 19, 8.

Schadow K (2003), 'Military/aerospace MEMS applications – AVT Task Group 078', *the RTO AVT Symposium on Novel Vehicle Concepts and Emerging Vehicle Technologies*, Brussels, Belgium, 7–10 April, and published in RTO-MP-104.

Schmidt G T (2011), 'INS/GPS Technology Trends', *Low-Cost Navigation Sensors and Integration Technology RTO-EN-SET-116(2011)*, NATO Research and Technology Organisation. Available from: http://www.rto.nato.int (accessed 28 November 2011).

© Woodhead Publishing Limited, 2013

Schmidt G T and Phillips R E (2011), 'INS/GPS Integration Architectures', *Low-Cost Navigation Sensors and Integration Technology RTO-EN-SET-116(2011)*, NATO Research and Technology Organisation. Available from: http://www.rto.nato.int (accessed 28 November 2011).

Schofield A R, Trusov A A and Shkel A M (2011),' Micromachined gyroscope concept allowing interchangeable operation in both robust and precision modes', *Sens Actuat A: Phys*, 165, 35–42.

SDI (2011), SDI500 IMU and SDN500 INS/GPS, Systron Donner Inertial. Available from: http://www.systron.com (accessed 28 November 2011).

Shkel A M (2006), 'Type I and Type II micromachined vibratory gyroscopes', *Proceedings of IEEE/ION Position Location and Navigation Symposium (PLANS)*, San Diego, CA, 25–27 April, 586–593.

Sung W-K, Dalal M and Ayazi F (2010), 'A 3 MHz spoke gyroscope with wide bandwidth and large dynamic range', *Proceedings of IEEE 23rd International Conference on Micro Electro Mechanical Systems (MEMS)*, Hong Kong, 24–28 January, pp. 104–107.

Tatar E, Alper S E, and Akin T (2011), 'Effect of quadrature error on the performance of a fully-decoupled MEMS gyroscope', *IEEE 24th International Conference on Micro Electro Mechanical Systems (MEMS)*, Cancun, Mexico, 23–27 January, 569–572.

Titterton D and Weston J (2005), *Strapdown Inertial Navigation Technology, Second Edition*, IEE and AIAA.

TRONICS (2011), MEMSOI. Available from: http://www.tronicsgroup.com/mems-foundry/memsoi-mpw-run-europractice (accessed 28 November 2011).

Trusov A A (2011), 'Allan variance analysis of noise modes in gyroscopes', Whitepaper, 18 March 2011. Available from: http://www.alexandertrusov.com (accessed 28 November 2011).

Waters R L and Jones T E, (2007), 'MEMS navigation-grade electro-optical accelerometer', in *Military Capabilities Enabled by Advances in Navigation Sensors Meeting Proceedings RTO-MP-SET-104*, Paper 12, NATO Research and Technology Organisation. Available from: http://www.rto.nato.int (accessed 28 November 2011).

Waters R, Tally C, Dick B, Jazo H, Fralick M, *et al.* (2010), 'Design and analysis of a novel electro-optical MEMS gyroscope for navigation applications', *IEEE Sensors 2010 Conference*, Waikoloa, Hawaii, 1–4 November, 1690–1695.

X-fab (2011), X-FAB platform technology XM-SC for inertial sensors. Available from: http://www.xfab.com/en/technology/mems/surface-micromachining/inertial-sensors.html (accessed 28 November 2011).

Zaman M F, Sharma A, Zhili H and Ayazi F (2008), 'A mode-matched silicon-yaw tuning-fork gyroscope with subdegree-per-hour Allan Deviation bias instability', *J Microelectromech Syst*, 117(6), 1526–1536.

© Woodhead Publishing Limited, 2013

9

MEMS for structural health monitoring in aircraft

M. GIGLIO, A. MANES and C. SBARUFATTI,
Politecnico di Milano, Italy

DOI: 10.1533/9780857096487.2.220

Abstract: Some possible applications for MEMS technology development in structural health monitoring (SHM) are investigated in this chapter, particularly exploring the area of piezoelectric based sensors and fiber Bragg grating optical technologies. Although the latter is not included among typical MEMS, its functioning not being based upon electric sources, its small dimensions and low logistic impact make it a micro optical mechanical system (MOMS).

Key words: structural health monitoring, structural diagnosis, crack, fuselage, MEMS, MOMS.

9.1 Introduction

Structural health monitoring (SHM) is today one of the most challenging research fields. However, the aerospace industry is trying to extend the duration of life-limited components, but a high level of control over the structures is necessary to guarantee both the aircraft availability and reliability. In effect due to advances in the evaluation of structural health by means of a SHM system, it could be possible to set up condition based maintenance (CBM). This approach means substituting a component according to its actual structural conditions instead of relying only on the design assumptions. The final aim is to update the scheduled maintenance intervals according to the actual condition of the structures. However, this is not an easy task, as it is governed and influenced by many variables, each one characterized by a stochastic distribution. Thus, the first step for developing such advanced technology would be the deployment of a robust damage detection system, able to recognize, locate and quantify the damage in a certain component. On the basis of this, maintenance stops can be optimized in order to maximize the availability with the minimum loss of reliability.

Currently, the health of aircraft structures is ensured with a thorough fatigue analysis in the design phase and a strict schedule of inspection during life. Only a few attempts to apply reliable methods to directly monitor the on-line damage from vibrations during lifetime of the aircraft have been carried out. The development of health and usage monitoring systems (HUMS) has received considerable attention from the aircraft community in recent years with the declared aim to increase flight safety, increase mission reliability, extend the duration of life-limited components and of course to reduce maintenance costs.

© Woodhead Publishing Limited, 2013

However, is important to underline that HUMS is mainly based on monitoring vibrations generated in components critical for flight performance. Data are continuously recorded using piezoelectric accelerometers; the data are processed and compared to a threshold value that describes the allowable damage. In particular, considering aircraft applications, an integrated and reliable system for monitoring possible damage by interpreting service parameters related to stresses inside the fuselage, and for evaluating the time inspections and remaining life (prognosis), is missing. The motivation for suggesting SHM is the potential capability to reduce the maintenance cost, which is a consistent fraction of the direct operating cost for both fixed and rotating wing aircrafts, thus playing an important role, especially in the case of the ageing aircrafts. The current state of the art is mainly represented only by devices that monitor vibrations generated in components critical for the flight performance. The new concept for SHM is embedded SHM, performed by a network of sensors positioned in the most critical areas of the aircraft that can collect data and evaluate degradation based on a complete knowledge of either the static or dynamic state of the fuselage together with advanced damage criteria. This sensor system could be mounted on new aircraft to define a more reliable, efficient and economic program of inspections, or on ageing airframes to perform life extension. The final aim is the maximization of both the aircraft availability and reliability, thus gradually modifying the maintenance procedures, setting the so-called condition based maintenance (CBM), and substituting or repairing a component according to its real load carrying capabilities and not just relying on design assumptions. Aircraft maintenance is time consuming, and often requires dismounting large structural portions in order to make the regions for inspection accessible to operators for manual surface scanning. It is clear that the deployment of a system able to automatically scan the structure for diagnosis and residual useful life (RUL) prognosis could optimize the aircraft utilization, which would be beneficial from both safety and economic perspectives.

Considering the differences in the maintenance approach due to the usage of such SHM systems, it is important to specify the differences with respect to classical non-destructive evaluation technologies (NDTs). NDTs can detect cracks at a very early stage of propagation, often detecting anomalies in the length order of 1 mm or less. However, the on-board detection system is expected to be designed for a longer target crack length (typically an order of magnitude greater when fuselage stiffened panels, as shown in Fig. 9.1, are considered). The difference lies in the associated maintenance procedure. Classical NDT technologies are manually used to scan the structure at fixed time intervals during the component/region lifetime, whereas the present SHM system is designed to be permanently installed and continuously operating to monitor the structure in real time. For instance, the specification guide for aircraft structures (Department of USA Defense, 2006) reports that damage tolerance should be respected for two panels (bays) of cracked skin plus the broken central stringer (or frame) for a

© Woodhead Publishing Limited, 2013

9.1 Example of a typical aeronautical structure, composed of a riveted stiffened skin.

structure classified as fail safe crack arrest, such as conventional skin stringer (or frame) construction. Thus, the possibility to automatically detect even a relatively large crack with a high level of reliability (Sbarufatti *et al.*, 2011a) would allow an increase in the machine's availability, thus sensibly reducing its operating costs.

However, it is important to consider that the system performances are directly related to the geometry of the structure being monitored, to its boundary conditions, and to the load acting on the structure, as well as to the sensor position and number. Considering the latter, a compromise design must be chosen between the performance level and the complexity of the sensor network. There is a need to reduce as far as possible the impact due to the installation of many sensors on the structure. Each acquisition node must be powered and must transmit data to a central unit, thus requiring a lot of cables and finally possibly resulting in an impractical solution. MEMS seem promising because of their small dimensions and reduced impact for installation. Even further, the continuous reduction in scale (for both sensor and circuit levels) is heading towards the concept of MEMS on chip. This means the possibility of constructing small reasoning nodes, able to acquire the required data, as well as to perform post-processing of the same data, thus transmitting only the relevant information to a central unit, with a large reduction in the required communication performances.

© Woodhead Publishing Limited, 2013

9.2 State-of-the-art structural health monitoring (SHM) application for aerospace structures

What follows is a selected review of SHM literature, from the early studies about health and usage monitoring systems, to the advanced demonstrators used for the on-line monitoring of damage on ageing structures. It is worth noting that, though the current chapter is focused on aircraft health monitoring, it is not only aerospace structures that are suitable for the installation of a SHM system, but also civil structures such as bridges, buildings, pipes, automotive, ships, etc., for which some applications already exist. The development path followed to deliver a robust system able to partially substitute the fail-safe design technique with the more efficient damage tolerant technique (Broek, 1979) is complicated. It involves areas of technology and expertise, such as non-destructive testing technologies, wireless and energy harvesting equipment, the ability to interpret and recognize the presence of damage from the data recorded through an acquisition system, as well as the ability to quantify the amount of damage and its location over the inspected surface.

9.2.1 From manual recording to SHM

The introduction of monitoring systems initially came from the necessity to record mission profiles in order to closely match the military aircraft design to its typical usage and maintenance profile. In 1974, a simple way of recording mission profiles was undertaken by the UK Armed Forces (Hall, 1976), consisting in a manual exercise in which pilots recorded after landing their estimates of the time spent in various flight conditions. Clearly the number of parameters must be limited and a considerable degree of inaccuracy was inevitable.

More detailed information can only come from a fully instrumented recording system. The main issue is then to identify which are the maneuvers and flight regimes of structural interest, requiring a flight load measurement program during which flight parameters will be recorded while the aircraft is flown through a range of standard conditions and maneuvers (system training). It is then necessary to manage ways of recognizing the interesting regimes from flight parameters, whose choice is crucial for the success of the program. Fatigue life consumption could then be monitored on individual aircrafts with varying degrees of accuracy by measuring relevant parameters. This has been done for many years on fixed wing aircrafts through accelerometers, but it has been found to be inadequate for helicopters, for which the number of damaging fatigue cycles is less controllable, due to harsh operational environment. The US Army's Structural Integrity Recording System (SIRS – 1981) (Farrel, 1981a,b) was developed for the Bell AH-1 Cobra, monitoring a large set of parameters, such as gross weight, airspeed, outside temperature, rotor speed, vertical acceleration, torque, etc. Then the equipment recorded the time when parameters fell in certain ranges typical of

© Woodhead Publishing Limited, 2013

certain flight conditions, estimating the life consumption of the machine. The lifecycle management of US Army helicopters is described in White (2008), which consists of monitoring the actual operations to identify damaging flight regimes, refining scheduled maintenance and predicting unscheduled maintenance. The time each airframe and component is exposed to damaging flight regimes is recorded, as well as operational environments, and correlated with the predetermined but constantly refined reliability–availability–maintainability (RAM) trends.

However, if loads are directly measured rather than estimated from flight parameters, some account of the maneuver's intensity would be taken, but losing the perception of the critical maneuver type. The drawbacks are that loads should be measured on many components and that the long-term reliability of strain gauges may be a problem as well as the presence of too many wires. Moreover, for rotating components (which means for shaft/rotor monitoring) the use of slip rings may be an issue, requiring an alternative means of signal transferring. The alternative could be the utilization of wireless communication protocols to connect the sensor with the data acquisition systems. A robust and cost-effective SHM solution is proposed in Farrar *et al.* (2001), obtained by integrating and extending technologies from various engineering and information technology disciplines, comprehending structural dynamics, wireless data acquisition, local actuation, micro-electromechanical systems (MEMS) technology and statistical pattern recognition algorithms. A prototype development is reported in Moya *et al.* (2008), which uses wireless communication protocols and digital MEMS sensors to perform vibration-based SHM. From the comparison with a classical accelerometers sensing network, the study proved that accurate modal testing can be carried out with standard wireless technology and MEMS.

Other problems consequently arise, the first one concerning that wires are also often used to power the sensors. In those cases, wireless communication technologies should be coupled with the energy harvesting criteria. MicroStrain Inc. (www.microstrain.com) is active in the development of wireless energy harvesting sensors for shipboard and aircraft SHM. The company recently conducted flight tests of a Bell M412 helicopter, demonstrating that energy harvesters can provide continuous, wireless operational load tracking of critical rotating structures without battery maintenance. Arms *et al.* (2008) developed and tested a fully programmable SHM system, designed to synchronize and record data from a range of wireless energy harvesting sensors (strain gauges, accelerometers and thermocouples), as well as hard-wired inertial sensors and data coming from the embedded GPS. However, although the power management for such systems is relevant, energy harvesting is outside the scope of the current chapter.

Moreover, the amount of data that need to be transferred should be carefully considered. The availability of procedures able to reduce transmission data volumes is a key aspect for the reliability and sustainability of the monitoring

© Woodhead Publishing Limited, 2013

system, in particular when several components are monitored at the same time and supervised by a single network control centre. A clustered star network topology seems to be the most adept for this kind of application, requiring the collection of data relative to a restricted region in a partial node, performing a first layer diagnosis and then communicating just the relevant information to a higher level collection node.

Almost all the monitoring techniques discussed so far have been aimed at reducing the unknowns associated with aircraft usage. Variations in strength of components still have to be statistically described and defects due to manufacturing or in-service damages are not yet specifically taken into account. In order to completely exploit the strength and the potential life of each individual element, it should be necessary to monitor the real current structural integrity. This is the basis of the 'damage-tolerant' philosophy discussed above, in which defects are assumed to be present in the structure, which then has to be designed so that they will not propagate to failure before being detected by inspections.

9.2.2 Model based SHM

With the increasing complexity of the SHM systems, came the necessity for increasingly accurate mathematical finite-element models to simulate crack effects on the structures, from the nucleation to the growing process, as well as to characterize new materials according to their fatigue performances. The idea developed by Sbarufatti *et al.* (2011a) is to introduce a massive usage of FEM-based data to simulate the material and structural fatigue behavior to reduce the costs associated with the development and testing of a structural monitoring system in all the possible service conditions (undamaged and damaged). In addition, the disposal of a physical model on which to calibrate the diagnostic and prognostic algorithms would allow a more physical appreciation of the structural behavior, thus creating a system hopefully more reliable than those just based on threshold criteria. The base of this advanced prognostic program is therefore the availability of detailed and reliable finite element models (FEM) of the structure with and without damage (Fig. 9.2). This would be the key step for the manipulation and optimization of information from sensor data, such as the identification of the damage-sensitive properties, derived from the measured response, which allow distinguishing between the undamaged and damaged structures. Comparing the healthy and cracked FEM results, the main objective should be the creation of a data matrix that contains the damage effects (stress, strain, mechanical wave propagation, etc.) accumulated in the monitored structure in terms of crack length and position, allowing for the best interpretation of the information obtained from the sensor network. In Sbarufatti *et al.* (2011b), a feed-forward Artificial Neural Network has been used to recognize some damage configurations, focusing on crack damage, in riveted skin-stringer configuration. A FEM-based training of the network was implemented, proving a good

© Woodhead Publishing Limited, 2013

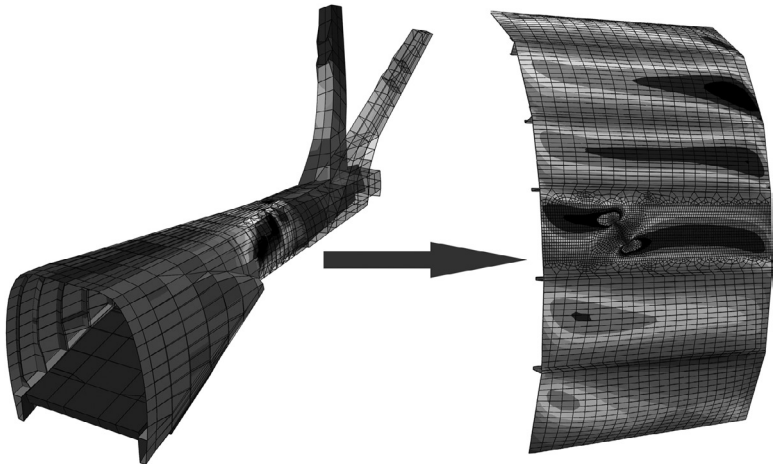

9.2 Finite element model of a helicopter rear fuselage, used to identify the most stressed region for mesh refinement and damage modeling.

performance in the test phase in terms of achieved resolution for damage identification.

9.2.3 Introduction of statistics

The accurate assessment of scheduled inspections and maintenance critically depends on the development of a quantitative methodology that integrates information from the state-of-the-art non-destructive evaluation (NDE) with the most advanced methods for the prediction of damage accumulation and structural integrity assessment. The overall problem in ageing aircraft life extension (which means ensuring airworthiness), regarding the probabilistic estimation of damage accumulation, was presented in Harlow and Wei (1999) as a central step toward the structural integrity and safety assessment, highlighting the necessity for the evaluation of the probability of damage detection (PoD) in relation to the probability of damage occurrence (PoO) and probability of false alarms (PFA). There are four possible detect/non-detect calls:

1. damage exists and is detected;
2. no damage exists but one is identified;
3. damage exists but is not detected; and
4. no damage exists and none is detected.

Both the mechanical aspect of damage accumulation and the probabilistic aspects of its evaluation and distribution should then be carefully considered (Sbarufatti *et al.*, 2010a). Bayesian statistics are then used in Zio and Peloni (2011), to

© Woodhead Publishing Limited, 2013

associate the uncertainties of the diagnostic system performances to the estimation of the residual useful life (RUL) distribution for the monitored component. The approach consisted in updating the *a priori* information about remaining life, according to the noised distribution coming from the diagnostic unit (in terms of crack dimension and position), thus generating a posterior knowledge about RUL, which is characterized by a lower variance.

9.2.4 Helicopter fuselage crack monitoring (HECTOR case study)

The approach described in Sections 9.2.2 and 9.2.3 is the most complete and its realization is the subject of HECTOR (helicopter fuselage crack monitoring and prognosis through on-board sensor network), a project coordinated by the European Defense Agency (EDA) in the framework of the Joint Investment Program on Innovative Concepts and Emerging Technologies (JIP-ICET). The aim of HECTOR is to increase the availability parameter by directly monitoring the damage while it is propagating inside the structure, the concept at the basis of the SHM systems discussed in this chapter, thus gaining instantaneous knowledge about the damage situation and setting the condition based maintenance (CBM). Although the methodology has been demonstrated for a helicopter structure, its validity can be extended to aircraft in general, as well as to the automotive and energy applications, given a model for the damage is available.

The base of this advanced diagnostic and prognostic program is the availability of finite element models (FEM) of the structure, with and without damage. This is the key step for the extraction of information from sensor data, such as the identification of the damage-sensitive properties, derived from the measured structural response, which allows distinguishing between the undamaged and damaged structures.

At a glance, sensors, smart algorithms and finite element models (FEM) are the three characters involved in the HECTOR methodology, each of them playing a substantial role inside the system.

The choice of the correct sensor technology is a key feature. In particular, two classes are evident: first, local sensors might be used to monitor regions were cracks already exist or are most probably expected; second, distributed sensing means a smart network of sensors, to be interpreted through a FEM database for diagnostic and prognostic purposes.

Algorithms are the 'brain' of the SHM. They receive the sensor data as real-time input, and treat them statistically in order to infer over the structural health condition of the monitored region. Nevertheless, if used alone, they lose the perception of physical conditions, as their decisions are only based upon predefined thresholds.

The role of FEM finite element simulations represents the 'experience' of the SHM. They provide some basic (and relatively low-cost) information that can be

© Woodhead Publishing Limited, 2013

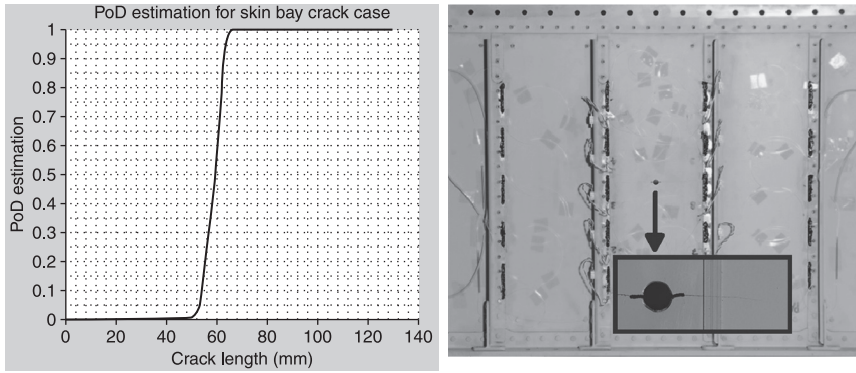

9.3 (a) Probability of detection (PoD) evaluated for the anomaly detection algorithm used inside HECTOR relative to the artificially initiated damage shown in (b).

used to train the algorithms to understand the physical reality behind raw sensor data. Now the output would be not just an alarm, but also the appreciation of damage position and criticality.

The methodology has been tested for crack monitoring over a typical stiffened skin aeronautical structure (Fig. 9.3). The sensor network, consisting of optical fiber Bragg grating (FGB) sensors, was optimized by means of a FEM-based procedure, selecting the best compromise configuration as a trade-off between network cost and maximum allowed crack length. The damage, consisting of a growing crack artificially initiated in the center of the panel (Fig. 9.3b), was selected as the worst case, or the one farthest from the sensors. The PoD of the system shown in Fig. 9.3a was calculated after the execution of five tests on the same damage configuration. The diagnostic system also proved to be particularly robust. A 10% uncertainty has been registered on the crack length associated with the damage recognition. Performances are by far expected to improve when damages approach the sensors or when more critical faults are present (i.e. a stringer failure).

9.3 MEMS devices for embedded SHM

Micromachining offers the potential for fabricating a range of micro-sensors and MEMS for structural applications including load, vibration and acoustics characterization and monitoring. Such micro-sensors are extremely small; they can be embedded into structural materials, can be mass-produced and are therefore potentially low cost. The state of the structure can be established through NDTs, applied manually by maintenance operators during scheduled stops, but this often requires the disassembling of many structural parts, thus large costs are associated

© Woodhead Publishing Limited, 2013

with the maintenance. The deployment of a low cost, low weight and small dimension technology (such as MEMS) is of particular interest for the realization of on-board automatic SHM.

In addition, a range of sensor types can be integrated onto a single chip with built-in electronics and ASICs (application-specific integrated circuits), thus providing a low power microsystem (Kim *et al.*, 2002). Such a basic configuration may further be packaged on the micro-chip or even organized at wafer level, with increasingly capable systems and subsystems as required for a complete sensor system. An example of innovative wafer-level packaging, or so-called '3-D integration', of the physical layers needed for extremely small nodes in future wireless sensor networks (WSN) is described in some detail in Flatscher *et al.* (2010). The required physical layers of a node in a WSN will typically include those illustrated also in the e-CUBES concept shown in Fig. 9.4 (www.e-cubes.org). The idea is to integrate power supply, power management, energy recuperation, RF communication, digital signal processing, memory, MEMS and other modules into the one, multifunctional heterogeneous device. The sensor modem, which has been selected for the demonstration of a 3-D integration concept, represents a tire pressure monitoring system (TPMS). The key elements of the complete system are a die-stack of a microcontroller, a RF transceiver, a pressure sensor and a bulk acoustic resonator (BAR). Other than the effective sensor unit size, the physical dimension of a node is determined by three main factors:

1. the size of the integrated circuits including the microcontroller, signal conditioning and radio circuits;
2. the minimum size of the antenna required for power-efficient communication; and
3. the power storage/battery and/or energy harvesting subsystem.

In order to realize highly miniaturized wireless sensor nodes, the technology used for their fabrication has to be carefully optimized. The fabrication of such

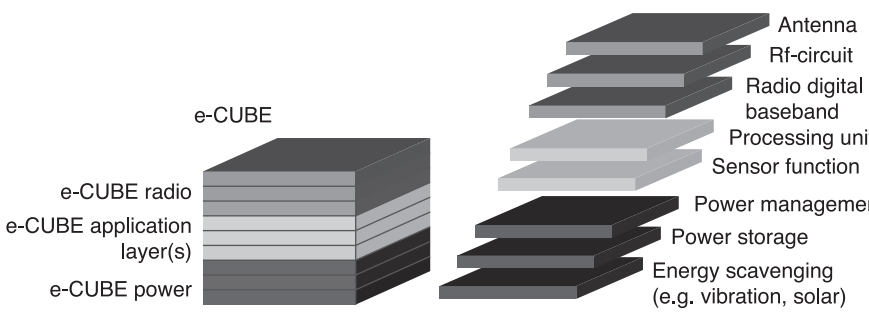

9.4 Image from the e-CUBES project (www.e-cubes.org) illustrating the multilayer concept for a wireless sensor network node.

© Woodhead Publishing Limited, 2013

e-CUBES is a typical example for the need of mixed approaches, taking advantage of a combination of different specific 3-D technologies (Janczyk *et al.*, 2007, 2008a,b; Ramm and Klumpp, 2008; Bieniek *et al.*, 2008). In particular, the so-called ICV-SLID technology has been adopted, based on inter-chip vias through the device substrates (through silicon vias) and metal bonding using solid-liquid-interdiffusion (SLID) soldering for simultaneous mechanical and the electrical connections. Interconnection techniques by hollow vias and Au stud bumps are used for stacking of sensor devices to the 3D-IC. Since integrated circuit technologies allow increasingly complex circuits in smaller sizes and with lower power levels, the main size limitations are therefore the antenna size and the power system. Given the integrated circuit consolidated technology, with respect to die size, power consumption and frequency capabilities, the achieved target size for the e-CUBES project was about $1\,cm^3$, while targeting $1 \times 1 \times 0.5\,mm$ dimensions in the future. Such a forthcoming e-CUBE could be integrated in a polymer-based 'patch' for integration into a tire for pressure monitoring or directly bonded to the airframe substrate, including metal wire patterns suitable for strain gauges or, if a larger size is allowed, antennae suitable for lower frequency RF-radio communications.

Moreover, packaged MEMS sensors may be integrated in a type of (networked) Smart Layer configuration (Boller, 2001a,b; Boller and Buderath, 2007) suitable for large-scale SHM systems. This concept is under development by the Stanford start-up company Acellent (www.acellent.com). However, a typical commercially available MEMS sensor package will likely be too thick to be directly applicable in thin foils. To reduce the build height of the sensors, 'unpackaged' MEMS sensors may be used.

In recent years, progress has been made to reduce the complexity of systems using MEMS sensors and devices. One example is microfluidics, where MEMS devices such as pressure and flow sensors and actuators may be integrated with flow channels and, for example, reactant chambers, especially for biomedical applications. Nevertheless, the Australian company SMSystems (www.smsystems.com.au) provides crack-detection sensors and a portable unit used for pressurizing/vacuum monitoring utilizing an emerging NDT technology known as comparative vacuum monitoring (CVM). Microfluidic channels are realized using MEMS-type technology in polymer foils, bonded to structural parts, the latter being a constitutive part of the channel itself. Given a depressurization is provided to the channels, the measure of the air flow induced by a crack passing through the sensor is an index of damage existence. This technology is particularly suitable for massive applications on composite structures, allowing the direct monitoring of the material curing process as well as the whole operational life of the considered component.

Many physical principles, already used for scheduled NDT-based maintenance, might be exploited and reproduced inside the MEMS reduced scale dimensions, among which are eddy currents, piezoelectricity/resistivity, surface traveling

© Woodhead Publishing Limited, 2013

waves, acoustic emission, potential drop, strain field sensitivity and FGB systems. Some examples are provided in the following paragraphs.

9.3.1 Eddy current based sensor

An on-chip eddy current sensor for proximity sensing and crack detection is reported in Sadler and Ahn (2001) for permanent structural monitoring. eddy current testing (ECT) works based on an interaction of a time-varying electromagnetic field with a conductive body according to Faraday's electromagnetic induction law. The principle of ECT is clearly depicted in Fig. 9.5. A time varying magnetic field is generated by providing an alternate current to a coil. The coil's magnetic field, interacting with a conductive object, generates circular (eddy) currents on it, which consequently produces the eddy current's magnetic field. The latter can either interact with the primary coil or with another dedicated secondary coil (dual coil sensor) and, most importantly, is dependent on the state (healthy or damaged) of the conductive element.

The described technology has so far been used by maintenance operators for manual scans of each surface for damage monitoring, and each crack type in particular. However, considering automatic testing, by fixing the distance between

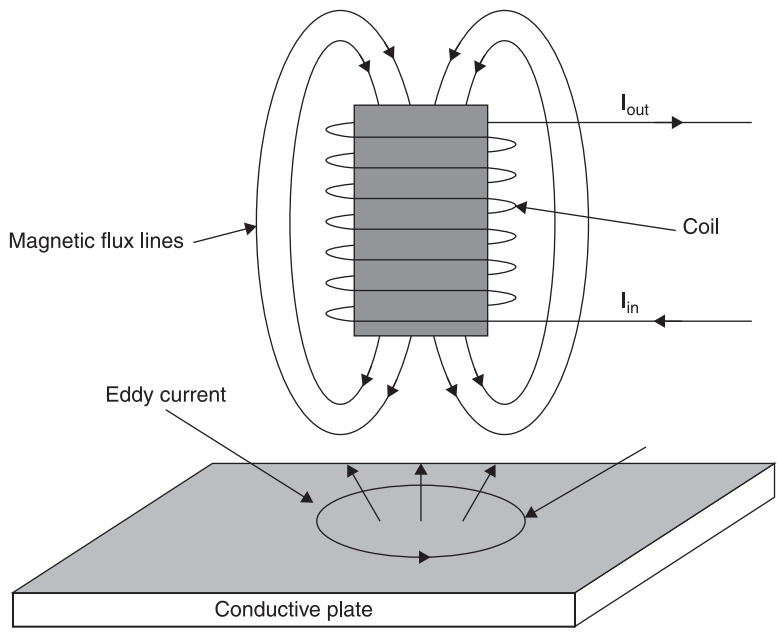

9.5 Eddy currents are generated in a conductive plate by a time varying current flowing in a coil located near the plate.

© Woodhead Publishing Limited, 2013

the sensor and target (i.e. a rivet hole), deviation in the measured signal can be interpreted as surface flaws, allowing an estimation of flaw dimensions. A dual coil sensor is presented in Sadler and Ahn (2001), where damage can be identified and quantified by monitoring the induced changes in the magnetic field, affecting the voltage coupled onto the sensing coil. The proposed sensor characteristics are reported in Table 9.1. The relatively low resistance and high inductance can be attributed, respectively, to the thick conductor lines obtained by means of a UV-LIGA (Qu *et al.*, 1998) lithography process and the semi-encapsulating Ni/Fe permalloy core. This combination results in the generation of large magnetic fields with low power dissipation from ohmic losses. In this way, the device is capable of generating large magnetic fields at low driving currents. In addition, the same technology could be extended to the development of an array-type sensor, which would likely be required in actual industrial ECT applications.

Concerning SHM performance, the described technology is able to detect damage at a very early stage (cracks have been clearly detected with depths of as little as 200 μm), also showing an extremely linear relation between crack length and output signal voltage. Nevertheless, its monitored region is restricted to a narrow region of a few millimeters, beyond which the sensitivity is significantly reduced. For this reason, it is suitable to monitor either existing crack development (in ageing aircrafts) or regions where crack nucleation is expected. Some attempts to extend the capability of eddy current technology to the scanning of relatively large monitored areas have been described in Washabaugh *et al.* (2002). The authors presented shaped-field sensors designed as conductive metallic windings, which are placed on a carrier, such as Kaptone using micro-fabrication techniques. A magnetic field is generated from one of these windings and then recorded by the other windings, thus allowing monitoring of crack propagation in metallic structures. The system can also be extended to a high-resolution eddy current imaging system by introducing a linear array of inductive sensing elements. Even further, the wavelength of the magnetic wave can be varied allowing the detection of cracks, inclusions and corrosion even in thicker metallic components. The system has been proven to work on cracked aluminum panels, around rivet holes and on a C-130 aircraft flight deck chine plate with hidden corrosion damage.

Table 9.1 Eddy current MEMS sensor characteristics

Sensor dimension	7 mm × 7 mm
Required input power	30 mW
Coil resistance	3 Ω
Coil inductance	1.5 μH
Frequency range	10–500 kHz
Coil thickness	20 μm
Full turns for each coil	13
Spacing between coils	30 μm

© Woodhead Publishing Limited, 2013

9.3.2 Surface acoustic wave (SAW) sensor

SAWs are mechanical waves that travel across an elastic solid medium, with low attenuation along the propagation direction but strong decay (exponential) into the bulk of the sample. These waves are useful for surface structure or shallow defects evaluation. SAWs are reflected or scattered by surface inhomogeneity and are therefore sensitive to existence or development of surface defects of the material. One of the advantages of the SAW method consists of investigation of a relatively large area with only one transducer (long distance control). If only surface defects are suspected, the use of surface acoustic waves is thus very efficient, being sensitive to the defects with dimensions $d \geq \lambda$ (λ represents the SAW wavelength), normal to the propagation direction.

Surface acoustic waves could thus be used for automatic structure monitoring and research is particularly active in this field. A wireless SAW based micro-sensor has been proposed in Varadan and Varadan (2000) and Varadan (2002), where MEMS, inter-digital transducers (IDTs) and required microelectronics and conformal antennas have been integrated in order to realize a programmable, robust and low cost passive micro-sensor (Kim *et al.*, 2002; Varadan and Varadan, 2000; Varadan, 2002). The sensor utilizes surface acoustic waves for detection of structural changes. The wave velocity and hence the oscillation frequency of a feedback loop containing an IDT device and a feedback amplifier are affected by changes in the mechanical or electrical boundary conditions in the wave path. As anticipated, the sensor principle is based on the fact that the wave traveling time between the IDTs changes with the variation of physical variables. As clearly depicted in Fig. 9.6, one of these IDTs acts as the device input and converts signal voltage variations into mechanical waves, based on the piezoelectricity generation.

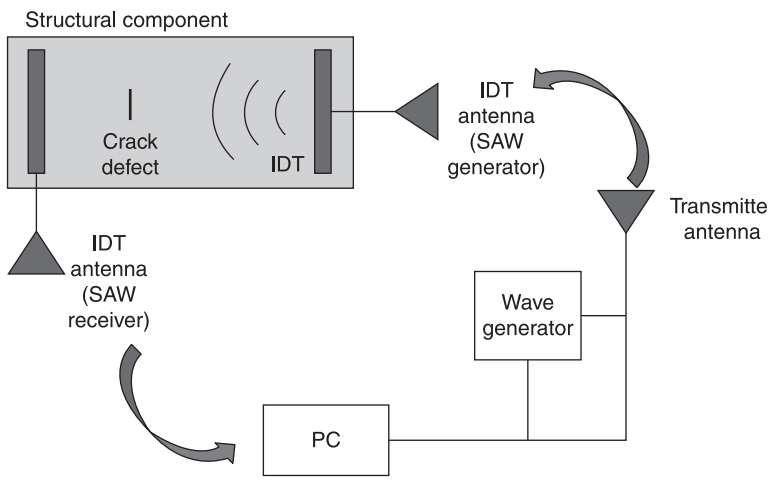

9.6 Scheme for a wireless IDT-based damage detection system.

© Woodhead Publishing Limited, 2013

The other IDT is employed as an output receiver to convert the mechanical waves back into output voltages. These devices are reciprocal in nature; as a result, signal voltages can be applied to both IDT with the same end result. Even more, a proper network of sensors could be designed, where each sensor is able to operate either as a wave generator or a receiver. Another advantage is that, when an IDT is directly connected to an antenna, the waves can be excited remotely by electromagnetic waves, thus generating a completely wireless sensor network system, not requiring power supply at sensor location.

Varadan and Varadan (2000) also showed the possibility of a MEMS IDT-based strain gauge. In fact, the traveling time of a SAW is directly proportional to the strain on the underlying component. As will be explained later, the strain field appears to be sensitive to the presence of damage, though the network sensitivity strongly depends on the sensor position, the monitored geometry, the damage type, position and extent as well as on the structure boundary conditions (applied load, environmental influences, etc.). Nevertheless, because of the possibilities for wireless communication and control, the adoption of IDT technology would allow for a strong reduction of the logistic impact due to the installation of a sensor network on airframes. However, it is necessary to consider that, when dealing with metallic conductive structures, the interferences and attenuation in signals would cause a strong increase in the communication packet error rate (Sbarufatti *et al.*, 2010b).

Smart SAW based sensor network

Piezoelectric materials can be used to measure stress and strain and can also be used to mechanically excite the structure to propagate stress waves and induce internal vibrations. Inputting a time-varying electrical signal to any of the actuators/sensors in a piezoelectric sensor network causes a propagating stress wave or propagating mechanical deformation to emanate from the sensor/actuator and travel through the material for detection by a plurality of neighboring sensors/actuators. The piezoelectric materials can be used in two sensing modes – active and passive. In active sensing mode, the actuators are externally excited to generate pre-selected diagnostic signals and transmit them to neighboring sensors, whose response can then be interpreted in terms of damage location and size or material property changes within the structure. In passive sensing mode, the piezoelectric sensors can be used as continuously monitoring sensors that 'listen' for external impact events. Piezoelectricity/resistivity can thus be used in order to deliver smart systems able to generate as well as to sense SAWs. Ideally, a sensor network can be installed on the monitored surface, thus scanning the structure for any occurring damage or anomaly.

Smart layers utilizing film embedded piezoelectric sensors have been proposed for SHM by several different research groups (Lin and Chang, 1998; Boller, 2001a,b; Kusaka and Qing, 2003; Lee *et al.*, 2004). The SMART layer™, developed by

© Woodhead Publishing Limited, 2013

Acellent Technologies (www.acellent.com), along with the SMART Suitcase™, can be used to generate and receive ultrasonic waves on structures. Piezoelectric elements are positioned according to structural needs on a Kapton Layer and are electrically wired by copper wiring using PCB techniques for the manufacturing process. The ultrasonic wave can be used for different purposes, one of which is to interrogate the condition of structures. With the network of actuators and sensors on the SMART layer, diagnostic signals can be sent from any actuator in the network to any neighboring sensor in the network, in many combinations forming various unique paths that cover the entire structure (Fig. 9.7). Depending on the application, various waveforms can be used for the diagnostic signal. The signal recorded by the SMART Suitcase™ can be analyzed with signal processing techniques to interpret the information. The diagnostic signals can potentially be used to detect structural damage, monitor in the service condition of structures, measure structural behavior, record environmental conditions, characterize material degradation and monitor manufacturing processes. To perform these various tasks using the diagnostic signal generated by the SMART layer™ and the SMART Suitcase™, software algorithms need to be developed. Currently, researchers at Acellent are using the SMART layer™ and SMART Suitcase™ to generate experimental data for this purpose. The SMART Layer®, including usable information processing, has to some extent been implemented in several tests, on both airplanes (F-16) and helicopters (RASCAL Black Hawk), as reported by the producers.

In Ihn and Chang (2004a,b), a piezoelectric based built-in diagnostic technique has been developed for monitoring fatigue crack growth in metallic structures. The technique uses diagnostic signals, generated from nearby piezoelectric actuators built into the structures, to detect crack growth. Guided Lamb waves were selected for actuators to maximize receiving sensor measurements. A physics-based damage index was developed relating sensor measurements to crack growth size. Two typical types of aircraft component were selected for tests to verify the proposed technique: riveted fuselage joints and composite bonded

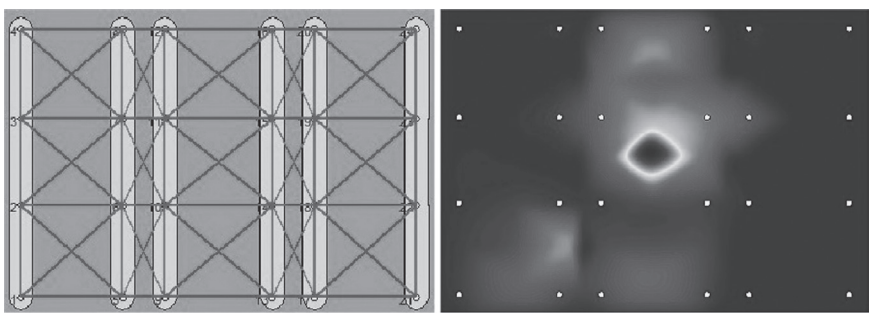

9.7 (a) Ultrasonic wave paths over a rectangular metallic panel and (b) damage localization after time domain post-processing.

© Woodhead Publishing Limited, 2013

repair patches with cracked aircraft parts. In riveted fuselage joints, the authors reported that the proposed technique can be used to detect crack lengths as small as 5 mm with certainty equal to that of conventional non-destructive testing (NDT), such as the eddy current testing and the ultrasonic scan methods. The results from the repair patch specimens also correlate well with visual inspections and clearly indicate that the technique can detect crack propagation underneath the patch.

9.3.3 Strain field-based SHM

Generally, damage to a structure can be defined as changes introduced into a system that adversely affects its current or future performance. Implicit in this definition is the concept that damage is not meaningful without a comparison between two different states of the system, one of which is assumed to represent the initial, and often undamaged, state. As an example, a crack that forms in a mechanical part produces a change in geometry that alters the stiffness characteristics of that part. Depending on the size and location of the crack and the loads applied to the system, the adverse effects of this damage can be either immediate or may take some time before they alter the system's performance. Damage can also result from scheduled discrete events such as aircraft landings and from unscheduled discrete events such as enemy fire on a military vehicle. In Sbarufatti *et al.* (2011a), the objective was to set up a diagnostic/prognostic system based upon strain field modifications due to the occurring damage, focusing the attention on fatigue type damages on metallic structures (cracks). Even thinking about bullet impacts in military applications, the assumption is that the evolution of the damage would be, however, a crack generated at the occurring notches.

In Sbarufatti *et al.* (2010a), it was demonstrated that the strain field sensitivity to crack damage can be exploited for structure monitoring; it also confirmed the possibility to accurately model with Finite Elements the static and fatigue dynamic behavior of a stiffened structure. However, the main issue was the strain sensitivity to the applied load. The monitored structures are often experiencing a load that is varying in time and, even worse, not easily predictable, due to environmental influences. The approach used hereafter consists in normalizing each sensor of a confined region with respect to the average value measured among all the sensors in the same region. In fact, the normalizing factor should be robust to the presence of the damage but only sensible to the applied load, thus allowing filtering of the load effect, without significantly altering the sensitivity to the crack. For a deeper insight into the problem, the interested reader should refer to Sbarufatti *et al.* (2010a).

Fiber Bragg grating (FBG) sensor application for SHM

Many strain gauges are available to date, based upon different physics, thus monitoring different parameters. Electrical resistance-based strain gauges and

© Woodhead Publishing Limited, 2013

optical fiber Bragg grating (FBG) sensors are the most common examples of strain gauges. Both are commonly used and their relative industrial experience is nowadays consolidated. However, the latter is particularly attractive, especially when a map or grid of sensors is required, as it allows a drastic reduction in the impact of sensor installation on existing structures.

The Bragg grating is usually photo-written in a standard telecommunication grade single-mode fiber. A virgin single-mode fiber consists of an ultra-clean thin rod with a core region in the center formed by doping with other materials to raise the refractive index. The standard dimension is 125 μm diameter for the entire fiber, while the centered core region has a diameter of around 9 μm, and a protective coating forms an outer layer. A laser illumination (in the ultraviolet spectral range) inscribes a refractive index modulation in the core of the fiber with a periodic pattern obtained through a photo-mask, which defines the periodicity. The extension of a Bragg grating for strain sensing purposes along the fiber is typically a few millimeters, which means that a Bragg grating can be regarded as a discrete point sensor for most purposes. The working principle is shown in Fig. 9.8.

In a measurement set-up, a broadband source (emitting a continuum of wavelengths) is introduced into an optical fiber. When the light hits the FBG, the wavelength matching the period of the grating is reflected and can be routed to a spectral detection unit via an optical coupler. When the grating is strained, the grating period will extend and the reflected wavelength peak will respond to this change in the grating period. A similar behavior occurs in compression, where the reflection peak moves to lower wavelengths. The main advantage comes from the multiplexing capability. After the first Bragg grating has reflected a certain wavelength light, a large light spectrum is still available, thus allowing inscribing of several Bragg gratings along one optical fiber at any desired positions, but characterized by different wavelength.

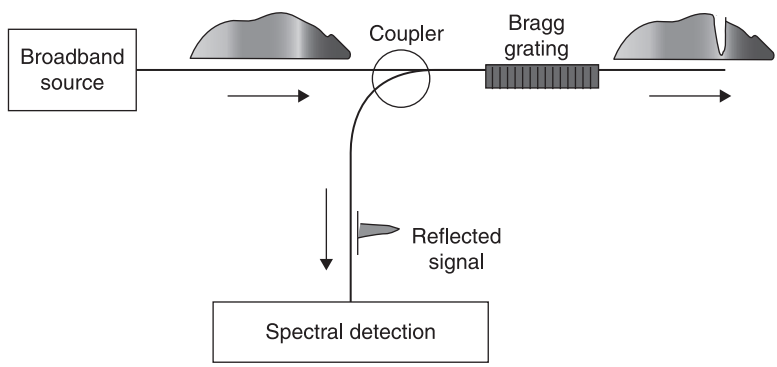

9.8 Fiber Bragg grating system working principle.

© Woodhead Publishing Limited, 2013

In order to separate the responses, each grating is inscribed with a different period so that the reflected spectrum will become a series of discrete peaks. The separation between each grating must be tailored to the application and the expected maximum strain or compression, so that the reflected peaks do not 'collide' with each other. FBGs for strain sensing are conveniently used in the 1550 nm telecommunications window where components such as couplers, detectors and light sources are readily available. The spectral width of the light source and the maximum expected strain for the application will determine how many FBGs can be accommodated along a single fiber. However, we can configure FBG sensors along many parallel fibers so that a large amount of sensors can be interrogated simultaneously.

FGB strain sensor system should be capable of providing a strain map of structures and thereby provide a warning system for damage identification. Further attractive features of such a system are immunity to electromagnetic interference, small dimensions and minimum weight and no need for local power supply at the sensor positions. The only power requirement is to run the interrogator and data analysis and storage equipment. The required instrumentation can be positioned in a convenient place, and passive connection fibers can connect all the sensor positions, as there are almost no fiber length limitations. The main drawback is the sensitivity of optical fiber to temperature; this generally requires temperature compensation. An easy solution is to deploy reference FBG sensors, which are not affected by strain and only respond to temperature changes for temperature compensation. The combined effect of fatigue loading and temperature on the sensitivity of Ormocer and polyimide coated FBGSs are determined in Frövel *et al.* (2010) for tensile and compression tests. The tests showed that both types of sensors performed satisfactorily before and after the 10^6 cycle fatigue tests of ±1200 microstrain. The Ormocer coated FBGSs showed a constant decrement of their sensitivity of about 2% after the fatigue cycling in the entire temperature range from −100 to 160°C, whilst polyimide coated sensors showed less than 1% changes but with higher standard deviations of the measured values.

The methodology for strain field-based SHM design is thoroughly described in Sbarufatti *et al.* (2010a,b), while Fig. 9.9 reports the FBG-based sensor network performances for crack detection, localization and quantification on aluminium reinforced skin fuselage panels. The detection algorithm output is shown in Fig. 9.9a as a function of crack length. In particular, a single crack was artificially initiated in the middle of the central bay and was made to propagate in the direction perpendicular to stringers. As shown, initially the algorithm output is almost zero, as the damage effect is very low, while it grows for larger crack lengths. The threshold level should be carefully determined in order to control the extent of false alarms without reducing the detection capabilities. After the alarm is generated, another algorithm can be activated to estimate the damage position and dimension. Figure 9.9b indicates the output of the localization unit versus the target damage position. Moreover, the performances in crack length quantification

© Woodhead Publishing Limited, 2013

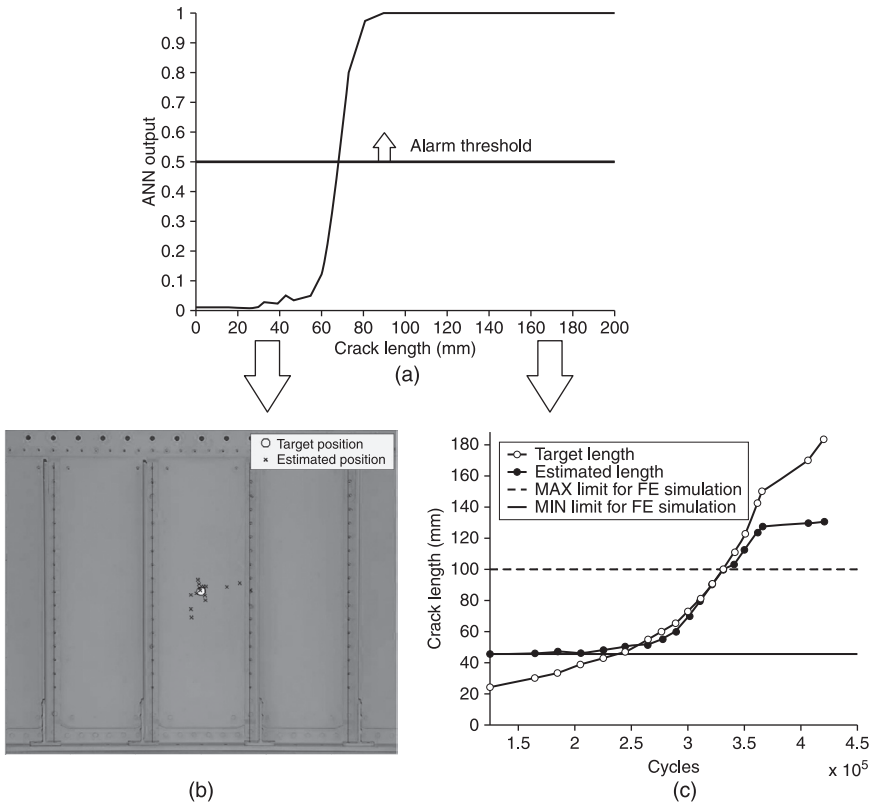

9.9 Output for the diagnostic algorithm developed for full damage characterization: (a) anomaly detection index; (b) damage localization; and (c) damage quantification.

are shown in Fig. 9.9c. As shown in the figure, the FEM simulated information had been provided inside a certain band of crack lengths. While the inferior limit for a correct quantification is clearly identifiable, a certain extrapolation capability was demonstrated for crack lengths exceeding the FEM simulation limit.

Typical strain field dependent SHM systems, like those described in Sbarufatti *et al.* (2011a), are based on static or quasi-static sensor acquisition. For instance, the work reported in Sbarufatti *et al.* (2011a) uses FBG multiplexed sensors with 1 kHz sampling rate. However, the same FBG sensor could be used to sense the strain wave propagating on a metallic medium and generated, for instance, by a piezoelectric actuator. In Betz *et al.* (2001, 2004), the identification of damage using Bragg grating sensors as ultrasonic receivers of Lamb waves is reported. Experiments were performed on aluminium plates to determine the severity of damage by varying the diameter of drilled holes. A reliable feature that could

© Woodhead Publishing Limited, 2013

serve as a damage index has been extracted, proving good correlation with the actual damage size. Nevertheless, the required acquisition frequency for the FBG system was around 460 kHz.

9.4 Conclusion and future trends

SHM consists today in the integration of sensors into structural components to automatize their diagnosis by means of automated signal processing, thus allowing for a real-time prognosis of the residual useful life. It uses sensors such as optical fibers, piezoelectric elements, micro-electromechanical systems (MEMS) or possibly even nanostructures, etc. These sensors allow monitoring of strains, acoustics, electrical fields, temperature, pressure, humidity, chemicals and possibly more. Information is retrieved either by wires but, when possible, even wireless. Sensor signals are processed using advanced data acquisition cards and multiplexers combined with FFT-analysers, wavelets, genetic algorithms and artificial neural networks, etc.

Nevertheless, SHM-related technological development described above is far from being at the limits. Much consideration and effort will be required to get the sensing and actuation devices attached onto or integrated into the structural material in an appropriate, reliable and cost-effective way. Also the parameters and damage types to be monitored is wide. When monitoring an airframe structure, we could face fatigue crack propagation, corrosion due to the harsh operational environment, and any damage due to accidental maneuvers such as a harsh landing, etc. For instance, relatively to corrosion, the Boeing company reports (Trego, 2003) that the major portion of the cost of inspecting aircraft for damage is associated with obtaining access to hidden parts of the airframe. In addition, there is the added cost associated with incidental damage that is done to the structure while gaining access to the hidden areas. Thus, there is a clear need to develop *in situ* sensors and the diagnostic and prognostic algorithms to monitor critical environments, in order to provide early and automatic warning relatively to hidden parts of the aircraft. Micro-electromechanical systems (MEMS) are a promising technology for SHM applications, from conventional accelerometers (vibration based SHM) to piezoelectric sensors and actuators and FBG-based optical systems. The latest developments have led to a remarkable reduction in size, cost and power consumption of these sensors. They can be mass produced, are small enough to be used in applications where conventional sensors would be intrusive, and are often combined with systems for wireless data transmission.

The usage of MEMS has made particularly attractive the possibility to have distributed sensing and, in particular, ‘smart sensing’. The essential difference between a smart sensor and a standard integrated sensor is its intelligence capabilities, or the presence of an on-board microprocessor. The microprocessor can be used for digital processing, analog to digital or frequency to code

© Woodhead Publishing Limited, 2013

conversions, calculations, and interfacing functions, which can facilitate self-diagnostics, self-identification or system diagnostic functions. It can also decide when to store data, and control when and for how long it will be operating, so as to minimize power consumption. Wireless technology will play an important role in SHM systems, especially if considering the increase in the number of sensors that are required for the detection of smaller and smaller defects, such as cracks and corrosion, or to increase the reliability of the same SHM systems.

Wireless global communication is important for facilitating low-cost, densely distributed sensing systems. Wireless links have been around for several years, and are now practically used in civil SHM, thus referring to large structures such as bridges and buildings (Spencer *et al.*, 2004). However, considering aerospace structures, two things have to be considered *a priori*. First, the packet error rate is strongly influenced by the presence of metal environments. Moreover, the interaction with on-board communication systems as well as the electromagnetic interference with other devices has to be carefully analysed. Nevertheless, further threats can be seen with respect to providing energy to the system elements. Batteries could be provided, or the system could charge itself by harvesting the energy from the structure, thus delivering a truly wireless SHM system. Last but not least, some hardware related issues have to be considered, among which are data acquisition, synchronization, available memory and transmission rate. The latter in particular has to be pushed to its limit, in order to make feasible the transmission of the huge amount of information recorder by the sensors distributed over the entire airframe.

Moreover, the continuing research and developments in materials, in particular at the micro- and nano-levels, open up new applications and sensing principles that are quickly addressed by the research community. In recent years, there has been increasing interest in moving from micromechanical to nanomechanical devices to increase data acquisition rates, improve force resolution and open the door to very high-frequency applications (Knobel and Cleland, 2003; Li *et al.*, 2006). Thanks to miniaturization down to micron- and nano-levels, the on-chip integration of functions (including sensing, data processing and storage and wireless communication) would also be pushed to the limit.

Research studies of sensing principles, materials and data processing technologies have thus the potential to revolutionize the aircraft maintenance, automating the costly and time-consuming procedure that nowadays mostly leads to the ‘no failure found’ information. Given this challenge, not only the aircraft availability will increase, but further potentials are foreseen in the possibility to obtain a remarkable weight saving for some components under the damage tolerant principle. Finally, standardization and certification procedures have to be developed in parallel, to make the new devices tempting from an industrial point of view.

© Woodhead Publishing Limited, 2013

9.5 References

Arms S W, Galbreath J H, Townsend C P, Churchill D L and Phan N (2008), 'Energy harvesting, wireless structural health monitoring system', *Proceedings of the 4th European Workshop on Structural Health Monitoring*, pp. 581–589.

Betz D, *et al.* (2001), 'Fiber-optic smart sensing of aviation structures', *Third International Workshop on Structural Health Monitoring*, pp. 306–315.

Betz D, *et al.* (2004), 'Damage identification using Lamb waves and fibre Bragg grating sensors', *Second European Workshop on Structural Health Monitoring*, pp. 1151–1158.

Bieniek T, *et al.* (2008), *e-CUBES Devices and Interconnects – Integrated Modelling and Simulation for Reliability Analysis*, MIXDES.

Boller, C (2001a), 'Aircraft structural health management', *Smart Mat Struct*, 10, 432–440.

Boller, C (2001b), 'Ways and options for aircraft structural health management', *Smart Mat Struct*, 10, 432–440.

Boller C and Buderath M (2007), 'Fatigue in aerostructures – where SHM can contribute to a complex subject', *Phil Trans R Soc*, 365, 561–587.

Broek D (1979), 'Damage tolerance in practice', *Fracture Mechanics Design Methodology*, AGARD Lecture Series, No 97.

Department of US Defense (2006), *Joint Service Specification Guide – Aircraft Structures*, JSSG-2006.

Farrar C R, Sohn H, Fugate M L and Czarnecki J J (2001), 'Integrated structural health monitoring'; *Proceedings of the SPIE – The International Society for Optical Engineering*, vol. 4335, *Advanced Non-destructive Evaluation for Structural and Biological Health Monitoring*, pp. 1–8.

Farrel T H (1981a), *Structural Integrity Recording System for US Army AH-1s helicopters*, USAAVRADCOM-TR-80-D-15, March 1981.

Farrel T H (1981b), *Structural Integrity Recording System for US Army AH-1s helicopters*, USAAVRADCOM-TR-81-D-6, March 1981.

Flatscher M, *et al.* (2010), 'A bulk acoustic wave (BAW) based transceiver for an in-tire-pressure monitoring sensor node', *IEEE J Solid-State Circ*, 45, 167–177.

Frövel M, del Olmo E, Carrión G and Pintado J M (2010), 'Influence of fatigue loads and temperature on the response of FBGS embedded in composite material for aerospace applications', *Proceedings of the Fifth European Workshop on Structural Health Monitoring*, Sorrento, Italy, 28 June–4 July, pp. 420–425.

Hall A D (1976), 'Helicopter design mission spectra', *AGARD Conference Proceedings*, No 206, April.

Harlow D G and Wei R P (1999), 'Probabilities of occurrence and detection of damage in air frame materials', *Fatigue Frac Engin Mat Struct*, 22, 427–436.

Ihn J B and Chang F K (2004a), 'Detection and monitoring of hidden fatigue crack growth using a built-in piezoelectric sensor/actuator network: I. Diagnostics', *Smart Mat Struct*, 13, 609–620.

Ihn J B and Chang F K (2004b), 'Detection and monitoring of hidden fatigue crack growth using a built-in piezoelectric sensor/actuator network: II. Validation using riveted joints and repair patches', *Smart Mat Struct*, 13, 621–630.

Janczyk G, *et al.* (2007), *Integrated Termo-Electro-mechanical Modelling of 3-D e-CUBES Structures*, MIXDES.

Janczyk G, *et al.* (2008a), *Heterogeneous System for Thermal Modelling and Simulations of Heterogeneous e-CUBES Devices*, MIXDES.

© Woodhead Publishing Limited, 2013

Janczyk G, *et al.* (2008b), 'Reliability issues of e-Cubes heterogeneous system integration', *Microelect Reliab*, 48, 1133–1138.

Kim J S, *et al.* (2002), 'Wireless health monitoring of cracks in structures with MEMS-IDT sensors', *Smart Struct Mat: Smart Electronics, Mems Nanotech*, 4700, 342–353.

Knobel R G and Cleland A N (2003), 'Nanometre-scale displacement sensing using a single electron transistor', *Nat Nanotech*, 424, 291–293.

Kusaka T and Qing P (2003), 'Characterization of Loading Effects on the Performance of SMART Layer Embedded or Surface-Mounted on Structures', in *Structural Health Monitoring 2003, from Diagnostic and Prognostic to Structural Health Management*, pp. 1539–1546.

Lee, S, Reddy J and Rostam-Abadi F (2004), 'Transient analysis of laminated composite plates with embedded smart-material layers', *Finite Elem Anal Des*, 40, 463–483.

Li M, Tang H and Roukes M L (2006), 'Ultra-sensitive NEMS-based cantilevers for sensing, scanned probe and very high-frequency applications', *Nat Nanotech*, 2, 114–120.

Lin M and Chang F (1998), 'Development of smart layer for built-in diagnostics for composite structures', *The 13th Annual ASC Technical Conferences on Composite Material, American Society of Composite, Baltimore, MD, 1998*, pp. 1–8.

Moya E, Torfs T, Peeters B, Vecchio A, Van Der Auweraer H, *et al.* (2008), 'Wireless sensor developments for Structural Health Monitoring', *Proceedings of the 4th European Workshop on Structural Health Monitoring*, pp. 606–613.

Qu W, *et al.* (1998), 'W-LIGA: A promising and low-cost variant for microsystem technology', *Proceedings of the Conference on Optoelectronic and Microelectronic Materials Devices*, pp. 380–383.

Ramm P and Klumpp A (2008), 'Through-silicon via technologies for extreme miniaturized 3D integrated wireless sensor systems (e-CUBES), *Proceedings of the International Interconnect Technology Conference*, pp. 7–9.

Sadler D J and Ahn C H (2001), 'On-chip eddy current sensor for proximity sensing and crack detection', *Sens Act*, A91, 340–345.

Sbarufatti C, Manes A and Giglio M (2010a), 'Probability of detection and false alarms for metallic aerospace panel health monitoring', *Proceedings of the 7th International Conference on CM and MFPT, BINDT*.

Sbarufatti C, Manes A and Giglio M, *et al.*, (2010b), 'Application of Structural Health Monitoring over a critical helicopter fuselage component', *Proceedings of the AIRTEC – HELI World*.

Sbarufatti, C, Manes A and Giglio M (2011a), 'HECTOR: one more step toward the embedded Structural Health Monitoring system', *Proceedings of the Third CEAS Air and Space Conference* – 21st AIDAA Congress.

Sbarufatti, C, Manes A and Giglio M (2011b), 'Advanced stochastic FEM-based artificial neural network for crack damage detection', *Proceedings of the Coupled Problems in Science and Engineering*.

Spencer B F, Ruiz-Sandoval M E and Kurata N (2004), 'Smart sensing technology: opportunities and challenges', *J Struct Cont Health Mon*, 11(4) 349–368.

Trego, A (2003), 'Installation of the Autonomous Structural Integrity Monitoring System', *Fourth International Workshop on Structural Health Monitoring*, Stanford, CA, pp. 863–870.

Varadan V K (2002), 'Wireless microsensors for health monitoring of structures', *Smart Struct, Dev Syst*, 4935, 526–536.

Varadan V K and Varadan V V (2000), 'Microsensors, Micro-Electromechanical Systems (MEMS), and electronics for smart structures and systems', *Smart Mat Struct*, 9, 953–972.

© Woodhead Publishing Limited, 2013

Washabaugh A, Zilberstein V, Schlicker D., Shay I, Grundy D, *et al.* (2002), 'Shaped field eddy-current sensors and arrays', *SPIE*, 4702, 63–75.

White D (2008), 'Structural health monitoring supports life cycle management of US army helicopters', *Proceedings of the 4th European Workshop on Structural Health Monitoring*, pp. 1192–1199.

Zio E and Peloni G (2011), 'Particle filtering prognostic estimation of the remaining useful life of nonlinear components', *Reliab Eng Syst Safety*, 96, 403–409.

© Woodhead Publishing Limited, 2013

10

MEMS for harsh environment sensors in aerospace applications: selected case studies

N. TILIAKOS,
Alliant Techsystems Operations, LLC, USA

DOI: 10.1533/9780857096487.2.245

Abstract: In this chapter we shall attempt to provide the reader with an understanding of what MEMS (micro-electromechanical systems) is and how it has become an enabling technology for some harsh environment aerospace applications, how it can contribute significantly to enhancing existing and future aerospace systems. We will explain what is meant by a harsh environment and how the engineer/scientist would need to accommodate his/her design to perform in this domain. Conveying this is perhaps best accomplished by presenting selected 'case studies', engineering examples of selected MEMS systems designed specifically for harsh environments in aerospace applications.

Key words: harsh environment MEMS, electronics cooling, high temperature Packaging, MEMS IMU, MEMS shear stress sensor, MEMS GNC.

10.1 Micro-electromechanical systems (MEMS)

The selected MEMS system case studies we have chosen include MEMS shear stress sensors, where we provide design, fabrication and testing details of this system as it applies to instrumentation for ground aero-propulsion wind tunnels, MEMS devices for thermal management of (aerospace) electronics cooling, and MEMS inertial measurement units (IMUs) for missile, guided munitions and high speed re-entry spacecraft guidance, navigation and control (GNC) applications. In addition, an overview of packaging for MEMS devices is presented, along with some of the necessary packaging attributes required for harsh environments. We close the chapter with a brief commentary on likely future trends for MEMS in aerospace applications and a short list of sources of further information.

10.1.1 Definition of MEMS

Micro-electromechanical systems is the synergistic combination of microelectronics and micron-sized mechanical structures or micro-machines, which together form an electro-mechanical system. In Japan, this technology is referred to as micro-machines, while in Europe it is microsystems technology (MST) and in the United States referred to as MEMS. The 'marriage' of microelectronics and micromechanical structures means that electrical circuits

© Woodhead Publishing Limited, 2013

and components are integrated into the mechanical device, enabling it to function as a sensor or actuator. This integration process can either occur during the microfabrication process or after the device is fabricated, such as during the packaging stage. In either case, design of the electrical circuit, the mechanical design of the sensor or actuator, such as the MEMS structure, and the packaging design should all occur concurrently early in the design process.

Many consider, the author included, MEMS to be an enabling technology, meaning that the MEMS device/system provides the overall product/system with a performance enhancing attribute. Some classic examples of a MEMS system, providing a product with a performance enhancing attribute, include MEMS accelerometers in automobiles triggering air bag deployment when a certain acceleration threshold is sensed, making automobiles safer and MEMS microphones and gyroscopes embedded in cell phones, tablets and computers, enabling these devices to provide user friendly features such as tilt detection, image stabilization, etc. Some examples of MEMS devices for aerospace applications are shown in Figs 10.1a, 10.1b and 10.1c.

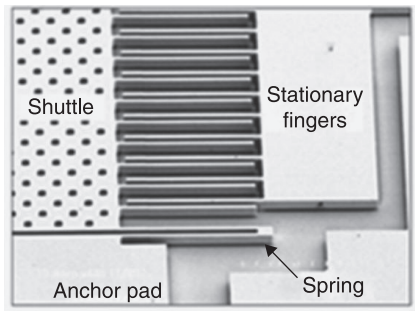

(a)

(b)

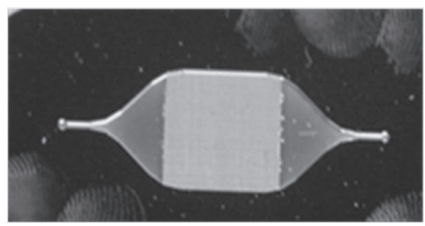

(c)

10.1 (a) SEM photo of a MEMS shear stress sensor, showing the inter-digited fingers, shuttle, anchor pad and spring; (b) array of high temperature MEMS heat flux sensors; (c) MEMS-based micro-catalytic reactor (devices were designed and tested at ATK GASL, photos courtesy of ATK GASL/Nicholas Tiliakos).

© Woodhead Publishing Limited, 2013

10.1.2 Defining the harsh environment

The definition of harsh environment is relative and perhaps subjective; however, the following characteristics may help define what we mean by such an environment:

- high temperature, »400 K or very low temperatures, <273 K;
- high pressures, »0.1 MPa, or vacuum;
- chemically reacting/oxidizing flowfields;
- radiation (e.g. electromagnetic, nuclear);
- presence of particulate matter to such a degree that it affects the MEMS device design;
- high acceleration/impulsive loads of more than the order of 10s of g (>98 m/s^2); and
- highly corrosive, e.g. oil wells, down-hole environments.

In short, a harsh environment could mean any condition in which the environment strongly influences the design, operation and performance of the sensor system, thereby requiring it to be accounted for at the onset of the requirements definition stage of the project. An example of a harsh aerospace environment is that of the flowfield surrounding a hypersonic vehicle (Fig. 10.2). This environment is characterized by high thermal loads (see the convective heat transfer coefficient (HTC), '$(h)_{turb}$' and adiabatic wall temperature ('$(T)_{aw}$' curves in Fig. 10.3) and structural/impulsive shock loads. This hypersonic flight environment is typically simulated by various aero-propulsion ground test facilities, such as those at ATK GASL (Fig. 10.4). Examples of the various MEMS devices tested at these facilities are also shown in Figs. 10.1a, 10.1b and 10.1c.

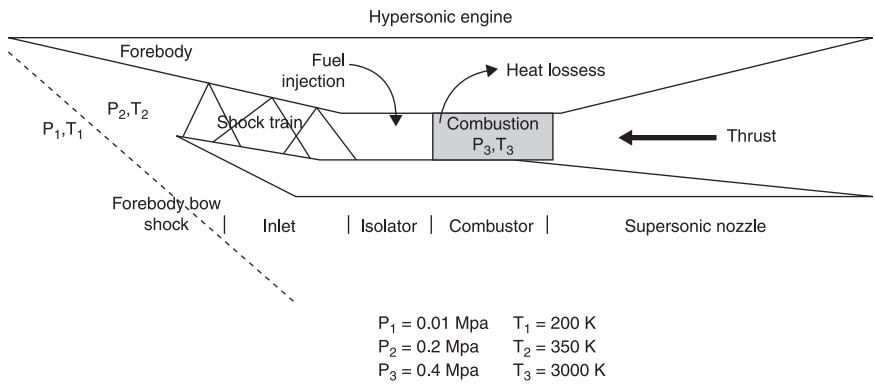

10.2 Schematic rendering of the various parts of a hypersonic aerospace vehicle, including the harsh environment.

© Woodhead Publishing Limited, 2013

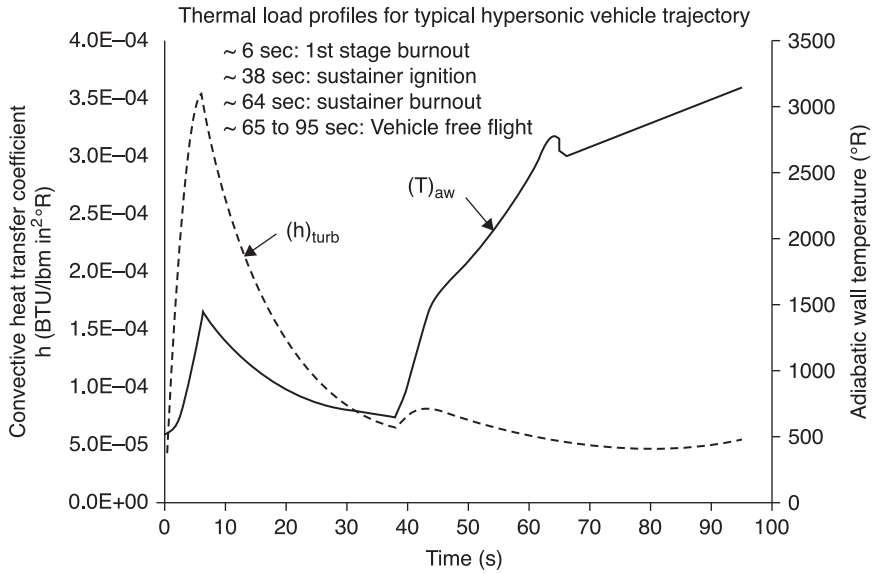

10.3 Thermal load profiles for a typical hypersonic vehicle trajectory.

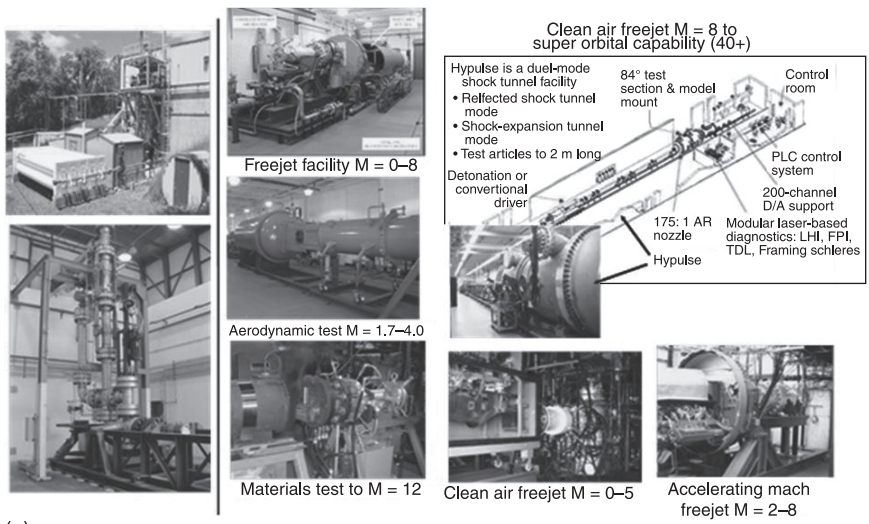
Freejet facility M = 0–8
Aerodynamic test M = 1.7–4.0
Materials test to M = 12
Clean air freejet M = 8 to super orbital capability (40+)
Hypulse is a duel-mode shock tunnel facility
• Reflected shock tunnel mode
• Shock-expansion tunnel mode
• Test articles to 2 m long
Detonation or convertional driver
84° test section & model mount
Control room
PLC control system
200-channel D/A support
175: 1 AR nozzle
Hypulse
Modular laser-based diagnostics: LHI, FPI, TDL, Framing schleres
Clean air freejet M = 0–5
Accelerating mach freejet M = 2–8

(a)

10.4 (a) Overview of some of the aero-propulsion ground test facilities at ATK GASL, NY; (b) MEMS shear stress sensor (see white circle on left side of photo), installed inside a supersonic nozzle in a ATK GASL aero-propulsion facility, being tested at high Mach number and high temperature (photos courtesy of ATK GASL/Nicholas Tiliakos).

© Woodhead Publishing Limited, 2013

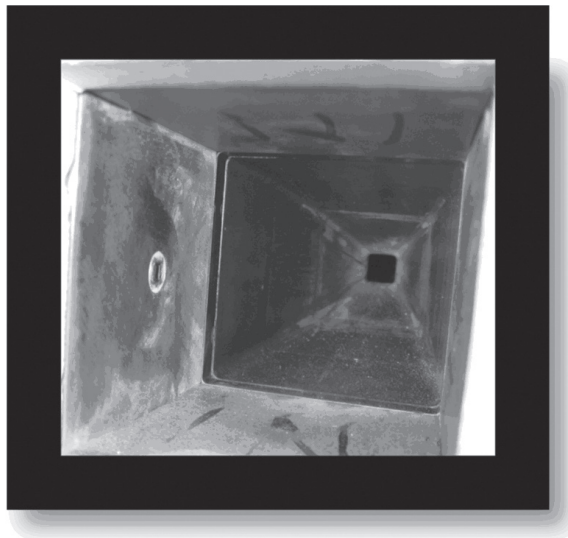

(b)

10.4 Continued.

10.1.3 MEMS in aerospace applications: overview

Before we can present a few selected case studies of MEMS harsh environment sensors for aerospace applications, we first answer the following questions:

- what aerospace applications are we considering?
- why even consider MEMS in aerospace applications?
- what is the 'aero-MEMS' market?
- what are some of the concerns/challenges of MEMS harsh environment sensors for aerospace applications?

Note that by 'aero-MEMS' market, we are considering both the commercial and military aerospace markets.

Compared to other markets (commercial electronics, industrial, etc.) the aerospace/defense market for 'aero-MEMS' is small but growing; and relatively low volume (10s–10 000s of devices . . . not millions!) but high price point, in the order of 10s to 100s US dollars per device versus pennies per MEMS device in the commercial sector. The commercial sector is driven by unit cost reduction, whereas the aero/defense industry is driven by device performance 'improving mission performance and reliability', and this in turn is driven by high performance and high reliability. There is an aero-MEMS market/interest in:

© Woodhead Publishing Limited, 2013

- acceleration measurement, e.g. MEMS accelerometers, MEMS gyroscopes for MEMS IMUs;
- MEMS pressure sensors, e.g. used by aircraft manufacturers to decrease maintenance costs;
- MEMS sensor suite, combining pressure, temperature, i.e. MEMS sensors on one monolithic substrate;
- sensor fusion algorithms;
- smart aerospace structures/MEMS health monitoring;
- micro-bolometers (night vision), motion sensors; and
- MEMS Safe and Arming (SandA) fuzes.

Aerospace applications and MEMS make a great combination, partly because MEMS devices directly address and satisfy the SWaP (Size, Weight and Power) requirements so important in the aerospace market and also because MEMS devices are an enabler for advanced aerospace systems, enhancing their performance in a potentially cost-effective manner. Table 10.1 presents some of the top-level aerospace application characteristics/requirements that are compatible with MEMS capabilities/attributes.

Though MEMS technology appears to provide a synergistic fit with aerospace requirements/applications, there are some concerns that need to be addressed before MEMS devices/systems become widely accepted and prevalent in this challenging, harsh environment. These concerns include:

- surviving the harsh environment, while providing high reliability and performance is a huge challenge. MEMS reliability needs to be proven, though

Table 10.1 Some top-level aerospace requirements met by MEMS technology

Aerospace industry requirement	Can MEMS achieve this?
1-High reliability (i.e. comparable to aerospace standards)	Yes-in some cases (e.g. accelerometers)*
2-High performance/repeatability performance	Yes-but depends on application
3-Stringent SWaP (Size, Weight and Power) requirements	Yes
4-Fast response (application specific)	Yes
5-All the above (1–4) in harsh environments (e.g. High 'g' loading, high temperatures/pressures, oxidizing environments)	In some Cases Yes
6-Tight tolerances/standards	TBD-aerospace standards re MEMS

* Packaging issues also play a role in MEMS device reliability

© Woodhead Publishing Limited, 2013

this may be device specific, even for the same technology application, perhaps due to lack of a MEMS standard in the aerospace field;
- over-coming the 'if it isn't broke why fix it' mentality, i.e. in many cases MEMS devices may outperform their macro-counterparts; however, the macro-counterparts are chosen because they perform well, have proven reliability and are cost effective, thereby ensuring their continued acceptance in the field;
- lack of heritage/maturity level: non-MEMS devices that perform similar functions to their MEMS counterpart (e.g. IMUs) have a heritage, are very reliable, cost effective and are proven to work over many years;
- lack of aerospace industry standards for MEMS: the number of years to develop and get to a commercially available state are a hurdle (e.g. 5+ years development, 10s of millions of US dollars), which challenges commercialization.

The aerospace industry needs to be convinced of the 'game changing' characteristics that MEMS can provide. It is challenging to convince an aerospace engineer that a MEMS device should replace a current legacy system (e.g. IMU), because that system is further down the learning curve and an unproven MEMS device (e.g. MEMS IMU) adversely affects the learning curve. Also, typical legacy systems cost is sometimes lower than a MEMS device. Consideration of MEMS at the start of product development would be helpful, otherwise the learning curve is too high. MEMS will make an impact on the aerospace market if it can be clearly shown that MEMS devices/systems increase product performance by orders of magnitude, while maintaining or increasing reliability, at a cost comparable to the legacy device/system. Dramatic improvements in aerospace product reliability and performance will spur the 'aero-MEMS' market, not necessarily price points.

10.2 Examples of MEMS harsh environment sensors in aerospace applications

10.2.1 Background: systems engineering view of MEMS harsh environment sensors

In this chapter we shall attempt to provide the reader with an understanding of what MEMS is and how it is an enabling technology for some harsh environment aerospace applications, how it can contribute significantly to enhancing existing and future aerospace systems and what is meant by a harsh environment and how the engineer/scientist would need to accommodate his/her design to perform in this domain. Conveying this is perhaps best accomplished by presenting 'case studies', with real life engineering examples, of MEMS systems designed specifically for harsh environments in aerospace applications. We caution the reader that this section is not meant to be an exhaustive literature review of past

© Woodhead Publishing Limited, 2013

and present MEMS systems for harsh environment aerospace applications, but instead a focused approach to a few select systems.

To start, we shall present an overview of typical requirements for these MEMS sensor systems, a systems engineering approach, followed by examples of a MEMS shear stress sensor, MEMS for electronics cooling/thermal management, MEMS gyroscopes and IMU for guidance/navigation and control (GNC) and MEMS packaging.

10.2.2 Systems engineering requirements overview for MEMS harsh environment sensors

During the engineering design process of any system, the initial task is to first define the system and its subsystems and then to capture the system (and eventually subsystem) requirements. This process is critical to engineering a successful product that will meet the customer requirements. If this step is incomplete, or worse is incorrect, the final system will not perform and may even be unsafe. For example, in the design of MEMS Safe and Arming fuzes, the engineer must design the system to only arm the fuze after a certain condition has been met. If this condition, for example acceleration load, is incorrectly specified or missed, the result could be disastrous: premature arming of a munition could lead to human casualties, incorrect target acquisition, mission failure, etc. A MEMS safe and arming (S and A) fuze is a micro-device that enables safe arming of a munition by sensing a condition (via a mechanical component) is met (e.g. acceleration loads) and then actuating another mechanical mechanism, typically a sliding spring, to arm the munition in preparation for its deployment (Robinson *et al.*, 2001). When assembling the system requirements for a MEMS sensor, we must consider the following (Fig. 10.5):

- Define and understand the system, for example, what components encompass the system that you are designing for? Are there subsystems? Does the system also include the structure into which the MEMS sensor and its packaging must interface with? How does the environment interact with the system?
- Communication with the customer is paramount to define the top level customer requirements. This must be done early and often until a final set of requirements has been approved by all parties involved. Note that the customer may not be the final end user, so that the parties involved in the systems requirements definition would include the engineers/program managers, customer(s) and end user(s).
- Knowledge of the environment that the final MEMS device/product will encounter or interface with must begin simultaneously with the assembly of the customer requirements. Understanding this environment may also come from the customer or end user.
- Need to understand the concept of operations ('CONOPS'). How will the system and its subsystems operate? And how will this operation tie back to the subsystem requirements?

© Woodhead Publishing Limited, 2013

© Woodhead Publishing Limited, 2013

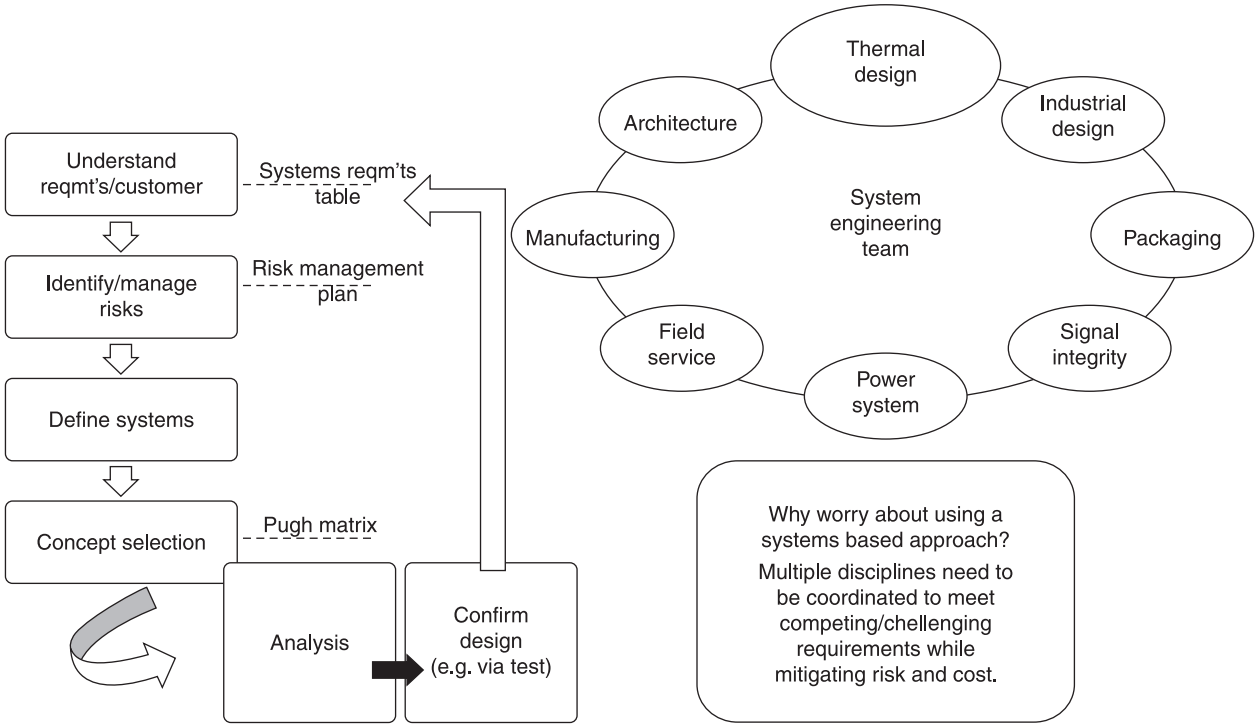

10.5 Schematic depicting concurrent systems engineering practices.

- Once the top-level customer requirements have been determined, there most likely will be derived requirements, which will usually fall out of the initial engineering analysis. For example, a general customer requirement might appear as 'the sensor must be flush-mounted to the aerospace vehicle and survive 1200 K static temperature'. The thermal-structural engineer may then determine that based on this temperature requirement and his/her understanding of the environment (e.g. is it oxidizing? is it high pressure?) that only a specific class of high temperature materials is available. However, because of the high temperature, the engineer must consider the potential for coefficient of thermal expansion (CTE) mismatch, either between the sensor and its own internal components or external components. This may now lead to the derived requirement that the sensor packaging should be of one monolithic material to minimize the overall strain and growth of the sensor and packaging components.
- Once the top level and derived requirements are set, a thorough first- and second-order engineering analysis begins. An initial design concept is achieved and iteration between the design, functionality and derived requirements begins as well.
- 'Concurrent engineering' is an approach where the various aspects of the engineering effort, for example, design, analysis, packaging, testing and fabrication/manufacturing planning, occur in parallel and early in the development work. This can be especially important in the development of MEMS sensors, where packaging cannot only consume a significant portion of a budget but also is critical to the implementation of the sensor. The importance of concurrent engineering is exemplified in the design, fabrication and development of a MEMS shear stress sensor for consideration on an aerospace flight vehicle. The MEMS sensor plus packaging design need to be considered together and early on in the requirements discussions, because even though most MEMS sensors encompass a very small form factor, in the order of mm, their packaging form factor could be in the order of centimeters, thereby making the installation of a MEMS sensor into an aerospace vehicle more challenging than originally thought. This is a factor that could also prohibit using the MEMS sensor, since valuable thermal protection panels would now require a large protrusion in order to accommodate the sensor potentially nullifying the original benefits of a non-intrusive MEMS sensor.

10.2.3 MEMS shear stress sensors

Motivation/sensor application

An integral part of assessing an aerospace vehicles' performance is accurate determination of its viscous drag and combustion efficiency, both of which are functions of surface shear stress forces. The measurement of shear stress is important for many practical reasons that include:

© Woodhead Publishing Limited, 2013

- improving the performance of aerospace vehicles by assessing and reducing viscous drag;
- understanding and characterizing laminar to turbulent boundary layer transition and separated flows (important for aerodynamic performance);
- thermal load assessment, using Reynolds Analogy;
- allow for calibration of computer code shear stress calculations;
- help identify when and where flow separation and boundary layer transition occurs in the engine flowpath; and
- the emerging field of active flow control. It should also be noted that the aerospace structure being interrogated could also be a turbine blade in a gas turbine engine, or wind turbine and not necessarily restricted to a vehicular structure.

In this case study, we shall direct our attention to a MEMS shear stress sensor designed for the harsh environment of aerospace vehicles, especially hypersonic aero-propulsion testing, a very challenging environment from which to extract useful data, based on the work of Tiliakos *et al.*, (2006, 2008a,b).

A MEMS-based shear stress sensor can be used to directly measure the shear stress on ground-based articles tested in hypersonic aero-propulsion tunnels, and eventually on flight-test articles. Typically, when attempting to determine combustor performance (i.e. efficiency) using computer codes, a value for the skin friction coefficient C_f is assumed, which is required as an input. Obtaining direct shear stress measurements, τ_{wall}, for example along a combustor or inlet wall (Fig. 10.2), will allow engineers to obtain a more accurate skin friction coefficient, since the two are related as:

$$\tau_{wall} = C_f \frac{1}{2}\rho V^2 \qquad [10.1]$$

where ρ is the fluid density (kg/m^3) and V is the local velocity (m/s). To understand how knowledge of the shear stress distribution relates to propulsive performance, we can relate the relative area change (dA/A), the relative total temperature change (dT_t/T_t) and momentum change in the flowpath to the change in Mach number distribution by combining the conservation of mass (assuming no species creation) Eq. 10.2, momentum, (assuming only forces are fluidic) Eq. 10.3 and energy Eq. 10.4 and utilizing the equation of state for a gas Eq. 10.5, and the differential form of Mach number in a 1-D formulation as follows, to obtain Eq. 10.6 (Smart, 2008):

$$\frac{d\rho}{\rho} + \frac{dV}{V} + \frac{dA}{A} \qquad [10.2]$$

$$\frac{dP}{P} + \frac{\gamma M^2}{2} + \frac{4C_f dx}{D} + \frac{\gamma M^2}{2}\frac{dV^2}{V^2} = 0, \qquad [10.3]$$

$$\frac{dT}{T} + \frac{(\gamma-1)}{2} M^2 \frac{dV^2}{V^2} = \left[1 + \frac{(\gamma-1)}{2} M^2\right]\frac{dT_t}{T_t} \qquad [10.4]$$

© Woodhead Publishing Limited, 2013

$$\frac{dp}{p} - \frac{d\rho}{\rho} - \frac{dT}{T} = 0 \qquad [10.5]$$

$$\frac{dM^2}{M^2} = \frac{2\left(1+\frac{(\gamma-1)}{2}M^2\right)}{1-M^2}\frac{dA}{A} + \frac{(1+\gamma M^2)\left(1+\frac{(\gamma-1)}{2}M^2\right)}{1-M^2}\frac{dT_t}{T_t} + \frac{\gamma M^2\left(1+\frac{(\gamma-1)}{2}M^2\right)}{1-M^2}\frac{4C_f dx}{D} \qquad [10.6]$$

Note that in the above equations: 'C_f' is the local skin friction coefficient; 'ρ' is the local fluidic density (kg/m^3); 'A' is the local cross-sectional area (m^2); 'V' is the local velocity (m/s); 'P' is the local pressure (Pa); 'γ' is the local specific heat ratio of the fluid; 'M' is the local Mach number, defined as the local velocity divided by the local speed of sound; 'D' is the diameter of the tube, a characteristic length (m); 'x' is the 1D position location in the stream; 'T' is the local static temperature (K); and 'T_t' is the total temperature of the flow (K).

The first term on the right-hand side (RHS) of Eq. 10.6 describes the effect of flowpath area change on the Mach number; the second term on the RHS of Eq. 10.6 relates the heat addition and total temperature effect on the Mach number, while the last term relates the effect of frictional forces, such as shear stress, on the Mach number distribution. If we know the flowpath area change and total temperature distributions, dA/A and dTt/Tt, along with the shear stress distribution from the sensor measurements, then we can integrate Eq. 10.6 to obtain the 1-D Mach number distribution in the flowpath. This information can also be used to back out the density, Eq. 10.2 and pressure, Eq. 10.3 distributions, which can ultimately be used to estimate vehicle performance parameters such as thrust, combustion efficiency and specific impulse, based on a 1-D formulation.

A MEMS-based shear stress sensor lends itself for harsh environment applications for aerospace applications for the following reasons:

- MEMS-based sensors, in general, satisfy the SWaP requirements well, i.e. Size, Weight and Power, since they are small, non-intrusive size, very low weight with minimal power consumption, compared to their macro-sensor counterparts;
- fast response; and
- wide dynamic range.

Background

Shear stress sensors use either direct or indirect methods for shear stress detection (Haritonidis, 1989). In the direct method the tangential force, such as shear, acts on a surface floating balance, thus giving the shear stress directly (Dhawan, 1953; Mabey and Gaudet, 1975). The deflection of the floating element is then

© Woodhead Publishing Limited, 2013

proportional to the shear force. Typically, bulky, mass-spring-dashpot type skin friction gauges are utilized inside a test article at a single discrete location. These 'macro' skin friction gauges require active cooling to remain below an operating temperature of 520 K. Furthermore, when using these, there is a need to trade off sensor spatial resolution with the ability of measuring small forces, while also having the measurement being prone to increased uncertainty due to misalignment, pressure gradients, acceleration, vibration and thermal expansion.

For indirect shear stress measuring methods, the shear stress is obtained by making measurements that are related to shear stress through some physical principle, for example heat transfer or velocity gradient. Some indirect measuring devices include Preston tubes (Preston, 1954), Stanton tubes (Hool, 1993) and hot-wire/hot-film surface mounted sensors (Rubesin *et al.*, 1975). Flow sensors based on heat transfer methods have a common problem in that the heat losses to the wall or substrate beneath the sensor are generally unknown, thus affecting the sensor's performance. Their validity in complex flowfields and/or with high heat transfer rates can be compromised. Furthermore, most available sensors are greatly limited in operating temperature, mostly due to their material capabilities.

The micro-machined devices discussed in Papen *et al.* (2001), Liu *et al.* (1994) and Zhe *et al.* (2001) measured shear stress levels in the range that was far below the range encountered in the supersonic/hypersonic flowfield environments typical of hypersonic aero-propulsion wind tunnels and are not well suited for harsh environment applications.

By taking advantage of MEMS fabrication techniques, issues associated with spatial resolution, frequency response, acceleration, vibration and pressure gradient, can be mitigated, since we are able to develop a sub-millimeter-sized sensor element that has hardly any mass and can respond quickly to changes in the flow (McCarthy *et al.*, 2003). Numerous other researchers have investigated measuring shear stress (Hyman *et al.*, 1999; Pan *et al.*, 1999; Wang *et al.*, 1999; Jiang *et al.*, 2000; Li *et al.*, 2008).

Relevant harsh environment

As discussed earlier, the harsh environment relevant to the application of a MEMS shear stress sensor presented here includes high temperature (≥800 K) and oxidizing flowfield for a sensor that will be embedded in a test article that is installed in an aero-propulsion tunnel (Fig. 10.4). The static pressures are relatively low, typically about 700 to 7000 Pa, with total pressures as high as 1.4 to 2.1 MPa and total temperatures up to 1600 K.

Sensor design

Earlier we discussed the importance of systems engineering practice, defining requirements at the beginning of a design effort and realizing that these

© Woodhead Publishing Limited, 2013

requirements would change and even evolve into derived requirements, thereby potentially changing the original design concept. According to Tiliakos *et al.* (2006, 2008a,b) the MEMS shear stress sensor prototype design shall meet the following requirements:

- *high temperature survivability*: (up to 1300 K) and must survive an oxidizing, chemically reacting environment;
- *chemically non-reacting*: the sensor could not chemically 'interact' with the environment;
- *non-intrusive*: the sensor could not physically or transductively interact with the environment;
- *wide dynamic range*: (10–10 000 Pa); and
- *high frequency response*: the sensor must react in a time frame that is faster than the turbulent timescale.

The high temperature survivability requires that the eventual sensor be fabricated out of silicon carbide (SiC) on an SOI (silicon-on-insulator) wafer, discussed below. The fact that the sensor was MEMS-based, with dimensions in the order of microns, with very low mass in the order of mg, and was installed flush mounted, ensured that it allowed for a high frequency response and was non-intrusive. In addition, the wide dynamic range (10–10 000 Pa) requirement will be satisfied by closed feedback loop electronics.

Sensor theory of operation/design

The sensor configuration and its operating principles are illustrated in Figs. 10.6a and 10.6b. A tangential aerodynamic force, F_{shear}, is applied on the sensing element proportional to the local shear stress. This force, $F_{shear} = K\delta(x)$, is transmitted to a free-floating shuttle supported on springs (Figs 10.1a, 10.6b and 10.7). The springs consist of pairs of folded cantilever beams at each end of the shuttle (Figs 10.6b and 10.8). When the shuttle translates, the gaps between electrodes attached to the shuttle and stationary electrodes vary, leading to a change of electrical capacitance (δC) between the two structures. This change of capacitance was measured with external circuitry and converted into a voltage signal, V_{sensed} (Fig. 10.6a). To increase the range of shear applied before the movable shuttle contacts the stationary structures, an electrostatic counterforce is applied to the shuttle by applying a potential difference, $V_{control}$, between the stationary and movable electrodes (Fig. 10.6a). The device is then maintained in the central position (i.e. 'null' condition) and the actuation voltage becomes the output quantity, via closed loop feedback control circuitry. This electric force feedback is what enables the sensor to measure a relatively wide range of shear stress, 10 to 10 000 Pa, one of the requirements discussed earlier.

The overall sensor design process consisted of defining a sensor geometry, which provided a measurable output at the lowest level of shear, and sufficient

© Woodhead Publishing Limited, 2013

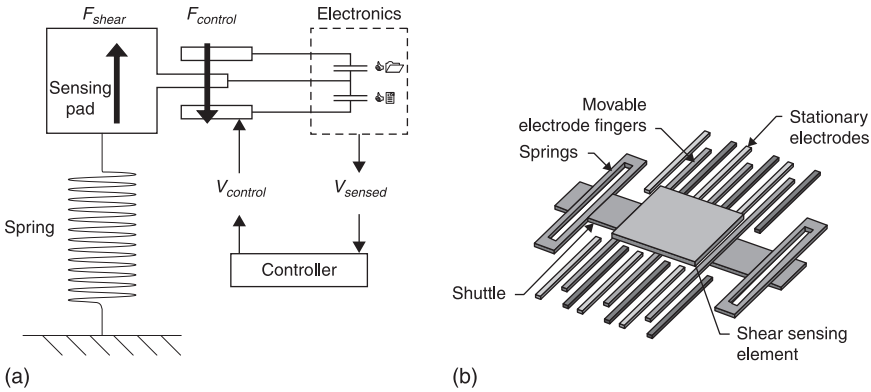

10.6 (a, b) MEMS shear stress sensor operating principle and configuration, discussed in (Tiliakos *et al.*, 2008a,b) (schematics obtained from Tiliakos *et al.* (2008a,b), courtesy of the author).

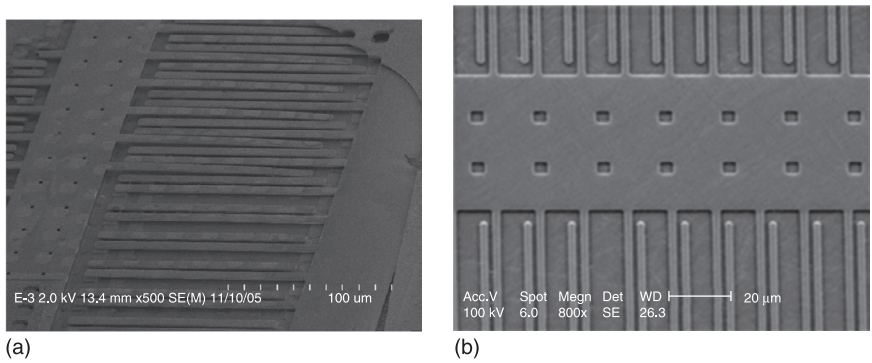

10.7 (a) SEM of MEMS shear stress sensor showing some of the fingers bending down, a result of inherent residual stresses; (b) SEM of improved design with minimal residual stress (photos courtesy of Tiliakos *et al.*, 2008a,b).

electrostatic force feedback to maintain the shuttle in a neutral position at the highest level of shear, all within the fabrication constraints imposed by the micro-fabrication technology, available circuitry and physical constraints. The surface micromachining process used set the thickness of each layer forming the device, but there was complete flexibility for the in-plane geometry, with minimum feature size of 2 microns. The sensor operation consisted of directly monitoring the shear force applied by the flow on a freely suspended sensing element flush, with the wall of an aero-propulsion wind tunnel nozzle at ATK GASL facilities in New York (Fig. 10.4b). The sensor was fabricated using MEMS micro-fabrication techniques and integrated the exposed sensing element, mechanical compliance,

© Woodhead Publishing Limited, 2013

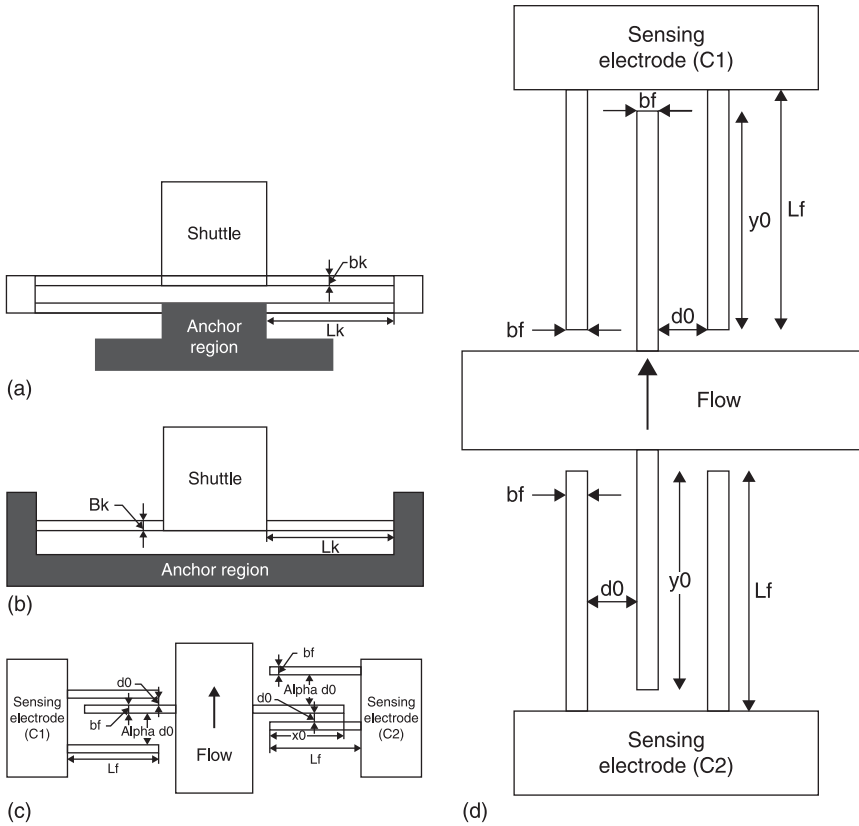

10.8 Spring configurations considered by Tiliakos *et al.* (2008a,b): (a) folded spring; (b) tensile spring; (c) perpendicular inter-digited finger orientation, w.r.t flow direction; (d) parallel inter-digited finger orientation (schematics obtained from Tiliakos *et al.* (2008a,b), courtesy of the author).

capacitive sensing and electrostatic force feedback on a chip. Each sensor had eight Ni contact pads (on the front sides, exposed to the flow) (Fig. 10.9), used to transmit sensor voltage signals to the data system and is discussed in detail in Tiliakos *et al.* (2008a,b).

Sensor design

In order to arrive at the current designs for the sensor element, various parameters were analyzed, such as:

- *spring type*: folded versus tensile beam springs (Fig. 10.8a,b);
- *parallel versus perpendicular finger layout* (Fig. 10.8c,d);

© Woodhead Publishing Limited, 2013

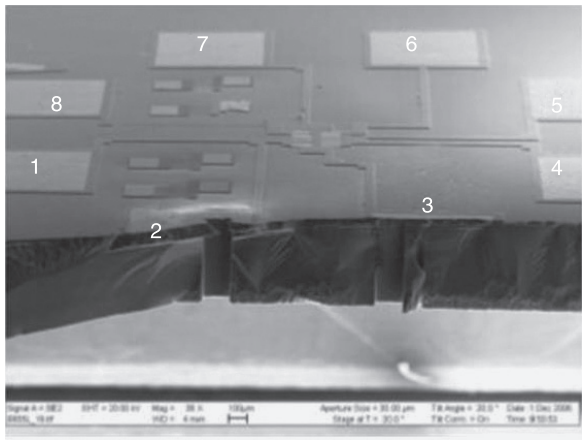

10.9 SEM photo of SiC film sensor element (cross-section) on 0.5 mm Si substrate showing pads (labeled numerically) and through-substrate vias for electrical connection (shown between pads '2' and '3') (photo obtained from Tiliakos *et al.* (2008b), courtesy of the author).

- *feature size*, i.e. 4 versus 8 μm thick structures;
- *number of electrodes/fingers*, N_f and finger length, L_f;
- *shuttle aspect ratio*: shuttle length to width ratio (L_s/w);
- *3 pad versus 4 pad layout*: (sense only versus sense and actuate);
- *finger width* × *finger gap options*: 2 × 2 μm and 3 × 3 μm.

The configuration for the two spring types, folded-beam design and the tensile-beam design, are shown in Figs 10.8a and 10.8b. The folded-beam design maximizes spring compliance, Eq. 10.7, while minimizing the spring length in the direction of displacement. However, the long beams are susceptible to the same out-of-plane bending from residual stress gradients as the shuttle fingers are (Fig. 10.7a). The tensile beam-design is less sensitive to stress gradients; however, 'spring-stiffening' can occur from the residual axial stress in the beam structures, Eq. 10.8 (Senturia, 2001).

$$K_{folded} = \frac{Ehb_k^2}{L_k^2} \qquad [10.7]$$

$$K_{tensile} = \frac{2Ehb_k^2}{L_k^2} \qquad [10.8]$$

where E = Young's modulus, h = device thickness, b_k = spring width and L_k = spring length. Two types of shuttle finger layouts were considered, parallel and perpendicular. In the perpendicular layout, the fingers are perpendicular to the

© Woodhead Publishing Limited, 2013

Table 10.2 Equations for the perpendicular and parallel MEMS shear stress sensor designs by (Tiliakos, *et al.*, 2008a,b)

Quantity formula	Perpendicular design	Parallel design
Differential capacitance	$dC(y) \approx 2N_f \varepsilon x_0 h \left[\frac{\alpha^2 - 1}{\alpha^2 d_0^2}\right] y$	$dC(y) = \frac{4N_f \varepsilon h}{d_0} y$
Sensitivity	$S = 2N_f \varepsilon x_0 h \left[\frac{\alpha^2 - 1}{\alpha^2 d_0^2}\right]$	$S = \frac{4N_f \varepsilon h}{d_0}$
Max. electrostatic force	$F \approx \frac{N_f \varepsilon x_0 h}{2} \left[\frac{\left(\alpha^2 - 1\right)}{\left(\alpha d_0\right)^2}\right] V^2$	$F = \frac{N_f \varepsilon h}{d_0} V^2$

N_f = number of fingers; ε = permittivity; x_0 = electrode overlap in x direction; y_0 = electrode overlap in y direction; d_0 = gap space; $\alpha = 4$ (gap spacing); V = applied voltage

flow and in the parallel layout, they are in line with the flow. A list of equations describing the relationship between the important parameters for each configuration is contained in Table 10.2. The perpendicular design necessitates that the stationary fingers are staggered with respect to the shuttle fingers, in order for a resultant electrostatic force to occur on the shuttle.

Sensor fabrication

To fabricate the harsh environment MEMS shear stress sensor, two main technologies were required: the SiC surface microfabrication process to form the shear sensor elements and a through substrate interconnect process to allow back-side packaging. As illustrated in Fig. 10.10, the SiC shear sensor is first fabricated using a surface micromachining/molding process in the top (device) layer of a SOI wafer. The interconnects are then formed through the silicon substrate to reach the under-side of the SiC sensors. Finally, the SiC device structures are released by removing the silicon that served as a mold for the SiC. The result is a chip with a SiC sensor element on one side that can be electrically contacted and packaged from the back side (Fig. 10.10), with the completed sensor, shown in Fig. 10.9 (Tiliakos *et al.*, 2008a,b), and completed sensor system, shown in Fig. 10.11.

Sensor packaging

Sensor packaging requirements are similar to sensor element requirements with regards to structural, temperature and environmental survival since, as is the case for the sensor element, the packaging will also be exposed to the flow.

© Woodhead Publishing Limited, 2013

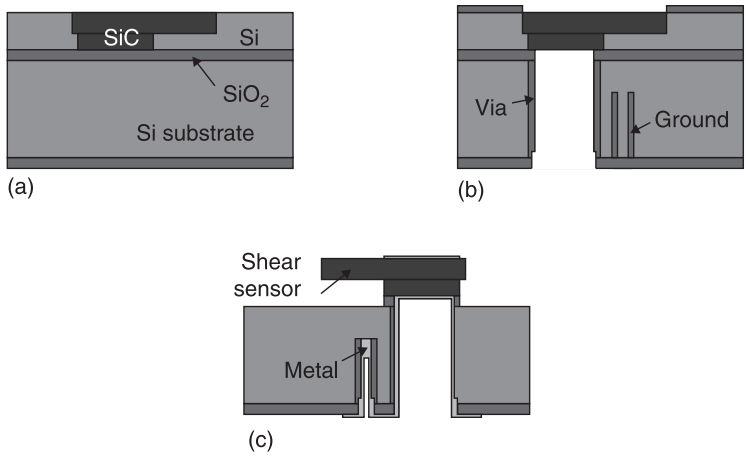

10.10 Fabrication of the MEMS shear stress sensor with through-substrate interconnection: (a) after SiC surface micromachining; (b) after through-substrate electrical interconnects; (c) final chip, after TSV metallization and release of SiC sensing element (Tiliakos *et al.*, 2008a,b).

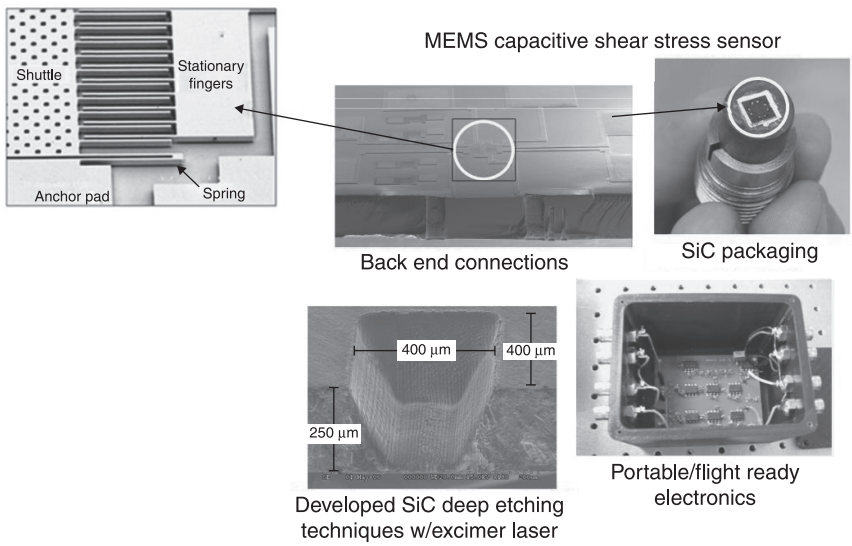

10.11 Photos of the entire MEMS shear stress sensor system (photos courtesy of Tiliakos *et al.*, 2008a,b).

The solution for the packaging was to leverage a proprietary process developed by the ATK team (Tiliakos *et al.*, 2008a,b), through which a die-pressed casting made of SiC was manufactured. The custom-made package conformed to the external square shape of the sensor element and allowed through holes (i.e.

© Woodhead Publishing Limited, 2013

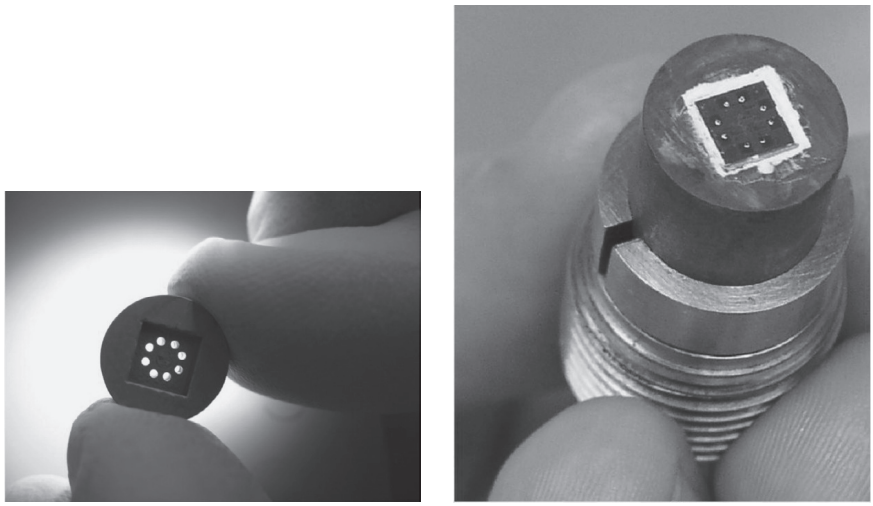

(a) (b)

10.12 Photos of the MEMS shear stress sensor element packaging: (a) SiC die-pressed pellet to hold sensor element; (b) complete assembly for installation into aero-propulsion tunnel at ATK, GASL, NY (photos obtained from Tiliakos *et al.* (2008b), courtesy of the author).

through silicon vias) to be created that matched the back-side pad pattern of the sensor chip. Figure 10.12 shows photos of the SiC die-pressed casting in which the sensor element was installed. The SiC casting material was pyrolized to temperatures over 1300 K during the forming process. Also shown in Fig. 10.12 is the full assembly in an inconel metal mounting fixture. The white filler material around the sensor element chip was custom-made ceramic filler based on SiC powder. Electrical connectivity was achieved by inserting small diameter wires through the holes in the SiC packaging and making contact with the metal pads on the under side of the sensor chip. Several wire types and high temperature electrically conductive epoxies were utilized to develop the best solution to this approach.

Sensor testing

Survivability in the high temperature, high shear environment of hypersonic flow is a challenging endeavor for any sensor, particularly a MEMS device exposed to the flow. As such, extensive cold testing, to calibrate the sensor, check out the various subsystems, the electronics, etc. were performed prior to hot-flow testing in aero-propulsion wind tunnels. Initial hot-flow tests were performed by Tiliakos *et al.* (2008a,b) with dummy sensor chips and SiC packaging pellets only, with the hardware and test fixture shown in Fig. 10.13. Testing was performed in an

© Woodhead Publishing Limited, 2013

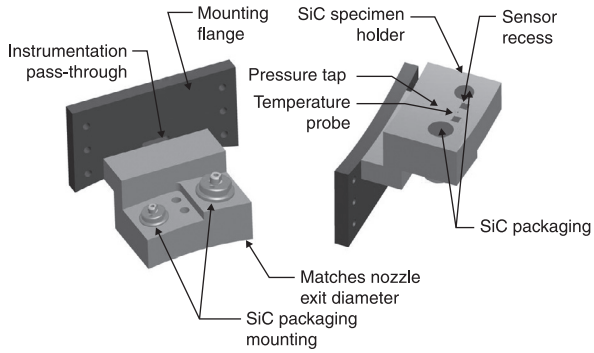

(a)

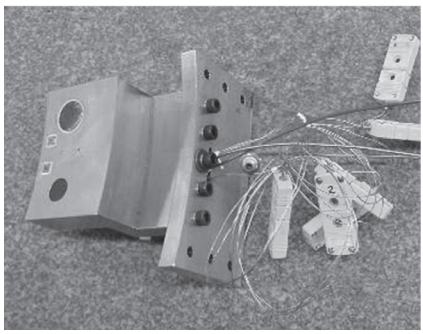

(b)

10.13 (a) Model drawings and (b) photo of the test hardware/fixture housing two dummy chip sensors and two packaging SiC pellet designs, installed for Mach 5 testing at ATK GASL, NY (photo obtained from Tiliakos *et al.* (2008b), courtesy of the author).

aero-propulsion wind tunnel at ATK GASL (Fig. 10.4a,b). The dummy sensor chips and SiC packaging pellets were mounted flush along the wall just downstream of a Mach 5 enthalpy facility nozzle (Fig. 10.4b). Pre-inspection and post-inspection photos of the samples, and further inspection of the sensor chips under the microscope, revealed no visible defects to the sensor chips or the SiC packaging pellets. Additional hot-flow testing of the assembled sensor unit shown in Fig. 10.11, in Mach 5 flow, also showed good survivability characteristics of the sensor element. Durations of the tests were from 45 to 90 sec. Shear levels were estimated at 500 to 700 Pa, with total temperature conditions at nearly 1000 K.

Voltage data from the shear stress sensor recorded for several hot-flow runs are shown in Fig. 10.14. Also shown are the predicted shear stress levels versus the Reynolds number determined from solving Eq. 10.9, and from using the measured pressure gradient at the sensor location. Well-established empirical formulations for the skin friction factor in smooth pipes or ducts is readily available in the

© Woodhead Publishing Limited, 2013

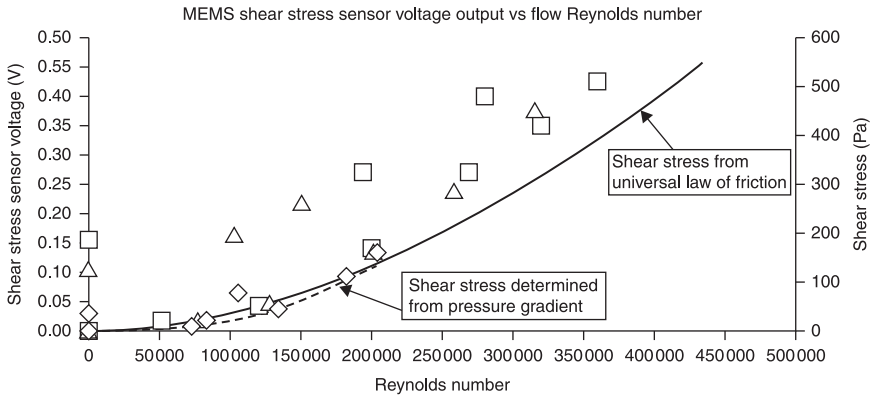

10.14 Shear stress sensor voltage data (symbols) from several runs, along with predicted shear stress levels using the universal law of friction equation and from the pressure gradient (data borrowed from Tiliakos *et al.*, 2008a).

literature, and thus can be leveraged to provide a referenced means of shear stress determination (Schlichting, 1979). According to Schlichting (1979), Prandtl's universal law of friction for smooth pipes provides an excellent empirical relationship for the determination of the shear factor in the case of very large Reynolds numbers, with this relationship being verified by the detailed measurements of Nikuradse, as well as others. The universal law of friction gives a straight line when $\frac{1}{\sqrt{\lambda}}$ is plotted against log (Re$\sqrt{\lambda}$), according to:

$$\frac{1}{\sqrt{\lambda}} = 2.0 \log\left(\frac{\bar{u}d}{\nu}\sqrt{\lambda}\right) - 0.8 \qquad [10.9]$$

where λ is the non-dimensional friction coefficient, equal to 64/Re, for laminar flow; Re is the Reynolds number equal to ρVD/μ; ρ is the fluid density (kg/m^3); V is the velocity (m/s); D(m) is a characteristic diameter of the circular pipe; and μ is the fluid absolute viscosity (Pa*sec). For non-circular pipes, the hydraulic diameter is used in place of the circular diameter, $d_h = \left(4A/\Pi\right)$, where A is the cross-sectional area and Π is the cross-sectional perimeter. As seen, the sensor voltage data closely follows both predicted shear stress level curves in the low Reynolds number range up to 200 000. For higher Reynolds numbers, the shear stress sensor voltages deviate from the curve predicted by Eq. 10.9. Hysteresis is observed for the shear stress sensor voltage as the flow in the pipe is stepped down from its maximum value. The level of hysteresis appears to be correlated with the maximum flow condition reached prior to reducing the flow rate, and may be attributed to a combination of environmental, mechanical and electrical issues.

Equation 10.9 was shown to be valid for subsonic and supersonic flow within pipes, and thus may be taken as our baseline for calibration purposes. Doing so,

© Woodhead Publishing Limited, 2013

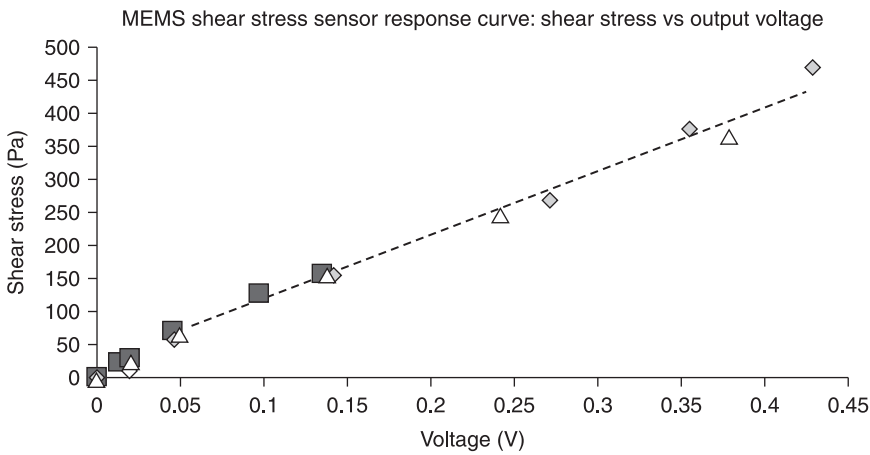

10.15 Response curve (shear stress vs voltage) for the MEMS sensor (data borrowed from Tiliakos *et al.*, 2008a).

and re-mapping the voltages versus the predicted shear stress, yields the response curve for the sensor (Fig. 10.15). Repeatability between the three different runs is good, and the results of Fig. 10.15 indicate that the response curve is slightly non-linear, near the voltage-low shear end of the graph. However, mostly the response curve is linear, which is expected since the capacitance linearly varies with the deflection of the shuttle (i.e. gap spacing between the stationary and moving fingers). Note that only the voltages measured during the flow-up condition are shown in the graph.

10.2.4 MEMS for thermal management in aerospace applications

Though electronics cooling/thermal management of electronics may not seem like an application that belongs in the category of 'harsh environment MEMS', the following should be considered. The trend in the heat fluxes, encountered by some current and future electronic devices (Ross, 2004), in the order of 10 to 100 W/cm^2, are comparable to the heat fluxes experienced, under certain conditions, by aerospace vehicles. Note that though the typical heat fluxes may be comparable, the static temperature over which these occur are drastically different, at most 450 K for electronics (Tummala, 2001) and more than 1200 K for certain aerospace platforms, for example rocket engines, gas turbine blades and hypersonic vehicle thermal loads (Fig. 10.3).

The demand for smaller, faster, more powerful consumer electronics is driving the need for faster CPUs, chips and electronics, which in turn is driving the quest for more innovative, capable and efficient thermal management techniques for

© Woodhead Publishing Limited, 2013

electronics cooling. The traditional approaches, for example natural convection, air cooled heat sinks and forced convection, are reaching their limits in terms of heat dissipation capabilities and HTC. The trend is now for thermal management technologies to provide higher HTCs, of more than 100 W/cm^2K, for heat fluxes in the order of 50 to more than 100 W/cm^2.

The field of consumer and military electronics is surging ahead with more sophisticated and powerful devices that are smaller and more portable than ever before. Such amazing technological advances also come with the challenge of cooling these power-hungry devices, in an efficient manner with ever-increasing constraints/requirements (e.g. lower weight, volume, cost and noise).

Some of the 'top-level' challenges encountered by MEMS devices for electronics cooling/thermal management are:

- to maintain low chip (junction) temperatures, below 390 K (though this could go as low as 360 K);
- high heat loads must be handled at the module level;
- better thermal control of the environment in which the electronic device is to be installed (e.g. the computer room, office space);
- to be able to deal with the overall rack heat load, competing requirements, higher performance, in smaller volume, harsh environment (high temperature, low pressure at high altitudes, vacuum/space, dust, etc.);
- application for military/aerospace electronics; and
- meeting competing requirements in a cost-effective way.

These challenges, and many others, become manageable by adopting and implementing a MEMS systems solution approach (Grace, 2010).

Some of the challenges of integrating and applying MEMS technology for electronics cooling, for example in heat sinks, include:

- Si/Cu CTE mismatch will lead to thermal and mechanical stresses, which contribute to fatigue and potential reliability issues;
- active MEMS based (e.g. synthetic jets, ionic fan) cooling methods require power consumption and therefore may be difficult to implement and be cost effective;
- humidity level, vibrational loads and particulate accumulation issues for aerospace electronics cooling at altitude;
- at altitude, the lower air densities lead to a decrease in the air flow rates available, requiring higher fan speeds or larger/noisier fans (Price and Short, 2007);
- materials incompatibility with refrigerants and solvents;
- MEMS component wear/tribology issues;
- necessity to keep MEMS fabrication costs low; and
- in the area of military/aerospace electronics, the military requirements in terms of temperature, service life and reliability are more stringent for thermal management than in the commercial sector.

© Woodhead Publishing Limited, 2013

MEMS for thermal management of aerospace electronics, though facing challenges, also offers potential creative solutions, since MEMS devices for electronics cooling can be integrated close to the heat source.

Much work has been and continues to be conducted in all areas of electronics cooling (e.g. forced air, liquid, jet impingement, spray cooling). Current electronics cooling technologies may seek to employ micro-pumps (Singhal, 2006), piezoelectric actuators (Sauciuc, 2007) or synthetic jets (Mahalingham *et al.*, 2007), to enhance cooling/heat transfer. While these technologies are promising, they also contribute to increasing the cooling system power consumption, as well as potentially requiring complex wiring. The focus of current state-of-the-art research in forced air cooling can be categorized in the following areas:

- improving heat fin design (e.g. pins, rectangular, ellipsoidal, etc.) (AAVID Thermalloy, 1996a,b; Short and Price, 2007);
- piezoelectric actuators (Sauciuc, 2007);
- micro-pumping technologies (Singhal, 2006);
- synthetic jets (Mahalingham *et al.*, 2007);
- fixed structures, for example dimples, attached to fins (Patrick, 2005); and
- advanced materials.

According to AAVID Thermalloy (1996a), staggered and augmented fins for air cooled systems can increase performance by 10% at 2 m/sec blower speed to 25% or more at 7.7 m/sec. AAVID Thermalloy (1996a) presents four distinct air cooled heat sink designs: standard rectangular fins; the control 'tuning fork' geometry, bent at certain locations with respect to the flow; bent fin model with three separate twisted sections that bend the flow; and flat fin heat sink cut to 120% of the control length. Test results show that the pressure drop for all four heat sink designs was similar, but the lowest overall system thermal resistance (0.08 K/W at 7.7 m/sec) was for the bent fin heat sink design. AAVID Thermalloy (1996a,b) presents similar discussion regarding augmented fins, noting that segmented heat sinks provide dramatic improvement in thermal performance, while limiting the pressure drop, ΔP penalty incurred. In the segmented or augmented-fin heat sinks, the fins are staggered, positioning the downstream leading edge of each fin section in the center of the air channel. Short and Price (2007) present some interesting results utilizing piezo fan technology, replacing conventional fan technology. The piezo fan technology relies on applying an alternating electric field to a piezoelectric material attached to a blade, resulting in a deformation of the piezo-material and an alternating blade motion. The vibratory motion generates air flow, used to cool electronics, serving to thin or disturb the boundary layer between the heat sink fins. Another option for MEMS in electronics cooling is synthetic jets (Mahalingham *et al.*, 2007), which are formed by the oscillation of a diaphragm bounding a cavity, producing an unsteady turbulent air jet. The diaphragm's oscillation can be achieved using piezoelectric and/or electromagnetic techniques. This approach offers significant increases in HTC and reduction in thermal resistance (~10%).

© Woodhead Publishing Limited, 2013

In the work outlined above, the researchers aim to provide heat transfer enhancements by thinning or perturbing the boundary layer in the heat transfer zone, at the expense of requiring additional power consumption. The challenge is to advance forced air cooling, for heat exchangers to provide cutting-edge thermal performance, while mitigating ΔP; any thermal management solution that requires increasing ΔP will ultimately be more costly, since fan or pump size/cost scales with increasing ΔP.

It is important that the thermal and MEMS engineers practice concurrent systems engineering practices, because integrating MEMS localized solutions into the cooling scheme may provide overall system performance improvements, with the challenges discussed earlier, albeit at the potential expense of subsystem performance. As an example, consider the heuristic Eq. 10.10, describing the overall system performance of a lap-top cooling system (Tiliakos, 2010):

$$\eta_{system} = \frac{Performance\left[f\ (Battery\ Life;\ \#\ Executable\ Instructions)\right]}{Average\ Total\ Power\ Consumption} = \left(\eta_{CPU}\eta_{Display}\eta_{cooling}\eta_{Battery}\right)$$

where η_{CPU}, $\eta_{Display}$, $\eta_{cooling}$ and $\eta_{Battery}$ represent the computer CPU, display, cooling subsystem and battery subsystem efficiencies, respectively $\overline{P}_c$ and represents the average power consumption of each CPU in the system. In Eq. 10.10, the CPU efficiency, $(\eta)_{CPU}$, is a function of CPU performance (i.e. number of instructions per second, voltage, number of nodes, operational frequency, heat dissipation, coefficient of performance of the heat sink fan and capacitance in the system). Equation 10.1 shows that the overall system performance and efficiency, η_{system}, is a function of the individual sub-systems' efficiencies. In addition, if the thermal engineer is willing to take a few percent decrement on the overall electronics cooling system efficiency, η_{system}, while simultaneously using a state-of-the-art battery (to maximize $\eta_{battery}$ or $\eta_{display}$, this may then allow utilization of less complex, less expensive and less efficient thermal management solutions, as long as the overall system performance still meets the system efficiency requirements. What this means is that it may make more sense to consider the system (not necessarily the subsystem) optimization as more important than $\eta_{cooling}$ when designing and/or selecting a thermal management technique. Optimization of the subsystems may not necessarily lead to an optimal system solution in terms of performance, cost and time to market; rather, strategic optimization of subsystem performance may be more worthwhile.

In summary, there are many opportunities for MEMS devices, for enabling better thermal management techniques for electronics cooling, whether they are employed as sensors (e.g. pressure, temperature) or actuators. The future in electronics cooling presents unique opportunities to the MEMS community for innovative solutions. Having also discussed the importance of a systems approach

© Woodhead Publishing Limited, 2013

to electronics cooling, it may be that future trends in providing innovative/cost effective thermal management techniques require hybrid cooling solutions that involve two different cooling techniques (MEMS or non-MEMS) in a 'staged' configuration. An example may be liquid cooling 'non-MEMS' techniques (2 phase) coupled with other MEMS based techniques (e.g. micro-channels, MEMS jet impingement or active air-cooled heat sinks). This also implies that integration of a MEMS-to-non-MEMS component solution will also require creative packaging technologies.

10.2.5 Packaging for harsh environment MEMS sensors

MEMS packaging serves a critical function, regardless of whether the environment is defined as 'harsh' or 'benign', which are of course relative terms. This function involves protecting the MEMS device from the environment, while at the same time enabling it to interface with the environment in a useful, sometimes non-intrusive manner, so it can accomplish its task, sensing and actuating. It is important to consider the packaging design and the design of the overall sensor and its subsystems, early on in the project, practicing concurrent engineering. The initial requirements need to be clearly cataloged, including the derived requirements, because in many cases they will drive the sensor and packaging designs together. It is also worth noting that MEMS packaging costs can take up to 70 to 80% of the overall product cost.

In the MEMS shear stress sensor design/development and testing effort conducted by Tiliakos *et al.* (2008a) discussed earlier, some of the major requirements of the packaging (Figs. 10.11 and 10.12) for that effort were high temperature survivability, minimal CTE mismatch between the sensor, adhesive and packaging, and compatibility with the environment. In many instances, these three 'top-level' requirements are relevant to all types of MEMS applications, but their derived requirements are application specific. For example, in the hypersonic/combusting environment for the MEMS shear stress sensor (Tiliakos *et al.*, 2008a), the derived requirements were based on the specific environment which, based on Computational Fluid Dynamics (CFD) and first-order engineering analysis, necessitated the following derived requirements:

1. Sensor/packaging/components must withstand an 800 to 1300 K oxidizing environment, with total pressures of up to 1.0 to 1.5 MPa and static pressures of up to 0.1 MPa;
2. Because of derived requirement (1), we had to minimize the CTE mismatch between all the sensor components to keep induced thermo-mechanical stresses to a minimum, to prevent unwanted component fatigue/cycling and also to mitigate spurious signals to the sensor generated from any induced stresses in both the MEMS sensor, its components and packaging. To keep the CTE mismatch to a minimum and/or to avoid it completely, only materials

© Woodhead Publishing Limited, 2013

with similar CTEs were selected, with the intent of keeping the number of different materials to a minimum; and

3. Compatibility with the environment means that the packaging will not chemically or electromagnetically react with the environment. This means that the packaging material must be chemically inert to the environment, with no surface reactions and/or catalytic reactions. Likewise, if the sensor is in an electromagnetic environment, induced electric fields in the packaging must be prevented, since these will likely interfere with the proper operation of the MEMS device and associated electronics, unless properly shielded. Another requirement, that was a direct consequence of the application, was that the MEMS shear stress sensor package (Figs. 10.11 and 10.12) had to be flush-mounted with the test article, to avoid any disturbance to the environment, that is, of the surrounding boundary layer. The MEMS package for the MEMS shear stress sensor, developed by Tiliakos *et al.* (2008a), was made as a monolithic piece, from SiC and survived testing at Alliant Techsystems (ATK GASL) aero-propulsion wind tunnels under the conditions of total temperature of 1220 K and total pressure of 1.5 MPa for 420 seconds continuous operation.

Packaging technology is categorized in terms of how the system interfaces with the environment, that is, capped and non-capped. Examples of MEMS products, which are typically sealed from the environment with a lid or cap, are accelerometers, gyroscopes and RF switches. For this type of packaging, hermetic sealing is a requirement, such that external gases, liquids, etc. are prevented from coming into contact with the MEMS device. The lids or caps are installed by various methods, including discrete assembly, wafer-to-wafer level bonding and wafer processing techniques (Evans, 2005).

In discrete assemblies, the MEMS system components are installed into the packaging and a lid is placed with special pick-and-place equipment. The materials used in the attachment process must be compatible with the overall system/package, with no outgassing into the MEMS structures (Evans, 2005). Wafer level bonding requires precise alignment of the MEMS wafer (which holds the MEMS devices) and a capping wafer. Bonding of the two wafers is typically performed in a gas or vacuum environment, with dicing leading to the final packaged MEMS devices.

Some of the packaging challenges include cost, size, induced stresses, electrical shielding, compatibility with environment, survivability, CTE mismatch, non-intrusiveness, inertness and reliability. In addition, contamination during assembly from particulates and providing a hermetically sealed packaging pose additional challenges. Selection of appropriate materials is critical to minimizing and eliminating some of these challenges (Gerke and Wesolek, 2006). Due to the high cost of MEMS packaging, many MEMS companies have transitioned from die-level packaging to wafer level packaging (WLP) (Frank, 2007). Also, the types of MEMs packaging varies, depending on the application, cost and the challenges that need to be addressed. Some of the packaging types include metal packages, ceramic, thin-film/multi-layer and plastic (Gerke and Wesolek, 2006).

© Woodhead Publishing Limited, 2013

This section provided a brief overview of MEMS packaging, its importance and some of the challenges. It may now be evident to the reader that the area of MEMS packaging poses a challenge that must be addressed on an application-specific basis, such that there is no general package solution. The reader is guided to the many useful references pertaining to MEMS packaging technology and techniques, some of which are cited in this chapter (Helvajian, 1999; Senturia, 2001; Tummala, 2001; Gerke and Wesolek, 2006).

10.2.6 MEMS inertial measurement: inertial measurement units (IMUs)

As discussed earlier, MEMS devices are compatible with the strict aerospace SWaP requirements. As with most aerospace systems, mission planners and engineers strive to minimize the size and weight of support systems, while attempting to maximize the payload to increase mission accomplishments/capabilities, and mitigating risks and hazards.

MEMS IMUs are providing tremendous technology-enabling features for the commercial market (e.g. smart cell phones, gaming equipment, cameras) and are increasingly attracting the attention of the aerospace/military sector. Harsh environment MEMS IMUs include the following aerospace applications:

- guidance, navigation and control (GNC) for high speed, high acceleration guided munitions, in the order of 1000 to 10 000 g, high-subsonic to supersonic speeds;
- GNC for re-entry spacecraft involved in entry, descent and landing (EDL) activities into planetary atmospheres, e.g. Mars entry;
- GNC activities on board small satellites/UAVs (Pollack *et al.*, 2009);
- weapons safe/arming and fuzing (Jones *et al.*, 1995; Pezous *et al.*, 2008);
- platform stabilization; and;
- personal (soldier)/vehicle navigation (Jones *et al.*, 1995).

One aerospace application, where MEMS technology is enabling and enhancing mission performance, is in the GNC of guided munitions, especially as a back-up to global positioning satellite (GPS) and as a primary GNC in GPS denied environments. There clearly are many aerospace applications where MEMS IMUs can play a vital role, as evidenced by the worldwide MEMS inertial sensing market having dramatically increased in the past 10 to 15 years, from about US$250 million of sales in 1995 to over US$2.5 billion sales in 2000 (Jones *et al.*, 1995). For MEMS IMU applications, the relevant harsh environment includes:

- very high and impulsive acceleration, on the order of 1000 to 100 000 g;
- space radiation environment, i.e. spacecraft/satellite GNC activities require radiation hardened electronics;
- potentially high temperatures, but typically less than the temperatures allowable for electronics;

© Woodhead Publishing Limited, 2013

- significant electro-magnetic interference (EMI) due to electronics jamming activities from an adversary; high vibrational loads: 20 to 3000 Hz (for 5–20 g) (El-Fatatry, 2004); and
- angular accelerations of >500 000 rad/s^2 for spinning gun launched munitions (El-Fatatry, 2004).

Not just the MEMS IMU device, but the entire *system*, such as associated electronics, antennas, power supplies, etc. must be compatible with this harsh environment. Note that a MEMS IMU would include some combination of accelerometers and gyroscopes.

Most US weapons use unguided ordnance, thereby requiring multiple rounds to ensure that a target is destroyed, resulting in increased risk of unwanted casualties, friendly fire, high ammunition usage rates, high cost and increased logistics. It has been shown (Jones *et al.*, 1995) that implementation of MEMS IMUs into munitions would result in a 10× reduction in required ordnance and a dramatic increase in hit probability, especially when combined with GPS technology, which provides affordable precision strike attributes without expensive ancillary equipment. Thus, MEMS technology becomes an enabler for better performing aerospace systems, with a significant positive impact on system cost, reliability and mission success. In many cases, because MEMS meets the SWaP requirements, existing munitions can be retro-fitted to accommodate the MEMS IMU subsystems into the overall aerospace platform. The estimated US Department of Defense (DoP) market for these 'smart munitions', such as precision guided munitions (PGMs) is 16 million units total, with an annual peacetime requirement of 250 000 to 500 000 units (Jones *et al.*, 1995). An example of existing, state-of-the-art smart guided munitions are ATK's precision guidance kit (PGK), which transforms existing artillery munitions (e.g. 155 mm) into 'smart munitions' by:

- integrating GPS-guided electronics into munitions deep fuze well;
- allowing the munition to generate its own power (no battery required); and
- combining guidance and fuzing into one device. Presently, this kit does not incorporate MEMS technology (Tiliakos, 2011).

Most PGMs today depend almost exclusively on GPS for positioning and navigation. There are many environments where GPS is denied, and in these instances MEMS IMUs could play a critical/enabling role. If military forces are operating in areas where GPS would be compromised (e.g. wooded/urban areas, inside buildings, under-water, etc.), then real-time positional data cannot be obtained without risking the mission and personnel by exposing themselves for better GPS data. Besides these environments, there are issues with GPS, including GPS receivers which must have a direct view of four satellites in order to acquire a 3-D positional fix. Even with four satellites in view, positioning information errors could occur, depending on the satellites' position, thereby possibly necessitating the need for more than four satellites to increase GNC accuracy

© Woodhead Publishing Limited, 2013

(Jones *et al.*, 1995). MEMS IMUs, with their low weight/size and minimal power consumption can provide a relatively inexpensive augmentation to GPS as a secondary system by providing updated data based on an initial GPS reference point, or as a primary system in GPS-denied environments. The MEMS IMU could also provide continuous data in the event of the GPS jamming or experiencing the issues discussed above (Jones *et al.*, 1995).

Regarding GNC for re-entry spacecraft involved in EDL activities into planetary atmospheres, for example Mars entry; past and present NASA missions to Mars have landed relatively light payloads, less than 1 metric ton. Future NASA missions have begun focusing on requiring the spacecraft to safely land 20 to 60 tons of payload onto the Martian surface, which will require enhanced EDL technology improvements (Adler *et al.*, 2010). In addition, the mission safety, reliability and performance will continue to be major requirements for all future NASA EDL systems. Some of NASA's EDL activities, which will require enhanced GNC improvements to the current state-of-the-art, include autonomous landing operations/GNC, hazard avoidance, precision landing, aero-capture and entry, advanced and reliable event triggers (e.g. parachute deployment, heat-shield jettison, descent phase initiation and precision landing) and manned autonomous landing operations (Adler *et al.*, 2010).

An example of a state-of-the-art MEMS IMU is shown in Fig. 10.16, by Milli Sensor Systems and Actuators (MSSA), which integrates high performance, single-degree-of-freedom MEMS gyroscopes and accelerometers on the same chip (McGeehon, 2009). The MSSA IMU instruments, the three MEMS gyros and six MEMS accelerometers, can be operated by programmable digital, field programmable gate array (FPGA) based or SOC-based control electronics, allowing them to be adaptable before and during the flight, providing re-calibration opportunities in a dynamic environment. These instruments can also operate in high-g environments. The combination of the sensor chip and digital electronics

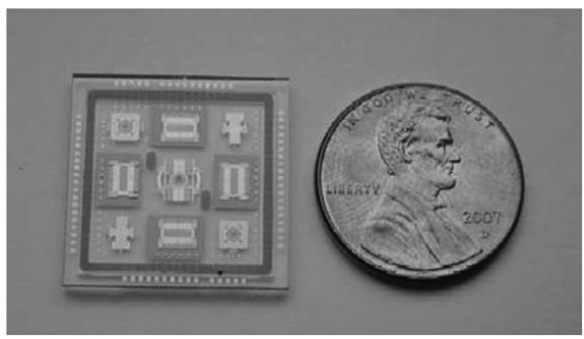

10.16 MSSA MEMS IMU sensor chip, housing three MEMS gyroscopes and six MEMS accelerometer on a chip the size of a US penny (photos courtesy of MSSA and Pollack *et al.*, 2009).

© Woodhead Publishing Limited, 2013

permits the complete MEMS IMU to be packaged in an enclosure the size of three-quarters, or integrated into the navigation system as a chip set. The single MEMS IMU sensor chip enables integration of inertial measurement with complementary navigation sensors in very small packages. The size of the single MEMS IMU sensor chip is in the order of a US penny (Fig. 10.16). The MEMS IMU sensor chip has planar *x*, *y* and *z*-axis gyroscopes and accelerometers in a single vacuum package. The three gyroscopes (arranged on a diagonal, from top left to bottom right) and the six accelerometers (Fig. 10.16) (doublets for each axis, in order to take out the effects of rotation) are all single degree of freedom instruments with very low cross-axis sensitivity and high-scale factor linearity. All instruments are aligned by the photo-mask to the precision of photolithography. The Pyrex substrate and cover provide mechanical and temperature stability.

Reliability is achieved by addressing the major IMU error sources in the design of the MEMS IMU sensor chip. Single degree of freedom designs, integration of all the instruments on the same chip, alignment of all the instruments on-chip, a single vacuum package, the use of materials to minimize mechanical and temperature instability minimize bias errors, offsets and scale factor errors, will allow for enhanced mission reliability, mission safety and performance. Built-in calibration permits monitoring the state of IMU performance, while vibration control and ruggedness maintains continuous operation of the IMU. The programmability of this MEMS IMU enables the rapid development, implementation and evaluation of new systems architectures for new missions. The features of the programmable MEMS IMU support 'mission-awareness' in hardware that complements the use of robust and adaptable models for sensor fusion to accomplish precision navigation and maneuvers. The system designer has direct control over parameters such as turn-on/turn-off, sampling rates, drive amplitudes, excitation frequencies, signal processing, filtering, data processing and data rates, for each gyroscope and accelerometer on the MEMS IMU chip (Fig. 10.16).

By calculating spacecraft position, velocity and heading (with corroboration from other on-board sensors, e.g. altimeters, Doppler radar), the spacecraft's real-time Mach # along with the corresponding trajectory dynamic pressure, can trigger an event by using these two pieces of information (e.g. supersonic parachute deployment, subsonic parachute deployment, heat-shield jettison, etc.). Such event triggering, using MEMS IMUs, will be more precise and accurate compared to event triggering based on timers. Coupled with corrective-predictive algorithms, trajectory dispersions will be reduced, thereby increasing mission reliability, success and improving safety.

An integrated MEMS IMU system designed for EDL activities will allow for real-time inputs from various on-board sensors (flush air data system, altimeter/laser/Doppler, etc.). Using the external sensor information (e.g. altitude data), the on-board atmospheric properties database for the planet (e.g. Mars) can be accessed, providing Martian pressure, temperature and altitude information. In

© Woodhead Publishing Limited, 2013

addition, the MEMS IMU system provides spacecraft velocity, acceleration and heading information. Knowing the density, pressure, temperature and spacecraft velocity, the spacecraft's dynamic pressure and Mach # state can be calculated. This derived information (derived from the interaction of external sensors with the MEMS IMU system) is then used in the spacecraft's on-board GNC computer to determine if an event trigger (based on Mach # and/or dynamic pressure) should occur. Event triggering off of the actual local/real-time environment is more accurate and reliable than triggering off a timer which, even if off by 1 to 2 seconds, could be extremely detrimental to the mission success since, at hypersonic or supersonic speeds, this delay would mean that the spacecraft has already traveled a distance in the order of several kilometers away from the required landing event point. In addition, for timed triggers, the spacecraft state estimate is reliant upon pre-flight predictions, which could be off.

10.3 Conclusion and future trends

While it is impossible to forecast the path of such an enabling technology as MEMS, one thing is certain: MEMS technology opens the engineers' imagination to a host of applications that it can enable, ranging from consumer products, for example cell phone image stabilization, to military/aerospace products, for example safer and more accurate munitions with MEMS IMUs.

This section will provide a brief overview of the tremendous mission enabling opportunities for MEMS in the aerospace field. The aerospace market, as discussed earlier in this chapter, is presently characterized by relatively low volume (10s to 10 000s of devices . . . not millions) but high price point on the order of 10s to 100s of US dollars per device versus pennies per device in the commercial sector. It is the author's opinion that, currently, the lack of clear aerospace standards for MEMS, both from the design/fabrication process to reliability/quality assurance, presently makes widespread acceptance of MEMS in the aerospace industry a challenge. However, this challenge can and should be addressed by a coordinated effort between the MEMS/aerospace industries, professional engineering societies and the relevant government agencies. Attempts have been made to provide judicious guidelines for MEMS devices in space applications (Stark, 1999). The reason why this is important is because the 'if it isn't broke, why fix it attitude' prevalent in the aerospace industry may change to: 'if we can use MEMS to make the system more reliable, cost effective and better performing, why not?' attitude. Once this occurs, MEMS will begin to gain more widespread acceptance in the aerospace industry, potentially allowing, for example, smart aircraft skin embedded with MEMS sensor systems that monitor the aircraft's structural health, while at the same time harvesting energy from the environment. This will require changing how the aerospace engineer views the aircraft structure and being convinced that the reliability and cost of this structure will not be adversely affected by the introduction of these 'smart', albeit potentially intrusive, MEMS devices into the aircraft.

© Woodhead Publishing Limited, 2013

In general, it is the author's belief that future trends of MEMS in aerospace applications will require the need for merging more capabilities into the MEMS system, such that fused mechanical, electrical, chemical and computational attributes will be the hallmark for these future MEMS devices, while increasing their reliability at a reasonable/competitive cost. In addition, MEMS may also serve as an enabler for nanotechnology devices, providing a bridge for nano-devices to interface with the macro-world, via the MEMS system. These future trends can be organized into the following broad category of applications.

10.3.1 Instrumentation/sensing

This category of applications can be further categorized into chemical, mechanical and fluidic sensors. In the area of chemical sensors, we can imagine MEMS chemical gas emission sensors integrated into gas turbine jet engines that will monitor the engine for fuel efficiency and optimal performance via feedback control and smart algorithms. Another application would be to utilize MEMS chemical sensors on aircraft for leak detection of hazardous substances. In the area of mechanical/fluidic sensors, MEMS skin friction sensors may be integrated into a suite with temperature and pressure sensors that can monitor various conditions inside the gas turbine engine (embedded in the casing or turbine blades) or external to the aircraft or missile. The sensors would detect possible ice build-up or other parameters of interest. For missile applications and smart bullets, it is conceivable that MEMS sensors would detect a condition on the missile body that would require actuation, forming an intelligent 'micro-adaptive flow control-on-a-chip' system. Such micro-adaptive flow control for missiles and small bullets is an application area of current and future interest. MEMS shear stress, pressure, temperature and heat flux sensors continue to be of interest for aerospace ground test/evaluation facilities, and will likely see more widespread application to flight articles. MEMS IMUs will also continue to draw interest for guidance, navigation and control applications for missiles and aerospace platforms in GPS denied environments. A future squadron of UAVs may utilize all types of MEMS suites, from chemical sensors to camera stabilization devices, to MEMS IMUs for autonomous fueling and autonomous flight operations.

10.3.2 Actuation

MEMS actuators by themselves have utility; however, when combined with MEMS sensors and a robust algorithm, could tremendously enhance an aerospace platform's performance and reliability. As mentioned above, smart micro-adaptive flow control is one area where MEMS actuators can be applied where we can imagine smaller, more accurate munitions, such as small projectiles or bullets that can accurately guide and steer their way to a target, thereby increasing mission success and minimizing friendly fire and collateral damage. Advanced engine fuel injection schemes for finer propellant atomization may benefit from MEMS sensors and actuators.

© Woodhead Publishing Limited, 2013

10.3.3 Energy harvesting

Energy/power harvesting is an area where MEMS may not only help enable but also will stand to benefit from as well. The only way to make MEMS systems in remote locations (aerospace platforms, underwater, bridges, etc.) economical, practical and implementable, is to provide them with energy harvesting subsystem capabilities, thereby reducing their maintenance needs for replacing batteries once they are depleted. Energy harvesting via solar, piezoelectric, electromagnetic, electrostatic and other means will provide opportunities for enabling MEMS sensor suites on aerospace platforms.

10.3.4 Smart aerospace structures/structural health monitoring

As mentioned earlier, embedded MEMS sensor suites within an aerospace vehicle's structure have many positive implications, but will have to pass several engineering attitude, cost and implementation hurdles. One area of health monitoring could be the monitoring of ammunition/ordnance depots on military bases, etc., where an array of MEMS sensors will ensure safe storage, transportation and accurate inventory of these vital systems. In addition, structural health monitoring of vital components in an aerospace system will ensure safe, reliable and cost-effective long-term performance of that system.

10.3.5 Wireless MEM/smart adaptive algorithms/ sensor fusion

Wireless MEMS is already an area of great interest and will continue to be in the foreseeable future, enabling most of what was discussed above. In addition, smart/ adaptive algorithms 'fused' into the MEMS sensor suite will help manage the tremendous amount of data gathered by these ubiquitous devices. This data will have to be coordinated with advanced algorithms, which monitor the appropriate times to record and transmit data, as well as power down the MEMS systems/ nodes for power conservation. In addition, programmability will allow the system designer to decide how best to reconfigure the MEMS system to handle different tasks, which will allow these systems to be more robust and adaptive to changing system needs and applications.

10.4 Sources of further information

There is an enormous array of references, journal publications, conference papers/ proceedings, and government roadmaps on MEMS, which all we have to do is 'google' the word MEMS to see. Some of the more established, though by no means the only publications, include the *IEEE Journal of Microelectromechanical*

© Woodhead Publishing Limited, 2013

Systems (JMEMS), *Sensors and Actuators Journal*, *MEMS Investor Journal* and others. Some of the heritage papers by Peterson (1986) and books by Senturia (2001), Tummala (2001), Kovacs (1998), Madou (2002) and Helvajian (1999) are notable references in MEMS sensors, packaging, MEMS transducers overview, micro-fabrication and aerospace systems, respectively (Van Heijster and Keizers, 2003; Wilson, 2011).

The author recommends for those just starting in MEMS to first take a course in MEMS that is part of a conference or offered by a professional engineering society, to obtain a good overview of the field. There are numerous MEMS conferences throughout the year in Europe, Asia and North America, which cover all aspects of MEMS for aerospace applications. Some of these conferences are sponsored by professional bodies such as ASME (American Society for Mechanical Engineers), IEEE (Institute of Electrical and Electronics Engineers), AIAA (American Institute for Aeronautics and Astronautics) and others (Osiander and Darrin, 2006). In addition, there are many outstanding academic research groups throughout the world working on MEMS technology for aerospace applications. In addition, some excellent on-line magazines that address MEMS include *Small Times*, *ElectroIQ* and *MEMS Investor Journal*. Some excellent websites include:

- http://www.grc.nasa.gov/WWW/sensors/
- http://www.memsnet.org/links/
- http://www.trimmer.net/

10.5 References

AAVID Thermalloy (1996a), Augmentation Improves Thermal Performance of Air Cooled Heat Sinks. Available at: http://www.seekic.com/mfg/4-Aavid/Application/36-Augmentation_Improves_Thermal_Performance_of_Air_Cooled_Heat_Sinks.html

AAVID Thermalloy (1996b), Augmented-Fin Air Cooled Heat Sinks. Available at: http://www.seekic.com/mfg/4-Aavid/Application/37-_AUGMENTED_FIN_AIR_COOLED_HEAT_SINKS_.html

Adler M, Wright A, Campbell C, Clark I, Engelund W, *et al.* (2010), *Draft Entry, Descent, and Landing Roadmap-Technology Area 09*, NASA, November.

Dhawan S (1953), *Direct Measurements of Skin Friction*, NACA TN 2567.

El-Fatatry A (2004), *MEMS Aerospace Applications*, NATO RTO Educational Notes, EN-AVT–105.

Evans D D (2005), 'Advances in MEMS packaging-design considerations', *ElectroIQ*, 13(4). Available at: http://www.electroiq.com/articles/ap/print/volume–13/issue–4/features/cover-story/advances-in-mems-packaging.html

Frank R (2007) 'Packaging Edges into the Spotlight', *Small Times*.

Gerke R D and Wesolek D M (2006), 'MEMS packaging for space Applications', in R Osiander, M Darrin and J L Champion, *MEMS and Microstructures in Aerospace Applications*, New York: Taylor and Francis Group, pp. 269–287.

Grace R (2010), 'Think outside the chip: MEMS-based systems solutions', *Sensors*, 30 April.

Haritonidis J H (1989), 'The measurement of wall shear stress', in *Advances in Fluid Mechanics Measurements*, Berlin and New York: Springer-Verlag, pp. 229–261.

© Woodhead Publishing Limited, 2013

Helvajian H (1999), *Microengineering Aerospace Systems*, California: The Aerospace Corporation.

Hool J H (1993) 'Measurement of skin friction using surface tubes,' *Aircraft Eng*, 28, 52.

Hyman D, Pan T, Reshotko E and Mehregany M (1999), *Microfabricated Shear Stress Sensors, Part 2: Testing and Calibration*, Vol 37, No 1.

Jiang F, Lee G B, Tai, Y C and Ho C M (2000), 'A flexible micro-machine-based shear stress sensor array and its application to separation-point detection', *Sensors and Actuators Journal*, 79, 194–203.

Iverson B D, Garimella S and Singhal V (2006), 'Micropumping technologies for electronics cooling', *Electronics Cooling*, 1 May.

Jones A, Flamm K, Gabriel K, Van Atta R and Mareth L (1995), *Microelectromechanical Systems Opportunities*, A Department of Defense dual-use technology industrial assessment.

Kovacs G (1998), *Micromachined Transducers Sourcebook*, New York: WCB McGraw-Hill.

Li Y, Chandrasekharan V, Bertolucci B, Nishida T, Cattafesta L and Sheplak M (2008), 'A MEMS shear stress sensor for turbulence measurements', A.I.A.A. 2008–269 conference paper, *46th A.I.A.A Aerospace Sciences Meeting and Exhibit*, Reno, NV, USA.

Liu C, Tai Y C, Huang J B and Ho C M (1994) *'Surface Micromachined Thermal Shear Stress Sensor', The 1st ASME Symposium on Application of Micro-Fabrication to Fluid Mechanics*; pp. 9–15.

Mabey D G and Gaudet L (1975), 'Some performance of small skin friction balances at supersonic speeds', *J Aircraft*, 12., 819–825.

Madou M (2002), *Fundamentals of Microfabrication*, New York: CRD Press.

Mahalingham R, Heffington S, Jones L and Williams R (2007), 'Synthetic jets for forced air cooling of electronics', *Electronics Cooling*, 13(2), May.

McCarthy M, Frechette L G, Modi V and Tiliakos N (2003), 'Initial development of a wall shear stress sensor for propulsion applications', in *Propulsion Measurement Sensor Development Workshop*, 12–13 May, Huntsville, AL.

McGeehon D (2009), 'Improving positional accuracy', *MDA TechUpdate*.

Osiander R and Darrin M (2006), 'Reliability practices for design and application of space-based MEMS', in R Osiander, M Darrin and J L Champion, *MEMS and Microstructures in Aerospace Applications*, New York: Taylor and Francis Group, pp. 327–367.

Pan T, Hyman D, Mehregany M, Reshotko E and Garverick S (1999), *Microfabricated Shear Stress Sensors, Part 1: Design and Fabrication*, Vol 37, No 1.

Papen T V, Ngo H D, Obermeier E, Schober M, Pirskawetz S, *et al.* (2001), 'A MEMS Surface Fence Sensor for Wall Shear Stress Measurement in Turbulent Flow Areas', in Proceedings of the 11th International Conference on Solid-State Sensors and Actuators, Transducers '01, vol. 2, Munich, Germany, 10–14 June, pp. 1476–1479.

Patrick W V (2005), 'Computations of Flow Structures and Heat Transfer in a Dimpled Channel at Low to Moderate Reynolds Number', MSc Thesis, Virginia Polytechnic Institute, VA.

Petersen K (1986), 'Silicon as a mechanical material', *MRS Proc*, 76, 99.

Pezous H, Sanchez M, Mathieu F, Dollat X, *et al.* (2008), 'Fabrication, assembly and tests of a MEMS-based safe, arm and fire device', *Proceedings of Power MEMS*, Japan.

Pollack J M, Hansen L J, Cardarelli D and Graven P (2009), 'Plug-N-Play (PnP) Micro-Electro-Mechanical System (MEMS) Inertial Measurement Unit (IMU): an enabling technology for small satellites', *23rd Annual AIAA/USU Conference on Small Satellites*.

Preston J H (1954), 'The Determination of turbulent skin friction by means of pitot tubes', *J R Aero Soc*, 58, 109–121.

© Woodhead Publishing Limited, 2013

Price D and Short B E (2007), 'Air-cooled, pin fin coldwall design for operation at altitude', *Electronics Cooling*, 1 August.

Robinson C H, Wood R H and Hoang T Q (2001), 'Development of inexpensive, ultra-miniature MEMS-based safety and arming (sanda) device for small-caliber munition fuzes', *US Army Tank Automotive Command (TACOM)*, Armament Research, Development and Engineering Center (ARDEC) Fuze Division, Adelphi, MD.

Ross P E (2004), 'Beat the heat', *IEEE Spectrum*, 41(5), 38–43.

Rubesin M W, Okuno A F, Mateer G G and Brosh A (1975), 'A hot-wire surface gauge for kin friction and separation detection measurements', *NASA TM X–62*, p. 465.

Sauciuc I (2007), 'Piezo actuators for electronics cooling', *Electronics Cooling*, 1 February.

Schlichting H (1979), *Boundary Layer Theory*, New York: McGraw-Hill.

Senturia S D (2001), *Microsystem Design*, Boston, MA: Kluwer Academic Publishers.

Short B E and Price D C (2007), 'Air-cooled, pin fin coldwall design for operation at altitude', *Electronics Cooling*, 13(3), 1 August.

Singhal V, Iverson B and Garimella S V (2006), 'Micropumping Technologies for Electronics Cooling', *Electronics Cooling*, 1 May 2006.

Smart M (2008), 'Scramjets', in Advances in Propulsion Technology for High Speed Aircraft, Educational Notes RTO-EN-AVT–150, 9(1), 9–38.

Stark B (1999), 'MEMS reliability assurance guidelines for space applications', *NASA JPL* 99(1), 1–312.

Tiliakos N, Papadopoulos G, Modi V, O'Grady A, McCarthy M, *et al.* (2006), 'MEMS Shear Stress Sensor for Hypersonic Aeropropulsion Test and Evaluation', in *Annual ITEA Technology Review*, Boston, MA.

Tiliakos N, Papadopoulos G, O'Grady A, Modi V, Larger R, *et al.* (2008a), 'Preliminary testing of a MEMS-based shear stress sensor for high speed flow applications', AIAA–2008–3948 paper, *26th AIAA Aerodynamic Measurement Technology and Ground Testing Conference*, Seattle, WA.

Tiliakos N, Papadopoulos G, O'Grady A, Modi V, Larger R, *et al.* (2008b), 'A MEMS-based shear stress sensor for high temperature applications', *46th AIAA Aerospace Sciences Meeting and Exhibit*, Reno, Nevada.

Tiliakos N (2010), 'MEMS-based system solutions for electronics cooling', *Micro Tech Conference*, Anaheim, USA.

Tiliakos N (2011), 'High-volume opportunities for MEMS in military applications: fuzes and guided munitions', *Sensors Tech Forum*, Boston, MA.

Tummala R R (2001), *Fundamentals of Microsystems Packaging*, New York: McGraw-Hill.

Van Heijster R and Keizers H (2003), 'Future trends for the application of MEMS in missiles and gun launched munitions', *RTO-MP–104 Conference Paper for AVT Symposium on Novel Vehicle Concepts and Emerging Vehicle Technologies*.

Wang X Q, Han Z, Jiang F, Tsao T, Lin Q, et al. (1999), 'A fully integrated shear stress sensor', *Proceedings of Transducers '99 Conference*.

Wilson J R (2011), 'The future of precision-guided munitions', *Military and Aerospace Electronics*, 1 December.

Zhe J, Farmer K R. and Modi V (2001), *'A MEMS Device for Measurement of Skin Friction with Capacitive Sensing*', Department of Mechanical Engineering, Columbia University, New York and Microelectronics Research Center, NJIT, Newark, NJ.

© Woodhead Publishing Limited, 2013

11

MEMS thrusters for nano- and pico-satellites

P. LOZANO, Massachusetts Institute of Technology, USA

DOI: 10.1533/9780857096487.2.283

Abstract: Nano- and pico-satellites are extraordinarily small spacecraft with masses and volumes of about 1 kg and 1 liter, respectively. Their inexpensive nature and relative ease for deployment has made them popular for increasingly challenging missions. The full potential of these satellites will only come to fruition if they are equipped with high-performance subsystems. Of these, propulsion has been challenging to scale down, given the stringent physical constraints associated with space thrusters. The fundamental principles of chemical and electric propulsion and their miniaturization potential are described in the context of the suitability of MEMS techniques in their design and manufacturing.

Key words: nano-satellites, pico-satellites, propulsion, electric propulsion, electrosprays, MEMS propulsion, ion engines, micropropulsion.

11.1 Introduction

Launched in 1957, Sputnik, the first man-made object to orbit the Earth, was by today's definition a small satellite. At about 80 kg, its capabilities were limited to the transmission of simple radio signals that went silent when the batteries, originally delivering a few watts, stopped working 22 days after launch. Since then, space capabilities, triggered first by political agendas and later by economic opportunity, have grown in a significant way. The most powerful and profitable satellites of today are platforms with in-orbit masses of several tons and power levels measured in tens of kilowatts. In the traditional space model, larger is better since improved capabilities have been associated with large, powerful satellites. This trend has also implied an increase in the cost of manufacturing, launching and maintaining space systems, limiting their development to a handful of nations and specialized large corporations.

However, the traditional model is currently being complemented, and sometimes even challenged, by recent technological developments and innovations. In particular, advances in MEMS have set in motion a number of different avenues, with the goal of miniaturizing spacecraft subsystems and payloads. This has become a motivation to take a fresh look at the traditional model and consider seriously the benefits of using smaller and cheaper satellites. 'Small' is, of course, not a well-defined word in this context but, in general, the community considers small satellites as those with in-orbit masses smaller than about 500 kg. In this broad category lies a subset that includes nano- (1–10 kg) and pico- (0.1–1 kg) satellites (Fig. 11.1). Smaller satellites are known as femto-

© Woodhead Publishing Limited, 2013

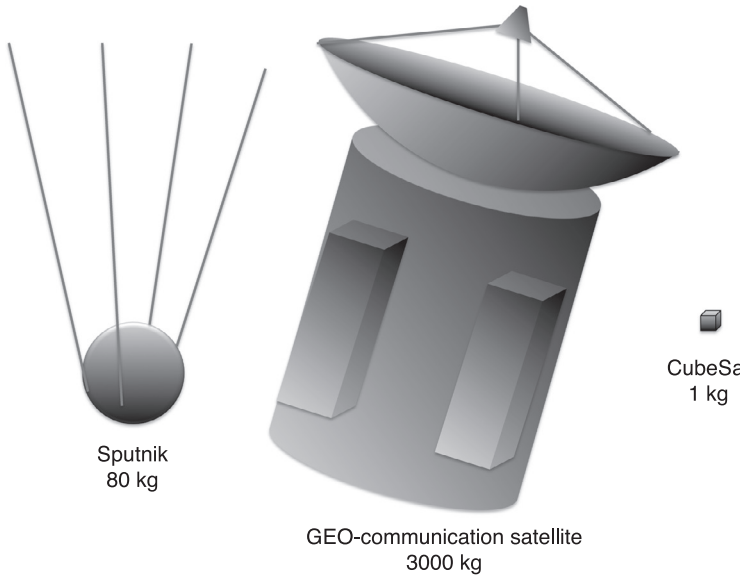

11.1 Relative sizes of Sputnik, a typical communication satellite and CubeSats.

satellites, including the so-called *chip-sats*, which are essentially all-MEMS devices (Muncheberg *et al.*, 1997; Barnhart *et al.*, 2007; Woellert *et al.*, 2011).

In the actual cost and schedule-constrained environment, *smaller* will very likely become the new *better*. Companies, universities and government agencies worldwide, many of them non-traditional space players, are discovering the benefits of developing small satellites, namely, relatively inexpensive space access and increased value per kg (and sometimes more importantly, per unit volume) of a given payload delivered to space. While small satellites will take advantage of improved capabilities of MEMS systems to carry out tasks normally associated with larger platforms, their true utility and impact will reveal itself when new and unorthodox applications are proposed and implemented. At the moment, it is difficult to predict the reach of this impact, although the most optimistic supporters suggest that small satellites, particularly in the *nano*-category, would do for space what the personal computer did for our society in the late 20th century, by allowing affordable access to space.

A number of challenges need to be overcome before such a vision becomes a reality. Some are programmatic, such as the availability of adequate launch services for small satellites beyond the traditional *piggyback* model, in which small satellites *hitchhike* to orbit in a rocket launching larger primary payloads. The main challenges are technical in nature. Of these, we focus on propulsion as an enabler of high-value missions. Up to now, most nano-satellites have not

© Woodhead Publishing Limited, 2013

featured propulsion. Instead, some of them rely on passive attitude control to achieve their mission, but in general nano-satellites have no mobility (e.g. 1 kg, 1 liter CubeSats). In some cases, simple and low performing cold-gas thrusters have been implemented, providing limited maneuverability. The vision stated above can only be carried forward with propulsion systems having the same, or better, performance than that of larger satellites.

While most satellite subsystems are amenable for efficient miniaturization, propulsion presents a set of unique challenges that so far have prevented the development of highly efficient and compact systems. Our goal here is to discuss these challenges and review potential solutions enabled by MEMS technologies.

11.2 Propulsion requirements

As mentioned in the introduction, the vast majority of small satellites today do not have propulsion. This is mostly a design necessity and budget constraint, rather than a mission choice. If it were readily available and affordable, then most small satellites, just as their larger counterparts, would include some form of propulsion. In this section, we assume that propulsion is indeed available and analyze the subsystem-level requirements.

The performance of any propulsion system can be characterized by the amount of force (or thrust) it produces, its specific impulse and, if using electrical energy, its efficiency. From a mission planner standpoint, this is all there is to know about the propulsion system, which at this level could be considered a black box. The properties of that *box* (size, mass, power) depend on the particular thruster technology.

The thrust is given by:

$$F = \dot{m}c \qquad [11.1]$$

where $\dot{m}$ is the mass flowrate into the thruster and c is the exhaust velocity relative to the accelerating spacecraft. If this velocity is constant, the specific impulse (total impulse per unit propellant weight) becomes:

$$I_{sp} = c/g \qquad [11.2]$$

where $g = 9.8\,\mathrm{m/s^2}$ is the Earth's sea-level gravitational acceleration. For an ideal rocket (under no gravitational, or any other external force) of initial wet (with full propellant tanks) mass m_0, the equation of motion can be solved to find the propellant mass fraction, m_p/m_0, as a function of vehicle change in velocity, ΔV:

$$\frac{m_p}{m_0} = 1 - \exp\left(-\frac{\Delta V}{c}\right) \qquad [11.3]$$

It is then clear from Eq. 11.1 and Eq. 11.3 that for a given thrust, higher specific impulse (or exhaust velocity) implies lower mass flow and subsequently a lower mass of propellant brought to orbit. In addition, from Eq. 11.3 we calculate the

© Woodhead Publishing Limited, 2013

propellant requirement for a particular ΔV. Equation 11.3 is known as the *rocket equation* and reflects the strong dependence (exponential) of propellant mass on specific impulse.

Most missions that make use of propulsion will have a particular ΔV requirement. From Eq. 11.1, thrust and *burn* time are linked through $\dot{m}$: achieving a mission, ΔV, will be faster at increased thrust. High thrust maneuvers are usually called *impulsive*, as they can be modeled as instantaneous changes in vehicle velocity for which the ideal rocket equation can be directly applied. However, low thrust maneuvers take longer, and in most cases of interest the situation will not be ideal as gravity forces, for instance, cannot be neglected. In those cases, the ΔV will be larger, leading to even longer burn times. From this perspective, it would appear that there is no incentive in using low thrust in space propulsion; however, optimal mission conditions typically occur with the combination of low thrust and high I_{sp}. This tradeoff is analyzed next.

When designing a space mission, it is highly advantageous to find conditions that maximize the payload mass fraction, m_{pay}/m_0, for a given ΔV. In a broad sense, this means minimizing total wet mass:

$$m_0 = m_s + m_p + m_{prop} \qquad [11.4]$$

where m_s is the structural mass and m_{prop} is the mass of the propulsion system, not including the propellant. At this point we need to introduce a distinction between chemical and electric propulsion (EP) thrusters.

In chemical thrusters, one or two chemical substances react to produce hot gasses that are accelerated while expanding in a nozzle, thus producing thrust. In this case, m_{prop} is constant and it is clear that the higher the I_{sp}, the lower the propellant use will be, thus minimizing the total wet mass. In electric thrusters, the energy of the exhaust does not come from a chemical reaction, but from electric power transferred to the particles that compromise the exhaust. Consequently, electric thrusters require external power P from a source that adds to the total wet mass of the satellite:

$$m_{prop} = \alpha P \quad \text{with} \quad P = \frac{Fc}{2\eta} \qquad [11.5]$$

where α is known as the specific mass (per unit power) of the EP system and η is its efficiency. The amount of energy per unit propellant mass of EP systems is much larger in general than that of chemical rockets. For instance, each water molecule in the reaction $H_2 + \frac{1}{2}O_2 \rightarrow H_2O$ will gain a kinetic energy of about 2.5 eV corresponding to an exhaust velocity of about 5 km/s, or an I_{sp} of 500 s (1 eV = 1.6×10^{-19} Joule). The energy in this case comes from the difference in bond strength of the molecules making up the reactants and products, which is constant. However, if electric power is used to accelerate singly charged water *ions*, there will be no upper limit on the kinetic energy achievable, as long as

© Woodhead Publishing Limited, 2013

velocities are not relativistic. For instance, applying 1000 eV/ion would accelerate these charged particles to 103 km/s, or an I_{sp} of more than 10 000 s. From Eq. 11.3, large I_{sp} translates into very low propellant fractions, so even with the additional mass brought by the required electrical source, it is possible to reduce the total mass over chemical systems. In fact, it is relatively straightforward to compute from Eq. 11.4 the first-order approximation to the optimal, I_{sp} (or exhaust velocity) for a given ΔV and burn time, $t_b = m_p/\dot{m}$:

$$c_{opt} \approx c^* - \Delta V/2 \quad \text{where} \quad c^* = \sqrt{\frac{2\eta t_b}{\alpha}} \qquad [11.6]$$

c^* is a characteristic velocity. The physical meaning of this quantity is if all elements of the spacecraft were removed leaving only the power plant mass, it would accelerate to this velocity. Therefore, c^* is the upper limit in achievable ΔV. In most cases of interest, ΔV is just a small fraction of c^*.

It is clear that high I_{sp} propulsion would be preferred for large ΔV requirements. However, the amount of power per unit mass in EP is very low compared to chemical systems, therefore EP is also characterized by low thrust and long burn times.

To summarize, chemical rockets provide large thrust and short burn times at the expense of heavy propellant use due to their low I_{sp}, while EP provides substantial propellant savings and the ability to reach high ΔV, at the expense of mission time.

Just as their larger counterparts, small satellites would require thrusters for main propulsion, attitude control and station keeping. Typically, main propulsion refers to considerable changes of orbital elements, such as altitude, eccentricity, inclination and others. Attitude control maneuvers are used to modify the orientation of the spacecraft, while station keeping is used to perform formation flight of a number of vehicles or counteract in-orbit perturbations, such as high altitude atmospheric drag, tidal forces or effects from gravitational non-uniformities. Each one of these maneuvers will have its own requirements in terms of ΔV and thrust for a particular set of initial conditions. Given the whole set of mission parameters, a propulsion alternative should be selected. As with any other space technology, this selection is not based only on performance, but also on cost and availability.

To learn more about EP systems and mission analysis, the reader is encouraged to consult the available literature (Jahn, 1968).

11.3 Propulsion technologies

In this section we present a brief review of different types of chemical and electric thrusters available today or in development. This presentation is based exclusively on the fundamental principles of these devices without considering their scalability to small satellites. The review is neither exhaustive nor detailed, and the reader is encouraged to browse the literature for additional information.

© Woodhead Publishing Limited, 2013

11.3.1 Chemical propulsion

By far, most flight-proven thruster systems have been of this kind and not surprisingly there is a large variety of thrusters that could be sub-categorized in many ways, for example in terms of propellant type or pressurization system, such as solid, liquid and hybrids, turbopumped, gas-pressurized, etc. (Sutton and Biblarz, 2001). Despite this variety, practically every chemical thruster is based on the same fundamental mechanism in which a gaseous substance of molecular weight μ and ratio of specific heat at constant pressure to specific heat at constant volume $\gamma = c_p/c_v$ contained in a chamber at high pressure, p_0 and temperature, T_0, accelerates through a convergent-divergent nozzle, while cooling down as internal energy is converted into kinetic energy during the nearly-isentropic gas expansion. The process continues until the exhaust reaches a pressure, p_e, at the nozzle exit of area, A_e. The thrust is then given by:

$$F = \dot{m}u_e + p_e A_e \quad \text{with} \quad u_e = \sqrt{\frac{2\gamma}{\gamma - 1}\frac{R}{\mu}T_0\left[1 - \left(\frac{p_e}{p_0}\right)^{\frac{\gamma-1}{\gamma}}\right]} \qquad [11.7]$$

where R is the universal gas constant (8.314 J/mol/K). Comparing this with Eq. 11.1, we find that the specific impulse (times g) is equal to the exhaust velocity, u_e, only when the expansion proceeds to $p_e = 0$. Of the two terms in Eq. 11.7, the first (direct thrust) dominates over the second (pressure thrust), so there is no advantage to increase p_e. The best performance occurs when the nozzle is matched, which in space operation would mean $p_e \approx 0$.

Most chemical thrusters will fall into one of the following categories (Fig. 11.2).

Cold gas thrusters

This is the simplest of all rockets and even though it is typically categorized as a chemical rocket, no chemical reactions are involved in its operation. A gas is stored in a vessel at high pressure and is injected directly through a control valve into the expansion nozzle. From Eq. 11.7, it is clear that the inherent low temperature of this device will yield low specific impulse (~80 s for ideal expansion of N_2 from $T_0 = 300$ K). Because of this, cold gas propulsion is restricted to very low ΔV maneuvers.

Liquid monopropellants

Among the most widely used space propulsion engines, monopropellants make use of a single reactive liquid, typically hydrazine (N_2H_4) that decomposes exothermically in the reaction, $2N_2H_4 \rightarrow 2NH_3 + H_2$, as it flows through a catalytic bed after being injected under pressure. The hot gas then expands through a nozzle

© Woodhead Publishing Limited, 2013

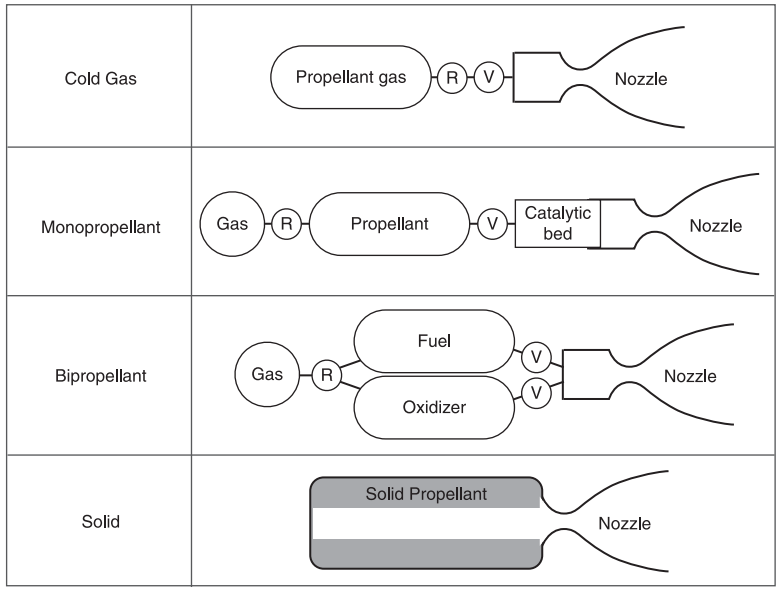

11.2 Illustration of chemical propulsion thrusters (R = regulator, V = valve).

producing thrust. The elevated temperature increases the specific impulse; however, high temperature triggers ammonia decomposition, which is an endothermic reaction that effectively limits the performance from 100 to 150 s. These thrusters have been traditionally used for station keeping in most satellites, for example, controlling north/south drifts of communication satellites in geostationary orbits.

Liquid bipropellants

In this type, the adiabatic flame temperature, T_0, is increased further by the use of efficient energetic combinations of fuels and oxidizers of low molecular weight. These are significantly more complex than monopropellants, and are used in applications requiring higher performance in terms of thrust and specific impulse. For example, the main engines of many launch vehicles and orbital upper stages make use of the combustion of cryogenically cooled liquid hydrogen and oxygen. The most efficient of these thrusters are able to reach an I_{sp} of about 450 s, very close to the theoretical maximum (e.g. Pratt and Whitney's RL-10). Part of the complexity of these engines is due to the pressurization mechanism. The high thrust required in many bipropellants for launch calls for the use of turbomachinery. The development of these engines can be singled out as one of the most expensive and complex, but also critical activities in space engineering. In space applications,

© Woodhead Publishing Limited, 2013

helium vessels are used to provide the required injection pressure, similar to monopropellants.

Solid propellants

Conceptually simpler than liquid rockets, the use of solid propellants minimize part count and complexity. Typical construction involves a relatively lightweight case and a mixture of oxidizer particles (in many cases ammonium perchlorate) bound together by a form of rubber, which acts as fuel (the binder). Formulations, such as aluminum, are sometimes added to improve operation. Once ignited, these formulations are designed to burn smoothly at known rates, thus producing a predictable thrust profile. The performance is just slightly lower than liquid bipropellants producing an exhaust of similar molecular weight. Their main application is in boosters to assist during the launch phase and in upper stages. Unlike mono- and bi-propellants, solid motors cannot be restarted, or stopped, after ignition. Their delivered impulse has significantly larger spread in target ΔV than liquid engines.

11.3.2 Electric Propulsion

As mentioned above, EP systems make use of an external source to increase the exhaust energy per unit mass, hence removing limitations in I_{sp}, improving performance in many traditional missions and enabling missions that simply cannot be realized using chemical propulsion. There are a large variety of thruster technologies in EP, some well-established and others still in development. Here we describe a few of these (Fig. 11.3), which are relevant to the context of this chapter.

Resistojets

In this type of thruster, electric energy is added to a regular chemical, or cold gas, thruster to improve I_{sp}. This is conceptually achieved by dissipating heat from a resistive element in contact with the working fluid. Resistojets have been applied to hydrazine thrusters where the higher temperature forces full ammonia decomposition, but still improves performance. Using this method, the specific impulse of a hydrazine monopropellant can be increased from 100 to 150 s to about 230 s, and more if, for example, hydrogen is used directly as the working gas.

Arcjets

Energy is added to the fluid through a high current arc discharge developing between a central coaxial cathode centered in the flow channel and the nozzle

© Woodhead Publishing Limited, 2013

material, which acts as the anode. Arc filaments are thin, but extremely hot, thus reaching high degrees of ionization, albeit at very low densities. The cross-sectional area of the arc effectively constricts the flow channel while preserving the same mass flowrate. This effectively increases the specific impulse. In its most promising implementation, using hydrogen as the propellant, the I_{sp} can reach 1000 s.

Electromagnetic engines

As in arcjets, strong discharges can produce highly ionized gases able to sustain large electric currents. When interacting with magnetic fields, either self-generated by the current itself or externally applied through auxiliary coils, this current produces vectorial volumetric forces ($\vec{f}$, [N/m^3]) on the plasma of the Lorentz type ($\vec{f} = \vec{j} \times \vec{B}$, where $\vec{j}$ is the current density vector [A/m^2] and $\vec{B}$ is the magnetic field vector, [T]), thus producing thrust. This is the working principle of magneto-hydrodynamic accelerators, including magneto-plasmadynamic thrusters (MPD). These devices are intended to work at high power and high flowrates, with predicted efficiencies around 50% and specific impulse in the 2000 to 5000 s range. A similar mechanism is used by pulsed plasma thrusters (PPT), which make use of solid *teflon* as a propellant. These thrusters are simple to build and operate, and achieve I_{sp} of about 1500 s. The main drawback is on their inherently low efficiency (<10%).

Gridded ion engines

In these thrusters, monoatomic, heavy gases (typically Xe) are partially ionized in a chamber through a dc or rf discharge. Some of the ions in the weakly ionized plasma are then accelerated through a pair of grids biased at high voltage. The grid potentials are selected to repel electrons from the volume between the grids, so a region of positive charge is generated, which eventually limits the amount of current that could be extracted as the field induced by these charges cancels out the applied field. Once extracted, the ion beam needs to be electrically neutralized using an external cathode that effectively pumps electrons out from the ionization chamber, thus avoiding spacecraft charging. These engines are highly efficient, up to 75%, and are able to deliver I_{sp} in the 3000 to 5000 s range.

Hall thrusters

Similar to ion engines, these devices generate weakly ionized plasma with ions accelerated by an electric field generated between a physical anode in the engine and a virtual equipotential downstream plane fixed by the external neutralizing cathode. In contrast to ion engines, Hall thrusters make use of a magnetic field that traps electrons in the engine volume for a sufficiently long time to produce

© Woodhead Publishing Limited, 2013

enough ionizing collisions with propellant neutrals. There is no need for gridded electrodes and consequently no space charge limitation. Varying with power level, the efficiency ranges between 20 and 60%, with an I_{sp} between 1200 and 2000 s.

Electrospray thrusters

These are similar to ion engines, as charged particles are accelerated between two electrodes biased to high voltages. The propellants in this case are conductive liquids (molten metals, liquid salts or electrolyte solutions), which are electrostatically stressed by the applied field. The electric traction is balanced by surface tension forces, thus forming sharp liquid menisci able to amplify the applied field by 2 to 3 orders of magnitude. The result of applying fields in the order of 0.1 to 10 billion volts per meter to conductive liquid surfaces is the generation of charged droplets, ions or both. These particles accelerate to high velocity producing thrust. Depending on the operational mode, the efficiency of electrosprays can be as high as 90%, with I_{sp} from 100 s (droplet mode) to 5000 s, or more (ion mode). Of particular interest is the use of ionic liquids (room-temperature molten salts) as propellants. These liquids do not evaporate in vacuum and produce pure ion beams. The main drawback of these thrusters (in main

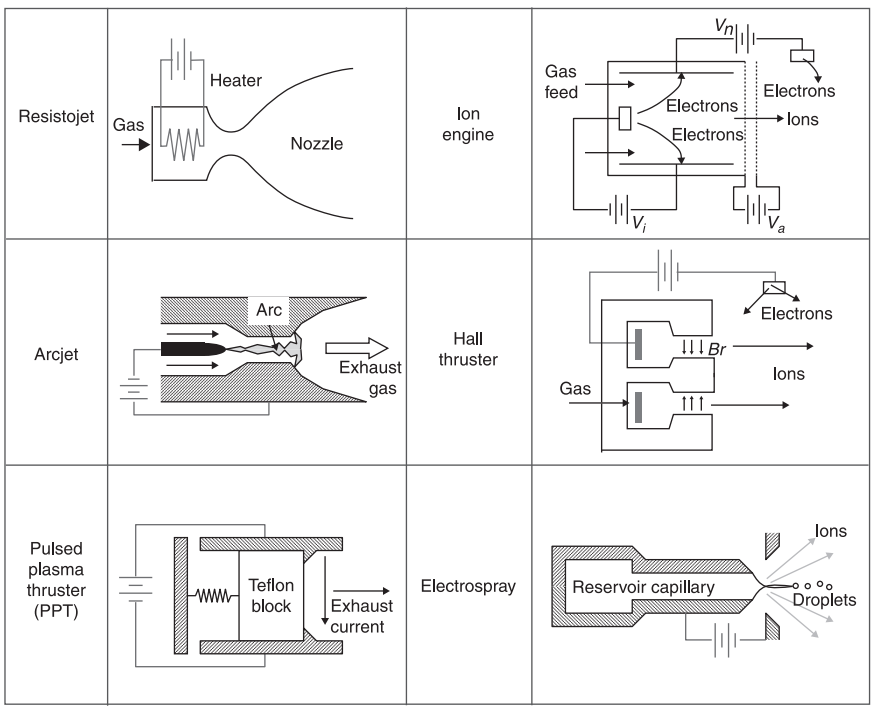

11.3 Illustration of electric propulsion thrusters.

© Woodhead Publishing Limited, 2013

propulsion applications) is that each electrified meniscus produces a very small thrust in the 0.1 to 1 μN range.

11.4 Miniaturizing propulsion systems

Once the need for mobility for pico- and nano-satellites has been established, and some of the propulsion fundamentals briefly reviewed, we proceed to discuss their scaling. There are two requirements for this:

1. As in regular satellites, the propulsion system needs to be **compact** enough to leave enough room for the rest of the spacecraft sub-subsystems. Volume tends to be the critical property in the actual launch model for small satellites (piggybacking), since the cost associated with delivering a given mass into orbit is not sensitive for ~1 kg objects. However, relatively strict volume allowances, sometimes driven by the launcher provider and primary payload requirements, and others by form-factor standardization, determines the fraction allocation for each subsystem, and as always the goal is to maximize payload fractions.
2. The propulsion system **performance** has to be similar, or better, to what is possible today in larger satellites. This requirement might seem to be artificial, since utility for small satellites has so far been directed towards secondary, or capability-limited tasks, and it may appear that there is no particular reason why the *status quo* should not be preserved. However, due to the foreseeable impact that highly capable small, inexpensive satellites would have, it seems a much more fruitful approach to aim toward the performance already displayed by state-of-the-art spacecraft.

Simple photographic scaling of a flight-proven propulsion system in a large satellite appears at first to be a solution addressing these two requirements. However, direct scaling of propulsion hardware is extremely challenging, because of physical limitations that do not allow for miniaturization while retaining the same level of performance, that is thrust density, specific impulse and efficiency.

The scaling will depend on the thruster type under consideration. To be more specific, but at the same time avoiding repetition, we group the scaling analysis on thruster type: i) chemical, ii) electrothermal, iii) electric gas-phase ionization, and iv) electric liquid-phase ionization.

11.4.1 Scaling of chemical thrusters

As discussed in Section 11.4 on ‘Miniaturizing propulsion systems’, chemical rockets, including cold gas thrusters, make use of the enthalpy added to a working fluid to accelerate it through an expansion nozzle.

Scaling a chemical thruster appears to have a benefit in terms of enhanced compactness. The reason for this is that for a device of size, s, the thrust varies as

© Woodhead Publishing Limited, 2013

s^2, while its mass changes as s^3. In consequence, the thrust per unit mass will change as s^{-1}. This assumes everything else in the thruster remains unchanged, such as photographic scaling. This interesting fact suggests that the smaller a thruster is, the better its thrust/weight performance will be, enabling not only in-space propulsion for small satellites, but perhaps advantageous launch capabilities. Unfortunately, the scaling is not linear and thrusters of this type require a number of ancillary components that are difficult to miniaturize.

Equation 11.7 can be used to examine the performance of these rockets. Except for cold gas engines, the enthalpy is increased through an exothermic reaction involving a single propellant and a catalyst, or a fuel-oxidizer combination. In most combustion problems the residence time is defined here as:

$$\tau \equiv \frac{s}{\upsilon} \qquad [11.8]$$

where υ is the fluid mean velocity, the parameter controlling both the ability of propellants to react and the rate of degradation of reaction products (i.e. ammonia decomposition in hydrazine monopropellants). If the residence time is too short, the process of combustion, including atomization, mixing and flame diffusion, might not proceed to completion before the fluid leaves through the nozzle. This becomes more critical with small s and for propellants and combinations of propellants that have to go through all combustion stages. This is the case for hydrocarbons, which are of great interest given their convenient storability properties when compared against gaseous propellants, which need to be stored under pressure. Unfortunately, hydrocarbons are difficult to atomize to the required levels in very small combustion chambers.

In addition, even with ideal flow and complete combustion, the specific impulse will only remain unchanged as long as the geometry of the nozzle (exit to throat area ratio) and adiabatic flame temperature in the combustion chamber, T_0, do not change as s is decreased. The heat flux to the wall (watts per unit area):

$$q = h_g(T_0 - T_w) = h_g \Delta T \qquad [11.9]$$

depends on h_g, the convection film coefficient, which determines the effectiveness of the heat transfer between the hot gases in the chamber and the thruster wall. The wall temperature is limited by materials properties and cannot be increased beyond what is possible using conventional materials, so in general T_w is constant, thus making ΔT roughly constant for high performance chemical propulsion. The film coefficient depends on gas properties (thermal conductivity, viscosity, specific heat and density), but it is also a function of gas velocity, roughly υ, and chamber or nozzle size, which scales as s. In particular, the film coefficient is found to increase at higher gas velocity and smaller sizes. The specific dependence is captured empirically in expressions such as (Sutton and Biblarz, 2001):

$$h_g \propto \frac{\upsilon^{0.8}}{s^{0.2}} \qquad [11.10]$$

© Woodhead Publishing Limited, 2013

It is clear from Eq. 11.9 and Eq. 11.10 that, as the thruster size decreases, the heat flux will increase and consequently more power density needs to be dissipated at a given temperature unless mass is added, or a way to cool down the thruster is provided. For miniature systems where these solutions are not desirable, we would then reduce ΔT as h_g increases, thus reducing the thruster specific impulse. In any event, this prevents photographic scaling as the relative dimension of the thruster needs to increase as the flow channel becomes smaller. These simple considerations ignore the effects of viscosity; as the thruster becomes smaller, the relative size of the boundary layers adjacent to the device walls become larger, and for very small thruster sizes they could occupy the whole channel. In large thrusters, losses associated with viscous drag are relatively small (a few percent decrease in performance), whereas in small chemical rockets, they could dominate the system-level efficiency. The adiabatic flame temperature could compensate for the lower I_{sp}, but this would exacerbate thermal loads limiting even more the degree of engine miniaturization.

Despite the scaling challenges due to incomplete combustion, heat dissipation and viscous losses, it is still possible to reduce the size of thrusters to fit in small satellites, with compromises on performance. Lower I_{sp}, for instance, increases the propellant mass ratio for a given mission, ΔV, thus increasing in proportion the size of the propellant tank. Perhaps the biggest challenge in miniaturizing chemical thrusters (and other types too) lies in scaling ancillary components, including high-pressure valves, flow controllers and regulators.

11.4.2 Scaling of electrothermal thrusters

The scaling of these devices is similar to that of chemical rockets, which is with similar thermal and flow issues. The main difference is in the ancillary components, as electric power is diverted toward the rocket chamber from a power processing unit (PPU) using a heat dissipation device. Small sizes (for the heater) here are in principle advantageous, since for a given heater resistivity and efficiency, the added power per unit mass varies as s^{-1}. The issue is how effective heat transfer could be, given the finite thermal conductivity and short residence time. These two issues dominate the scaling of electrothermal thrusters and prevent miniaturization of existing flight-proven hardware.

11.4.3 Electric gas phase ionization

The fundamental characteristic in this category of high I_{sp} thrusters is the production and acceleration of an ionized gas or plasma. Plasmas are generated and sustained through collisions of electrons with injected neutrals via rf or dc discharges. Efficient ionization requires a relatively small mean free path of ionizing collisions of the electron population with neutrals:

© Woodhead Publishing Limited, 2013

$$\lambda = \frac{1}{n_e Q} \qquad [11.11]$$

Q is the collision cross-section (in m^2) and n_e is the number density of electrons, or plasma density, in the chamber (in m^{-3}). The mean free path needs to scale with the device size, s, for the probability of ionization to remain unchanged. From Eq. 11.11, we see that n_e should scale as s^{-1}. Q is essentially constant and equal to the cross-section of the neutral species. In consequence, as the thruster becomes smaller, the plasma density needs to increase. A higher density results in more thrust per unit area, but also higher particle flux to the walls of the device. The effect of this is a decrease in efficiency, as the energy invested in creating charged particles is lost, in addition to an increase in heat flux. Similar to chemical rockets, a larger thruster mass or active cooling would be required to alleviate thermal loads.

In addition, a magnetic field, B, is used to trap electrons inside the device. The characteristic dimension controlling this confinement is the Larmor radius:

$$r_L = \frac{m\bar{c}}{eB} \qquad [11.12]$$

which also scales with s. For a fixed electron charge to mass ratio (e/m), this means that B must change as s^{-1}. This assumes constant electron thermal velocity, $\bar{c}$, which is a fair approximation since the electron energy controlling electron motion is selected to maximize ionization probabilities for a given propellant gas. If electromagnets are used to generate the field, this means higher magnet power and therefore a further decrease in propulsion system efficiency. One of the main concerns in scaling plasma thrusters to very small sizes is the erosion of components due to the increase of ion flux lost to the device walls. This is the fundamental life-limiting mechanism of these types of thrusters and even though they are able to operate at high I_{sp}, their ΔV characteristics could be limited by their potentially short lifetime.

The conclusion is that gas phase plasma thrusters, just as chemical rockets, cannot retain performance with photographic scaling. Nevertheless, and despite the unavoidable compromises in performance, it is possible to miniaturize this type of engine for applications in pico-/nano-satellites through careful engineering design and advanced manufacturing processes. The successful implementation in very small satellites would also require the miniaturization of ancillary components. For instance, reducing the size of the efficient and successful NSTAR NASA ion engine (flown aboard the *Deep Space 1* technology demonstrator spacecraft and in the *Dawn* probe on a mission to explore asteroids Vesta and Ceres) would require miniaturization of a large number of high-pressure valves, tanks, regulators and at least six independent power supplies in the PPU, not counting the power and control electronics required by the propellant delivery system.

© Woodhead Publishing Limited, 2013

11.4.4 Scaling of liquid phase ionization thrusters

In this category we have electrospray thrusters operating with electrically conductive liquid propellants. While we use the term ionization, the physical process to produce charged species is different from the gas phase ionization, in which particles are originally neutral. In electrosprays, an electric field, E, on the liquid surface effectively produces a force, or traction on the charged species. Depending on the field polarity, positive or negative ions migrate rapidly toward the liquid-vacuum interface (surface charge relaxation). These ions could be in solution, in the case of liquid electrolytes, could be positive atomic nuclei in the case of liquid metals, or bi-polar ionic molecules or atoms, as in molten salts. Since the liquid is a free surface, its shape changes according to the acting force (electric pressure) when balanced by surface tension, σ, until reaching a surface curvature proportional to r^{-1}:

$$\frac{1}{2}\varepsilon_0 E^2 \approx \frac{2\sigma}{r} \qquad [11.13]$$

where $\varepsilon_0 = 8.854 \times 10^{-12}$ F/m is the permittivity of vacuum. This force tends to produce sharp menisci that intensify the field, thus increasing the force and making the menisci even sharper until becoming, under ideal conditions, conical. These liquid structures are known as Taylor cones. The field is so intense near the apex of a Taylor Cone that charge emission occurs. Depending on operating conditions and liquid properties, the outcome of this process could be a thin charged jet issuing from the tip of the cone. Subsequently, this thin jet breaks up into charged droplets forming a spray. Alternatively, the force on ions at the apex of the cone could overwhelm their binding forces in the liquid (molecular and coulombic) and produce ion extraction, a process known as field-assisted ion evaporation. Droplet emission produces more thrust for a given current than ion emission, although the specific impulse in the ion mode is much larger.

Regardless of the operational mode, the relevant physics of charge emission in electrosprays are confined to very small volumes. For instance, ion emission from an ionic liquid (a room temperature molten salt) can be produced from a meniscus with a characteristic size of about 5 μm. According to Eq. 11.13, the required field to produce a Taylor Cone of that size would be about 10^7 V/m. This is at least two orders of magnitude lower than the field required for ion evaporation in ionic liquids, or about 10^9 V/m. In practice, electrodes in the 1 mm size range are biased to voltages of about 1 kV (except liquid metals, needing about 10 times more voltage) to obtain the field required for Taylor Cone formation. The cone itself then serves as a field amplifier to produce, in our example, ion emission from a region about 20 nm near the cone apex. This is a dramatic change of scales encompassing nearly six orders of magnitude, with the most relevant physics occurring at the smallest of all. The consequence for miniaturization is very clear; electrosprays are already miniaturized. In fact, the challenge in this case is to scale

© Woodhead Publishing Limited, 2013

up, since individual Taylor cones produce thrust levels in the 0.01 to 1 μN range, which are too small for most applications, even for the smallest of nano/pico-satellites. In a practical implementation, a large number of emitters need to be fired simultaneously in parallel to obtain useful thrust. The challenge is fundamentally in manufacturing, with some physical constraints. For instance, the size of the smallest Taylor cone is determined by the lengthscale at which viscous losses produce a pressure drop in the order of the electrostatic pressure. The minimum spacing between adjacent Taylor cones distributed on a surface array for parallel firing is limited by particle interception on extracting electrodes, deformation of materials and electric/hydraulic isolation. All these factors tend to set the scale of individual electrospray emitters to a value much smaller to that achievable by current manufacturing processes.

The efficiency of these thrusters is determined by their electrical properties and not the physical size or the number of emitters fired simultaneously, therefore efficiency considerations are focused on the PPU. Finally, as in all other thrusters, true miniaturization would only be achieved if ancillary components, which dominate the mass, volume and power budgets, scale down favorably. Of particular interest is the pure ionic mode, in which passive flow through porous media is achieved and therefore no pressurized containers, or valves, pipes or neutralizer, if operated in the bipolar mode, are required.

11.5 MEMS thrusters

Given the scaling considerations of each thruster type, it is clear that miniaturization compatible with MEMS processes with future implementation in pico- and nano-satellites is not practical for the whole spectrum of available and developing technologies. In fact, only a few examples have been proposed and described in the literature, which are for the most part in line with compatibility considerations between MEMS materials and processes and specific propulsion requirements. In practice, it is necessary to determine whether the use of MEMS is advantageous in the manufacturing of propulsion systems for very small satellites. Positive attributes, such as compactness, low tolerance in assemblies, batch processing, modularity and low cost, are clearly desirable, as long as thruster performance is retained, or exceeded, when compared to conventional propulsion systems.

A thorough survey of propulsion systems for nano-satellites in the 1 kg category, or CubeSats, was recently published (Mueller *et al.*, 2010). In this review, the authors discuss a wide range of propulsion technologies that could be miniaturized for their use in nano-satellites. Only a handful of them involved MEMS materials and processes. In many instances, it was correctly emphasized that thrusters themselves tend to be the smallest component in the propulsion system (i.e. chamber plus nozzle in chemical rockets), while most of the system mass and volume is taken up by subcomponents, such as valves, pipes, power converters, sensors and other actuators. In this context, the use of MEMS technologies would

© Woodhead Publishing Limited, 2013

be most beneficial, not in the manufacturing of the thrust-delivery device, but in the miniaturized fabrication of ancillary components. This argument implies that practically all propulsion systems for small satellites have the potential to benefit from MEMS techniques. However, for the sake of brevity, we will only focus on design considerations for systems that have been, or are likely to be, fully implemented with MEMS.

Hybrid approaches, such as conventionally fabricated chemical and EP engines, are therefore excluded from this discussion, including plasma thrusters that rely on weakly ionized gases, such as Ion Engines and Hall Thrusters. Given the intrinsic difficulties in scaling down these devices (described in Section 11.4 on 'Miniaturizing propulsion systems'), it is unlikely that they would benefit from MEMS, except again in the context of contributing to the compactness of ancillary components. The natural division of technologies is once more between chemical and EP engines. Design considerations involving MEMS are different in most cases. In the next section, we discuss the relevance of these considerations in the context of some thruster examples described in the literature. The interested reader is encouraged to consult the cited references for a more detailed description of a particular technology.

11.6 Design considerations of MEMS thrusters

11.6.1 Chemical (gas/liquid propellants) MEMS propulsion

The operational and performance characteristics of chemical propulsion engines are very sensitive to a number of intrinsic properties of this type of system, including:

Feed pressure and thermal management

Best performance for chemical rockets is achieved at pressures sufficiently large such that the gas expanding from the main chamber to the nozzle exit behaves like a continuum fluid, such that there are enough collisions between gas particles. High pressure also promotes combustion by improving reaction kinetics. In addition, best performance is achieved at high adiabatic flame temperature. As discussed in previous sections, high pressure and temperature present a number of challenges when scaling thrusters down. These challenges set the requirements for the MEMS device design, the process to build it and the corresponding selection of materials. A critical issue is the ability to effectively bond materials of dissimilar coefficient of thermal expansion. In many instances, these differences produce bonds that are either under compressive or tensile stresses at temperatures different than the bonding temperature. Operationally, this introduces a common failure mode of thermally active devices. Given that many of these materials will operate at high pressure, high strength is important too. Fortunately, the yield

© Woodhead Publishing Limited, 2013

strength of silicon, by far the most widely used material in MEMS, is adequate for high-pressure operation. In addition, silicon displays excellent anodic bond strength, enabling the stacking of multi-wafer structures. Other related materials, such as silicon carbide, also have potential to increase the resistance of pressure vessels, while still providing some of the flexibility that characterizes microfabricated structures. Temperature control of silicon-based thrusters is possible due to the relatively high thermal conductivity (on a par with aluminum), relaxing some of the concerns encountered when designing the cooling strategy for such small devices.

Thruster feedthroughs

A common difficulty in the design and implementation of MEMS devices is packaging and connectivity with external components. In chemical thrusters, because of their relatively low specific impulse, the amount of propellant supplied to the chamber could be substantial relative to the size of the device. In most cases, propellants are pressurized before they are delivered into the chamber. This makes the union between supply line and thruster a particularly sensitive element that requires close attention. The challenge is to retain tolerances and dimensions consistent with the desired scaling of the thruster. It is not surprising that in many cases these connections become larger and heavier than the thruster.

Propellant management

Propellant storage requirements for small thrusters are similar to those used by regular chemical propulsion. The fundamental limitation in both cases is set by the strength of materials used in the construction of propellant tanks. The most desirable condition maximizes yield strength and minimizes mass density. Additional constraints, such as chemical compatibility, are important too. In many instances, composite materials meet such a combination of properties. Here as well, attachment of low profile, but reliable and strong feedthroughs is essential. Equally important are the miniaturization of ancillary components, such as pressure regulators, pipes and control and isolation valves. As mentioned before, these components could easily dominate the mass, volume and power budget of the propulsion system. Fixed pressure mini-regulators and piezo-controlled valves are examples that have the potential to improve the compactness of these systems.

Boundary layer thickness

Even if the miniaturization of chemical thruster components is successful, it is unlikely that scaled performance relative to larger rockets could be maintained. Regular chemical thrusters effectively transform gas internal energy into kinetic energy through an adequately shaped expansion nozzle. Non-idealities, such as

© Woodhead Publishing Limited, 2013

the appearance of shocks, flow separation and viscous losses across the boundary layers developing at the walls reduce the energy conversion efficiency. At small scales, boundary layers become particularly relevant, since their fully developed thickness could easily become as large as the thruster flow channel. This reduces the efficiency, such that the performance decreases with respect to a large nozzle for the same adiabatic flame temperature. In fact, the expansion characteristics become much less sensitive to the actual shape at small scales (Bayt, 1999; Bruccoleri *et al.*, 2012), as the assumption normally used to first approximate the nozzle geometry breaks down and losses dominate.

A few interesting MEMS-based chemical propulsion examples can be found in the open literature. One of the most evolved examples corresponds to a cold gas thruster (Stenmark and Lang, 1997). The system is a self-contained MEMS module that includes four thruster heads, each one with its own control valve capable of regulating flow, thus allowing for throttle ability. While the specific impulse is still intrinsically limited to low values in these devices (about 60 s), the contribution to implementing a full build using MEMS is substantial and could potentially be extended to other types of propulsion in need of miniaturized ancillary flow control components.

Such extension would be extremely valuable, and well coupled, to efforts to miniaturize monopropellants and bipropellant thruster systems using MEMS techniques. For instance, the work of Hitt *et al*. (2001) describes a system in which hydrogen peroxide decomposes exothermically to produce thrust. The highlight if this work lies in the interesting design at the microscopic level achieved by deep reactive ion etching (DRIE) in silicon. It is based on the production of pillars in a rectangular chamber with a silver catalyst deposited on the surface. Tests of this concept have been encouraging, although challenges in achieving full decomposition at small scales remain. Such a concept is otherwise promising and as mentioned above, would benefit substantially from advanced solutions to the problem of controlling flows via MEMS structures.

Bi-propellant thrusters have also the potential to benefit from MEMS approaches. As discussed above, these thrusters are complex and, in general, more challenging to implement than mono-propellants, cold gas thrusters and other types of propulsion. It is also true that bi-propellants achieve the highest performance of all chemical rocket types, and therefore an implementation using MEMS would be beneficial. The state-of-the-art bi-propellant MEMS engine is probably best represented by the work described in Protz (2004), in which a series of patterned silicon wafers are anodically bonded in a relatively thin stack containing practically all the flow elements of a regular bi-propellant engine. As such, the design needs to account for high pressures and temperatures, particularly in the cooling channels and combustion chamber.

Preliminary tests of this thruster indicate that it is indeed possible to operate a bi-propellant engine at small scales, although unavoidable challenges would remain. For example, most tests were carried out using gaseous propellants, which

© Woodhead Publishing Limited, 2013

are not practical in space or launch applications due to storability limitations under pressure. The ideal bi-propellant engine would work with easily storable liquid propellants and would avoid pressurized canisters to achieve the required operating pressure conditions. These rockets would benefit substantially from a MEMS-based pressurization system. Along these lines, researchers have demonstrated that some critical fundamental challenges in MEMS processing could be overcome by building a turbomachinery-based pressurization system commensurate with the bi-propellant thruster package. As in other cases, operational challenges remain and some of these will likely drive design changes (Jamonet, 2002).

11.6.2 Chemical (solid propellants) MEMS propulsion

While sharing some of the issues of liquid/gas propellants, solid fuels have the advantage of easier storability, since they do not need to be externally pressurized and do not require ancillary propellant management components that are challenging to miniaturize. However, because of their reduced dimensions, the expected performance would suffer in similar ways, as described above for liquid propellants.The application of solid propellants is more restricted, since they cannot be restarted and their impulse delivery is not as accurate, making the total ΔV in general larger than necessary for a given mission. Nevertheless, due to their simplicity, they can be used in small packages and compensate for this disadvantage by operating both in parallel to vary thrust and in series to control effective burn time and perform a number of in-orbit maneuvers. Several promising MEMS implementations of this approach have been described in the literature, including digitally addressable micro-chamber solid burners and various propellant formulations (Rossi *et al.*, 2001; Zhang *et al.*, 2005; Chaalane *et al.*, 2007). Such addressable configurations should be capable of providing maneuverability to nano-satellites by selective firing of individual chambers. Higher controllability and longer lifetimes would require relatively high chamber aspect ratios and higher micro-chamber densities. Isolating adjacent chambers from each other when firing remains as one of the main design challenges. This becomes more difficult the closer the chambers are to each other for materials with fixed thermal properties. Successful high density implementation of this concept will require the use of thermally insulating materials compatible with MEMS processes, such as some variety of ceramics. Other manufacturing challenges remain; for instance, it is important to generate sufficient pressure in the chamber to sustain effective combustion. To this end, researchers have included isolation membranes that do not burst until the pressure has reached operational values. The overall concept of MEMS solid thrusters is interesting due to the potential compactness and simplified operation. More work is still required to improve the performance of these devices, such that they reach higher values of I_{sp}, since currently the use of propellant is significantly less efficient than even cold gas thrusters.

© Woodhead Publishing Limited, 2013

11.6.3 Resistojet MEMS propulsion

Similar in principle to chemical systems, these devices share some of their design characteristics. In particular, their MEMS implementation is targeted to improve the poor ΔV capability of low I_{sp} cold gas propulsion. However, due to the reduced scales and subsequent short residence times, direct heat transfer of the gas from the chamber walls is ineffective. An interesting solution (Ketsdever *et al.*, 2005) involves operation at significantly lower pressures, such that the mean free path for particle collisions is larger than the device size, and therefore the gas particles are more likely to collide directly with the device walls, effectively thermalizing at the temperature of the heated surfaces and eventually exiting the thruster at the corresponding (higher) thermal velocity. The so-called free molecule micro-resistojet (FMMR) is one of the few examples of resistojets using MEMS. The FMMR thruster heads are micromachined in silicon using conventional photolithographic techniques, making it very compact. This concept becomes promising for applications in nano-/pico-satellites when coupled with miniature propellant management components and efficient heating elements. Its performance is somewhat better than cold gas thrusters reaching an lsp of 70 to 80*s* with water at about 250°C. A potential drawback is the low energy conversion efficiency, since only a small fraction of the thermal energy required to heat the device walls ends up as kinetic energy of the free molecules in the jet.

11.6.4 MEMS electric discharge thrusters

There are only a few gas phase ionization thrusters compatible with MEMS developed so far and these are still in a relatively low developmental stage. It is therefore premature to predict how applicable they will be to small satellites in the near/mid-term. The exception in this group is the PPT, which is better understood at a scale that is not too large in comparison with MEMS devices. However, it is unlikely that the efficiency of PPTs will improve at small scales, as some of the physical considerations discussed in previous sections of this chapter suggest. For instance, some preliminary testing of PPT MEMS thrusters yielded efficiencies as low as 1% or even lower. Though the thrusters are small, their corresponding PPUs would be disproportionally large. Nevertheless, we could envisage applications for small thruster heads acting on strategic locations of large space structures, such as telescopes and other systems.

11.6.5 Electrospray thrusters

The very small size of electrified menisci, coupled with recent developments in micro- and nano-manufacturing and propellant technology, allow electrospray thrusters to situate themselves as a unique technology amenable for miniaturization down to MEMS and, possibly, nEMS scales. Historically, electrospray propulsion

© Woodhead Publishing Limited, 2013

was first proposed in the form of charged-droplet emitters (colloid thrusters) back in the 1960s and 1970s (Khayms, 2000). During that time, it was recognized that multiple emitters, in this case capillary tubes fed through some form of direct pressurized injection, would be required to obtain enough thrust at relatively high specific impulse. In those days, the concept of nano-/pico-satellites was practically nonexistent and projected missions for these thrusters were targeting high ΔV at good efficiency of conventionally sized spacecraft. This required the development of multiple emitter arrays, which were fabricated with ordinary machine-shop manufacturing. Because of this, only a limited number of individual emitters could be reliably assembled together. This meant that each emitter was forced to produce high currents of charged droplets. This effectively meant low specific charge to mass ratio of particles and large flowrates. The consequence of this is that for the high I_{sp} envisioned for these thrusters' very high voltages, sometimes up to 100 kV were required. Eventually, colloid thrusters were abandoned in lieu of ion engines. The forceful approach of those days has recently been replaced with the subtle high performance emission from single emitters, carefully controlled and multiplexed at scales only achievable by micro-manufacturing techniques. Even though this new approach is ideal for very small satellites, it does not exclude its application to all satellites by multiplexing not emitters, but arrays of emitters, or thruster modules.

The flexibility of operation featured by electrospray thrusters allows MEMS designs in different configurations. Here we present a few examples of electrospray MEMS thrusters described in the literature.

Capillary emitter arrays

These were part of the first implementation of electrospray thrusters using MEMS. Capillary flow for electrosprays is relatively well understood from the early tests carried out during the 1960s and 1970s and adequate propellants such as doped glycerol required such a configuration. One of the first attempts at microfabricating capillary arrays in silicon is described in Paine (2002). In this design, emitters would be fabricated in silicon and distributed on a 2-D planar surface. The design called for emitters separated from a gold extractor by silicon on insulator (SOI) wafer. The propellant planned for this thruster was formamide doped with LiCl. This propellant was suggested in earlier studies (Fernandez and Loscertales, 1994), in which adequate fluids were sought to replace glycerol. Ideal fluids for this application would have relatively low viscosity, high electrical conductivity and low volatility. Formamide was found to be adequate in these attributes. This design, based on MEMS, was innovative enough to revitalize the field and focus the attention on microfabrication techniques for the assembly of electrospray thrusters.

However, it was suggested in subsequent work (Velásquez-García *et al.*, 2006) that such an approach would be unable to produce stable emission from all

© Woodhead Publishing Limited, 2013

capillaries. The pressure drop (hydraulic impedance) would not be high enough along individual channels to allow emission from adjacent emitters. The proposed solution was to increase the length of the channel to enhance the hydraulic drop. The required new length was much larger than the thickness of silicon wafers, thus eliminating the possibility of having a compact 2-D structure. In its place, parallel channels were carved on and *sandwiched* between silicon wafers, and emission would be produced from the edge of the device. This 1-D concept included a *clip-on* structure to hold the extractor slit, but its frontal area was much larger than the active electrospray area, making the net thrust density much smaller compared to what could be accomplished with 2-D emitter arrays. In addition, since they work in the droplet regime, both of these concepts would require valves and a pump, which as mentioned before, are difficult to miniaturize.

The ideal situation would be to retain the 2-D structure but increase the aspect ratio of the capillaries. In through-wafer etching, this effectively means reducing the diameter to sizes on the order of 1 micron. This has two disadvantages, first, from Eq. 11.13, the field required to produce a Taylor cone becomes larger, which for a fixed emitter/extractor geometry means larger operating voltages, introducing then additional electric isolation difficulties. Second, such small capillaries are prone to clogging due to impurities on the liquid, or due to vapor lock from bubbles trapped in the closed propellant system. An ingenious mitigation of these problems was proposed in Krpoun *et al.* (2009). The new configuration is similar to that of Paine (2002), but instead of increasing the capillary aspect ratio, each emitter is filled with a collection of microspheres sintered in place, that effectively act as a resistive element to liquid flow.

Externally wetted arrays

Besides the much-improved manufacturing capabilities, the reinvigorated interest in electrospray propulsion has been fueled by the use of ionic liquids as propellants. Ionic liquids are organic-based room temperature molten salts. They are ideal liquids for electrospray applications, as they have negligible vapor pressure, good electric conductivity and a wide variety of physical and chemical properties. The breakthrough in this area came when experiments with capillary emitters using the ionic liquid EMI-BF_4 resulted in a transition from a droplet mode to one in which only ions are emitted (Romero-Sanz *et al.*, 2003). This was a completely new regime that would allow electrosprays to operate in a similar way to ion engines, but without recurring to gas phase ionization and therefore without all associated scaling difficulties. Since these liquids do not evaporate in vacuum, it became possible to use an externally wetted architecture similar to that of liquid metal ion sources (Lozano and Martinez-Sanchez, 2005).

In the first implementation, ionic liquids wet a tungsten needle previously sharpened and electrochemically treated to enhance wetting by the ionic liquid. It was later found that not only EMI-BF_4 but a wide variety of other liquids will

© Woodhead Publishing Limited, 2013

produce pure ion emission, in stark contrast with capillary emitters. These sources are known as ionic liquid ion sources (ILIS). There are many benefits of using such an open architecture. Clogging is less likely, as the liquid has multiple paths to arrive to the tip and concerns about trapped gas are mostly eliminated. Importantly, such configuration does not require valves or backpressure to work. The only control variable is the applied voltage, thus simplifying the operation and eliminating the cumbersome requirement for miniaturizing ancillary components other than the PPU. However, it was also determined that operation in the pure ionic regime requires periodic alternation of the voltage polarity at frequencies in the order of 1 Hz, so that ions of the polarity not extracted by the field do not accumulate and produce corrosion (Lozano and Martinez-Sanchez, 2004).

The first MEMS implementation of this concept was carried out in silicon (Gassend *et al.*, 2009). The process makes use of plasma-enhanced chemical vapor deposition (PECVD) and DRIE to produce high aspect ratio sharp structures. One of the main challenges with this approach is the inability of most ionic liquids to wet silicon. The implemented solution included the growth of black silicon (nano-grass), which under some conditions promoted wetting. These ideas were further extended to include an extractor electrode that could be manually assembled by a clip mechanism.

Porous metal arrays

One of the main drawbacks of the externally wetted configuration on silicon pertains to the transport of propellant from a reservoir to the roughened silicon substrate. An option would be to actively pump the fluid onto the surface, but that complicates the design by introducing unnecessary ancillary components. A solution to this problem would be to produce emitter arrays on a porous substrate and let capillary action alone transport the propellant from a reservoir on the back of the device. Porous silicon appears to be an alternative; however, porosity is confined to the surface of the wafer. In addition, even if the porosity in silicon could be extended through the bulk, for capillary action to drive flow from the reservoir toward the tips, the pore size needs to be either uniform or decrease from the back of the wafer.

Current methods to produce porous silicon yield the opposite porosity gradient. The use of porous metal substrates has been proposed to solve this problem (Legge and Lozano, 2011). The challenge has shifted to the microfabrication of sharp emitters on porous metals. As a viable alternative, electrochemical etching of 2-D structures (Fig. 11.4) could be achieved by using a dry mask to protect the metal bulk from contamination by regular photoresists. In order to avoid distortion of the porous structure at the surface of the substrate, it is necessary to guarantee etching in a regime in which the diffusion of electrochemical products controls the metal dissolution process, thus giving smooth surfaces from where emission

© Woodhead Publishing Limited, 2013

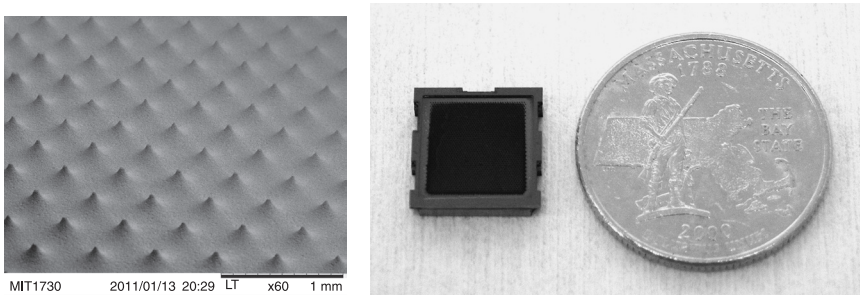

11.4 Left: Example of micro-tip emitter arrays fabricated on porous metals; right: packaged porous metal electrospray thruster.

could occur (Courtney, 2011). The porous metal substrate could then be integrated with a silicon package including extractor electrodes.

This process has been used to produce a prototype for an ion electrospray propulsion system (iEPS) for CubeSats (Fig. 11.5), which would allow up to 16 thrusters and a PPU to be included in one of these small satellites, while not taking more than one-quarter to one-third of the total mass and volume of the spacecraft (Lozano and Courtney, 2010). Each thruster head contains approximately 500 porous micro tips spaced 450 micron from each other. Since the device is

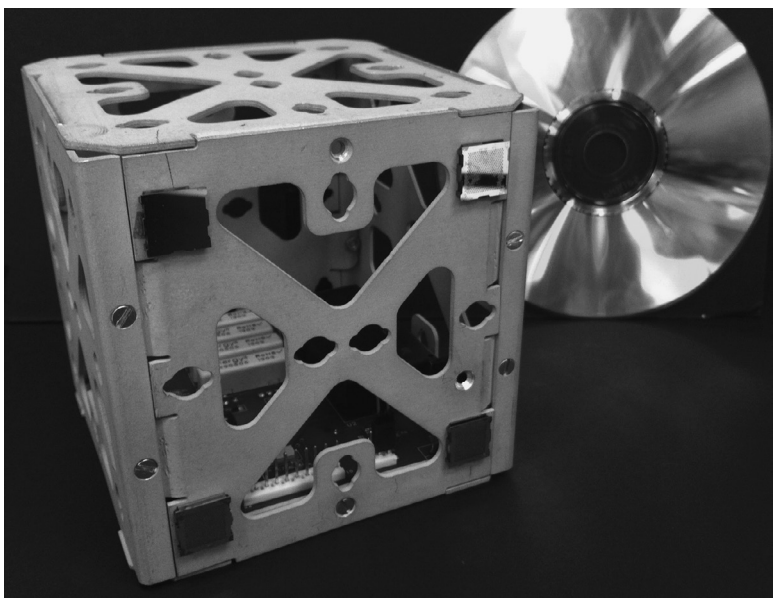

11.5 The ion electrospray propulsion system (iEPS) is an alternative to provide mobility to nano-satellites. The photo shows four laboratory iEPS thrusters and PPU card in an 1U CubeSat.

© Woodhead Publishing Limited, 2013

micro-etched on porous metal, it needs to be integrated with a silicon package. The use of dissimilar materials in MEMS, particularly in space applications, presents a number of design constraints, such as different thermal expansion characteristics and the ability to bond wafers together. As with other types of electrospray MEMS thrusters, the main challenge is to provide sufficient electric and hydraulic isolation against voltage differences in the order of 1 kV in a device with very small size tolerances and virtually *soaked* in a conductive liquid.

11.7 Future trends

In conclusion, the application of MEMS processes and techniques toward the design and fabrication of propulsion systems for nano- and pico-satellites provides a degree of flexibility that only recently has started to become a tangible possibility. The prospects for the future are tantalizing. Adding propulsion to very small satellites would allow them to undertake high performance missions so far restricted to large space platforms. For instance, propulsion would allow groups of small satellites to fly in formation cooperatively, thus enabling a whole suite of applications in communications, surveillance, science, etc., by taking advantage of fractionated and distributed architectures. The lifecycle costs associated with pico- and nano-satellites are relatively small, allowing a large number of non-traditional space players to participate with new applications and novel missions. The market for small satellites could grow significantly in the next decade, due to the great flexibility afforded by the combination of low cost and enhanced capabilities. Here again, propulsion will play an important role, as increasingly more small satellites will be able to operate in orbits that cannot afford the accumulation of disabled spacecraft. In all likelihood, the international community will reach an agreement to ensure that small satellites are de-orbited after their projected end of life to avoid further accumulation of manmade space debris. In upper lower Earth orbits (LEO), propulsion is the only practical method to force spacecraft re-entry.

There are a number of propulsion technologies amenable for miniaturization using MEMS. Some of these are based on chemical reactions, while others take advantage of the high propellant efficiency of ion propulsion. The use of MEMS materials and processes in this field is fundamentally different to usual practice, requiring the breed of a new type of propulsion specialist. An understanding of thermodynamic cycles and traditional manufacturing is no longer enough to succeed when designing propulsion systems for very small satellites. In addition, engineers will require an understating of materials science, nano-engineering, applied quantum physics, ion optics, plasma physics and other cross-cutting disciplines.

As the field of propulsion for pico- and nano-satellites evolves, attention should shift to the equally important miniaturization of ancillary components and, in the

© Woodhead Publishing Limited, 2013

case of electric thrusters, more compact and efficient PPUs. The outlook for some technologies, such as electrospray propulsion, is very interesting. In the near future, MEMS versions of these thrusters should be able to include thrusters, propellant management and power and control electronics, all in a single small package. Particularly interesting for small systems would be the use of high efficiency solar panels, such as recently developed inverted meta-morphic (IMM) cells that promise specific power values on the order of 100 W/kg with efficiencies as high as 30%. Using these technologies, it is not inconceivable to think of swarms of small robotic spacecraft exploring simultaneously all corners of the inner solar system, or the deployment of very complex and capable communications or remote sensing architectures. Interestingly, such ambitious plans would cost a fraction of the price tag of actual systems as enabled by the ingenuity of MEMS applied to propulsion systems and will certainly change the paradigm of access to space.

11.8 References

Barnhart D J, Vladimirova T and Sweeting M N (2007), 'Very-small-satellite design for distributed space missions', *J Spacecraft Rockets*, 44(6), 1294–1306.

Bayt R L (1999), 'Analysis, fabrication and testing of a MEMS-based micropropulsion system', PhD Thesis, MIT.

Bruccoleri A R, Leiter R, Drela M and Lozano P (2012), 'Experimental effects of nozzle geometry on flow efficiency at low Reynolds numbers', *J Prop Power*, 28(1), 96–105.

Chaalane A, Rossi C and Esteve D (2007), 'The formulation and testing of new solid propellant mixture (DB + x%BP) for a new MEMS-based microthruster', *Sens and Actu A*, 138, 161–166.

Courtney D G (2011), 'Ionic liquid ion source emitter arrays fabricated on bulk porous substrates for spacecraft propulsion', PhD Thesis, MIT.

Fernandez de la Mora J and Loscertales I G (1994), 'The current transmitted through an electrified conical meniscus', *J Fl Mech*, 260, 155–184.

Gassend B, Velasquez-Garcia L F, Akinwande A I and Martinez-Sanchez M (2009), 'A microfabricated planar electrospray array ionic liquid ion source with integrated extractor,' *J Microelect Syst*, 18(3), 679–694.

Hitt D L, Zakrzwski C M and Thomas M A (2001), 'MEMS-based satellite micropropulsion via catalyzed hydrogen peroxide decomposition', *Smart Mat Struct*, 10, 1163–1175.

Jahn R G (2006), *Physics of Electric Propulsion*, Dover, UK: McGraw-Hill.

Jamonet L (2002), 'Testing of a microrocket engine turbopump', SM Thesis, MIT.

Ketsdever A D, Lee R H and Lilly T C (2005), 'Performance testing of a microfabricated propulsion system for nanosatellite applications', *J Micromech Microeng*, 15, 2254–2263.

Khayms V (2000), 'Advanced propulsion for microsatellites', PhD Thesis, MIT.

Krpoun R, Smith K L, Stark J P W and Shea H R (2009), 'Tailoring the hydraulic impedance of out-of-plane micromachined electrospray sources with integrated electrodes', *Appl Phys Lett*, 94, 163502.

Legge R and Lozano P (2011), 'Electrospray propulsion based on emitters microfabricated in porous metals', *J Prop Power*, 27(2), 485–495.

Lozano P and Martinez-Sanchez M (2004), 'Ionic liquid ion sources: Suppression of electrochemical reactions using voltage alternation', *J Coll Interface Sci*, 280, 149–154.

© Woodhead Publishing Limited, 2013

Lozano P and Martinez-Sanchez M (2005), 'Ionic liquid ion sources: Characterization of externally wetted emitters', *J Coll Interface Sci*, 282, 412–421.

Lozano P C and Courtney D G (2010), 'On the development of high specific impulse electric propulsion thrusters for small satellites', 1915685, *The Small Satellites Systems and Services – The 4S Symposium*.

Mueller J, Hofer R, Parker M and Ziemer J (2010), 'Survey of propulsion technologies applicable to CubeSats', *57th JANNAF Propulsion Meeting*, Colorado Springs, CO.

Muncheberg S, Krischke M and Lemke N (1997), 'Nano-satellites and microsystems technology – Capabilities, limitations and applications', *Acta Astronautica*, 39(9–12), 799–808.

Paine M D (2002), 'A micro-fabricated colloid microthruster: high voltage electrostatic fields on a MEMS device', PhD Dissertation, University of Southampton.

Protz C S (2004), 'Experimental investigation of microfabricated bipropellant rocket engines', PhD Thesis, MIT.

Romero-Sanz I, Bocanegra R and Fernandez de la Mora J (2003), 'Source of heavy molecular ions based in Taylor Cones of ionic liquids operating in the pure ionic regime', *J Appl Phys*, 94(5), 3599–3605.

Rossi C, Conto T D, Esteve D and Larangot B (2001), 'Design, fabrication and modeling of MEMS-based microthrusters for space application', *Smart Mat Struct*, 10, 1156–1162.

Stenmark L and Lang M (1997), 'Micro propulsion thrusters and technologies', *2nd European Spacecraft Propulsion Conference, ESA SP-398*, pp. 399–405, 27–29 May. http://www.sscspace.com/about-the-ssc-group/ssc-companies/nanospace

Sutton G P and Biblarz O (2001), *Rocket Propulsion Elements*, New York: John Wiley and Sons.

Velásquez-García L F, Akinwande A I and Martínez-Sánchez M (2006), 'A microfabricated linear array of electrospray emitters for thruster applications', *J Microelect Syst*, 15(5), 1260–1271.

Woellert K, Ehrenfreund P, Ricco A J and Hertzfeld H (2011), 'CubeSats: Cost-effective science and technology platforms for emerging and developing nations', *Adv Space Res*, 47, 663–684.

Zhang K L, Chou S K, Ang S S and Tang X S (2005), 'A MEMS-based solid propellant microthruster with Au/Ti igniter', *Sens Act A*, 122, 113–123.

© Woodhead Publishing Limited, 2013

12

MEMS enabling space exploration and exploitation

R. OSIANDER and A. DARRIN,
The Johns Hopkins University Applied Physics Laboratory, USA

DOI: 10.1533/9780857096487.2.311

Abstract: This chapter covers the use of MEMS technology for space exploration and exploitation. Most current uses for MEMS in space applications are single devices in place of typically larger mechanical or electronic parts. Future spacecraft systems and instruments will consist of holistically integrated micromechanical and electronic parts. This chapter discusses both the use of MEMs in spacecraft systems and subsystems and in instrument and sensor applications. The chapter concludes with a section on the uniqueness of the space environment and reliability concerns of the space environment. To consider MEMS devices for space flight application, it is important to understand the environmental impacts.

Key words: nano-sat, satellite, spacecraft, sun sensor, attitude, GNC, magnetometer, spectrometer, radiation effects.

12.1 Introduction

There are numerous drivers for the miniaturization of space vehicles and their respective components in today's cost constrained environment. These drivers include low cost, low power consumption, low mass and low volume, while MEMS show an increased tolerance to the space environment when compared to conventional macroscale electro-mechanical devices. The commercial markets show a dramatic cost reduction via mass production of MEMS devices; these cost savings have yet to be realized in the space arena as a niche market looking for a small number of instruments or custom devices. The price advantage of MEMS in mass production may be less of a concern here than other drivers, the first being the very low mass and volume that enables a reduction in launch costs. Low power consumption is a factor for most MEMS devices, which have electrostatic actuation. In addition, there is a very small thermal constraint as it takes lower power to maintain temperature. The small size allows MEMS components to be resistant to vibration, shock and in some cases radiation, which will be discussed further. With the small components we can devise highly integrated, multi-functional components that simplify the systems. The unique nature of batch fabrication allows low cost mass production of larger arrays, another advantage that also has been seen in the electronics world. Space applications include components for traditional satellites subsystems as well as unique instrument capabilities for the scientific payloads. Typically, MEMS is an enabling technology, such as the mirror array for the James

© Woodhead Publishing Limited, 2013

Webb Space Telescope (JWST). The size reduction makes MEMS devices applicable for Nano-sats and Pico-sats (Osiander *et al.*, 2005).

12.2 Future trends in spacecraft – small satellites

Most current uses for MEMS in space applications are single devices in place of typically larger mechanical or electronic parts. Future spacecraft systems and instruments, such as the JWST, will consist of holistically integrated micromechanical and electronic parts. The path toward achieving economical, reliable high performance and accelerated space satellite development has been long and difficult. The idea of accessing space became a reality in the late 1950s, causing an explosive growth of development in military and scientific capabilities taking the space industry by storm. During this time, advancement in mission capacity was priority, not cost or schedule. While military space technology remained secret and mainly engaged with the Cold War, the National Aeronautics and Space Administration (NASA) and the European Space Agency (ESA) among others, successfully demonstrated increasingly complex scientific space missions. Space systems matured into large, complex, multi-mission satellites as launch vehicle technology increased carrying capacity. While the importance and challenge of maintaining a space presence was important, a shift in the focus of the space industry toward low cost, quick development spacecraft spurred a revisit to smaller satellites and missions. Continuing the advancement of space technology with less funding led to a variety of economical launch vehicle developments and increased usage of commercially available components.

With the end of the Cold War and public concern with expensive space missions, NASA introduced the Discovery Program in 1992 under the Faster, Better, Cheaper initiative to demonstrate low-cost interplanetary exploration with small satellites. Most of all, many priceless lessons were learned that have improved modern space program development for the military and science.

Many early space satellites are considered as small satellites. Satellites were constrained to be small because launch vehicles at that time were modified sub-orbital rockets not specifically designed to enter space with large payloads. In 1958, the first successful US space satellite, Explorer 1, was an 8.32 kg payload and launched to perigee 358 km by a Juno I rocket having a maximum payload capacity of 11 kg. Since then, many different launch vehicles have been developed to accommodate a variety of payload capacities ranging over 5 tons. Mass of a satellite design is directly related to a large component of program cost, the launch vehicle. An estimated launch cost of $20 000 per kg drives many programs to design small satellites (Sutherland, 2012). Advancements in miniaturization of satellite subsystems have created new small satellite classifications. Small satellites are categorized by mass (Fig. 12.1).

Modern small satellite mission capabilities are far beyond their predecessors. Satellite subsystems adopt consumer electronic designs, much like the cell phone,

© Woodhead Publishing Limited, 2013

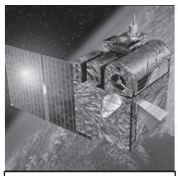	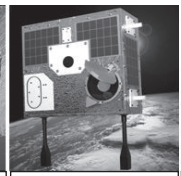	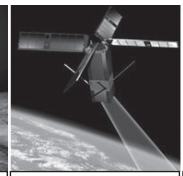	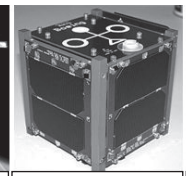	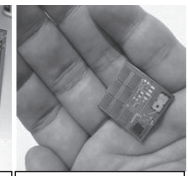
Mini (100–180 kg)	Micro (10–100 kg)	Nano (1–10 kg)	Pico (0.01–1 kg)	Femto (1–10 g)
Myriade bus: 120 kg known as Astrosat-100 2011 French military constellation, ELISA	MOST telescope: 53 kg Canada's first and only space telescope and world's smallest 2003	MBD 3U bus: 5 kg military mission capable design for the department of defense	CSTB1 1U bus: 1 kg 2007 Boeing's tech demonstration captured ground images with a CMOS camera	Cornell's sprite: 10 g 2011 satellite-on-a-chip to create a distributed wireless multi-point space sensor network

12.1 Definitions of very small spacecraft and respective examples.

to reduce size of components and deliver increased processing and battery efficiency. Availability of commercially off-the-shelf parts (COTS) plays a large role in making small satellites more appealing. COTS components for Nano- and Pico-size satellites are emerging, but are mostly of academic research quality. For achieving performance in a very small footprint, MEMS technologies become enablers. In 1999, California Polytechnic State University and Stanford University standardized a miniature satellite with intentions of conducting economical academic space research (Heidt *et al.*, 2001). Commonly used standard CubeSat dimensions are classified as 1 U (10 cm^3) and 3 U (30 × 10 × 10 cm), and must weigh less than 5.0 kg. The modest weight and volume requirements enable 'piggy back' launches, called rideshares, to split costs or use extra available space on launch vehicles.

12.3 MEMS in spacecraft subsystems

All spacecraft can be divided into the spacecraft bus and payload(s) (commercial, military or scientific). Especially with the recent push to smaller, less expensive spacecraft, MEMS devices have found their way into both the bus subsystems as well as the payloads. Spacecraft subsystems, which use MEMS technology, include guidance, navigation and control (GNC), communications and thermal control. Micro-propulsion will be discussed in another chapter in this collection, but with the small thrust levels, it is typically used only for spacecraft control.

12.3.1 Guidance, navigation and control (GNC)

The GNC system is one of the most critical systems on any spacecraft, responsible for executing the typical space mission operational functions such as orbital insertion, Sun acquisition, Earth acquisition, science target acquisition, pointing and tracking and orbital/trajectory Delta-V propulsive maneuvers. It consists of the attitude sensors such as star trackers and sun sensors, inertial measurement

© Woodhead Publishing Limited, 2013

units, actuators, typically momentum wheels and thrusters. MEMS devices have found applications in all of them.

To determine the spacecraft attitude, any quantity sensitive to it, for example the magnetic field vector or the angle to the sun or a star, can be used. They can be divided into course sensors, such as magnetometers, sun sensors, Earth horizon sensors and fine sensors, such as fine sun sensors and star cameras.

Very sensitive MEMS magnetometers have been developed for science measurements, and will be discussed later. Given the uncertainties in the magnetic field model, about 0.3 to 0.5° in low-earth orbit (LEO), the magnetometer sensitivity requirements for magnetometers as an attitude sensor are relatively weak, at a range of about ±60 μT, with a sensitivity of ±10 nT. MEMS magnetometers have been developed based on miniaturization of flux gates, as well as the Lorentz force acting on MEMS resonating bars and membranes. Since only the direction of the magnetic field is sensitive to attitude, another sensor such as a sun sensor is required. Xylophone bar magnetometers are based on a classical resonating xylophone bar. A sinusoidal current is supplied to the bar oscillating at the fundamental transverse resonant mode of the bar. When an external magnetic field is present, the resulting Lorentz force causes the bar to vibrate at its fundamental frequency with an amplitude directly proportional to the vertical component of the ambient magnetic field (Lamy *et al.*, 2010). One such approach to a xylophone magnetometer is illustrated in Fig. 12.2.

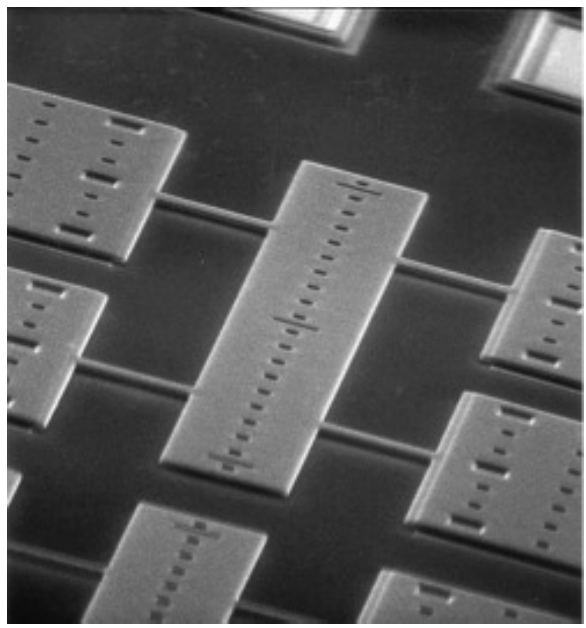

12.2 Example of xylophone style magnetometer. (Courtesy The Johns Hopkins University Applied Physics Laboratory.)

© Woodhead Publishing Limited, 2013

Sun sensors determine the direction to the sun, and work like a sundial. At MEMS dimensions, problems due to diffraction and reduced angular deflection arise when the masks approach MEMS dimensions. An example of a MEMS sun sensor is the JPL micro sun sensor (Liebe and Mobasser, 2001). In geosynchronous Earth orbit (GEO), Earth horizon sensors can be used for attitude measurements (in LEO, they only can tell up or down). They measure the thermal emission of the Earth and are based on an infrared detector or imager, a technology grown in recent years with the uncooled infrared imagers based on MEMS fabrication. Another way to measure attitude is by measuring the Earth's gravitational attraction with a MEMS-based gravity gradient sensor (Ghose and Shea, 2009).

Star trackers are similar to sun sensors, but sense the position of several stars at once and provide a more accurate attitude determination. They typically use an array of charge-coupled devices (CCDs) with very low power requirements, and can be combined with MEMS mirrors to allow for smart tracking (Clark, 2001). Attitude in LEO can also be determined via the global positioning system (GPS). One contribution MEMS is making to GPS is the fabrication of ultra-small atomic clocks (Lalgudi Venkatraman, 2011).

Gyroscopes and accelerometers are the building blocks of most spacecraft GNC systems. They are called inertial sensors, since their operation takes advantage of an object's inertia. Unlike attitude sensors, inertial measurements can only provide attitude via integration and therefore require some absolute attitude reference measurement to overcome integration of errors.

The technologies commonly used in today's inertial reference units (IRUs), for example in the Hubble space telescope (HST), include high performance mechanical (spinning mass) gyros, ring laser gyros and fiber optic gyros, with masses of a few kilograms and power requirements of 20 watts. MEMS gyroscopes, as discussed already, provide an opportunity to reduce mass and power drastically. The accuracy of a gyroscope is largely determined by its bias stability or drift rate, its angle random walk (ARW) and its scale factor stability, and depends strongly on the proof mass, a challenge for MEMS devices. The overwhelming majority of MEMS research and development activities to date have been focused on gyroscopes in either the high performance tactical class or in the consumer class. Realizing the importance for space applications, NASA, especially JPL, as well as ESA, have invested in the MEMS gyroscope technology for space applications. Figure 12.3 shows a JPL miniature single-axis vibratory Coriolis force MEMS gyroscope, which uses a large post rigidly attached to the center of the device formed by the four electrodes' proof mass to increase sensitivity (George, 2003).

The development of MEMS accelerometers has been driven by the demand of the automobile industry for an inexpensive accelerometer as an airbag sensor. For consumer applications, MEMS accelerometers and gyroscopes are integrated electrically and mechanically to create full 6-DOF IMUs, even employing Kalman filter processing. It is only a matter of time before they are used in spacecraft systems, which requires at least radiation hard electronics and proven durability.

© Woodhead Publishing Limited, 2013

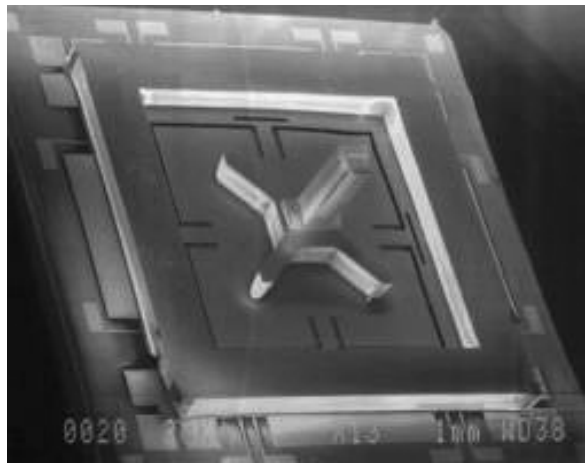

12.3 MEMS–based gyros offer the advantages of small volume and mass, low power, and reduced cost through batch fabrication. (Image courtesy of NASA/ Caltech JPL.)

There are two fundamental ways to control the attitude, either by applying torques on the external via propulsion, or by changing the angular momentum with reaction wheels. Of course, any such action, for example the spring supported launch of a probe or the start of a motor, will cause a change in the attitude if not compensated. Micro-propulsion is discussed elsewhere in this book. However, it is important to know that the specific impulse and the control capability of some of the micro-propulsion systems is sufficient to provide means of attitude control for even larger spacecraft.

Reaction wheels use electric motors to torque against high-inertia rotors or 'wheels'. When the motor exerts a torque on the wheel, an equal and opposite reaction torque is applied to the spacecraft. Micro-wheels of 100 mm diameter, micromachined in a stack of silicon wafers, have been demonstrated for attitude control and energy storage (Peczalski *et al.*, 2001). The small inertia of a typical MEMS device will make them less efficient and can only be compensated by extremely high speeds, which challenges the reliability requirements for such devices.

The use of MEMS microsystems for space mission applications has the potential to completely change the design and development of future spacecraft GNC systems. Their low cost, mass, power and size volume, and capability to mass-produce make MEMS GNC sensors ideal for science and exploration missions that look for performance and functionality in smaller and less expensive spacecraft. The challenge for MEMS engineers remains to achieve navigational class sensor performance and qualification to the harsh space radiation environment.

© Woodhead Publishing Limited, 2013

12.3.2 Communication systems

The communications subsystem receives and demodulates signals sent up from the ground station (uplink) and modulates and sends signals back to the ground station (downlink). The system is also responsible for any communication with other satellites. The uplink signal consists of commands and range tones, which are signals first transmitted by the ground station, and then received and retransmitted by the satellite. The delay is used to determine the satellite's distance from the station. In addition to range tones, the downlink signal includes telemetry for spacecraft status and any payload data. The downlink signal is usually coherent in phase with the uplink signal, which allows for Doppler shift detection of spacecraft velocity.

The signal frequency range for ground to satellite communications is anywhere from 0.2 to 50 GHz, depending on the application. Uplink and telemetry downlink data rates are typically less than 1 kbit/s, and are transmitted using low-bandwidth, wide-beam antennas. When payload data requires a higher transmission rate, high-gain, directional antennas are used. These antennas need to be steered either mechanically or electrically. Mechanical steering places additional demands on the attitude determination and control subsystem, which must balance the reaction forces caused by antenna movement.

One of the most exciting applications of MEMS for microwave communications in spacecraft concerns the implementation of 'active aperture phase array antennas' (Selleri and Toso, 2009). These systems consist of groups of antennas phase-shifted from each other to take advantage of constructive and destructive interference in order to achieve high directionality. Such systems allow for electronically steered radiated and received beams, which have greater agility and will not interfere with the satellite's position. They have been implemented with solid-state components; however, these systems are power-hungry, and have large insertion losses and problems with linearity. In contrast, phase shifters implemented with micro-electro mechanical switches have lower insertion loss and require less power. This makes MEMS an enabling technology for lightweight, low-power electronically steerable antennas for small satellites.

Microwave and RF MEMS are also applicable to commercial communication satellites, where communications systems make up the payload as well as being part of the satellite bus. These systems require many switches for signal routing and redundancy. In the past, they have been implemented by large electromechanical switches or by power-hungry solid-state switches. MEMS offer a lightweight, low-power alternative to such switches. Additional applications for MEMS in spacecraft communications systems include higher performance filters for transmitter/receiver circuits.

12.3.3 Thermal control

Thermal control systems are an integral part of all spacecraft and instruments, maintaining the temperature within a range required to function properly. The

© Woodhead Publishing Limited, 2013

basic heat sources in a spacecraft are the instruments, heaters or solar absorption, while the only heat loss mechanism is radiation. Thermal control uses heat pipes, thermal switches, heaters and louvers to move heat from the basic heat sources in a spacecraft onto radiators and away from instruments. Traditionally, thermal control has been more passive, designing the satellite in a way that radiators are thermally connected to the heat source and maintain a constant temperature. Often heaters or louvers are used to give it some control. The thermal mass of small satellites is very small and requires higher sophistication of control; especially since reduced radiator size as well as available heater power does not support the traditional approach. Unfortunately, thermal properties do not scale, that is a thin MEMS device has a smaller thermal resistance and thermal capacitance than a macroscopic device, and will only work for thermal control at the device level. MEMS-based thermal control devices are louvers, thermal switches, thermostat switches, heat pipes and, potentially, Stirling coolers or micropumps in the future.

The only way to remove heat from a spacecraft is by rejecting the heat from a radiator surface into space. Conventional louvers have been used traditionally to control the amount of cooling for a fixed size radiator. They typically provide closed to open effective emissivity variation of 0.1 to 0.6 over areas from 200 to 6000 cm^2. Disadvantages of traditional louver assemblies for small satellites are the size and weight, and the sensitivity to the solar position.

MEMS shutters and louvers have been suggested very early, as a means of thermal control using MEMS for nano- and pico-satellites (Osiander *et al.*, 2004). The Johns Hopkins University Applied Physics Laboratory (JHU APL), together with NASA Goddard Space Flight Center (NASA/GSFC) has designed, fabricated and tested a number of louver and shutter designs using MEMS surface micromachining. Figure 12.4 shows a radiator assembly with 36 MEMS die, each containing 72 shutter arrays, which were fabricated with the Sandia National Laboratory's SUMMIT5 process, assembled at JHU and flown with other approaches on the NASA/GSFC Space Technology 5 (ST-5) mission, launched in 2006, as demonstration technology for variable emittance coatings. This radiator was inspected to have 95% of the shutters working, was fully space-qualified, including thermal vacuum, vibration and shock, and was designed to survive shutter failure due to electrical shorts and micro-particles.

Thermal switches are active thermal control devices that allow the connection or disconnection of the thermal contact between two surfaces. Thermal switches are typically installed between an insulated spacecraft structure and an external radiator, for example between the battery on the Mars rover and the structure or the radiator. Various types of paraffin are often used in the thermal switches to create conduction paths when melted materials expand and bring components in close contact. A radiator based on electrostatic switching the contact between the radiator surface and the substrate has also been demonstrated (Beasley *et al.*, 2004).

Heat pipes are used to spread the heat within the structure and between the heat source and the sink, for example the radiator. They achieve this through a capillary

© Woodhead Publishing Limited, 2013

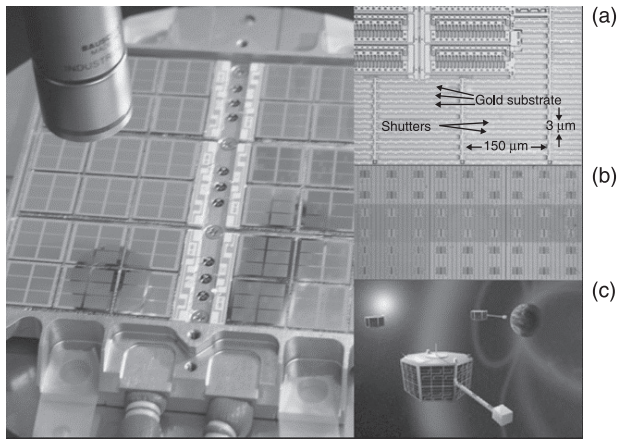

12.4 The ST5 MEMS radiator, consisting of 36 Shutter dies. (a) Close-up of the shutters and electrostatic motors.) (b) Close-up of part of the Shutter die. Each die contains 76 of these sections (9 shown. (Source: JHU/APL). (c) Artist's conception of the ST5 spacecraft constellation (Courtesy The Johns Hopkins University Applied Physics Laboratory).

driven, fluid phase change process in sealed tubes partially filled with a working fluid and a capillary wick acting as the pump. Large heat transfer rates can be achieved at an almost constant temperature in the system. MEMS-based heat exchange techniques have been investigated for cooling the central processing unit (CPU) on ground applications. The Sandia National Laboratories have developed micromachined vapor chamber heat spreaders and has patented a passively 'smart' heat transfer mechanism to remove heat dissipated by computer chips in the 50 watts/cm^2 range. MEMS-based heat pipes can address one of the basic issues in spacecraft thermal control, heat dissipation from densely packaged electronic parts assembled in electronic boxes.

MEMS pumps have applications in another thermal control system, fluid loops. In their simplified form, they consist of a pumping device, a heat exchanger and a space radiator. They are operated under the principle of forced liquid convective cooling. They require evaporator, condenser, reservoir and liquid and vapor lines, which can be etched into a silicon wafer, with a glass wafer with grooves etched for capillary pumping as a cover plate.

Stirling cooling, another active thermal control method, is theoretically able to achieve the maximum efficiency in cooling. Several MEMS-based active cooling systems, based on a Stirling cooler, have been suggested. Because heat dissipation is directly related to the volume to be cooled, thermal cycling occurs much faster in micro devices than in macro devices. MEMS thermal control devices may become a critical element in the demand for nano/micro-satellites, as they offer unique size, power and weight advantages.

© Woodhead Publishing Limited, 2013

12.4 MEMS in space science instrumentation

There are a number of insertion points for MEMS into scientific instruments, based on the advantages of microsystems. The small size of a MEMS device, and the small features with high aspect ratios, allow mechanically strong structures to be built with very small thermal conduction paths and small thermal capacities. Such devices can be used in micro-bolometers and allow the detection and imaging of particles and electromagnetic radiation from X-rays to mm-waves with very high resolution. The technology also allows small shutters or mirrors to be built, which can block or deflect light from a single pixel in a telescope such as the JWST, which is designated to replace the HST. The small dimensions also allow for building ultra-small plasma detectors and mass spectrometers with sufficient electric fields at very small supply voltages.

Science instruments can be divided into different groups based on the missions. For Earth and Solar Sciences, and in some respects, planetary and deep space missions, the detection, investigation and mapping of electromagnetic fields, particle distributions and gravitational fields are important. Instruments to be employed are plasma and ion detectors, magnetometers and accelerometers. For the observation of stars and planetary emissions, telescopes and spectrometers are of importance. Here, MEMS instruments can act as the detector such as a bolometer, or can improve the operation of the telescopes, as in the case of the JWST. For planetary exploration, MEMS instruments can help reduce the size and weight of planetary landers. Instruments such as hygrometers, seismometers, mass spectrometers and the magnetic resonance force microscope could be used for robotic and human exploration. Other instruments, those that measure the environmental conditions within the spacecraft or habitat, for example medical diagnosis instrumentations, or environmental monitors such as oxygen detectors, could be applied for human space exploration.

12.4.1 Electromagnetic field and particle detection for space science

MEMS-based detectors for electromagnetic fields and particles are expected to be important for future planetary and deep space missions, and their use in a constellation of satellites for the mapping of ion distributions or magnetic fields, as envisioned in some Earth Science mission concepts.

Typical plasma spectrometers, such as the Cassini INMS, designed to measure the positive ion and neutral environments of Saturn's icy satellites and rings, are rather large, require a huge amount of electrical power, are expensive and could not be easily implemented into 20 to 50 small satellites. Different micromachined designs have been investigated to generate electrostatic analyzers. One instrument, the MEMS-based flat plasma spectrometer, built by the JHU APL and the US Airforce Academy (USAFA), was mounted at the International Space Station in

© Woodhead Publishing Limited, 2013

2011 (Feldmesser *et al.*, 2010). This instrument, including sensor head array, printed circuit board with amplifier array electronics, power supply and chassis has been designed and built to occupy a volume of approximately 200 cm^3 in a 0.5 kg, 300 mW package.

The determination of planetary electric and magnetic fields and their interactions with the solar wind and other charged particles, have been an important focus for past space missions and in future mission planning. Magnetic measurements are essential for the maps used in satellite orientation and navigation, as well as for geophysical mapping of the Earth's electromagnetic field. For the Oersted mission, the fluxgate magnetometer's noise level was in the order of about 100 pT at 1 Hz, for deep space mission sensitivities below these levels are desirable. Initial attempts to micromachine fluxgates have resulted in sensitivities of the order of around 100 nT. Other miniature magnetometers have been based on magneto-resistance or giant magneto-resistance, which can achieve about 10 nT sensitivities at very high frequencies and relatively low noise levels. Magnetometer designs that have been successfully micromachined have been based on the torque or magneto-striction created by a ferromagnetic material, or the Lorentz force. An interesting approach for space application, where large current carrying supply lines can change the magnetic environment around the magnetic boom, is the use of such a magnetometer with remote interrogations.

The measurement of electric fields in space is important to investigate wave processes in space plasma. A prototype for a micromachined device based on a split Langmuir probe, consisting of two conductive plates in a small distance, was tested on board the Prognoz-10 satellite (Korepanov, 2002).

Precise and absolute measurement of magnetic fields is central for future planetary, solar and interplanetary missions. Atomic magnetometers have a history in space dating back more than 40 years, and they have flown in space vehicles ranging from high-altitude balloons to high-profile interplanetary missions. Present instruments of this type require significant resources, and their size, mass and power impose significant constraints on their use in space. Recent breakthroughs in microfabricated atomic devices have demonstrated reductions of resources by one to two orders of magnitude over conventional instruments, by incorporating micromachined elements into the devices and by using lasers rather than lamps as the excitation source. The fundamental technology is a miniature rubidium (Rb) vapor cell of chip-scale dimensions, fabricated by using micro-electromechanical systems techniques. These vapor cells have been used as frequency references in clocks, but by using suitable atomic transitions, they also function as magnetometers. The Rb vapor cell is enclosed by a ceramic heater (Fig. 12.5), and finally fabricated into a magnetic field sensor, all optical components of which have been evaluated for radiation tolerance to at least 50 krad(Si) of both proton and gamma radiation. In the assembled sensor, the microfabricated Rb vapor cell is illuminated with circular-polarized light from a vertical-cavity surface-emitting laser (VCSEL), and the resonant response of the atoms is detected by a photodiode (Korth *et al.*, 2010).

© Woodhead Publishing Limited, 2013

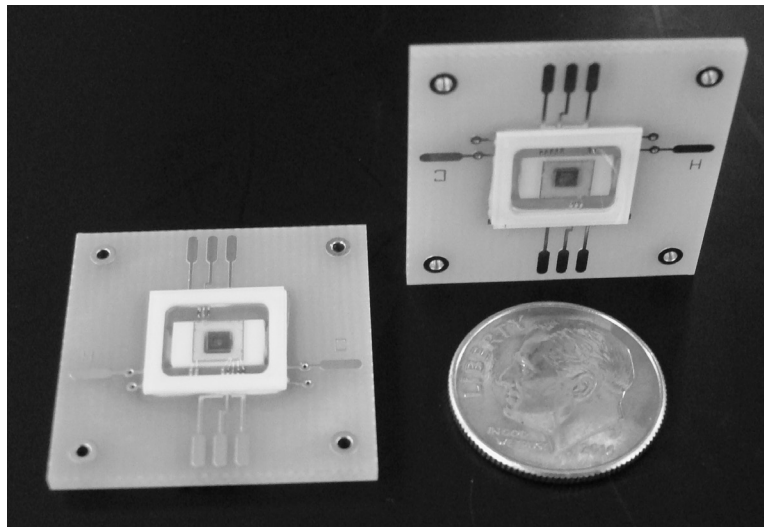

12.5 Miniature rubidium (Rb) vapor cell of chip-scale dimensions fabricated by using micro-electromechanical systems techniques. (Courtesy The Johns Hopkins University Applied Physics Laboratory.)

12.4.2 Telescopes and spectrometers

The development of optical MEMS components during the telecom boom of the late 1990s has provided building blocks for a new generation of space-based optical devices. Micromachined silicon slits and apertures provide a high degree of precision for critical optical paths, and have been used in spaceflight dual slit spectrometers. More dramatically, micro-opto-electromechanical systems (MOEMS) can deflect certain image areas to a spectrometer, can block other areas, or can be used to correct for optical aberrations in the telescope or the instrument. An example is the near infrared spectrograph (NIRSpec) for the JWST, which will have MOEMS devices as an integral part of the instrument (Li *et al.*, 2010). Targets in the field of view are normally selected by opening groups of shutters in a micro-shutter array (MSA) to form multiple apertures. Images of the shutters and the array are shown in Fig. 12.6. Another application, and one that is relatively well established, is in bolometers. Here, the small pixel size enabled by MEMS and the resulting small thermal capacities allow for integration of large arrays of very small bolometric devices, which can be used to detect radiation from the mm wave range all the way up to X-rays and particles.

A similar application is the use of dense arrays of MEMS mirrors in adaptive optics for space telescopes. This application requires that the mirror be positioned continuously and not just toggled between two positions. On terrestrial telescope applications, adaptive optics compensate for atmospheric turbulence during

© Woodhead Publishing Limited, 2013

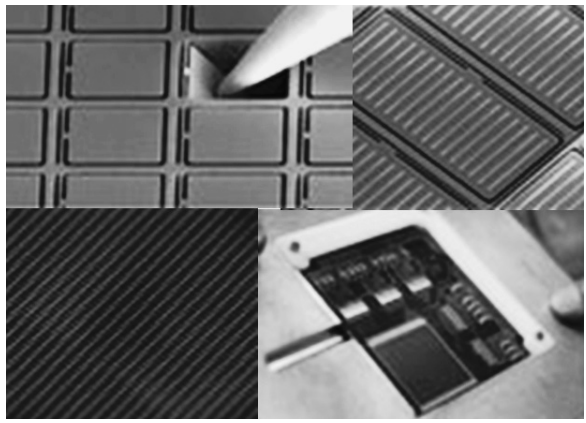

12.6 Images of the near infrared spectrograph (NIRSpec). Microshutters on the James Webb Space Telescope. Manual shutter operation (top left), shutters closed (top right), shutter array (bottom left) and shutter assembly (bottom right) (courtesy NASA).

observations. In principle, very faint objects can be imaged during long exposures, provided there is a bright 'reference beacon' nearby to allow the AO system to analyze the atmospheric effects. The same optics could be used in space-based applications to replace high-precision heavy-weight mirrors with light-weight mirrors corrected via adaptive optics.

The size of spectrometers, especially infrared spectrometers, has been rapidly reduced in recent years, due to uncooled IR detectors with ultra-small pixel size and modern micromachining techniques. Infrared spectrometers are some of the most important instruments since most molecules show a characteristic 'fingerprint' spectrum within this range, and reduction in size for these instruments will have a major impact on space-based observations. Their development has been propelled in recent years due to the sensor need for chemical and biological agent detection. One example is a Fabry–Perot based interferometer, which consists of two flat, parallel, semi-transparent silicon membranes coated with films of high reflectivity and low absorption. The pass band of the etalon is determined by the separation between the plates, which is generally varied using MEMS actuators based on thermal, electrostatic or piezoelectric effects (Barry *et al.*, 2000; Mott *et al.*, 2002; Sinclair *et al.*, 2004). Another approach for a MEMS infrared interferometer is the use of programmable diffraction gratings (Butler *et al.*, 2001; Sinclair *et al.*, 2004). Small ribbons, which constitute an optical grating, are actuated electrostatically to change the grating constant and therefore the transmission or reflection spectrum of the device. In correlation spectroscopy, a spectrum of interest is programmed into the grating and correlated with the received thermal infrared radiation to detect and identify substances such as chemical agents or pollutants in the environment.

© Woodhead Publishing Limited, 2013

The recent development of uncooled infrared imagers demonstrates the advantages of microstructures for thermal transport (Daly *et al.*, 2004). For small MEMS structures, very little absorption of infrared light (or any energy, including mm waves or X-rays) in these small structures with small thermal mass and low thermal conductance can generate a temperature rise easily measured due to thermal expansion or thermoelectric effects. The advantage of IR bolometers is that they can be used at ambient temperatures and are almost wavelength independent. Bolometers can be used not only for infrared radiation, but also for any other radiation such as X-rays (Jerominek *et al.*, 2009; Tralshawala *et al.*, 2000). MEMS are an enabling technology for these position sensitive spectrometers, which require the small size for resolution as well as for small thermal capacities.

12.4.3 MEMS sensors for planetary missions

All of the scientific spacecraft instruments discussed so far are essentially remote sensing devices, measuring photons, fields or particles from orbiting spacecraft. Equally important is the ability to measure the properties such as chemical composition encountered on a planet's surface or in its atmosphere. For example, mass spectrometers have been used in the exploration of our planetary system by robotic spacecraft to Venus, Mars, Jupiter, the Moon, the comet Halley, and most recently Saturn and its moon Titan. Other instruments, including X-ray spectrometers, nuclear magnetic resonance and scanning electron microscopes, have been flown or proposed for use in planetary exploration missions in order to identify the composition of planetary soils *in situ*. Traditionally, these instruments are large and consume a lot of power. Miniaturization would allow these instruments to be incorporated onto small multiple entry probes, autonomous rovers and sample handling systems such as robotic arms, booms and drills. MEMS technology will allow developing highly miniaturized versions of these instruments, subject to the requirement that they maintain the performance of existing spaceflight instruments, or add new capabilities such as to carry out analytical chemistry in the lab-on-a-chip integrated package.

In a mass spectrometer, ions are being introduced to the instrument by the sample handling system, and then separated by their charge to mass ratio in a mass filter, such as magnetic sectors, quadrupoles and RF ion traps. Another approach is time-of-flight measurements, in which ions of constant initial kinetic energy but different mass are separated by their flight times due to their differences in velocity. Work on MEMS-based mass spectrometers has been reported for all these approaches, but instrument performance has fallen far short of the requirements for a spaceflight mass spectrometer, and the need for additional research and development in this area is obvious.

Another *in situ* instrument is nuclear magnetic resonance as a very sensitive way to detect the presence of water, and therefore a desirable instrument on any

© Woodhead Publishing Limited, 2013

explorer mission. Recent approaches, potentially being built entirely on a MEMS/microelectronics platform, are based on magnetic resonance force microscopy, where the force applied by the spins rotating in a RF filed on a micromachined resonant cantilever beam with a magnetic particle is measured via interferometric techniques. Such instruments could potentially be used in space exploration as element detectors for landers. While it is difficult to imagine the instrumentation for future spacecraft, which will be enabled or improved by the integration of MEMS, it is obvious from the examples that this path has been started, and there are devices that can be inserted into space systems, as well as devices that are already designed and fabricated for specific missions.

12.5 Reliability concerns in the space environment

MEMS devices used in space missions are exposed to many different types of environments. These environments include manufacturing, assembly, test and qualification at the part, board and assembly levels. Subsystem and system level environments include pre-launch, launch and mission. Each of these environments contributes unique stress factors. To assure long-life performance, numerous factors must be considered in relation to the mission environment when determining requirements to be imposed at the piece part (MEMS device) level. The high reliability required of all space equipment is achieved through the use of good design practices, design margins (e.g. de-rating) and manufacturing process controls, which are imposed at each level of fabrication and assembly. Design margins ensure that space equipment is capable of performing its mission in the space environment. The manufacturing process controls are intended to ensure that a product of known quality is manufactured to meet the design requirements and that any required changes are made based on a documented baseline.

12.5.1 Thermal effects

Spacecraft may receive radiant thermal energy from two sources: incoming solar radiation (solar constant, reflected solar energy, albedo) and outgoing long wave radiation (OLR) emitted by the Earth and the atmosphere (Bonnie and James, 1994). High temperature causes adverse effects on spacecraft system parts and components, such as cracking, separation, wear-out, corrosion and performance degradation. These temperature-related defects may affect the electronic parts, the mechanical parts and the materials in a spacecraft.

The temperature of the spacecraft pre-launch and launch environment is controlled by the supply of conditioned air furnished to the spacecraft through its fairing. The launch vehicle itself also controls the pre-launch thermal environment. Spacecraft typically require a temperature range of 9 to 37°C. The highest ascent temperatures measured on the inside of the payload fairing have ranges from 27°C for the Orbiter to 204°C for the Delta and Atlas vehicles.

© Woodhead Publishing Limited, 2013

Ageing effects of temperature are modeled after the Arrhenius or Eyring equations, which can be used to estimate the longevity of the subsystem. However, the activation energy is based on electrochemical effects, which may not be the predominant failure mode, especially in the mechanical aspects of the MEMS device. Lack of an established reliability base remains a precautionary note when evaluating MEMS for space applications. Accelerated stress testing can be used to activate latent failure mechanisms. The temperatures used for accelerated testing at the parts level are more extreme than the temperatures used to test components and systems. The latter temperatures exceed the worst case predictions for the mission operating conditions to provide additional safety margins.

In many cases, the space environment presents extreme thermal stress on the spacecraft. High temperature extremes result from the exposure to direct sunlight and low temperature extremes result because there is no atmosphere to contain the heat when not exposed to the sun. This cycling between temperature extremes can aggravate thermal expansion mismatches between materials and assemblies. Large cyclic temperature changes in temperature can cause cracking, separation and other reliability problems for temperature sensitive parts. For example, in a typical 550 km LEO, there would be approximately 15 eclipse cycles over a 24-hour period. In a GEO, there would be only 90 cycles in a year, with a maximum shadow time of 1.2 hours per day. Temperature cycling is also a major cause of fatigue-related solder joint failures.

12.5.2 Mechanical effects of shock, acceleration and vibration

Mechanical factors that must be considered are acceleration, random vibration, acoustic vibration and shock. The effects of these factors must be considered during the launch phase, during the time of deployment of the system, and to a lesser degree, when in orbit or planetary trajectory. Qualification at the component level includes vibration, shock and thermal vacuum tests. Acceleration loads experienced by the payload consist of static or steady state, and dynamic or vibration loads. For the Shuttle program, payloads are subjected to acceleration and vibration during re-entry and during emergency or nominal landings (as well as the normal ascent acceleration and vibration-load events).

The vibration environment during launches can reach accelerations of 10 g at frequencies up to 1000 Hz. Vibration effects must also be considered in the design of MEMS assemblies. When the natural frequency of the system and the forcing frequency coincide, the amplitude of the vibration could become large and destructive. MEMS assemblies must be designed so that the natural frequencies are much greater than the forcing frequencies of the system. In general, due to the low mass of MEMS devices, the effect of vibration will be minimal but assuredly must be taken into consideration with the packaging. For example, long wire bond leads have reached harmonic frequencies causing failures during qualification tests.

© Woodhead Publishing Limited, 2013

Random vibration and multi-vibration tests (i.e. swept sine, or frequency sine combined with random vibration) are typically performed. Even commercial manufacturers of mass-produced MEMS devices, such as accelerometers for air bag deployment, have incorporated shock and drop tests to their routing quality screens.

12.5.3 Chemical effects

Chemical effects on MEMS devices include high humidity environments, out-gassing and atomic oxygen (AO). Moisture from high humidity environments can have serious deleterious effects on MEMS devices. Moisture causes corrosion, swelling and loss of strength, as well as stiction and oxide bridging. To protect against moisture effects, electronic packages are typically hermetically sealed. However, many MEMS devices, especially those used for environmental sensors, cannot be hermetically sealed and require additional precautions. Moisture exposure during mission and launch is limited by the control of the environment. Prior to launch, the humidity of storage and processing must be controlled.

Materials used in near proximity or enclosed hermetically with optical components or surface sensors – which might include exposed MEMS devices – require stringent collected volatile condensable materials (CVCM) percentages of less than 0.05%. Out-gassing is of particular concern from such parts as wire, cable and connectors. Materials for space electronics must be able to meet a unique set of requirements, including stability under high vacuum and the radiation of space (stability in high AO and UV conditions). AO can attack exposed MEMS devices and impact their electronic and mechanical properties. AO exists in significant amounts around LEOs and around Mars. It is highly reactive; exposure to AO tends to cause metals to develop an oxide on their surface, whereas polymers tend to lose mass and undergo a change in surface morphology. Due to their high reactivity with AO, polymers and other composites need to be protected. In general, AO will not be a concern to many of the MEMS materials, especially for applications that do not require exterior exposure.

12.5.4 Radiation effects

Most of the investigations of radiation damage by charged particles, including electrons, protons and heavy ions ($Z > 2$) have been in electronic, opto-electronic and optical devices. Those results can be partially applied to the case of radiation damage in MEMS.

Radiation effects in electronic circuits, consisting of complementary metal-oxide-semiconductor (CMOS) or bipolar transistors, may be severe and have been investigated for a long time. These effects are still important for MEMS devices, which in general are somewhat connected to CMOS electronics, especially as COTS components with high integration.

© Woodhead Publishing Limited, 2013

When charged particles interact with the bound electrons in the atoms, they leave in their wake a track of charge consisting of electrons and holes. Most of the radiation damage that occurs in MEMS can be attributed to the charge liberated when energetic ions traverse the device. Ions passing through metal layers in MEMS generate electrons, which are a tiny fraction of the electrons already present, and so have no effect on MEMS performance. In contrast, ions passing through may become trapped at sites where they can reside for long time periods. Their presence distorts the electric fields in the immediate vicinity of those sites, and can cause long-term device degradation in the form of increased leakage currents and, eventually, functional failure. These are typically called total ionizing dose (TID) effects, because the device performance degradation depends on the total amount of charge generated over time. The effects of TID on MEMS can be in either the electronic or mechanical parts of the device, or both. Single-event effects, where a single particle is interacting with the material and liberates sufficient charge to cause an effect, typically do not affect mechanical MEMS structures.

12.5.5 Particulates

Another environmental effect, typically only seen for environmentally exposed MEMS devices, are particulates. In zero gravity, a significant reliability concern is posed by loose or floating particles. In the process of manufacturing integrated circuits or discrete semiconductor devices, loose conductive particles (e.g. solder balls, weld slag, flakes of metal plating, semiconductor chips, die attach materials, etc.) can be within the device packaging prior to seal. In a zero gravity environment, these particles may float about within the package and bridge metallization runs, short bond wires and otherwise damage electronic circuitry. The use of a particle capture test through sticky tapes and other getter type materials is one mitigation approach. The inability to 'blow off' particulates with an inert gas where release structures are present reinforces the need for an effective contaminant control program.

12.6 Conclusion

This chapter serves as an introduction and overview to MEMS insertion into space applications. It is clearly evident from this overview that MEMS hold great promise for almost every component application in space vehicles. Current uses are single devices in place of typically larger mechanical or electronic parts. However, it will not be long before entire systems are replaced with micron scale components. This chapter introduced many of these potential applications. For scientific instruments to communication systems, the breadth of potential opportunities is impressive. The use of microsystem fabrication techniques will revolutionize size and functionality of future scientific instrumentation as well as

© Woodhead Publishing Limited, 2013

spacecraft. Distributed nano-satellites enabled by MEMS technology will further our ability to explore and exploit the space environment.

12.7 References

Barry R K, Satyapal S, Greenhouse M A, Barclay R, Amato D D, *et al.* (2000), 'Near IR Fabry–Perot interferometer for wide field, low resolution hyperspectral imaging on the next generation space telescope', *Proc SPIE*, 4013, 861.

Beasley M A, Firebaugh S L, Edwards R L, Keeney A C and Osiander R (2004), 'MEMS thermal switch for spacecraft thermal control', *Proc SPIE*, 5344, 98.

Bonnie F and James C (1994), *The Natural Space Environment Effects on Spacecraft*, NASA Reference Publication 1350.

Butler M A, Senturia S D, Deutsch E R, Sinclair M B, Sweatt W C, *et al.* (2001) 'A MEMS-based programmable diffraction grating for optical holography in the spectral domain', *Technical Digest – International Electron Devices Meeting IEDM 2001*, p. 909.

Clark N (2001), 'Intelligent star tracker', *Proc SPIE*, 4592, 216.

Daly J T, Johnson E A, Bodkin A, Stevenson W A and White D A (2000), 'Recent advances in miniaturization of infrared spectrometers', *Proc SPIE*, 3953, 70.

Feldmesser H S, Darrin M, Osiander R, Paxton L J, Rogers A Q, *et al.* (2010), 'Canary-ion spectroscopy for ionospheric sensing', *Proc SPIE*, 7691, 76910.

George T (2003), 'Overview of MEMS/NEMS technology development for space applications at NASA/JPL', *Pro SPIE*, 5116, 136.

Ghose K and Shea H (2009), 'Fabrication and testing of a MEMS based earth sensor', *Proc IEEE*, p. 327.

Heidt H, Puig-Suari J, Moore A S, Nakasuka S and Twiggs R T (2001), 'CubeSat: a new generation of pico-satellite for education and industry low-cost space experimentation', *Proceedings of the Utah State University Small Satellite Conference*, Logan, UT.

Jerominek H, Pope T D, Alain C, Zhang R, Lehoux M, *et al.* (2009), '128 × 128 pixel uncooled bolometric FPA for IR detection and imaging', *Proc SPIE*, 3436, 585.

Korepanov V (2002), 'Electromagnetic sensors for microsatellites', *Proc IEEE Sens*, p. 1718.

Korth H, Strohbehn K, Tejada F, Andreon A, McVeigh S, *et al.* (2010), 'Chip-scale absolute scalar magnetometer for space applications', *Johns Hopkins APL Technical Digest*, 28(3), 248.

LalgudiVenkatraman V, Pétremand Y, Affolderbach C, Mileti G, de Rooij N, *et al.* (2011), 'Microfabrication and packaging of a rubidium vapor cell as a plasma light source for MEMS atomic clocks', *Proc Transducers, IEEE*, 1907.

Lamy H, Niyonzima I, Rochus P and Rochus V (2010), 'A xylophone bar magnetometer for micro/pico satellites', *ActaAstro*, 67(7–8), 793.

Li M J, Brown A D, Kutyrev A, Moseley S and Mikula V (2010), 'JWST microshutter array system and beyond', *Proc SPIE*, 7594, 75940N.

Liebe C C and Mobasser S (2001), 'MEMS based sun sensor', *IEEE Aerospace Conf Proc*, 3, 31565.

Mott D B, Barclay R, Bier A, Chen T, DiCamillo B, *et al.* (2002), 'Micromachined tunable Fabry–Perot filters for infrared astronomy', *Proc SPIE*, 4841, 578.

Osiander R, Firebaugh S L, Champion J L, Farrar D and Darrin A G (2004) 'Micro-electromechanical devices for satellite thermal control', *IEEE Sens J*, 4, 525.

© Woodhead Publishing Limited, 2013

Osiander R, Darrin A G and Champion J L (2005), *MEMS and Microstructures in Aerospace Applications*, Boca Raton, FL: CRC Press.

Peczalski A, Elgersma M, Quenon D, Jacobs, J (2001), 'Micro-wheels for attitude control and energy storage in small satellites', *IEEE Aerospace Conf Proc*, 5, 52483.

Selleri S and Toso G (Eds.) (2009), *Active Antennas for Space Applications, International Journal of Antennas and Propagation* (Special Issue), Hindawi Publishing Corporation.

Sinclair M B, Pfeifer K B, Butler M A, Senturia S D, Deutsch E R, *et al.* (2004) 'A MEMS-based correlation radiometer', *Proc SPIE*, 5346, 37.

Sutherland B (2012), *Modern Warfare, Intelligence and Deterrence: the Technologies that are Transforming Them*, New Jersey: John Wiley & Sons, p. 79.

Tralshawala N, Aslam S, Brekosky R P, Chen T C, Figueroa Feliciano E, *et al.* (2000), 'Design and fabrication of superconducting transition edge X-ray calorimeters', in *Nuclear Instruments and Methods in Physics Research, Section A: Accelerators, Spectrometers, Detectors and Associated Equipment*, 444(1), p. 188.

© Woodhead Publishing Limited, 2013

Index

AAVID Thermalloy, 269
accelerometer, 8–13, 193–5
  bias stability peak-peak value, 195
  Colibrys MEMS accelerometer *vs.* Honeywell QA2030, 195
  mixed-signal high-order sigma-delta dual-quantisation loop, 193
  system dynamics after 6000 g shock, 194
active damping, 30
active drag reduction
  actuators, 166–72
    basic design of zero-net-mass-flux 'synthetic' jet, 167
  future trends, 172–3
  micro-electromechanical systems (MEMS) devices in aerospace applications, 153–73
  overview, 153–60
    contrasting perspectives, 157–60
    streamwise velocity and pressure instantaneous contours, 158
    transport CO_2 emissions by mode, 155
  surface sensors, 160–6
active sensing mode, 234
'aero-MEMS' market, 248
aerospace
  MEMS pressure and flow sensors for automotive engine management, 78–103
    concentration, density and fuel quality sensors, 95–7
    design process, 81–6
    flow sensors, 89–94
    looking forward, 103
    packaging MEMS sensors for harsh environments, 99–103
    pressure sensor, 86–9
    sensor signal conditioning, 97–8
    sensors used in system/engine management, 78–81
  micro-electromechanical systems (MEMS) devices for active drag reduction, 153–73
    actuators, 166–72
    future trends, 172–3
    overview, 153–60
    surface sensors, 160–6
air bag, 6
air quality, 143
aircraft
  MEMS for structural health monitoring, 220–41
    MEMS devices for embedded SHM, 228–40
    promising developments, 240–1
    state of the art application for aerospace structures, 223–8
    typical aeronautical structure, 222
  micro-electro mechanical system (MEMS) inertial navigation systems, 177–216
    future trends, 216
    global positioning system (GPS), 207–16
    microfabrication, 189–207
    overview, 177–89
alignment, 206
Allan variance (AVAR), 202–4
  analysis results, 203
amplitude shift keying (ASK), 66
Analog Device ADXL50, 12
Analog Device ADXL78, 12
Analog Device ADXRS612, 17
analog-to-digital converter (ADC), 63
angle random walk (ARW), 315
angular rate sensor, 13–19, 39–45

© Woodhead Publishing Limited, 2013

angular velocity sensors, 39–41
performance requirements for different gyroscopes, 40
micromachined gyroscope technology, 42–5
tuning fork, 43–5
vibrating-wheel, 43
vibratory, 42
operating principles, 41–2
gyroscopes using Coriolis Effect, 41
anti-lock braking system (ABS), 4, 30
anti skid control (ASC), 30
application-specific integrated circuits (ASICs), 229
arcjets, 290–1
ARINC 429, 80
Arrhenius equation, 326
automotive engine management
MEMS pressure and flow sensors for aerospace application, 78–103
concentration, density and fuel quality sensors, 95–7
design process, 81–6
flow sensors, 89–94
looking forward, 103
packaging MEMS sensors for harsh environments, 99–103
pressure sensor, 86–9
sensor signal conditioning, 97–8
sensors used in system management, 78–81
automotive and aircraft sensor networks, 80–1
MAF and MAP sensor, 79
automotive radar sensors
radio-frequency micro-electromechanical systems (RF MEMS), 106–34
components, 110–21
front-end technology, 121–6
overview, 106–10
radar beam steering technology, 126–33
automotive safety integrated levels (ASIL), 50
automotive tire pressure monitoring systems
applications – state of the art TPMS module, 57–8
electrical components of battery, 58
rim-based mounting of an OEM, 57
applications and solutions, 55–9
direct and indirect TPMS systems, 55–6
direct systems, 56–7
schematic, 56
future applications, 74–5
commodity – system reduction costs, 74–5
integration into tire, 75
MEMS, 54–76
power management, 67–74
pressure sensors and technologies, 59–65
requirements, 65–7
life-time vs current consumption, 67
pressure sensor, 65–6
standards and protocol, 66–7
systems with localisation, 59
typical display, 59
systems without localisation, 58–9
typical display of TPMS warning lamp, 58
automotive vehicles
MEMS for passenger safety, 3–26
accelerometers for crash sensing systems, 8–13
angular rate sensors for rollover detection systems, 13–19
future trends in safety sensing systems, 23–5
passenger safety systems, 4–8
strain gauges for occupant sensing systems, 19–23
autonomous cruise control (ACC), 106
avionic full-duplex (AFDX), 80
axes misalignment, 205

ball-in-tube sensor, 8
barometric absolute pressure (BAP), 79
Bayesian statistics, 226–7
bias, 204–5
bias instability, 205
bias variation over temperature, 205
BiCMOS, 12
body frame, 182
bolometers, 324
boundary layer approximation, 154
bulk-acoustic wave, 72
bulk micromachining (BMM), 60–1
pressure sensor as triple stack, 61

capacitive effect, 11
capacitive/piezo-resistive detection schemes, 62–4
pressure sensor with analog-to-digital conversion, 63

© Woodhead Publishing Limited, 2013

Wheatstone bridge configuration for pressure sensor, 63
capacitive pressure sensors, 88–9
carouseling, 207
Cassini INMS, 320
charged-droplet emitters, 304
chemical propulsion, 288–90
chemical propulsion thrusters, 289
cold gas thrusters, 288
design considerations, 299–302
boundary layer thickness, 300–2
feel pressure and thermal management, 299–300
propellant management, 300
thruster feedthroughs, 300
liquid bipropellants, 289–90
liquid monopropellants, 288–9
solid propellants, 290
chemical vapour deposition (CVD), 87
chip-sats, 284
climate control, 142–4
microfabricated sensors for measuring temperature and humidity, 144
closed-loop inertial sensors, 201–2
cold gas thrusters, 288
collected volatile condensable materials (CVCM), 327
colloid thrusters, 304
comparative vacuum monitoring (CVM), 230
complementary metal oxide semiconductor (CMOS), 62
complex flow, 154–5
computational fluid dynamics (CFD), 81
concept of operations (CONOPS), 252
concurrent engineering, 254
condition based maintenance (CBM), 220, 221, 227
coning error, 207
constant bias, 205
continuous-wave radar (CWR), 108–9
controller area network (CAN), 80
Coriolis effect, 14–16, 41–2, 196
mass flow sensors, 93–4
roll sensor, 16
correlation spectroscopy, 323
crash sensing systems
accelerometers, 8–13
background, 8–9
ball-in-tube sensor and rolamite sensor, 8
MEMS sensors implementation, 11–13
MEMS sensors implementation, 11–13
manufacturing processes comments, 12–13
system integration, 13
technical details of typical devices, 12
vehicle showing sensors scheme, 13
operation principles for MEMS sensors, 9–11
mass-spring damper system, 9
cross-axis response, 205–6
cruise control, 138
CubeSats, 298

3-D integration, 229
deep reactive ion etching (DRIE), 83
dielectric barrier discharge (DBD), 168
differential pressure flow sensors, 89–91
digital signal processor (DSP), 38
dimples, 169–72
active dimple formation through buckling, 172
circular EAP actuator, 171
direction cosine matrix (DCM), 182–3, 186
distributed front airbag sensing system, 8
distributed MEMS transmission line phase shifter, 115–16
low-loss distributed 2-bit W-band MEMS DMTL phase shifter, 116
Domain Controller ECU
integration of all inertial sensors, 48–50
sensor cluster, 49
six degrees of freedom (DoF) into vehicle, 49
driving techniques, 16–17
MEMS sensors, 17

earth-centered earth-fixed (ECEF) frame, 181
earth-centered inertial (ECI) frame, 181
Eddy current based sensor, 231–2
Eddy current MEMS sensor characteristics, 232
Eddy currents generated in conductive plate, 231
eddy current testing (ECT), 231
electric propulsion, 290–3
arcjets, 290–1
electromagnetic engines, 291
electrospray thrusters, 292–3
gridded ion engines, 291
hall thrusters, 291–2
illustration, 292
resistojets, 290

© Woodhead Publishing Limited, 2013

electrically programmable memory (EPROM), 97
electroacoustic wave resonator, 118
electromagnetic engines, 291
electromagnetic wave resonator, 118
electromechanical wave resonator, 118
electromechanically tunable capacitor, 112
electronic control unit, 5
electronic stability control (ESC), 29
  description of system, 31–4
  inertial devices, 47–8
    combo sensor, 47
electrospray thrusters
  design considerations, 303–8
    capillary emitter arrays, 304–5
    externally wetted arrays, 305–6
    ion electrospray propulsion system, 307
    micro-tip emitter arrays fabricated on porous metal, 307
    porous metal arrays, 306–8
electrostatic actuation, 110–11
electrostatically actuated capacitive shunt switch, 111
electrostatically actuated series switch, 111
Elk test *see* moose test
energy harvesting, 71–4
error operator, 188
Euler angle, 183–4
exhaust gas recirculation (EGR) system, 79
Eyring equation, 326

Fabry–Perot based interferometer, 323
failure modes and effects analysis (FMEA), 50
failure modes effects and diagnostic analysis (FMEDA), 50
Federal Motor Vehicle Safety Standards (FMVSS), 54
fiber Bragg grating (FBG) sensor
  application for SHM, 236–40
  FBG system working principle, 237
fibre Bragg grating (FBG), 163
fibre optic pressure sensors, 89
Fisher-Tropsch (FT), 97
flow sensors, 89–94
  Coriolis mass, 93–4
    cross-section of vacuum packaging and gettering approach, 94
    MEMS chip and resonating microtube, 94
  differential pressure, 89–91
    jet mounted Pitot tube, 90
    pitot-static or prandtl tube, 91
  hot wire, 91–3
    bidirectional thin-film thermal anemometer, 92
    hybrid ceramic hot wire flow sensor integrated into fuel injector, 93
  MEMS pressure sensors for automotive engine management and aerospace application, 78–103
    concentration, density and fuel quality sensors, 95–7
    design process, 81–6
    looking forward, 103
    packaging MEMS sensors for harsh environments, 99–103
    pressure sensor, 86–9
    sensor signal conditioning, 97–8
    sensors used in system/engine management, 78–81
fluctuation skin-friction, 163
force deflector types, 19–21
  schematic diagram, 20
forced convection, 162
forward longitudinal crashes, 6
free molecule micro-resistojet (FMMR), 303

g^2-sensitivity, 206
gimbaled
  stable platform mechanisation, 179–80
    inertial navigation system, 179
global navigation satellite system (GNSS), 178
global positioning system (GPS), 178–9, 207–16
  INS complementary characteristics, 208
gridded ion engines, 291
gyrocompassing, 206
gyroscope, 40
  g-sensitivity, 206
Gyrotron angular rate tachometer, 40

Hall Effect, 14
hall thrusters, 291–2
health and usage monitoring systems (HUMS), 220
HECTOR (helicopter fuselage crack monitoring and prognosis through onboard sensor network), 227–8
high-pulse repetition frequency (HPRF) mono-pulse Doppler-radar front-end, 121–3

© Woodhead Publishing Limited, 2013

complete 38-GHz RF MEMS-based front end, 122
transmit and receive mode radiation characteristic, 123
hot wire flow sensors, 91–3
Hubble space telescope (HST), 315
hybrid laminar flow control (HLFC), 156

ICV-SLID technology, 230
impulsive, 286
incoming solar radiation, 325
inertial measurement unit (IMU), 177–8
aerospace applications, 213–16
AIS SiIMU02 MEMS IMU, 214
DARPA MEMS IMU, 213
Honeywell HG1930 MEMS IMU, 214
inertial navigation system (INS)
future trends, 216
global positioning system (GPS), 207–16
micro-electro mechanical system (MEMS) for aircraft, 177–216
microfabrication, 189–207
overview, 177–89
ISA, IMU and INS relationship, 178
roll, yaw and pitch axis definition for an airplane, 178
inertial reference frame, 181–2
e -frame strapdown mechanisation, 181
inertial reference units (IRU), 315
inertial sensor assembly (ISA), 177–8
inertial sensors, 189–202, 315
accelerometer and gyro biases for different grades of IMU, 190
current accelerometer technology applications, 191
current gyro technology applications, 192
noise characteristics, 202–7
Inland Transport Committee for Tire Pressure Monitoring, 54
inline DC-contact MEMS series switch, 112
INS/GPS system
aerospace applications, 213–16
AIS SiNAV MEMS INS/GPS, 215
attitude errors using INS simulations, 216
position and velocity errors using INS simulations, 215
deeply coupled architecture, 212–13
illustration, 212
loosely coupled architecture
illustration, 211
tightly coupled architecture, 211–12
illustration, 211–12
integrated circuits (IC), 81
inter-digital transducer (IDT), 233
international reference meridian (IRM), 181
international reference pole (IRP), 181
inverted meta-morphic (IMM) cells, 309
ion Electrospray Propulsion System (iEPS), 307
ionic liquid ion sources (ILIS), 306
ISO 21750, 2206, 54
ISO 9141-2, 80

James Webb Space Telescope (JWST), 312
John Hopkins University Applied Physics Laboratory (JHU APL), 318

Kalman filter, 208–9
application to aid INS, 210–13
INS error model, 209–10
Kapton Layer, 235

laminar boundary layer, 154
Larmor radius, 296
lateral acceleration sensor, 34
leaky-wave antenna (LWA), 128–9
scattering parameters, 129
unit cell, 128
whole chip, wire bonds and membranes, 130
liquid bipropellants, 289–90
liquid monopropellants, 288–9
local frame, 182
long-range radar (LRR), 108, 110
Lorentz force, 314, 321

manifold absolute pressure (MAP), 78
mass air flow (MAF), 78
mass spectrometer, 324
mass-spring-damper system, 9
mechanical package design, 99–100
mechanically driven antenna platform, 129–32
proposed RF antenna and design layout, 131
radiation beam pattern, 132
Melexis MLX80807/8, 22
MEMS-based Faraday cage, 118, 121
MEMS sensors
accelerometer in ESC, 35–9
ASIC circuit improvements, 37–8

© Woodhead Publishing Limited, 2013

digital communication capability, 38
packaging, 38–9
transducer, 36–7
accelerometer used in active suspension, 51–2
active damping system using three single-axis low-g sensors, 52
angular rate sensor, 39–45
automotive Vehicle Stability Control applications, 29–53
sensor fusion, 46–7
combo sensors, 46
vehicle architecture challenges, 46–51
ESC integration and airbag sensors into airbag ECU, 48
ESC sensor cluster including inertial devices, 47–8
ESC sensor integrated into ESC ECU, 48
functional safety challenges, 50
future trends, 50–1
integration of all inertial sensors into Domain Controller ECU, 48–50
MEMS-switched true-time delay phase-shifter network, 114–15
MEMS transducer, 36–7
x-axis capacitive accelerometer, 36
metal-oxide gas sensors, 143
micro-electromechanical system (MEMS), 245–51
aerospace applications, 248, 250–1
top-level aerospace requirements met by MEMS technology, 250
aircraft structural health monitoring, 220–41
MEMS devices for embedded SHM, 228–40
promising developments, 240–1
state of the art application for aerospace structures, 223–8
typical aeronautical structure, 222
automotive tire pressure monitoring systems, 54–76
future TPMS applications, 74–5
market, 55
power management, 67–74
pressure sensors and technologies, 59–65
TPMS applications and solutions, 55–9
TPMS requirements, 65–7
concentration, density and fuel quality sensors, 95–7
automotive ethanol concentration sensor based on fuel's dielectric constant, 95
density plot for ethanol-gasoline at 25°C, 96
density ranges of various liquids and fluids, 96
defining the harsh environment, 247–8, 249
aero-propulsion ground test facilities, 249
schematic rendering of various parts of hypersonic aerospace vehicle, 247
thermal load profiles for typical hypersonic vehicle trajectory, 248
definition, 245–6
design process, 81–6
fabrication, 82–6
devices for active drag reduction in aerospace applications, 153–73
actuators, 166–72
future trends, 172–3
overview, 153–60
surface sensors, 160–6
enabling space exploration and exploitation, 311–29
future trends in spacecraft, 312–13
reliability concerns of space environment, 325–8
space science instrumentation, 320–5
spacecraft subsystems, 313–19
examples of MEMS devices, 246
fabrication, 82–6
four different structures, 84
process steps for polysilicon Wheatstone bridge on stainless steel, 85
steps for making silicon absolute piezo-resistive pressure sensor, 83
future trends
actuation, 278
energy harvesting, 279
instrumentation/sensing, 278
smart aerospace structures/structural health monitoring, 279
wireless MEM/smart adaptive algorithms/sensor fusion, 279
future trends in safety sensing systems, 23–5
environment monitoring systems, 25
passenger monitoring systems, 24
vehicle monitoring systems, 24–5

© Woodhead Publishing Limited, 2013

harsh environment sensors in aerospace applications, 245–79
examples, 251–77
MEMS inertial measurement, 273–7
MSSA MEMS IMU Sensor Chip, 275
packaging for harsh environments, 271–3
schematic depicting concurrent systems engineering practices, 253
systems engineering requirements overview, 252–4
systems engineering view of harsh environment sensors, 251–2
thermal management in aerospace applications, 267–71
inertial navigation systems for aircraft, 177–216
future trends, 216
global positioning system (GPS), 207–16
microfabrication, 189–207
overview, 177–89
market share of automotive MEMS in 2009, 4
MEMS thrusters for nano- and pico-satellites, 283–309
design considerations, 299–308
future trends, 308–9
MEMS thrusters, 298–9
miniaturising propulsion systems, 293–8
propulsion requirements, 285–7
propulsion technologies, 287–93
packaging sensors for harsh environments, 99–103
interior construction of stainless steel diaphragm pressure sensors, 102
plastic packaged silicon pressure sensor, 101
three pin connector on an automotive MAP sensor, 102
passenger safety in automotive vehicles, 3–26
accelerometers for crash sensing systems, 8–13
angular rate sensors for rollover detection systems, 13–19
passenger safety systems, 4–8
strain gauges for occupant sensing systems, 19–23
pressure and flow sensors for automotive engine management and aerospace application, 78–103
flow sensors, 89–94
looking forward, 103
pressure sensor, 86–9
sensors used in system/engine management, 78–81
pressure sensors and technologies, 59–65
bulk micromachining of sensor devices, 60–1
detection schemes capacitive/piezo-resistive, 62–4
motion detection, 64–5
summary, 65
surface micromachining of sensor devices, 61–2
regulations history, 54–5
short overview of TPMS regulations and standards, 55
sensor signal conditioning, 97–8
automotive MAP package showing ASIC and MEMS pressure sensor, 98
shear stress sensors, 254–67
background, 256–7
design, 257–8, 260–2
element packaging, 264
entire MEMS shear stress sensor system, 263
equations for perpendicular and parallel sensor designs, 262
fabrication, 262
fabrication of MEMS shear stress sensor with through-substrate interconnection, 263
model drawings and test hardware/fixture housing, 265
motivation/sensor application, 254–6
operating principle and configuration, 259
packaging, 262–4
relevant harsh environment, 257
response curve, 267
SEM showing some fingers bending down and improved design with minimal residual stress, 259
sensor theory of operation/design, 258–9
SiC film sensor element, 261
spring configuration, 260
testing, 264–7
voltage data, 266
micro-electromechanical systems (MEMS)
passenger comfort in vehicles, 137–46
auditory comfort, 145–6

© Woodhead Publishing Limited, 2013

climate control, 142–4
future trends, 146
overview, 137–40
seating adjustment, 140–2
visual comfort, 144–5
micro-machines, 245
micro-opto-electromechanical systems (MOEMS), 322
micro-pillar technique, 163
microfabrication, 189–207
MicroStrain Inc., 224
microsystems technology (MST), 245
MIL-STD-1553 multiplexing protocol, 80
moose test, 31
motion detection, 64–5
monolithic MEMS integration of pressure membrane and accelerometer, 64

NASA Goddard Space Flight Center (NASA/GSFC), 318
natural laminar flow control (NLFC), 156
navigation equation, 182–9, 185–8
operational inertial-, earth-, navigation- and body-frames, 186
navigation frame, 181–2
near infrared spectrograph (NIRSpec), 322
non-destructive evaluation technologies (NDTs), 221
nuclear magnetic resonance, 324–5

occupant sensing systems
background, 19
Delphi's Passive Occupant Detection System, 20
MEMS sensor implementation, 22–3
manufacturing processes comments, 22–3
system integration, 23
technical details of typical devices, 22
MEMS sensor operation principles, 19–22
strain gauges, 19–23
occupied bandwidth (OBW), 66
original equipment manufacturer (OEM), 57
oscillators, 14, 118, 120–1
mass oscillating within a housing and mass movement, 15
MEMS variable Faraday cage, 120
outgoing long wave radiation (OLR), 325

packaging, 38–9
stacked die configuration of digital XY accelerometer, 39
passenger comfort
auditory comfort, 145–6
climate control, 142–4
future trends, 146
micro-electromechanical systems (MEMS) in vehicles, 137–46
overview, 137–40
comfort feedback loop with sensor, decision-maker and actuator, 139
MEMS role, 139–40
scope, 137–8
seating adjustment, 140–2
visual comfort, 144–5
passenger safety, 4–8
crash event, 6
crash event classification, 6–8
forward longitudinal crash types, 7
vehicular translations, 7
MEMS in automotive vehicles, 3–26
accelerometers for crash sensing systems, 8–13
angular rate sensors for rollover detection systems, 13–19
future trends in safety sensing systems, 23–5
passenger safety systems, 4–8
strain gauges for occupant sensing systems, 19–23
protection system, 5
Passive Occupant Detection System, 19
passive sensing mode, 234
phase-shift keying (PSK), 108
phase shifters, 114–18
piezoelectric effect, 10
piezoresistive effect, 10–11
piezoresistive pressure sensors, 87–8
Pirani gauge, 91
Pitot tube, 90
plasma etching, 83
plasma spectrometers, 320
position rate equation, 188
power density spectrum (PDS), 73
power down, 70–1
power management, 67–74
battery lifetime model, 67–8
typical share of energy consumption over lifetime of TPMS module, 68
energy harvesting, 71–4
block diagram of 2.4Ghz demonstrator, 72

© Woodhead Publishing Limited, 2013

filtered measurement data of z-axis acceleration signal at inner liner, 73
schematic cross-section of an electrostatic vibration harvester, 74
size comparison of 2.4Ghz TPMS demonstrator PCB vs 1 Euro Cent coin, 71
vibration energy harvester mounted on test PCB with load resistor, 74
LF receiver and protocol, 69–70
typical datagram format of current TPMS module, 69
power down, 70–1
active and inactive parts of TPM sensor, 70
RF transmission and protocol, 68–9
typical datagram of current TPMS module, 69
power spectral density (PSD), 202–4
predicted mean vote (PMV), 139
pressure sensor, 86–9
capacitive, 88–9
fibre optic, 89
MEMS flow sensors for automotive engine management and aerospace application, 78–103
concentration, density and fuel quality sensors, 95–7
design process, 81–6
flow sensors, 89–94
looking forward, 103
packaging MEMS sensors for harsh environments, 99–103
sensor signal conditioning, 97–8
sensors used in system/engine management, 78–81
piezoresistive, 87–8
requirements, 65–6
TPMS MEMs sensor pressure measurement over temperature, 66
printed circuit board, 38, 97
propulsion technologies, 287–93
chemical propulsion, 288–90
cold gas thrusters, 288
illustration, 289
liquid bipropellants, 289–90
liquid monopropellants, 288–9
solid propellants, 290
electric propulsion, 290–3
arcjets, 290–1
electromagnetic engines, 291
electrospray thrusters, 292–3
gridded ion engines, 291
hall thrusters, 291–2
illustration, 292
resistojets, 290
Protection technologies, 4–5
pulse-Doppler radar, 109
pulsed massless jet, 168–9
axisymmetric model with sting projection, 169
drag coefficient map for axial harmonic forcing, 169

quaternion, 184–5

radio-frequency micro-electromechanical systems (RF MEMS)
automotive radar sensors, 106–34
components, 110–21
oscillators, 118, 120–1
phase shifters, 114–18
switches and tunable capacitors, 110–14
front-end technology, 121–6
38-GHz car-radar front-end, 121–3
77-GHz car-radar front-end, 123–6
overview, 106–10
car radar sensors requirements, 110
LRR and SRR combination, 107
sensor types and architecture, 107–9
radar beam steering technology, 126–33
mechanically driven antenna platform, 129–32
MEMS reconfigurable Vee-antennas, 133
MEMS steerable leaky-wave antennas, 128–9
MEMS tuneable reflective microwave surface, 126–8
rapid distortion theory (RDT), 158
reconfigurable Vee-antennas
E-plane beam-steering pattern, 134
micro-mechanical concept, 133
reflective electronic display, 145
Rescue technologies, 5
residual useful life (RUL), 221, 227
resistojets, 290
resonant structure types, 21–2
schematic diagram, 21
Response technologies, 4
ride discomfort index (RDI), 139
rideshares, 313
Robert Borsch 77-GHz automotive-radar front-end, 123–6
77-GHz MEMS automotive radar radiation characteristics, 125

© Woodhead Publishing Limited, 2013

77-GHz MEMS automotive radar realised by RFMEMSSP4T switch and Rotman lens, 125
two 77-GHz RF MEMS, 124
rocket equation, 286
rolamite sensor, 9
roll over protection, 6
rollover detection systems
angular rate sensors, 13–19
background, 13–14
MEMS sensor operation principles, 14–17
MEMS sensor implementation, 17–19
example, 18
manufacturing processes comments, 18
system integration, 18–19
technical details, 17–18

Sandia National Laboratories, 319
satellites, nano- and pico-
design considerations of MEMS thrusters, 299–308
chemical (gas/liquid propellants) MEMS propulsion, 299–302
chemical (solid propellants) MEMS propulsion, 302
electrospray thrusters, 303–8
MEMS electric discharge thrusters, 303
resistojet MEMS propulsion, 303
future trends, 308–9
MEMS thrusters, 283–309, 298–9
miniaturising propulsion systems, 293–8
chemical thrusters scaling, 293–5
electric gas phase ionisation, 295–6
electrothermal thrusters scaling, 295
liquid phase ionisation thrusters scaling, 297–8
propulsion requirements, 285–7
propulsion technologies, 287–93
chemical propulsion, 288–90
electric propulsion, 290–3
relative sizes of Sputnik, 284
scale factor, 205
Schuler tuning, 207
sculling error, 207
seating adjustment, 140–2
sensor array with thin-film electrodes, 141
sensing techniques, 16–17
sensor fusion, 46–7
separation control, 159
serial peripheral interface (SPI), 38
short-range radar (SRR), 107–8, 110
application, 108
signal-to-noise ration (SNR), 63
skin friction sensors, 161–4
heat loss from a wall- mounted thermal sensor, 161
single micro pillar and pillar array, 163
SMART layer, 234–5
SMART Suitcase, 235
smart windows, 144
solid propellants, 290
space application, 311–29
future trends in spacecraft, 312–13
definitions of very small spacecraft and respective examples, 313
MEMS in space science instrumentation, 320–5
electromagnetic field and particle detection for space science, 320–2
MEMS sensors for planetary missions, 324–5
miniature rubidium vapour cell, 322
near-infrared spectrograph (NIRSpec) Microshutters, 323
telescopes and spectrometers, 322–4
MEMS in spacecraft subsystems, 313–19
communication systems, 317
guidance, navigation and control (GNC), 313–16
MEMS–based gyros, 316
ST5 MEMS radiator, 319
thermal control, 317–19
xylophone style magnetometer, 314
reliability concerns of space environment, 325–8
chemical effects, 327
mechanical effects of shock, acceleration and vibration, 326–7
particulates, 328
radiation effects, 327–8
thermal effects, 325–6
space science instrumentation, 320–5
electromagnetic field and particle detection for space science, 320–2
MEMS sensors for planetary missions, 324–5
miniature rubidium vapour cell, 322
near-infrared spectrograph (NIRSpec) Microshutters, 323
telescopes and spectrometers, 322–4
spacecraft subsystems, 313–19
communication systems, 317

© Woodhead Publishing Limited, 2013

guidance, navigation and control (GNC), 313–16
MEMS–based gyros, 316
ST5 MEMS radiator, 319
thermal control, 317–19
xylophone style magnetometer, 314
split Langmuir probe, 321
StabiliTrak system, 31
steering wheel angle sensor, 34
stirling cooling, 319
Strain field-based SHM, 236–40
FBG sensor application for SHM, 236–40
fiber Bragg grating system working principle, 237
output for diagnostic algorithm developed for full damage characterisation, 239
strain gauges, 19–23
strapdown error equations, 188–9
strapdown system technology
inertial navigation system, 180
structural health monitoring (SHM), 220–41
MEMS devices for embedded SHM, 228–40
Eddy current based sensor, 231–2
multilayer concept for Wireless Sensor Network node, 229
Strain field-based SHM, 236–40
surface acoustic wave (SAW) sensor, 233–6
promising developments, 240–1
state of the art application for aerospace structures, 223–8
finite element model of helicopter rear fuselage, 226
from manual recording to SHM, 223–5
helicopter fuselage crack monitoring (HECTOR case study), 227–8
introduction to statistics, 226–7
model based SHM, 225–6
Probability of detection evaluated for anomaly detection algorithm, 228
typical aeronautical structure, 222
Structural Integrity Recording System (SIRS), 223–4
surface acoustic wave (SAW) sensor, 233–6
scheme for wireless IDT-based damage detection system, 233
smart SAW based sensor network, 234–6
ultrasonic wave paths over rectangular metallic panel and damage localisation, 235
surface-fence concept, 162
surface micromachining (SMM), 60, 61–2
schematic cross-section of BICMOS-based SMM pressure sensor with package, 62
surface pressure transducers, 164–6
capacitance transducer function and design, 165
silicon Nitride pressure sensor, 164
switch, 110–14
in- line DC-contact MEMS series, 112
RF MEMS comparison, 113
two most commonly used electrostatically actuated type, 111
switched capacitor banks, 112
Systron Donner, 16–17

tangential aerodynamic force, 258
Taylor cones, 297
thermal anemometers *see* hot wire flow sensors
thermal design, 99
thin film hot thin film flow sensors, 92
time triggered protocol (TTP), 80
tire pressure monitoring system (TPMS), 229
total ionising dose (TID), 328
touch-down mode, 165–6
transport rate, 187
Transportation Recall Enhancement, Accountability and Documentation (TREAD Act), 54
tunable capacitors, 110–14
tunable dielectric-block loaded-line phase-shifter, 116–18
binary-coded 4.25-bit W-band monocrystalline-silicon, 117
W-band RF MEMS phase shifters comparison, 119
tuneable reflective microwave surface, 126–8
MEMS-based HIS with induced tunable gradient, 127
periodic high-impedance metamaterial surface, 126
phase shifter based on a dielectric rod waveguide (DRW), 128
tuning fork gyroscopes, 43–5
configuration when angular velocity along vertical axis, 43

© Woodhead Publishing Limited, 2013

principle operation, 44
SEM image, 44
turbulence, 157
turbulent boundary layer, 154

ultra-wide band (UWB) sensor, 107–8

vehicle area network (VAN), 80
vehicle stability control, 30–5
applications in MEMS sensors, 29–53
accelerometer in ESC, 35–9
accelerometers used in active suspension, 51–2
angular rate sensor, 39–45
vehicle architecture challenges and sensor fusion, 46–51
ESC system description, 31–4
main ESC components, 33
market trends, legislation and mandates, 34–5
overview, 29–30
short history, 30–1
sensotronic brake control system of Mercedes-Benz 211 series E-Class sedan, 32
vertical-cavity surface-emitting laser (VCSEL), 321
vibrating-wheel gyroscopes, 43
vibratory gyroscope, 42, 196–201
3-D model of the mode-decoupled gyroscope structure, 198
combination of a 1-DoF drive-mode resonator and a 1-DoF sense- mode resonator, 196
degenerate, anti-phase *x* – and *y*-vibratory modes, 200
quadrature cancellation electrodes, 199
whole-angle mode, 200
virtual sensor, 81
visual comfort, 144–5
electrochromic behaviour, 145

wheel speed sensor, 34
wireless sensor networks (WSN), 229

xylophone magnetometer, 314

yaw rate sensor, 34

zero-net-mass-flux jet, 167

© Woodhead Publishing Limited, 2013